

# **From Nuclei to Compact Stars**



# Contents

<b>1. Participants</b>	<b>1659</b>
1.1. ICRA <span>Net</span> participants . . . . .	1659
1.2. On going collaborations . . . . .	1659
1.3. Graduate Students . . . . .	1660
<b>2. Brief Description of the Research Activities</b>	<b>1661</b>
2.1. Nuclear and Atomic Astrophysics . . . . .	1661
2.2. White Dwarf Physics and Astrophysics . . . . .	1666
2.3. Neutron Star Physics and Astrophysics . . . . .	1669
2.4. Neutron Star Physics with Gamma Ray Bursts . . . . .	1674
2.5. Emission-Radiation Mechanisms of White Dwarfs and Neutron Stars . . . . .	1676
2.6. Exact Solutions of the Einstein-Maxwell equations in Astrophysics . . . . .	1677
2.7. Critical fields and Non Linear Electrodynamics Effects in Neutron Stars and Black Holes . . . . .	1678
<b>3. Publications 2013</b>	<b>1679</b>
3.1. Refereed Journals . . . . .	1679
3.1.1. Printed . . . . .	1679
3.1.2. Accepted for publication (in press) . . . . .	1679
3.1.3. Submitted . . . . .	1679
3.1.4. In preparation . . . . .	1680
<b>4. Publications (before 2013)</b>	<b>1681</b>
4.1. Refereed Journals . . . . .	1681
4.2. Conference Proceedings . . . . .	1682
<b>5. APPENDICES</b>	<b>1687</b>
<b>A. Nuclear and Atomic Astrophysics</b>	<b>1689</b>
A.1. On gravitationally and electro-dynamically bound massive nuclear density cores . . . . .	1689
A.1.1. Introduction . . . . .	1689
A.1.2. The relativistic Thomas-Fermi equation and the beta equilibrium condition . . . . .	1691
A.1.3. The ultra-relativistic analytic solutions . . . . .	1693

A.1.4.	New results derived from the analytic solutions . . . . .	1696
A.1.5.	Estimates of gravitational effects in a Newtonian approximation . . . . .	1697
A.1.6.	Possible applications to neutron stars . . . . .	1698
A.1.7.	Conclusions . . . . .	1699
A.2.	On the relativistic Thomas-Fermi treatment of compressed atoms and compressed nuclear matter cores of stellar dimensions . .	1701
A.2.1.	Introduction . . . . .	1701
A.2.2.	The Thomas-Fermi model for compressed atoms: the Feynman-Metropolis-Teller treatment . . . . .	1703
A.2.3.	The relativistic generalization of the Feynman-Metropolis-Teller treatment . . . . .	1707
A.2.4.	Comparison and contrast with approximate treatments	1712
A.2.5.	Application to nuclear matter cores of stellar dimensions	1720
A.2.6.	Compressional energy of nuclear matter cores of stellar dimensions . . . . .	1728
A.2.7.	Conclusions . . . . .	1730
A.3.	The relativistic Feynman-Metropolis-Teller equation of state at finite temperatures . . . . .	1734
A.3.1.	Introduction . . . . .	1734
A.3.2.	The relativistic FMT treatment . . . . .	1735
A.3.3.	Numerical integration of the equations and the EOS . .	1739
A.3.4.	Application to nuclear matter cores of stellar dimensions	1746
A.3.5.	Conclusions . . . . .	1751
A.4.	On Magnetic Fields in Rotating Nuclear Matter Cores of Stellar Dimensions . . . . .	1753
A.4.1.	Introduction . . . . .	1753
A.4.2.	The Relativistic Thomas-Fermi equation . . . . .	1754
A.4.3.	The ultra-relativistic analytic solutions . . . . .	1756
A.4.4.	Rotating Nuclear Matter Cores of Stellar Dimensions in Classical Electrodynamics . . . . .	1756
A.4.5.	Conclusions . . . . .	1759
<b>B.</b>	<b>White Dwarfs Physics and Astrophysics</b>	<b>1761</b>
B.1.	The relativistic Feynman-Metropolis-Teller theory for white dwarfs in general relativity . . . . .	1761
B.1.1.	Introduction . . . . .	1761
B.1.2.	The Equation of State . . . . .	1765
B.1.3.	General relativistic equations of equilibrium . . . . .	1778
B.1.4.	Mass and radius of general relativistic stable white dwarfs	1782
B.1.5.	Conclusions . . . . .	1789
B.2.	On general relativistic uniformly rotating white dwarfs . . . . .	1791
B.2.1.	Introduction . . . . .	1791
B.2.2.	Spacetime geometry and Hartle's formalism . . . . .	1793

B.2.3.	Limits on the stability of rotating white dwarfs . . . . .	1793
B.2.4.	WD structure and stability boundaries . . . . .	1798
B.2.5.	The maximum mass . . . . .	1801
B.2.6.	The minimum rotation period . . . . .	1802
B.2.7.	Occurrence of secular axisymmetric instability . . . . .	1804
B.2.8.	Spin-up and spin-down evolution . . . . .	1807
B.2.9.	Astrophysical implications . . . . .	1808
B.2.10.	Concluding remarks . . . . .	1810
B.2.11.	Supplementary information . . . . .	1811
B.3.	SGRs and AXPs as rotation powered massive white dwarfs . .	1821
B.3.1.	Introduction . . . . .	1821
B.3.2.	SGRs and AXPs within the white dwarf model . . . . .	1822
B.3.3.	SGRs and AXPs within the magnetar model . . . . .	1826
B.3.4.	Observations of massive fast rotating highly magnetized white dwarfs . . . . .	1831
B.3.5.	Rotational instability of white dwarfs . . . . .	1832
B.3.6.	Glitches and outbursts in SGRs and AXPs . . . . .	1834
B.3.7.	Magnetosphere emission from white dwarfs . . . . .	1835
B.3.8.	The connection with supernova remnants . . . . .	1838
B.3.9.	On the fiducial neutron star and white dwarf parame- ters in light of recent theoretical progress . . . . .	1840
B.3.10.	Conclusions and remarks . . . . .	1841
B.4.	SGR 0418+5729 and Swift J1822.3-1606 as massive fast rotating highly magnetized white dwarfs . . . . .	1844
B.4.1.	Introduction . . . . .	1844
B.4.2.	Rotation powered white dwarfs . . . . .	1846
B.4.3.	Structure and stability of rotating white dwarfs . . . . .	1847
B.4.4.	SGR 0418+5729 . . . . .	1848
B.4.5.	Swift J1822.3-1606 . . . . .	1854
B.4.6.	1E 2259+586 . . . . .	1857
B.4.7.	Concluding Remarks . . . . .	1861
B.5.	A white dwarf merger as progenitor of the AXP 4U 0142+61? .	1864
B.5.1.	A model for 4U 0142+61 . . . . .	1865
B.5.2.	Conclusions . . . . .	1871
B.6.	Finite temperature effects on the mass-radius relation of white dwarfs . . . . .	1872
B.6.1.	The ultra low-mass white dwarf companion of PSR J1738+03331874	
B.6.2.	Discussion . . . . .	1876
B.7.	Dynamical instability of white dwarfs and breaking of spheri- cal symmetry under the presence of extreme magnetic fields .	1878
B.7.1.	Introduction . . . . .	1878
B.7.2.	Ultramagnetized white dwarfs . . . . .	1879
B.7.3.	Equation of state and virial theorem violation . . . . .	1881

B.7.4.	Breaking of spherical symmetry and quadrupole instability . . . . .	1884
B.7.5.	Microscopic instabilities . . . . .	1885
B.7.6.	General relativistic effects . . . . .	1887
B.7.7.	Evolutionary path . . . . .	1889
B.7.8.	Conclusions . . . . .	1889
<b>C.</b>	<b>Neutron Stars Physics and Astrophysics</b>	<b>1891</b>
C.1.	Self-gravitating system of degenerate neutrons, protons and electrons in beta equilibrium . . . . .	1891
C.1.1.	Introduction . . . . .	1891
C.1.2.	The impossibility of a solution with local charge neutrality . . . . .	1893
C.1.3.	The solution with global charge neutrality . . . . .	1895
C.1.4.	Numerical integration of the equilibrium equations . . . . .	1896
C.1.5.	Conclusions . . . . .	1899
C.2.	The Klein first integrals in an equilibrium system with electromagnetic, weak, strong and gravitational interactions . . . . .	1900
C.2.1.	Introduction . . . . .	1900
C.2.2.	The Constitutive General Relativistic Equations . . . . .	1901
C.2.3.	The Thermodynamic Laws and the Field Equations in the Spherically Symmetric Case . . . . .	1904
C.2.4.	Constancy of the Klein potentials and beta equilibrium . . . . .	1907
C.2.5.	Concluding Remarks . . . . .	1909
C.3.	The constitutive equations of a self-gravitating system of neutrons, protons and electrons . . . . .	1911
C.3.1.	Introduction . . . . .	1911
C.3.2.	Einstein-Maxwell-Thomas-Fermi equations in the degenerate case . . . . .	1912
C.3.3.	Newtonian limit . . . . .	1916
C.3.4.	Introducing strong interactions . . . . .	1917
C.3.5.	Finite temperature effects . . . . .	1920
C.3.6.	Concluding Remarks . . . . .	1925
C.4.	Neutron stars fulfilling all fundamental interactions . . . . .	1929
C.4.1.	Introduction . . . . .	1929
C.4.2.	The Constitutive Relativistic Equations . . . . .	1930
C.4.3.	Neutron star structure . . . . .	1941
C.4.4.	Observational constraints on the mass-radius relation . . . . .	1948
C.4.5.	Comparison with the traditional TOV treatment . . . . .	1948
C.4.6.	Concluding Remarks . . . . .	1952
C.5.	Uniformly rotating neutron stars . . . . .	1954
C.5.1.	Introduction . . . . .	1954
C.5.2.	Hartle's slow rotation approximation . . . . .	1958
C.5.3.	Stability of uniformly rotating neutron stars . . . . .	1960

---

C.5.4.	Structure of uniformly rotating neutron stars . . . . .	1963
C.5.5.	Neutron star mass-radius relation . . . . .	1968
C.5.6.	Deformation of the neutron star . . . . .	1970
C.5.7.	Core and crust moment of inertia . . . . .	1976
C.5.8.	Observational constraints . . . . .	1976
C.5.9.	Concluding remarks . . . . .	1979
C.5.10.	Supplementary material . . . . .	1982
C.6.	On the surface tension of neutron star matter . . . . .	1985
C.6.1.	Introduction . . . . .	1985
C.6.2.	Surface properties for neutron star matter without grav- itational interaction . . . . .	1988
C.6.3.	Surface properties for neutron star matter with gravita- tional interaction . . . . .	2003
C.6.4.	Surface tension for the system with small electron density	2009
C.6.5.	Summary . . . . .	2014
C.7.	On the cooling of globally neutral neutron stars . . . . .	2017
C.7.1.	Thermal evolution equations . . . . .	2018
C.7.2.	General relativistic isothermality . . . . .	2019
C.7.3.	Occurrence of the direct Urca process . . . . .	2019
C.7.4.	Cooling curves . . . . .	2019
C.7.5.	Conclusions . . . . .	2021
C.8.	Thermal evolution of neutron stars: global and local charge neutrality cases . . . . .	2023
C.8.1.	Thermal evolution equations . . . . .	2025
C.8.2.	Cooling curves and relaxation time . . . . .	2025
C.9.	Realistic versus fiducial parameters of rotating neutron stars .	2029
C.9.1.	Neutron star's quantities . . . . .	2032
C.9.2.	Accuracy of approximate analytic formulas for the Ke- plerian sequence . . . . .	2034
C.9.3.	Accuracy of approximate analytic formulas for the mo- ment of inertia . . . . .	2037
C.9.4.	Implications on the magnetic-dipole model of pulsars .	2039
C.9.5.	Conclusions . . . . .	2044
<b>D.</b>	<b>Neutron Stars Physics with Gamma-Ray Bursts</b>	<b>2045</b>
D.1.	Cooling of young neutron stars in GRBs associated to Super- novae . . . . .	2045
D.1.1.	Introduction . . . . .	2045
D.1.2.	Cooling of Young, Hot Neutron Stars . . . . .	2046
D.1.3.	Late X-Ray Emission in GRBs associated to Supernovae: URCAs . . . . .	2049
D.1.4.	Neo-Neutron Star Luminosity and the URCAs . . . . .	2050
D.1.5.	Discussion and Conclusions . . . . .	2054

---

D.2. Gravitational Waves versus Electromagnetic Emission in Gamma-Ray Bursts . . . . .	2055
D.2.1. Global versus local charge neutrality . . . . .	2055
D.2.2. GRB 090227B . . . . .	2057
D.2.3. Inference of neutron star binary parameters . . . . .	2058
D.2.4. Gravitational wave emission . . . . .	2061
D.2.5. Conclusions . . . . .	2067
<b>E. Exact Solutions of the Einstein-Maxwell equations in Astrophysics</b>	<b>2069</b>
E.1. On the relativistic precession and oscillation frequencies of test particles around rapidly rotating compact stars . . . . .	2069
E.1.1. Introduction . . . . .	2069
E.1.3. Orbital Motion Frequencies on the Equatorial Plane . . . . .	2073
E.1.4. Accuracy of Ryan's Analytic Formulas . . . . .	2084
E.1.5. Accuracy of PRS solution . . . . .	2087
E.1.6. The Relativistic Precision Model . . . . .	2088
E.1.7. Concluding Remarks . . . . .	2091
E.1.8. Supplementary information . . . . .	2094
<b>F. Critical Fields and Non-linear Electrodynamics Effects in Astrophysics</b>	<b>2099</b>
F.1. On the black hole mass-formula in nonlinear electrodynamics . . . . .	2099
F.1.1. Introduction . . . . .	2099
F.1.2. Field Equations . . . . .	2101
F.1.3. Reversible and Irreversible transformations . . . . .	2102
F.1.4. Weak Field Lagrangians . . . . .	2103
F.1.5. The Black Hole Mass Formula . . . . .	2107
F.1.6. Transformations in the outer horizon . . . . .	2109
F.1.7. Energy decomposition for any nonlinear theory . . . . .	2110
F.1.8. Discussion . . . . .	2112
<b>Bibliography</b>	<b>2115</b>

# 1. Participants

## 1.1. ICRA Net participants

- D. Arnett (Steward Observatory, University of Arizona, USA)
- D. Bini (Istituto Nazionale per l'Applicazione del Calcolo, Italy)
- H. Kleinert (Free University of Berlin , Germany)
- V. Popov (ITEP, Moscow, Russia)
- Jorge A. Rueda (ICRA Net, University of Rome, Italy)
- R. Ruffini (ICRA Net, University of Rome, Italy)
- S.-S. Xue (ICRA Net, University of Rome, Italy)

## 1.2. On going collaborations

- K. Boshkayev (University of Almaty, Kazakhstan)
- E. Gacía-Berro (Universitat Politècnica de Catalunya, Spain)
- P. LorénAguilar (University of Exeter, United Kingdom)
- B. Külebi (Institut de Ciències de l'Espai, Spain)
- M. Malheiro (Instituto Tecnológico de Aeronáutica, Brazil)
- H. Mosquera (Universidade Estadual Vale do Acaraú, Brazil)
- R. Negreiros (Universidade Federal de Fluminense, Brazil)
- L. Pachón (Universidad de Antioquia, Colombia)
- D. Pugliese (Queen Mary University of London, United Kingdom)
- H. Quevedo (Universidad Nacional Autónoma de México, Mexico)
- C. Valenzuela (Universidad del Valle, Colombia)

### **1.3. Graduate Students**

- R. Belvedere (ICRANet, University of Rome, Italy)
- D. Cáceres (ICRANet, University of Rome, Italy)
- F. Gomes de Oliveira (ICRANet, University of Rome, Italy and Université de Nice Sophia-Antipolis, France)
- S. Martins de Carvalho (ICRANet, University of Rome, Italy and Université de Nice Sophia-Antipolis, France)
- J. Pereira (ICRANet, University of Rome, Italy and Université de Nice Sophia-Antipolis, France)
- Y. Wu (ICRANet, University of Rome, Italy and Université de Nice Sophia-Antipolis, France)

## 2. Brief Description of the Research Activities

The study of compact objects such as white dwarfs, neutron stars and black holes requires the interplay between nuclear and atomic physics together with relativistic field theories e.g. general relativity, quantum electrodynamics, quantum chromodynamics, as well as particle physics. In addition to the physical aspects, the study of astrophysical scenarios characterized by the presence of a compact object has also started to be focus of extensive research within our group. The research which has been done and is currently being developed within our group can be divided into the following topics:

1. Nuclear and Atomic Astrophysics
2. White Dwarfs Physics and Astrophysics
3. Neutron Stars Physics and Astrophysics
4. Emission-Radiation Mechanisms of White Dwarfs and Neutron Stars
5. Neutron Star Physics and Astrophysics with Gamma Ray Bursts
6. Exact Solutions of the Einstein and Einstein-Maxwell equations in Astrophysics
7. Critical Fields and Non-linear Electrodynamics Effects in Astrophysics

### 2.1. Nuclear and Atomic Astrophysics

Within this subject of research we study the properties and processes occurring in compact stars such as white dwarfs and neutron stars in which nuclear and atomic physics have to be necessarily applied. We focus on the properties of nuclear matter under extreme conditions of density and pressure found in these objects. The equation of state of the matter in compact star interiors is studied in detail taking into account all the interactions between the constituents within a full relativistic framework.

The aim is to have a unified approach for nuclei, superheavy nuclei up to atomic numbers of the order of  $10^5$ – $10^6$ , and what we have denominated “nuclear matter cores of stellar dimensions”:

- characterized by atomic number of the order of  $10^{57}$ ;
- composed by a degenerate fluid of neutrons, protons and electrons in  $\beta$ -equilibrium;
- globally neutral configurations;
- expected to be kept at nuclear density by self gravity.

The study of all these objects going from the microscopic to the macroscopic is at the base of the theory of white dwarfs, neutron stars, hyperon stars, strange quark stars, and other related compact objects.

It is known that the Thomas-Fermi model has been extensively applied in atomic physics, also has been applied extensively in atomic physics in its relativistic form as well as in the study of atoms with heavy nuclei (see Gombás, 1949, for instance). Similarly there have been considerations of relativistic Thomas-Fermi model for quark stars pointing out the existence of critical electric fields on their surfaces (Alcock et al., 1986). Similar results have also been obtained in the transition at very high densities, from the normal nuclear matter phase in the core to the color-flavor-locked phase of quark matter in the inner core of hybrid stars (Alford et al., 2001). However, no example exists to the application of the electromagnetic Thomas-Fermi model to white dwarfs and neutron stars.

The analysis of superheavy nuclei has historically represented a major field of research, developed by Prof. V. Popov and Prof. W. Greiner and their schools. This same problem was studied in the context of the relativistic Thomas-Fermi equation also by R. Ruffini and L. Stella, already in the '80s. The recent approach was started with the Ph.D. Thesis of M. Rotondo and has shown the possibility to extrapolate this treatment of superheavy nuclei to the case of nuclear matter cores of stellar dimensions (see appendix A.1). The very unexpected result has been that also around these massive cores there is the distinct possibility of having an electromagnetic field close to the critical value

$$E_c = \frac{m_e^2 c^3}{e \hbar} \approx 1.3 \times 10^{16} \text{ Volt cm}^{-1},$$

localized in a very narrow shell of the order of the electron Compton wavelength (see Fig. 2.1).

The welcome result was that all the analytic work developed by Prof. V. Popov and the Russian school can be applied using scaling laws satisfied by the relativistic Thomas-Fermi equation to the case of nuclear matter cores of stellar dimensions, if the  $\beta$ -equilibrium condition is properly taken into account. This has been the result obtained and published by Ruffini, Rotondo and Xue already in 2007. Since then, a large variety of problems has emerged, which have seen the direct participation of ICRA<sub>Net</sub> Professors, graduate students,

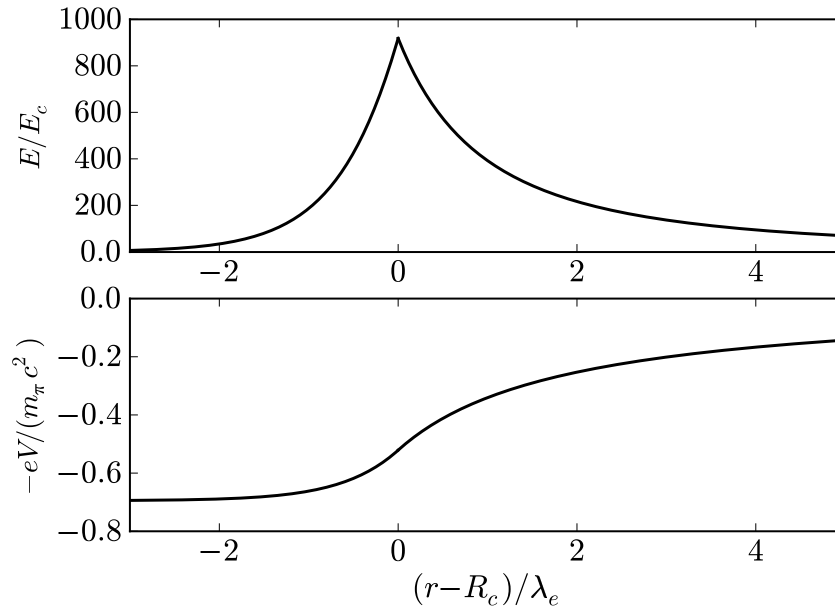


**Figure 2.1.:** Upper panel: electric field around the surface of a nuclear matter core of stellar dimensions in units of the critical field  $E_c$ . Lower panel: electron Coulomb potential  $-eV$ . Here  $R_c$  denotes the core radius and  $\lambda_e = \hbar/(m_e c)$  is the electron Compton wavelength.

postdocs, as well as collaborators worldwide including Prof. V. W. Greiner, Prof. Popov, Prof. D. Arnett and the Nobel Prize Awarded, Prof. G. 't Hooft.

One of the crucial issues to be debated is the stability of such cores under the competing effects of self-gravity and Coulomb repulsion. It has been demonstrated their stability against nuclear fission, as opposed to the case of heavy nuclei; see appendix A.1. In particular, on the basis of Newtonian gravitational energy considerations it has been found the existence of a possible new island of stability for mass numbers

$$A > A_R = 0.039 \left( \frac{N_p}{A} \right)^{1/2} \left( \frac{m_{\text{Planck}}}{m_n} \right)^3,$$

where  $N_p$  is the number of protons,  $A$  is the total number of baryons,  $m_n$  is the neutron mass and  $m_{\text{Planck}} = \sqrt{\hbar c/G}$  is the Planck mass.

The equilibrium against Coulomb repulsion originates now from the combined effect of the screening of the relativistic electrons, of the surface tension due to strong interactions, and of the gravitational interaction of these massive cores. By enforcing the condition of  $\beta$ -equilibrium, it has been also obtained a generalization to the relation between the mass number  $A$  and atomic number  $N_p$  which encompasses phenomenological expressions (see appendix A.1 for details).

All these considerations have been made for an isolated core with constant proton density whose boundary has been sharply defined by a step function. No external forces are exerted. Consequently, the Fermi energy of the electrons has been assumed to be equal to zero.

Different aspects concerning these macroscopic systems have been also considered. For instance, the analysis of the electron distribution around such cores in both the case of global charge neutrality and the case of not global charge neutrality has been presented by R. Ruffini, M. Rotonondo and S.-S. Xue in *Neutral nuclear core versus super charged one*, Proc. 11th Marcel Grossmann Meeting, 2008.

The assumption of a sharp proton density profile has been relaxed and, consequently, a smooth surface modeled by a Woods-Saxon-like proton distribution has been introduced in *The Extended Nuclear Matter Model with Smooth Transition Surface* by Jorge A. Rueda H., B. Patricelli, M. Rotonondo, R. Ruffini, S.-S. Xue, , Proc. 3rd Stueckelberg Workshop on Relativistic Field Theories, 2008. The presence of overcritical electric fields close to their surface has been confirmed also in this more general case.

The existence of the scaling laws of the ultrarelativistic Thomas-Fermi equation (see appendix A.1) has led to the very exciting possibility of having macroscopic configurations of nuclear matter in  $\beta$ -equilibrium exhibiting strong electric fields on their surfaces. In order to go one step further towards a more realistic description of macroscopic configurations as white dwarfs and neutron stars, further improvements and extensions must be applied to the starting model.

It is therefore interesting, in order to approach both the complex problem of a neutron star core and its interface with the neutron star crust and the problem of the equilibrium of gas in a white dwarf taking into account all possible global electromagnetic interactions between the nucleus and the relativistic electrons, to extend the model to the compressed case in which the Fermi energy of electrons turns to be positive.

The analysis of globally neutral and compressed configurations composed by a nucleus made of relativistic degenerate neutrons and protons surrounded by relativistic degenerate electrons in  $\beta$ -equilibrium has been recently accomplished. This work generalized the Feynman-Metropolis-Teller treatment of compressed atoms to relativistic regimes, and the concept of compressed nuclear matter cores of stellar dimensions was introduced (see appendix A.2 for details).

In the relativistic generalization of the Feynman-Metropolis-Teller approach, the equation to be integrated is the relativistic Thomas-Fermi equation. The integration of this equation does not admit any regular solution for a point-like nucleus and both the nuclear radius and the nuclear composition have necessarily to be taken into account. This introduces a fundamental difference from the non-relativistic Thomas-Fermi model where a point-like nucleus was adopted.

Due to the introduction of the concept of Wigner-Seitz cells, the study of degenerate compressed matter in white dwarfs can be addressed. This problem presents, still today, open issues of great interest such as the equilibrium of the electron gas and the associated nuclear component, taking into account the electromagnetic, the gravitational and the weak interactions formulated in a correct special and general relativistic framework.

A complete analysis of the properties of such configurations as a function of the compression can be duly done through the relativistic generalization of the Feynman-Metropolis-Teller approach (see appendix A.2 for details).

It has been then possible to derive a consistent equation of state for compressed matter which generalizes both the uniform free-electron fluid approximation, adopted for instance by Chandrasekhar (1931b) in his famous treatment of white dwarfs, and the well-known work of Salpeter (1961a) which describes the electrodynamic and relativistic effects by a sequence of approximations. Apart from taking into account all possible electromagnetic and special relativistic corrections to the equation of state of white dwarf matter, the new equation of state that incorporates the  $\beta$ -equilibrium condition, leads to a self-consistent calculation of the onset for inverse  $\beta$ -decay as function of the Fermi energy of electrons or the density of the system. This is very important for the analysis of the stability of white dwarfs against gravitational collapse (see below and appendix B.1).

The extension of the above works to the case of finite temperatures is part of the doctoral work of S. Martins de Carvalho. The generalization of the relativistic Feynman-Metropolis-Teller treatment to the case  $T \neq 0$  has been already accomplished, see appendix A.3. The inclusion of finite temperature effects is becoming of primary importance in view of the recent discoveries of ultra-low mass white dwarfs with masses  $\lesssim 0.2M_{\odot}$  (Antoniadis et al. 2012,2013), which are companion of neutron stars in relativistic binaries. These low-mass white dwarfs represent the perfect arena for testing the equation of state of compressed matter since the central densities of these objects are expected to be  $\lesssim 10^6 \text{ g cm}^{-3}$ , where the degenerate approximation breaks down and so thermal effects cannot be neglected.

A related topic of current interest concerns the case of rotating nuclear matter cores of stellar dimensions. The induced magnetic field by electric field rotation has been recently obtained (see appendix A.4). Such analysis has been done in the framework of classical electrodynamics under the assumption of uniform rigid rotation of the macroscopic nuclear cores in the non-compressed case. For rotation periods of the order of  $\sim 10 \text{ ms}$ , overcritical magnetic fields has been obtained near the surface of the configuration.

In neutron star cores, nuclear matter is under very extreme conditions of density and pressure. The importance of the strong interactions between nucleons at such extreme pressures it has been known for years (see e.g. Cameron, 1970; Shapiro and Teukolsky, 1983a). However, due to the absence of a complete theory of the strong interactions, and due to the impossibility

of performing terrestrial experiments with similar extreme pressure-density conditions, the equation of state of nuclear matter at densities larger than the nuclear saturation density  $\sim 2.7 \times 10^{14}$  g/cm<sup>3</sup>, is still today unknown. The construction of nuclear equations of state combined with a fully consistent formulation of the equations of equilibrium in general relativity both for white dwarfs and neutron stars is an active topic of research within our group. In the recent past, some graduate theses of our group were devoted to this topic, for instance the works of M. Rotondo and Jorge A. Rueda, which were soon followed by the ones of D. Pugliese, R. Belvedere, K. Boshkayev. Currently, S. Martins de Carvalho and Y. Wu are developing their graduate theses following these guidelines.

### 2.2. White Dwarf Physics and Astrophysics

A branch of research which is currently under continuous evolution corresponds to the extension to the case of general relativity, all the previous theory about the Thomas-Fermi model and the relativistic Thomas-Fermi model, applied initially to the study of heavy nuclei, superheavy nuclei as well as to the theoretical hypothesis of nuclear matter cores of stellar dimensions. The aim is to construct a self-consistent theory of self-gravitating systems obeying relativistic quantum statistics, electromagnetic, weak and strong interactions in the framework of general relativity, from which it is possible to study the properties of compact objects, such as white dwarfs and neutron stars.

The recent generalization of the Feynman-Metropolis-Teller treatment to relativistic regimes, which led to a new equation of state of white dwarf matter (see appendix A.2), has been recently used to construct equilibrium configurations of white dwarfs in general relativity (see appendix B.1).

The description of the inverse  $\beta$ -decay within the relativistic Feynman-Metropolis-Teller equation of state in conjunction with general relativity, leads to a self-consistent calculation of the critical mass of white dwarfs (see appendix B.1 for details). The numerical value of the mass, of the radius, and of the critical mass of white dwarfs turn to be smaller with respect to the ones obtained with approximate equations of state (see e.g. Hamada and Salpeter, 1961). Therefore, the analysis of compressed atoms following the relativistic Feynman-Metropolis-Teller treatment has important consequences in the determination of the mass-radius relation of white dwarfs, leading to the possibility of a direct confrontation of these results with observations, in view of the current great interest for the cosmological implications of the type Ia supernovae.

The generalization of the above general relativistic theory of white dwarfs to the case of rotation is the thesis work of K. Boshkayev; see appendix B.2 for details. The entire family of uniformly rotating stable white dwarfs has been already obtained by studying the mass-shedding, the inverse  $\beta$ -decay, pyc-

nonnuclear reactions, as well as the axisymmetric instabilities. Both the maximum mass and the minimum(maximum) rotation period(frequency) have been obtained for selected nuclear compositions. This work is relevant for the evolution of massive white dwarfs and type Ia supernovae. Besides, it has been successfully applied to the description of soft-gamma-ray repeaters (SGRs) and anomalous X-ray pulsars (AXPs) within a model based on rotation powered white dwarfs, as shown in appendixes B.3–B.5.

SGRs and AXPs are a class of compact objects that show interesting observational properties: rotational periods in the range  $P \sim (2\text{--}12)$  s, a narrow range with respect to the wide range of ordinary pulsars  $P \sim (0.001\text{--}10)$  s; spin-down rates  $\dot{P} \sim (10^{-13}\text{--}10^{-10})$ , larger than ordinary pulsars  $\dot{P} \sim 10^{-15}$ ; strong outburst of energies  $\sim (10^{41}\text{--}10^{43})$  erg, and for the case of SGRs, giant flares of even large energies  $\sim (10^{44}\text{--}10^{47})$  erg, not observed in ordinary pulsars.

The recent observation of SGR 0418+5729 with a rotational period of  $P = 9.08$  s, an upper limit of the first time derivative of the rotational period  $\dot{P} < 6.0 \times 10^{-15}$ , and an X-ray luminosity of  $L_X = 6.2 \times 10^{31}$  erg/s, promises to be an authentic Rosetta Stone, a powerful discriminant for alternative models of SGRs and AXPs. The loss of rotational energy of a neutron star with this spin-down rate  $\dot{P}$  cannot explain the X-ray luminosity of SGR 0418+5729, excluding the possibility of identifying this source as an ordinary spin-down powered pulsar. The inferred upper limit of the surface magnetic field of SGR 0418+5729  $B < 7.5 \times 10^{12}$  G, describing it as a neutron star within the magnetic braking scenario, is well below the critical field challenging the power mechanism based on magnetic field decay purported in the magnetar scenario.

We have shown that the observed upper limit on the spin-down rate of SGR 0418+5729 is, instead, perfectly in line with a model based on a massive fast rotating highly magnetized white dwarf of mass  $M = 1.4M_\odot$ , radius  $R = 10^3$  km, and moment of inertia  $I \approx 10^{49}$  g cm<sup>2</sup>. We analyze the energetics of all SGRs and AXPs including their outburst activities and show that they can be well explained through the change of rotational energy of the white dwarf associated to the observed sudden changes of the rotational period, the glitches. All SGRs and AXPs can be interpreted as rotating white dwarfs that generate their energetics from the rotational energy and therefore there is no need to invoke the magnetic field decay of the magnetar model. Details can be found in appendix B.3. The above calculation of the range of minimum rotation periods of massive white dwarfs,  $0.3 \lesssim P_{min} \lesssim 2.2$  seconds, depending on the nuclear composition (see appendix B.2), implies the rotational stability of SGRs and AXPs. The relatively long minimum period of <sup>56</sup>Fe rotating white dwarfs  $\sim 2.2$  seconds, implies that the objects describing SGRs and AXPs have are made of chemical compositions lighter than <sup>56</sup>Fe, e.g. <sup>12</sup>C or <sup>16</sup>O.

We have analyzed within the white dwarf model of SGRs and AXPs, SGR 0418+5729 and Swift J1822.3-1606 the so-called *low magnetic field magnetars*;

see appendix B.4. The request of the rotational stability of the white dwarf gives bounds for the mass, radius, moment of inertia and magnetic field, through the analysis of constant rotation period sequences of uniformly rotating white dwarfs. We have also analyzed the emission properties of these two objects in the optical band, and inferred the cyclotron frequencies associated to their magnetic fields which might cause absorption features in the optical wavelengths (see appendix B.4). Concerning the emission in the high-energy bands, such as X and gamma-rays, it is part of the graduate work of D. Cáceres.

We are in addition considering the possible progenitors of these massive fast rotating highly magnetized white dwarfs. Recent smoothed particle hydrodynamics (SPH) simulations of white dwarfs mergers (Garcia-Berro et al. 2012) indicate that the outcomes of these binaries are white dwarfs with the above desirable properties, and thus they can be progenitors of SGRs and AXPs. Specifically, the products of these mergers consist of a hot central white dwarf surrounded by a heavy rapidly rotating disk. We applied these considerations to the specific case of 4U 0142+61 (see appendix B.5) and show that the merger of a double degenerate system can explain the characteristics of this peculiar AXP.

The request of the rotational stability of the white dwarf outcome of the merger gives bounds for the mass, radius, moment of inertia and magnetic field. Assuming a carbon composition, we find that the mass and radius of 4U 0142+61 must be in the range  $1.16\text{--}1.39 M_{\odot}$  and  $0.0014\text{--}0.0086 R_{\odot}$ . We followed the post-merger cooling and rotation evolution of the newly formed white dwarf. We show that this scenario accounts for the observed infrared excess and the emission observed in the other optical bands. We demonstrate that the observed properties of 4U 0142+6 are consistent with a  $\sim 1.2 M_{\odot}$  white dwarf, remnant of the coalescence of an original system made of two white dwarfs of masses  $0.6 M_{\odot}$  and  $1.0 M_{\odot}$ . Finally, we infer a post-merging age  $\tau_{\text{WD}} \approx 64$  kyr, and a magnetic field  $B \approx 2 \times 10^8$  G. Evidence for such a magnetic field may come from the possible detection of the electron cyclotron absorption feature observed between the *B* and *V* bands at a frequency  $\nu \approx 10^{15}$  Hz in the spectrum of 4U 0142+61. Details can be found in appendix B.5.

We now turn from the above massive white dwarfs to low-mass white dwarfs. Recent observations of relativistic white dwarf-neutron star binaries has led to the discovery that the white dwarfs in these systems are light objects with masses  $\lesssim 0.2 M_{\odot}$  (Antoniadis et al. 2012,2013). These objects should have densities lower than  $\sim 10^6$  g cm $^{-3}$ , where thermal effects might become relevant. In this line the generalization of the relativistic Feynman-Metropolis-Teller treatment to the case of finite temperatures acquires importance (see appendix A.3). We have used this new equation of state to construct the mass-radius relation of white dwarfs at finite temperatures in a wide range of central densities; we refer to appendix B.6 for details. We analyze in particular the white dwarf companion of the pulsar PSR J1738+0333,

which is expected to have a mass  $\sim 0.18M_{\odot}$  (Antoniadis et al. 2012). Using the observed surface effective temperature and surface gravity of the white dwarf we infer that the central core temperature of the object should be close to  $\sim 2 \times 10^7$  K.

Going back to magnetized white dwarfs, it has been recently purported by Das and Mukhopadhyay (2013) that the presence of a extremely large uniform magnetic field of order  $10^{18}$  G in the interior of a white dwarf, increases the maximum mass of the star from the traditional Chandrasekhar value,  $\approx 1.44 M_{\odot}$ , to a new upper bound  $\approx 2.58 M_{\odot}$ . Such a much larger limit would make these astrophysical objects viable candidates for the explanation of the superluminous population of type Ia supernovae. We show in App. B.7 that the new mass limit was obtained neglecting several macro and micro physical aspects such as gravitational, dynamical stability, breaking of spherical symmetry, general relativity, inverse  $\beta$  decay, and pycnonuclear fusion reactions. These effects are relevant for the self-consistent description of the structure and assessment of stability of these objects. When accounted for, they lead to the conclusion that the existence of such ultramagnetized white dwarfs in nature is very unlikely due to violation of minimal requests of stability, and therefore the canonical Chandrasekhar mass limit of white dwarfs has to be still applied.

## 2.3. Neutron Star Physics and Astrophysics

In the earliest description of neutron stars in the works of Tolman (1939) and Oppenheimer and Volkoff (1939) only a gas of neutrons was considered and the equations of equilibrium (hereafter TOV equations) were written in the Schwarzschild metric. They considered the model of a degenerate gas of neutrons to hold from the center to the border, with the density monotonically decreasing away from the center.

In the intervening years, more realistic neutron star models have been presented challenging the original considerations of Tolman (1939) and Oppenheimer and Volkoff (1939). The TOV equations considered the existence of neutrons all the way to the surface of the star. The presence of neutrons, protons and electrons in  $\beta$ -equilibrium were instead introduced by Harrison et al. (1965). Still more important, the neutron stars have been shown to be composed of two sharply different components: the core at nuclear and supra-nuclear densities consisting of degenerate neutrons, protons and electrons in  $\beta$ -equilibrium and a crust of white dwarf like material, namely a nuclei lattice in a background of degenerate electrons (see Harrison et al., 1965; Baym et al., 1971a, for details). Further works describing the nuclear interactions were later introduced. Clearly all these considerations departed profoundly from the Oppenheimer and Volkoff (1939) assumption.

The matching between the core and the crust is still today an open issue in

neutron star physics. In order to handle with this interesting problem, a step-by-step procedure is needed. In such a case, the neutron, proton, and electron fluid is confined within the core radius due to the compression exerted by the crust component of the neutron star.

Most of the effort have been given to the construction of self-consistent solutions of the equations of equilibrium for neutron stars in general relativity taking into account the traditionally neglected electromagnetic interaction. In nearly all the scientific literature on neutron stars, a “local approach”, where the equation of state of neutron star matter is constructed ignoring global gravitational and Coulombian effects by assuming not only flat space but also local charge neutrality, has been traditionally used. The gravitational effects are then taken into account by embedding such an equation of state into the TOV equations of hydrostatic equilibrium.

We have introduced a new approach which thanks to the existence of scaling laws can apply to compressed atoms as well as to massive nuclear matter cores of stellar dimensions. This approach on the compressed atom has already given a new contribution in the study of white dwarfs. It represents the first self-consistent calculation taking into due account the electromagnetic contribution in a relativistic treatment of the Thomas-Fermi equation, within global formulation of the equilibrium of white dwarfs in general relativity.

The application of the above results to the case of neutron stars is much more complex and it has been approached stepwise. As a first step we have considered the application of this novel approach to the case of a system of neutrons, protons, and electrons in  $\beta$ -equilibrium at zero temperatures within general relativity (see appendix C.1). The crucial role of the generalized Fermi energy of particles, for short Klein potentials, and their constancy on the entire equilibrium configuration has been outlined. Such a solution, although does not represent a realistic model for a neutron star, contains all the essential physics of the phenomenon of gravito-polarization in neutron star interiors: the existence of an electric potential and consequently an electric field over the entire configuration has been there evidenced.

We have there proved, for the case of this simplified example where strong interactions are neglected, that the traditional approach of describing the system imposing the condition of local charge neutrality and solving the corresponding TOV equations is conceptually inconsistent. We have then substitute the condition of local charge neutrality with the condition of global charge neutrality and derived the correct equations which we have called the Einstein-Maxwell-Thomas-Fermi system. The boundary conditions are also different from a traditional Cauchy data with the values of the functions and first derivatives at the center into a boundary condition at the center and delicate eigenvalue problem at the boundary determining the condition of charge neutrality at the border (see appendix C.1). The conceptual differences and the alternative mathematical equations of the two approaches, the ones im-

posing local versus global charge neutrality, lead to the presence of additional electrodynamic global structures. However, in this specific simple example, they do not give significant quantitative differences in the mass-radius relation for the equilibrium configurations. A very different situation occurs when strong interactions are also taken into account.

The next step has been to introduce self-consistently the strong interactions in the construction of the equilibrium configurations. We have indeed recently generalized the Einstein-Maxwell-Thomas-Fermi equations to the case of strong interactions, see appendix C.2 for details. There the major aim has been to prove the constancy of the Klein potentials in the case in which the nuclear interactions are described by a Lagrangian including in addition to the gravitational, electromagnetic, and weak interactions, also the presence of  $\sigma$ ,  $\omega$ , and  $\rho$  virtual mesons that mediate the nuclear interactions.

We have also extended to finite temperatures the theoretical treatment of gravito-polarization for a system of neutrons, protons and electrons in  $\beta$ -equilibrium, taking into account strong interactions modeled through the exchange of  $\sigma$ ,  $\omega$  and  $\rho$  virtual mesons (see appendix C.3 for details). The crucial role of the Klein potentials of particles is outlined as well as the condition of isothermality of Tolman. We have shown that, the gravito-polarization effect although energetically much weaker than the corresponding gravitational and thermal effects, do survive in the case of finite temperatures. Their role, when strong interactions are considered, is of fundamental astrophysical importance.

The construction of realistic neutron stars with core and crust satisfying global (but not local) charge neutrality has been already accomplished (see appendix C.4). The solutions lead to a new structure of the star: a positively charged core at supranuclear densities surrounded by an electronic distribution of thickness  $\sim \hbar/(m_e c) \sim 10^2 \hbar/(m_\pi c)$  of opposite charge, as well as a neutral crust at lower densities. Inside the core there is a Coulomb potential well of depth  $\sim m_\pi c^2/e$ . The constancy of the Klein potentials in the transition from the core to the crust, impose the presence of an overcritical electric field  $\sim (m_\pi/m_e)^2 E_c$ . For each central density, an entire family of core-crust interface boundaries can be constructed, each of them reaching the neutrality point at a different electron density at the edge of the crust. This leads consequently to crusts with masses and thickness smaller than the ones obtained from the traditional TOV treatment, resulting in a novel neutron star mass-radius relation.

The generalization of this important work to the case of uniformly rotating neutron stars has been already accomplished (see appendix C.5). This part of the graduate thesis of R. Belvedere has been based on the previous results obtained by K. Boshkayev for the case of rotating white dwarfs. We determine the equilibrium configurations by solving the Einstein-Maxwell-Thomas-Fermi equations within the slow rotation formalism by Hartle. We integrate these equations of equilibrium for different central densities and

circular angular velocities and compute the mass, polar and equatorial radii, angular momentum, eccentricity, moment of inertia, as well as quadrupole moment  $Q$  of the configurations. Both the Keplerian mass-shedding limit and the axisymmetric secular instability are used to construct the new mass-radius relation. We compute the maximum and minimum masses and rotation frequencies of neutron stars.

The analysis of the properties of the core-crust interface, such as its surface and Coulomb energies, are being studied by Y. Wu, as part of his graduate work (see appendix C.6, for details). We study the instability against Bohr-Wheeler surface deformations in the case of neutron stars obeying global charge neutrality. Assuming the core-crust transition at nuclear density  $\rho_{core} \approx 2.7 \times 10^{14} \text{ g cm}^{-3}$ , we find that the instability sets the upper limit to the crust density,  $\rho_{crust}^{crit} \approx 1.2 \times 10^{14} \text{ g cm}^{-3}$ . This result implies a non-zero lower limit to the maximum electric field of the core-crust transition surface and makes inaccessible a limit of quasi-local charge neutrality reachable in the limit  $\rho_{crust} = \rho_{core}$ . The general framework presented in this work can be also applied to study the stability of sharp phase-transitions in hybrid stars as well as in strange stars both bare and with outer crust. The results of this work open the way to a more general analysis of the stability of these transition surfaces accounting for other effects such as gravitational binding, centrifugal repulsion, magnetic field induced by rotating electric field and therefore magnetic dipole-dipole interactions.

We turn now to the thermal evolution of neutron stars, which is part of the PhD thesis of Sheyse M. de Carvalho. Some properties of neutron stars, such as the equation of state and the composition in their cores are still uncertain. All the microscopic calculations are model dependent and give us a variety of possible equations of state with different compositions of the core. Owing to the strong sensitivity of the thermal evolution of a neutron star to its microscopic and macroscopic properties, the simulation of the neutron star cooling is one of the potential methods to probe their interior structure. As we show in Apps. C.7 and C.8, the theoretical cooling curves depend on the adopted stellar interior, emissivities, heat capacity and thermal conductivity.

Neutron stars have temperatures around  $10^{11}$  K at birth, but gradually cool down in a process realized by two channels: neutrino emission from the stellar body and heat conduction from the internal layers in the surface resulting in a photon emission. We neglect the possible reheating mechanisms, the magnetic fields, and the superfluidity effects. In Apps. C.7 and C.8 we compute the cooling curves, namely the thermal evolution, of the neutron stars with global neutrality and to compare them with the locally neutral neutron star (TOV-like) cooling curves.

The cooling curves have been computed considering the isothermal approximation in App. C.7, that is we first do not take into account the thermal relaxation phase in which the core and the crust of the neutron star are thermally decoupled. The size and mass fraction of the neutron star core where

the direct Urca is active for the case of NL3 parametrization of the nuclear model was also computed. The full cooling curves are computed in App. C.8. We noticed a different behavior of the thermal relaxation phase with respect to the locally neutral neutron stars, when the density at the base of the crust is lower than  $\approx 5 \times 10^{13} \text{ g cm}^{-3}$ . We conclude that in a very thin crust with a small or absent inner crust, some neutrino emission processes are blocked keeping the crust hotter for longer times, so increasing the time for the interior to reach isothermality.

It is clear from all the above discussion on neutron stars, that in the intervening years from the seminal work of Oppenheimer and Volkoff (1939), much more has been learned concerning the equation of state including the nuclear interactions, and on a more complex description of the structure parameters and stability of both static and rotating neutron stars. In spite of this fact, it is common in the pulsar literature to infer neutron star astrophysical observables such as surface magnetic field and luminosity by adopting as fiducial structure parameters for the mass, radius, and moment of inertia,  $M = 1.4 M_{\odot}$ ,  $R = 10 \text{ km}$ ,  $I = 10^{45} \text{ g cm}^2$ , respectively. The same argument applies to the use of some analytic formulas existing in the literature for the determination of the maximum rotation frequency (see e.g. Lattimer and Prakash, 2004a) and of the moment of inertia (see e.g. Ravenhall and Pethick, 1994; Lattimer and Schutz, 2005) of a neutron star. However, it is clear that both different theoretical models or, for a fixed model, different structure parameters by varying central density and/or rotation frequency, can give rise to quite different quantitative estimates of the astrophysical quantities.

In App. C.9, we summarize a recent work part of the PhD thesis of R. Belvedere, in which it is analyzed the consequences of using fiducial parameters and analytic formulas for the Keplerian sequence and moment of inertia, on the estimation of pulsar observables. We construct the Keplerian sequence of globally and locally neutral neutron stars and compare qualitatively and quantitatively our results with the approximate analytic formula given by Lattimer and Prakash (2004a). We analyze specifically the case of the fastest observed pulsar PSR J1748–2446ad (Hessels et al., 2006a) with a frequency of 716 Hz, which is often used in the literature to constraint the mass-radius relation and so the EOS of neutron stars (see e.g. Trümper, 2011). Then, we calculate the moment of inertia of globally and locally neutral neutron stars and compare and contrast the results with the approximate formulas given by Ravenhall and Pethick (1994) and also Lattimer and Schutz (2005) for the moment of inertia as a function of the star compactness. Finally, we turn to the astrophysical observables of pulsars and analyze the estimates of the magnetic field and radiation efficiency of the high-magnetic field pulsars class. We compare and contrast the values of realistic neutron star configurations with the ones derived using the above fiducial parameters, with which fields larger than the quantum critical value for vacuum breakdown,  $B_c = m_e^2 c^2 / (e \hbar) \approx 4.4 \times 10^{13} \text{ G}$ , are obtained (see e.g. Ng and Kaspi, 2011).

## 2.4. Neutron Star Physics with Gamma Ray Bursts

The progenitors and emission mechanisms leading to the most energetic radiation observed in astrophysics, the Gamma Ray Bursts (GRBs), are studied. Focus is given to the termed GRB-Supernova connection and to Short GRBs. The binary progenitors of these systems are studied in detail with particular emphasis on the role played by neutron stars.

It is understood that the Supernovae (SNe) associated to Gamma Ray Bursts (GRBs) are of type Ib/c. However, the temporal coincidence of the GRB and the SN represents still a major enigma of Relativistic Astrophysics. A novel concept has been recently proposed for explaining the temporal coincidence of some Gamma Ray Bursts (GRBs) with an associated Supernova (SN) in terms of the gravitational collapse of a neutron star to a Black Hole (BH), induced by a type Ib/c SN explosion (see Rueda and Ruffini, 2012, and the report of activities of the GRB group). There, based on the pioneer idea of Ruffini et al. (2008a), the specific case of a close (orbital period  $< 1$  h) binary system composed of an evolved star with a neutron star companion has been considered. We have computed in (Rueda and Ruffini, 2012) the accretion rate onto the neutron star of the material expelled from the explosion of the core progenitor as a type Ib/c SN, and give the explicit expression of the accreted mass as a function of the nature of the components and binary parameters. We showed that the NS can reach, in a few seconds, the critical mass and consequently gravitationally collapses to a Black Hole. This gravitational collapse process leads to the emission of the GRB.

We have recently applied in (Izzo et al., 2012a) the above considerations to the case of GRB 090618 (see also report of activities of the GRB group), for which there is evidence of a SN  $\sim 10$  days after the GRB occurrence. We compute the progenitor binary parameters: the mass of the neutron star companion,  $M_{\text{NS}}$ , and the mass of the SN core progenitor,  $M_{\text{core}}$ , are in the following mass ranges:  $1.8 \lesssim M_{\text{NS}}/M_{\odot} \lesssim 2.1$  and  $3 \leq M_{\text{core}}/M_{\odot} \leq 8$ . We have also discussed in (Rueda and Ruffini, 2012; Izzo et al., 2012a) the complementarity of these considerations to alternative processes explaining long and short GRBs.

It is clear that after the occurrence of the SN and the GRB emission, the outcome is represented, respectively, by a NS and a BH. A possible strong evidence of the NS formation is represented by the observation of a characteristic late ( $t = 10^8$ – $10^9$  s) X-ray emission that has been interpreted as originated by the young ( $t \sim 1$  minute–(10–100) years), hot ( $T \sim 10^7$ – $10^8$  K) NS, which we have called neo-NS (see Negreiros et al. (2012) and appendix D.1, for details). This has been indeed observed in GRB 090618 (Izzo et al., 2012b) and also in GRB 101023 (Penacchioni et al., 2012). If the NS and the BH are gravitationally bound they give origin to a new kind of binary system, which can lead itself to the merging of the NS and the BH and consequently to a new process of gravitational collapse of the NS into the BH. In this case the

system could originate a yet additional process of GRB emission and possibly a predominant emission in gravitational waves.

The traditional study of neutron star cooling has been generally applied to quite old objects as the Crab Pulsar (957 years) or the Central Compact Object in Cassiopeia A (330 years) with an observed surface temperature  $\sim 10^6$  K. However, as we just mentioned in GRB-SN systems there is possible evidence of the cooling of neutron stars with surface temperatures  $\sim 10^7$ – $10^8$  K. The traditional thermal processes taking place in the neutron star crust might be enhanced by the extreme high temperature conditions of neo-neutron star and therefore the study of the thermal behavior especially of the crust of neo-neutron stars deserve the appropriate attention. This issue is part of the graduate work of S. Martins de Carvalho. The influence of possible fallback accretion after the SN explosion, as well as the study of possible thermal emission processes in the early evolution of the neo-neutron stars is being studied within the thesis work of F. Gomes de Oliveira.

We now turn to the so-called short GRBs. The progress obtained from the Fermi-GBM and Konus-Wind satellites has been used to identify through the analysis of GRB 090227B (Muccino et al., 2013) the new class of genuinely short GRBs: short bursts with the same inner engine of the long GRBs but endowed with a severely low value of the baryon load,  $B \equiv M_B c^2 / E_{tot}^{GRB} \lesssim 5 \times 10^{-5}$ , where  $M_B$  is the mass of the baryons engulfed by the expanding ultrarelativistic  $e^+e^-$  plasma of energy  $E_{tot}^{GRB}$ . The emission from these GRBs mainly consists in a first emission, the peak GRB (P-GRB), followed by a softer emission squeezed on the first one. The typical separation between the two components is expected to be shorter than 1–10 ms.

A special case is GRB 090227B. From the 16 ms time-binned light curves a significant thermal emission in the first 96 ms, which has been identified with the P-GRB, has been found Muccino et al. (2012). The subsequent emission is identified with the extended afterglow. The P-GRB of 090227B has the highest temperature ever observed,  $k_B T = 517$  keV, where  $k_B$  is the Boltzmann constant. Other properties of the GRB have been computed, e.g. the total energy emitted  $E_{tot}^{GRB}$ , Baryon load  $B$ , Lorentz factor at transparency  $\Gamma_{tr}$ , cosmological redshift  $z$ , intrinsic duration of the GRB emission  $\Delta t$ , and average density of the CircumBurst Medium (CBM)  $\langle n_{CBM} \rangle$ ; we refer to Muccino et al. (2013) for further details.

These quantitative results lead to the conclusion that the progenitor of GRB 090227B is a neutron star binary: (1) the natal kicks velocities imparted to a neutron star binary at birth can be even larger than  $200 \text{ km s}^{-1}$  and therefore a binary system can runaway to the halo of its host galaxy, clearly pointing to a very low average number density of the CBM; (2) the very large total energy, which we can indeed infer in view of the absence of beaming, and the very short time scale of emission point again to a neutron star binary; (3) as we shall show below the very small value of the baryon load is strikingly consistent with two neutron stars having small crusts, in line with the recent

neutron star theory (Belvedere et al., 2012). This first identification of a genuinely short GRB has allowed us to compute for the first time the total energy release in form of gravitational waves from a neutron star binary merger that leads to the emission of a GRB, which we show in App D.2.

In App D.2 we show that the observations of the genuinely short GRB 090227B lead to crucial information on the binary neutron star progenitor. The data obtained from the electromagnetic spectrum allows to probe crucial aspects of the correct theory of neutron stars and their equation of state. The baryon load parameter  $B$  obtained from the analysis of GRB 090227B, leads to a remarkable agreement of the baryonic matter expected to be ejected in a neutron star binary merger and validate a choice of the parameters of the binary components,  $M_1 = M_2 = 1.34M_\odot$ , and  $R_1 = R_2 = 12.24$  km.

We computed the dynamics of the neutron star binary progenitor prior to the merger and emission of the GRB. We compare and contrast the classic description of the dynamics with the more general one given by the framework of the effective one-body formalism, which we use up to 4-PN order. We estimate the detectability of GRB 090227B by the Advanced LIGO interferometer, by computing the signal-to-noise ratio up to the contact point of the binary components, for the theoretically inferred cosmological redshift,  $z = 1.61$  (Muccino et al., 2013). We also estimate the redshift at which Advanced LIGO would detect this GRB with a signal-to-noise ratio equal to five; we obtained  $z \approx 0.08$ . From the dynamics, we then estimated the total energy release in form of gravitational waves (see Table D.3). From this, we concluded that the emission of electromagnetic radiation in a GRB by a binary neutron star system is at least one order of magnitude larger than the gravitational wave emission.

There are other applications connected with GRBs where the physics of neutron stars plays an important role and where the different aspects of a detailed description of the neutron star interior described in this report acquire a specific value. This is the case of the process of induced gravitational collapse described at the beginning of this summary. We refer for further details on this process, the distinction between long and short GRBs, as well as the GRB-SN connection, to the report of the GRB group.

## 2.5. Emission-Radiation Mechanisms of White Dwarfs and Neutron Stars

In this new topic, we are studying the possible emission mechanisms of white dwarfs and neutron stars. We are thus interested in the radiation generated in the magnetospheres of magnetized white dwarfs and neutron stars. Both energetics and spectrum of different radiation mechanisms operating in the magnetosphere of compact objects are analyzed and applied to the observa-

tions of white dwarfs and neutron star pulsars, Soft Gamma-Ray Repeaters (SGRs), X-ray pulsars (ordinary and anomalous), and other similar systems. This is one of the main fields of the Ph. D. work of D. Cáceres.

There are some preliminary results regarding the high-energy emission in X and Gamma rays from magnetized white dwarfs. It comes out that a massive ( $M \sim M_{\odot}$ ), fast rotating ( $P \sim 1$  s), highly magnetized ( $B \sim 10^8$  G), can emit persistent high-energy emission as a by-product of the pair-creation process in the magnetosphere. The positrons bombard the polar caps of the magnetosphere producing an X-ray emission with luminosities of the order of  $10^{35}$  erg  $s^{-1}$ . This is in line with what observed in SGRs and AXPs and similar mechanisms are also at work in ordinary pulsars. We are currently preparing a manuscript with the first application of this work to some SGRs and AXPs.

## 2.6. Exact Solutions of the Einstein-Maxwell equations in Astrophysics

We analyze the ability of analytic exact solutions of the Einstein-Maxwell equations to describe the exterior spacetime of compact stars like white dwarfs and neutron stars. The problem of matching between interior and exterior spacetimes is addressed in detail. The effect of the quadrupole moment on the properties of the spacetime is also investigated. Particular attention is given to the application of exact solutions in astrophysics, e.g. the dynamics of particles around compact stars and its relevance in astrophysical systems like X ray binaries.

Thus, whether analytic exact vacuum(electrovacuum) solutions of the Einstein(Einstein-Maxwell) field equations can accurately describe or not the exterior spacetime of compact stars remains still an interesting open question. As an attempt to establish their level of accuracy, the radii of the Innermost Stable Circular Orbits (ISCOs) of test particles given by analytic exterior spacetime geometries have been compared with the ones given by numerical solutions for neutron stars obeying a realistic equation of state. It has been so shown that the six-parametric solution of Pachón, Rueda, and Sanabria (2006) (hereafter PRS) is more accurate to describe the neutron star ISCO radii than other analytic models.

In this line, Pachón et al. (2012) have recently proposed an additional test of accuracy for analytic exterior geometries based on the comparison of orbital frequencies of neutral test particles. The Keplerian, frame-dragging, as well as the precession and oscillation frequencies of the radial and vertical motions of neutral test particles for the Kerr and PRS geometries have been computed in (Pachón et al., 2012). Then, they were compared with the numerical values obtained by Morsink and Stella (1999) for realistic neutron stars.

Contrary to what previously stated in the literature, it has been identified the role of high-order multipole moments such as the mass quadrupole and current octupole in the determination of the orbital frequencies, especially in the rapid rotation regime. These results are relevant to cast a separatrix between black holes and neutron star signatures as well as probe the nuclear matter equation of state and neutron star parameters from the Quasi-Periodic Oscillations (QPOs) observed in Low Mass X-Ray Binaries. We refer to (Pachón et al., 2012) and appendix E.1, for further details.

## **2.7. Critical fields and Non Linear Electrodynamics Effects in Neutron Stars and Black Holes**

We turn now to a more theoretical topic: the effects of non-linear electrodynamics minimally coupled to gravity. We construct new analytic and numeric solutions to the Einstein-Maxwell equations representing black holes or the exterior field of a compact star. Some astrophysical applications are studied in detail such as the extractable energy of black holes, the mass-formula of the black hole; see for instance appendix F.1. This is part of the graduate work of J. Pereira.

## 3. Publications 2013

### 3.1. Refereed Journals

#### 3.1.1. Printed

1. Jorge A. Rueda, G. Aznar-Siguán, K. Boshkayev, E. García-Berro, L. Izzo, P. Lorén-Aguilar, R. Ruffini, *A white dwarf merger as progenitor of the AXP 4U 0142+61?*, *ApJ Letters* **772**, L24 (2013).
2. K. Boshkayev, L. Izzo, Jorge A. Rueda, R. Ruffini, *SGR 0418+5729, Swift J1822.3-1606, and 1E 2259+586 as massive fast rotating highly magnetized white dwarfs*, *A&A*. **555**, A151 (2013).
3. K. Boshkayev, Jorge A. Rueda, R. Ruffini, I. Siutsou, *On general relativistic uniformly rotating white dwarfs*, *ApJ* **762**, 117 (2013).
4. Jorge A. Rueda, R. Ruffini, *On the general relativistic Thomas-Fermi theory of white dwarfs and neutron stars*, *Il Nuovo Cimento C* **36**, 145 (2013).
5. Jorge A. Rueda, R. Ruffini, *On the Einstein-Maxwell-Thomas-Fermi equations for white dwarfs and neutron stars*, *Int. J. Mod. Phys. D*. **22**, 1360007 (2013).

#### 3.1.2. Accepted for publication (in press)

1. S. Martins de Carvalho, M. Rotondo, Jorge A. Rueda, R. Ruffini, *The relativistic Feynman-Metropolis-Teller treatment at finite temperatures and its effects on mass-radius relation of white dwarfs*, *Phys. Rev. C*.
2. R. Belvedere, Jorge A. Rueda, R. Ruffini, *Uniformly rotating neutron stars in the global and local charge neutrality cases*, *Nuclear Physics A*.
3. Jorge A. Rueda, R. Ruffini, *Strong, weak, electromagnetic, and gravitational interactions in neutron stars*, *Int. J. Mod. Phys. D*.

#### 3.1.3. Submitted

1. J. G. Coelho, R. M. Jr. Marinho, M. Malheiro, R. Negreiros, Jorge A. Rueda, R. Ruffini, *Dynamical instability of white dwarfs and breaking of spherical*

- symmetry under the presence of extreme magnetic fields*, submitted to Phys. Rev. Lett.
2. J. Pereira, H. Mosquera-Cuesta, Jorge A. Rueda, R. Ruffini, *On the black hole mass-formula in nonlinear electrodynamics*, submitted to Phys. Lett. B.
  3. Jorge A. Rueda, R. Ruffini, Yuan-Bin Wu, S.-S. Xue, *On the surface tension of neutron star matter with global charge neutrality*, submitted to Phys. Rev. C.
  4. S. Martins de Carvalho, Jorge A. Rueda, R. Ruffini, *On the cooling of globally neutral neutron stars*, submitted to J. Korean Phys. Soc.
  5. D. L. Cáceres, Jorge A. Rueda, R. Ruffini, *On the stability of ultramagnetized white dwarfs*, submitted to J. Korean Phys. Soc.
  6. K. Boshkayev, Jorge A. Rueda, R. Ruffini, I. Siutsou, *General relativistic white dwarfs and their astrophysical implications*, submitted to J. Korean Phys. Soc.

#### 3.1.4. In preparation

1. S. Martins de Carvalho, R. Negreiros, Jorge A. Rueda, R. Ruffini, *Thermal evolution of neutron stars: global and local charge neutrality cases*, to be submitted to A&A.
2. R. Belvedere, Jorge A. Rueda, R. Ruffini, *Fiducial versus realistic parameters of neutron stars*, to be submitted to A&A Letters.
3. R. Belvedere, Jorge A. Rueda, R. Ruffini, *On the magnetic field of pulsars with realistic neutron star configurations*, to be submitted to ApJ Letters.
4. F. Gomes de Oliveira, Jorge A. Rueda, R. Ruffini, *Gravitational waves versus electromagnetic emission in gamma-ray bursts*, to be submitted to ApJ.
5. J. Pereira, Jorge A. Rueda, R. Ruffini, *Thin shell stability of globally neutral neutron stars*, to be submitted to Phys. Rev. D.
6. D. L. Cáceres, Jorge A. Rueda, R. Ruffini, *On the minimum mass of magnetized neutron stars*, to be submitted to Phys. Rev. D.

## 4. Publications (before 2013)

### 4.1. Refereed Journals

1. L. Izzo, Jorge A. Rueda, R. Ruffini, *GRB 090618: a candidate of a neutron star gravitational collapse to a black hole induced by a type Ib/c supernova*, *A&A*, 548, L5 (2012).
2. Jorge A. Rueda, R. Ruffini, *On the induced gravitational collapse of a neutron star to a black hole by a type Ib/c supernova*, *ApJ* **758**, L7 (2012).
3. L. A. Pachón, Jorge A. Rueda, C. Valenzuela, *On the relativistic precession and oscillation frequencies of test particles around rapidly rotating compact stars*, *ApJ* **756**, 82 (2012).
4. M. Malheiro, Jorge A. Rueda, R. Ruffini, *SGRs and AXPs as rotation-powered massive white dwarfs*, *Publ. Astron. Soc. Japan* **64**, 56 (2012).
5. R. Belvedere, D. Pugliese, Jorge A. Rueda, R. Ruffini, S.-S. Xue, *Neutron star equilibrium configurations within a fully relativistic theory with strong, weak, electromagnetic, and gravitational interactions*, *Nuclear Physics A* **883**, 1 (2012).
6. R. Negreiros, C. L. Bianco, Jorge A. Rueda, R. Ruffini, *Cooling of young neutron stars in GRB associated to supernovae*, *A&A* **540**, A12 (2012).
7. Jorge A. Rueda, R. Ruffini, and S.-S. Xue, *The Klein first integrals in an equilibrium system with electromagnetic, weak, strong and gravitational interactions*, *Nuclear Physics A* **872**, 286 (2011).
8. M. Rotondo, Jorge A. Rueda, R. Ruffini, S.-S. Xue, *Relativistic Feynman-Metropolis-Teller theory for white dwarfs in general relativity*, *Phys. Rev. D* **84**, 084007 (2011).
9. M. Rotondo, Jorge A. Rueda, R. Ruffini, S.-S. Xue, *The self-consistent general relativistic solution for a system of degenerate neutrons, protons and electrons in  $\beta$ -equilibrium*, *Phys. Lett. B* **701**, 667 (2011).
10. M. Rotondo, Jorge A. Rueda, R. Ruffini, S.-S. Xue, *Relativistic Thomas-Fermi treatment of compressed atoms and compressed nuclear matter cores of stellar dimensions*, *Phys. Rev. C* **83**, 045805 (2011).

11. M. Rotondo, R. Ruffini, S.-S. Xue, and V. S. Popov, *On gravitationally and electrodynamically bound nuclear matter cores of stellar dimensions*, Int. J. Mod. Phys. D **20**, 1995 (2011).
12. Jorge A. Rueda, R. Ruffini, *Towards a Relativistic Thomas-Fermi Theory of White Dwarfs and Neutron Stars*, Int. J. Mod. Phys. E **20**, 141 (2011).
13. K. Boshkayev, Jorge A. Rueda, R. Ruffini, *On the Maximum Mass of General Relativistic Uniformly Rotating White Dwarfs*, Int. J. Mod. Phys. E **20**, 136 (2011).
14. Jorge A. Rueda, M. Rotondo, R. Ruffini, S.-S. Xue, *On compressed nuclear matter: from nuclei to neutron stars*, Int. J. Mod. Phys. D **20**, 1789 (2011).
15. Jorge A. Rueda, Michael Rotondo, Remo Ruffini, She-Sheng Xue, *A self-consistent approach to neutron stars*, J. Korean Phys. Soc. **57**, 560 (2010).
16.  $e^-e^+$  pair creation by vacuum polarization around electromagnetic black holes, C. Cherubini, A. Geralico, Jorge A. Rueda H., R. Ruffini, Phys. Rev. D **79**, 124002 (2009).
17. R. Ruffini, M. Rotondo and S.-S. Xue, *Electrodynamics for nuclear Matter in bulk*, Int. J. Mod. Phys. D **16**, 1 (2007).
18. R. Ruffini and L. Stella, *Some comments on the relativistic Thomas-Fermi model and the Vallarta-Rosen equation*, Phys. Lett. B **102**, 442 (1981).
19. J. Ferreira, R. Ruffini and L. Stella, *On the relativistic Thomas-Fermi model*, Phys. Lett. B **91**, 314 (1980).

## 4.2. Conference Proceedings

1. R. Belvedere, Jorge A. Rueda, R. Ruffini, S.-S. Xue *Neutron star equilibrium configurations within a fully relativistic theory with strong, weak, electromagnetic, and gravitational interactions*, Current Issues on Relativistic Astrophysics, South Korea (2012).
2. K. Boshkayev, Jorge A. Rueda, R. Ruffini, *SGRs and AXPs AXPs as Massive Fast Rotating Highly Magnetized White Dwarfs*, Current Issues on Relativistic Astrophysics, South Korea (2012).
3. S. Martins de Carvalho, Jorge A. Rueda, R. Ruffini, *On the relativistic Feynman-Metropolis-Teller equation of state at finite temperatures and low-mass white dwarfs*, Current Issues on Relativistic Astrophysics, South Korea (2012).

4. Jorge A. Rueda, R. Ruffini, *Fundamental interactions in neutron stars*, 13th Marcel Grossmann Meeting, Sweden (2012).
5. S. Martins de Carvalho, Jorge A. Rueda, R. Ruffini, *On the relativistic Feynman-Metropolis-Teller equation of state at finite temperatures and low-mass white dwarfs*, 13th Marcel Grossmann Meeting, Sweden (2012).
6. K. Boshkayev, Jorge A. Rueda, R. Ruffini, *SGRs and AXPs as Massive Fast Rotating Highly Magnetized White Dwarfs: Bounds on the Mass, Moment of Inertia and Magnetic Fields*, 13th Marcel Grossmann Meeting, Sweden (2012).
7. K. Boshkayev, Jorge A. Rueda, R. Ruffini, *On General Relativistic Uniformly Rotating White Dwarfs*, 13th Marcel Grossmann Meeting, Sweden (2012).
8. R. Belvedere, Jorge A. Rueda, R. Ruffini, S.-S. Xue *Neutron star equilibrium configurations within a fully relativistic theory with strong, weak, electromagnetic, and gravitational interactions*, 13th Marcel Grossmann Meeting, Sweden (2012).
9. Jorge A. Rueda, *SGRs and AXPs as massive fast rotating highly magnetized white dwarfs*, 39th COSPAR Scientific Assembly, India (2012).
10. K. Boshkayev, *Fast Rotating White Dwarfs as Precursors of Type Ia supernovae and Millisecond Pulsars*, 39th COSPAR Scientific Assembly, India (2012).
11. R. Belvedere, Jorge A. Rueda, R. Ruffini, *Moment of inertia, radii, surface emission from a new theoretical understanding of Neutron Stars*, 39th COSPAR Scientific Assembly, India (2012).
12. K. Boshkayev, Jorge A. Rueda, R. Ruffini, *Rotating white dwarfs and their stability*, CompStar: the physics and astrophysics of compact stars, Tahiti (2012).
13. R. Belvedere, Jorge A. Rueda, R. Ruffini, *Neutron star equilibrium configurations within a fully relativistic theory with strong, weak, electromagnetic, and gravitational interactions*, CompStar: the physics and astrophysics of compact stars, Tahiti (2012).
14. K. Boshkayev, Jorge A. Rueda, R. Ruffini, *Stability of Rotating Nuclear Matter Cores of Stellar Dimensions*, CompStar: Equation of State for Compact Star Interiors and Supernovae, Croatia (2012).
15. R. Belvedere, Jorge A. Rueda, R. Ruffini, *Neutron star equilibrium configurations*, CompStar: Equation of State for Compact Star Interiors and Supernovae, Croatia (2012).

16. M. Rotondo, Jorge A. Rueda, R. Ruffini, S.-S. Xue, *On Degenerate Compressed Atoms and Compressed Nuclear Matter Cores of Stellar Dimensions*, Int. J. Mod. Phys. Conf. S. **12**, 203 (2012).
17. K. Boshkayev, M. Rotondo, R. Ruffini, *On Magnetic Fields in Rotating Nuclear Matter Cores of Stellar Dimensions*, Int. J. Mod. Phys.: Conf. S. **12**, 58 (2012).
18. Jorge A. Rueda, R. Ruffini, S.-S. Xue, *Electrostatic Configurations Crossover Neutron Star Core*, Proc. 12th Marcel Grossmann Meeting, 1042 (2012).
19. Jorge A. Rueda, M. Rotondo, R. Ruffini, S.-S. Xue, *A New Family of Neutron Star Models: Global Neutrality versus Local Neutrality*, Proc. 12th Marcel Grossmann Meeting, 1039 (2012).
20. M. Rotondo, Jorge A. Rueda, R. Ruffini, S.-S. Xue, *From Compressed Atoms to Compressed Massive Nuclear Density Cores*, Proc. 12th Marcel Grossmann Meeting, 1036 (2012).
21. M. Malheiro, Jorge A. Rueda, R. Ruffini, *SGRs and AXPs: White Dwarf Pulsars versus Magnetars*, Proc. "The X-ray Universe 2011", Germany (2011).
22. R. Belvedere, Jorge A. Rueda, R. Ruffini, *Mass, Radius and Moment Of Inertia of Neutron Stars*, Proc. 2nd Ferrara Workshop on "X-ray Astrophysics up to 511 keV", Italy (2011).
23. S. Martins de Carvalho, C. Argüelles, Jorge A. Rueda, R. Ruffini, *SGRs and AXPs: White Dwarf Pulsars versus Magnetars*, Proc. "The X-ray Universe 2011", Germany (2011).
24. Jorge A. Rueda, M. Rotondo, R. Ruffini, and S.-S. Xue, *On the relativistic Feynman-Metropolis-Teller equation of state and general relativistic white-dwarfs*, Proceedings of Science, PoS(Texas2010), 269 (2011).
25. D. Pugliese, Jorge A. Rueda, R. Ruffini, and S.-S. Xue, *A general relativistic Thomas-Fermi treatment of neutron star cores*, Proceedings of Science, PoS(Texas 2010), 271 (2011).
26. R. Belvedere, *On the structure of the crust of neutron stars*, Proceedings of Science, PoS(Texas 2010), 270 (2011).
27. K. Boshkayev, *On the Stability of Rotating Nuclear Matter Cores of Stellar Dimensions*, Proceedings of Science, PoS(Texas 2010), 275 (2011).
28. K. Boshkayev, Jorge A. Rueda, and R. Ruffini, *On the minimum rotational period of fast rotating white dwarfs*, Proc. Erasmus Mundus IRAP PhD Workshop "From Nuclei to White Dwarfs to Neutron Stars", Eds. A. Mezzacappa, World Scientific (2011).

- 
29. Jorge A. Rueda, D. Pugliese, M. Rotondo, R. Ruffini, S.-S. Xue, *A general relativistic Thomas-Fermi treatment of neutron stars cores I. The case of non-interacting particles*, Proc. 2nd Galileo-Xu Guangqi Meeting, Italy (2010).
  30. Jorge A. Rueda, D. Pugliese, M. Rotondo, R. Ruffini, S.-S. Xue, *A general relativistic Thomas-Fermi treatment of neutron stars cores II. Generalized Fermi energies and beta equilibrium in the strongly interacting case*, Proc. 2nd Galileo-Xu Guangqi Meeting, Italy (2010).
  31. K. Boshkayev, M. Rotondo, and R. Ruffini, *On Magnetic Fields in Rotating Nuclear Matter Cores of Stellar Dimensions*, Proc. 2nd Galileo-Xu Guangqi Meeting, Italy (2010).
  32. R. Mohammadi, Jorge A. Rueda, R. Ruffini, and S.-S. Xue, *The solution of the Thomas-Fermi equation in the presence of strong magnetic fields*, Proc. 2nd Galileo-Xu Guangqi Meeting, Italy (2010).
  33. Jorge A. Rueda, R. Ruffini, S.-S. Xue, *On the electrostatic structure of neutron stars*, AIP Conf. Proc. 1205, 143 (2010).
  34. Jorge A. Rueda H., B. Patricelli, M. Rotondo, R. Ruffini, S.-S. Xue, *The Extended Nuclear Matter Model with Smooth Transition Surface*, Proc. 3rd Stueckelberg Workshop on Relativistic Field Theories, Italy (2008).
  35. B. Patricelli, J. A. Rueda H., R. Ruffini *On the Crust of Neutron Stars*, Proc. 3rd Stueckelberg Workshop on Relativistic Field Theories, Pescara, Italy (2008).
  36. R. Ruffini, M. Rotondo and S.-S. Xue, *Neutral nuclear core vs super charged one*, Proc. 11th Marcel Grossmann Meeting, Eds. R. Jantzen, H. Kleinert, R. Ruffini, World Scientific, Singapore (2008).
  37. B. Patricelli, M. Rotondo and R. Ruffini, *On the Charge to Mass Ratio of Neutron Cores and Heavy Nuclei*, AIP Conf. Proc. **966**, 143 (2008).
  38. M. Rotondo, R. Ruffini and S.-S. Xue, *On the Electrodynamical properties of Nuclear matter in bulk*, AIP Conf. Proc. **966**, 147 (2008).
  39. B. Patricelli, M. Rotondo, J. A. Rueda H. and R. Ruffini, *The Electrodynamics of the Core and the Crust components in Neutron Stars*, AIP Conf. Proc. **1059**, 68 (2008).
  40. R. Ruffini, *The Role of Thomas-Fermi approach in Neutron Star Matter*, Proceedings of the 9<sup>th</sup> International Conference "Path Integrals-New trends and perspectives", Eds. W. Janke and A. Pelster, World Scientific, Singapore (2008).

#### 4. Publications (before 2013)

---

41. R. Ruffini, M. Rotondo, S.-S. Xue, *The Thomas-Fermi Approach and Gamma-Ray Bursts*, AIP Conf. Proc. **1053**, 243 (2008).
42. Jorge A. Rueda, B. Patricelli, M. Rotondo, R. Ruffini, and S. S. Xue, *The Extended Nuclear Matter Model with Smooth Transition Surface*, Proc. 3rd Stueckelberg Workshop on Relativistic Field Theories, Italy (2008).

## 5. APPENDICES



# A. Nuclear and Atomic Astrophysics

## A.1. On gravitationally and electrostatically bound massive nuclear density cores

### A.1.1. Introduction

Models involving  $e^+e^-$  plasmas of total energy  $\leq 10^{55}$  ergs originating from a vacuum polarization process during the formation of a black hole are being studied to explain a variety of ultra-relativistic astrophysics events (Ruffini et al., 2010b; Cherubini et al., 2009; Aksenov et al., 2007). The formation of such a Kerr-Newman black hole with overcritical electromagnetic fields can only occur during the process of gravitational collapse, e.g., of two coalescing neutron stars. Accordingly in this article we consider new electrostatic properties of massive nuclear density cores which have been neglected in the astrophysics literature. This issue has been overlooked in the traditional description of neutron stars by considering only neutrons (Oppenheimer and Volkoff, 1939) or by imposing *ab initio* local charge neutrality, i.e., local identity of the densities of protons and electrons  $n_p = n_e$ , thus bypassing the description of any possible electrostatic effect (Harrison et al., 1965; Baym et al., 1971a).

The model we consider here generalizes the relativistic Thomas-Fermi treatment for neutral atoms with heavy nuclei (Pieper and Greiner, 1969; Müller et al., 1972; Greenberg and Greiner, 1982; Popov, 1971b; Zeldovich and Popov, 1972; Migdal et al., 1976). The study of neutral atoms with nuclei of mass number  $A \sim 10^2$ – $10^6$  is a classic problem of theoretical physics (Zeldovich and Popov, 1972; Ruffini et al., 2010b). Special attention has been given to a possible vacuum polarization process and the creation of  $e^+e^-$  pairs (Pieper and Greiner, 1969; Zeldovich and Popov, 1972; Ruffini et al., 2010b) as well as to the study of nuclear stability against Coulomb repulsion (Greenberg and Greiner, 1982). The existence of electric fields larger than the critical value  $E_c = m_e^2 c^3 / (e\hbar)$  near their surfaces (Popov, 1971b) has also been shown. We have generalized these models by enforcing the beta equilibrium conditions (Ruffini et al., 2007b).

We have then extrapolated those results by numerical integration to the case of massive nuclear density cores of mass  $\approx 1M_\odot$  and radius  $R_c \approx 10$  km

(Ruffini et al., 2007b). Such a massive nuclear density core is a globally neutral system of  $N_n$  neutrons,  $N_p$  protons and  $N_e$  electrons in beta equilibrium at nuclear density having mass numbers  $A \sim (m_{\text{Planck}}/m_n)^3$  where  $m_n$  ( $m_e$ ) is the neutron (electron) mass and  $m_{\text{Planck}} = (\hbar c/G)^{1/2}$  (Ruffini et al., 2007b). As in the nuclear model (Migdal et al., 1976), the proton distribution is here assumed to be constant up to the core radius  $R_c$ . We have obtained configurations with global charge neutrality  $N_p = N_e$  but  $n_p \neq n_e$ , in contrast with the local condition  $n_p = n_e$  traditionally assumed in astrophysics. As a result electric fields of critical value are confirmed to exist, near the surface, also in the case of massive nuclear density cores in analogy to the case of heavy nuclei.

Recently a new dimensionless form of the relativistic Thomas-Fermi treatment for a nuclear density core has been obtained which reveals the existence of new scaling laws for this model.

In this article we present a unified treatment extending from heavy nuclei to massive nuclear density cores by using an explicit analytic solitonic solution of the new dimensionless form of the relativistic Thomas-Fermi equation. We confirm the existence of and give an analytic expression for the overcritical electric field near the surface of massive nuclear density cores already obtained in (Ruffini et al., 2007b) by numerical integration. Furthermore there are a variety of new results made possible by the new analytic formulation. First we give an explicit expression for the Coulomb energy of such cores, demonstrating their stability against nuclear fission, as opposed to the case of heavy nuclei. Secondly on the basis of Newtonian gravitational energy considerations we propose the existence of a possible new island of stability for mass numbers  $A > A_R = 0.039 \left(\frac{N_p}{A}\right)^{1/2} \left(\frac{m_{\text{Planck}}}{m_n}\right)^3$ . The equilibrium against Coulomb repulsion originates now from the combined effect of the screening of the relativistic electrons, of the surface tension due to strong interactions and of the gravitational interaction of the massive dense cores. By enforcing the condition of beta equilibrium, we also obtain a generalized relation between the mass number  $A$  and atomic number  $N_p$  which encompasses previous phenomenological expressions.

All the above solutions have been obtained assuming the electron Fermi energy to be equal to zero. The necessity and the methodology of extending these results to the case of compressed atoms along the lines of the Feynman-Metropolis-Teller treatment (Feynman et al., 1949), corresponding to positive values of the Fermi energy of electrons, are outlined here. We also motivate the clear necessity and the general methodology of justifying the above results using a self-consistent general relativistic treatment of the system. These ideas will be pursued in detail elsewhere.

### A.1.2. The relativistic Thomas-Fermi equation and the beta equilibrium condition

It has been known since the classic work of Fermi (Fermi, 1950) that the phenomenological drop model of the nucleus gives excellent results for a variety of properties including the isobaric behavior and nuclear fission. In addition to the masses of the baryonic components and the asymmetry energy and pairing term, the mass formula contains terms estimating the surface tension energy of the nucleus (Fermi, 1950)

$$\varepsilon_s = 17.5 \cdot A^{2/3} \text{ MeV}, \quad (\text{A.1.1})$$

and the Coulomb energy (Fermi, 1950)

$$\varepsilon_c = \frac{3\alpha N_p^2}{5R_c}, \quad (\text{A.1.2})$$

where  $R_c = r_0 A^{1/3}$ ,  $r_0 = 1.5 \cdot 10^{-13}$  cm and the numerical factors are derived by fitting the observational data. From the extremization of the mass formula the following relation between  $A$  and  $N_p$  is obtained (Fermi, 1950)

$$N_p \simeq \left[ \frac{2}{A} + \frac{3}{200} \frac{1}{A^{1/3}} \right]^{-1}, \quad (\text{A.1.3})$$

which in the limit of small  $A$  gives

$$N_p \simeq \frac{A}{2}. \quad (\text{A.1.4})$$

The analysis of the stability of the nucleus against finite deformation leads to a stability condition against fission given by the equality of the surface energy term to the Coulomb energy. This leads to the condition (Fermi, 1950)

$$\frac{N_p^2}{A} < 45. \quad (\text{A.1.5})$$

A novel situation occurs when super-heavy nuclei ( $A > \tilde{A} \sim 10^4$ ) are examined (Ferreirinho et al., 1980; Ruffini et al., 2007b). The distribution of electrons penetrates inside the nucleus: a much smaller effective net charge of the nucleus occurs due to the screening of relativistic electrons (Migdal et al., 1976; Ferreira et al., 1980). In Ruffini and Stella (1981) a definition of an effective nuclear charge due to the penetration of the electrons was presented. A treatment based on the relativistic Thomas-Fermi model has been developed in order to describe the penetration of the electrons and their effective screening of the positive nuclear charge. In particular, by assuming

$N_p \simeq A/2$ , Pieper and Greiner (1969); Müller et al. (1972); Greenberg and Greiner (1982) and Popov (1971b); Zeldovich and Popov (1972); Migdal et al. (1976) in a series of papers were able to solve the non-linear Thomas-Fermi equation. It was demonstrated in Migdal et al. (1976) that the effective positive nuclear charge is confined to a small layer of thickness  $\sim \hbar/\sqrt{\alpha}m_\pi c$  where  $m_\pi$  is the pion mass and as usual  $\alpha = e^2/\hbar c$ . Correspondingly electric fields of strength much larger than the critical value  $E_c$  for vacuum polarization at the surface of the core are created. However, the creation of electron-positron pairs due to the vacuum polarization process does not occur because of the Pauli blocking by the degenerate electrons Ruffini et al. (2010b).

Here we generalize the work of Pieper and Greiner (1969); Müller et al. (1972); Greenberg and Greiner (1982) and Popov (1971b); Zeldovich and Popov (1972); Migdal et al. (1976). We have relaxed the condition  $N_p \simeq A/2$  adopted by Popov and Greiner as well as the condition  $N_p \simeq [2/A + 3/200A^{1/3}]^{-1}$  adopted by Ferreira et al. (1980). Instead we explicitly impose the beta decay equilibrium between neutrons, protons and electrons. We then extrapolate such model to the case  $A \approx (m_{\text{Planck}}/m_n)^3 \sim 10^{57}$ . A supercritical field still exists in a shell of thickness  $\sim \hbar/\sqrt{\alpha}m_\pi c$  at the core surface, and a charged lepton-baryonic core is surrounded by an oppositely charged leptonic component. Such massive nuclear density cores, including the leptonic component, are globally neutral.

As usual we assume that the protons are distributed at constant density  $n_p$  within a radius

$$R_c = \Delta \frac{\hbar}{m_\pi c} N_p^{1/3}, \quad (\text{A.1.6})$$

where  $\Delta$  is a parameter such that  $\Delta \approx 1$  ( $\Delta < 1$ ) corresponds to nuclear (supranuclear) densities when applied to ordinary nuclei. The overall Coulomb potential satisfies the Poisson equation

$$\nabla^2 V(r) = -4\pi e [n_p(r) - n_e(r)], \quad (\text{A.1.7})$$

with the boundary conditions  $V(\infty) = 0$  (due to the global charge neutrality of the system) and finiteness of  $V(0)$ . The density  $n_e(r)$  of the electrons of charge  $-e$  is determined by the Fermi energy condition on their Fermi momentum  $P_e^F$ ; we assume here

$$E_e^F = [(P_e^F c)^2 + m_e^2 c^4]^{1/2} - m_e c^2 - eV(r) = 0, \quad (\text{A.1.8})$$

which leads to

$$n_e(r) = \frac{(P_e^F)^3}{3\pi^2 \hbar^3} = \frac{1}{3\pi^2 \hbar^3 c^3} \left[ e^2 V^2(r) + 2m_e c^2 eV(r) \right]^{3/2}. \quad (\text{A.1.9})$$

By introducing  $x = r/[\hbar/m_\pi c]$ ,  $x_c = R_c/[\hbar/m_\pi c]$  and  $\chi/r = eV(r)/c\hbar$ , the relativistic Thomas-Fermi equation takes the form

$$\frac{1}{3x} \frac{d^2\chi(x)}{dx^2} = -\frac{\alpha}{\Delta^3} \theta(x_c - x) + \frac{4\alpha}{9\pi} \left[ \frac{\chi^2(x)}{x^2} + 2 \frac{m_e}{m_\pi} \frac{\chi}{x} \right]^{3/2}, \quad (\text{A.1.10})$$

where  $\chi(0) = 0, \chi(\infty) = 0$ . The neutron density  $n_n(r)$  is determined by the Fermi energy condition on their Fermi momentum  $P_n^F$  imposed by beta decay equilibrium

$$\begin{aligned} E_n^F &= [(P_n^F c)^2 + m_n^2 c^4]^{1/2} - m_n c^2 \\ &= [(P_p^F c)^2 + m_p^2 c^4]^{1/2} - m_p c^2 + eV(r), \end{aligned} \quad (\text{A.1.11})$$

which in turn is related to the proton and electron densities by Eqs. (A.1.7), (A.1.9) and (A.1.10). These equations have been integrated numerically (see Ruffini et al. (2007b)).

### A.1.3. The ultra-relativistic analytic solutions

In the ultrarelativistic limit, the relativistic Thomas-Fermi equation admits an analytic solution. Introducing the new function  $\phi$  defined by  $\phi = \frac{4^{1/3}}{(9\pi)^{1/3}} \Delta \frac{\chi}{x}$  and the new variables  $\hat{x} = (12/\pi)^{1/6} \sqrt{\alpha} \Delta^{-1} x$ ,  $\xi = \hat{x} - \hat{x}_c$ , where  $\hat{x}_c = (12/\pi)^{1/6} \sqrt{\alpha} \Delta^{-1} x_c$ , then Eq. (A.1.10) becomes

$$\frac{d^2 \hat{\phi}(\xi)}{d\xi^2} = -\theta(-\xi) + \hat{\phi}(\xi)^3, \quad (\text{A.1.12})$$

where  $\hat{\phi}(\xi) = \phi(\xi + \hat{x}_c)$ . The boundary conditions on  $\hat{\phi}$  are:  $\hat{\phi}(\xi) \rightarrow 1$  as  $\xi \rightarrow -\hat{x}_c \ll 0$  (at the massive nuclear density core center) and  $\hat{\phi}(\xi) \rightarrow 0$  as  $\xi \rightarrow \infty$ . The function  $\hat{\phi}$  and its first derivative  $\hat{\phi}'$  must be continuous at the surface  $\xi = 0$  of the massive nuclear density core. Equation (A.1.12) admits an exact solution

$$\hat{\phi}(\xi) = \begin{cases} 1 - 3 \left[ 1 + 2^{-1/2} \sinh(a - \sqrt{3}\xi) \right]^{-1}, & \xi < 0, \\ \frac{\sqrt{2}}{(\xi + b)}, & \xi > 0, \end{cases} \quad (\text{A.1.13})$$

where the integration constants  $a$  and  $b$  have the values  $a = \text{arcsinh}(11\sqrt{2}) \approx 3.439$ ,  $b = (4/3)\sqrt{2} \approx 1.886$ . Next we evaluate the Coulomb potential energy

function

$$eV(\xi) = \left(\frac{9\pi}{4}\right)^{1/3} \frac{1}{\Delta} m_\pi c^2 \hat{\phi}(\xi), \quad (\text{A.1.14})$$

and by differentiation, the electric field

$$E(\xi) = - \left(\frac{3^5 \pi}{4}\right)^{1/6} \frac{\sqrt{\alpha} m_\pi^2 c^3}{\Delta^2 e \hbar} \hat{\phi}'(\xi). \quad (\text{A.1.15})$$

Details are given in Figs. A.1 and A.2.

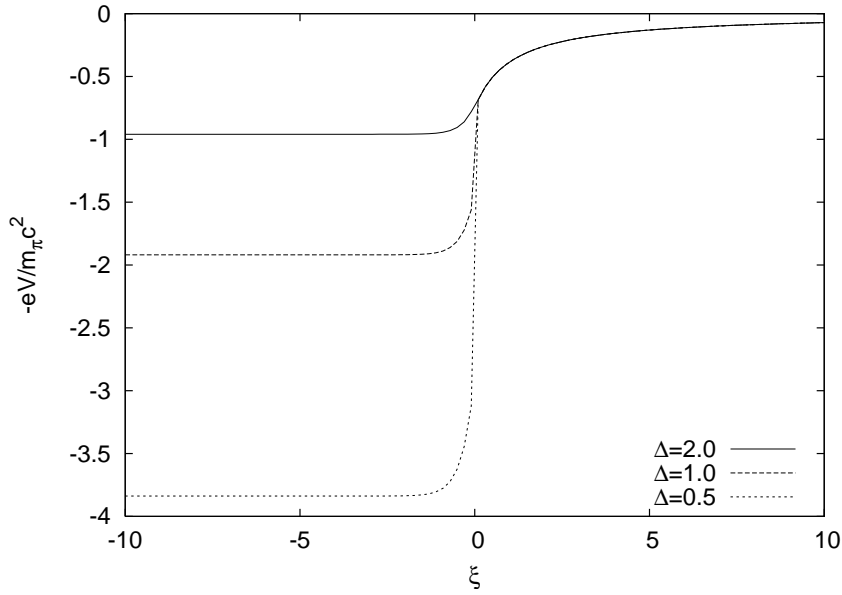


**Figure A.1.:** The electron Coulomb potential energy  $-eV$ , in units of pion mass  $m_\pi$  is plotted as a function of the radial coordinate  $\xi = \hat{x} - \hat{x}_c$ , for selected values of the density parameter  $\Delta$ .

We now estimate three crucial quantities:

1) the Coulomb potential at the center of the configuration,

$$eV(0) \approx \left(\frac{9\pi}{4}\right)^{1/3} \frac{1}{\Delta} m_\pi c^2, \quad (\text{A.1.16})$$

2) the electric field at the surface of the core

$$E_{\max} \approx 0.95 \sqrt{\alpha} \frac{1}{\Delta^2} \frac{m_\pi^2 c^3}{e \hbar} = 0.95 \frac{\sqrt{\alpha}}{\Delta^2} \left(\frac{m_\pi}{m_e}\right)^2 E_c. \quad (\text{A.1.17})$$

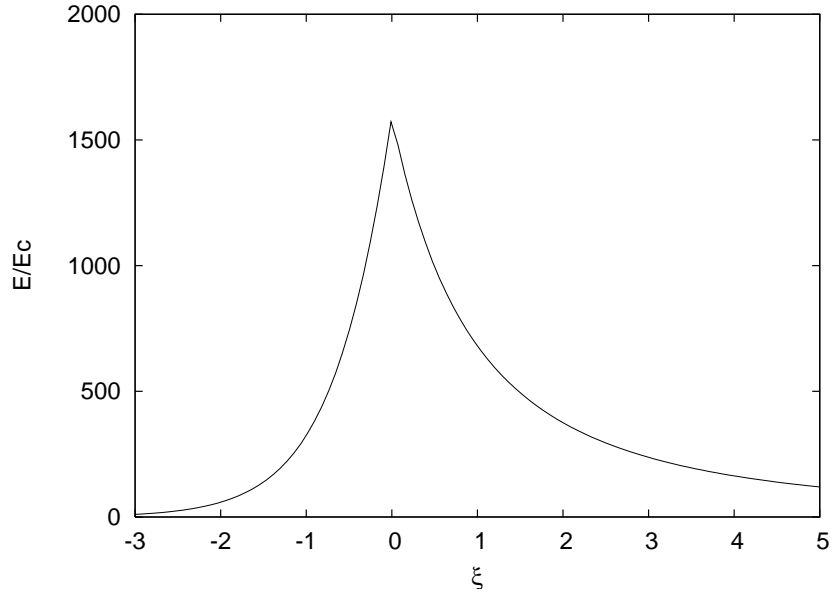


**Figure A.2.:** The electric field is plotted in units of the critical field  $E_c$  as a function of the radial coordinate  $\xi$  for  $\Delta=2$ , showing a sharp peak at the core radius.

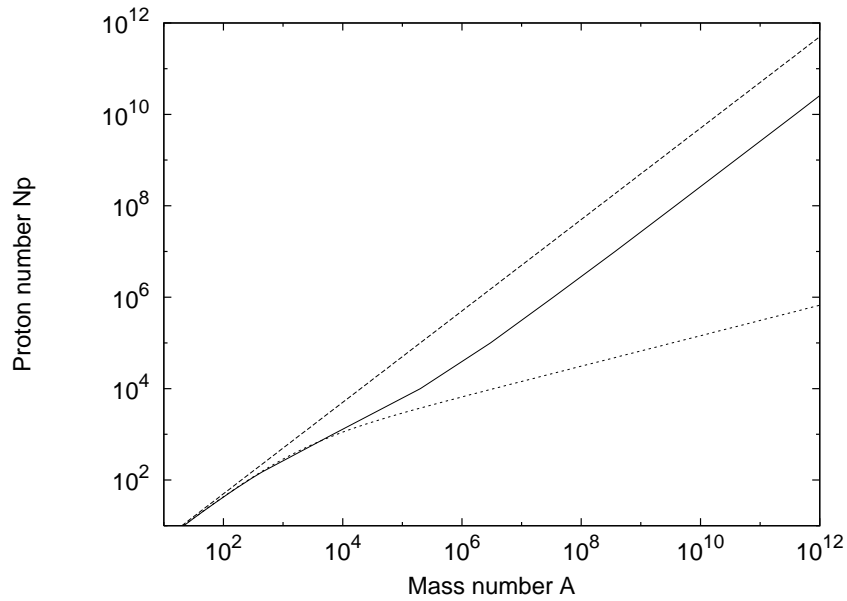


**Figure A.3.:** The  $A$ - $N_p$  relation at nuclear density (solid line) obtained from first principles compared with the phenomenological expressions given by  $N_p \simeq A/2$  (dashed line) and Eq. (A.1.3) (dotted line). The asymptotic value, for  $A \rightarrow (m_{\text{Planck}}/m_n)^3$ , is  $N_p \approx 0.0046A$ .

3) the Coulomb electrostatic energy of the core

$$\mathcal{E}_{\text{em}} = \int \frac{E^2}{8\pi} d^3r \approx 0.15 \frac{3\hbar c(3\pi)^{1/2}}{4\Delta\sqrt{\alpha}} A^{2/3} \frac{m_\pi c}{\hbar} \left(\frac{N_p}{A}\right)^{2/3}. \quad (\text{A.1.18})$$

These three quantities are functions only of the pion mass  $m_\pi$ , the density parameter  $\Delta$  and of the fine structure constant  $\alpha$ . Their formulas apply over the entire range from superheavy nuclei with  $N_p \sim 10^3$  all the way up to massive cores with  $N_p \approx (m_{\text{Planck}}/m_n)^3$ .

#### A.1.4. New results derived from the analytic solutions

Starting from the analytic solutions of the previous section we obtain the following new results.

a) Using the solution (A.1.13), we have obtained a new generalized relation between  $A$  and  $N_p$  for any value of  $A$ . In the limit of small  $A$  this result agrees well with the phenomenological relations given by Eqs. (A.1.3) and (A.1.4), as is clearly shown in Fig. A.3. It appears that the explicit evaluation of the beta equilibrium, in contrast with the previously adopted Eqs.(3,4), leads to an effect comparable in magnitude and qualitatively similar to the asymmetry energy in the phenomenological liquid drop model.

b) The charge-to-mass ratio of the effective charge  $Q$  at the core surface to the core mass  $M$  is given by

$$\frac{Q}{\sqrt{GM}} \approx \frac{E_{\text{max}} R_c^2}{\sqrt{G} m_n A} \approx \frac{m_{\text{Planck}}}{m_n} \left(\frac{1}{N_p}\right)^{1/3} \frac{N_p}{A}. \quad (\text{A.1.19})$$

For superheavy nuclei with  $N_p \approx 10^3$ , the charge-to-mass ratio for the nucleus is

$$\frac{Q}{\sqrt{GM}} > \frac{1}{20} \frac{m_{\text{Planck}}}{m_n} \sim 10^{18}. \quad (\text{A.1.20})$$

Gravitation obviously plays no role in the stabilization of these nuclei.

Instead for massive nuclear density cores where  $N_p \approx (m_{\text{Planck}}/m_n)^3$ , the ratio  $Q/\sqrt{GM}$  given by Eq. (A.1.19) is simply

$$\frac{Q}{\sqrt{GM}} \approx \frac{N_p}{A}, \quad (\text{A.1.21})$$

which is approximatively 0.0046 (see Fig. A.3). It is well-known that the charge-to-mass-ratio (A.1.21) smaller than 1 evidences the equilibrium of self-gravitating mass-charge system both in Newtonian gravity and general relativity (see, e.g., Chandrasekhar (1992)).

c) For a massive core at nuclear density the criterion of stability against fission ( $\mathcal{E}_{em} < 2\mathcal{E}_s$ ) is satisfied. In order to see this we use Eqs. (A.1.1) and (A.1.18)

$$\frac{\mathcal{E}_{em}}{2\mathcal{E}_s} \approx 0.15 \frac{3}{8} \sqrt{\frac{3\pi}{\alpha}} \frac{1}{\Delta} \left(\frac{N_p}{A}\right)^{2/3} \frac{m_\pi c^2}{17.5 \text{ MeV}} \sim 0.1 < 1. \quad (\text{A.1.22})$$

### A.1.5. Estimates of gravitational effects in a Newtonian approximation

In order to investigate the possible effects of gravitation on these massive neutron density cores we proceed to some qualitative and quantitative estimates based on the Newtonian approximation.

a) The *maximum* Coulomb energy per proton is given by Eq. (A.1.16) where the potential is evaluated at the center of the core. The Newtonian gravitational potential energy per proton (of mass  $m_p$ ) in the field of a massive nuclear density core with  $A \approx (m_{\text{Planck}}/m_n)^3$  is given by

$$\mathcal{E}_g = -G \frac{M m_p}{R_c} = -\frac{1}{\Delta} \frac{m_{\text{Planck}}}{m_n} \frac{m_\pi c^2}{N_p^{1/3}} \simeq -\frac{m_\pi c^2}{\Delta} \left(\frac{A}{N_p}\right)^{1/3}. \quad (\text{A.1.23})$$

Since  $A/N_p \sim 0.0046$  (see Fig. A.3) for any value of  $\Delta$ , the gravitational energy is larger in magnitude than and opposite in sign to the Coulomb potential energy per proton of Eq. (A.1.16) so the system should be gravitationally stable.

b) There is yet a more accurate derivation of the gravitational stability based on the analytic solution of the Thomas-Fermi equation Eq. (A.1.12). The Coulomb energy  $\mathcal{E}_{em}$  given by (A.1.18) is mainly distributed within a thin shell of width  $\delta R_c \approx \hbar \Delta / (\sqrt{\alpha} m_\pi c)$  and proton number  $\delta N_p = n_p 4\pi R_c^2 \delta R_c$  at the surface. To ensure the stability of the system, the attractive gravitational energy of the thin proton shell

$$\mathcal{E}_{gr} \approx -3 \frac{G}{\Delta} \frac{A^{4/3}}{\sqrt{\alpha}} \left(\frac{N_p}{A}\right)^{1/3} m_n^2 \frac{m_\pi c}{\hbar} \quad (\text{A.1.24})$$

must be larger than the repulsive Coulomb energy (A.1.18). For small  $A$ , the gravitational energy is always negligible. However, since the gravitational energy increases proportionally to  $A^{4/3}$  while the Coulomb energy only increases proportionally to  $A^{2/3}$ , the two must eventually cross, which occurs

at

$$A_R = 0.039 \left( \frac{N_p}{A} \right)^{1/2} \left( \frac{m_{\text{Planck}}}{m_n} \right)^3. \quad (\text{A.1.25})$$

This establishes a *lower* limit for the mass number  $A_R$  necessary for the existence of an island of stability for massive nuclear density cores. The *upper* limit of the island of stability will be determined by general relativistic effects.

c) Having established the role of gravity in stabilizing the Coulomb interaction of the massive nuclear density core, we outline the importance of the strong interactions in determining its surface. We find for the neutron pressure at the surface:

$$P_n = \frac{9}{40} \left( \frac{3}{2\pi} \right)^{1/3} \left( \frac{m_\pi}{m_n} \right) \frac{m_\pi c^2}{(\hbar/m_\pi c)^3} \left( \frac{A}{N_p} \right)^{5/3} \frac{1}{\Delta^5}, \quad (\text{A.1.26})$$

and for the surface tension, as extrapolated from nuclear scattering experiments,

$$P_s = - \left( \frac{0.13}{4\pi} \right) \frac{m_\pi c^2}{(\hbar/m_\pi c)^3} \left( \frac{A}{N_p} \right)^{2/3} \frac{1}{\Delta^2}. \quad (\text{A.1.27})$$

We then obtain

$$\frac{|P_s|}{P_n} = 0.39 \cdot \Delta^3 \left( \frac{N_p}{A} \right) = 0.24 \cdot \frac{\rho_{\text{nucl}}}{\rho_{\text{surf}}}, \quad (\text{A.1.28})$$

where  $\rho_{\text{nucl}} = 3m_n A / 4\pi R_c^3$ . The relative importance of the nuclear pressure and nuclear tension is a very sensitive function of the density  $\rho_{\text{surf}}$  at the surface.

It is important to emphasize a major difference between nuclei and the massive nuclear density cores treated in this article: the gravitational binding energy in these massive nuclear density cores is instead  $\varepsilon_{\text{gr}} \approx GM_\odot m_n / R_c \approx 0.1 m_n c^2 \approx 93.8 \text{ MeV}$ . In other words it is much bigger than the nuclear energy in ordinary nuclei  $\varepsilon_{\text{nuclear}} \approx \hbar^2 / m_n r_0^2 \approx 28.8 \text{ MeV}$ .

### A.1.6. Possible applications to neutron stars

All the above considerations have been made for an isolated massive core at constant density whose boundary has been sharply defined by a step function. No external forces are exerted. Consequently due to the global charge neutrality, the Fermi energy of the electrons has been assumed to be equal to zero. In the earliest description of neutron stars in the work of Oppenheimer and Volkoff (1939) only a gas of neutrons was considered and the equation

of equilibrium was written in the Schwarzschild metric. They considered the model of a degenerate gas of neutrons to hold from the center to the border, with the density monotonically decreasing away from the center.

In the intervening years a more realistic model has been presented challenging the original considerations of Tolman (1939); Oppenheimer and Volkoff (1939). Their TOV equations considered the existence of neutrons all the way to the surface of the star. The presence of neutrons, protons and electrons in beta equilibrium were instead introduced in Harrison et al. (1965). Still more important the neutron stars have been shown to be composed of two sharply different components: the core at nuclear and/or supra-nuclear density consisting of neutrons, protons and electrons and a crust of white dwarf like material, namely of degenerate electrons in a nuclei lattice (Harrison et al., 1965; Baym et al., 1971a). The pressure and the density of the core are mainly due to the baryons while the pressure of the crust is mainly due to the electrons with the density due to the nuclei and possibly with some free neutrons due to neutron drip (see e.g. Baym et al. (1971a)). Further works describing the nuclear interactions were later introduced (see e.g. Haensel et al. (2007)). Clearly all these considerations departed profoundly from the TOV approximation. The matching between the core component and the crust is the major unsolved problem. To this issue this article introduces some preliminary results in a simplified model which has the advantage to present explicit analytic solutions.

In all the above treatments in order to close the system of equations the condition of local charge neutrality  $n_e = n_p$  was adopted without a proof. The considerations of massive neutron density cores presented in this article offer an alternative to the local charge neutrality condition  $n_e = n_p$ . In a specific example which can be solved also analytically such condition is substituted by the Thomas-Fermi relativistic equations implying  $n_e \neq n_p$  and an overall charge neutral system ( $N_e = N_p$ ). The condition of global charge neutrality as opposed to the local one, leads to the existence of overcritical electric fields at the core surface which may be relevant in the description of neutron stars.

### A.1.7. Conclusions

We have first generalized the treatment of heavy nuclei by enforcing the condition of beta equilibrium in the relativistic Thomas-Fermi equation, avoiding the imposition of  $N_p \simeq A/2$  between  $N_p$  and  $A$  traditionally assumed in the literature. In doing so we have obtained (see Fig. A.3) an  $A - N_p$  relation which extends the ones adopted in the literature. Using the existence of scaling laws for the system of equations considered, we extend the results obtained for heavy nuclei to the case of massive nuclear density cores. The novelty in this article is to show how both the considerations of heavy nuclei and of systems of macroscopic astrophysical dimensions can take advantage

from a rigorous and analytic solution of the Thomas-Fermi relativistic equations and the beta equilibrium conditions. This task is achieved by obtaining explicit analytic solutions fulfilling precise boundary conditions and using the scaling laws introduced in this article.

Indeed the Thomas-Fermi treatment has been considered also in the context of quark stars with a charge and a density distribution analogous to the one of massive nuclear density cores we consider in this article Itoh (1970); Witten (1984); Alcock et al. (1986); Kettner et al. (1995); Usov (1998). There are however a variety of differences both in the boundary conditions adopted and in the solution obtained. In the present article we show that we can indeed obtain overcritical electric fields at nuclear density on macroscopic scales of  $R_c \approx 10$  Km and  $M \approx 1M_\odot$  for existing field theories involving only neutrons, protons and electrons and their fundamental interactions and no quarks present. We obtain explicit analytic solutions of the relativistic Thomas-Fermi equations, self-consistently solved with the condition of beta equilibrium. Such analytic solutions allow to give explicit expressions for the Coulomb energy, surface energy and Newtonian gravitational energy of such massive nuclear density cores.

These cores are stable against fission (see Eq. (A.1.22)), the surface tension determines the sharpness of their boundary (see Eq. (A.1.28)) and the gravitational interaction, at Newtonian level, balances the Coulomb repulsion for mass numbers larger than the critical value given by Eq. (A.1.25).

As a by-product of these results, we also conclude that the arguments often quoted concerning limits on the electric fields of an astrophysical system based on a free test particle (the dust approximation) considering only the gravitational and electric interactions

$$(E_{\max})_{\text{dust}} \approx \frac{m_e m_n c^3}{e \hbar} \frac{m_n}{m_{\text{Planck}}}, \quad (\text{A.1.29})$$

$$\left(\frac{Q}{\sqrt{GM}}\right)_{\text{dust}} \approx \sqrt{G} \frac{m_e}{e} = \frac{1}{\sqrt{\alpha}} \frac{m_e}{m_{\text{Planck}}}, \quad (\text{A.1.30})$$

appear to be inapplicable for  $A \sim (m_{\text{Planck}}/m_n)^3$ . Here nuclear densities are reached and the roles of *all* fundamental interactions, including weak and strong interactions in addition to the electromagnetic and gravitational ones and including as well quantum statistics, have to be taken into account through the relativistic Thomas-Fermi model. Eqs. (A.1.29) and (A.1.30) are replaced by Eqs. (A.1.17) and (A.1.21),

$$E_{\max} \approx \frac{0.95\sqrt{\alpha} m_{\text{Planck}}}{\Delta^2} \frac{m_{\text{Planck}}}{m_e} \left(\frac{m_\pi}{m_n}\right)^2 (E_{\max})_{\text{dust}}, \quad (\text{A.1.31})$$

$$\frac{Q}{\sqrt{GM}} \approx \frac{N_p}{A} \sqrt{\alpha} \frac{m_{\text{Planck}}}{m_e} \left(\frac{Q}{\sqrt{GM}}\right)_{\text{dust}}. \quad (\text{A.1.32})$$

## **A.2. On the relativistic Thomas-Fermi treatment of compressed atoms and compressed nuclear matter cores of stellar dimensions**

### **A.2.1. Introduction**

In a classic article Baym et al. (1971a) presented the problem of matching, in a neutron star, a liquid core, composed of  $N_n$  neutrons,  $N_p$  protons and  $N_e$  electrons, to the crust taking into account the electro-dynamical and surface tension effects. After discussing the different aspects of the problem they concluded: *The details of this picture requires further elaboration; this is a situation for which the Thomas-Fermi method is useful.* This statement, in first instance, may appear surprising: the Thomas-Fermi model has been extensively applied in atomic physics (see e.g. Gombás (1949); March (1957); Lundqvist and March (1983)), also has been applied extensively in atomic physics in its relativistic form (see e.g. Ferreira et al. (1980); Ruffini and Stella (1981)) as well as in the study of atoms with heavy nuclei in the classic works of Migdal et al. (1976, 1977). Similarly there have been considerations of relativistic Thomas-Fermi model for quark stars pointing out the existence of critical electric fields on their surfaces (see e.g. Alcock et al. (1986); Usov (1998)). Similar results have also been obtained by Alford et al. (2001) in the transition at very high densities, from the normal nuclear matter phase in the core to the color-flavor-locked phase of quark matter in the inner core of hybrid stars. No example exists of the application of the electromagnetic Thomas-Fermi model for neutron stars. This problem can indeed be approached with merit by studying the simplified but rigorous concept of a nuclear matter core of stellar dimensions which fulfills the relativistic Thomas-Fermi equation as discussed by Ruffini et al. (2007b), by Rotondo et al. (2011e) and by Popov (2010). As we will see this work leads to the prediction of the existence of a critical electric field at the interface between the core and the crust of a neutron star.

In Ruffini et al. (2007b) and Rotondo et al. (2011e) it is described a degenerate system of  $N_n$  neutrons,  $N_p$  protons and  $N_e$  electrons constrained to a constant density distribution for the protons and it is solved the corresponding relativistic Thomas-Fermi equation and derived for the neutrons the distribution following the implementation of the beta equilibrium condition. This generalizes e.g. the works of Migdal et al. (1976, 1977); Popov (1971b,a) and Pieper and Greiner (1969); Greenberg and Greiner (1982) by eliminating the constraint  $N_p \approx A/2$ , clearly not valid for heavy nuclei, and enforcing self-consistently in a new relativistic Thomas-Fermi equation the condition of beta equilibrium. Using then the existence of scaling laws we have extended in Rotondo et al. (2011e) the results from heavy nuclei to the case of nuclear matter cores of stellar dimensions. In both these treatments we had assumed

the Fermi energy of the electrons  $E_e^F = 0$ . The aim of this article is to proceed with this dual approach and to consider first the case of compressed atoms and then, using the existence of scaling laws, the compressed nuclear matter cores of stellar dimensions with a positive value of their electron Fermi energies.

It is well known that Salpeter has been among the first to study the behavior of matter under extremely high pressures by considering a Wigner-Seitz cell of radius  $R_{WS}$  (Salpeter, 1961a). Salpeter assumed as a starting point the nucleus point-like and a uniform distribution of electrons within a Wigner-Seitz cell, and then considered corrections to the above model due to the inhomogeneity of electron distribution. The first correction corresponds to the inclusion of the lattice energy  $E_C = -(9N_p^2\alpha)/(10R_{WS})$ , which results from the point-like nucleus-electron Coulomb interaction and, from the electron-electron Coulomb interaction inside the cell of radius  $R_{WS}$ . The second correction is given by a series-expansion of the electron Fermi energy about the average electron density  $n_e$  of the uniform approximation. The electron density is then assumed equals to  $n_e[1 + \epsilon(r)]$  with  $\epsilon(r)$  considered as infinitesimal. The Coulomb potential energy is assumed to be the one of the point-like nucleus with the uniform distribution of electrons of density  $n_e$  thus the correction given by  $\epsilon(r)$  is neglected on the Coulomb potential. The electron distribution is then calculated at first-order by expanding the relativistic electron kinetic energy about its value given by the uniform approximation considering as infinitesimal the ratio  $eV/E_e^F$  between the Coulomb potential energy  $eV$  and the electron Fermi energy  $E_e^F = \sqrt{[cP_e^F(r)]^2 + m_e^2c^4} - m_e c^2 - eV$ . The inclusion of each additional Coulomb correction results in a decreasing of the pressure of the cell  $P_S$  by comparison to the uniform one.

It is quite difficult to assess the self-consistency of all the recalled different approximations adopted by Salpeter. In order to validate and also to see the possible limits of the Salpeter approach, we consider the relativistic generalization of the Feynman, Metropolis, Teller treatment (Feynman et al., 1949) which takes automatically and globally into account all electromagnetic and special relativistic contributions. We show explicitly how this new treatment leads in the case of atoms to electron distributions markedly different from the ones often adopted in the literature of constant electron density distributions. At the same time it allows to overcome some of the difficulties in current treatments.

Similarly the point-like description of the nucleus often adopted in literature is confirmed to be unacceptable in the framework of a relativistic treatment.

In Sec. A.2.2 we first recall the non-relativistic treatment of the compressed atom by Feynman, Metropolis and Teller. In Sec. A.2.3 we generalize that treatment to the relativistic regime by integrating the relativistic Thomas-Fermi equation, imposing also the condition of beta equilibrium. In Sec. A.2.4

we first compare the new treatment with the one corresponding to a uniform electron distribution often used in the literature and to the Salpeter treatment. We also compare and contrast the results of the relativistic and the non-relativistic treatment.

In Sec. A.2.5, using the same scaling laws adopted by Ruffini et al. (2007b) and Rotondo et al. (2011e) we turn to the case of nuclear matter cores of stellar dimensions with mass numbers  $A \approx (m_{\text{Planck}}/m_n)^3 \sim 10^{57}$  or  $M_{\text{core}} \sim M_{\odot}$  where  $m_n$  is the neutron mass and  $m_{\text{Planck}} = (\hbar c/G)^{1/2}$  is the Planck mass. Such a configuration presents global but not local charge neutrality. Analytic solutions for the ultra-relativistic limit are obtained. In particular we find:

1) explicit analytic expressions for the electrostatic field and the Coulomb potential energy,

2) an entire range of possible Fermi energies for the electrons between zero and a maximum value  $(E_e^F)_{\text{max}}$ , reached when  $R_{WS} = R_c$ , which can be expressed analytically,

3) the explicit analytic expression of the ratio between the proton number  $N_p$  and the mass number  $A$  when  $R_{WS} = R_c$ .

We turn then in Sec. A.2.6 to the study of the compressional energy of the nuclear matter cores of stellar dimensions for selected values of the electron Fermi energy. We show that the solution with  $E_e^F = 0$  presents the largest value of the electro-dynamical structure.

We finally summarize the conclusions in Sec. A.2.7.

## A.2.2. The Thomas-Fermi model for compressed atoms: the Feynman-Metropolis-Teller treatment

### The classical Thomas-Fermi model

The Thomas-Fermi model assumes that the electrons of an atom constitute a fully degenerate gas of fermions confined in a spherical region by the Coulomb potential of a point-like nucleus of charge  $+eN_p$ . Feynman, Metropolis and Teller have shown that this model can be used to derive the equation of state of matter at high pressures by considering a Thomas-Fermi model confined in a Wigner-Seitz cell of radius  $R_{WS}$  (Feynman et al., 1949).

We recall that the condition of equilibrium of the electrons in an atom, in the non-relativistic limit, is expressed by

$$\frac{(P_e^F)^2}{2m_e} - eV = E_e^F, \quad (\text{A.2.1})$$

where  $m_e$  is the electron mass,  $V$  is the electrostatic potential and  $E_e^F$  is their constant Fermi energy.

The electrostatic potential fulfills, for  $r > 0$ , the Poisson equation

$$\nabla^2 V = 4\pi e n_e, \quad (\text{A.2.2})$$

where the electron number density  $n_e$  is related to the Fermi momentum  $P_e^F$  by

$$n_e = \frac{(P_e^F)^3}{3\pi^2 \hbar^3}. \quad (\text{A.2.3})$$

For neutral atoms and ions  $n_e$  vanishes at the boundary so the electron Fermi energy is, respectively, zero or negative. In the case of compressed atoms  $n_e$  does not vanish at the boundary while the Coulomb potential energy  $eV$  does. Consequently  $E_e^F$  is positive.

Defining

$$eV(r) + E_e^F = e^2 N_p \frac{\phi(r)}{r}, \quad (\text{A.2.4})$$

and introducing the new dimensionless radial coordinate  $\eta$  as

$$r = b\eta \quad \text{with} \quad b = \frac{(3\pi)^{2/3}}{2^{7/3}} \frac{1}{N_p^{1/3}} \frac{\hbar^2}{m_e e^2} = \frac{\sigma}{N_p^{1/3}} r_{Bohr}, \quad (\text{A.2.5})$$

where  $\sigma = (3\pi)^{2/3}/2^{7/3} \approx 0.88$ ,  $r_{Bohr} = \hbar^2/(m_e e^2)$  is the Bohr radius, we obtain the following expression for the electron number density

$$n_e(\eta) = \frac{N_p}{4\pi b^3} \left( \frac{\phi(\eta)}{\eta} \right)^{3/2}, \quad (\text{A.2.6})$$

and then Eq. (A.2.2) can be written in the form

$$\frac{d^2 \phi(\eta)}{d\eta^2} = \frac{\phi(\eta)^{3/2}}{\eta^{1/2}}, \quad (\text{A.2.7})$$

which is the classic Thomas-Fermi equation. A first boundary condition for this equation follows from the point-like structure of the nucleus

$$\phi(0) = 1. \quad (\text{A.2.8})$$

A second boundary condition comes from the conservation of the number of electrons  $N_e = \int_0^{R_{WS}} 4\pi n_e(r) r^2 dr$

$$1 - \frac{N_e}{N_p} = \phi(\eta_0) - \eta_0 \phi'(\eta_0), \quad (\text{A.2.9})$$

where  $\eta_0 = R_{WS}/b$  defines the radius  $R_{WS}$  of the Wigner-Seitz cell. In the case

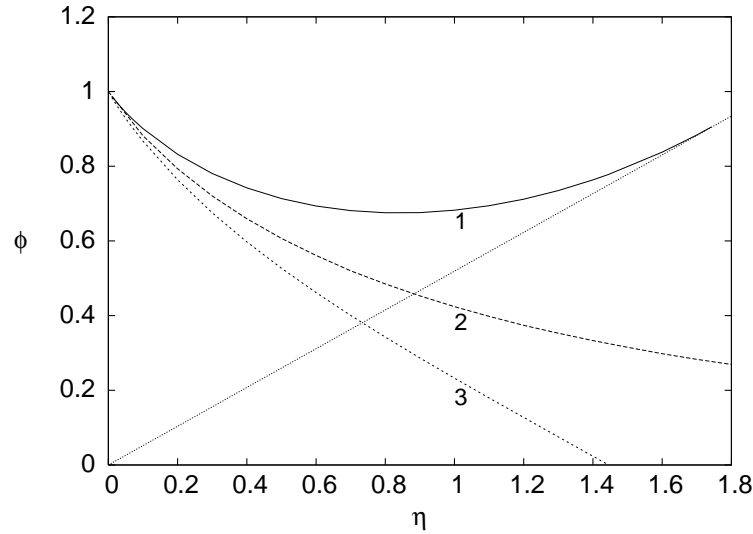


**Figure A.4:** Physically relevant solutions of the Thomas-Fermi Equation (A.2.7) with the boundary conditions (A.2.8) and (A.2.9). The curve 1 refers to a neutral compressed atom. The curve 2 refers to a neutral free atom. The curve 3 refers to a positive ion. The dotted straight line is the tangent to the curve 1 at the point  $(\eta_0, \phi(\eta_0))$  corresponding to overall charge neutrality (see Eq. (A.2.9)).

of compressed atoms  $N_e = N_p$  so the Coulomb potential energy  $eV$  vanishes at the boundary  $R_{WS}$ . As a result, using Eqs. (A.2.1) and (A.2.3), the Fermi energy of electrons satisfies the universal relation

$$\frac{\sigma r_{Bohr}}{e^2} \frac{E_e^F}{N_p^{4/3}} = \frac{\phi(\eta_0)}{\eta_0}, \quad (\text{A.2.10})$$

while the Wigner-Seitz cell radius  $R_{WS}$  satisfies the universal relation

$$\frac{R_{WS}}{\sigma r_{Bohr} N_p^{-1/3}} = \eta_0. \quad (\text{A.2.11})$$

Therefore in the classic treatment  $\eta_0$  can approach zero and consequently the range of the possible values of the Fermi energy extends from zero to infinity.

The results are summarized in Figs. A.4 and A.5.

### The Thomas-Fermi-Dirac model

Dirac has introduced modifications to the original Thomas-Fermi theory to include effects of the exchange interaction (Dirac, 1930). In this case the con-

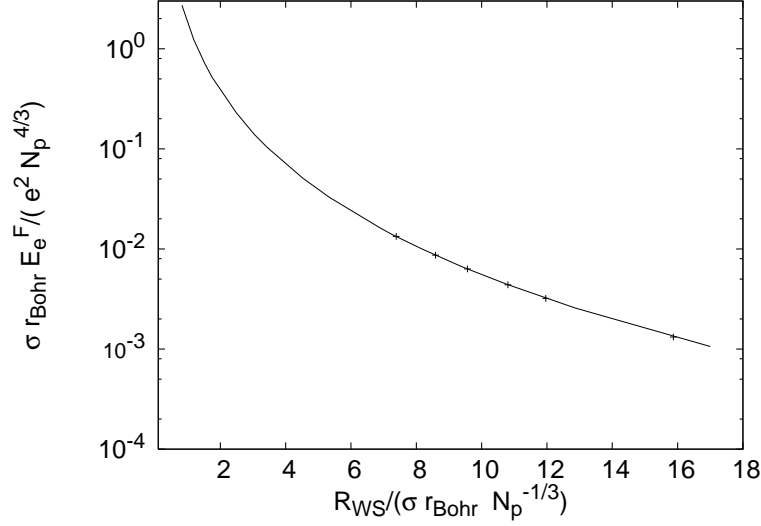


**Figure A.5.:** The electron Fermi energy  $E_e^F$ , in units of  $e^2 N_p^{4/3} / (\sigma r_{Bohr})$  is plotted as a function of the Wigner-Seitz cell radius  $R_{WS}$ , in units of  $\sigma r_{Bohr} N_p^{-1/3}$  (see Eqs. (A.2.10), (A.2.11)). Points refer to the numerical integrations of the Thomas-Fermi equation (A.2.7) performed originally by Feynman, Metropolis and Teller in Feynman et al. (1949).

dition of equilibrium of the electrons in the atom is generalized as follows

$$\frac{(P_e^F)^2}{2m_e} - eV - \frac{e^2}{\pi\hbar} P_e^F = E_e^F. \quad (\text{A.2.12})$$

The electron number density is now connected to the Coulomb potential energy by

$$n_e = \frac{1}{3\pi^5} \frac{1}{r_{Bohr}^3} \left[ 1 + \sqrt{1 + 2\pi^2 \frac{r_{Bohr}}{e^2} (eV + E_e^F)} \right]^3. \quad (\text{A.2.13})$$

Defining

$$\frac{1}{2\pi^2} \frac{e^2}{r_{Bohr}} + eV(r) + E_e^F = e^2 N_p \frac{\chi(r)}{r}, \quad (\text{A.2.14})$$

the Eq. (A.2.2) can be written in dimensionless form as

$$\frac{d^2\phi(\eta)}{d\eta^2} = \eta \left[ d + \left( \frac{\phi(\eta)}{\eta} \right)^{1/2} \right]^3, \quad (\text{A.2.15})$$

where  $d = (3/(32\pi^2))^{1/3}(1/N_p)^{2/3}$ . The boundary condition for Eq. (A.2.15) are  $\phi(0) = 1$  and  $\eta_0\phi'(\eta_0) = \phi(\eta_0)$ .

### A.2.3. The relativistic generalization of the Feynman-Metropolis-Teller treatment

#### The relativistic Thomas-Fermi model for atoms

In the relativistic generalization of the Thomas-Fermi equation the point-like approximation of the nucleus must be abandoned (Ferreirinho et al., 1980; Ruffini and Stella, 1981) since the relativistic equilibrium condition

$$E_e^F = \sqrt{(P_e^F c)^2 + m_e^2 c^4} - m_e c^2 - eV(r), \quad (\text{A.2.16})$$

which generalizes the Eq. (A.2.1), would lead to a non-integrable expression for the electron density near the origin. Consequently we adopt an extended nucleus. Traditionally the radius of an extended nucleus is given by the phenomenological relation  $R_c = r_0 A^{1/3}$  where  $A$  is the number of nucleons and  $r_0 = 1.2 \times 10^{-13}$  cm. Further it is possible to show from the extremization of the semi-empirical Weizsacker mass-formula that the relation between  $A$  and  $N_p$  is given by (see e.g. Segré (1977) and Ferreirinho et al. (1980))

$$N_p \approx \left[ \frac{2}{A} + \frac{2a_C}{a_A} \frac{1}{A^{1/3}} \right]^{-1} \approx \left[ \frac{2}{A} + \frac{3}{200} \frac{1}{A^{1/3}} \right]^{-1}, \quad (\text{A.2.17})$$

where  $a_C \approx 0.71$  MeV,  $a_A \approx 93.15$  MeV are the Coulomb and the asymmetry coefficients respectively. In the limit of small  $A$  Eq. (A.2.17) gives

$$N_p \approx \frac{A}{2}. \quad (\text{A.2.18})$$

In Rotondo et al. (2011e) we have relaxed the condition  $N_p \approx A/2$  adopted e.g. in Migdal et al. (1977) as well as the condition  $N_p \approx [2/A + 3/(200A^{1/3})]^{-1}$  adopted e.g. in Ferreirinho et al. (1980); Ruffini and Stella (1981) by imposing explicitly the beta decay equilibrium between neutron, protons and electrons.

In particular, following the previous treatments (see e.g. Rotondo et al. (2011e)), we have assumed a constant distribution of protons confined in a

radius  $R_c$  defined by

$$R_c = \Delta \frac{\hbar}{m_\pi c} N_p^{1/3}, \quad (\text{A.2.19})$$

where  $m_\pi$  is the pion mass and  $\Delta$  is a parameter such that  $\Delta \approx 1$  ( $\Delta < 1$ ) corresponds to nuclear (supranuclear) densities when applied to ordinary nuclei. Consequently, the proton density can be written as

$$n_p(r) = \frac{N_p}{\frac{4}{3}\pi R_c^3} \theta(R_c - r) = \frac{3}{4\pi} \frac{m_\pi^3 c^3}{\hbar^3} \frac{1}{\Delta^3} \theta(R_c - r), \quad (\text{A.2.20})$$

where  $\theta(x)$  is the Heaviside function which by definition is given by

$$\theta(x) = \begin{cases} 0, & x < 0, \\ 1, & x > 0. \end{cases} \quad (\text{A.2.21})$$

The electron density is given by

$$n_e(r) = \frac{(P_e^F)^3}{3\pi^2 \hbar^3} = \frac{1}{3\pi^2 \hbar^3 c^3} \left[ e^2 V^2(r) + 2m_e c^2 e V(r) \right]^{3/2}, \quad (\text{A.2.22})$$

where  $V$  is the Coulomb potential.

The overall Coulomb potential satisfies the Poisson equation

$$\nabla^2 V(r) = -4\pi e [n_p(r) - n_e(r)], \quad (\text{A.2.23})$$

with the boundary conditions  $V(\infty) = 0$  (due to global charge neutrality) and finiteness of  $V(0)$ .

Using Eqs. (A.2.4), (A.2.5) and replacing the particle densities (A.2.20) and (A.2.22) into the Poisson equation (A.2.23) we obtain the relativistic Thomas-Fermi equation

$$\frac{d^2 \phi(\eta)}{d\eta^2} = -\frac{3\eta}{\eta_c^3} \theta(\eta_c - \eta) + \frac{\phi^{3/2}}{\eta^{1/2}} \left[ 1 + \left( \frac{N_p}{N_p^{crit}} \right)^{4/3} \frac{\phi}{\eta} \right]^{3/2}, \quad (\text{A.2.24})$$

where  $\phi(0) = 0$ ,  $\phi(\infty) = 0$  and  $\eta_c = R_c/b$ . The critical number of protons  $N_p^{crit}$  is defined by

$$N_p^{crit} = \sqrt{\frac{3\pi}{4}} \alpha^{-3/2}, \quad (\text{A.2.25})$$

where, as usual,  $\alpha = e^2/(\hbar c)$ .

It is interesting that by introducing the new dimensionless variable

$$x = \frac{r}{\lambda_\pi} = \frac{b}{\lambda_\pi} \eta, \quad (\text{A.2.26})$$

and the function

$$\chi = \alpha N_p \phi, \quad (\text{A.2.27})$$

where  $\lambda_\pi = \hbar/(m_\pi c)$ , Eq. (A.2.24) assumes a canonical form, the master relativistic Thomas-Fermi equation (see Ruffini (2008a))

$$\frac{1}{3x} \frac{d^2 \chi(x)}{dx^2} = -\frac{\alpha}{\Delta^3} \theta(x_c - x) + \frac{4\alpha}{9\pi} \left[ \frac{\chi^2(x)}{x^2} + 2 \frac{m_e \chi}{m_\pi x} \right]^{3/2}, \quad (\text{A.2.28})$$

where  $x_c = R_c/\lambda_\pi$  with the boundary conditions  $\chi(0) = 0$ ,  $\chi(\infty) = 0$ . The neutron density  $n_n(r)$ , related to the neutron Fermi momentum  $P_n^F = (3\pi^2 \hbar^3 n_n)^{1/3}$ , is determined, as in the previous case Rotondo et al. (2011e), by imposing the condition of beta equilibrium

$$\begin{aligned} E_n^F &= \sqrt{(P_n^F c)^2 + m_n^2 c^4} - m_n c^2 \\ &= \sqrt{(P_p^F c)^2 + m_p^2 c^4} - m_p c^2 + eV(r), \end{aligned} \quad (\text{A.2.29})$$

which in turn is related to the proton density  $n_p$  and the electron density by Eqs. (A.2.22), (A.2.23). Integrating numerically these equations we have obtained a new generalized relation between  $A$  and  $N_p$  for any value of  $A$ . In the limit of small  $A$  this result agrees with the phenomenological relations given by Eqs. (A.2.17, A.2.18), as is clearly shown in Fig. (A.6).

### The relativistic Thomas-Fermi model for compressed atoms

We turn now to the case of compressed atoms in which the electron Fermi energy is positive. The relativistic generalization of the equilibrium condition (A.2.1) now reads

$$E_e^F = \sqrt{(P_e^F c)^2 + m_e^2 c^4} - m_e c^2 - eV(r) > 0. \quad (\text{A.2.30})$$

Adopting an extended-nucleus with a radius given by Eq. (A.2.19) and a proton density given by Eq. (A.2.20) the Poisson equation (A.2.23), with the fol-

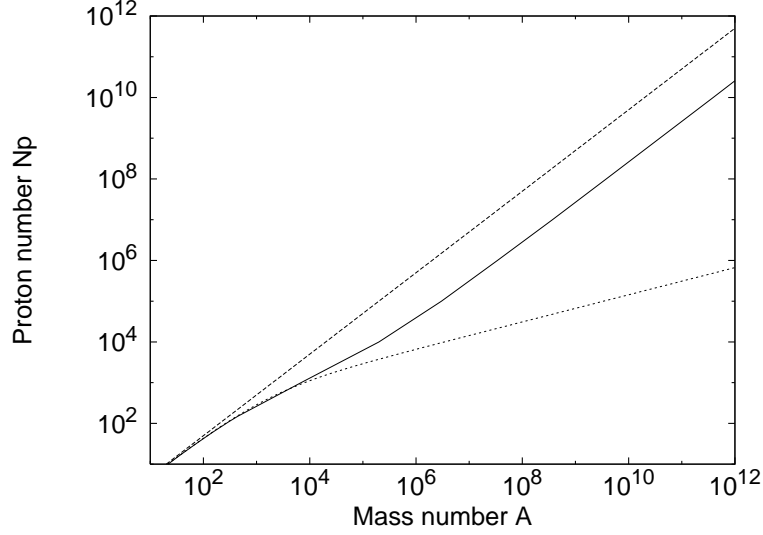


**Figure A.6.:** The  $A$ - $N_p$  relation at nuclear density (solid line) obtained from first principles compared with the phenomenological expressions given by  $N_p \approx A/2$  (dashed line) and Eq. (A.2.17) (dotted line). The asymptotic value, for  $A \rightarrow (m_{\text{Planck}}/m_n)^3$ , is  $N_p \approx 0.0046A$ .

lowing electron density

$$n_e(r) = \frac{(P_e^F)^3}{3\pi^2\hbar^3} = \frac{1}{3\pi^2\hbar^3 c^3} \left[ e^2 \hat{V}^2(r) + 2m_e c^2 e \hat{V}(r) \right]^{3/2}, \quad (\text{A.2.31})$$

gives again the master relativistic Thomas-Fermi equation (A.2.28) where  $\chi/r = e\hat{V}(r)/(c\hbar)$  and  $e\hat{V} = eV + E_e^F$ .

In this case Eq. (A.2.28) has to be integrated with the boundary conditions  $\chi(0) = 0$ ,  $\chi(x_{WS}) = x_{WS}\chi'(x_{WS})$ ,  $x_{WS} = R_{WS}/\lambda_\pi$ . Using Eqs. (A.2.4), (A.2.26) and (A.2.27) we obtain the electron Fermi energy in the form

$$E_e^F = m_\pi c^2 \frac{\chi(x_{WS})}{x_{WS}}. \quad (\text{A.2.32})$$

The neutron density  $n_n(r)$ , related to the neutron Fermi momentum  $P_n^F = (3\pi^2\hbar^3 n_n)^{1/3}$ , is determined by imposing the condition of beta equilibrium

$$\begin{aligned} E_n^F &= \sqrt{(P_n^F c)^2 + m_n^2 c^4} - m_n c^2 \\ &= \sqrt{(P_p^F c)^2 + m_p^2 c^4} - m_p c^2 + eV(r) + E_e^F. \end{aligned} \quad (\text{A.2.33})$$

Using this approach, it is then possible to determine the beta equilibrium nuclide as a function of the density of the system. Infact, electrons and pro-

tons can be converted to neutrons in inverse beta decay  $p + e^- \rightarrow n + \nu_e$  if the condition  $E_n^F < \sqrt{(P_p^F c)^2 + m_p^2 c^4} - m_p c^2 + eV(r) + E_e^F$  holds. The condition of equilibrium (A.2.33) is crucial, for example, in the construction of a self-consistent equation of state of high energy density matter present in white dwarfs and neutron star crusts. In the case of zero electron Fermi energy the generalized  $A - N_p$  relation of Fig. (A.6) is obtained.

### The relativistic Thomas-Fermi-Dirac model for compressed atoms

We now take into account the exchange corrections to the relativistic Thomas-Fermi equation (A.2.28). In this case we have (see Migdal et al. (1977) for instance)

$$E_e^F = \sqrt{(cP_e^F)^2 + m_e^2 c^4} - m_e c^2 - eV - \frac{\alpha}{\pi} cP_e^F = \text{constant}. \quad (\text{A.2.34})$$

Introducing the function  $\chi(r)$  as before

$$E_e^F + eV = e\hat{V} = \hbar c \frac{\chi}{r}, \quad (\text{A.2.35})$$

we obtain the electron number density

$$n_e = \frac{1}{3\pi^2 \hbar^3 c^3} \left\{ \gamma (m_e c^2 + e\hat{V}) + [(e\hat{V})^2 + 2m_e c^2 e\hat{V}]^{1/2} \right. \\ \left. \times \left[ \frac{(1 + \gamma^2)(m_e c^2 + e\hat{V})^2 - m_e^2 c^4}{(m_e c^2 + e\hat{V})^2 - m_e^2 c^4} \right]^{1/2} \right\}^3, \quad (\text{A.2.36})$$

where  $\gamma = (\alpha/\pi)/(1 - \alpha^2/\pi^2)$ .

If we take the approximation  $1 + \gamma^2 \approx 1$  the above equation becomes

$$n_e = \frac{1}{3\pi^2 \hbar^3 c^3} \left\{ \gamma (m_e c^2 + e\hat{V}) + [(e\hat{V})^2 + 2m_e c^2 e\hat{V}]^{1/2} \right\}^3. \quad (\text{A.2.37})$$

The second term on the right-hand-side of Eq. (A.2.37) has the same form of the electron density given by the relativistic Thomas-Fermi approach without the exchange correction (A.2.31) and therefore the first term shows the explicit contribution of the exchange term to the electron density.

Using the full expression of the electron density given by Eq. (A.2.36) we

obtain the relativistic Thomas-Fermi-Dirac equation

$$\begin{aligned} \frac{1}{3x} \frac{d^2\chi(x)}{dx^2} = & -\frac{\alpha}{\Delta^3} \theta(x_c - x) + \frac{4\alpha}{9\pi} \left\{ \gamma \left( \frac{m_e}{m_\pi} + \frac{\chi}{x} \right) + \left[ \left( \frac{\chi}{x} \right)^2 + 2 \frac{m_e}{m_\pi} \frac{\chi}{x} \right]^{1/2} \right. \\ & \times \left. \left[ \frac{(1 + \gamma^2)(m_e/m_\pi + \chi/x)^2 - (m_e/m_\pi)^2}{(m_e/m_\pi + \chi/x)^2 - (m_e/m_\pi)^2} \right]^{1/2} \right\}^3, \end{aligned} \quad (\text{A.2.38})$$

which by applying the approximation  $1 + \gamma^2 \approx 1$  becomes

$$\frac{1}{3x} \frac{d^2\chi(x)}{dx^2} = -\frac{\alpha}{\Delta^3} \theta(x_c - x) + \frac{4\alpha}{9\pi} \left\{ \gamma \left( \frac{m_e}{m_\pi} + \frac{\chi}{x} \right) + \left[ \left( \frac{\chi}{x} \right)^2 + 2 \frac{m_e}{m_\pi} \frac{\chi}{x} \right]^{1/2} \right\}^3. \quad (\text{A.2.39})$$

The boundary conditions for Eq. (A.2.38) are  $\chi(0) = 0$  and  $\chi(x_{WS}) = x_{WS}\chi'(x_{WS})$ . The neutron density can be obtained as before by using the beta equilibrium condition (A.2.33) with the electron Fermi energy given by Eq. (A.2.34).

In Fig. A.7 we show the results of the numerical integration of the relativistic Thomas-Fermi equation (A.2.28) and of the relativistic Thomas-Fermi-Dirac equation (A.2.38) for helium, carbon and iron. In particular, we show the electron Fermi energy multiplied by  $N_p^{-4/3}$  as a function of the ratio  $R_{WS}/R_c$  between the Wigner-Seitz cell radius  $R_{WS}$  and the nucleus radius  $R_c$  given by Eq. (A.2.19).

The effects of the exchange term are appreciable only in the low density (low compression) region, i.e. when  $R_{WS} \gg R_c$  (see Fig. A.7). We can then conclude in total generality that the correction given by the Thomas-Fermi-Dirac exchange term is, small in the non-relativistic low compression (low density) regime, and negligible in the relativistic high compression (high density) regime.

#### A.2.4. Comparison and contrast with approximate treatments

There exists in the literature a variety of semi-qualitative approximations adopted in order to describe the electron component of a compressed atom (see e.g. Bürvenich et al. (2007) for applications of the uniform approximation and e.g. Chabrier and Potekhin (1998a); Potekhin et al. (2009); Douchin and Haensel (2001); Haensel and Zdunik (1990a,b), for applications of the Salpeter approximate treatment).

We shall see how the relativistic treatment of the Thomas-Fermi equation affects the current analysis of compressed atoms in the literature by introducing qualitative and quantitative differences which deserve attention.

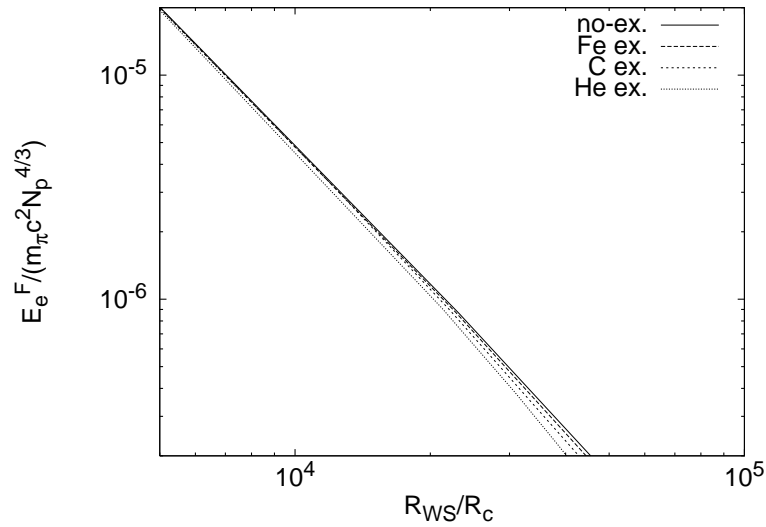


**Figure A.7.:** The electron Fermi energy in units of  $m_{\pi}c^2N_p^{4/3}$  is plotted for helium, carbon and iron, as a function of the ratio  $R_{WS}/R_c$  in the relativistic Feynman-Metropolis-Teller (FMT) treatment with and without the exchange effects. Here  $R_{WS}$  denotes the Wigner-Seitz cell radius and  $R_c$  is the nucleus radius as given by Eq. (A.2.19). It is clear that the exchange terms are appreciable only in the low density region and are negligible as  $R_{WS} \rightarrow R_c$ .

### Relativistic FMT treatment vs. relativistic uniform approximation

One of the most used approximations in the treatment of the electron distribution in compressed atoms is the one in which, for a given nuclear charge  $+eN_p$ , the Wigner-Seitz cell radius  $R_{WS}$  is defined by

$$N_p = \frac{4\pi}{3} R_{WS}^3 n_e, \quad (\text{A.2.40})$$

where  $n_e = (P_e^F)^3 / (3\pi^2 \hbar^3)$ . The Eq. (A.2.40) ensures the global neutrality of the Wigner-Seitz cell of radius  $R_{WS}$  assuming a uniform distribution of electrons inside the cell.

We shall first compare the Feynman-Metropolis-Teller treatment, previously introduced, with the uniform approximation for the electron distribution. In view of the results of the preceding section, hereafter we shall consider the non-relativistic and the relativistic formulation of the Feynman-Metropolis-Teller treatment with no Thomas-Fermi-Dirac exchange correction.

In Fig. A.8 we have plotted the electron number density obtained from Eq. (A.2.31) where the Coulomb potential is related to the function  $\chi$ , which is obtained from numerical integration of the relativistic Thomas-Fermi equation (A.2.28) for different compressions for helium and iron. We have normalized the electron density to the average electron number density  $n_0 = 3N_e / (4\pi R_{WS}^3) = 3N_p / (4\pi R_{WS}^3)$  as given by Eq. (A.2.40).

We can see in Fig. A.8 how our treatment, based on the numerical integration of the relativistic Thomas-Fermi equation (A.2.28) and imposing the condition of beta equilibrium (A.2.33), leads to electron density distributions markedly different from the constant electron density approximation.

From Eqs. (A.2.30), (A.2.40) and taking into account the global neutrality condition of the Wigner-Seitz cell  $eV(R_{WS}) = 0$ , the electron Fermi energy in the uniform approximation can be written as

$$E_e^F \simeq \left[ -\frac{m_e}{m_\pi} + \sqrt{\left(\frac{m_e}{m_\pi}\right)^2 + \left(\frac{9\pi}{4}\right)^{2/3} \frac{N_p^{2/3}}{x_{WS}^2}} \right] m_\pi c^2. \quad (\text{A.2.41})$$

We show in Fig. A.9 the electron Fermi energy as a function of the average electron density  $n_0 = 3N_e / (4\pi R_{WS}^3) = 3N_p / (4\pi R_{WS}^3)$  in units of the nuclear density  $n_{nuc} = 3A / (4\pi \Delta^3 N_p \lambda_\pi^3)$ . For selected compositions we show the results for the relativistic Feynman-Metropolis-Teller treatment, based on the numerical integration of the relativistic Thomas-Fermi equation (A.2.28), and for the relativistic uniform approximation.

As clearly shown in Fig. A.8 and summarized in Fig. A.9 the relativistic treatment leads to results strongly dependent at low compression from the

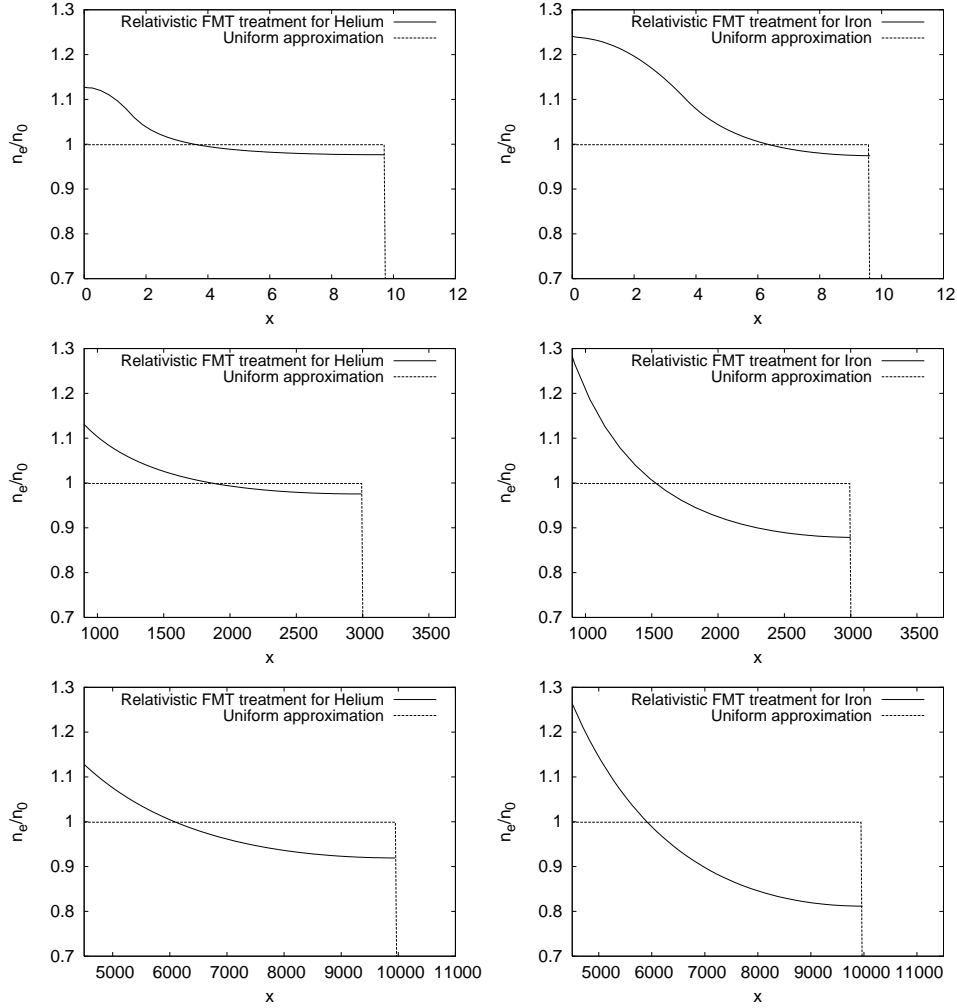


**Figure A.8.:** The electron number density  $n_e$  in units of the average electron number density  $n_0 = 3N_e/(4\pi R_{WS}^3)$  is plotted as a function of the dimensionless radial coordinate  $x = r/\lambda_\pi$  for the selected compressions  $x_{WS} = 9.7$  (upper panels),  $x_{WS} = 3 \times 10^3$  (middle panels) and  $x_{WS} = 10^4$  (bottom panels), in both the relativistic Feynman, Metropolis, Teller approach and the uniform approximation respectively for helium (panels on the left) and iron (panels on the right).

nuclear composition. The corresponding value of the electron Fermi energy derived from a uniform approximation overevaluates the true electron Fermi energy (see Fig. A.9). In the limit of high compression the relativistic curves asymptotically approach the uniform one (see also Fig. A.8).

The uniform approximation becomes exact in the limit when the electron Fermi energy acquires its maximum value as given by

$$(E_e^F)_{max} \simeq \left[ -\frac{m_e}{m_\pi} + \sqrt{\left(\frac{m_e}{m_\pi}\right)^2 + \left(\frac{3\pi^2}{2}\right)^{2/3} \left(\frac{N_p}{A}\right)^{2/3}} \right] m_\pi c^2, \quad (\text{A.2.42})$$

which is attained when  $R_{WS}$  coincides with the nuclear radius  $R_c$ . Here, the maximum electron Fermi energy (A.2.42) is obtained by replacing in Eq. (A.2.41) the value of the normalized Wigner-Seitz cell radius  $x_{WS} = x_c = R_c/\lambda_\pi \approx [(3/2)\pi]^{1/3} A^{1/3}$ .

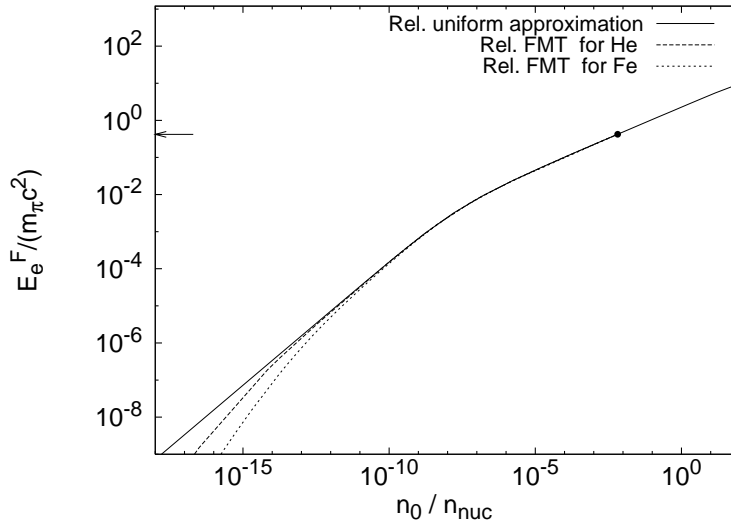


**Figure A.9.:** The electron Fermi energy  $E_e^F$  in units of the pion rest energy is plotted as a function of the average electron density  $n_0 = 3N_e/(4\pi R_{WS}^3)$  in units of the nuclear density  $n_{nuc} = 3A/(4\pi\Delta^3 N_p \lambda_\pi^3)$  for a uniform approximation (solid line), compared and contrasted to the ones obtained considering the relativistic Feynman, Metropolis, Teller approach. The arrow and the dot indicate the value of the maximum electron Fermi energy as given by Eq. (A.2.42), consistent with the finite size of the nucleus.

### Relativistic FMT treatment vs. Salpeter approximate treatment

Corrections to the uniform distribution were also studied by Salpeter (1961a) and his approximations are largely applied in physics (see e.g. Chabrier and

Potekhin (1998a); Potekhin et al. (2009)) and astrophysics (see e.g. Douchin and Haensel (2001); Haensel and Zdunik (1990a,b)).

Keeping the point-like nucleus assumption, Salpeter (1961a) studied the corrections to the above models due to the inhomogeneity of the electron distribution inside the Wigner-Seitz cell. He expressed an analytic formula for the total energy of a Wigner-Seitz cell based on Coulomb corrections to the uniform distribution of electrons. The first correction corresponds to the inclusion of the lattice energy  $E_C = -(9N_p^2\alpha)/(10R_{WS})$ , which results from the point-like nucleus-electron Coulomb interaction and, from the electron-electron Coulomb interaction inside the cell of radius  $R_{WS}$ . The second correction is given by a series-expansion of the electron Fermi energy about the average electron density  $n_e$  given by Eq. (A.2.40) the uniform approximation  $n_e = 3N_p/(4\pi R_{WS}^3)$ . The electron density is then assumed equals to  $n_e[1 + \epsilon(r)]$  with  $\epsilon(r)$  considered as infinitesimal. The Coulomb potential energy is assumed to be the one of the point-like nucleus with the uniform distribution of electrons of density  $n_e$ , thus the correction given by  $\epsilon(r)$  is neglected on the Coulomb potential. The electron distribution is then calculated at first-order by expanding the relativistic electron kinetic energy

$$\begin{aligned}\epsilon_k &= \sqrt{[cP_e^F(r)]^2 + m_e^2c^4} - m_e c^2 \\ &= \sqrt{(3\pi^2 n_e)^{2/3}[1 + \epsilon(r)]^{2/3} + m_e^2c^4} - m_e c^2,\end{aligned}\quad (\text{A.2.43})$$

about its value given by the uniform approximation

$$\epsilon_k^{\text{unif}} = \sqrt{(3\pi^2 n_e)^{2/3} + m_e^2c^4} - m_e c^2,\quad (\text{A.2.44})$$

considering as infinitesimal the ratio  $eV/E_e^F$  between the Coulomb potential energy  $eV$  and the electron Fermi energy  $E_e^F = \sqrt{[cP_e^F(r)]^2 + m_e^2c^4} - m_e c^2 - eV$ .

The effect of the Dirac electron-exchange correction (Dirac, 1930) on the equation of state was also considered by Salpeter (1961a). However, adopting the general approach of Migdal et al. (1977), these effects are negligible in the relativistic regime (see Subsec. A.2.3).

The inclusion of each additional Coulomb correction results in a decreasing of the pressure of the cell  $P_S$ . However, despite to be very interesting in identifying piecewise contributions to the total pressure, the validity of the Salpeter approach needs a verification by a more general treatment. For instance, the failure of the Salpeter formulas can be seen at densities of the order of  $\sim 10^2 - 10^3 \text{ g cm}^{-3}$  for nuclei with large  $N_p$ , as in the case of iron, where the pressure becomes negative (see Table (A.1)). Therefore, the problem of solving the relativistic Thomas-Fermi equation within the Feynman, Metropolis, Teller approach becomes a necessity, since this approach gives all the possible

**Table A.1.:** Pressure for iron as a function of the density  $\rho$  in the uniform approximation ( $P$ ), in the Salpeter approximation ( $P_S$ ) and in the relativistic Feynman-Metropolis-Teller approach ( $P_{FMTrel}$ ). Here  $x_S = P_{e,S}^F / (m_e c)$ ,  $x_{FMTrel} = P_e^F / (m_e c)$  are respectively the normalized Salpeter Fermi momentum and the relativistic Feynman-Metropolis-Teller Fermi momentum.

$\rho$ (g/cm <sup>3</sup> )	$x_S$	$x_{FMTrel}$	$P$ (bar)	$P_S$ (bar)	$P_{FMTrel}$ (bar)
$2.63 \times 10^2$	0.05	0.0400	$2.9907 \times 10^{10}$	$-1.8800 \times 10^8$	$9.9100 \times 10^9$
$2.10 \times 10^3$	0.10	0.0857	$9.5458 \times 10^{11}$	$4.4590 \times 10^{11}$	$5.4840 \times 10^{11}$
$1.68 \times 10^4$	0.20	0.1893	$3.0227 \times 10^{13}$	$2.2090 \times 10^{13}$	$2.2971 \times 10^{13}$
$5.66 \times 10^4$	0.30	0.2888	$2.2568 \times 10^{14}$	$1.8456 \times 10^{14}$	$1.8710 \times 10^{14}$
$1.35 \times 10^5$	0.40	0.3887	$9.2964 \times 10^{14}$	$8.0010 \times 10^{14}$	$8.0790 \times 10^{14}$
$2.63 \times 10^5$	0.50	0.4876	$2.7598 \times 10^{15}$	$2.4400 \times 10^{15}$	$2.4400 \times 10^{15}$
$4.53 \times 10^5$	0.60	0.5921	$6.6536 \times 10^{15}$	$6.0040 \times 10^{15}$	$6.0678 \times 10^{15}$
$7.19 \times 10^5$	0.70	0.6820	$1.3890 \times 10^{16}$	$1.2693 \times 10^{16}$	$1.2810 \times 10^{16}$
$1.08 \times 10^6$	0.80	0.7888	$2.6097 \times 10^{16}$	$2.4060 \times 10^{16}$	$2.4442 \times 10^{16}$
$2.10 \times 10^6$	1.00	0.9853	$7.3639 \times 10^{16}$	$6.8647 \times 10^{16}$	$6.8786 \times 10^{16}$
$3.63 \times 10^6$	1.20	1.1833	$1.6902 \times 10^{17}$	$1.5900 \times 10^{17}$	$1.5900 \times 10^{17}$
$5.77 \times 10^6$	1.40	1.3827	$3.3708 \times 10^{17}$	$3.1844 \times 10^{17}$	$3.1898 \times 10^{17}$
$8.62 \times 10^6$	1.6	1.5810	$6.0754 \times 10^{17}$	$5.7588 \times 10^{17}$	$5.7620 \times 10^{17}$
$1.23 \times 10^7$	1.80	1.7790	$1.0148 \times 10^{18}$	$9.6522 \times 10^{17}$	$9.6592 \times 10^{17}$
$1.68 \times 10^7$	2.0	1.9770	$1.5981 \times 10^{18}$	$1.5213 \times 10^{18}$	$1.5182 \times 10^{18}$
$3.27 \times 10^7$	2.50	2.4670	$4.1247 \times 10^{18}$	$3.9375 \times 10^{18}$	$3.9101 \times 10^{18}$
$5.66 \times 10^7$	3.00	2.965	$8.8468 \times 10^{18}$	$8.4593 \times 10^{18}$	$8.4262 \times 10^{18}$
$1.35 \times 10^8$	4.00	3.956	$2.9013 \times 10^{19}$	$2.7829 \times 10^{19}$	$2.7764 \times 10^{19}$
$2.63 \times 10^8$	5.00	4.939	$7.2160 \times 10^{19}$	$6.9166 \times 10^{19}$	$6.9062 \times 10^{19}$
$8.85 \times 10^8$	7.50	7.423	$3.7254 \times 10^{20}$	$3.5700 \times 10^{20}$	$3.5700 \times 10^{20}$

Coulomb and relativistic contributions automatically and correctly.

### Relativistic FMT treatment vs. non-relativistic FMT treatment

We now compare and contrast the Fermi energy, given by Eq. (A.2.32), of a compressed atom in the non-relativistic and the relativistic limit (see Fig. A.10).

There are major differences:

- 1) The electron Fermi energy in the relativistic treatment is strongly dependent on the nuclear composition, while the non-relativistic treatment presents a universal behavior in the units of Fig. A.10. In the limit of low densities the relativistic curves approach the universal non-relativistic curve. In the non-relativistic treatment the ratio  $E_e^F / (m_\pi c^2 N_p^{4/3})$  does not depend on the num-

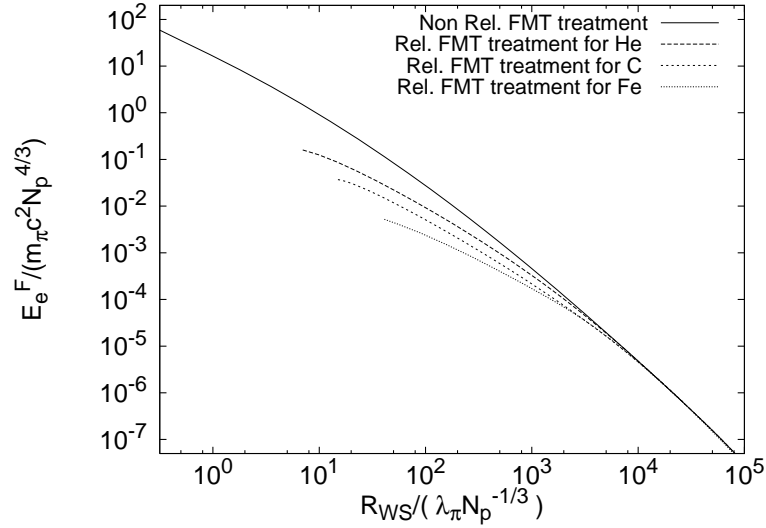


**Figure A.10.:** The electron Fermi energies in units of  $m_{\pi}c^2N_p^{4/3}$  for helium, carbon and iron are plotted as a function of the ratio  $R_{WS}/(\lambda_{\pi}N_p^{-1/3})$  respectively in the non-relativistic and in the relativistic Feynman-Metropolis-Teller (FMT) treatment. The dimensionless quantities have been chosen in order to obtain an universal curve in the non relativistic treatment following Eqs. (A.2.10) and (A.2.11). The relativistic treatment leads to results of the electron Fermi energy dependent on the nuclear composition and systematically smaller than the non-relativistic ones. The electron Fermi energy can attain arbitrary large values, in the non relativistic treatment, as the point-like nucleus is approached.

ber of protons  $N_p$  if the Wigner-Seitz cell radius  $R_{WS}$  is multiplied by  $N_p^{1/3}$  (see Eqs. (A.2.10), (A.2.11)). This universality is lost in the relativistic treatment since there is no way to eliminate the dependence of the electron Fermi energy on the nuclear composition (see Eq. (A.2.28)).

2) The relativistic treatment leads to values of the electron Fermi energy consistently smaller than the ones of the non-relativistic treatment.

3) While in the non-relativistic treatment the electron Fermi energy can reach, by compression, infinite values as  $R_{WS} \rightarrow 0$ , in the relativistic treatment it reaches a perfectly finite value given by Eq. (A.2.42) attained when  $R_{WS}$  coincides with the nuclear radius  $R_c$ .

It is clear then, from above considerations, the relativistic treatment of the Thomas-Fermi equation introduces significant differences from the current approximations in the literature: a) the uniform electron distribution (Bürvenich et al., 2007), b) the approximate perturbative solutions departing from the uniform distribution (Salpeter, 1961a) and c) the non-relativistic treatment (Feynman et al., 1949). We have recently applied these results of the relativistic Feynman, Metropolis, Teller treatment of a compressed atom to the study of white dwarfs and their consequences on the determination of their masses, radii and critical mass (Rotondo et al., 2011b).

### A.2.5. Application to nuclear matter cores of stellar dimensions

We turn now to nuclear matter cores of stellar dimensions of  $A \simeq (m_{\text{Planck}}/m_n)^3 \sim 10^{57}$  or  $M_{\text{core}} \sim M_{\odot}$ .

Following the treatment presented in Rotondo et al. (2011e), we use the existence of scaling laws and proceed to the ultra-relativistic limit of Eqs. (A.2.20), (A.2.28), (A.2.31), (A.2.33). For positive values of the electron Fermi energy  $E_e^F$ , we introduce the new function  $\phi = 4^{1/3}(9\pi)^{-1/3}\chi\Delta/x$  and the new variable  $\hat{x} = kx$  where  $k = (12/\pi)^{1/6}\sqrt{\alpha}\Delta^{-1}$ , as well as the variable  $\xi = \hat{x} - \hat{x}_c$  in order to describe better the region around the core radius.

Eq. (A.2.28) becomes

$$\frac{d^2\hat{\phi}(\xi)}{d\xi^2} = -\theta(-\xi) + \hat{\phi}(\xi)^3, \quad (\text{A.2.45})$$

where  $\hat{\phi}(\xi) = \phi(\xi + \hat{x}_c)$  and the curvature term  $2\hat{\phi}'(\xi)/(\xi + \hat{x}_c)$  has been neglected.

The Coulomb potential energy is given by

$$eV(\xi) = \left(\frac{9\pi}{4}\right)^{1/3} \frac{1}{\Delta} m_{\pi} c^2 \hat{\phi}(\xi) - E_e^F, \quad (\text{A.2.46})$$

corresponding to the electric field

$$E(\xi) = - \left( \frac{3^5 \pi}{4} \right)^{1/6} \frac{\sqrt{\alpha} m_\pi^2 c^3}{\Delta^2 e \hbar} \hat{\phi}'(\xi), \quad (\text{A.2.47})$$

and the electron number-density

$$n_e(\xi) = \frac{1}{3\pi^2 \hbar^3 c^3} \left( \frac{9\pi}{4} \right) \frac{1}{\Delta^3} (m_\pi c^2)^3 \hat{\phi}^3(\xi). \quad (\text{A.2.48})$$

In the core center we must have  $n_e = n_p$ . From Eqs. (A.2.20) and (A.2.48) we then have that, for  $\xi = -\hat{x}_c$ ,  $\hat{\phi}(-\hat{x}_c) = 1$ .

In order to consider a compressed nuclear density core of stellar dimensions, we then introduce a Wigner-Seitz cell determining the outer boundary of the electron distribution which, in the new radial coordinate  $\xi$  is characterized by  $\xi^{WS}$ . In view of the global charge neutrality of the system the electric field goes to zero at  $\xi = \xi^{WS}$ . This implies, from Eq. (A.2.47),  $\hat{\phi}'(\xi^{WS}) = 0$ .

We now turn to the determination of the Fermi energy of the electrons in this compressed core. The function  $\hat{\phi}$  and its first derivative  $\hat{\phi}'$  must be continuous at the surface  $\xi = 0$  of the nuclear density core.

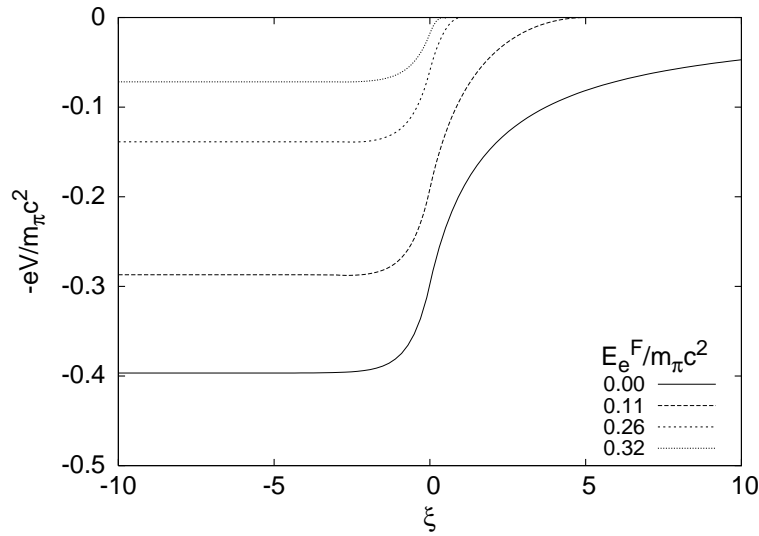


**Figure A.11.:** The electron Coulomb potential energies in units of the pion rest energy in a nuclear matter core of stellar dimensions with  $A \simeq 10^{57}$  or  $M_{core} \sim M_\odot$  and  $R_c \approx 10^6$  cm, are plotted as a function of the dimensionless variable  $\xi$ , for different values of the electron Fermi energy also in units of the pion rest energy. The solid line corresponds to the case of null electron Fermi energy. By increasing the value of the electron Fermi energy the electron Coulomb potential energy depth is reduced.

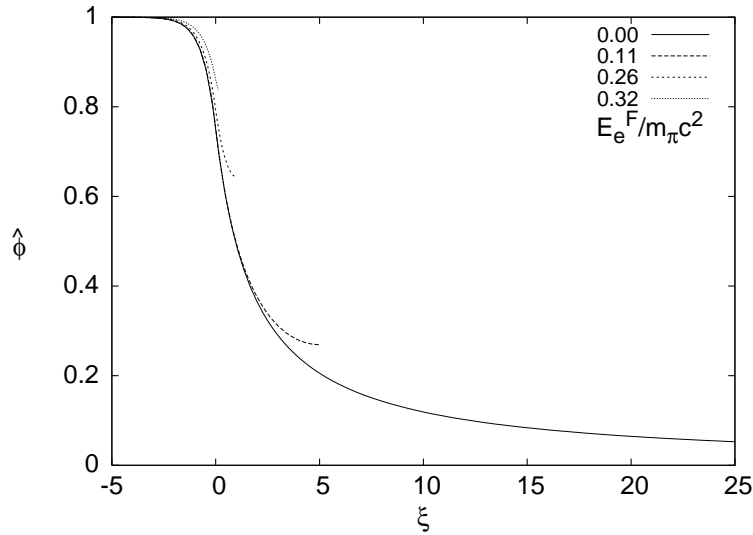


**Figure A.12.:** Solutions of the ultra-relativistic Thomas-Fermi equation (A.2.45) for different values of the Wigner-Seitz cell radius  $R_{WS}$  and correspondingly of the electron Fermi energy in units of the pion rest energy as in Fig. A.11, near the core surface. The solid line corresponds to the case of null electron Fermi energy.

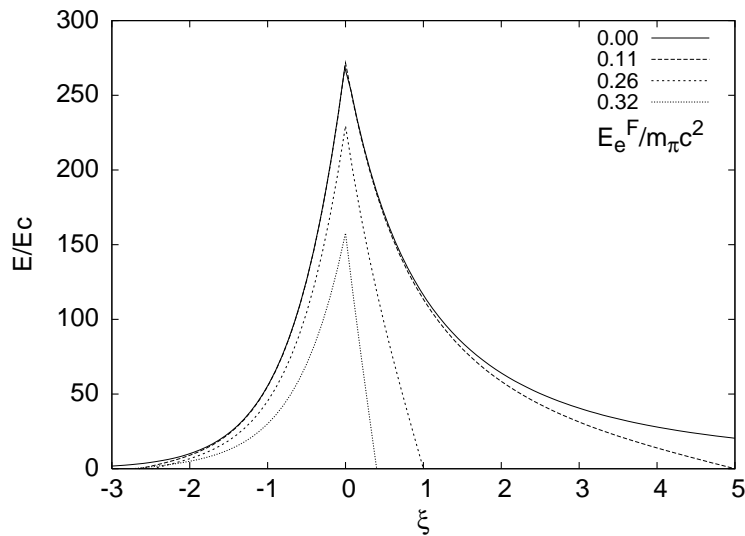


**Figure A.13.:** The electric field in units of the critical field for vacuum polarization  $E_c = m_e^2 c^3 / (e \hbar)$  is plotted as a function of the coordinate  $\xi$ , for different values of the electron Fermi energy in units of the pion rest energy. The solid line corresponds to the case of null electron Fermi energy. To an increase of the value of the electron Fermi energy it is found a reduction of the peak of the electric field.

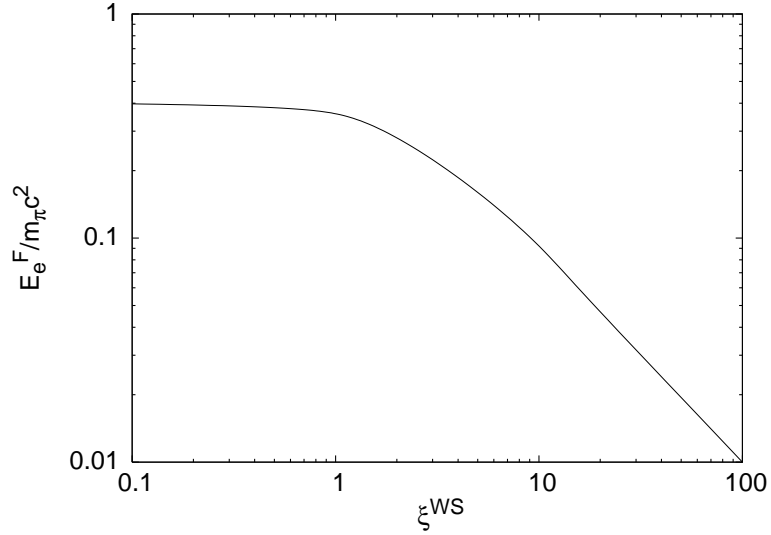


**Figure A.14.:** The Fermi energy of electrons in units of the pion rest energy is plotted for different Wigner-Seitz cell dimensions (i.e for different compressions)  $\xi^{WS}$  in the ultra-relativistic approximation . In the limit  $\xi^{WS} \rightarrow 0$  the electron Fermi energy approaches asymptotically the value  $(E_e^F)_{max}$  given by Eq. (A.2.63).

This boundary-value problem can be solved analytically and indeed Eq. (A.2.45) has the first integral,

$$2[\hat{\phi}'(\xi)]^2 = \begin{cases} \hat{\phi}^4(\xi) - 4\hat{\phi}(\xi) + 3, & \xi < 0, \\ \hat{\phi}^4(\xi) - \hat{\phi}^4(\xi^{WS}), & \xi > 0, \end{cases} \quad (\text{A.2.49})$$

with boundary conditions at  $\xi = 0$ :

$$\begin{aligned} \hat{\phi}(0) &= \frac{\hat{\phi}^4(\xi^{WS}) + 3}{4}, \\ \hat{\phi}'(0) &= -\sqrt{\frac{\hat{\phi}^4(0) - \hat{\phi}^4(\xi^{WS})}{2}}. \end{aligned} \quad (\text{A.2.50})$$

Having fulfilled the continuity condition we integrate Eq. (A.2.49) obtaining for  $\xi \leq 0$

$$\hat{\phi}(\xi) = 1 - 3 \left[ 1 + 2^{-1/2} \sinh(a - \sqrt{3}\xi) \right]^{-1}, \quad (\text{A.2.51})$$

where the integration constant  $a$  has the value

$$\sinh(a) = \sqrt{2} \left( \frac{11 + \hat{\phi}^4(\xi^{WS})}{1 - \hat{\phi}^4(\xi^{WS})} \right). \quad (\text{A.2.52})$$

In the interval  $0 \leq \xi \leq \xi^{WS}$ , the field  $\hat{\phi}(\xi)$  is implicitly given by

$$F \left( \arccos \frac{\hat{\phi}(\xi^{WS})}{\hat{\phi}(\xi)}, \frac{1}{\sqrt{2}} \right) = \hat{\phi}(\xi^{WS})(\xi - \xi^{WS}), \quad (\text{A.2.53})$$

where  $F(\varphi, k)$  is the elliptic function of the first kind, and  $F(0, k) \equiv 0$ . For  $F(\varphi, k) = u$ , the inverse function  $\varphi = F^{-1}(u, k) = \text{am}(u, k)$  is the well known Jacobi amplitude. In terms of it, we can express the solution (A.2.53) for  $\xi > 0$  as,

$$\hat{\phi}(\xi) = \hat{\phi}(\xi^{WS}) \left\{ \cos \left[ \text{am} \left( \hat{\phi}(\xi^{WS})(\xi - \xi^{WS}), \frac{1}{\sqrt{2}} \right) \right] \right\}^{-1}. \quad (\text{A.2.54})$$

In the present case of  $E_e^F > 0$  the ultra-relativistic approximation is indeed always valid up to  $\xi = \xi^{WS}$  for high compression factors, i.e. for  $R_{WS} \simeq R_c$ . In the case  $E_e^F = 0$ ,  $\xi^{WS} \rightarrow \infty$ , there is a breakdown of the ultra-relativistic approximation when  $\xi \rightarrow \xi^{WS}$ .

Details are given in Figs. A.11, A.12, A.13.

We can now estimate two crucial quantities of the solutions: the Coulomb potential at the center of the configuration and the electric field at the surface of the core

$$eV(0) \simeq \left( \frac{9\pi}{4} \right)^{1/3} \frac{1}{\Delta} m_\pi c^2 - E_e^F, \quad (\text{A.2.55})$$

$$E_{\text{max}} \simeq 2.4 \frac{\sqrt{\alpha}}{\Delta^2} \left( \frac{m_\pi}{m_e} \right)^2 E_c |\hat{\phi}'(0)|, \quad (\text{A.2.56})$$

where  $E_c = m_e^2 c^3 / (e\hbar)$  is the critical electric field for vacuum polarization. These functions depend on the value  $\hat{\phi}(\xi^{WS})$  via Eqs. (A.2.49)–(A.2.53). At the boundary  $\xi = \xi^{WS}$ , due to the global charge neutrality, both the electric field  $E(\xi^{WS})$  and the Coulomb potential  $eV(\xi^{WS})$  vanish. From Eq. (A.2.46), we determine the value of  $\hat{\phi}(\xi)$  at  $\xi = \xi^{WS}$

$$\hat{\phi}(\xi^{WS}) = \Delta \left( \frac{4}{9\pi} \right)^{1/3} \frac{E_e^F}{m_\pi c^2}, \quad (\text{A.2.57})$$

as a function of the electron Fermi energies  $E_e^F$ . From the above Eq. (A.2.57),

one can see that there exists a solution, characterized by the value of electron Fermi energy

$$\frac{(E_e^F)_{max}}{m_\pi c^2} = \frac{1}{\Delta} \left( \frac{9\pi}{4} \right)^{1/3}, \quad (\text{A.2.58})$$

such that  $\hat{\phi}(\xi^{WS}) = 1$ . From Eq. (A.2.53) and  $\zeta = 0$ , we also have

$$\xi^{WS}(\hat{\phi}(\xi^{WS})) = \left\{ \frac{1}{\hat{\phi}(0)} F \left[ \arccos \left( 4 - \frac{3}{\hat{\phi}(0)} \right), \frac{1}{\sqrt{2}} \right] \right\}. \quad (\text{A.2.59})$$

For  $\hat{\phi}(\xi^{WS}) = 1$ , from Eq. (A.2.50) follows  $\hat{\phi}(0) = 1$  hence Eq. (A.2.59) becomes

$$\xi^{WS}(\hat{\phi}(0)) = F \left[ 0, \frac{1}{\sqrt{2}} \right]. \quad (\text{A.2.60})$$

It is well known that if the inverse Jacobi amplitude  $F[0, 1/\sqrt{2}]$  is zero, then

$$\xi^{WS}(\hat{\phi}(\xi^{WS}) = \hat{\phi}(0) = 1) = 0. \quad (\text{A.2.61})$$

Indeed from  $\hat{\phi}(\xi^{WS}) = 1$  follows  $\hat{\phi}(0) = 1$  and  $\xi^{WS} = 0$ . When  $\xi^{WS} = 0$  from Eq. (A.2.50) follows  $\hat{\phi}'(0) = 0$  and, using Eq. (A.2.56),  $E_{max} = 0$ . In other words for the value of  $E_e^F$  fulfilling Eq. (A.2.57) no electric field exists on the boundary of the core and from Eq. (A.2.48) and Eqs. (A.2.19, A.2.20) it follows that indeed this is the solution fulfilling both global  $N_e = N_p$  and local  $n_e = n_p$  charge neutrality. In this special case, starting from Eq. (A.2.33) and  $A = N_p + N_n$ , we obtain

$$(E_e^F)_{max}^{3/2} = \frac{\frac{9\pi}{4} (\hbar c)^3 \frac{A}{R_c^3} - (E_e^F)_{max}^3}{2^{3/2} \left[ \left( \frac{9\pi}{4} (\hbar c)^3 \frac{A}{R_c^3} - (E_e^F)_{max}^3 \right)^{2/3} + m_n^2 c^4 \right]^{3/4}}. \quad (\text{A.2.62})$$

In the ultra-relativistic approximation  $(E_e^F)_{max}^3 / \frac{9\pi}{4} (\hbar c)^3 \frac{A}{R_c^3} \ll 1$  so Eq. (A.2.62) can be approximated to

$$(E_e^F)_{max} = 2^{1/3} \frac{m_n}{m_\pi} \gamma \left[ -1 + \sqrt{1 + \frac{\beta}{2\gamma^3}} \right]^{2/3} m_\pi c^2, \quad (\text{A.2.63})$$

where

$$\beta = \frac{9\pi}{4} \left( \frac{\hbar}{m_n c} \right)^3 \frac{A}{R_c^3}, \quad \gamma = \sqrt{1 + \beta^{2/3}}. \quad (\text{A.2.64})$$

The corresponding limiting value to the  $N_p/A$  ratio is obtained as follows

$$\frac{N_p}{A} = \frac{2\gamma^3}{\beta} \left[ -1 + \sqrt{1 + \frac{\beta}{2\gamma^3}} \right]^2. \quad (\text{A.2.65})$$

Inserting Eqs. (A.2.63), (A.2.64) in Eq. (A.2.65) one obtains the ultra-relativistic limit of Eq. (A.2.42), since the electron Fermi energy, in view of the scaling laws introduced in Rotondo et al. (2011e), is independent of the value of  $A$  and depends only on the density of the core.

The  $N_p$ -independence in the limiting case of maximum electron Fermi energy attained when  $R_{WS} = R_c$ , in which the ultra-relativistic treatment approaches the uniform one, and the  $N_p$ -dependence for smaller compressions  $R_{WS} > R_c$  can be understood as follows. Let see the solution to the ultra-relativistic equation (A.2.45) for small  $\zeta > 0$ . Analogously to the Feynman-Metropolis-Teller approach to the non-relativistic Thomas-Fermi equation, we solve the ultra-relativistic equation (A.2.45) for small  $\zeta$ . Expanding  $\hat{\phi}(\zeta)$  about  $\zeta = 0$  in a semi convergent power series,

$$\frac{\hat{\phi}(\zeta)}{\hat{\phi}(0)} = 1 + \sum_{n=2}^{\infty} a_n \zeta^{n/2} \quad (\text{A.2.66})$$

and substituting it into the ultra-relativistic equation (A.2.45), we have

$$\sum_{k=3}^{\infty} a_k \frac{k(k-2)}{4} \zeta^{(k-4)/2} = \phi^2(0) \exp \left[ 3 \ln \left( 1 + \sum_{n=2}^{\infty} a_n \zeta^{n/2} \right) \right]. \quad (\text{A.2.67})$$

This leads to a recursive determination of the coefficients:

$$\begin{aligned} a_3 &= 0, a_4 = \phi^2(0)/2, a_5 = 0, a_6 = \phi^2(0)a_2/2, a_7 = 0, \\ a_8 &= \phi^2(0)(1 - a_2^2)/8, \dots, \end{aligned} \quad (\text{A.2.68})$$

with  $a_2 = \hat{\phi}'(0)/\hat{\phi}(0)$  determined by the initial slope, namely, the boundary condition  $\hat{\phi}'(0)$  and  $\hat{\phi}(0)$  in Eq. (A.2.50):

$$\hat{\phi}(0) = \frac{\hat{\phi}^4(\zeta^{WS}) + 3}{4}, \quad \hat{\phi}'(0) = -\sqrt{\frac{\hat{\phi}^4(0) - \hat{\phi}^4(\zeta^{WS})}{2}} \quad (\text{A.2.69})$$

Thus the series solution (A.2.66) is uniquely determined by the boundary value  $\hat{\phi}(\zeta^{WS})$  at the Wigner-Seitz cell radius.

Now we consider the solution up to the leading orders

$$\begin{aligned}\hat{\phi}(\xi) &= \hat{\phi}(0) + \hat{\phi}'(0)\xi + \frac{1}{2}\hat{\phi}^3(0)\xi^2 + \frac{1}{2}\hat{\phi}^3(0)a_2\xi^3 \\ &+ \frac{1}{8}\hat{\phi}^3(0)(1 - a_2^2)\xi^4 + \dots\end{aligned}\quad (\text{A.2.70})$$

Using Eq. (A.2.70), the electron Fermi energy (A.2.57) becomes

$$\begin{aligned}E_e^F &= (E_e^F)_{max} \left[ 1 + a_2\bar{\xi}^{WS} + \frac{1}{2}\hat{\phi}^2(0)(\bar{\xi}^{WS})^2 + \frac{1}{2}\hat{\phi}^2(0)a_2(\bar{\xi}^{WS})^3 \right. \\ &\left. + \frac{1}{8}\hat{\phi}^2(0)(1 - a_2^2)(\bar{\xi}^{WS})^4 + \dots \right] \hat{\phi}(0),\end{aligned}\quad (\text{A.2.71})$$

where  $(E_e^F)_{max} = (9\pi/4)^{1/3}\Delta^{-1}$  is the maximum Fermi energy which is attained when the Wigner-Seitz cell radius equals the nucleus radius  $R_c$  (see Eq. A.2.58). For  $\hat{\phi}(\bar{\xi}^{WS}) < 1$ , we approximately have  $\hat{\phi}(0) = 3/4$ ,  $\hat{\phi}'(0) = -(3/4)^2/\sqrt{2}$  and the initial slope  $a_2 = \hat{\phi}'(0)/\hat{\phi}(0) = -(3/4)/\sqrt{2}$ . Therefore Eq. (A.2.71) becomes

$$\begin{aligned}E_e^F &\approx (E_e^F)_{max} \left[ 1 - \frac{3}{4\sqrt{2}}\bar{\xi}^{WS} + \frac{1}{2}\left(\frac{3}{4}\right)^2(\bar{\xi}^{WS})^2 - \frac{1}{2^{3/2}}\left(\frac{3}{4}\right)^3(\bar{\xi}^{WS})^3 \right. \\ &\left. + \frac{1}{8}\left(\frac{3}{4}\right)^2\left(\frac{41}{32}\right)(\bar{\xi}^{WS})^4 + \dots \right].\end{aligned}\quad (\text{A.2.72})$$

By the definition of the coordinate  $\xi$ , we know all terms except the first term in the square bracket depend on the values of  $N_p$ . In the limit of maximum compression when the electron Fermi energy acquires its maximum value, namely when  $\bar{\xi}^{WS} = 0$ , the electron Fermi energy (A.2.72) is the same as the one obtained from the uniform approximation which is independent of  $N_p$ . For smaller compressions, namely for  $\bar{\xi}^{WS} > 0$  the electron Fermi energy deviates from the one given by the uniform approximation becoming  $N_p$ -dependent.

In Fig. A.14 we plot the Fermi energy of electrons, in units of the pion rest energy, as a function of the dimensionless parameter  $\bar{\xi}^{WS}$  and, as  $\bar{\xi}^{WS} \rightarrow 0$ , the limiting value given by Eq. (A.2.63) is clearly displayed.

In Alcock et al. (1986), in order to study the electro-dynamical properties of strange stars, the ultra-relativistic Thomas-Fermi equation was numerically solved in the case of bare strange stars as well as in the case of strange stars with a crust (see e.g. curves (a) and (b) in Fig. 6 of Alcock et al. (1986)). In Fig. 6 of Alcock et al. (1986) was plotted what they called the Coulomb potential energy, which we will denote as  $V_{\text{Alcock}}$ . The potential  $V_{\text{Alcock}}$  was plotted for different values of the electron Fermi momentum at the edge of

the crust. Actually, such potential  $V_{\text{Alcock}}$  is not the Coulomb potential  $eV$  but it coincides with our function  $e\hat{V} = eV + E_e^F$ . Namely, the potential  $V_{\text{Alcock}}$  corresponds to the Coulomb potential shifted by the the Fermi energy of the electrons. We then have from Eq. (A.2.46)

$$e\hat{V}(\xi) = \left(\frac{9\pi}{4}\right)^{1/3} \frac{1}{\Delta} m_\pi c^2 \hat{\phi}(\xi) = V_{\text{Alcock}}. \quad (\text{A.2.73})$$

This explains why in Alcock et al. (1986), for different values of the Fermi momentum at the crust the depth of the potential  $V_{\text{Alcock}}$  remains unchanged. Instead, the correct behavior of the Coulomb potential is quite different and, indeed, its depth decreases with increasing of compression as can be seen in Fig. A.11.

### A.2.6. Compressional energy of nuclear matter cores of stellar dimensions

We turn now to the compressional energy of these family of compressed nuclear matter cores of stellar dimensions each characterized by a different Fermi energy of the electrons. The kinematic energy-spectra of complete degenerate electrons, protons and neutrons are

$$\epsilon^i(p) = \sqrt{(pc)^2 + m_i^2 c^4}, \quad p \leq P_i^F, \quad i = e, p, n. \quad (\text{A.2.74})$$

So the compressional energy of the system is given by

$$\mathcal{E} = \mathcal{E}_B + \mathcal{E}_e + \mathcal{E}_{\text{em}}, \quad \mathcal{E}_B = \mathcal{E}_p + \mathcal{E}_n, \quad (\text{A.2.75})$$

$$\mathcal{E}_i = 2 \int_i \frac{d^3 r d^3 p}{(2\pi\hbar)^3} \epsilon^i(p), \quad i = e, p, n, \quad \mathcal{E}_{\text{em}} = \int \frac{E^2}{8\pi} d^3 r. \quad (\text{A.2.76})$$

Using the analytic solution (A.2.54) we calculate the energy difference between two systems,  $I$  and  $II$ ,

$$\Delta\mathcal{E} = \mathcal{E}(E_e^F(II)) - \mathcal{E}(E_e^F(I)), \quad (\text{A.2.77})$$

with  $E_e^F(II) > E_e^F(I) \geq 0$ , at fixed  $A$  and  $R_c$ .

We first consider the infinitesimal variation of the total energy  $\delta\mathcal{E}_{\text{tot}}$  with respect to the infinitesimal variation of the electron Fermi energy  $\delta E_e^F$

$$\delta\mathcal{E} = \left[ \frac{\partial\mathcal{E}}{\partial N_p} \right]_{VWS} \left[ \frac{\partial N_p}{\partial E_e^F} \right] \delta E_e^F + \left[ \frac{\partial\mathcal{E}}{\partial VWS} \right]_{N_p} \left[ \frac{\partial VWS}{\partial E_e^F} \right] \delta E_e^F. \quad (\text{A.2.78})$$

For the first term of this relation we have

$$\begin{aligned} \left[ \frac{\partial \mathcal{E}}{\partial N_p} \right]_{V^{WS}} &= \left[ \frac{\partial \mathcal{E}_p}{\partial N_p} + \frac{\partial \mathcal{E}_n}{\partial N_p} + \frac{\partial \mathcal{E}_e}{\partial N_p} + \frac{\partial \mathcal{E}_{em}}{\partial N_p} \right]_{V^{WS}} \\ &\simeq \left[ E_p^F - E_n^F + E_e^F + \frac{\partial \mathcal{E}_{em}}{\partial N_p} \right]_{V^{WS}}, \end{aligned} \quad (\text{A.2.79})$$

where the general definition of chemical potential  $\partial \epsilon_i / \partial n_i = \partial \mathcal{E}_i / \partial N_i$  is used ( $i = e, p, n$ ) neglecting the mass defect  $m_n - m_p - m_e$ . Further using the condition of the beta-equilibrium (A.2.33) we have

$$\left[ \frac{\partial \mathcal{E}}{\partial N_p} \right]_{V^{WS}} = \left[ \frac{\partial \mathcal{E}_{em}}{\partial N_p} \right]_{V^{WS}}. \quad (\text{A.2.80})$$

For the second term of the Eq. (A.2.78) we have

$$\begin{aligned} \left[ \frac{\partial \mathcal{E}}{\partial V^{WS}} \right]_{N_p} &= \left[ \frac{\partial \mathcal{E}_p}{\partial V^{WS}} + \frac{\partial \mathcal{E}_n}{\partial V^{WS}} + \frac{\partial \mathcal{E}_e}{\partial V^{WS}} + \frac{\partial \mathcal{E}_{em}}{\partial V^{WS}} \right]_{N_p} \\ &= \left[ \frac{\partial \mathcal{E}_e}{\partial V^{WS}} \right]_{N_p} + \left[ \frac{\partial \mathcal{E}_{em}}{\partial V^{WS}} \right]_{N_p}, \end{aligned} \quad (\text{A.2.81})$$

since in the process of increasing the electron Fermi energy namely, by decreasing the radius of the Wigner-Seitz cell, the system by definition maintains the same number of baryons  $A$  and the same core radius  $R_c$ .

Now  $\delta \mathcal{E}$  reads

$$\delta \mathcal{E} = \left\{ \left[ \frac{\partial \mathcal{E}_e}{\partial V^{WS}} \right]_{N_p} \frac{\partial V^{WS}}{\partial E_e^F} + \left[ \frac{\partial \mathcal{E}_{em}}{\partial V^{WS}} \right]_{N_p} \frac{\partial V^{WS}}{\partial E_e^F} + \left[ \frac{\partial \mathcal{E}_{em}}{\partial N_p} \right]_{V^{WS}} \frac{\partial N_p}{\partial E_e^F} \right\} \delta E_e^F, \quad (\text{A.2.82})$$

so only the electromagnetic energy and the electron energy give non-null contributions.

From this equation it follows that

$$\Delta \mathcal{E} = \Delta \mathcal{E}_{em} + \Delta \mathcal{E}_e, \quad (\text{A.2.83})$$

where  $\Delta \mathcal{E}_{em} = \mathcal{E}_{em}(E_e^F(II)) - \mathcal{E}_{em}(E_e^F(I))$  and  $\Delta \mathcal{E}_e = \mathcal{E}_e(E_e^F(II)) - \mathcal{E}_e(E_e^F(I))$ .

In the particular case in which  $E_e^F(II) = (E_e^F)_{max}$  and  $E_e^F(I) = 0$  we obtain

$$\Delta \mathcal{E} \simeq 0.75 \frac{3^{5/3}}{2} \left( \frac{\pi}{4} \right)^{1/3} \frac{1}{\Delta \sqrt{\alpha}} \left( \frac{\pi}{12} \right)^{1/6} N_p^{2/3} m_\pi c^2, \quad (\text{A.2.84})$$

which is positive.

The compressional energy of a nuclear matter core of stellar dimensions increases with its electron Fermi energy as expected.

### A.2.7. Conclusions

The results presented in this article are in the realm of theoretical physics of nuclear physics and of atomic physics and give special attention to relativistic effects. They generalize to the relativistic regimes classical results obtained by Feynman, Metropolis and Teller (Feynman et al., 1949) and, by the introduction of scaling laws, they generalize the classical results obtained by Migdal et al. (1976, 1977); Rotondo et al. (2011e) in heavy nuclei to massive cores of  $\sim M_{\odot}$ . As such they find their justification. They acquire also special meaning in astrophysics: the considerations contained in Secs. I–IV lead to a consistent treatment of white dwarfs and the ones in Secs. V and VI lead to a deeper understanding of neutron star physics.

We have generalized to the relativistic regime the classic work of Feynman, Metropolis and Teller by solving the relativistic Thomas-Fermi equation in a Wigner-Seitz cell corresponding to a compressed atom. The integration of this equation does not admit regular solutions for a point-like nucleus and both the nuclear radius and the nuclear composition have necessarily to be taken into account (Ferreirinho et al., 1980; Ruffini and Stella, 1981). This introduces a fundamental difference from the non-relativistic Thomas-Fermi model where a point-like nucleus is traditionally adopted.

As in previous works by Ferreira et al. (1980), Ruffini and Stella (1981) and Rotondo et al. (2011e), the protons in the nuclei have been assumed to be at constant density, the electron distribution has been derived by the relativistic Thomas-Fermi equation and the neutron component by the beta equilibrium between neutrons, protons and electrons.

We have examined, for completeness, the relativistic generalization of the Thomas-Fermi-Dirac equation by taking into due account the exchange terms (Dirac, 1930), adopting the general approach of Migdal et al. (1977), and shown that these effects, generally small, can be neglected in the relativistic treatment.

There are marked differences between the relativistic and the non-relativistic treatments.

The first is that the existence of a finite size nucleus introduces a limit to the compressibility: the dimension of the Wigner-Seitz cell can never be smaller than the nuclear size. Consequently the electron Fermi energy which in the non-relativistic approach can reach arbitrarily large values, reaches in the present case a perfectly finite value: an expression for this finite value of the electron Fermi energy has been given in analytic form. There are in the literature many papers adopting a relativistic treatment for the electrons, with a point-like approximation for the nucleus, which are clearly inconsistent (see e.g. Chabrier and Potekhin (1998a) and Potekhin et al. (2009)).

The second is the clear difference of the electron distribution as a function of the radius and of the nuclear composition as contrasted to the uniform approximation (see Fig. A.8 of Sec. A.2.4), often adopted in the literature (see

e.g. Bürvenich et al. (2007)). Therefore the validity of inferences based on a uniform approximation should be duly verified both in the relativistic and in the non-relativistic regime.

The third is that the relativistic Feynman-Metropolis-Teller treatment allows to treat precisely the electro-dynamical interaction within a compressed atom with all the relativistic corrections. This allows to validate and in some cases overcome the difficulties of treatments describing the electro-dynamical effect by a sequence of successive approximations. This is the case of validation of the Salpeter approach at high densities and the overcome of negative pressures at low densities. The new treatment evidences a softening of the dependence of the electron Fermi energy on the compression factor, as well as a gradual decrease of the exchange terms in proceeding from the non-relativistic to the fully relativistic regimes. It is then possible to derive, as shown in Table A.1 of Sec. A.2.4, a consistent equation of state for compressed matter.

The equation of state obtained in Table A.1 of Sec. A.2.4 has been recently applied to the study of the general relativistic white-dwarf equilibrium configurations by Rotondo et al. (2011b). The contribution of quantum statistics, weak and electromagnetic interactions here considered have been further generalized there by considering the contribution of the general relativistic equilibrium of white dwarf matter. This is expressed by the simple formula  $\sqrt{g_{00}}\mu_{ws} = \text{constant}$ , which links the chemical potential of the Wigner-Seitz cell  $\mu_{ws}$  with the general relativistic gravitational potential  $g_{00}$  at each point of the configuration. The configuration outside each Wigner-Seitz cell is strictly neutral and therefore no global electric field is necessary to warranty the equilibrium of the white dwarf. These equations modify the ones used by Chandrasekhar by taking into due account the Coulomb interaction between the nuclei and the electrons as well as inverse beta decay. They also generalize the work of Salpeter by considering a unified self-consistent approach to the Coulomb interaction in each Wigner-Seitz cell. The consequences on the numerical value of the Chandrasekhar-Landau mass limit have been then presented as well as on the mass-radius relation of white dwarfs (Rotondo et al., 2011b). This leads to the possibility of a direct confrontation of these results with observations, in view of the current great interest for the cosmological implications of the type Ia supernovae (Phillips, 1993; Riess et al., 1998; Perlmutter et al., 1999; Riess et al., 2004) and in the case of low mass white dwarf companion of the Pulsar PSRJ1141-6545 (Kramer, 2010) as well as the role of white dwarfs in novae.

In Secs. V and VI we have then extrapolated these results to the case of nuclear matter cores of stellar dimensions for  $A \approx (m_{\text{Planck}}/m_n)^3 \sim 10^{57}$  or  $M_{\text{core}} \sim M_{\odot}$ . The aim here is to explore the possibility of obtaining for these systems a self-consistent solution presenting global and not local charge neutrality. The results generalize the considerations presented in the previous article by Rotondo et al. (2011e) corresponding to a nuclear matter core of stel-

lar dimensions with null Fermi energy of the electrons. The ultra-relativistic approximation allows to obtain analytic expressions for the fields in the case of positive electron Fermi energies. An entire family of configurations exist with values of the Fermi energy of the electrons ranging from zero to a maximum value  $(E_e^F)_{max}$  which is reached when the Wigner-Seitz cell coincides with the core radius. The configuration with  $E_e^F = (E_e^F)_{max}$  corresponds to the configuration with  $N_p = N_e$  and  $n_p = n_e$ : for this limiting value of the Fermi energy the system fulfills both the global and the local charge neutrality and, correspondingly, no electro-dynamical structure is present in the core. The other configurations present generally overcritical electric fields close to their surface. The configuration with  $E_e^F = 0$  has the maximum value of the electric field at the core surface, well above the critical value  $E_c$  (see Fig. A.11, Fig. A.12 and Fig. A.13 of Section A.2.5). All these cores with overcritical electric fields are stable against the vacuum polarization process due to the Pauli blocking by the degenerate electrons (see e.g. Ruffini et al. (2010b)). We have also compared and contrasted our treatment of the relativistic Thomas-Fermi solutions to the corresponding one addressed in the framework of strange stars by Alcock et al. (1986), pointing out in these treatments some inconsistency in the definition of the Coulomb potential. We have finally compared the compressional energy of configurations with selected values of the electron Fermi energy.

The above problem is theoretically well defined, represents a necessary step in order to approach the more complex problem of a neutron star core and its interface with the neutron star crust.

Neutron stars are composed of two sharply different components: the liquid core at nuclear and/or supra-nuclear density consisting of neutrons, protons and electrons and a crust of degenerate electrons in a lattice of nuclei (see e.g. Baym et al. (1971a)) and Harrison et al. (1965)) and possibly of free neutrons due to neutron drip when this process occurs (see e.g. Baym et al. (1971a)). Consequently, the boundary conditions for the electrons at the surface of the neutron star core will have generally a positive value of the electron Fermi energy in order to take into account the compressional effects of the neutron star crust on the core. The case of zero electron Fermi energy corresponds to the limiting case of absence of the crust.

In a set of interesting papers Glendenning (1992); Glendenning and Pei (1995); Christiansen and Glendenning (1997); Glendenning and Schaffner-Bielich (1999); Christiansen et al. (2000); Glendenning (2001) have relaxed the local charge neutrality condition for the description of the mixed phases in hybrid stars. In such configurations the global charge neutrality condition, as opposed to the local one, is applied to the limited regions where mixed phases occur while in the pure phases the local charge neutrality condition still holds. We have generalized Glendenning's considerations by looking to a violation of the local charge neutrality condition on the entire configuration, still keeping its overall charge neutrality. This effect cannot occur locally, and

requires a global description of the equilibrium configuration. To exemplify this novel approach we have considered in Rotondo et al. (2011d) the simplest, nontrivial, self-gravitating system of degenerate neutrons, protons and electrons in beta equilibrium in the framework of relativistic quantum statistics and the Einstein-Maxwell equations. The impossibility of imposing the condition of local charge neutrality on such systems is proved in complete generality. The crucial role of the constancy of the generalized electron Fermi energy is emphasized and consequently the coupled system of the general relativistic Thomas-Fermi equations and the Einstein-Maxwell equations is solved. We then give an explicit solution corresponding to a violation of the local charge neutrality condition on the entire star, still fulfilling the global charge neutrality when electromagnetic, weak and general relativistic effects are taken into account.

The results presented in the second part of this article on nuclear matter cores of stellar dimensions evidence the possibility of having the existence of critical electromagnetic fields at the core surface.

## A.3. The relativistic Feynman-Metropolis-Teller equation of state at finite temperatures

### A.3.1. Introduction

We have recently generalized in Ref. Rotondo et al. (2011c) to relativistic regimes the classic work of Feynman, Metropolis and Teller (FMT) Feynman et al. (1949), solving a compressed atom by the Thomas-Fermi equation in a Wigner-Seitz cell. The integration of this equation does not admit any regular solution for a point-like nucleus and both the nuclear radius and the nuclear composition have necessarily to be taken into account Ferreira et al. (1980); Ruffini and Stella (1981). This introduces a fundamental difference from the non-relativistic Thomas-Fermi model where a point-like nucleus is adopted. So, this approach improves all previous treatments of the equation of state (EOS) of a compressed atom, including the classic work of Salpeter Salpeter (1961a), in the following aspects: 1) in order to guarantee self-consistency with a relativistic treatment of the electrons, the point-like assumption of the nucleus is abandoned introducing a finite sized nucleus; 2) the Coulomb interaction energy is fully calculated without any approximation by solving numerically the relativistic Thomas-Fermi equation for each given nuclear composition; 3) the energy-density of the system is calculated taking into account the contributions of the nuclei, of the Coulomb interactions as well as of the relativistic electrons; 4) the  $\beta$ -equilibrium between neutrons, protons and electrons is also taken into account leading to a self-consistent calculation of the threshold density for triggering the inverse  $\beta$ -decay of a given nucleus.

We have shown in Ref. Rotondo et al. (2011b) how these effects are important in the determination of the macroscopic structure of general relativistic white dwarfs, for instance we demonstrated the relevance of the above items 4) and 5) to determine the critical mass of white dwarfs against gravitational collapse, which can be induced either by the inverse  $\beta$  decay or by general relativistic effects. More recently, the relativistic FMT EOS has been used to determine general relativistic equilibrium configurations of rotating white dwarfs Boshkayev et al. (2013b).

In this work we extend our previous work Rotondo et al. (2011c) on the degenerate relativistic FMT treatment by including the effects of finite temperatures. Besides being interesting by its own, the inclusion of finite temperature effects is becoming of primary importance in view of the recent discoveries of ultra-low mass white dwarfs with masses  $\lesssim 0.2M_{\odot}$  Antoniadis et al. (2013a, 2012), companion of neutron stars in relativistic binaries. These low-mass white dwarfs represent the perfect arena for testing the EOS of compressed matter since the central densities of these objects are expected to be  $\lesssim 10^6 \text{ g cm}^{-3}$ , where the degenerate approximation breaks down and

so thermal effects cannot be neglected. The generalization of the relativistic FMT model presented here represent serves also as an extension of previous works in which the non-relativistic Thomas-Fermi model has been used to describe the physics of the low density layers of neutron stars including their atmospheres (see e.g. Ref. Thorolfsson et al. (1998)). The proper treatment of the relativistic and Coulomb effects corrects the over and underestimate of the total pressure at high and low densities respectively, which occurs in non-relativistic Thomas-Fermi models and in the approximate Coulomb corrections of Salpeter Salpeter (1961a); see Rotondo et al. (2011c), for further details.

Besides the generalization of the EOS of compressed matter, we follow the steps in Rotondo et al. (2011c) and extrapolate the treatment to the case of compressed nuclear matter cores of stellar dimensions introduced in : macroscopic cores composed of neutrons, protons, and electron in  $\beta$  equilibrium and with mass numbers  $A \sim (m_{\text{Planck}}/m_n)^3 \sim 10^{57}$ , hence masses  $M_{\text{core}} \sim M_{\odot}$ ; expected to be bound by self-gravity. These objects are idealized configurations that reflect the properties of macroscopic nuclear matter systems such as neutron stars.

The paper is organized as follows: first in Sec. A.3.2 we briefly describe the relativistic FMT treatment both in the completely degenerate case and the extension to finite temperatures. Then in Sec. A.3.3 we summarize the results of the numerical integration of the equations and describe the general properties of the new EOS. In Sec. A.3.4 we extend the formulation to the case of the nuclear matter cores of stellar dimensions introduced in Rotondo et al. (2011c). Finally the conclusions are presented in Sec. A.3.5.

### A.3.2. The relativistic FMT treatment

#### The degenerate case

We briefly describe now the relativistic generalization of the classic FMT treatment of compressed atoms recently achieved in Rotondo et al. (2011c). One of the main differences is that, in order to allow for the presence of a cloud of relativistic electrons (see e.g. Ferreira et al. (1980); Ruffini and Stella (1981)), the point-like nucleus approximation must be abandoned. The relativistic equilibrium condition of compressed atoms for the degenerate case is expressed by

$$E_e^F = \sqrt{c^2(P_e^F)^2 + m_e^2 c^4} - m_e^2 c^2 - eV(r) = \text{constant} > 0, \quad (\text{A.3.1})$$

where  $V$  denotes the Coulomb potential,  $P_e^F$  is the electron Fermi momentum and  $E_e^F$  denotes the Fermi energy of electrons. In Ref. Rotondo et al. (2011c), we adopted a constant distribution of protons confined in a radius

$R_c = \Delta \lambda_\pi Z^{\frac{1}{3}}$ , where  $\lambda_\pi = \hbar/(m_\pi c)$  is the pion Compton wavelength, with  $m_\pi$  the pion rest mass, and  $Z$  is the number of protons. The parameters  $\Delta$  is such that at nuclear density,  $\Delta \approx (r_0/\lambda_\pi)(A/Z)^{1/3}$ , where  $r_0 \approx 1.2$  fm and  $A$  is the atomic weight; so in the case of ordinary nuclei  $\Delta \approx 1$ . The proton density can be then written as

$$n_p(r) = \frac{Z}{\frac{4}{3}\pi R_c^3} \theta(r - R_c), \quad (\text{A.3.2})$$

where  $\theta(r - R_c)$  is the Heaviside function centered at the core/nucleus radius,  $r = R_c$ . The electron density follows from Fermi-Dirac statistics and is given by

$$n_e(r) = \frac{(P_e^F)^3}{3\pi^2 \hbar^3} = \frac{1}{3\pi^2 \hbar^3 c^3} [\hat{V}^2(r) + 2m_e c^2 \hat{V}(r)]^{\frac{3}{2}}, \quad (\text{A.3.3})$$

where  $\hat{V} = e\hat{V} + E_e^F$  and we have used the equilibrium condition (A.3.1).

By introducing the dimensionless quantities  $x = r/\lambda_\pi$ ,  $x_c = R_c/\lambda_\pi$ ,  $\chi/r = \hat{V}(r)/(\hbar c)$  and replacing the particle densities into the Poisson Equation

$$\nabla^2 V = 4\pi e(n_p - n_e), \quad (\text{A.3.4})$$

we obtain the relativistic Thomas-Fermi equation

$$\frac{1}{3x} \frac{d^2 \chi(x)}{dx^2} = -\frac{\alpha}{\Delta^3} \theta(x_c - x) + \frac{4\alpha}{9\pi} \left[ \frac{\chi^2(x)}{x^2} + \frac{2m_e}{m_\pi} \frac{\chi(x)}{x} \right]^{\frac{3}{2}}. \quad (\text{A.3.5})$$

The above differential equation has to be integrated subjected to the boundary conditions

$$\chi(0) = 0, \quad \left. \frac{d\chi}{dx} \right|_{x=0} > 0, \quad \left. \frac{d\chi}{dx} \right|_{x=x_{WS}} = \frac{\chi(x_{WS})}{x_{WS}}, \quad (\text{A.3.6})$$

where the latter condition ensures the global charge neutrality at the Wigner-Seitz cell radius  $R_{WS}$ , and  $x_{WS} = R_{WS}/\lambda_\pi$  is the dimensionless cell radius.

The total energy of the Wigner-Seitz cell can be written as the sum of three contributions

$$E_{WS} = E_N + E_k + E_C, \quad (\text{A.3.7})$$

where

$$E_N = M_N(A, Z)c^2, \quad (\text{A.3.8})$$

$$E_k = \int_0^{R_{WS}} 4\pi r^2 (\mathcal{E}_e - m_e n_e) dr, \quad (\text{A.3.9})$$

$$E_C = \frac{1}{2} \int_{R_c}^{R_{WS}} 4\pi r^2 e [n_p(r) - n_e(r)] V(r) dr, \quad (\text{A.3.10})$$

are the nucleus, kinetic, and Coulomb energy of the cell. For the nucleus mass,  $M_N(A, Z)$ , we adopt experimental values, and  $\mathcal{E}_e$  is the electron energy density

$$\begin{aligned}\mathcal{E}_e &= \frac{2}{(2\pi\hbar)^3} \int_0^{P_e^F} \sqrt{c^2 p^2 + m_e^2 c^4} 4\pi p^2 dp, \\ &= \frac{m_e^4 c^5}{8\pi^2 \hbar^3} [x_e \sqrt{1 + x_e^2} (1 + 2x_e^2) - \operatorname{arcsinh}(x_e)],\end{aligned}\quad (\text{A.3.11})$$

where we have avoided double-counting of the electrons rest-energy and the nucleus Coulomb energy which are already accounted for in the experimental values of nuclear masses.

The total pressure at the border of the Wigner-Seitz cell is exerted only by the relativistic degenerate electron gas

$$\begin{aligned}P_{\text{FMT}}^{\text{rel}} &= \frac{1}{3} \frac{2}{(2\pi\hbar)^3} \int_0^{P_e^{F,\text{WS}}} \frac{c^2 p^2}{\sqrt{c^2 p^2 + m_e^2 c^4}} 4\pi p^2 dp, \\ &= \frac{m_e^4 c^5}{8\pi^2 \hbar^3} [x_e \sqrt{1 + x_e^2} (2x_e^2/3 - 1) + \operatorname{arcsinh}(x_e)]\end{aligned}\quad (\text{A.3.12})$$

where  $x_e = P_e^{F,\text{WS}}/(m_e c) \equiv P_e^F(R_{\text{WS}})/(m_e c)$  is the dimensionless electron Fermi momentum, often called relativistic parameter, evaluated at the radius of the Wigner-Seitz cell,  $R_{\text{WS}}$ .

A detailed analysis of this EOS and how it generalizes previous works based either on non-relativistic electrons or on the uniform approximation of the electron gas or on first order corrections of it owing to Coulomb effects can be found in Refs. Rotondo et al. (2011c,b).

### Generalization of the EOS to finite temperatures

We turn now to consider a relativistic gas of electrons at temperature  $T \neq 0$  surrounding the finite sized and positively charged nucleus. We assume the proton number density as in the degenerate case, i.e. given by Eq. (A.3.3), and we can write the electron number density following Fermi-Dirac statistics as

$$n_e = \frac{2}{(2\pi\hbar)^3} \int_0^\infty \frac{4\pi p^2 dp}{\exp\left[\frac{\tilde{E}(p) - \tilde{\mu}_e(p)}{k_B T}\right] + 1},\quad (\text{A.3.13})$$

where  $k_B$  is the Boltzmann constant,  $\tilde{\mu}_e$  is the electron chemical potential with the rest-mass subtracted off, and  $\tilde{E}(p) = \sqrt{c^2 p^2 + m_e^2 c^4} - m_e c^2$ , with  $p$  and  $m_e$  the electron momentum and rest-mass, respectively.

Introducing the degeneracy parameter  $\eta = \tilde{\mu}_e/(k_B T)$ ,  $t = \tilde{E}(p)/(k_B T)$  and

$\beta = k_B T / (m_e c^2)$ , we can write the electron number density as

$$n_e = \frac{8\pi\sqrt{2}}{(2\pi\hbar)^3} m^3 c^3 \beta^{3/2} [F_{1/2}(\eta, \beta) + \beta F_{3/2}(\eta, \beta)], \quad (\text{A.3.14})$$

where

$$F_k(\eta, \beta) \equiv \int_0^\infty \frac{t^k \sqrt{1 + (\beta/2)t}}{1 + e^{t-\eta}} dt \quad (\text{A.3.15})$$

is the relativistic Fermi-Dirac integral.

We consider configurations with temperatures  $T \ll m_e c^2 / k_B \approx 5.94 \times 10^9$  K, so we will not take into account the presence of anti-particles. Using the same dimensionless quantities and replacing the particle densities into the Poisson equation we obtain the generalization of the relativistic Thomas-Fermi equation at finite temperatures

$$\frac{d^2\chi(x)}{dx^2} = -4\pi\alpha x \left\{ \frac{3}{4\pi\Delta^3} \theta(x_c - x) - \frac{\sqrt{2}}{\pi^2} \left( \frac{m_e}{m_\pi} \right)^3 \beta^{3/2} [F_{1/2}(\eta, \beta) + \beta F_{3/2}(\eta, \beta)] \right\}, \quad (\text{A.3.16})$$

where we have defined a new Thomas-Fermi function  $\chi$  by  $\tilde{\mu}_e = k_B T \eta = \hbar\chi/r$ , and used the electron equilibrium condition which now reads

$$\tilde{\mu}_e - eV = k_B T \eta - eV = \text{constant}, \quad (\text{A.3.17})$$

with  $V$  the Coulomb potential.

The Eq. (A.3.16) must be integrated subjected to the same boundary conditions as in the degenerate case, given by Eq. (A.3.6).

For the present case at finite temperature, the total energy of each Wigner-Seitz can be again written as

$$E_{\text{WS}} = E_N + E_k + E_C, \quad (\text{A.3.18})$$

but now the nucleus energy

$$E_N = M_N(A, Z)c^2 + U_{\text{th}}, \quad U_{\text{th}} = \frac{3}{2}k_B T, \quad (\text{A.3.19})$$

accounts for the internal energy of nuclei,  $U_{\text{th}}$ , which we here adopt as an ideal gas. Quantum corrections to the ion fluid considered here can be straightforwardly computed following previous treatments such as Stolzmann and Bloecker (1996); Chabrier and Potekhin (1998b); Potekhin and Chabrier (2000).

The electron kinetic energy is given by Eq. (A.3.9) but in this case the elec-

tron energy density is

$$\varepsilon_e = m_e c^2 n_e + \frac{\sqrt{2}}{\pi^2 \hbar^3} m_e^4 c^5 \beta^{5/2} [F_{3/2}(\eta, \beta) + \beta F_{5/2}(\eta, \beta)], \quad (\text{A.3.20})$$

and finally the Coulomb energy is computed again as in Eq. (A.3.10) with the electron density now given by Eq. (A.3.14).

The total density and pressure are then given by

$$\rho = \frac{E_{\text{WS}}/c^2}{V_{\text{WS}}}, \quad (\text{A.3.21})$$

$$P = P_N + P_e, \quad (\text{A.3.22})$$

where

$$P_N = \frac{2}{3} \frac{U_{\text{th}}}{V_{\text{WS}}} = \frac{k_B T}{V_{\text{WS}}}, \quad (\text{A.3.23})$$

$$P_e = \frac{2^{3/2}}{3\pi^2 \hbar^3} m_e^4 c^5 \beta^{5/2} \left[ F_{3/2}(\eta_{\text{WS}}, \beta) + \frac{\beta}{2} F_{5/2}(\eta_{\text{WS}}, \beta) \right], \quad (\text{A.3.24})$$

with  $\eta_{\text{WS}}$  is the value of  $\eta$  at the boundary of the Wigner-Seitz cell whose volume is  $V_{\text{WS}} = 4\pi R_{\text{WS}}^3/3$ .

### A.3.3. Numerical integration of the equations and the EOS

For a given chemical composition ( $Z, A$ ), temperature  $T$  (i.e.  $\beta$ ), and Wigner-Seitz cell radius  $x_{\text{WS}}$ , the relativistic Thomas-Fermi equation (A.3.16) is integrated subjected to the boundary conditions (A.3.6). We thus obtain both the Coulomb potential and the function  $\eta$  inside the given Wigner-Seitz cell. With the knowledge of  $\eta_{\text{WS}}$ , we proceed to evaluate first the energy of the cell by Eqs. (A.3.18–A.3.20) and subsequently the EOS through Eqs. (A.3.21–A.3.24). Thus, for given composition and temperature, we repeat the above steps for different cell radii, which give us different compression levels of the system, and therefore leads to different densities and pressures, hence the EOS. These steps can be performed for different compositions and temperatures; the results are discussed below.

#### Properties of the EOS

As we showed in Ref. Rotondo et al. (2011c), as a result of the Coulomb interaction duly accounted for in the relativistic Thomas-Fermi treatment, the distribution of the electrons inside a Wigner-Seitz cell is not uniform. In order to show the effects of the temperature, in Fig. A.15 we show as an example the electron number density inside a Wigner-Seitz cell of  $^{56}\text{Fe}$  at a density of

$30 \text{ g cm}^{-3}$  and for temperatures  $T = [0, 10^7, 10^{10}] \text{ K}$ .

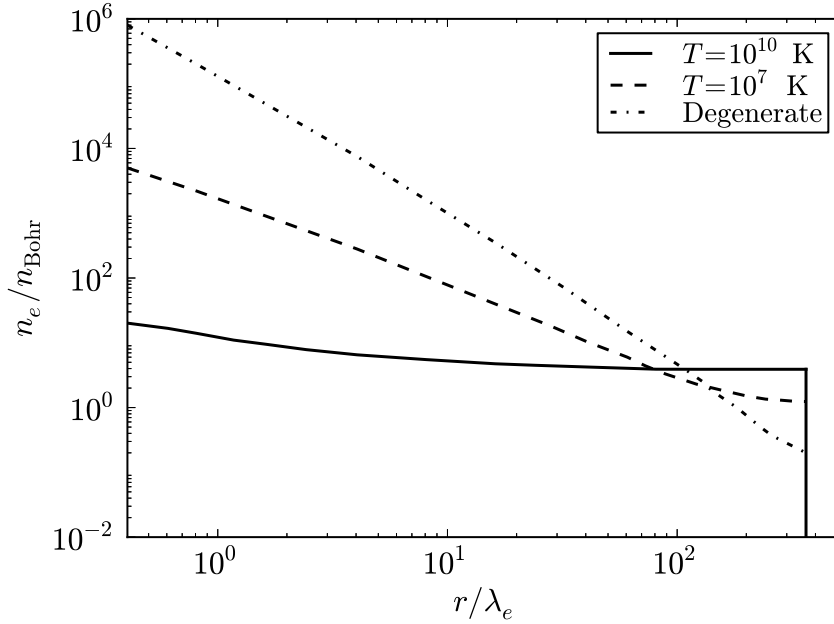


**Figure A.15.:** Electron number density inside a Wigner-Seitz cell of  $^{56}\text{Fe}$  at a density of  $30 \text{ g cm}^{-3}$  at selected temperatures. Here  $n_{\text{Bohr}} = 3/(4\pi R_{\text{Bohr}}^3) \approx 1.6 \times 10^{24} \text{ cm}^{-3}$ , where  $R_{\text{Bohr}} = \hbar/(e^2 m_e) \approx 5.3 \times 10^{-9} \text{ cm}$ , is the Bohr radius. In this example we have used both low density and high temperatures up to  $10^{10} \text{ K}$  in order to show an extreme example of electron density flattening.

We can see in Fig. A.15 how the effect of the temperature tends to homogenize inside the cell. In addition, we notice that the larger the temperature the larger the value of the electron density at the border of the Wigner-Seitz cell, thus increasing the electron pressure. This effect can be clearly seen in Fig. A.16 where we show the value of the electron number density evaluated at the cell radius,  $R_{\text{WS}}$ , as a function of the density for the temperatures  $T = [10^4, 10^5, 10^6, 10^7, 10^8] \text{ K}$ , for a given chemical composition,  $^{12}\text{C}$ .

The volume of the Wigner-Seitz cell,  $V_{\text{WS}} = 4\pi R_{\text{WS}}^3/3$ , determines the density of the system  $\rho$  given by Eq. (A.3.21); the smaller the volume the larger the density. In Fig. A.17 we show the density of the system as a function of the Wigner-Seitz cell radius  $R_{\text{WS}}$  for a temperature  $T = 10^7 \text{ K}$  and chemical composition  $^{12}\text{C}$ .

It is important to mention that often in the literature is used as density of the system the quantity  $\rho = AM_u n_e / Z$ , which clearly corresponds to the rest-mass density of nuclei in the system (assuming a uniform distribution of electrons), where  $M_u = 1.6604 \times 10^{-24} \text{ g}$  is the unified atomic mass. We can see from Eq. (A.3.7) that this is equivalent to neglect the internal and Coulomb energy of the cells. However, as we showed in Refs. Rotondo et al. (2011c,b), the inclusion of the Coulomb and electron kinetic energies are important at

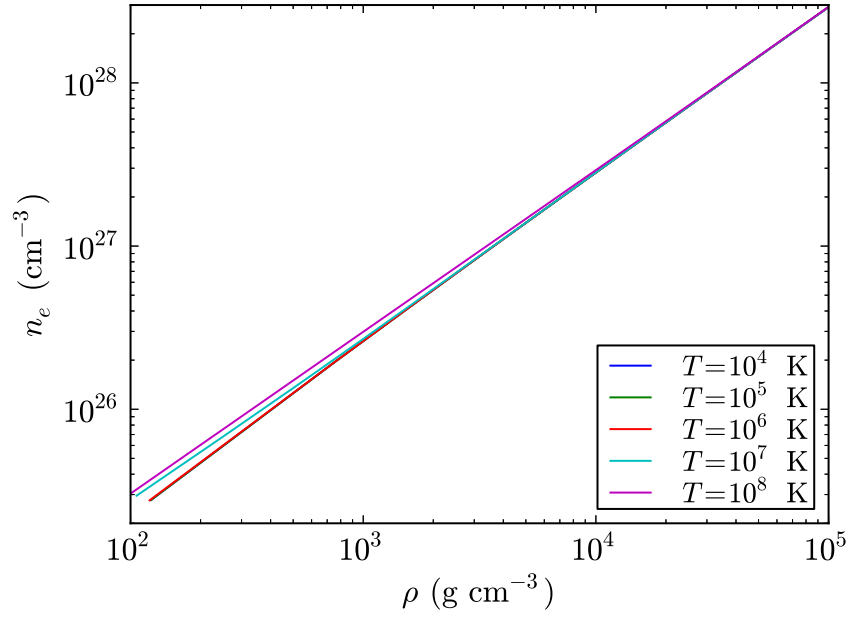


**Figure A.16.:** Electron number density at the radius of a Wigner-Seitz cell of  $^{12}\text{C}$  as a function of the density (A.3.21) for the selected temperatures  $T = [10^4, 10^5, 10^6, 10^7, 10^8]$  K.

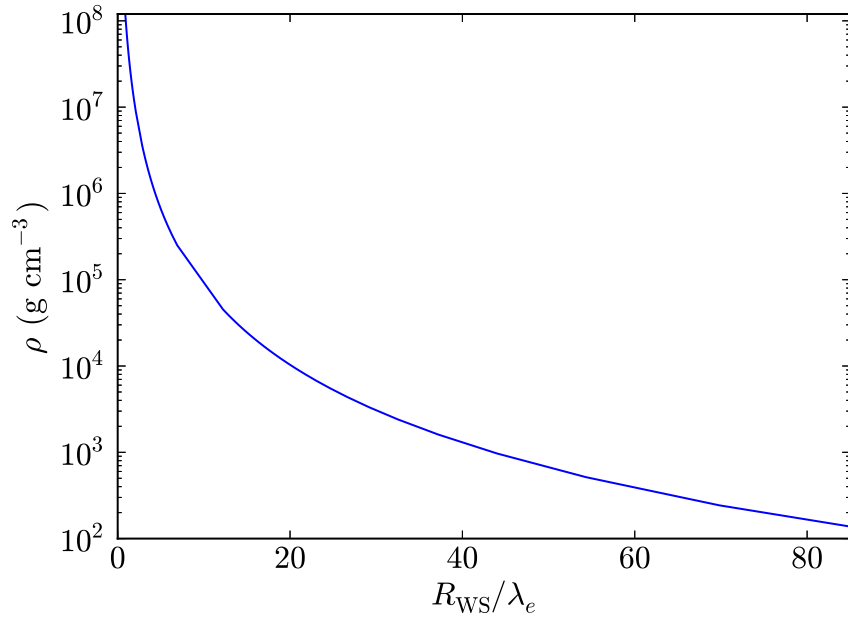


**Figure A.17.:** Total density (in  $\text{g cm}^{-3}$ ) of the system as a function of the radius of the Wigner-Seitz cell (in units of the electron Compton wavelength  $\lambda_e = \hbar / (m_e c) \approx 3.9 \times 10^{-11}$  cm) in the case of  $^{12}\text{C}$  at a temperature  $T = 10^7$  K.

low and high densities, respectively. In particular, the contribution of the kinetic energy of the electrons to the energy density is fundamental in the determination of the critical density for the gravitational collapse of  $^{12}\text{C}$  white dwarfs Rotondo et al. (2011b). We show in Fig. A.18 the effect on the EOS of using as density of the system only the nuclei rest-mass,  $\rho = AM_u n_e / Z$ , instead of the full mass density given by Eq. (A.3.21) with the energy of the Wigner-Seitz cell given by Eq. (A.3.7), which takes into account the internal energy (thermal and electron kinetic energies) as well as the Coulomb energy of the Wigner-Seitz cell.

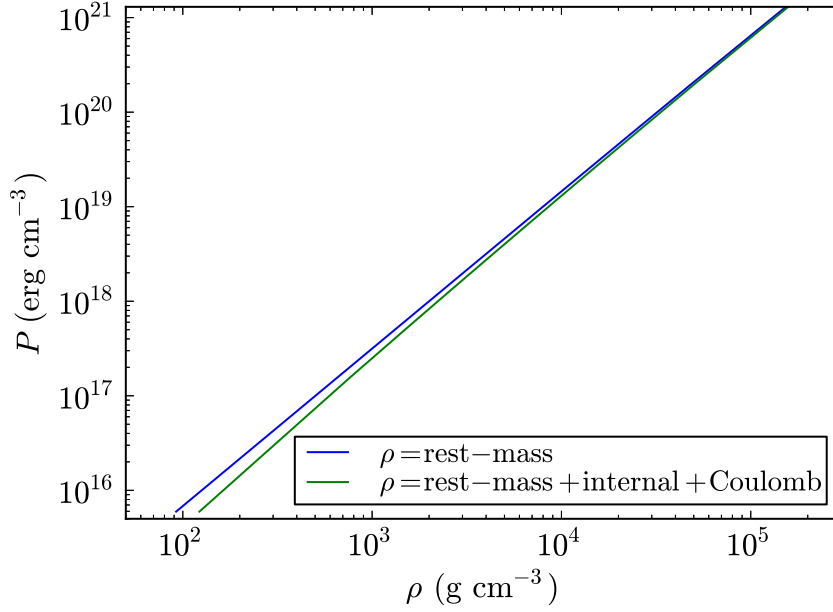


**Figure A.18.:** Total pressure as a function of the matter density  $\rho = AM_u n_e / Z$  and  $\rho = E_{\text{WS}} / (c^2 V_{\text{WS}})$  which includes the internal (nuclei thermal and electron kinetic energies) and Coulomb energy in the Wigner-Seitz cell. In this example the composition is  $^{12}\text{C}$  and the temperature  $T = 10^4$  K.

The effects of finite temperatures are clearly expected to be important at low densities, where the system loses its degeneracy. The point where the EOS should start to deviate from its degenerate behavior can be estimated by equating the degenerate and ideal gas pressures for the electron component. Assuming the electrons as non-relativistic we have,  $n_e k_B T = (3\pi^2)^{2/3} \hbar^2 n_e^{5/3} / m_e$ , from which we obtain that temperature effects are important for densities

$$\rho \lesssim 1.5 \times 10^3 \left( \frac{T}{10^7 \text{ K}} \right)^{3/2} \text{ g cm}^{-3}, \quad (\text{A.3.25})$$

where we have used  $A/Z \approx 2$  and  $\rho \approx AM_u n_e / Z$ . In Fig. A.19 we compare the relativistic degenerate FMT EOS Rotondo et al. (2011c,b) and its general-

ization at finite temperatures presented in this work, for the cases  $T = 10^7$  and  $10^8$  K and  $^{12}\text{C}$  chemical composition. For these specific temperatures,  $T = 10^7$  and  $10^8$  K, we see that deviations of the degenerate EOS start at a density  $\rho \approx 2 \times 10^4$  and  $\approx 10^6$  g cm $^{-3}$ , respectively. For the same temperatures, Eq. (A.3.25) estimate deviations from degeneracy at  $\rho \approx 1.5 \times 10^3$  and  $\approx 4.8 \times 10^4$  g cm $^{-3}$ , respectively. Thus, the lower the temperature the better the estimate given by Eq. (A.3.25); the reason for this is that for larger temperatures the system will loose the degeneracy at larger densities where the non-relativistic approximation for the electrons breaks down.

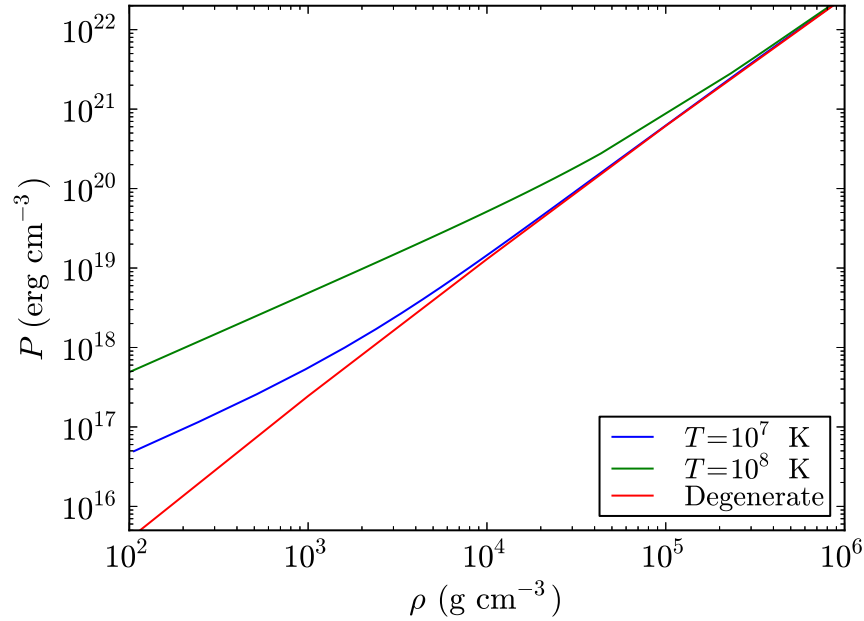


**Figure A.19.:** Comparison of the EOS for  $^{12}\text{C}$  at temperatures  $T = [0, 10^7, 10^8]$  K.

We summarize the finite temperature generalization of the relativistic FMT EOS in Fig. A.21, where we plot as an example the total pressure (A.3.22) as a function of the total density of the system (A.3.21) at temperatures  $T = [10^4, 10^5, 10^6, 10^7, 10^8]$  K and for a chemical composition,  $^{12}\text{C}$ . All the above features of the EOS are general and therefore applied also to chemical compositions other than  $^{12}\text{C}$ .

### Inverse $\beta$ decay and pycnonuclear reactions

We turn now to the finite temperature effects on the inverse  $\beta$  decay instability. It is known that white dwarfs may become unstable against the inverse  $\beta$  decay process  $(Z, A) \rightarrow (Z - 1, A)$  through the capture of energetic electrons. In order to trigger such a process the electron energy must be larger

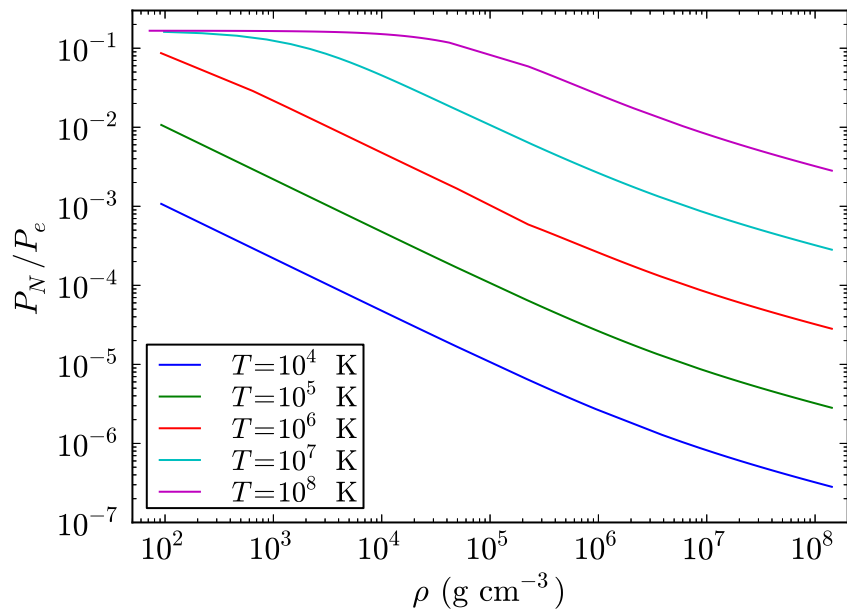


**Figure A.20.:** Nuclei to electron pressure ratio as a function of the mass density in the case of  $^{12}\text{C}$  white dwarf for selected temperatures in the range  $T = 10^4\text{--}10^8$  K.

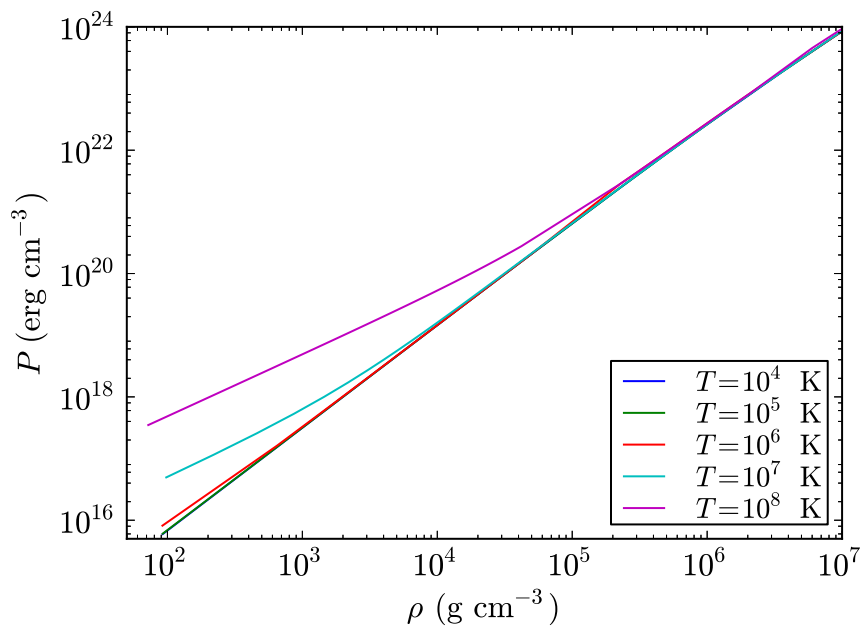


**Figure A.21.:** Total pressure as a function of the mass density in the case of  $^{12}\text{C}$  white dwarf for selected temperatures in the range  $T = 10^4\text{--}10^8$  K.

than the mass difference between the initial nucleus  $(Z, A)$  and the final nucleus  $(Z - 1, A)$ . This threshold energy is denoted as  $\epsilon_Z^\beta$ . Usually it is satisfied  $\epsilon_Z^\beta - 1 < \epsilon_Z^\beta$  and therefore the initial nucleus undergoes two successive decays, i.e.  $(Z, A) \rightarrow (Z - 1, A) \rightarrow (Z - 2, A)$ ; see e.g. Refs. Salpeter (1961b); Shapiro and Teukolsky (1983b).

The critical density  $\rho_{crit}^\beta$  is then obtained numerically by looking for the density at which the electron energy equals  $\epsilon_Z^\beta$ . In Table II of Ref. Rotondo et al. (2011b) we showed that, in the degenerate case, the threshold energies to trigger the inverse  $\beta$  process for  ${}^4\text{He}$ ,  ${}^{12}\text{C}$ ,  ${}^{16}\text{O}$ , and  ${}^{56}\text{Fe}$  are reached at densities,  $1.37 \times 10^{11}$ ,  $3.88 \times 10^{10}$ ,  $1.89 \times 10^{10}$ , and  $1.14 \times 10^9$  g cm $^{-3}$ , respectively. Since the effects of temperatures  $T \lesssim 10^8$  K are important at densities  $\rho \lesssim 10^6$  g cm $^{-3}$  (see Figs. A.19 and A.21), we found that the critical densities for the occurrence of the inverse  $\beta$  decay instability are roughly the same as the ones computed in the degenerate approximation.

We turn now to the pycnonuclear reactions. In a nuclei lattice the nuclear reactions proceed with the overcoming of the Coulomb barrier between neighbor nuclei. At zero temperatures,  $T = 0$ , the Coulomb barrier can be overcome due to the zero-point energy of the nuclei (see e.g. Salpeter and van Horn (1969); Shapiro and Teukolsky (1983b))

$$E_p = \hbar\omega_p, \quad \omega_p = \sqrt{\frac{4\pi e^2 Z^2 \rho}{A^2 M_u^2}}. \quad (\text{A.3.26})$$

The number of pycnonuclear reactions per unit volume per unit time increases with the density of the system Salpeter and van Horn (1969) and any effect that reduces the Coulomb barrier will increase the cross-section of the reaction. The inclusion of the temperature could then lead to thermo-enhanced pycnonuclear rates (see e.g. Refs. Salpeter and van Horn (1969); Gasques et al. (2005)). The astrophysical importance of pycnonuclear reactions e.g. in the theory of white dwarfs relies on the fact that for instance the  ${}^{12}\text{C}+{}^{12}\text{C}$  pycnonuclear fusion, leading to  ${}^{24}\text{Mg}$ , is possible in a time scale shorter than a Hubble time,  $\tau_{\text{pyc}} < 10$  Gyr, for densities  $\sim 10^{10}$  g cm $^{-3}$ . Such a density turns to be larger than the critical density  $\sim 3 \times 10^9$  g cm $^{-3}$  for the double inverse  $\beta$  decay of  ${}^{24}\text{Mg}$  into  ${}^{24}\text{Ne}$  by electron capture (see e.g. Salpeter (1961a); Shapiro and Teukolsky (1983b)), which destabilize the white dwarf due to sudden decrease of its electron pressure. For instance, following the updated reaction rates of Ref. Gasques et al. (2005), we recently computed Boshkayev et al. (2013b) the critical density for pycnonuclear instability in general relativistic uniformly rotating  ${}^{12}\text{C}$  white dwarfs, at zero temperatures. It comes out that the instability agent of white dwarfs can be either general relativistic effects or inverse  $\beta$  decay or pycnonuclear reactions or rotation through mass-shedding or secular instabilities (see Boshkayev et al.

(2013b), for details).

The electrons around the nuclei lead to a screening of the positive charge of the nucleus reducing the Coulomb barrier; hence their proper inclusion could in principle increase the reaction rates. On the other hand, we showed in Figs. A.15 and A.16 two different effects owing to the finite temperature: 1) it tends to flatten the electron distribution, thus changing the electron screening of the Coulomb potential with respect to the degenerate case; and 2) it increases the electron density hence the pressure at the border of the cell. These effects clearly could lead to consequences on the estimates of the rates of the pycnonuclear reactions (see e.g. Potekhin and Chabrier (2012)).

However, the inclusion of these combined effects within the pycnonuclear reactions treatment, following a fully relativistic approach of the electron gas and the Coulomb interactions as the one presented here, is a most difficult and complex task that deserves to be the subject of a fully separate work, and therefore will not be addressed here.

### A.3.4. Application to nuclear matter cores of stellar dimensions

#### The degenerate case

In Ref. Rotondo et al. (2011c) we extended the relativistic FMT model to what we have called nuclear matter cores of stellar dimensions: objects with mass numbers  $A \sim (m_{\text{Planck}}/m_n)^3 \sim 10^{57}$ , thus with corresponding masses  $M_{\text{core}} \sim M_{\odot}$ . These systems are expected to represent idealized macroscopic objects composed of neutrons, protons, and electrons in  $\beta$  equilibrium and kept bound by self-gravity, such as the cores of neutron stars.

Following our treatment in Ref. Rotondo et al. (2011c), we use the existence of scaling laws and proceed to the ultra-relativistic limit of Eqs. (A.3.3) and (A.3.5). For positive values of the electron Fermi energy  $E_e^F$ , we introduce the new function  $\phi = 4^{1/3}(9\pi)^{-1/3}\chi\Delta/x$  and the new variable  $\hat{x} = kx$  where  $k = (12/\pi)^{1/6}\sqrt{\alpha}\Delta^{-1}$ , as well as the variable  $\zeta = \hat{x} - \hat{x}_c$  in order to describe better the region around the core radius.

Thus, Eq. (A.3.5) becomes

$$\frac{d^2\hat{\phi}(\zeta)}{d\zeta^2} = -\theta(-\zeta) + \hat{\phi}(\zeta)^3, \quad (\text{A.3.27})$$

where  $\hat{\phi}(\zeta) = \phi(\zeta + \hat{x}_c)$  and the term  $2\hat{\phi}'(\zeta)/(\zeta + \hat{x}_c)$  has been neglected, namely we introduce a plane-parallel approximation.

The Coulomb potential energy is given by

$$eV(\zeta) = \left(\frac{9\pi}{4}\right)^{1/3} \frac{1}{\Delta} m_{\pi} c^2 \hat{\phi}(\zeta) - E_e^F, \quad (\text{A.3.28})$$

corresponding to the electric field

$$E(\xi) = - \left( \frac{3^5 \pi}{4} \right)^{1/6} \frac{\sqrt{\alpha} m_\pi^2 c^3}{\Delta^2 e \hbar} \frac{d\hat{\phi}}{d\xi}, \quad (\text{A.3.29})$$

and the electron number-density

$$n_e(\xi) = \frac{1}{3\pi^2 \hbar^3 c^3} \left( \frac{9\pi}{4} \right) \frac{1}{\Delta^3} (m_\pi c^2)^3 \hat{\phi}^3(\xi), \quad (\text{A.3.30})$$

and the function  $\hat{\phi}(\xi)$  satisfies  $\hat{\phi}(-\hat{x}_c) = 1$ .

In order to consider a compressed nuclear density core of stellar dimensions, we then introduce a Wigner-Seitz cell determining the outer boundary of the electron distribution which, in the new radial coordinate  $\xi$  is characterized by  $\xi_{\text{WS}}$ . In view of the global charge neutrality of the system the electric field goes to zero at  $\xi = \xi_{\text{WS}}$ . This implies, from Eq. (A.3.29),  $d\hat{\phi}/d\xi = 0$  at  $\xi = \xi_{\text{WS}}$ .

We now turn to the determination of the Fermi energy of the electrons in this compressed core. The function  $\hat{\phi}$  and its first derivative  $d\hat{\phi}/d\xi$  must be continuous at the core surface  $\xi = 0$ .

This boundary-value problem can be solved analytically and indeed Eq. (A.3.27) has the first integral,

$$2 \left( \frac{d\hat{\phi}}{d\xi} \right)^2 = \begin{cases} \hat{\phi}^4(\xi) - 4\hat{\phi}(\xi) + 3, & \xi < 0, \\ \hat{\phi}^4(\xi) - \hat{\phi}^4(\xi_{\text{WS}}), & \xi > 0, \end{cases} \quad (\text{A.3.31})$$

with boundary conditions at  $\xi = 0$ :

$$\begin{aligned} \hat{\phi}(0) &= \frac{\hat{\phi}^4(\xi_{\text{WS}}) + 3}{4}, \\ \left. \frac{d\hat{\phi}}{d\xi} \right|_{\xi=0} &= - \sqrt{\frac{\hat{\phi}^4(0) - \hat{\phi}^4(\xi_{\text{WS}})}{2}}. \end{aligned} \quad (\text{A.3.32})$$

Having fulfilled the continuity condition we integrate Eq. (A.3.31) obtaining for  $\xi \leq 0$

$$\hat{\phi}(\xi) = 1 - 3 \left[ 1 + 2^{-1/2} \sinh(a - \sqrt{3}\xi) \right]^{-1}, \quad (\text{A.3.33})$$

where the integration constant  $a$  has the value

$$\sinh(a) = \sqrt{2} \left( \frac{11 + \hat{\phi}^4(\xi_{\text{WS}})}{1 - \hat{\phi}^4(\xi_{\text{WS}})} \right). \quad (\text{A.3.34})$$

In the interval  $0 \leq \xi \leq \xi_{\text{WS}}$ , the field  $\hat{\phi}(\xi)$  is implicitly given by

$$F\left(\arccos\frac{\hat{\phi}(\xi_{\text{WS}})}{\hat{\phi}(\xi)}, \frac{1}{\sqrt{2}}\right) = \hat{\phi}(\xi_{\text{WS}})(\xi - \xi_{\text{WS}}), \quad (\text{A.3.35})$$

where  $F(\varphi, k)$  is the elliptic function of the first kind, and  $F(0, k) \equiv 0$ . For  $F(\varphi, k) = u$ , the inverse function  $\varphi = F^{-1}(u, k) = \text{am}(u, k)$  is the well known Jacobi amplitude. We can thus express the solution (A.3.35) for  $\xi > 0$  as

$$\hat{\phi}(\xi) = \frac{\hat{\phi}(\xi_{\text{WS}})}{\cos\left[\text{am}\left(\hat{\phi}(\xi_{\text{WS}})(\xi - \xi_{\text{WS}}), \frac{1}{\sqrt{2}}\right)\right]}. \quad (\text{A.3.36})$$

### The finite temperature case

A nuclear matter core of stellar dimensions, by definition, is a system composed by neutrons, protons and electrons at nuclear density and in  $\beta$  equilibrium, hence the number of protons  $Z$  and neutrons  $N_n = A - Z$  satisfy  $N_n \gg Z$ . Typically, in such a degenerate massive cores we have  $A/Z \approx 10^2$ , so at nuclear density the neutron gas will have a Fermi energy  $E_n^F$  of the order of

$$E_n^F \sim \frac{P_n^F}{2m_n} \sim (3\pi^2)^{2/3} \frac{\hbar^2}{2m_n} \left(\frac{A - Z}{A} \frac{\rho_{\text{nuc}}}{m_n}\right)^{2/3} \sim 60 \text{ MeV}, \quad (\text{A.3.37})$$

where we have used a nuclear density value  $\rho_{\text{nuc}} \approx 2.7 \times 10^{14} \text{ g cm}^{-3}$  and  $1 - Z/A \approx 1$ . Assuming a temperature such that  $T \ll T_n^F = E_n^F/k_B \approx 7 \times 10^{11} \text{ K}$ , the neutron chemical potential  $\mu_n$  can be expanded as

$$\mu_n = E_n^F \left[ 1 - \frac{\pi^2}{12} \left(\frac{k_B T}{E_n^F}\right)^2 - \frac{\pi^4}{80} \left(\frac{k_B T}{E_n^F}\right)^4 + \dots \right]. \quad (\text{A.3.38})$$

Correspondingly, the protons have Fermi energy  $E_p^F \sim (Z/A)^{2/3} E_n^F \sim \text{MeV}$ , so for temperatures  $k_B T \ll E_p^F \approx 1 \text{ MeV}$ , Eq. (A.3.38) applies also for protons

$$\mu_p = E_p^F \left[ 1 - \frac{\pi^2}{12} \left(\frac{k_B T}{E_p^F}\right)^2 - \frac{\pi^4}{80} \left(\frac{k_B T}{E_p^F}\right)^4 + \dots \right]. \quad (\text{A.3.39})$$

As a result, for temperatures  $k_B T \lesssim 1 \text{ MeV}$ , both neutrons and protons can be treated as degenerate particles whereas in this limit electrons are semi-degenerate and ultra-relativistic. In the case of ordinary nuclei, due their high isospin symmetry ( $A/Z \approx 2$ ), both neutrons and protons can be treated as degenerate particles until  $T \approx (Z/A)^{2/3} E_n^F/k_B \sim 38 \text{ MeV}$ .

Since in the ultra-relativistic limit for electrons their kinetic energy  $\epsilon$  is sim-

ply  $pc$ , the condition  $\mu_e/(k_B T) \gg 1$  holds. Consequently the integral

$$I = \int_0^\infty \frac{f(\epsilon)d\epsilon}{\exp\left(\frac{\epsilon-\mu_e}{k_B T}\right) + 1}, \quad (\text{A.3.40})$$

with  $f(\epsilon) = \epsilon^2$  appearing in the electron density given by Eq. (A.3.13) can be expanded as

$$I = \int_0^{\mu_e} f(\epsilon)d\epsilon + 2(k_B T)^2 f'(\mu_e) \int_0^\infty \frac{z}{e^z + 1} dz + \frac{1}{3}(k_B T)^4 f'''(\mu_e) \int_0^\infty \frac{z^3}{e^z + 1} dz + \dots, \quad (\text{A.3.41})$$

where

$$\int_0^\infty \frac{z^{x-1}}{e^z + 1} dz = (1 - 2^{1-x})\Gamma(x) \sum_{n=1}^\infty \frac{1}{n^x}, \quad (\text{A.3.42})$$

with  $\Gamma$  the Gamma function and  $\mu_e$  the chemical potential of electrons and a prime denotes derivative with respect to  $\epsilon$ . We thus obtain the result

$$I = \int_0^{\mu_e} f(\epsilon)d\epsilon + \frac{\pi^2}{6}(k_B T)^2 f'(\mu_e) + \frac{7\pi^4}{360}(k_B T)^4 f'''(\mu_e) + \dots, \quad (\text{A.3.43})$$

and retaining only the first term in  $T$  we have

$$I \approx \frac{\mu_e^3}{3} + \frac{\pi^2}{6}(k_B T)^2 \mu_e. \quad (\text{A.3.44})$$

As previously discussed for a nuclear massive core of stellar dimensions we can assume the planar approximation so, introducing the same dimensionless quantities as before, the Poisson equation assumes the form

$$\frac{d^2 \hat{\phi}}{d\tilde{\zeta}^2} = -\theta(\tilde{\zeta} - \tilde{\zeta}_c) + \hat{\phi}^3 + s\hat{\phi}, \quad (\text{A.3.45})$$

where  $s = (2\pi^4)^{1/3} \Delta^2 (k_B T)^2 / (3^{4/3} m_\pi^2 c^2)$ .

The Coulomb potential is given by

$$eV(\tilde{\zeta}) = \left(\frac{9\pi}{4}\right)^{1/3} \frac{1}{\Delta} m_\pi c^2 \hat{\phi}(\tilde{\zeta}) - C, \quad (\text{A.3.46})$$

with  $C = (9\pi/4)^{1/3} \Delta^{-1} m_\pi c^2 \hat{\phi}(\tilde{\zeta}_{\text{WS}})$ , the electric field is given by the same

expression as Eq. (A.3.29), and the electron number density is

$$n_e(\xi) = \frac{(m_\pi c^2)^3}{3\pi^2 \hbar^3 c^3} \left[ \left( \frac{9\pi}{4} \right) \frac{1}{\Delta^3} \hat{\phi}^3(\xi) + \frac{\pi^2}{2} \left( \frac{9\pi}{4} \right)^{1/3} \frac{1}{\Delta} \left( \frac{k_B T}{m_\pi c^2} \right)^2 \hat{\phi}(\xi) \right]. \quad (\text{A.3.47})$$

The global charge neutrality of the system imposes the boundary condition that the electric field vanishes at  $\xi = \xi_{WS}$ . This implies  $d\hat{\phi}/d\xi|_{\xi=\xi_{WS}} = 0$ . The function  $\hat{\phi}$  and its first derivative  $d\hat{\phi}/d\xi$  must be continuous at the surface  $\xi = 0$  of the nuclear density core. This boundary-value problem can be solved analytically and indeed Eq. (A.3.45) has the first integral,

$$2 \left( \frac{d\hat{\phi}}{d\xi} \right)^2 = \begin{cases} \hat{\phi}^4(\xi) + 2s\hat{\phi}^2 - 4\hat{\phi}(\xi) + 3 - 2s, & \xi \leq 0, \\ \hat{\phi}^4(\xi) + 2s\hat{\phi}^2 - \hat{\phi}^4(\xi_{WS}) - 2s\hat{\phi}^2(\xi_{WS}), & \xi > 0, \end{cases} \quad (\text{A.3.48})$$

with boundary conditions at  $\xi = 0$ :

$$\hat{\phi}(0) = \frac{\hat{\phi}^4(\xi_{WS}) + 3}{4} + \frac{s}{2} [\hat{\phi}^2(\xi_{WS}) - 1], \quad (\text{A.3.49})$$

$$\left. \frac{d\hat{\phi}}{d\xi} \right|_{\xi=0} = - \left\{ \frac{\hat{\phi}^4(0) - \hat{\phi}^4(\xi_{WS})}{2} + s[\hat{\phi}^2(0) - \hat{\phi}^2(\xi_{WS})] \right\}^{1/2}. \quad (\text{A.3.50})$$

The solution of Eq. (A.3.48) in the interior region  $\xi \leq 0$  is then

$$\hat{\phi}(\xi) = 1 - (s+3) \left[ 1 + \left( \frac{s+1}{2} \right)^{1/2} \sinh(\beta - \sqrt{s+3}\xi) \right]^{-1}, \quad (\text{A.3.51})$$

with

$$\sinh \beta = \sqrt{\frac{2}{s+1}} \left\{ \frac{11 + \hat{\phi}^4(\xi_{WS}) + 2s[\hat{\phi}^2(\xi_{WS}) + 1]}{1 - \hat{\phi}^4(\xi_{WS}) - 2s[\hat{\phi}^2(\xi_{WS}) - 1]} \right\}. \quad (\text{A.3.52})$$

In the exterior region  $\xi > 0$  the solution of Eq. (A.3.48) is

$$\hat{\phi}(\xi) = \frac{\sqrt{-s + \sqrt{s^2 + G}}}{\cos \left( \text{am} \left[ (s^2 + G)^{1/4} (\xi - \xi_{WS}), \frac{1}{2} + \frac{s}{2\hat{\phi}^2(\xi_{WS})} \right] \right)}, \quad (\text{A.3.53})$$

where  $G = \hat{\phi}^4(\xi_{WS}) + 2s\hat{\phi}^2(\xi_{WS})$ . It can be seen how in the limit  $T \rightarrow 0$  ( $s \rightarrow 0$ ), the solution at finite temperatures given by Eqs. (A.3.51), (A.3.52), and (A.3.53) becomes the degenerate solution Eqs. (A.3.33), (A.3.34), and (A.3.36), respectively.

From Eqs. (A.3.50) follows that the peak of the electric field at the surface of the core is larger than the corresponding value obtained for  $T = 0$ . In fact

we have, for any temperature  $T > 0$  and level of compression  $\xi_{\text{WS}} \neq 0$

$$\left| \left( \frac{d\hat{\phi}}{d\xi} \right)_{\xi=0} \right|_{T>0} > \left| \left( \frac{d\hat{\phi}}{d\xi} \right)_{\xi=0} \right|_{T=0}. \quad (\text{A.3.54})$$

As in the degenerate case, in the limit  $\xi_{\text{WS}} \rightarrow 0$ , the global charge neutrality  $N_e = Z$  and the local charge neutrality  $n_e = n_p$  are recovered and at the surface of the massive core no electrodynamical structure is present.

The above analytic equations can be used only in the ultra-relativistic regime of the electron gas; it can then be checked from the above formulation that at such high compressions we have  $\hat{\phi}(\xi)|_{T>0} \approx \hat{\phi}(\xi)|_{T=0}$ . More specifically, corrections due to thermal effects on the density of ultra-relativistic electrons are smaller than 1% for  $T \lesssim 0.1 \text{ MeV}/k_B \approx 10^9 \text{ K}$ .

### A.3.5. Conclusions

The Feynman-Metropolis-Teller treatment of compressed matter Rotondo et al. (2011c) has been here generalized to the case of finite temperatures. We have thus obtained the EOS formed by nuclei and electrons by solving the finite temperature relativistic Thomas-Fermi equation (A.3.16) within globally neutral Wigner-Seitz cells. We emphasize in this work on the electron component and the Coulomb interaction between ions and electrons fully computed within a relativistic Thomas-Fermi approach with finite sized nuclei, and therefore applicable to any relativistic regime of the electrons and densities. This work generalizes other treatments based on either a uniform distribution of electrons or the classic Thomas-Fermi treatment; see e.g. Thorolfsson et al. (1998). The quantum corrections to the classic ideal ion fluid considered in this work can be straightforwardly introduced in their corresponding ranges of relevance as done in previous treatments; see e.g. Stolzmann and Bloeker (1996); Chabrier and Potekhin (1998b); Potekhin and Chabrier (2000, 2013).

We have shown the general features of the new EOS and compared and contrasted the effects owing to the non-zero temperature with respect to the degenerate case. We have checked that the onset of the inverse  $\beta$  decay instability is not modified for temperatures  $T \lesssim 10^8 \text{ K}$  and therefore the zero-temperature critical densities computed in Ref. Rotondo et al. (2011b) can be safely used. The enhancement and flattening of the electron density inside the cell for larger temperatures could have relevant effect in the pycnonuclear reaction rates in the interior of white dwarfs and/or in the low density layers of accreting neutron stars.

Deviations from the degenerate EOS have been shown to occur in the regions of interest of low-mass white dwarfs and in the outermost layers of neutron star crusts. Ultra-low mass white dwarfs  $M_{\text{WD}} \sim 0.2M_{\odot}$  Anto-

niadis et al. (2013a, 2012) have been found in binary systems with neutron stars companions. These objects have central densities  $\lesssim 10^6 \text{ g cm}^{-3}$ , where the degenerate approximation breaks down and so thermal effects cannot be neglected. The application of the treatment presented in this work to these configurations is under current consideration.

Following our previous work Rotondo et al. (2011c), we have then extrapolated the treatment to macroscopic systems with mass numbers  $A \approx (m_{\text{Planck}}/m_n)^3 \sim 10^{57}$ , corresponding to masses  $M_{\text{core}} \approx M_{\odot}$ . We showed that the presence of the temperature enhances the maximum electric field in the core surface of these objects.

## A.4. On Magnetic Fields in Rotating Nuclear Matter Cores of Stellar Dimensions

### A.4.1. Introduction

Neutron stars are mainly detected as pulsars, whose regular pulsations in the radio, X-ray, and optical bands are produced by constant, ordered magnetic fields that are the strongest known in the Universe. However the origin of the magnetic field in the neutron stars is not fully understood, so far. Nevertheless in the literature one may find various hypotheses explaining the formation of the magnetic field (Ginzburg, 1964; Woltjer, 1964; Ruderman, 1972, 1995; Reisenegger, 2001, 2007; Reisenegger et al., 2007). The simplest hypothesis to explain the presence of the strong fields observed in neutron stars is the conservation of the magnetic flux already present in the progenitor stars during the gravitational collapse. This idea is based on the assumption that all stars at all stages of their evolution have some magnetic field, due to electronic currents circulating in their interiors. Thus this argument led to the prediction of the fields  $B \approx 10^{12}$  G in neutron stars a few years before the discovery of pulsars (Ginzburg, 1964; Woltjer, 1964). However, there is no detailed physical picture of such a flux conserving collapse. Thompson and Duncan (1993) put forward the hypothesis that newborn neutron stars are likely to combine vigorous convection and differential rotation making a dynamo process operate in them. They predicted fields up to  $10^{15} - 10^{16}$  G in neutron stars with few millisecond initial periods, and suggested that such fields could explain much of the phenomenology associated with Soft Gamma Repeaters and Anomalous X-ray Pulsars (Thompson and Duncan, 1995, 1996).

Probably, these processes are not mutually exclusive. A strong field might be present in the collapsing star, but later be deformed and perhaps amplified by some combination of convection, differential rotation, and magnetic instabilities (Tayler, 1973; Spruit, 2002). The relative importance of these ingredients depends on the initial field strength and rotation rate of the star. For both mechanisms, the field and its supporting currents are not likely to be confined to the solid crust of the star, but distributed in most of the stellar interior, which is mostly a fluid mixture of neutrons, protons, electrons, and other, more exotic particles.

Unlike aforementioned hypotheses which are based on the assumptions that all stars are magnetized or charged with some net charge different from zero, we explore the system recently considered by Ruffini et al. (2007b). According to that work the system consisting of degenerate neutrons, protons and electrons in beta equilibrium is globally neutral and expected to be kept at nuclear density by self gravity. In what follows these systems are termed as Nuclear Matter Cores of Stellar Dimensions. Despite the global neutrality the charge distribution turned out to be different from zero inside and out-

side (near the surface) the star. The magnitude of the net charge inside and outside the core is equal, but the sign is opposite. Such an effect takes place as a consequence of the beta equilibrium, the penetration of electrons into the core, hence the screening of the core charge and global charge neutrality. As a result of this effect, one may show the presence of an electric field close to the critical value  $E_c = m_e^2 c^3 / e \hbar$  near the surface of the massive cores, although localized in a very narrow shell. Thus in this case the magnetic field of the neutron star may be generated only if it spins like pulsars, even though the progenitor star has not been magnetized or electrically charged.

#### A.4.2. The Relativistic Thomas-Fermi equation

The Thomas-Fermi equation is the exact theory for atoms, molecules and solids as  $Z \rightarrow \infty$  (Lieb and Simon, 1973). The relativistic Thomas-Fermi theory developed for the study of atoms for heavy nuclei with  $Z = 10^6$  (Ferreirinho et al., 1980; Ruffini and Stella, 1981) gives important basic new information on the study of nuclear matter in bulk in the limit of  $A = (m_{Planck}/m_n)^3$  nucleons of mass  $m_n$  and on its electrodynamic properties. The analysis of nuclear matter bulk in neutron stars composed of degenerate gas of neutrons, protons and electrons, has traditionally been approached by implementing microscopically the charge neutrality condition by requiring the electron density  $n_e(r)$  to coincide with the proton density  $n_p(r)$ ,

$$n_e(r) = n_p(r). \quad (\text{A.4.1})$$

It is clear however that especially when conditions close to the gravitational collapse occur, there is an ultra-relativistic component of degenerate electrons whose confinement requires the existence of very strong electromagnetic fields, in order to guarantee the overall charge neutrality of the neutron star. Under these conditions equation (A.4.1) will be necessarily violated.

Using substantially a statistical approach based on the relativistic Thomas-Fermi equation, Ferreirinho et al. (1980); Ruffini and Stella (1981) have analyzed the electron densities around an extended nucleus in a neutral atom all the way up to  $Z = 6000$ . They have shown the effect of penetration of the electron orbital well inside the nucleus, leading to a screening of the nuclei positive charge and to the concept of an “effective” nuclear charge distribution.

In the work of Ruffini et al. (2007b) and Rotondo et al. (2011e) the relativistic Thomas-Fermi equation has been used to extrapolate the treatment of super heavy nuclei to the case of nuclear matter cores of stellar dimensions. These cores represent the inner part of neutron stars and are characterized by an atomic number of order of  $A = (m_{Planck}/m_n)^3 \approx 10^{57}$ , composed of degenerate  $N_n$  neutrons,  $N_p$  protons and  $N_e$  electrons in beta equilibrium and expected to be kept at nuclear density by self gravity. It has been shown that

near the surface of the massive cores it is possible to have an electric field close to the critical value  $E_c$ , although localized in a very narrow shell of the order of the  $\lambda_e$  electron Compton wavelength. Now let us review the main assumptions and results of those works.

According to Ruffini et al. (2007b) and Rotondo et al. (2011e) the protons are distributed at constant density  $n_p$  within a radius

$$R_c = \Delta \frac{\hbar}{m_\pi c} N_p^{1/3}, \quad (\text{A.4.2})$$

where  $\Delta$  is a parameter such that  $\Delta \approx 1$  ( $\Delta < 1$ ) corresponds to nuclear (supranuclear) densities when applied to ordinary nuclei. The overall Coulomb potential satisfies the Poisson equation

$$\nabla^2 V(r) = -4\pi e [n_p(r) - n_e(r)], \quad (\text{A.4.3})$$

with the boundary conditions  $V(\infty) = 0$  (due to the global charge neutrality of the system) and finiteness of  $V(0)$ . The density  $n_e(r)$  of the electrons of charge  $-e$  is determined by the Fermi energy condition on their Fermi momentum  $P_e^F$ ; we assume here

$$E_e^F = [(P_e^F c)^2 + m_e^2 c^4]^{1/2} - m_e c^2 - eV(r) = 0, \quad (\text{A.4.4})$$

which leads to

$$n_e(r) = \frac{(P_e^F)^3}{3\pi^2 \hbar^3} = \frac{1}{3\pi^2 \hbar^3 c^3} [e^2 V^2(r) + 2m_e c^2 eV(r)]^{3/2}. \quad (\text{A.4.5})$$

Introducing the dimensionless quantities  $x = r/[\hbar/m_\pi c]$ ,  $x_c = R_c/[\hbar/m_\pi c]$  and  $\chi/r = eV(r)/c\hbar$ , the relativistic Thomas-Fermi equation takes the form

$$\frac{1}{3x} \frac{d^2 \chi(x)}{dx^2} = -\frac{\alpha}{\Delta^3} H(x_c - x) + \frac{4\alpha}{9\pi} \left[ \frac{\chi^2(x)}{x^2} + 2 \frac{m_e}{m_\pi} \frac{\chi}{x} \right]^{3/2}, \quad (\text{A.4.6})$$

where  $\alpha = e^2/(\hbar c)$  is the fine structure constant,  $H(x_c - x)$  is the Heaviside step function and the boundary conditions for  $\chi(x)$  are  $\chi(0) = 0, \chi(\infty) = 0$ . The neutron density  $n_n(r)$  is determined by the Fermi energy condition on their Fermi momentum  $P_n^F$  imposed by beta decay equilibrium

$$E_n^F = [(P_n^F c)^2 + m_n^2 c^4]^{1/2} - m_n c^2 = [(P_p^F c)^2 + m_p^2 c^4]^{1/2} - m_p c^2 + eV, \quad (\text{A.4.7})$$

which in turn is related to the proton and electron densities by Eqs. (A.4.3), (A.4.5) and (A.4.6).

### A.4.3. The ultra-relativistic analytic solutions

In the ultrarelativistic limit with the planar approximation the relativistic Thomas-Fermi equation admits an analytic solution. Introducing the new function  $\phi$  defined by  $\phi = 4^{1/3}(9\pi)^{-1/3}\Delta\chi/x$  and the new variables  $\hat{x} = (12/\pi)^{1/6}\sqrt{\alpha}\Delta^{-1}x$ ,  $\xi = \hat{x} - \hat{x}_c$ , where  $\hat{x}_c = (12/\pi)^{1/6}\sqrt{\alpha}\Delta^{-1}x_c$ , Eq. (A.4.6) becomes

$$\frac{d^2\hat{\phi}(\xi)}{d\xi^2} = -H(-\xi) + \hat{\phi}(\xi)^3, \quad (\text{A.4.8})$$

where  $\hat{\phi}(\xi) = \phi(\xi + \hat{x}_c)$ . The boundary conditions on  $\hat{\phi}$  are:  $\hat{\phi}(\xi) \rightarrow 1$  as  $\xi \rightarrow -\hat{x}_c \ll 0$  (at the nuclear matter core center) and  $\hat{\phi}(\xi) \rightarrow 0$  as  $\xi \rightarrow \infty$ . The function  $\hat{\phi}$  and its first derivative  $\hat{\phi}'$  must be continuous at the surface  $\xi = 0$  of the nuclear matter core of stellar dimensions. Hence equation (A.4.8) admits an exact solution

$$\hat{\phi}(\xi) = \begin{cases} 1 - 3 \left[ 1 + 2^{-1/2} \sinh(a - \sqrt{3}\xi) \right]^{-1}, & \xi < 0, \\ \frac{\sqrt{2}}{(\xi + b)}, & \xi > 0, \end{cases} \quad (\text{A.4.9})$$

where the integration constants  $a$  and  $b$  have the values  $a = \text{arccosh}(9\sqrt{3}) \approx 3.439$ ,  $b = (4/3)\sqrt{2} \approx 1.886$ . Next we evaluate the Coulomb potential function

$$V(\xi) = \left( \frac{9\pi}{4} \right)^{1/3} \frac{m_\pi c^2}{\Delta e} \hat{\phi}(\xi), \quad (\text{A.4.10})$$

and by differentiation, the electric field

$$E(\xi) = - \left( \frac{3^5 \pi}{4} \right)^{1/6} \frac{\sqrt{\alpha} m_\pi^2 c^3}{\Delta^2 e \hbar} \hat{\phi}'(\xi). \quad (\text{A.4.11})$$

Details are given in Figs. A.22 and A.23.

### A.4.4. Rotating Nuclear Matter Cores of Stellar Dimensions in Classical Electrodynamics

In section A.4.2 and A.4.3 we have seen that in the massive nuclear density cores the electric charge distribution is different from zero, although it is globally neutral. In this section we investigate the case when this charge distribution is allowed to rotate with the constant angular velocity  $\Omega$  around the axis of symmetry. Thus the magnetic field of the resultant current density is calculated in terms of the charge distribution.

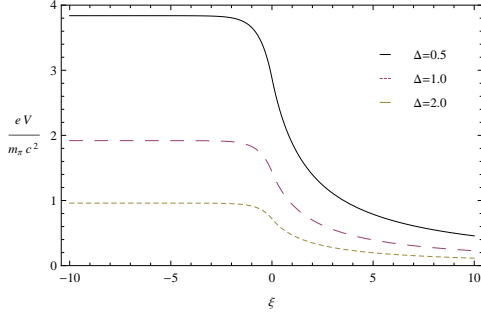


**Figure A.22.:** The electron Coulomb potential energy  $eV$ , in units of pion mass  $m_\pi$  is plotted as a function of the radial coordinate  $\xi = \hat{x} - \hat{x}_c$ , for selected values of the density parameter  $\Delta$ .

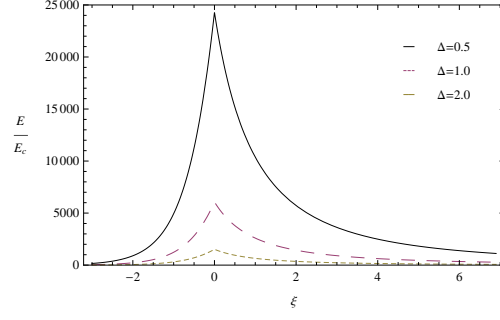


**Figure A.23.:** The electric field is plotted in units of the critical field  $E_c$  as a function of the radial coordinate  $\xi$ , showing a sharp peak at the core radius, for selected values of  $\Delta$ .

Consider a charge distribution moving in a such way that at every point in space the charge density and the current density remain constant. In this case the magnetic field is defined by

$$\mathbf{B}(\mathbf{r}) = \nabla \times \mathbf{A}(\mathbf{r}), \quad \mathbf{A}(\mathbf{r}) = (\boldsymbol{\Omega}/c^2) \times \mathbf{F}(\mathbf{r}), \quad \mathbf{F}(\mathbf{r}) = \frac{1}{4\pi} \int \frac{\mathbf{r}'\rho(\mathbf{r}')d^3\mathbf{r}'}{|\mathbf{r} - \mathbf{r}'|}, \quad (\text{A.4.12})$$

where  $\mathbf{A}$  is the vector potential of the magnetic field,  $\mathbf{F}(\mathbf{r})$  is the "superpotential" in general form. In the case of spherical symmetry,  $\mathbf{F}(\mathbf{r})$  may be taken as radial (see Marsh (1982)). Writing  $\mathbf{F}(\mathbf{r}) = \mathbf{e}_r F(r)$ , where  $\mathbf{e}_r$  is the unit radial vector, one has

$$F(r) = \frac{1}{r^2} \int_0^r r'^2 \frac{d}{dr'} [r'V(r')] dr'. \quad (\text{A.4.13})$$

This expression allows to calculate the magnetic field due to rotation of any spherically symmetric distribution of charge in terms of its electrostatic Coulomb potential. Note that in fact due to rotation the shape of the neutron star must deviate from spherical symmetry. Since we are interested in the estimation of the order of the magnetic field the distortions to the shape of the star can be neglected for simplicity. Thus the magnetic field is defined by

$$\mathbf{B}(\mathbf{r}) = B_r \mathbf{e}_r + B_\theta \mathbf{e}_\theta, \quad B_r = \frac{2\Omega F}{c^2 r} \cos \theta, \quad B_\theta = -\frac{2\Omega}{c^2} \left[ \frac{F}{r} + \frac{r}{2} \frac{d}{dr} \left( \frac{F}{r} \right) \right] \sin \theta, \quad (\text{A.4.14})$$

where  $B_r$  is the radial component and  $B_\theta$  is the angular component of the magnetic field,  $\theta$  is the angle between  $r$  and  $z$  axis, and  $\mathbf{e}_\theta$  is the unit vector along  $\theta$ . Consequently the expression for the magnitude (the absolute value)

of the magnetic field can be written as

$$B(r, \theta) = \frac{\Omega r}{c^2} \sqrt{\left(\frac{2F}{r^2}\right)^2 + \left\{ \frac{4F}{r^2} \frac{d}{dr} \left(\frac{F}{r}\right) + \left[ \frac{d}{dr} \left(\frac{F}{r}\right) \right]^2 \right\} \sin^2 \theta}. \quad (\text{A.4.15})$$

Using the relation between  $r$  and  $\xi$

$$r = R_c + \left(\frac{\pi}{12}\right)^{1/6} \frac{\Delta}{\sqrt{\alpha}} \frac{\hbar}{m_\pi c} \xi, \quad (\text{A.4.16})$$

one may estimate the value of the magnetic field. In Figs. A.24, A.25, A.26 and A.27 details are given.

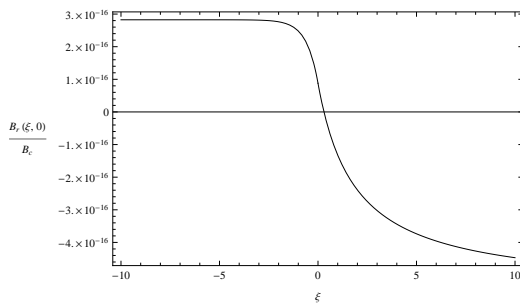


**Figure A.24.:** The radial component of the magnetic field is plotted as a function of the radial coordinate  $\xi$  in units of the critical field  $B_c = m_c^2 c^3 / e \hbar \approx 4.5 \times 10^{13}$  G. Here the period is taken to be  $P = 10$  ms,  $\theta = 0$ ,  $\Delta = 1$  and the radius of the core  $R_c = 10$  km. Note that  $B_r$  is considered at the poles of star, where it has maximum value. Outside the star  $B_r$  has very small negative value and it tends to zero. Because of visualization difficulties it is not seen in the figure.

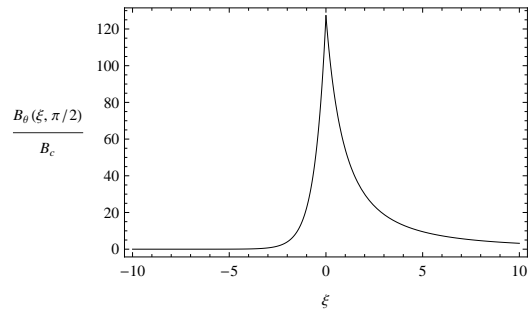


**Figure A.25.:** The angular component of the magnetic field is plotted in units of the  $B_c$ . Here  $P = 10$  ms,  $\theta = \pi/2$ ,  $\Delta = 1$  and  $R_c = 10$  km. Note that  $B_\theta$  is considered at the equator, where it has maximum value. Inside the star it has very small constant negative value. Outside the star first it becomes negative (the value is very small) then it tends to zero. Because of scale problems this behavior is not seen from the figure.

Examining the Fig. A.24 one can see very small value of  $B_r$  which almost does not make a significant contribution to the magnitude of the field, except for the poles of the star. On the contrary,  $B_\theta$  Fig. A.25 has values exceeding the critical magnetic field near the surface of the core although localized in a narrow region between positively and negatively charged shells as expected. Outside the core the magnetic field becomes negative. The magnitude of the

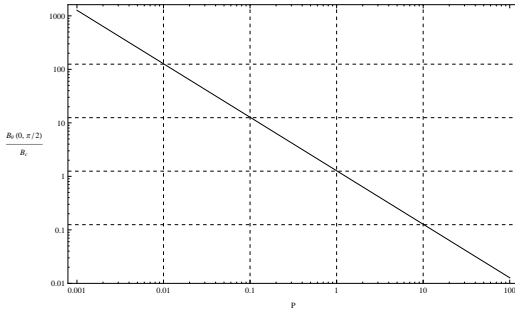


**Figure A.26.:** The magnitude of the magnetic field is plotted as a function of the period of the star  $P$  in the units of the critical field  $B_c$  at the surface of the core  $R_c = 10 \text{ km}$  on the equator in the logarithmic scale.

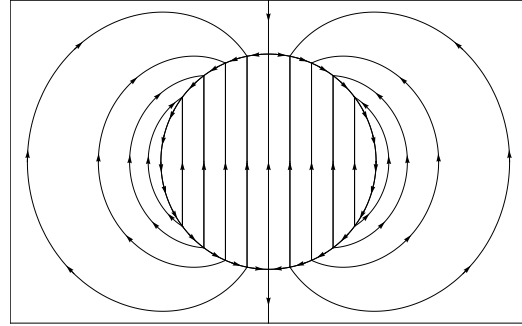


**Figure A.27.:** The magnetic lines of forces. Outside the star the magnetic field looks like a dipole field. Extra lines along the surface of the star indicate overcritical value of the field between positively and negatively charged shells.

field has very small and eventually vanishing values. This effect can not be seen from the figures, because of visualization difficulties.

In Fig. A.26 the magnitude of the magnetic field is presented as a function of the rotational period  $P$  on the surface of the core at the equator. Practically it demonstrates the upper limit of possible values of the magnetic field in the range between  $1 \text{ ms}$  and  $100 \text{ s}$ . Fig. A.27 represents magnetic lines of force inside, outside and on the surface of the star. It turned out that the lines of force of the overcritical magnetic field are oppressed between two shells along the surface of the core.

### A.4.5. Conclusions

In this paper we have investigated the behavior of the magnetic field induced due to rotation on the basis of the research works considered in Ruffini et al. (2007b) and Rotondo et al. (2011e) using the technique developed by Marsh (1982).

For this purpose considering a rotating neutron star with the period of  $10 \text{ ms}$  we have obtained the magnetic field of order of the critical field near the surface of the star and analyzed the magnetic lines of forces.

According to our results the magnetic fields of the neutron stars could be generated due to the rotation of the star as a whole rigid body. We believe that the generation of the magnetic field due to the rotation is the reason for the formation of the constant magnetic fields at the initial moments of neutron stars birth.

The problem of investigating the magnetic field in general relativity for a

self-gravitating system of degenerate fermions in beta equilibrium is beyond the scope of the present work. We expect to investigate this problem in the nearest future.

# B. White Dwarfs Physics and Astrophysics

## B.1. The relativistic Feynman-Metropolis-Teller theory for white dwarfs in general relativity

### B.1.1. Introduction

The necessity of introducing the Fermi-Dirac statistics in order to overcome some conceptual difficulties in explaining the existence of white dwarfs leading to the concept of degenerate stars was first advanced by (Fowler, 1926) in a classic paper. Following that work, Stoner (1929) introduced the effect of special relativity into the Fowler considerations and he discovered the critical mass of white dwarfs

$$M_{\text{crit}}^{\text{Stoner}} = \frac{15}{16} \sqrt{5\pi} \frac{M_{\text{Pl}}^3}{\mu^2 m_n^2} \approx 3.72 \frac{M_{\text{Pl}}^3}{\mu^2 m_n^2}, \quad (\text{B.1.1})$$

where  $M_{\text{Pl}} = \sqrt{\hbar c / G} \approx 10^{-5}$  g is the Planck mass,  $m_n$  is the neutron mass, and  $\mu = A/Z \approx 2$  is the average molecular weight of matter which shows explicitly the dependence of the critical mass on the chemical composition of the star.

Following the Stoner's work, Chandrasekhar (1931b) pointed out the relevance of describing white dwarfs by using an approach, initiated by Milne (1930), of using the mathematical method of the solutions of the Lane-Emden polytropic equations (Emden, 1907). The same idea of using the Lane-Emden equations taking into account the special relativistic effects to the equilibrium of stellar matter for a degenerate system of fermions, came independently to Landau (1932). Both the Chandrasekhar and Landau treatments were explicit in pointing out the existence of the critical mass

$$M_{\text{crit}}^{\text{Ch-L}} = 2.015 \frac{\sqrt{3\pi}}{2} \frac{M_{\text{Pl}}^3}{\mu^2 m_n^2} \approx 3.09 \frac{M_{\text{Pl}}^3}{\mu^2 m_n^2}, \quad (\text{B.1.2})$$

where the first numerical factor on the right hand side of Eq. (B.1.2) comes from the boundary condition  $-(r^2 du/dr)_{r=R} = 2.015$  (see last entry of Table 7 on Pag. 80 in Emden (1907)) of the  $n = 3$  Lane-Emden polytropic equation.

Namely for  $M > M_{\text{crit}}^{\text{Ch-L}}$ , no equilibrium configuration should exist.

Some of the basic assumptions adopted by Chandrasekhar and Landau in their idealized approach e.g. the treatment of the electron as a free-gas without taking into due account the electromagnetic interactions, as well as the stability of the distribution of the nuclei against the gravitational interaction led to some criticisms by Eddington (1935). It was unfortunate that the absence of interest of E. Fermi on the final evolution of stars did not allow Fermi himself to intervene in these well-posed theoretical problems (Boccaletti and Ruffini, 2010). Indeed, we are showing in this article how the solution of the conceptual problems of the white dwarf models, left open for years, can be duly addressed by considering the relativistic Thomas-Fermi model of the compressed atom (see Subsec. B.1.2 and Sec. B.1.4).

The original work on white dwarfs was motivated by astrophysics and found in astrophysics strong observational support. The issue of the equilibrium of the electron gas and the associated component of nuclei, taking into account the electromagnetic, the gravitational and the weak interactions is a theoretical physics problem, not yet formulated in a correct special and general relativistic context.

One of the earliest alternative approaches to the Chandrasekhar-Landau work was proposed by Salpeter (1961a). He followed an idea originally proposed by Frenkel (1928): to adopt in the study of white dwarfs the concept of a Wigner-Seitz cell. Salpeter introduced to the lattice model of a point-like nucleus surrounded by a uniform cloud of electrons, corrections due to the non-uniformity of the electron distribution (see Subsec. B.1.2 for details). In this way Salpeter (1961a) obtained an analytic formula for the total energy in a Wigner-Seitz cell and derived the corresponding equation of state of matter composed by such cells, pointing out explicitly the relevance of the Coulomb interaction.

The consequences of the Coulomb interactions in the determination of the mass and radius of white dwarfs, was studied in a subsequent paper by Hamada and Salpeter (1961) by using the equation of state constructed in Salpeter (1961a). They found that the critical mass of white dwarfs depends in a nontrivial way on the specific nuclear composition: the critical mass of Chandrasekhar-Landau which depends only on the mass to charge ratio of nuclei  $A/Z$ , now depends also on the proton number  $Z$ .

This fact can be seen from the approximate expression for the critical mass of white dwarfs obtained by Hamada and Salpeter (1961) in the ultrarelativistic limit for the electrons

$$M_{\text{crit}}^{\text{H\&S}} = 2.015 \frac{\sqrt{3\pi}}{2} \frac{1}{\mu_{\text{eff}}^2} \frac{M_{\text{Pl}}^3}{m_n^2}, \quad (\text{B.1.3})$$

where

$$\mu_{\text{eff}} = \mu \left( \frac{P_S}{P_{\text{Ch}}} \right)^{-3/4}, \quad (\text{B.1.4})$$

being  $P_S$  the pressure of the Wigner-Seitz cell obtained by Salpeter (1961a) (see Subsec. B.1.2) and  $P_{\text{Ch}}$  is the pressure of a free-electron fluid used by Chandrasekhar (see Subsec. B.1.2). The ratio  $P_S/P_{\text{Ch}}$  is a function of the number of protons  $Z$  (see Eq. (20) in Salpeter (1961a)) and it satisfies  $P_S/P_{\text{Ch}} < 1$ . Consequently, the effective molecular weight satisfies  $\mu_{\text{eff}} > \mu$  and the critical mass of white dwarfs turns to be smaller than the original one obtained by Chandrasekhar-Landau (see Eq. (B.1.2)).

In the mean time, the problem of the equilibrium gas in a white dwarf taking into account possible global electromagnetic interactions between the nucleus and the electrons was addressed by Olson and Bailyn (1975, 1976). They well summarized the status of the problem: Traditional models for the white dwarf are non-relativistic and electrically neutral. Although an electric field is needed to support the pressureless nuclei against gravitational collapse, the star is treated essentially in terms of only one charge component, where charge neutrality is assumed. Their solution to the problem invokes the breakdown of the local charge neutrality and the presence of an overall electric field as a consequence of treating also the nuclei inside the white dwarf as a fluid. They treated the white dwarf matter through a two-fluid model not enforcing local charge neutrality. The closure equation for the Einstein-Maxwell system of equations was there obtained from a minimization procedure of the mass-energy of the configuration. This work was the first pointing out the relevance of the Einstein-Maxwell equations in the description of an astrophysical system by requiring global and non local charge neutrality. As we will show here, this interesting approach does not apply to the case of white dwarfs. It represents, however, a new development in the study of neutron stars (see e.g. Rotondo et al. (2011d))

An alternative approach to the Salpeter treatment of a compressed atom was reconsidered in gur (2000) by applying for the first time to white dwarfs a relativistic Thomas-Fermi treatment of the compressed atom introducing a finite size nucleus within a phenomenological description (see also Bertone and Ruffini (2000)).

Recently, the study of a compressed atom has been revisited in Rotondo et al. (2011c) by extending the global approach of Feynman et al. (1949) taking into account weak interactions. This treatment takes also into account all the Coulomb contributions duly expressed relativistically without the need of any piecewise description. The relativistic Thomas-Fermi model has been solved by imposing in addition to the electromagnetic interaction also the weak equilibrium between neutrons, protons and electrons self-consistently. This presents some conceptual differences with respect to previous approaches and can be used in order both to validate and to establish their limitations.

In this article we apply the considerations presented in Rotondo et al. (2011c) of a compressed atom in a Wigner-Seitz cell to the description of non-rotating white dwarfs in general relativity. This approach improves all previous treatments in the following aspects:

1. In order to warranty self-consistency with a relativistic treatment of the electrons, the point-like assumption of the nucleus is abandoned introducing a finite sized nucleus (Rotondo et al., 2011c). We assume for the mass as well as for charge to mass ratio of the nucleus their experimental values instead of using phenomenological descriptions based on the semi-empirical mass-formula of Weizsacker (see e.g. Gur (2000); Bertone and Ruffini (2000)).
2. The electron-electron and electron-nucleus Coulomb interaction energy is calculated without any approximation by solving numerically the relativistic Thomas-Fermi equation for selected energy-densities of the system and for each given nuclear composition.
3. The energy-density of the system is calculated taking into account the contributions of the nuclei, of the Coulomb interactions as well as of the relativistic electrons; the latter being neglected in all previous treatments. This particular contribution turns to be very important at high-densities and in particular for light nuclear compositions e.g.  ${}^4\text{He}$  and  ${}^{12}\text{C}$ .
4. The  $\beta$ -equilibrium between neutrons, protons, and electrons is also taken into account leading to a self-consistent calculation of the threshold density for triggering the inverse  $\beta$ -decay of a given nucleus.
5. The structure of the white dwarf configurations is obtained by integrating the general relativity equations of equilibrium.
6. Due to 4) and 5) we are able to determine if the instability point leading to a maximum stable mass of the non-rotating white dwarf is induced by the inverse  $\beta$ -decay instability of the composing nuclei or by general relativistic effects.

Paradoxically, after all this procedure which takes into account many additional theoretical features generalizing the Chandrasekhar-Landau and the Hamada and Salpeter works, a most simple equation is found to be fulfilled by the equilibrium configuration in a spherically symmetric metric. Assuming the metric

$$ds^2 = e^{\nu(r)}c^2dt^2 - e^{\lambda(r)}dr^2 - r^2d\theta^2 - r^2\sin^2\theta d\varphi^2, \quad (\text{B.1.5})$$

we demonstrate how the entire system of equations describing the equilibrium of white dwarfs, taking into account the weak, the electromagnetic and

the gravitational interactions as well as quantum statistics all expressed consistently in a general relativistic approach, is simply given by

$$\sqrt{g_{00}}\mu_{ws} = e^{\nu(r)/2}\mu_{ws}(r) = \text{constant}, \quad (\text{B.1.6})$$

which links the chemical potential of the Wigner-Seitz cell  $\mu_{ws}$ , duly solved by considering the relativistic Feynman-Metropolis-Teller model following Rotondo et al. (2011c), to the general relativistic gravitational potential at each point of the configuration. The overall system outside each Wigner-Seitz cell is strictly neutral and no global electric field exists, contrary to the results reported in Olson and Bailyn (1976). The same procedure will apply as well to the case of neutron star crusts.

The article is organized as follows. In Sec. B.1.2 we summarize the most common approaches used for the description of white dwarfs and neutron star crusts: the uniform approximation for the electron fluid (see e.g. Chandrasekhar (1931b)); the often called lattice model assuming a point-like nucleus surrounded by a uniform electron cloud (see e.g. Baym et al. (1971b)); the generalization of the lattice model due to Salpeter (1961a); the Feynman, Metropolis and Teller approach (Feynman et al., 1949) based on the non-relativistic Thomas-Fermi model of compressed atoms and, the relativistic generalization of the Feynman-Metropolis-Teller treatment recently formulated in Rotondo et al. (2011c).

In Sec. B.1.3 we formulate the general relativistic equations of equilibrium of the system and show how, from the self-consistent definition of chemical potential of the Wigner-Seitz cell and the Einstein equations, comes the equilibrium condition given by Eq. (B.1.6). In addition, we obtain the Newtonian and the first-order post-Newtonian equations of equilibrium.

Finally, we show in Sec. B.1.4 the new results of the numerical integration of the general relativistic equations of equilibrium and discuss the corrections to the Stoner critical mass  $M_{\text{crit}}^{\text{Stoner}}$ , to the Chandrasekhar-Landau mass limit  $M_{\text{crit}}^{\text{Ch-L}}$ , as well as to the one of Hamada and Salpeter  $M_{\text{crit}}^{\text{H\&S}}$ , obtained when all interactions are fully taken into account through the relativistic Feynman-Metropolis-Teller equation of state (Rotondo et al., 2011c).

## B.1.2. The Equation of State

There exists a large variety of approaches to model the equation of state of white dwarf matter, each one characterized by a different way of treating or neglecting the Coulomb interaction inside each Wigner-Seitz cell, which we will briefly review here. Particular attention is given to the calculation of the self-consistent chemical potential of the Wigner-Seitz cell  $\mu_{ws}$ , which plays a very important role in the conservation law (B.1.6) that we will derive in Sec. B.1.3.

### The uniform approximation

In the uniform approximation used by Chandrasekhar (1931b), the electron distribution as well as the nucleons are assumed to be locally constant and therefore the condition of local charge neutrality

$$n_e = \frac{Z}{A_r} n_N, \quad (\text{B.1.7})$$

where  $A_r$  is the average atomic weight of the nucleus, is applied. Here  $n_N$  denotes the nucleon number density and  $Z$  is the number of protons of the nucleus. The electrons are considered as a fully degenerate free-gas and then described by Fermi-Dirac statistics. Thus, their number density  $n_e$  is related to the electron Fermi-momentum  $P_e^F$  by

$$n_e = \frac{(P_e^F)^3}{3\pi^2\hbar^3}, \quad (\text{B.1.8})$$

and the total electron energy-density and electron pressure are given by

$$\begin{aligned} \varepsilon_e &= \frac{2}{(2\pi\hbar)^3} \int_0^{P_e^F} \sqrt{c^2 p^2 + m_e^2 c^4} 4\pi p^2 dp \\ &= \frac{m_e^4 c^5}{8\pi^2 \hbar^3} [x_e \sqrt{1 + x_e^2} (1 + 2x_e^2) - \text{arcsinh}(x_e)], \end{aligned} \quad (\text{B.1.9})$$

$$\begin{aligned} P_e &= \frac{1}{3} \frac{2}{(2\pi\hbar)^3} \int_0^{P_e^F} \frac{c^2 p^2}{\sqrt{c^2 p^2 + m_e^2 c^4}} 4\pi p^2 dp \\ &= \frac{m_e^4 c^5}{8\pi^2 \hbar^3} [x_e \sqrt{1 + x_e^2} (2x_e^2/3 - 1) + \text{arcsinh}(x_e)], \end{aligned} \quad (\text{B.1.10})$$

where we have introduced the dimensionless Fermi momentum  $x_e = P_e^F / (m_e c)$  with  $m_e$  the electron rest-mass.

The kinetic energy of nucleons is neglected and therefore the pressure is assumed to be only due to electrons. Thus the equation of state can be written as

$$\varepsilon_{\text{unif}} = \varepsilon_N + \varepsilon_e \approx \frac{A_r}{Z} M_u c^2 n_e + \varepsilon_e, \quad (\text{B.1.11})$$

$$P_{\text{unif}} \approx P_e, \quad (\text{B.1.12})$$

where  $M_u = 1.6604 \times 10^{-24}$  g is the unified atomic mass and  $\varepsilon_e$  and  $P_e$  are given by Eqs. (B.1.9–B.1.10).

Within this approximation, the total self-consistent chemical potential is given by

$$\mu_{\text{unif}} = A_r M_u c^2 + Z \mu_e, \quad (\text{B.1.13})$$

where

$$\mu_e = \frac{\mathcal{E}_e + P_e}{n_e} = \sqrt{c^2(P_e^F)^2 + m_e^2 c^4}, \quad (\text{B.1.14})$$

is the electron free-chemical potential.

As a consequence of this effective approach which does not take into any account the Coulomb interaction, it is obtained an effective one-component electron-nucleon fluid approach where the kinetic pressure is given by electrons of mass  $m_e$  and their gravitational contribution is given by an effective mass  $(A_r/Z)M_u$  attached to each electron (see e.g. Landau and Lifshitz (1980)). This is even more evident when the electron contribution to the energy-density in Eq. (B.1.11) is neglected and therefore the energy-density is attributed only to the nuclei. Within this approach followed by Chandrasekhar (1931b), the equation of state reduces to

$$\mathcal{E}_{\text{Ch}} = \frac{A_r}{Z} M_u c^2 n_e, \quad (\text{B.1.15})$$

$$P_{\text{Ch}} = P_{\text{unif}} = P_e. \quad (\text{B.1.16})$$

### The lattice model

The first correction to the above uniform model, corresponds to abandon the assumption of the electron-nucleon fluid through the so-called “lattice” model which introduces the concept of Wigner-Seitz cell: each cell contains a point-like nucleus of charge  $+Ze$  with  $A$  nucleons surrounded by a uniformly distributed cloud of  $Z$  fully-degenerate electrons. The global neutrality of the cell is guaranteed by the condition

$$Z = V_{\text{ws}} n_e = \frac{n_e}{n_{\text{ws}}}, \quad (\text{B.1.17})$$

where  $n_{\text{ws}} = 1/V_{\text{ws}}$  is the Wigner-Seitz cell density and  $V_{\text{ws}} = 4\pi R_{\text{ws}}^3/3$  is the cell volume.

The total energy of the Wigner-Seitz cell is modified by the inclusion of the Coulomb energy, i.e

$$E_L = \mathcal{E}_{\text{unif}} V_{\text{ws}} + E_C, \quad (\text{B.1.18})$$

being

$$E_C = E_{e-N} + E_{e-e} = -\frac{9}{10} \frac{Z^2 e^2}{R_{\text{ws}}}, \quad (\text{B.1.19})$$

where  $\mathcal{E}_{\text{unif}}$  is given by Eq. (B.1.11) and  $E_{e-N}$  and  $E_{e-e}$  are the electron-nucleus

and the electron-electron Coulomb energies

$$E_{e-N} = - \int_0^{R_{ws}} 4\pi r^2 \left( \frac{Ze}{r} \right) en_e dr = - \frac{3 Z^2 e^2}{2 R_{ws}}, \quad (\text{B.1.20})$$

$$E_{e-e} = \frac{3 Z^2 e^2}{5 R_{ws}}. \quad (\text{B.1.21})$$

The self-consistent pressure of the Wigner-Seitz cell is then given by

$$P_L = - \frac{\partial E_L}{\partial V_{ws}} = P_{unif} + \frac{1}{3} \frac{E_C}{V_{ws}}, \quad (\text{B.1.22})$$

where  $P_{unif}$  is given by Eq. (B.1.12). It is worth to recall that the point-like assumption of the nucleus is incompatible with a relativistic treatment of the degenerate electron fluid (see Ferreira et al. (1980); Ruffini and Stella (1981) for details). Such an inconsistency has been traditionally ignored by applying, within a point-like nucleus model, the relativistic formulas (B.1.9) and (B.1.10) and their corresponding ultrarelativistic limits (see e.g. Salpeter (1961a)).

The Wigner-Seitz cell chemical potential is in this case

$$\mu_L = E_L + P_L V_{ws} = \mu_{unif} + \frac{4}{3} E_C. \quad (\text{B.1.23})$$

By comparing Eqs. (B.1.12) and (B.1.22) we can see that the inclusion of the Coulomb interaction results in a decreasing of the pressure of the cell due to the negative lattice energy  $E_C$ . The same conclusion is achieved for the chemical potential from Eqs. (B.1.13) and (B.1.23).

### Salpeter approach

A further development to the lattice model came from Salpeter (1961a) whom studied the corrections due to the non-uniformity of the electron distribution inside a Wigner-Seitz cell.

Following the Chandrasekhar (1931b) approximation, Salpeter also neglects the electron contribution to the energy-density. Thus, the first term in the Salpeter formula for the energy of the cell comes from the nuclei energy (B.1.15). The second contribution is given by the Coulomb energy of the lattice model (B.1.19). The third contribution is obtained as follows: the electron density is assumed as  $n_e[1 + \epsilon(r)]$ , where  $n_e = 3Z/(4\pi R_{ws}^3)$  is the average electron density as given by Eq. (B.1.17), and  $\epsilon(r)$  is considered infinitesimal. The Coulomb potential energy is assumed to be the one of the point-like nucleus surrounded by a uniform distribution of electrons, so the correction given by  $\epsilon(r)$  on the Coulomb potential is neglected. The electron distribution is then calculated at first-order by expanding the relativistic electron kinetic

energy

$$\begin{aligned}\epsilon_k &= \sqrt{[cP_e^F(r)]^2 + m_e^2 c^4} - m_e c^2 \\ &= \sqrt{\hbar^2 c^2 (3\pi^2 n_e)^{2/3} [1 + \epsilon(r)]^{2/3} + m_e^2 c^4} - m_e c^2,\end{aligned}\quad (\text{B.1.24})$$

about its value in the uniform approximation

$$\epsilon_k^{\text{unif}} = \sqrt{\hbar^2 c^2 (3\pi^2 n_e)^{2/3} + m_e^2 c^4} - m_e c^2,\quad (\text{B.1.25})$$

considering as infinitesimal the ratio  $eV/E_e^F$  between the Coulomb potential energy  $eV$  and the electron Fermi energy

$$E_e^F = \sqrt{[cP_e^F(r)]^2 + m_e^2 c^4} - m_e c^2 - eV.\quad (\text{B.1.26})$$

The influence of the Dirac electron-exchange correction (Dirac, 1930) on the equation of state was also considered by Salpeter (1961a). However, adopting the general approach of Migdal et al. (1977), it has been shown that these effects are negligible in the relativistic regime (Rotondo et al., 2011c). We will then consider here only the major correction of the Salpeter treatment.

The total energy of the Wigner-Seitz cell is then given by (see Salpeter (1961a) for details)

$$E_S = E_{\text{Ch}} + E_C + E_S^{TF},\quad (\text{B.1.27})$$

being

$$E_S^{TF} = -\frac{162}{175} \left(\frac{4}{9\pi}\right)^{2/3} \alpha^2 Z^{7/3} \mu_e,\quad (\text{B.1.28})$$

where  $E_{\text{Ch}} = \mathcal{E}_{\text{Ch}} V_{\text{ws}}$ ,  $E_C$  is given by Eq. (B.1.19),  $\mu_e$  is given by Eq. (B.1.14), and  $\alpha = e^2/(\hbar c)$  is the fine structure constant.

Correspondingly, the self-consistent pressure of the Wigner-Seitz cell is

$$P_S = P_L + P_{TF}^S,\quad (\text{B.1.29})$$

where

$$P_{TF}^S = \frac{1}{3} \left(\frac{P_e^F}{\mu_e}\right)^2 \frac{E_S^{TF}}{V_{\text{ws}}}.\quad (\text{B.1.30})$$

The Wigner-Seitz cell chemical potential can be then written as

$$\mu_S = \mu_L + E_{TF}^S \left[ 1 + \frac{1}{3} \left(\frac{P_e^F}{\mu_e}\right)^2 \right].\quad (\text{B.1.31})$$

From Eqs. (B.1.29) and (B.1.31), we see that the inclusion of each additional Coulomb correction results in a further decreasing of the pressure and of the

chemical potential of the cell. The Salpeter approach is very interesting in identifying piecewise Coulomb contribution to the total energy, to the total pressure and, to the Wigner-Seitz chemical potential. However, it does not have the full consistency of the global solutions obtained with the Feynman-Metropolis-Teller approach (Feynman et al., 1949) and its generalization to relativistic regimes (Rotondo et al., 2011c) which we will discuss in detail below.

### The Feynman-Metropolis-Teller treatment

Feynman et al. (1949) showed how to derive the equation of state of matter at high pressures by considering a Thomas-Fermi model confined in a Wigner-Seitz cell of radius  $R_{ws}$ .

The Thomas-Fermi equilibrium condition for degenerate non-relativistic electrons in the cell is expressed by

$$E_e^F = \frac{(P_e^F)^2}{2m_e} - eV = \text{constant} > 0, \quad (\text{B.1.32})$$

where  $V$  denotes the Coulomb potential and  $E_e^F$  denotes the Fermi energy of electrons, which is positive for configurations subjected to external pressure, namely, for compressed cells.

Defining the function  $\phi(r)$  by  $eV(r) + E_e^F = e^2 Z \phi(r)/r$ , and  $\eta$  by  $r = b\eta$ , where  $b = (3\pi)^{2/3} (\lambda_e/\alpha) 2^{-7/3} Z^{-1/3}$ , being  $\lambda_e = \hbar/(m_e c)$  the electron Compton wavelength; the Poisson equation from which the Coulomb potential  $V$  is calculated self-consistently becomes

$$\frac{d^2\phi(\eta)}{d\eta^2} = \frac{\phi(\eta)^{3/2}}{\eta^{1/2}}. \quad (\text{B.1.33})$$

The boundary conditions for Eq. (B.1.33) follow from the point-like structure of the nucleus  $\phi(0) = 1$  and, from the global neutrality of the Wigner-Seitz cell  $\phi(\eta_0) = \eta_0 d\phi/d\eta|_{\eta=\eta_0}$ , where  $\eta_0$  defines the dimensionless radius of the Wigner-Seitz cell by  $\eta_0 = R_{ws}/b$ .

For each value of the compression, e.g.  $\eta_0$ , it corresponds a value of the electron Fermi energy  $E_e^F$  and a different solution of Eq. (B.1.33), which determines the self-consistent Coulomb potential energy  $eV$  as well as the self-consistent electron distribution inside the cell through

$$n_e(\eta) = \frac{Z}{4\pi b^3} \left[ \frac{\phi(\eta)}{\eta} \right]^{3/2}. \quad (\text{B.1.34})$$

In the non-relativistic Thomas-Fermi model, the total energy of the Wigner-Seitz cell is given by (see Slater and Krutter (1935); Feynman et al. (1949) for

details)

$$E_{\text{ws}} = E_N + E_k^{(e)} + E_C, \quad (\text{B.1.35})$$

being

$$E_N = M_N(Z, A)c^2, \quad (\text{B.1.36})$$

$$\begin{aligned} E_k^{(e)} &= \int_0^{R_{\text{ws}}} 4\pi r^2 \mathcal{E}_e[n_e(r)] dr \\ &= \frac{3}{7} \frac{Z^2 e^2}{b} \left[ \frac{4}{5} \eta_0^{1/2} \phi^{5/2}(\eta_0) - \phi'(0) \right], \end{aligned} \quad (\text{B.1.37})$$

$$\begin{aligned} E_C &= E_{e-N} + E_{e-e} \\ &= -\frac{6}{7} \frac{Z^2 e^2}{b} \left[ \frac{1}{3} \eta_0^{1/2} \phi^{5/2}(\eta_0) - \phi'(0) \right], \end{aligned} \quad (\text{B.1.38})$$

where  $M_N(Z, A)$  is the nucleus mass,  $\mathcal{E}_e[n_e(r)]$  is given by Eq. (B.1.9) and  $E_{e-N}$  and  $E_{e-e}$  are the electron-nucleus Coulomb energy and the electron-electron Coulomb energy, which are given by

$$E_{e-N} = - \int_0^{R_{\text{ws}}} 4\pi r^2 \left( \frac{Ze}{r} \right) n_e(r) dr, \quad (\text{B.1.39})$$

$$E_{e-e} = \frac{1}{2} \int_0^{R_{\text{ws}}} 4\pi r^2 n_e(\vec{r}) dr \int_0^{R_{\text{ws}}} 4\pi r'^2 \frac{en_e(\vec{r}')}{|\vec{r} - \vec{r}'|} dr'. \quad (\text{B.1.40})$$

From Eqs. (B.1.37) and (B.1.38) we recover the well-known relation between the total kinetic energy and the total Coulomb energy in the Thomas-Fermi model (Slater and Krutter, 1935; Feynman et al., 1949)

$$E_k^{(e)} = E_k^{\text{unif}}[n_e(R_{\text{ws}})] - \frac{1}{2} E_C, \quad (\text{B.1.41})$$

where  $E_k^{\text{unif}}[n_e(R_{\text{ws}})]$  is the non-relativistic kinetic energy of a uniform electron distribution of density  $n_e(R_{\text{ws}})$ , i.e.

$$E_k^{\text{unif}}[n_e(R_{\text{ws}})] = \frac{3}{5} Z^* \mu_e(R_{\text{ws}}), \quad (\text{B.1.42})$$

with  $Z^*$  defined by

$$Z^* = V_{\text{ws}} n_e(R_{\text{ws}}), \quad (\text{B.1.43})$$

and  $\mu_e(R_{\text{ws}}) = \hbar^2 [3\pi^2 n_e(R_{\text{ws}})]^{2/3} / (2m_e)$ .

The self-consistent pressure of the Wigner-Seitz cell in the non-relativistic Thomas-Fermi model is (see Slater and Krutter (1935); Feynman et al. (1949) for details)

$$P_{\text{TF}} = \frac{2}{3} \frac{E_k^{\text{unif}}[n_e(R_{\text{ws}})]}{V_{\text{ws}}}. \quad (\text{B.1.44})$$

The pressure of the Thomas-Fermi model (B.1.44) is equal to the pressure of a free-electron distribution of density  $n_e(R_{\text{ws}})$ . Being the electron density inside the cell a decreasing function of the distance from the nucleus, the electron density at the cell boundary,  $n_e(R_{\text{ws}})$ , is smaller than the average electron distribution  $3Z/(4\pi R_{\text{ws}}^3)$ . Then, the pressure given by (B.1.44) is smaller than the one given by the non-relativistic version of Eq. (B.1.10) of the uniform model of Subsec. B.1.2. Such a smaller pressure, although faintfully given by the expression of a free-electron gas, contains in a self-consistent fashion all the Coulomb effects inside the Wigner-Seitz cell.

The chemical potential of the Wigner-Seitz cell of the non-relativistic Thomas-Fermi model can be then written as

$$\mu_{\text{TF}} = M_N(Z, A)c^2 + Z^* \mu_e(R_{\text{ws}}) + \frac{1}{2}E_C, \quad (\text{B.1.45})$$

where we have used Eqs. (B.1.41)–(B.1.43).

Integrating by parts the total number of electrons

$$Z = \int_0^{R_{\text{ws}}} 4\pi r^2 n_e(r) dr = Z^* + I(R_{\text{ws}}), \quad (\text{B.1.46})$$

where

$$I(R_{\text{ws}}) = \int_0^{R_{\text{ws}}} \frac{4\pi}{3} r^3 \frac{\partial n_e(r)}{\partial r} dr, \quad (\text{B.1.47})$$

we can rewrite finally the following semi-analytical expression of the chemical potential (B.1.45) of the cell

$$\begin{aligned} \mu_{\text{TF}} = & M_N(Z, A)c^2 + Z \mu_e^{\text{unif}} \left[ 1 + \frac{I(R_{\text{ws}})}{Z} \right]^{2/3} \\ & + \mu_e^{\text{unif}} I(R_{\text{ws}}) \left[ 1 + \frac{I(R_{\text{ws}})}{Z} \right]^{2/3} + \frac{1}{2}E_C, \end{aligned} \quad (\text{B.1.48})$$

where  $\mu_e^{\text{unif}}$  is the electron free-chemical potential (B.1.14) calculated with the average electron density, namely, the electron chemical potential of the uniform approximation. The function  $I(R_{\text{ws}})$  depends explicitly on the gradient of the electron density, i.e. on the non-uniformity of the electron distribution.

In the limit of absence of Coulomb interaction both the last term and the function  $I(R_{\text{ws}})$  in Eq. (B.1.48) vanish and therefore in this limit  $\mu_{\text{TF}}$  reduces to

$$\mu_{\text{TF}} \rightarrow \mu_{\text{unif}}, \quad (\text{B.1.49})$$

where  $\mu_{\text{unif}}$  is the chemical potential in the uniform approximation given by Eq. (B.1.13).

### The relativistic Feynman-Metropolis-Teller treatment

We recall now how the above classic Feynman, Metropolis, and Teller treatment of compressed atoms has been recently generalized to relativistic regimes (see Rotondo et al. (2011c) for details). One of the main differences in the relativistic generalization of the Thomas-Fermi equation is that, the point-like approximation of the nucleus, must be abandoned since the relativistic equilibrium condition of compressed atoms

$$E_e^F = \sqrt{c^2(P_e^F)^2 + m_e^2c^4} - m_e c^2 - eV(r) = \text{constant} > 0, \quad (\text{B.1.50})$$

would lead to a non-integrable expression for the electron density near the origin (see e.g. Ferreira et al. (1980); Ruffini and Stella (1981)).

It is then assumed a constant distribution of protons confined in a radius  $R_c$  defined by

$$R_c = \Delta \lambda_\pi Z^{1/3}, \quad (\text{B.1.51})$$

where  $\lambda_\pi = \hbar/(m_\pi c)$  is the pion Compton wavelength. If the system is at nuclear density  $\Delta \approx (r_0/\lambda_\pi)(A/Z)^{1/3}$  with  $r_0 \approx 1.2$  fm. Thus, in the case of ordinary nuclei (i.e., for  $A/Z \approx 2$ ) we have  $\Delta \approx 1$ . Consequently, the proton density can be written as

$$n_p(r) = \frac{Z}{\frac{4}{3}\pi R_c^3} \theta(r - R_c) = \frac{3}{4\pi} \left( \frac{1}{\Delta \lambda_\pi} \right)^3 \theta(r - R_c), \quad (\text{B.1.52})$$

where  $\theta(r - R_c)$  denotes the Heaviside function centered at  $R_c$ . The electron density can be written as

$$n_e(r) = \frac{(P_e^F)^3}{3\pi^2 \hbar^3} = \frac{1}{3\pi^2 \hbar^3 c^3} \left[ \hat{V}^2(r) + 2m_e c^2 \hat{V}(r) \right]^{3/2}, \quad (\text{B.1.53})$$

where  $\hat{V} = eV + E_e^F$  and we have used Eq. (B.1.50).

The overall Coulomb potential satisfies the Poisson equation

$$\nabla^2 V(r) = -4\pi e [n_p(r) - n_e(r)], \quad (\text{B.1.54})$$

with the boundary conditions  $dV/dr|_{r=R_{\text{ws}}} = 0$  and  $V(R_{\text{ws}}) = 0$  due to the global charge neutrality of the cell.

By introducing the dimensionless quantities  $x = r/\lambda_\pi$ ,  $x_c = R_c/\lambda_\pi$ ,  $\chi/r = \hat{V}(r)/(\hbar c)$  and replacing the particle densities (B.1.52) and (B.1.53) into the Poisson equation (B.1.54), it is obtained the relativistic Thomas-Fermi equation (Ruffini, 2008a)

$$\frac{1}{3x} \frac{d^2 \chi(x)}{dx^2} = -\frac{\alpha}{\Delta^3} \theta(x_c - x) + \frac{4\alpha}{9\pi} \left[ \frac{\chi^2(x)}{x^2} + 2 \frac{m_e}{m_\pi} \frac{\chi(x)}{x} \right]^{3/2}, \quad (\text{B.1.55})$$

which must be integrated subjected to the boundary conditions  $\chi(0) = 0$ ,  $\chi(x_{\text{WS}}) \geq 0$  and  $d\chi/dx|_{x=x_{\text{WS}}} = \chi(x_{\text{WS}})/x_{\text{WS}}$ , where  $x_{\text{WS}} = R_{\text{WS}}/\lambda_{\pi}$ .

The neutron density  $n_n(r)$ , related to the neutron Fermi momentum  $P_n^F = (3\pi^2\hbar^3 n_n)^{1/3}$ , is determined by imposing the condition of beta equilibrium

$$E_n^F = \sqrt{c^2(P_n^F)^2 + m_n^2 c^4} - m_n c^2 = \sqrt{c^2(P_p^F)^2 + m_p^2 c^4} - m_p c^2 + eV(r) + E_e^F, \quad (\text{B.1.56})$$

subjected to the baryon number conservation equation

$$A = \int_0^{R_c} 4\pi r^2 [n_p(r) + n_n(r)] dr. \quad (\text{B.1.57})$$

In Fig. B.1 we see how the relativistic Feynman-Metropolis-Teller treatment leads to electron density distributions markedly different from the constant electron density approximation. The electron distribution is far from being uniform as a result of the solution of Eq. (B.1.55), which takes into account the electromagnetic interaction between electrons and between the electrons and the finite sized nucleus. Additional details are given in Rotondo et al. (2011c).

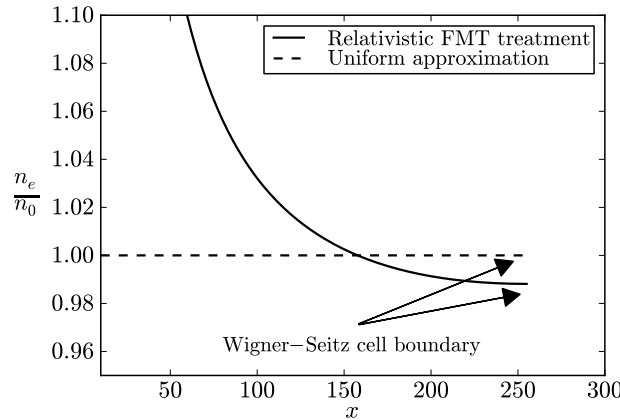


**Figure B.1.:** The electron number density  $n_e$  in units of the average electron number density  $n_0 = 3Z/(4\pi R_{\text{WS}}^3)$  inside a Wigner-Seitz cell of  $^{12}\text{C}$ . The dimensionless radial coordinate is  $x = r/\lambda_{\pi}$  and Wigner-Seitz cell radius is  $x_{\text{WS}} \approx 255$  corresponding to a density of  $\sim 10^8 \text{ g/cm}^3$ . The solid curve corresponds to the relativistic Feynman-Metropolis-Teller treatment and the dashed curve to the uniform approximation. The electron distribution for different levels of compression as well as for different nuclear compositions can be found in Rotondo et al. (2011c).

Rotondo et al. (2011e) have shown how the solution of the relativistic Thomas-Fermi equation (B.1.55) together with the self-consistent implementation of the  $\beta$ -equilibrium condition (B.1.56) leads, in the case of zero electron Fermi energy ( $E_e^F = 0$ ), to a theoretical prediction of the  $\beta$ -equilibrium line, namely a theoretical  $Z$ - $A$  relation. Within this model the mass to charge ratio  $A/Z$  of nuclei is overestimated, e.g. in the case of  ${}^4\text{He}$  the overestimate is  $\sim 3.8\%$ , for  ${}^{12}\text{C} \sim 7.9\%$ , for  ${}^{16}\text{O} \sim 9.52\%$ , and for  ${}^{56}\text{Fe} \sim 13.2\%$ . These discrepancies are corrected when the model of the nucleus considered above is improved by explicitly including the effects of strong interactions. This model, however, illustrates how a self-consistent calculation of compressed nuclear matter can be done including electromagnetic, weak, strong as well as special relativistic effects without any approximation. This approach promises to be useful when theoretical predictions are essential, for example in the description of nuclear matter at very high densities, e.g. nuclei close and beyond the neutron drip line.

The densities in white dwarf interiors are not highly enough to require such theoretical predictions. Therefore, in order to ensure the accuracy of our results we use for  $(Z, A)$ , needed to solve the relativistic Thomas-Fermi equation (B.1.55), as well as for the nucleus mass  $M_N(Z, A)$ , their known experimental values. In this way we take into account all the effects of the nuclear interaction.

Thus, the total energy of the Wigner-Seitz cell in the present case can be written as

$$E_{\text{FMT}}^{\text{rel}} = E_N + E_k^{(e)} + E_C, \quad (\text{B.1.58})$$

being

$$E_N = M_N(Z, A)c^2, \quad (\text{B.1.59})$$

$$E_k^{(e)} = \int_0^{R_{\text{ws}}} 4\pi r^2 (\mathcal{E}_e - m_e n_e) dr, \quad (\text{B.1.60})$$

$$E_C = \frac{1}{2} \int_{R_c}^{R_{\text{ws}}} 4\pi r^2 e [n_p(r) - n_e(r)] V(r) dr, \quad (\text{B.1.61})$$

where  $M_N(Z, A) = A_r M_u$  is the experimental nucleus mass, e.g. for  ${}^4\text{He}$ ,  ${}^{12}\text{C}$ ,  ${}^{16}\text{O}$  and  ${}^{56}\text{Fe}$  we have  $A_r = 4.003, 12.01, 16.00$  and  $55.84$  respectively. In Eq. (B.1.61) the integral is evaluated only outside the nucleus (i.e. for  $r > R_c$ ) in order to avoid a double counting with the Coulomb energy of the nucleus already taken into account in the nucleus mass (B.1.59). In order to avoid another double counting we subtract to the electron energy-density  $\mathcal{E}_e$  in Eq. (B.1.60) the rest-energy density  $m_e c^2 n_e$  which is also taken into account in the nucleus mass (B.1.59).

The total pressure of the Wigner-Seitz cell is given by

$$P_{\text{FMT}}^{\text{rel}} = P_e [n_e(R_{\text{ws}})], \quad (\text{B.1.62})$$

where  $P_e[n_e(R_{\text{ws}})]$  is the relativistic pressure (B.1.10) computed with the value of the electron density at the boundary of the cell.

The electron density at the boundary  $R_{\text{ws}}$  in the relativistic Feynman-Metropolis-Teller treatment is smaller with respect to the one given by the uniform density approximation (see Fig. B.1). Thus, the relativistic pressure (B.1.62) gives systematically smaller values with respect to the uniform approximation pressure (B.1.10) as well as with respect to the Salpeter pressure (B.1.29).

In Fig. B.2 we show the ratio between the relativistic Feynman-Metropolis-Teller pressure  $P_{\text{FMT}}^{\text{rel}}$  (B.1.62) and the Chandrasekhar pressure  $P_{\text{Ch}}$  (B.1.10) and the Salpeter pressure  $P_{\text{S}}$  (B.1.29) in the case of  $^{12}\text{C}$ . It can be seen how  $P_{\text{FMT}}^{\text{rel}}$  is smaller than  $P_{\text{Ch}}$  for all densities as a consequence of the Coulomb interaction. With respect to the Salpeter case, we have that the ratio  $P_{\text{FMT}}^{\text{rel}}/P_{\text{S}}$  approaches unity from below at large densities as one should expect.

However, at low densities  $\lesssim 10^4\text{--}10^5 \text{ g/cm}^3$ , the ratio becomes larger than unity due to the defect of the Salpeter treatment which, in the low density non-relativistic regime, leads to a drastic decrease of the pressure and even to negative pressures at densities  $\lesssim 10^2 \text{ g/cm}^3$  or higher for heavier nuclear compositions e.g.  $^{56}\text{Fe}$  (see Salpeter (1961a); Rotondo et al. (2011c) and Table B.1). This is in contrast with the relativistic Feynman-Metropolis-Teller treatment which matches smoothly the classic Feynman-Metropolis-Teller equation of state in that regime (see Rotondo et al. (2011c) for details).

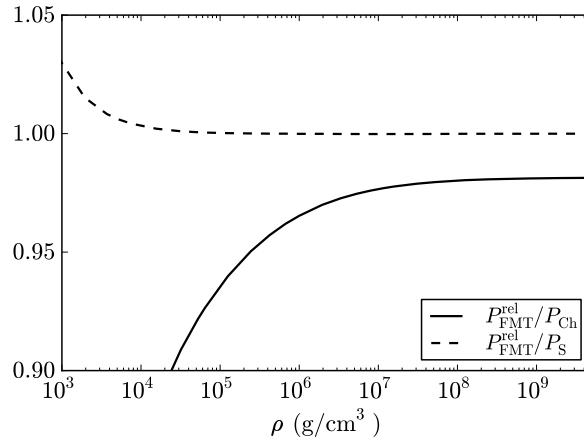


**Figure B.2.:** Ratio of the pressures in the different treatments as a function of the density for  $^{12}\text{C}$  white dwarfs (see Table B.1). The solid curve corresponds to the ratio between the relativistic Feynman-Metropolis-Teller pressure  $P_{\text{FMT}}^{\text{rel}}$  given by Eq. (B.1.62) and the Chandrasekhar pressure  $P_{\text{Ch}}$  given by Eq. (B.1.10). The dashed curve corresponds to the ratio between the relativistic Feynman-Metropolis-Teller pressure  $P_{\text{FMT}}^{\text{rel}}$  given by Eq. (B.1.62) and the Salpeter pressure  $P_{\text{S}}$  given by Eq. (B.1.29).

$\rho$	$P_{\text{Ch}}$	$P_{\text{S}}$	$P_{\text{FMT}}^{\text{rel}}$
10	$1.46731 \times 10^{14}$	$-1.35282 \times 10^{13}$	$4.54920 \times 10^{14}$
40	$1.47872 \times 10^{15}$	$4.60243 \times 10^{14}$	$7.09818 \times 10^{14}$
70	$3.75748 \times 10^{15}$	$1.60860 \times 10^{15}$	$2.05197 \times 10^{15}$
$10^2$	$6.80802 \times 10^{15}$	$3.34940 \times 10^{15}$	$3.90006 \times 10^{15}$
$10^3$	$3.15435 \times 10^{17}$	$2.40646 \times 10^{17}$	$2.44206 \times 10^{17}$
$10^4$	$1.45213 \times 10^{19}$	$1.28976 \times 10^{19}$	$1.28965 \times 10^{19}$
$10^5$	$6.50010 \times 10^{20}$	$6.14494 \times 10^{20}$	$6.13369 \times 10^{20}$
$10^6$	$2.62761 \times 10^{22}$	$2.54932 \times 10^{22}$	$2.54431 \times 10^{22}$
$10^7$	$8.46101 \times 10^{23}$	$8.28899 \times 10^{23}$	$8.27285 \times 10^{23}$
$10^8$	$2.15111 \times 10^{25}$	$2.11375 \times 10^{25}$	$2.10896 \times 10^{25}$
$10^9$	$4.86236 \times 10^{26}$	$4.78170 \times 10^{26}$	$4.76613 \times 10^{26}$
$10^{10}$	$1.05977 \times 10^{28}$	$1.04239 \times 10^{28}$	$1.03668 \times 10^{28}$

**Table B.1.:** Equation of state for  $^{12}\text{C}$  within the different treatments. The pressure in the uniform approximation for  $\mu = 2$  is  $P_{\text{Ch}}$ , the Salpeter pressure is  $P_{\text{S}}$  and the relativistic Feynman-Metropolis-Teller pressure is  $P_{\text{FMT}}^{\text{rel}}$ . The units for the density are  $\text{g}/\text{cm}^3$  and for the pressure  $\text{dyn}/\text{cm}^2$ .

No analytic expression of the Wigner-Seitz cell chemical potential can be given in this case, so we only write its general expression

$$\mu_{\text{FMT}}^{\text{rel}} = E_{\text{FMT}}^{\text{rel}} + P_{\text{FMT}}^{\text{rel}} V_{\text{ws}}, \quad (\text{B.1.63})$$

where  $E_{\text{FMT}}^{\text{rel}}$  and  $P_{\text{FMT}}^{\text{rel}}$  are given by Eqs. (B.1.58) and (B.1.62) respectively. The above equation, contrary to the non-relativistic formula (B.1.45), in no way can be simplified in terms of its uniform counterparts. However, it is easy to check that, in the limit of no Coulomb interaction  $n_e(R_{\text{ws}}) \rightarrow 3Z/(4\pi R_{\text{ws}}^3)$ ,  $E_{\text{C}} \rightarrow 0$ , and  $E_k \rightarrow \mathcal{E}_{\text{Ch}} V_{\text{ws}}$  and, neglecting the nuclear binding and the proton-neutron mass difference, we finally obtain

$$\mu_{\text{FMT}}^{\text{rel}} \rightarrow \mu_{\text{unif}}, \quad (\text{B.1.64})$$

as it should be expected.

Now we summarize how the equation of state of compressed nuclear matter can be computed in the Salpeter case and in the relativistic Feynman-Metropolis-Teller case, parameterized by the total density of the system:

(i) For a given radius  $R_{\text{ws}}$  of the Wigner-Seitz cell the relativistic Thomas-Fermi equation (B.1.55) is integrated numerically and the density of the configuration is computed as  $\rho = E_{\text{FMT}}^{\text{rel}}/(c^2 V_{\text{ws}})$  where  $E_{\text{FMT}}^{\text{rel}}$  is the energy of the cell given by Eq. (B.1.58).

(ii) For that value of the density, the radius of the Wigner-Seitz cell in the

Salpeter treatment is

$$R_{\text{ws}} = \left( \frac{3A_r M_u}{4\pi\rho} \right)^{1/3}, \quad (\text{B.1.65})$$

where Eq. (B.1.15) has been used. On the contrary, in the relativistic Feynman-Metropolis-Teller treatment no analytic expression relating Wigner-Seitz cell radius and density can be written.

(iii) From this Wigner-Seitz cell radius, or equivalently using the value of the density, the electron density in the Salpeter model is computed from the assumption of uniform electron distribution and the charge neutrality condition, i.e. Eq. (B.1.15). In the relativistic Feynman-Metropolis-Teller treatment, the electron number density at the boundary of the Wigner-Seitz cell is, following Eq. (B.1.53), given by

$$n_e^{\text{relFMT}} = \frac{1}{3\pi^2 \lambda_\pi^3} \left[ \frac{\chi^2(x_{\text{ws}})}{x_{\text{ws}}^2} + 2 \frac{m_e}{m_\pi} \frac{\chi(x_{\text{ws}})}{x_{\text{ws}}} \right]^{3/2}, \quad (\text{B.1.66})$$

where the function  $\chi(x)$  is the solution of the relativistic Thomas-Fermi equation (B.1.55).

(iv) Finally, with the knowledge of the electron density at  $R_{\text{ws}}$ , the pressure can be calculated. In the Salpeter approach it is given by Eq. (B.1.29) while in the relativistic Feynman-Metropolis-Teller case it is given by Eq. (B.1.62).

### B.1.3. General relativistic equations of equilibrium

Outside each Wigner-Seitz cell the system is electrically neutral, thus no overall electric field exists. Therefore, the above equation of state can be used to calculate the structure of the star through the Einstein equations. Introducing the spherically symmetric metric (B.1.5), the Einstein equations can be written in the Tolman-Oppenheimer-Volkoff form Tolman (1939); Oppenheimer and Volkoff (1939)

$$\frac{dv(r)}{dr} = \frac{2G}{c^2} \frac{4\pi r^3 P(r) / c^2 + M(r)}{r^2 \left[ 1 - \frac{2GM(r)}{c^2 r} \right]}, \quad (\text{B.1.67})$$

$$\frac{dM(r)}{dr} = 4\pi r^2 \frac{\mathcal{E}(r)}{c^2}, \quad (\text{B.1.68})$$

$$\frac{dP(r)}{dr} = -\frac{1}{2} \frac{dv(r)}{dr} [\mathcal{E}(r) + P(r)], \quad (\text{B.1.69})$$

where we have introduced the mass enclosed at the distance  $r$  through  $e^{\lambda(r)} = 1 - 2GM(r)/(c^2 r)$ ,  $\mathcal{E}(r)$  is the energy-density and  $P(r)$  is the total pressure.

We turn now to demonstrate how, from Eq. (B.1.69), it follows the general relativistic equation of equilibrium (B.1.6), for the self-consistent Wigner-

Seitz chemical potential  $\mu_{\text{ws}}$ . The first law of thermodynamics for a zero temperature fluid of  $N$  particles, total energy  $E$ , total volume  $V$ , total pressure  $P = -\partial E/\partial V$ , and chemical potential  $\mu = \partial E/\partial N$  reads

$$dE = -PdV + \mu dN, \quad (\text{B.1.70})$$

where the differentials denote arbitrary but simultaneous changes in the variables. Since for a system whose surface energy can be neglected with respect to volume energy, the total energy per particle  $E/N$  depends only on the particle density  $n = N/V$ , we can assume  $E/N$  as an homogeneous function of first-order in the variables  $N$  and  $V$  and hence, it follows the well-known thermodynamic relation

$$E = -PV + \mu N. \quad (\text{B.1.71})$$

In the case of the Wigner-Seitz cells, Eq. (B.1.71) reads

$$E_{\text{ws}} = -P_{\text{ws}}V_{\text{ws}} + \mu_{\text{ws}}, \quad (\text{B.1.72})$$

where we have introduced the fact that the Wigner-Seitz cells are the building blocks of the configuration and therefore we must put in Eq. (B.1.71)  $N_{\text{ws}} = 1$ . Through the entire article we have used Eq. (B.1.72) to obtain from the knowns energy and pressure, the Wigner-Seitz cell chemical potential (see e.g. Eqs. (B.1.13) and (B.1.23)). From Eqs. (B.1.70) and (B.1.71) we obtain the so-called Gibbs-Duhem relation

$$dP = nd\mu. \quad (\text{B.1.73})$$

In a white dwarf the pressure  $P$  and the chemical potential  $\mu$  are decreasing functions of the distance from the origin. Thus, the differentials in the above equations can be assumed as the gradients of the variables which, in the present spherically symmetric case, become just derivatives with respect to the radial coordinate  $r$ . From Eq. (B.1.73) it follows the relation

$$\frac{dP_{\text{ws}}}{dr} = n_{\text{ws}} \frac{d\mu_{\text{ws}}}{dr}. \quad (\text{B.1.74})$$

From Eqs. (B.1.69), (B.1.72) and (B.1.74) we obtain

$$n_{\text{ws}}(r) \frac{d\mu_{\text{ws}}(r)}{dr} = -\frac{1}{2} \frac{dv(r)}{dr} n_{\text{ws}}(r) \mu_{\text{ws}}(r), \quad (\text{B.1.75})$$

which can be straightforwardly integrated to obtain the first integral

$$e^{v(r)/2} \mu_{\text{ws}}(r) = \text{constant}. \quad (\text{B.1.76})$$

The above equilibrium condition is general and it also applies for non-zero temperature configurations ( see e.g. Klein (1949)). In such a case, it can be

shown that in addition to the equilibrium condition (B.1.76) the temperature of the system satisfies the Tolman isothermality condition  $e^{\nu(r)/2}T(r) = \text{constant}$  Tolman (1930); Tolman and Ehrenfest (1930).

### The weak-field non-relativistic limit

In the weak-field limit we have  $e^{\nu/2} \approx 1 + \Phi$ , where the Newtonian gravitational potential has been defined by  $\Phi(r) = \nu(r)/2$ . In the non-relativistic mechanics limit  $c \rightarrow \infty$ , the chemical potential  $\mu_{\text{ws}} \rightarrow \tilde{\mu}_{\text{ws}} + M_{\text{ws}}c^2$ , where  $\tilde{\mu}_{\text{ws}}$  denotes the non-relativistic free-chemical potential of the Wigner-Seitz cell and  $M_{\text{ws}}$  is the rest-mass of the Wigner-Seitz cell, namely, the rest-mass of the nucleus plus the rest-mass of the electrons. Applying these considerations to Eq. (B.1.76) we obtain

$$e^{\nu/2}\mu_{\text{ws}} \approx M_{\text{ws}}c^2 + \tilde{\mu}_{\text{ws}} + M_{\text{ws}}\Phi = \text{constant}. \quad (\text{B.1.77})$$

Absorbing the Wigner-Seitz rest-mass energy  $M_{\text{ws}}c^2$  in the constant on the right-hand-side we obtain

$$\tilde{\mu}_{\text{ws}} + M_{\text{ws}}\Phi = \text{constant}. \quad (\text{B.1.78})$$

In the weak-field non-relativistic limit, the Einstein equations (B.1.67)–(B.1.69) reduce to

$$\frac{d\Phi(r)}{dr} = \frac{GM(r)}{r^2}, \quad (\text{B.1.79})$$

$$\frac{dM(r)}{dr} = 4\pi r^2 \rho(r), \quad (\text{B.1.80})$$

$$\frac{dP(r)}{dr} = -\frac{GM(r)}{r^2} \rho(r), \quad (\text{B.1.81})$$

where  $\rho(r)$  denotes the rest-mass density. The Eqs. (B.1.79)–(B.1.80) can be combined to obtain the gravitational Poisson equation

$$\frac{d^2\Phi(r)}{dr^2} + \frac{2}{r} \frac{d\Phi(r)}{dr} = 4\pi G\rho(r). \quad (\text{B.1.82})$$

In the uniform approximation (see Subsec. B.1.2), the equilibrium condition given by Eq. (B.1.78) reads

$$\tilde{\mu}_e + \frac{A_r}{Z} M_u \Phi = \text{constant}, \quad (\text{B.1.83})$$

where we have neglected the electron rest-mass with respect to the nucleus rest-mass and we have divided the equation by the total number of electrons  $Z$ . This equilibrium equation is the classical condition of thermodynamic

equilibrium assumed for non-relativistic white dwarf models (see e.g. Landau and Lifshitz (1980) for details).

Introducing the above equilibrium condition (B.1.83) into Eq. (B.1.82), and using the relation between the non-relativistic electron chemical potential and the particle density  $n_e = (2m_e)^{3/2} \tilde{\mu}_e^{3/2} / (3\pi^2 \hbar^3)$ , we obtain

$$\frac{d^2 \tilde{\mu}_e(r)}{dr^2} + \frac{2}{r} \frac{d\tilde{\mu}_e(r)}{dr} = - \frac{2^{7/3} m_e^{3/2} (A_r/Z)^2 m_N^2 G}{3\pi \hbar^3} \tilde{\mu}_e^{3/2}(r), \quad (\text{B.1.84})$$

which is the correct equation governing the equilibrium of white dwarfs within Newtonian gravitational theory (Landau and Lifshitz, 1980). It is remarkable that the equation of equilibrium (B.1.84), obtained from the correct application of the Newtonian limit, does not coincide with the equation given by Chandrasekhar (1931b,a, 1935, 1939), which, as correctly pointed out by Eddington (1935), is a mixture of both relativistic and non-relativistic approaches. Indeed, the consistent relativistic equations should be Eq. (B.1.76). Therefore a dual relativistic and non-relativistic equation of state was used by Chandrasekhar. The pressure on the left-hand-side of Eq. (B.1.81) is taken to be given by relativistic electrons while, the term on the right-hand-side of Eq. (B.1.80) and (B.1.81) (or the source of Eq. (B.1.82)), is taken to be the rest-mass density of the system instead of the total relativistic energy-density. Such a procedure is equivalent to take the chemical potential in Eq. (B.1.78) as a relativistic quantity. As we have seen, this is inconsistent with the weak-field non-relativistic limit of the general relativistic equations.

### The Post-Newtonian limit

Indeed, if one were to treat the problem of white dwarfs approximately without going to the sophistications of general relativity, but including the effects of relativistic mechanics, one should use at least the equations in the post-Newtonian limit. The first-order post-Newtonian expansion of the Einstein equations (B.1.67)–(B.1.69) in powers of  $P/\mathcal{E}$  and  $GM/(c^2 r)$  leads to the equilibrium equations (Ciufolini and Ruffini, 1983)

$$\frac{d\Phi(r)}{dr} = - \frac{1}{\mathcal{E}(r)} \left[ 1 - \frac{P(r)}{\mathcal{E}(r)} \right] \frac{dP(r)}{dr}, \quad (\text{B.1.85})$$

$$\frac{dM(r)}{dr} = 4\pi r^2 \frac{\mathcal{E}(r)}{c^2}, \quad (\text{B.1.86})$$

$$\begin{aligned} \frac{dP(r)}{dr} = & - \frac{GM(r)}{r^2} \frac{\mathcal{E}(r)}{c^2} \left[ 1 + \frac{P(r)}{\mathcal{E}(r)} + \frac{4\pi r^3 P(r)}{M(r)c^2} \right. \\ & \left. + \frac{2GM(r)}{c^2 r} \right], \end{aligned} \quad (\text{B.1.87})$$

where Eq. (B.1.87) is the post-Newtonian version of the Tolman-Oppenheimer-Volkoff equation (B.1.69).

Replacing Eq. (B.1.74) into Eq. (B.1.85) we obtain

$$\left[1 - \frac{P(r)}{\mathcal{E}(r)}\right] \frac{d\mu_{\text{ws}}(r)}{dr} + \frac{\mathcal{E}(r)/c^2}{n_{\text{ws}}(r)} \frac{d\Phi(r)}{dr} = 0. \quad (\text{B.1.88})$$

It is convenient to split the energy-density as  $\mathcal{E} = c^2\rho + U$ , where  $\rho = M_{\text{ws}}n_{\text{ws}}$  is the rest-energy density and  $U$  the internal energy-density. Thus, Eq. (B.1.88) becomes

$$\begin{aligned} \frac{d\mu_{\text{ws}}(r)}{dr} + M_{\text{ws}} \frac{d\Phi(r)}{dr} - \frac{P(r)}{\mathcal{E}(r)} \frac{d\mu_{\text{ws}}(r)}{dr} \\ + \frac{U/c^2}{n_{\text{ws}}(r)} \frac{d\Phi(r)}{dr} = 0, \end{aligned} \quad (\text{B.1.89})$$

which is the differential post-Newtonian version of the equilibrium equation (B.1.76) and where the post-Newtonian corrections of equilibrium can be clearly seen. Applying the non-relativistic limit  $c \rightarrow \infty$  to Eq. (B.1.89):  $P/\mathcal{E} \rightarrow 0$ ,  $U/c^2 \rightarrow 0$ , and  $\mu_{\text{ws}} \rightarrow M_{\text{ws}}c^2 + \tilde{\mu}_{\text{ws}}$ , we recover the Newtonian equation of equilibrium (B.1.78).

### B.1.4. Mass and radius of general relativistic stable white dwarfs

#### Inverse $\beta$ -decay instability

It is known that white dwarfs may become unstable against the inverse  $\beta$ -decay process  $(Z, A) \rightarrow (Z - 1, A)$  through the capture of energetic electrons (see e.g. Hund (1936); Landau (1938); Zel'Dovich (1958a); Harrison et al. (1958)). In order to trigger such a process, the electron Fermi energy must be larger than the mass difference between the initial nucleus  $(Z, A)$  and the final nucleus  $(Z - 1, A)$ . We denote this threshold energy as  $\epsilon_Z^\beta$ . Usually it is satisfied  $\epsilon_{Z-1}^\beta < \epsilon_Z^\beta$  and therefore the initial nucleus undergoes two successive decays, i.e.  $(Z, A) \rightarrow (Z - 1, A) \rightarrow (Z - 2, A)$  (see e.g. Salpeter (1961a); Shapiro and Teukolsky (1983a)). Some of the possible decay channels in white dwarfs with the corresponding known experimental threshold energies  $\epsilon_Z^\beta$  are listed in Table B.2. The electrons in the white dwarf may eventually reach the threshold energy to trigger a given decay at some critical density  $\rho_{\text{crit}}^\beta$ . Configurations with  $\rho > \rho_{\text{crit}}^\beta$  become unstable (see Harrison et al. (1958); Salpeter (1961a) for details).

Within the uniform approximation, e.g. in the case of the Salpeter equation of state Salpeter (1961a), the critical density for the onset of inverse  $\beta$ -decay

Decay	$\epsilon_Z^\beta$	$\rho_{\text{crit}}^{\beta,\text{relFMT}}$	$\rho_{\text{crit}}^{\beta,\text{unif}}$
${}^4\text{He} \rightarrow {}^3\text{H} + n \rightarrow 4n$	20.596	$1.39 \times 10^{11}$	$1.37 \times 10^{11}$
${}^{12}\text{C} \rightarrow {}^{12}\text{B} \rightarrow {}^{12}\text{Be}$	13.370	$3.97 \times 10^{10}$	$3.88 \times 10^{10}$
${}^{16}\text{O} \rightarrow {}^{16}\text{N} \rightarrow {}^{16}\text{C}$	10.419	$1.94 \times 10^{10}$	$1.89 \times 10^{10}$
${}^{56}\text{Fe} \rightarrow {}^{56}\text{Mn} \rightarrow {}^{56}\text{Cr}$	3.695	$1.18 \times 10^9$	$1.14 \times 10^9$

**Table B.2.:** Onset of inverse beta decay instability for  ${}^4\text{He}$ ,  ${}^{12}\text{C}$ ,  ${}^{16}\text{O}$  and  ${}^{56}\text{Fe}$ . The experimental inverse  $\beta$ -decay energies  $\epsilon_Z^\beta$  are given in MeV and they have been taken from Table 1 of Audi et al. (2003a). The corresponding critical density for the uniform electron density model,  $\rho_{\text{crit}}^{\beta,\text{unif}}$  given by Eq. (B.1.90), is given in  $\text{g}/\text{cm}^3$  as well as the critical density  $\rho_{\text{crit}}^{\beta,\text{relFMT}}$  for the relativistic Feynman-Metropolis-Teller case. The numerical values of  $\epsilon_Z^\beta$  are taken from Audi et al. (2003a), see also Shapiro and Teukolsky (1983a)

is given by

$$\rho_{\text{crit}}^{\beta,\text{unif}} = \frac{A_r}{Z} \frac{M_u}{3\pi^2 \hbar^3 c^3} [(\epsilon_Z^\beta)^2 + 2m_e c^2 \epsilon_Z^\beta]^{3/2}, \quad (\text{B.1.90})$$

where Eq. (B.1.15) has been used.

Because the computation of the electron Fermi energy within the relativistic Feynman-Metropolis-Teller approach Rotondo et al. (2011c) involves the numerical integration of the relativistic Thomas-Fermi equation (B.1.55), no analytic expression for  $\rho_{\text{crit}}^\beta$  can be found in this case. The critical density  $\rho_{\text{crit}}^{\beta,\text{relFMT}}$  is then obtained numerically by looking for the density at which the electron Fermi energy (B.1.50) equals  $\epsilon_Z^\beta$ .

In Table B.2 we show, correspondingly to each threshold energy  $\epsilon_Z^\beta$ , the critical density both in the Salpeter case  $\rho_{\text{crit}}^{\beta,\text{unif}}$  given by Eq. (B.1.90) and in the relativistic Feynman-Metropolis-Teller case  $\rho_{\text{crit}}^{\beta,\text{relFMT}}$ . It can be seen that  $\rho_{\text{crit}}^{\beta,\text{relFMT}} > \rho_{\text{crit}}^{\beta,\text{unif}}$  as one should expect from the fact that, for a given density, the electron density at the Wigner-Seitz cell boundary satisfies  $n_e^{\text{relFMT}} < n_e^{\text{unif}}$ . This means that, in order to reach a given energy, the electrons within the relativistic Feynman-Metropolis-Teller approach must be subjected to a larger density with respect to the one given by the approximated Salpeter analytic formula (B.1.90).

### General relativistic instability

The concept of the critical mass has played a major role in the theory of stellar evolution. For Newtonian white dwarfs the critical mass is reached asymptotically at infinite central densities of the object. One of the most important

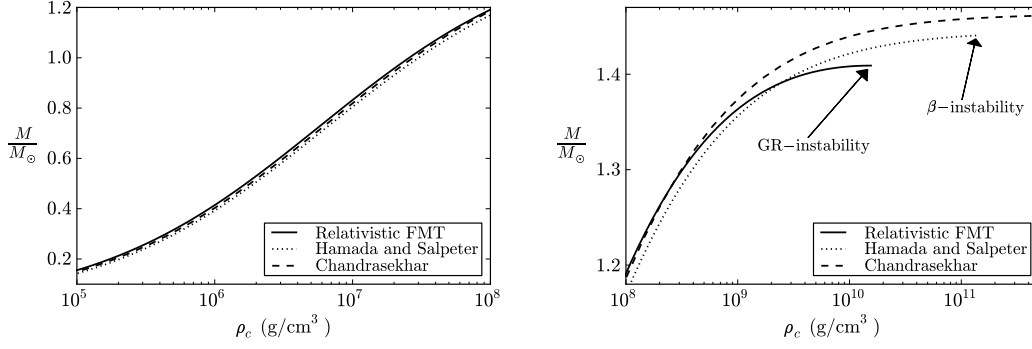


**Figure B.3.:** Mass in solar masses as a function of the central density in the range (left panel)  $10^5$ – $10^8$   $\text{g}/\text{cm}^3$  and in the range (right panel)  $10^8$ – $5 \times 10^{11}$   $\text{g}/\text{cm}^3$  for  ${}^4\text{He}$  white dwarfs. The solid curve corresponds to the present work, the dotted curves are the Newtonian configurations of Hamada and Salpeter and the dashed curve are the Newtonian configurations of Chandrasekhar.

general relativistic effects is to shift this critical point to some finite density  $\rho_{\text{crit}}^{\text{GR}}$ .

This general relativistic effect is an additional source of instability with respect to the already discussed instability due to the onset of inverse  $\beta$ -decay which, contrary to the present general relativistic one, applies also in the Newtonian case by shifting the maximum mass of Newtonian white dwarfs to finite densities (see e.g. Harrison et al. (1958)).

### Numerical results

In Figs. B.3–B.10 we have plotted the mass-central density relation and the mass-radius relation of general relativistic  ${}^4\text{He}$ ,  ${}^{12}\text{C}$ ,  ${}^{16}\text{O}$  and  ${}^{56}\text{Fe}$  white dwarfs. In particular, we show the results for the Newtonian white dwarfs of Hamada and Salpeter (1961), for the Newtonian white dwarfs of Chandrasekhar (1931b) and the general relativistic configurations obtained in this work based on the relativistic Feynman-Metropolis-Teller equation of state (Rotondo et al., 2011c).

Since our approach takes into account self-consistently both  $\beta$ -decay equilibrium and general relativity, we can determine if the critical mass is reached due either to inverse  $\beta$ -decay instability or to the general relativistic instability.

A comparison of the numerical value of the critical mass as given by Stoner (1929), Eq. (B.1.1), by Chandrasekhar (1931b) and Landau (1932), Eq. (B.1.2), by Hamada and Salpeter (1961) and, by the treatment presented here can be found in Table B.3.

From the numerical integrations we have obtained:

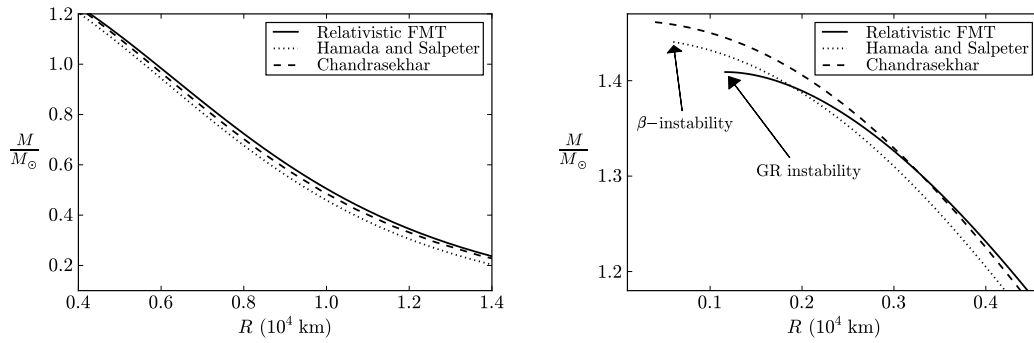


**Figure B.4.:** Mass in solar masses as a function of the radius in units of  $10^4$  km for  ${}^4\text{He}$  white dwarfs. The left and right panels show the configurations for the same range of central densities of the corresponding panels of Fig. B.3. The solid curve corresponds to the present work, the dotted curves are the Newtonian configurations of Hamada and Salpeter and the dashed curve are the Newtonian configurations of Chandrasekhar.

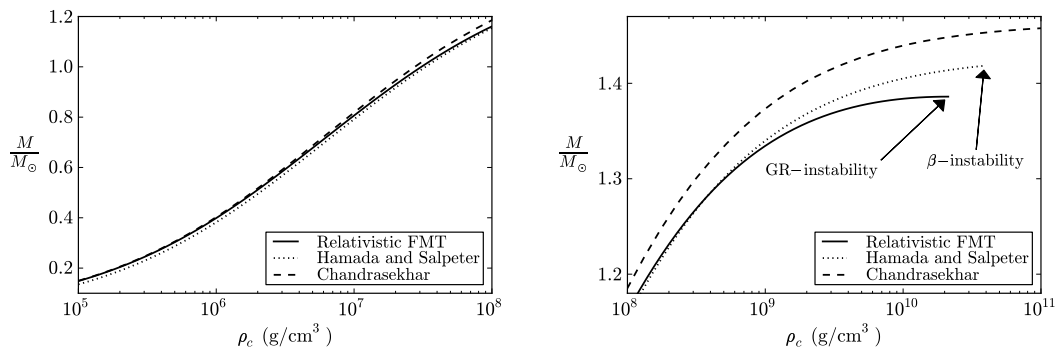


**Figure B.5.:** Mass in solar masses as a function of the central density in the range (left panel)  $10^5$ – $10^8$   $\text{g}/\text{cm}^3$  and in the range (right panel)  $10^8$ – $10^{11}$   $\text{g}/\text{cm}^3$  for  ${}^{12}\text{C}$  white dwarfs. The solid curve corresponds to the present work, the dotted curves are the Newtonian configurations of Hamada and Salpeter and the dashed curve are the Newtonian configurations of Chandrasekhar.

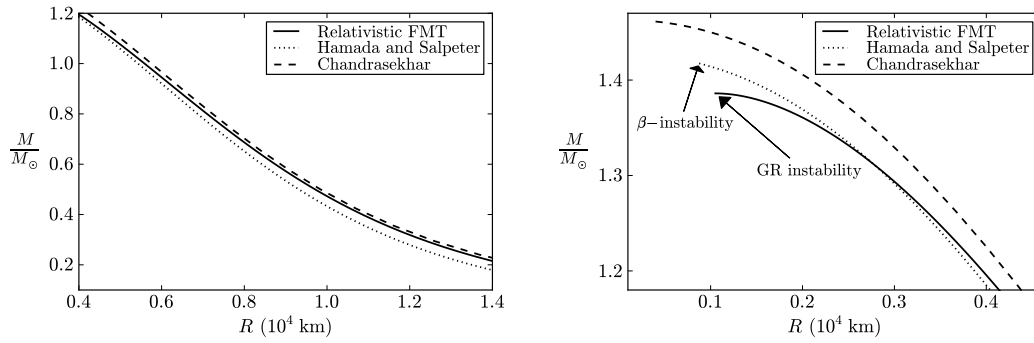


**Figure B.6.:** Mass in solar masses as a function of the radius in units of  $10^4$  km for  $^{12}\text{C}$  white dwarfs. The left and right panels show the configurations for the same range of central densities of the corresponding panels of Fig. B.5. The solid curve corresponds to the present work, the dotted curves are the Newtonian configurations of Hamada and Salpeter and the dashed curve are the Newtonian configurations of Chandrasekhar.

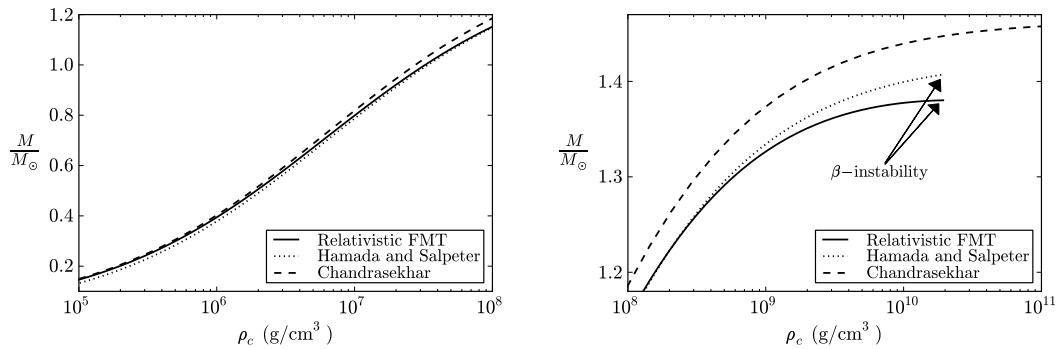


**Figure B.7.:** Mass in solar masses as a function of the central density in the range (left panel)  $10^5$ – $10^8$   $\text{g}/\text{cm}^3$  and in the range (right panel)  $10^8$ – $10^{11}$   $\text{g}/\text{cm}^3$  for  $^{16}\text{O}$  white dwarfs. The solid curve corresponds to the present work, the dotted curves are the Newtonian configurations of Hamada and Salpeter and the dashed curve are the Newtonian configurations of Chandrasekhar.

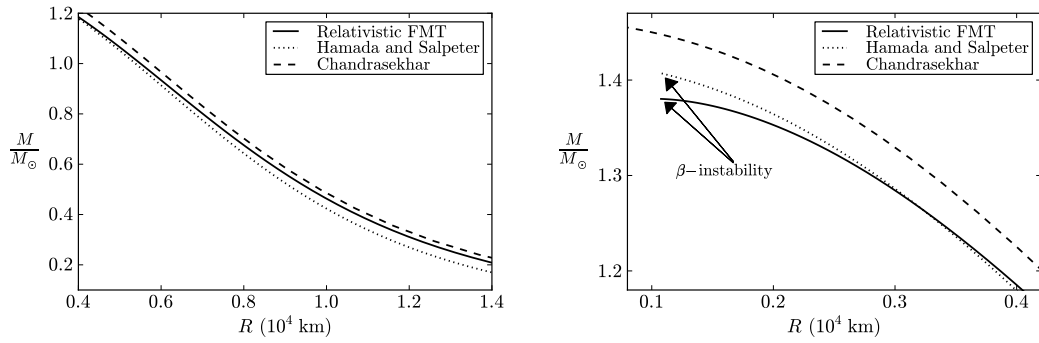


**Figure B.8.:** Mass in solar masses as a function of the radius in units of  $10^4$  km for  $^{16}\text{O}$  white dwarfs. The left and right panels show the configurations for the same range of central densities of the corresponding panels of Fig. B.7. The solid curve corresponds to the present work, the dotted curves are the Newtonian configurations of Hamada and Salpeter and the dashed curve are the Newtonian configurations of Chandrasekhar.

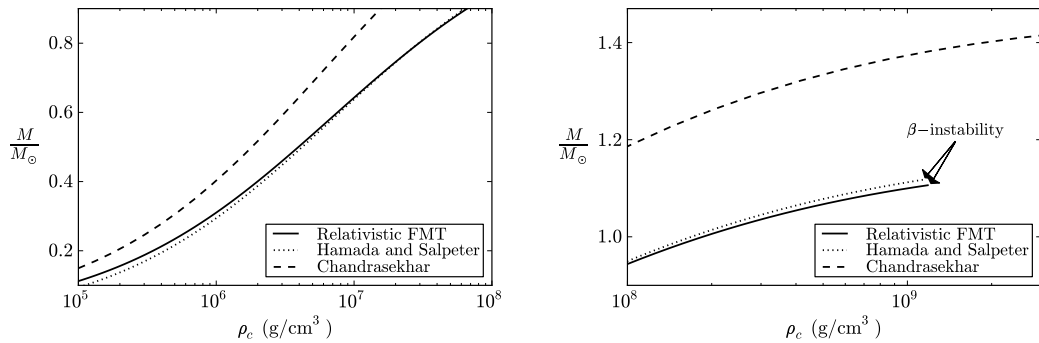


**Figure B.9.:** Mass in solar masses as a function of the central density in the range (left panel)  $10^5$ – $10^8$   $\text{g}/\text{cm}^3$  and in the range (right panel)  $10^8$ – $3 \times 10^9$   $\text{g}/\text{cm}^3$  for  $^{56}\text{Fe}$  white dwarfs. The solid curve corresponds to the present work, the dotted curves are the Newtonian configurations of Hamada and Salpeter and the dashed curve are the Newtonian configurations of Chandrasekhar.

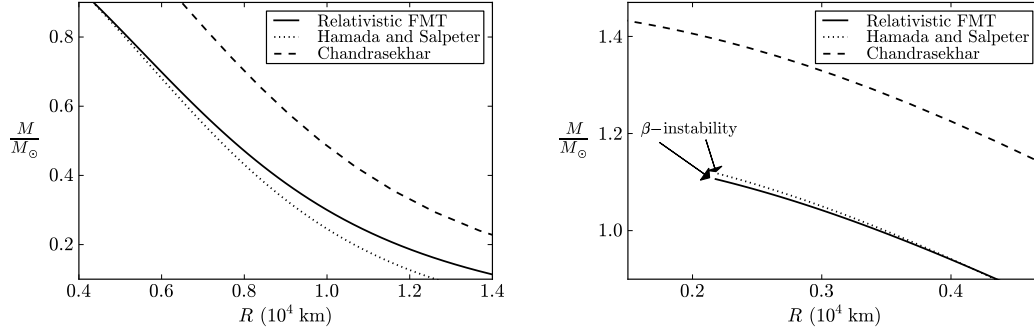


**Figure B.10.:** Mass in solar masses as a function of the radius in units of  $10^4$  km for  $^{56}\text{Fe}$  white dwarfs. The left and right panels show the configurations for the same range of central densities of the corresponding panels of Fig. B.9. The solid curve corresponds to the present work, the dotted curves are the Newtonian configurations of Hamada and Salpeter and the dashed curve are the Newtonian configurations of Chandrasekhar.

1.  $^4\text{He}$  and  $^{12}\text{C}$  white dwarfs satisfy  $\rho_{\text{crit}}^{\text{GR}} < \rho_{\text{crit}}^{\beta}$  (see Figs. B.3–B.6 and Tables B.2 and B.3), so they are unstable with respect to general relativistic effects. The critical density of  $^{12}\text{C}$  white dwarfs is  $\sim 2.12 \times 10^{10} \text{ g/cm}^3$ , to be compared with the value  $2.65 \times 10^{10} \text{ g/cm}^3$  obtained from calculations based on general relativistic corrections to the theory of polytropes (see e.g. Shapiro and Teukolsky (1983a)).
2. White dwarfs composed of heavier material than  $^{12}\text{C}$ , e.g.  $^{16}\text{O}$  and  $^{56}\text{Fe}$  are unstable due to inverse  $\beta$ -decay of the nuclei (see Figs. B.7–B.10 and Tables B.2 and B.3). It is worth to notice that the correct evaluation of general relativistic effects and of the combined contribution of the electrons to the energy-density of the system introduce, for  $^{12}\text{C}$  white dwarfs, a critical mass not due to the inverse beta decay. When the contribution of the electrons to the energy-density is neglected (e.g. Chandrasekhar (1931b) and Hamada and Salpeter (1961), see Eq. (B.1.15)) the critical density for Carbon white dwarfs is determined by inverse beta decay irrespective of the effects of general relativity.
3. It can be seen from Figs. B.3–B.10 that the drastic decrease of the Salpeter pressure at low densities (see Salpeter (1961a); Rotonondo et al. (2011c) and Table B.1 for details) produces an underestimate of the mass and the radius of low density (low mass) white dwarfs.
4. The Coulomb effects are much more pronounced in the case of white dwarfs with heavy nuclear compositions e.g.  $^{56}\text{Fe}$  (see Figs. B.9 and B.10).

	$\rho_{\text{crit}}^{\text{H\&S}}$	$M_{\text{crit}}^{\text{H\&S}} / M_{\odot}$	$\rho_{\text{crit}}^{\text{FM\&Trel}}$	$M_{\text{crit}}^{\text{FM\&Trel}} / M_{\odot}$
${}^4\text{He}$	$1.37 \times 10^{11}$	1.44064	$1.56 \times 10^{10}$	1.40906
${}^{12}\text{C}$	$3.88 \times 10^{10}$	1.41745	$2.12 \times 10^{10}$	1.38603
${}^{16}\text{O}$	$1.89 \times 10^{10}$	1.40696	$1.94 \times 10^{10}$	1.38024
${}^{56}\text{Fe}$	$1.14 \times 10^9$	1.11765	$1.18 \times 10^9$	1.10618

**Table B.3.:** Critical density and corresponding critical mass for the onset of gravitational collapse of the Newtonian  ${}^4\text{He}$ ,  ${}^{12}\text{C}$ ,  ${}^{16}\text{O}$  and  ${}^{56}\text{Fe}$  white dwarfs of Hamada and Salpeter (1961), based on the Salpeter equation of state (Salpeter, 1961a), and of the corresponding general relativistic configurations obtained in this work based on the relativistic Feynman-Metropolis-Teller equation of state (Rotondo et al., 2011c). Densities are in  $\text{g}/\text{cm}^3$  and masses in solar masses. For the sake of comparison, the critical mass of Stoner (B.1.1) and of the one of Chandrasekhar-Landau (B.1.2) are  $M_{\text{crit}}^{\text{Stoner}} \sim 1.72M_{\odot}$  and  $M_{\text{crit}}^{\text{Ch-L}} \sim 1.45M_{\odot}$ , for the average molecular weight  $\mu = A_r/Z = 2$ .

### B.1.5. Conclusions

We have addressed the theoretical physics aspects of the white dwarf configurations of equilibrium, quite apart from the astrophysical application.

The recently accomplished description of a compressed atom within the global approach of the relativistic Feynman, Metropolis and Teller (Rotondo et al., 2011c) has been here solved within the Wigner-Seitz cell and applied to the construction of white dwarfs in the framework of general relativity. From a theoretical physics point of view, this is the first unified approach of white dwarfs taking into account consistently the gravitational, the weak, the strong and the electromagnetic interactions, and it answers open theoretical physics issues in this matter. No analytic formula for the critical mass of white dwarfs can be derived and, on the contrary, the critical mass can be obtained only through the numerical integration of the general relativistic equations of equilibrium together with the relativistic Feynman-Metropolis-Teller equation of state.

The value of the critical mass and the radius of white dwarfs in our treatment and in the Hamada and Salpeter (1961) treatment becomes a function of the composition of the star. Specific examples have been given in the case of white dwarfs composed of  ${}^4\text{He}$ ,  ${}^{12}\text{C}$ ,  ${}^{16}\text{O}$  and  ${}^{56}\text{Fe}$ . The results of Chandrasekhar, of Hamada and Salpeter and ours have been compared and contrasted (see Table B.3 and Figs. B.3–B.10).

The critical mass is a decreasing function of  $Z$  and Coulomb effects are more important for heavy nuclear compositions. The validity of the Salpeter approximate formulas increases also with  $Z$ , namely for heavy nuclear compositions the numerical values of the masses as well as of the radii of white dwarfs obtained using the Salpeter equation of state are closer to the ones ob-

tained from the full numerical integration of the general relativistic treatment presented here.

Turning now to astrophysics, the critical mass of white dwarfs is today acquiring a renewed interest in view of its central role in the explanation of the supernova phenomena (Phillips, 1993; Riess et al., 1998; Perlmutter et al., 1999; Riess et al., 2004). The central role of the critical mass of white dwarfs as related to supernova was presented by Hoyle and Fowler (1960) explaining the difference between type I and type II Supernova. This field has developed in the intervening years to a topic of high precision research in astrophysics and, very likely, both the relativistic and the Coulomb effects outlined in this article will become topic of active confrontation between theory and observation. For instance, the underestimate of the mass and the radius of low density white dwarfs within the Hamada and Salpeter (1961) treatment (see Figs. B.3–B.10) leads to the possibility of a direct confrontation with observations in the case of low mass white dwarfs e.g. the companion of the Pulsar J1141-6545 (Kramer, 2010).

We have finally obtained a general formula in Eq. (B.1.76) as a “first integral” of the general relativistic equations of equilibrium. This formula relates the chemical potential of the Wigner-Seitz cells, duly obtained from the relativistic Feynman-Metropolis-Teller model (Rotondo et al., 2011c) taking into account weak, nuclear and electromagnetic interactions, to the general relativistic gravitational potential at each point of the configuration. Besides its esthetic value, this is an important tool to examine the radial dependence of the white dwarf properties and it can be also applied to the crust of a neutron star as it approaches to the physical important regime of neutron star cores.

The formalism we have introduced allows in principle to evaluate subtle effects of a nuclear density distribution as a function of the radius and of the Fermi energy of the electrons and of the varying depth of the general relativistic gravitational potential. The theoretical base presented in this article establishes also the correct framework for the formulation of the more general case when finite temperatures and magnetic fields are present. This treatment naturally opens the way to a more precise description of the crust of neutron stars, which will certainly become an active topic of research in view of the recent results by Goriely et al. (2011a,b) on the importance of the Coulomb effects in the r-process nucleosynthesis of the crust material during its post-ejection evolution in the process of gravitational collapse and/or in the merging of neutron star binaries.

## **B.2. On general relativistic uniformly rotating white dwarfs**

### **B.2.1. Introduction**

The relevance of rotation in enhancing the maximum stable mass of a white dwarf (WD) have been discussed for many years both for uniform rotation (see e.g. James, 1964; Anand, 1965; Roxburgh and Durney, 1966; Monaghan, 1966; Geroyannis and Hadjopoulos, 1989) and differential rotation (see e.g. Ostriker and Bodenheimer, 1968; Ostriker and Tassoul, 1969; Tassoul and Ostriker, 1970; Durisen, 1975). Newtonian gravity and post-Newtonian approximation have been mainly used to compute the structure of the star, with the exception of the work of Arutyunyan et al. (1971), where rotating white dwarfs (RWDs) were computed in full General Relativity (GR). From the microscopical point of view, the equation of state (EOS) of cold WD matter has been assumed to be either the one of a microscopically uniform degenerate electron fluid used by Chandrasekhar (1931b) in his classic work, or assumed to have a polytropic form.

However, as shown first by Salpeter (1961a) in the Newtonian case and then by (Rotondo et al., 2011c,b) in General Relativity (GR), a detailed description of the EOS taking into account the effects of the Coulomb interaction are essential for the determination of the maximum stable mass of non-rotating WDs. Specific microphysics of the ion-electron system forming a Coulomb lattice, together with the detail computation of the inverse  $\beta$ -decays and the pycnonuclear reaction rates, play a fundamental role.

A new EOS taking into account the finite size of the nucleus, the Coulomb interactions, and the electroweak equilibrium in a self-consistent relativistic fashion has been recently obtained by Rotondo et al. (2011c). This relativistic Feynman-Metropolis-Teller (RFMT) EOS generalizes both the Chandrasekhar (1931b) and Salpeter (1961a) works in that a full treatment of the Coulomb interaction is given through the solution of a relativistic Thomas-Fermi model. This leads to a more accurate calculation of the energy and pressure of the Wigner-Seitz cells, hence a more accurate EOS. It has been shown how the Salpeter EOS overestimates at high densities and underestimates at low densities the electron pressure. The application of this new EOS to the structure of non-rotating  ${}^4\text{He}$ ,  ${}^{12}\text{C}$ ,  ${}^{16}\text{O}$  and  ${}^{56}\text{Fe}$  was recently done in (Rotondo et al., 2011b). The new mass-radius relations generalize the works of Chandrasekhar (1931b) and Hamada and Salpeter (1961); smaller maximum masses and a larger minimum radii are obtained. Both GR and inverse  $\beta$ -decay can be relevant for the instability of non-rotating WDs depending on the nuclear composition, as we can see from Table B.4, which summarizes some results of Rotondo et al. (2011b).

We here extend the previous results of Rotondo et al. (2011b) for uniformly

Composition	$\rho_{\text{crit}}^{J=0}$ (g/cm <sup>3</sup> )	Instability	$M_{\text{max}}^{J=0} / M_{\odot}$
<sup>4</sup> He	$1.56 \times 10^{10}$	GR	1.40906
<sup>12</sup> C	$2.12 \times 10^{10}$	GR	1.38603
<sup>16</sup> O	$1.94 \times 10^{10}$	inverse $\beta$ -decay	1.38024
<sup>56</sup> Fe	$1.18 \times 10^9$	inverse $\beta$ -decay	1.10618

**Table B.4.:** Critical density and mass for the gravitational collapse of non-rotating <sup>4</sup>He, <sup>12</sup>C, <sup>16</sup>O and <sup>56</sup>Fe WDs in GR obtained by Rotondo et al. (2011b), based on the RFMT EOS Rotondo et al. (2011c). We indicate in the third column if the critical density is due either to inverse  $\beta$ -decay or to general relativistic effects.

RWDs at zero temperatures obeying the RFMT EOS. We use the Hartle’s approach (Hartle, 1967) to solve the Einstein equations accurately up to second order approximation in the angular velocity of the star. We calculate the mass  $M$ , equatorial  $R_{eq}$  and polar  $R_p$  radii, angular momentum  $J$ , eccentricity  $\epsilon$ , and quadrupole moment  $Q$ , as a function of the central density  $\rho_c$  and rotation angular velocity  $\Omega$  of the WD. We construct also RWD models for the Chandrasekhar and Salpeter EOS and compare and contrast the differences with the RFMT ones.

We analyze in detail the stability of RWDs both from the microscopic and macroscopic point of view in Sec. B.2.3. Besides the inverse  $\beta$ -decay instability, we also study the limits to the matter density imposed by zero-temperature pycnonuclear fusion reactions using up-to-date theoretical models (Gasques et al., 2005; Yakovlev et al., 2006). The mass-shedding limit as well as the secular axisymmetric instability boundary are calculated.

The general structure and stability boundaries of <sup>4</sup>He, <sup>12</sup>C, <sup>16</sup>O and <sup>56</sup>Fe WDs are discussed in in Sec. B.2.4. From the maximally rotating models (mass-shedding sequence), we calculate in Sec. B.2.5 the maximum mass of uniformly rotating <sup>4</sup>He, <sup>12</sup>C, <sup>16</sup>O and <sup>56</sup>Fe WDs for the Chandrasekhar, Salpeter, and RFMT EOS, and compare the results with the existing values in the literature. We calculate the minimum(maximum) rotation period(frequency) of a RWD for the above nuclear compositions, taking into account both inverse  $\beta$ -decay and pycnonuclear restrictions to the density; see Sec. B.2.6.

We discuss in Sec. B.2.7 the axisymmetric instabilities found in this work. A comparison of Newtonian and general relativistic WDs presented in App. B.2.11 show that this is indeed a general relativistic effect. Furthermore, we estimate in App. B.2.11 the accuracy of the “slow” rotation approximation (power-series solutions up to order  $\Omega^2$ ) for the determination of the maximally rotating sequence of WDs. In this line, we calculate the rotation to gravitational energy ratio and the deviations from spherical symmetry.

In addition, we construct in Sec. B.2.8 constant rest-mass evolution tracks of RWDs at fixed chemical composition and show that RWDs may experi-

ence both spin-up and spin-down epochs while loosing angular momentum, depending on their initial mass and rotation period.

Finally, in Sec. B.2.9 we outline some astrophysical implications of the results presented in this work, which we summarized in Sec. B.2.10.

### B.2.2. Spacetime geometry and Hartle's formalism

Hartle (1967) described for the first time the structure of rotating objects approximately up to second order terms in the angular velocity of the star  $\Omega$ , within GR. In this "slow" rotation approximation, the solution of the Einstein equations in the exterior vacuum can be written in analytic closed form in terms of the total mass  $M$ , angular momentum  $J$  and quadrupole moment  $Q$  of the star (see App. B.2.11). The interior metric is constructed by solving numerically a system of ordinary differential equations for the perturbation functions (see Hartle, 1967; Hartle and Thorne, 1968, for details).

The spacetime geometry up to order  $\Omega^2$ , with an appropriate choice of coordinates is, in geometrical units  $c = G = 1$ , described by (Hartle, 1967)

$$\begin{aligned}
 ds^2 &= \left\{ e^{v(r)} [1 + 2h_0(r) + 2h_2(r)P_2(\cos\theta)] - \omega^2 r^2 \sin^2\theta \right\} dt^2 \\
 &+ 2\omega r^2 \sin^2\theta dt d\phi - e^{\lambda(r)} \left[ 1 + 2 \frac{m_0(r) + m_2(r)P_2(\cos\theta)}{r - M^{J=0}(r)} \right] dr^2 \\
 &- r^2 [1 + 2k_2(r)P_2(\cos\theta)] (d\theta^2 + \sin^2\theta d\phi^2), \tag{B.2.1}
 \end{aligned}$$

where  $P_2(\cos\theta)$  is the Legendre polynomial of second order,  $e^{v(r)}$  and  $e^{\lambda(r)} = [1 - 2M^{J=0}(r)/r]^{-1}$ , and  $M^{J=0}(r)$  are the metric functions and mass of the corresponding static (non-rotating) solution with the same central density as the rotating one. The angular velocity of local inertial frames  $\omega(r)$ , proportional to  $\Omega$ , as well as the functions  $h_0$ ,  $h_2$ ,  $m_0$ ,  $m_2$ ,  $k_2$ , proportional to  $\Omega^2$ , must be calculated from the Einstein equations (see Hartle, 1967; Hartle and Thorne, 1968, for details); their analytic expressions in the vacuum case can be found in App. B.2.11.

The parameters  $M$ ,  $J$  and  $Q$ , are then obtained for a given EOS from the matching procedure between the internal and external solutions at the surface of the rotating star. The total mass is defined by  $M = M^{J \neq 0} = M^{J=0} + \delta M$ , where  $M^{J=0}$  is the mass of a static (non-rotating) WD with the same central density as  $M^{J \neq 0}$ , and  $\delta M$  is the contribution to the mass due to rotation.

### B.2.3. Limits on the stability of rotating white dwarfs

#### The mass-shedding limit

The velocity of particles on the equator of the star cannot exceed the Keplerian velocity of "free" particles, computed at the same location. In this limit,

particles on the star's surface keep bound to the star only due to a balance between gravity and centrifugal forces. The evolution of a star rotating at this Keplerian rate is accompanied by loss of mass, becoming thus unstable (see e.g. Stergioulas, 2003, for details). A procedure to obtain the maximum possible angular velocity of the star before reaching this limit was developed e.g. by Friedman et al. (1986a). However, in practice, it is less complicated to compute the mass-shedding (or Keplerian) angular velocity of a rotating star,  $\Omega_K^{J \neq 0}$ , by calculating the orbital angular velocity of a test particle in the external field of the star and corotating with it at its equatorial radius,  $r = R_{eq}$ .

For the Hartle-Thorne external solution, the Keplerian angular velocity can be written as (see e.g. Torok et al. (2008) and App. B.2.11, for details)

$$\Omega_K^{J \neq 0} = \sqrt{G \frac{M}{R_{eq}^3} \left[ 1 - jF_1(R_{eq}) + j^2F_2(R_{eq}) + qF_3(R_{eq}) \right]}, \quad (\text{B.2.2})$$

where  $j = cJ/(GM^2)$  and  $q = c^4Q/(G^2M^3)$  are the dimensionless angular momentum and quadrupole moment, and the functions  $F_i(r)$  are defined in App. B.2.11. Thus, the numerical value of  $\Omega_K^{J \neq 0}$  can be computed by gradually increasing the value of the angular velocity of the star,  $\Omega$ , until it reaches the value  $\Omega_K^{J \neq 0}$  expressed by Eq. (B.2.2).

It is important to analyze the issue of the accuracy of the slow rotation approximations, e.g. accurate up to second order in the rotation expansion parameter, for the description of maximally rotating stars as WDs and neutron stars (NSs). We have performed in App. B.2.11 a scrutiny of the actual physical request made by the slow rotation regime. Based on this analysis, we have checked that the accuracy of the slow rotation approximation increases with the density of the WD, and that the mass-shedding (Keplerian) sequence of RWDs can be accurately described by the  $\Omega^2$  approximation within an error smaller than the one found for rapidly rotating NSs,  $\lesssim 6\%$ .

### The turning-point criterion and secular axisymmetric instability

In a sequence of increasing central density the mass of non-rotating star is limited by the first maximum of the  $M-\rho_c$  curve, i.e. the turning-point given by the maximum mass,  $\partial M/\partial \rho_c = 0$ , marks the secular instability point and it coincides also with the dynamical instability point if the perturbation obeys the same EOS as of the equilibrium configuration (see e.g. Shapiro and Teukolsky, 1983a, for details). The situations is, however, much more complicated in the case of rotating stars; the determination of axisymmetric dynamical instability points implies to find the perturbed solutions with zero frequency modes, that is, perturbed configurations whose energy (mass) is the same as the unperturbed (equilibrium) one, at second order. However, Friedman et al. (1988) formulated, based on the works of Sorkin (1981, 1982),

a turning-point method to locate the points where secular instability sets in for uniformly rotating relativistic stars: along a sequence of rotating stars with fixed angular momentum and increasing central density, the onset of secular axisymmetric instability is given by

$$\left( \frac{\partial M(\rho_c, J)}{\partial \rho_c} \right)_J = 0. \quad (\text{B.2.3})$$

Thus, configurations on the right-side of the maximum mass of a  $J$ -constant sequence are secularly unstable. After the secular instability sets in, the configuration evolves quasi-stationarily until it reaches a point of dynamical instability where gravitational collapse should take place (see Stergioulas, 2003, and references therein). The secular instability boundary thus separates stable from unstable stars. It is worth stressing here that the turning-point of a constant  $J$  sequence is a sufficient but not a necessary condition for secular instability and therefore it establishes an absolute upper bound for the mass (at constant  $J$ ). We construct the boundary given by the turning-points of constant angular momentum sequences as given by Eq. (B.2.3). The question whether dynamically unstable RWDs can exist or not on the left-side of the turning-point boundary remains an interesting problem and deserves further attention in view of the very recent results obtained by Takami et al. (2011) for some models of rapidly rotating NSs.

### Inverse $\beta$ -decay instability

It is known that a WD might become unstable against the inverse  $\beta$ -decay process  $(Z, A) \rightarrow (Z - 1, A)$  through the capture of energetic electrons. In order to trigger such a process, the electron Fermi energy (with the rest-mass subtracted off) must be larger than the mass difference between the initial  $(Z, A)$  and final  $(Z - 1, A)$  nucleus. We denote this threshold energy as  $\epsilon_Z^\beta$ . Usually it is satisfied  $\epsilon_{Z-1}^\beta < \epsilon_Z^\beta$  and therefore the initial nucleus undergoes two successive decays, i.e.  $(Z, A) \rightarrow (Z - 1, A) \rightarrow (Z - 2, A)$  (see e.g. Salpeter (1961a); Shapiro and Teukolsky (1983a)). Some of the possible decay channels in WDs with the corresponding known experimental threshold energies  $\epsilon_Z^\beta$  are listed in Table B.5. The electrons in the WD may eventually reach the threshold energy to trigger a given decay at some critical density  $\rho_{\text{crit}}^\beta$ . Since the electrons are responsible for the internal pressure of the WD, configurations with  $\rho > \rho_{\text{crit}}^\beta$  become unstable due to the softening of the EOS as a result of the electron capture process (see e.g. Salpeter, 1961a). In Table B.5, correspondingly to each threshold energy  $\epsilon_Z^\beta$ , the critical density  $\rho_{\text{crit}}^\beta$  given by the RFMT EOS is shown; see Rotondo et al. (2011b) for details.

Decay	$\epsilon_Z^\beta$ (MeV)	$\rho_{\text{crit}}^\beta$ (g/cm <sup>3</sup> )
${}^4\text{He} \rightarrow {}^3\text{H} + n \rightarrow 4n$	20.596	$1.39 \times 10^{11}$
${}^{12}\text{C} \rightarrow {}^{12}\text{B} \rightarrow {}^{12}\text{Be}$	13.370	$3.97 \times 10^{10}$
${}^{16}\text{O} \rightarrow {}^{16}\text{N} \rightarrow {}^{16}\text{C}$	10.419	$1.94 \times 10^{10}$
${}^{56}\text{Fe} \rightarrow {}^{56}\text{Mn} \rightarrow {}^{56}\text{Cr}$	3.695	$1.18 \times 10^9$

**Table B.5.:** Onset for the inverse  $\beta$ -decay of  ${}^4\text{He}$ ,  ${}^{12}\text{C}$ ,  ${}^{16}\text{O}$  and  ${}^{56}\text{Fe}$ . The experimental values of the threshold energies  $\epsilon_Z^\beta$  have been taken from Table 1 of Audi et al. (2003b); see also (Shapiro and Teukolsky, 1983a). The corresponding critical density  $\rho_{\text{crit}}^\beta$  are for the RFMT EOS (see Rotondo et al., 2011b)

### Pycnonuclear fusion reactions

In our WD model, we assume a unique nuclear composition  $(Z, A)$  throughout the star. We have just seen that inverse  $\beta$ -decay imposes a limit to the density of the WD over which the current nuclear composition changes from  $(Z, A)$  to  $(Z - 1, A)$ . There is an additional limit to the nuclear composition of a WD. Nuclear reactions proceed with the overcoming of the Coulomb barrier by the nuclei in the lattice. In the present case of zero temperatures  $T = 0$ , the Coulomb barrier can be overcome because the zero-point energy of the nuclei (see e.g. Shapiro and Teukolsky, 1983a)

$$E_p = \hbar\omega_p, \quad \omega_p = \sqrt{\frac{4\pi e^2 Z^2 \rho}{A^2 M_u^2}}, \quad (\text{B.2.4})$$

where  $e$  is the fundamental charge and  $M_u = 1.6605 \times 10^{-24}$  g is the atomic mass unit.

Based on the pycnonuclear rates by Zel'Dovich (1958b); Cameron (1959), Salpeter (1961a) estimated that in a time of 0.1 Myr,  ${}^1\text{H}$  is converted into  ${}^4\text{He}$  at  $\rho \sim 5 \times 10^4$  g cm<sup>-3</sup>,  ${}^4\text{He}$  into  ${}^{12}\text{C}$  at  $\rho \sim 8 \times 10^8$  g cm<sup>-3</sup>, and  ${}^{12}\text{C}$  into  ${}^{24}\text{Mg}$  at  $\rho \sim 6 \times 10^9$  g cm<sup>-3</sup>. The threshold density for the pycnonuclear fusion of  ${}^{16}\text{O}$  occurs, for the same reaction time 0.1 Myr, at  $\rho \sim 3 \times 10^{11}$  g cm<sup>-3</sup>, and for 10 Gyr at  $\sim 10^{11}$  g cm<sup>-3</sup>. These densities are much higher than the corresponding density for inverse  $\beta$ -decay of  ${}^{16}\text{O}$ ,  $\rho \sim 1.9 \times 10^{10}$  g cm<sup>-3</sup> (see Table B.5). The same argument applies to heavier compositions e.g.  ${}^{56}\text{Fe}$ ; so pycnonuclear reactions are not important for heavier than  ${}^{12}\text{C}$  in WDs.

It is important to analyze the case of  ${}^4\text{He}$  WDs in detail. At densities  $\rho_{\text{pyc}} \sim 8 \times 10^8$  g cm<sup>-3</sup> a  ${}^4\text{He}$  WD should have a mass  $M \sim 1.35M_\odot$  (see e.g. Fig. 3 in Rotondo et al., 2011b). However, the mass of  ${}^4\text{He}$  WDs is constrained to lower values from their previous thermonuclear evolution: a cold star with mass  $> 0.5M_\odot$  have already burned an appreciable part of its He-

lithium content at earlier stages. Thus, WDs of  $M > 0.5M_{\odot}$  with  ${}^4\text{He}$  cores are very unlikely (see Hamada and Salpeter, 1961, for details). It should be stressed that  ${}^4\text{He}$  WDs with  $M \lesssim 0.5M_{\odot}$  have central densities  $\rho \sim 10^6 \text{ g cm}^{-3}$  (Rotondo et al., 2011b) and at such densities pycnonuclear reaction times are longer than 10 Gyr, hence unimportant. However, we construct in this work  ${}^4\text{He}$  RWDs configurations all the way up to their inverse  $\beta$ -decay limiting density for the sake of completeness, keeping in mind that the theoretical  ${}^4\text{He}$  WDs configurations with  $M \gtrsim 0.5M_{\odot}$  could actually not be present in any astrophysical system.

From the above discussion we conclude that pycnonuclear reactions can be relevant only for  ${}^{12}\text{C}$  WDs. It is important to stress here that the reason for which the pycnonuclear reaction time,  $\tau_{pyc}^{\text{C+C}}$ , determines the lifetime of a  ${}^{12}\text{C}$  WD is that reaction times  $\tau_{pyc}^{\text{C+C}} < 10 \text{ Gyr}$  are achieved at densities  $\sim 10^{10} \text{ g cm}^{-3}$ , lower than the inverse  $\beta$  decay threshold density of  ${}^{24}\text{Mg}$ ,  ${}^{24}\text{Mg} \rightarrow {}^{24}\text{Na} \rightarrow {}^{24}\text{Ne}$ ,  $\rho \sim 3.2 \times 10^9 \text{ g cm}^{-3}$  (see e.g. Salpeter, 1961a; Shapiro and Teukolsky, 1983a). Thus, the pycnonuclear  ${}^{12}\text{C}+{}^{12}\text{C}$  fusion produces unstable  ${}^{24}\text{Mg}$  that almost instantaneously decay owing to electron captures, and so the WD becomes unstable as we discussed in Subsec. B.2.3.

However, the pycnonuclear reaction rates are not known with precision due to theoretical and experimental uncertainties. Hamada and Salpeter (1961) had already pointed out in their work that the above pycnonuclear density thresholds are reliable only within a factor 3 or 4. The uncertainties are related to the precise knowledge of the Coulomb tunneling in the high density low temperature regime relevant to astrophysical systems, e.g. WDs and NSs, as well as with the precise structure of the lattice; impurities, crystal imperfections, as well as the inhomogeneities of the local electron distribution and finite temperature effects, also affect the reaction rates. The energies for which the so-called astrophysical  $S$ -factors are known from experiments are larger with respect to the energies found in WD and NS crusts, and therefore the value of the  $S$ -factors have to be obtained theoretically from the extrapolation of experimental values using appropriate nuclear models, which at the same time are poorly constrained. A detailed comparison between the different theoretical methods and approximations used for the computation of the pycnonuclear reaction rates can be found in (Gasques et al., 2005; Yakovlev et al., 2006).

The  $S$ -factors have been computed in (Gasques et al., 2005; Yakovlev et al., 2006) using up-to-date nuclear models. Following these works, we have computed the pycnonuclear reaction times for C+C fusion as a function of the density as given by Eq. (B.2.27),  $\tau_{pyc}^{\text{C+C}}$ , which we show in Fig. B.11; we refer to App. B.2.11 for details.

We obtain that for  $\tau_{pyc}^{\text{C+C}} = 10 \text{ Gyr}$ ,  $\rho_{pyc} \sim 9.26 \times 10^9 \text{ g cm}^{-3}$  while, for  $\tau_{pyc}^{\text{C+C}} = 0.1 \text{ Myr}$ ,  $\rho_{pyc} \sim 1.59 \times 10^{10} \text{ g cm}^{-3}$ , to be compared with the value  $\rho \sim 6 \times 10^9 \text{ g cm}^{-3}$  estimated by Salpeter (1961a). In order to compare

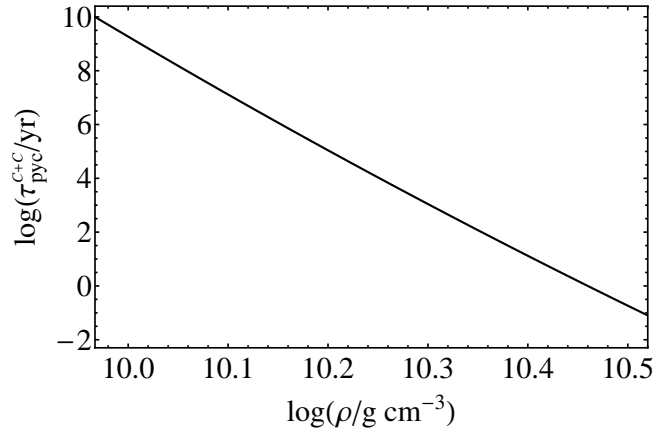


**Figure B.11.** Pycnonuclear reaction times at zero temperature for C+C fusion as a function of the density.

the threshold densities for inverse  $\beta$ -decay and pycnonuclear fusion rates, we shall indicate in our mass-density and mass-radius relations the above two density values corresponding to these two lifetimes. It is important to stress that the computation of the pycnonuclear reactions rates is subjected to theoretical and experimental uncertainties (see Gasques et al., 2005, for details). For instance, Hamada and Salpeter (1961) stated that these pycnonuclear critical densities are reliable within a factor 3 or 4. If three times larger, the above value of  $\rho_{\text{pyc}}$  for  $\tau_{\text{pyc}}^{\text{C+C}} = 0.1$  Myr becomes  $\rho_{\text{pyc}} \sim 4.8 \times 10^{10} \text{ g cm}^{-3}$ , larger than the inverse  $\beta$ -decay threshold density  $\rho_{\beta}^{\text{C}} \sim 3.97 \times 10^{10} \text{ g cm}^{-3}$  (see Table B.5). As we will see in Sec. B.2.7, the turning-point construction leads to an axisymmetric instability boundary in the density range  $\rho_{\text{crit}}^{\text{C},J=0} = 2.12 \times 10^{10} < \rho < \rho_{\beta}^{\text{C}} \text{ g cm}^{-3}$  in a specific range of angular velocities. This range of densities is particularly close to the above values of  $\rho_{\text{pyc}}$  which suggests a possible competition between different instabilities at high densities.

#### B.2.4. WD structure and stability boundaries

The structure of uniformly RWDs have been studied by several authors (see e.g. James, 1964; Anand, 1965; Roxburgh and Durney, 1966; Monaghan, 1966; Geroyannis and Hadjopoulos, 1989). The issue of the stability of both uniformly and differentially rotating WDs has been studied as well (see e.g. Ostriker and Bodenheimer, 1968; Ostriker and Tassoul, 1969; Tassoul and Ostriker, 1970; Durisen, 1975). All the above computations were carried out within Newtonian gravity or at the post-Newtonian approximation. The EOS of cold WD matter has been assumed to be either the one of a microscopically uniform degenerate electron fluid, which we refer hereafter as Chandrasekhar EOS (Chandrasekhar, 1931b), or assuming a polytropic EOS. How-

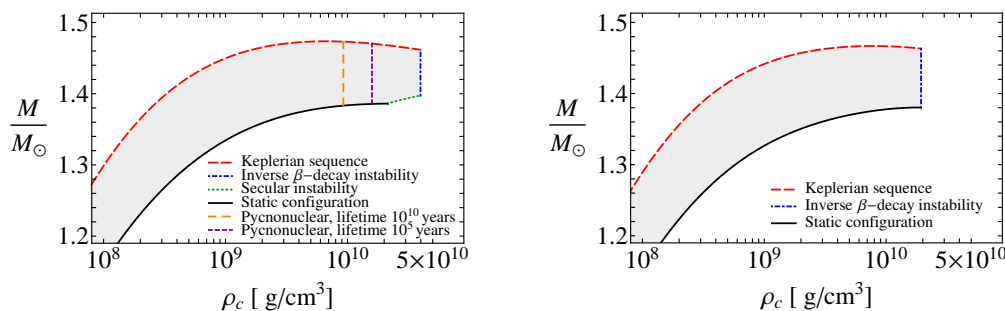


**Figure B.12.:** Mass in solar masses versus the central density for  $^{12}\text{C}$  (left panel) and for  $^{16}\text{O}$  (right panel) WDs. The solid curve corresponds to the mass of non-rotating WDs, the Keplerian sequence is the red thick dashed curve, the blue thick dotted-dashed curve is the inverse  $\beta$  instability boundary, and the green thick solid curve is the axisymmetric instability boundary. The orange and purple dashed boundaries correspond to the pycnonuclear densities for reaction times  $\tau_{pyc} = 10$  Gyr and 0.1 Myr, respectively. All rotating stable WDs are in the shaded region.

ever, microscopic screening caused by Coulomb interactions as well as the process of inverse  $\beta$ -decay of the composing nuclei cannot be properly studied within such EOS (see Rotondo et al., 2011c,b, for details).

The role of general relativistic effects, shown in Rotondo et al. (2011b), has been neglected in all the above precedent literature. The only exception to this rule is, up to our knowledge, the work of Arutyunyan et al. (1971), who investigated uniformly RWDs for the Chandrasekhar EOS within GR. They use an  $\Omega^2$  approximation following a method developed by Sedrakyan and Chubaryan (1968), independently of the work of Hartle (1967). A detailed comparison of our results with the ones of Arutyunyan et al. (1971) can be found in App. B.2.11.

In Figs. B.12–B.13 we show the mass-central density relation and the mass-radius relation of general relativistic rotating  $^{12}\text{C}$  and  $^{16}\text{O}$  WDs. We explicitly show the boundaries of mass-shedding, secular axisymmetric instability, inverse  $\beta$ -decay, and pycnonuclear reactions.

Turning now to the rotation properties, in Fig. B.14 we show the  $J$ - $M$  plane especially focusing on RWDs with masses larger than the maximum non-rotating mass, hereafter Super-Chandrasekhar WDs (SCWDs). It becomes clear from this diagram that SCWDs can be stable only by virtue of their non-zero angular momentum: the lower-half of the stability line of Fig. B.14, from  $J = 0$  at  $M/M_{max}^{J=0}$  all the way up to the value of  $J$  at  $M_{max}^{J \neq 0} \sim 1.06M_{max}^{J=0}$ , determines the critical(minimum) angular momentum under which a SCWDs becomes unstable. The upper half of the stability line determines, instead, the maximum angular momentum that SCWDs can have.

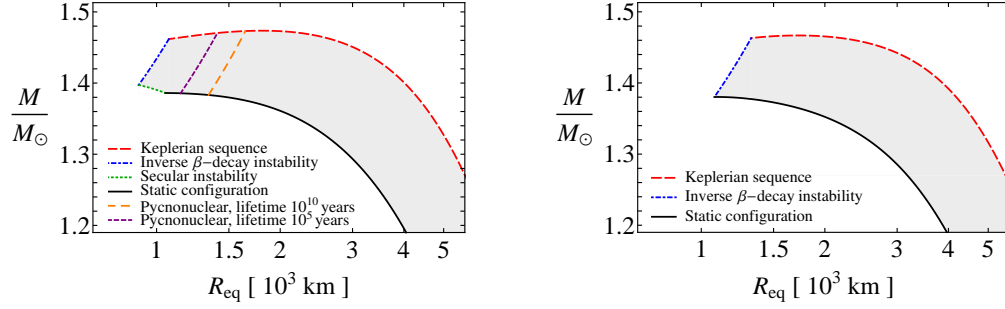


**Figure B.13.:** Mass in solar masses versus the equatorial radius in units of  $10^3$  km for  $^{12}\text{C}$  (left panel) and for  $^{16}\text{O}$  (right panel) WDs. The left and right panels show the configurations for the same range of central densities of the corresponding panels of Fig. B.12.

Composition	$\rho_{M_{max}^{J \neq 0}}$	$k$	$M_{max}^{J=0}/M_{\odot}$	$R_{M_{max}^{J=0}}$	$P_{min}$	$R_p^{P_{min}}$	$R_{eq}^{P_{min}}$	$(T/ W )^{P_{min}}$	$\epsilon^{P_{min}}$	$j^{P_{min}}$	$q^{P_{min}}$
$^4\text{He}$	$5.46 \times 10^9$	1.0646	1.40906	1163	0.284	564	736	0.0163	0.642	1.004	526
$^{12}\text{C}$	$6.95 \times 10^9$	1.0632	1.38603	1051	0.501	817	1071	0.0181	0.647	1.287	1330
$^{16}\text{O}$	$7.68 \times 10^9$	1.0626	1.38024	1076	0.687	1005	1323	0.0194	0.651	1.489	2263
$^{56}\text{Fe}$	$1.18 \times 10^9$	1.0864	1.10618	2181	2.195	2000	2686	0.0278	0.667	2.879	23702

**Table B.6.:** Properties of uniformly rotating general relativistic  $^4\text{He}$ ,  $^{12}\text{C}$ ,  $^{16}\text{O}$  and  $^{56}\text{Fe}$  WDs:  $\rho_{M_{max}^{J \neq 0}}$  is the central density in  $\text{g cm}^{-3}$  corresponding to the rotating maximum mass  $M_{max}^{J \neq 0}$ ;  $k$  is the dimensionless factor used to express the rotating maximum mass  $M_{max}^{J \neq 0}$  as a function of the non-rotating maximum mass  $M_{max}^{J=0}$  of WDs, in solar masses, obtained in Rotondo et al. (2011b), as defined in Eq. (B.2.5); the corresponding minimum radius is  $R_{M_{max}^{J=0}}$ , in km;  $P_{min}$  is the minimum rotation period in seconds. We recall that the configuration with  $P_{min}$  is obtained for a WD rotating at the mass-shedding limit and with central density equal to the critical density for inverse  $\beta$ -decay (see Table B.5 and the right panel of Fig. B.16). The polar  $R_p^{P_{min}}$  and equatorial  $R_{eq}^{P_{min}}$  radii of the configuration with  $P_{min}$  are also given in km. The quantity  $(T/|W|)^{P_{min}}$  is the ratio between the kinetic and binding energies, the parameter  $\epsilon^{P_{min}}$  is the eccentricity of the star, rotating at  $P_{min}$ . Finally,  $j^{P_{min}}$  and  $q^{P_{min}}$  are the dimensionless angular momentum and quadrupole moment of WDs, respectively.

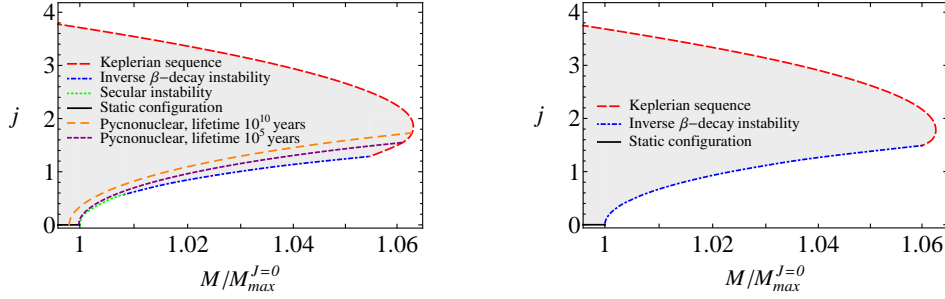


**Figure B.14.:** Dimensionless angular momentum  $j \equiv cJ/(GM^2)$  versus the mass of rotating  $^{12}\text{C}$  (left panel) and  $^{16}\text{O}$  (right panel) WDs, normalized to the maximum non-rotating mass. All rotating stable WDs are in the shaded region.

Nuclear Composition	EOS	$\rho_{M_{max}^{J \neq 0}}$ (g/cm <sup>3</sup> )	$R_p^{M_{max}^{J \neq 0}}$ (km)	$R_{eq}^{M_{max}^{J \neq 0}}$ (km)	$M_{max}^{J \neq 0}/M_\odot$	$P^{M_{max}^{J \neq 0}}$ (sec)
$\mu = 2$	Chandrasekhar	$1.07 \times 10^{10}$	1198.91	1583.47	1.5159	0.884
	Salpeter	$1.07 \times 10^{10}$	1193.08	1575.94	1.4996	0.883
$^4\text{He}$	RFMT	$5.46 \times 10^9$	1458.58	1932.59	1.5001	1.199
	Salpeter	$1.08 \times 10^{10}$	1183.99	1564.16	1.4833	0.878
$^{12}\text{C}$	RFMT	$6.95 \times 10^9$	1349.15	1785.98	1.4736	1.074
	Salpeter	$1.09 \times 10^{10}$	1178.88	1556.68	1.4773	0.875
$^{16}\text{O}$	RFMT	$7.68 \times 10^9$	1308.09	1730.65	1.4667	1.027
	Salpeter	$1.14 \times 10^9$	2002.43	2693.17	1.2050	2.202
$^{56}\text{Fe}$	RFMT	$1.18 \times 10^9$	2000.11	2686.06	1.2017	2.195

**Table B.7.:** The maximum rotating mass of general relativistic uniformly rotating  $^4\text{He}$ ,  $^{12}\text{C}$ ,  $^{16}\text{O}$  and  $^{56}\text{Fe}$  WDs for different EoS.  $\rho_{M_{max}^{J \neq 0}}$ ,  $R_p^{M_{max}^{J \neq 0}}$ ,  $R_{eq}^{M_{max}^{J \neq 0}}$ , and  $P^{M_{max}^{J \neq 0}}$  are central density, polar and equatorial radii, and rotation period of the configuration with the maximum mass,  $M_{max}^{J \neq 0}$ .

### B.2.5. The maximum mass

The maximum masses of rotating WDs belongs to the Keplerian sequence (see Figs. B.12–B.14) and it can be expressed as

$$M_{max}^{J \neq 0} = k M_{max}^{J=0}, \quad (\text{B.2.5})$$

where  $M_{max}^{J=0}$  is the maximum stable mass of non-rotating WDs and  $k$  is a numerical factor that depends on the chemical composition, see Table B.6 for details. For  $^4\text{He}$ ,  $^{12}\text{C}$ ,  $^{16}\text{O}$ , and  $^{56}\text{Fe}$  RWDs, we found  $M_{max}^{J \neq 0} \sim 1.500, 1.474, 1.467, 1.202 M_\odot$ , respectively.

In Table B.7 we compare the properties of the configuration with maximum mass using different EOS, namely Chandrasekhar  $\mu = 2$ , Salpeter, and RFMT EOS. A comparison with classical results obtained with different treatments and EOS can be found in App. B.2.11.

It is worth mentioning that the maximum mass of RWDs is not associated with a critical maximum density for gravitational collapse. This is in con-

Nuclear composition	EoS	$\rho_{\text{crit}}^{\beta}$ (g/cm <sup>3</sup> )	$R_p^{P_{\text{min}}}$ (km)	$R_{\text{eq}}^{P_{\text{min}}}$ (km)	$M_{P_{\text{min}}}^{J \neq 0} / M_{\odot}$	$P_{\text{min}}$ (sec)
$\mu = 2$	Chandra	$1.37 \times 10^{11}$	562.79	734.54	1.4963	0.281
	Salpeter	$1.37 \times 10^{11}$	560.41	731.51	1.4803	0.281
<sup>4</sup> He	RFMT	$1.39 \times 10^{11}$	563.71	735.55	1.4623	0.285
	Salpeter	$3.88 \times 10^{10}$	815.98	1070.87	1.4775	0.498
<sup>12</sup> C	RFMT	$3.97 \times 10^{10}$	816.55	1071.10	1.4618	0.501
	Salpeter	$1.89 \times 10^{10}$	1005.62	1324.43	1.4761	0.686
<sup>16</sup> O	RFMT	$1.94 \times 10^{10}$	1005.03	1323.04	1.4630	0.687
	Salpeter	$1.14 \times 10^9$	2002.43	2693.17	1.2050	2.202
<sup>56</sup> Fe	RFMT	$1.18 \times 10^9$	2000.11	2686.06	1.2018	2.195

**Table B.8.:** The minimum rotation period of general relativistic rotating <sup>4</sup>He, <sup>12</sup>C, <sup>16</sup>O and <sup>56</sup>Fe WDs.  $\rho_{\text{crit}}^{\beta}$  is the critical density for inverse  $\beta$  decay.  $M_{P_{\text{min}}}^{J \neq 0}$ ,  $R_p^{P_{\text{min}}}$ , and  $R_{\text{eq}}^{P_{\text{min}}}$  are the mass, polar, and equatorial radii corresponding to the configuration with minimum rotation period,  $P_{\text{min}}$ .

trast with the non-rotating case where the configuration of maximum mass (turning-point) corresponds to a critical maximum density over which the WD is unstable against gravitational collapse.

The angular momentum  $J$  along the mass-shedding sequence is not constant and thus the turning-point criterion (B.2.3) does not apply to this sequence. Therefore the configuration of maximum rotating mass (B.2.5) does not separate stable from secular axisymmetrically unstable WDs. We have also verified that none of the RWDs belonging to the mass-shedding sequence is a turning-point of some  $J = \text{constant}$  sequence, and therefore they are indeed secularly stable. We therefore extend the Keplerian sequence all the way up to the critical density for inverse  $\beta$  decay,  $\rho_{\text{crit}}^{\beta}$ , see Table B.5 and Fig. B.12.

### B.2.6. The minimum rotation period

The minimum rotation period  $P_{\text{min}}$  of WDs is obtained for a configuration rotating at Keplerian angular velocity, at the critical inverse  $\beta$ -decay density; i.e. is the configuration lying at the crossing point between the mass-shedding and inverse  $\beta$ -decay boundaries, see Figs. B.12 and B.14. For <sup>4</sup>He, <sup>12</sup>C, <sup>16</sup>O, and <sup>56</sup>Fe RWDs we found the minimum rotation periods  $\sim 0.28, 0.50, 0.69$  and  $2.19$  seconds, respectively (see Table B.6 for details). In Table B.7 we compare the properties of the configuration with minimum rotation period using different EOS, namely Chandrasekhar  $\mu = 2$ , Salpeter, and RFMT EOS.

In the case of <sup>12</sup>C WDs, the minimum period 0.50 seconds have to be compared with the value obtained assuming as critical density the threshold for pycnonuclear reactions. Assuming lifetimes  $\tau_{\text{pyc}}^{\text{C}+\text{C}} = 10$  Gyr and 0.1 Myr, corresponding to critical densities  $\rho_{\text{pyc}} \sim 9.26 \times 10^9$  g cm<sup>-3</sup> and  $\rho_{\text{pyc}} \sim 1.59 \times 10^{10}$  g cm<sup>-3</sup>, we obtain minimum periods  $P_{\text{min}}^{\text{pyc}} = 0.95$  and  $0.75$  seconds, respectively.

It is interesting to compare and contrast some classical results with the ones presented in this work. Using post-Newtonian approximation, Roxburgh and Durney (1966) analyzed the problem of dynamical stability of maximally

rotating RWDs, i.e. WDs rotating at the mass-shedding limit. The result was a minimum polar radius of 363 km, assuming the Chandrasekhar EOS with  $\mu = 2$ . The Roxburgh critical radius is rather small with respect to our minimum polar radii, see Table B.6. It is clear that such a small radius would lead to a configuration with the central density over the limit established by inverse  $\beta$ -decay: the average density obtained for the Roxburgh's critical configuration is  $\sim 1.47 \times 10^{10}$  g/cm<sup>3</sup>, assuming the maximum mass  $1.48M_{\odot}$  obtained in the same work (see Table B.9 in App. B.2.11). A configuration with this mean density will certainly have a central density larger than the inverse  $\beta$ -decay density of <sup>12</sup>C and <sup>16</sup>O,  $3.97 \times 10^{10}$  g/cm<sup>3</sup> and  $1.94 \times 10^{10}$  g/cm<sup>3</sup>, respectively (see Table B.5). The rotation period of the WD at the point of dynamical instability of Roxburgh must be certainly shorter than the minimum values presented here.

The above comparison is in line with the fact that we did not find any turning-point that cross the mass-shedding sequence (see Figs. B.12–B.13). Presumably, ignoring the limits imposed by inverse  $\beta$ -decay and pycnonuclear reactions, the boundary determined by the turning-points could cross at some higher density the Keplerian sequence. Such a configuration should have a central density very similar to the one found by Roxburgh and Durney (1966).

In the work of Arutyunyan et al. (1971) the problem of the minimum rotation period of a WD was not considered. However, they showed their results for a range of central densities covering the range of interest of our analysis. Thus, we have interpolated their numerical values of the rotation period of WDs in the Keplerian sequence and calculated the precise values at the inverse  $\beta$ -decay threshold for <sup>4</sup>He, <sup>12</sup>C, and <sup>16</sup>O that have  $\mu = 2$  and therefore in principle comparable to the Chandrasekhar EOS results with the same mean molecular weight. We thus obtained minimum periods  $\sim 0.31, 0.55, 0.77$  seconds, in agreement with our results (see Table B.8).

It is important to stress that, although it is possible to compare the results using the Chandrasekhar EOS  $\mu = 2$  with the ones obtained for the RFMT EOS, both qualitative and quantitative differences exist between the two treatments. In the former a universal mass-density and mass-radius relation is obtained assuming  $\mu = 2$  while, in reality, the configurations of equilibrium depend on the specific values of  $Z$  and  $A$  in non-trivial way. For instance, <sup>4</sup>He, <sup>12</sup>C, and <sup>16</sup>O have  $\mu = 2$  but the configurations of equilibrium are rather different. This fact was emphasized by Hamada and Salpeter (1961) in the Newtonian case and further in GR by Rotondo et al. (2011b), for non-rotating configurations. In Fig. B.15 we present a comparison of the mass-density and mass-radius for the universal Chandrasekhar  $\mu = 2$  and the RFMT EOS for specific nuclear compositions.

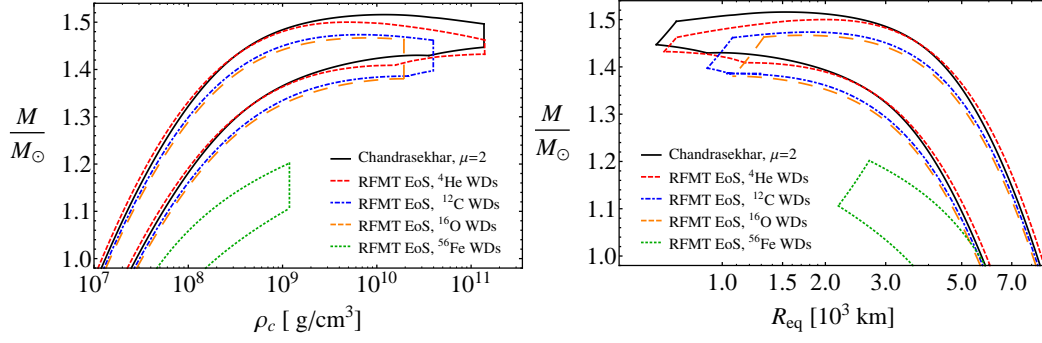


**Figure B.15.** Mass versus central density (left panel) and mass versus equatorial radius (right panel) for general relativistic WDs using the Chandrasekhar and the RFMT EOS.

### B.2.7. Occurrence of secular axisymmetric instability

Regarding the stability of rotating WDs, Ostriker and Bodenheimer (1968); Ostriker and Tassoul (1969); Durisen (1975) showed that uniformly rotating Newtonian polytropes and WDs described by the uniform degenerate electron fluid EOS are axisymmetrically stable at any rotation rate. In clear contrast with these results, we have shown here that uniformly RWDs can be indeed be secularly axisymmetric unstable as can be seen from Figs. B.12–B.14 (green boundary). We have constructed in App. B.2.11 Newtonian RWDs for the Chandrasekhar EOS and compare the differences with the general relativistic counterpart. Apart from the quantitative differences for the determination of the mass at high densities, it can be seen from Fig. B.17 (left panel) the absence of turning-points in the Newtonian mass-density relation. This can be understood from the fact that the maximum stable mass of non-rotating WDs is, in the Newtonian case, reached formally at infinite central density. We should then expect that turning-points will appear only from a post-Newtonian approximation, where the critical mass is shifted to finite densities (see e.g. Roxburgh and Durney, 1966, for the calculation of dynamical instability for post-Newtonian RWDs obeying the Chandrasekhar EOS).

In this respect the Fig. B.14 is of particular astrophysical relevance. Configurations lying in the filled region are stable against mass-shedding, inverse  $\beta$ -decay and secular axisymmetric instabilities. RWDs with masses smaller than the maximum non-rotating mass (Sub-Chandrasekhar WDs), i.e.  $M^{J \neq 0} < M_{max}^{J=0}$ , can have angular momenta ranging from a maximum at the mass-shedding limit all the way down to the non-rotating limit  $J = 0$ . SCWDs, however, are stabilized due to rotation and therefore there exist a minimum angular momentum,  $J_{min} > 0$ , to guarantee their stability. We have shown above that secular axisymmetric instability is relevant for the determination of this minimum angular momentum of SCWDs (see green boundary

in Fig. B.14). It is interesting to note in this respect that from our results it turns out that SCWDs with *light chemical compositions* such as  ${}^4\text{He}$  and  ${}^{12}\text{C}$ , are unstable against *axisymmetric*, inverse  $\beta$ -decay and mass-shedding instabilities. On the opposite, in SCWDs with *heavier chemical compositions*, such as  ${}^{16}\text{O}$  and  ${}^{56}\text{Fe}$ , the secular axisymmetric instability does not take place; see Fig. B.14. The existence of the new boundary due to secular axisymmetric instability is a critical issue for the evolution of SCWDs since their lifetime might be reduced depending on their initial mass and angular momentum.

From the quantitative point of view, we have found that axisymmetric instability sets in for  ${}^{12}\text{C}$  SCWDs in the range of masses  $M_{max}^{J=0} < M \lesssim 1.397M_{\odot}$ , for some specific range of rotation periods  $\gtrsim 1.24$  seconds. We can express the minimum rotation period that a SCWD with a mass  $M$  within the above mass range can have through the fitting formula

$$P_{axi} = 0.062 \left( \frac{M - M_{max}^{J=0}}{M_{\odot}} \right)^{-0.67} \text{ seconds}, \quad (\text{B.2.6})$$

where  $M_{max}^{J=0}$  is the maximum mass of general relativistic non-rotating  ${}^{12}\text{C}$  WDs,  $M_{max}^{J=0} \approx 1.386M_{\odot}$  (see Table B.4 and Rotondo et al. (2011b)). Thus, Eq. (B.2.6) describes the rotation periods of the configurations along the green-dotted boundary in Figs. B.12, B.13, and B.14. Correspondingly, the central density along this instability boundary varies from the critical density of static  ${}^{12}\text{C}$  WDs,  $\rho_{crit}^{C,J=0} = 2.12 \times 10^{10} \text{ g cm}^{-3}$  (see Table B.4), up to the inverse  $\beta$ -decay density,  $\rho_{\beta}^C = 3.97 \times 10^{10} \text{ g cm}^{-3}$  (see Table B.5).

It is important to note that at the lower edge of the density range for axisymmetric instability,  $\rho_{crit}^{C,J=0}$ , the timescale of C+C pycnonuclear reactions are  $\tau_{pyc}^{C+C} \approx 339 \text{ yr}$  (see Fig. B.11). It becomes then of interest to compare this timescale with the corresponding one of the secular axisymmetric instability that sets in at the same density.

The growing time of the secular instability is given by the dissipation time driven either by gravitational radiation or viscosity (Chandrasekhar, 1970). However, gravitational radiation reaction is expected to drive secular instabilities for systems with rotational to gravitational energy ratio  $T/|W| \sim 0.14$ , the bifurcation point between McClaurin spheroids and Jacobi ellipsoids (see Chandrasekhar, 1970, for details). Therefore, we expect gravitational radiation to become important only for differentially rotating WDs, which can attain more mass and more angular momentum (Ostriker and Bodenheimer, 1968). In the present case of general relativistic uniformly RWDs, only the viscosity timescale  $\tau_v$  is relevant. A rotating star that becomes secularly unstable first evolve with a characteristic time  $\tau_v$  and eventually reach a point of dynamical instability, thus collapsing within a time  $\tau_{dyn} \approx \Omega_K^{-1} \sim \sqrt{R^3/GM} \lesssim 1 \text{ s}$ , where  $R$  is the radius of the star (see e.g. Stergioulas, 2003).

The viscosity timescale can be estimated as  $\tau_v = R^2\rho/\eta$  (see e.g. Lindblom, 1987), where  $\rho$  and  $\eta$  are the density and viscosity of the star. The viscosity of a WD assuming degenerate relativistic electrons is given by (Durisen, 1973)

$$\eta_{fluid} = 4.74 \times 10^{-2} \frac{H_\Gamma(Z)}{Z} \rho^{5/3} \left[ \left( \frac{\rho}{2 \times 10^6} \right)^{2/3} + 1 \right]^{-1}, \quad (\text{B.2.7})$$

where  $H_\Gamma(Z)$  is a slowly varying dimensionless constant that depends on the atomic number  $Z$  and the Coulomb to thermal energy ratio

$$\Gamma = \frac{e^2 Z^2}{k_B T} \left( \frac{4\pi}{3} \frac{\rho}{2ZMu} \right)^{1/3}, \quad (\text{B.2.8})$$

where  $k_B$  is the Boltzmann constant and  $A \simeq 2Z$  has been used.

The expression (B.2.7) is valid for values of  $\Gamma$  smaller than the critical value for crystallization  $\Gamma_{cry}$ . The critical  $\Gamma_{cry}$  is not well constrained but its value should be of the order of  $\Gamma_{cry} \sim 100$  (see e.g. Durisen, 1973; Shapiro and Teukolsky, 1983a). The critical value  $\Gamma_{cry}$  defines a crystallization temperature  $T_{cry}$  under which the system behaves as a solid. For  $\Gamma_{cry} \sim 100$ , we have  $T_{cry} \approx 8 \times 10^7 [\rho / (10^{10} \text{ g cm}^{-3})]^{1/3}$  K, for  $Z = 6$ . When  $\Gamma$  approaches  $\Gamma_{cry}$  the viscosity can increase drastically to values close to (van Horn, 1969; Durisen, 1973)

$$\eta_{cry} = 4.0 \times 10^{-2} \left( \frac{Z}{7} \right)^{2/3} \rho^{5/6} \exp[0.1(\Gamma - \Gamma_{cry})]. \quad (\text{B.2.9})$$

For instance, we find that at densities  $\rho_{crit}^{C,J=0}$  and assuming a central temperature  $T \gtrsim 0.5T_{cry}$  with  $T_{cry} \approx 10^8$  K, the viscous timescale is in the range  $10 \lesssim \tau_v \lesssim 1000$  Myr, where the upper limit is obtained using Eq. (B.2.7) and the lower limit with Eq. (B.2.9). These timescales are longer than the pycnonuclear reaction timescale  $\tau_{pyc}^{C+C} = 339$  yr at the same density. So, if the pycnonuclear reaction rates are accurate, it would imply that pycnonuclear reactions are more important to restrict the stability of RWDs with respect to the secular instability. However, we have to keep in mind that, as discussed in Sec. B.2.3, the pycnonuclear critical densities are subjected to theoretical and experimental uncertainties, which could in principle shift them to higher values. For instance, a possible shift of the density for pycnonuclear instability with timescales  $\tau_{pyc}^{C+C} \sim 1$  Myr to higher values  $\rho_{pyc}^{C+C} > \rho_{crit}^{C,J=0}$ , would suggest an interesting competition between secular and pycnonuclear instability in the density range  $\rho_{crit}^{C,J=0} < \rho < \rho_\beta^C$ .

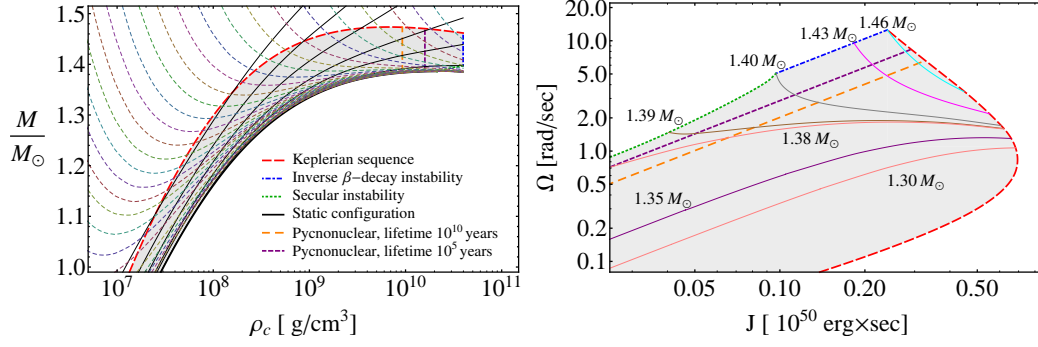


**Figure B.16.:** Left panel: mass versus the central density for  $^{12}\text{C}$  RWDs. The solid black curves correspond to  $J=\text{constant}$  sequences, where the static case  $J = 0$  the thickest one. The color thin-dashed curves correspond to  $\Omega=\text{constant}$  sequences. The Keplerian sequence is the red thick dashed curve, the blue thick dotted-dashed curve is the inverse  $\beta$ -decay instability boundary, and the green thick dotted curve is the axisymmetric secular instability boundary. Right panel: contours of constant rest-mass in the  $\Omega - J$  plane; RWDs that evolve along a track with  $\partial\Omega/\partial J > 0$  spin-down by losing angular momentum while, the ones with  $\partial\Omega/\partial J < 0$ , spin-up.

### B.2.8. Spin-up and spin-down evolution

It is known that at constant rest-mass  $M_0$ , entropy  $S$  and chemical composition  $(Z, A)$ , the spin evolution of a RWD is given by (see Shapiro et al., 1990, for details)

$$\dot{\Omega} = \frac{\dot{E}}{\Omega} \left( \frac{\partial\Omega}{\partial J} \right)_{M_0, S, Z, A}, \quad (\text{B.2.10})$$

where  $\dot{\Omega} \equiv d\Omega/dt$  and  $\dot{E} \equiv dE/dt$ , with  $E$  the energy of the star.

Thus, if a RWD is losing energy by some mechanism during its evolution, that is  $\dot{E} < 0$ , the change of the angular velocity  $\Omega$  in time depends on the sign of  $\partial\Omega/\partial J$ ; RWDs that evolve along a track with  $\partial\Omega/\partial J > 0$ , will spin-down ( $\dot{\Omega} < 0$ ) and the ones following tracks with  $\partial\Omega/\partial J < 0$  will spin-up ( $\dot{\Omega} > 0$ ).

In Fig. B.16 we show, in the left panel, the  $\Omega = \text{constant}$  and  $J = \text{constant}$  sequences in the mass-central density diagram and, in the right panel, contours of constant rest-mass in the  $\Omega - J$  plane.

The sign of  $\partial\Omega/\partial J$  can be analyzed from the left panel plot of Fig. B.16 by joining two consecutive  $J = \text{constant}$  sequences with an horizontal line and taking into account that  $J$  decreases from left to right and from up to down. The angular velocity  $\Omega$ , instead, decreases from right to left and from up to down for SCWDs and, for sub-Chandrasekhar WDs, from left to right and from up to down. We note that, in the SCWDs region  $\Omega = \text{constant}$  sequences satisfy  $\partial\Omega/\partial\rho_c < 0$  while, in the sub-Chandrasekhar region, both

$\partial\Omega/\partial\rho_c < 0$  and  $\partial\Omega/\partial\rho_c > 0$  appear (see minima). SCWDs can only either spin-up by angular momentum loss or spin-down by gaining angular momentum. In the latter case, the RWD becomes decompressed with time increasing its radius and moment of inertia, and then SCWDs following this evolution track will end at the mass-shedding limit (see Fig. B.16). Some evolutionary tracks of sub-Chandrasekhar WDs and SCWDs are shown in the right panel of Fig. B.16. It is appropriate to recall here that Shapiro et al. (1990) showed that spin-up behavior by angular momentum loss occurs for rapidly rotating Newtonian polytropes if the polytropic index is very close to  $n = 3$ , namely for an adiabatic index  $\Gamma \approx 4/3$ . It was shown explicitly by Geroyannis and Pappasotiropoulos (2000) that these conditions are achieved only by Super-Chandrasekhar polytropes.

Besides the confirmation of the above known result for SCWDs in the general relativistic case, we report here the presence of minima  $\partial\Omega/\partial\rho_c = 0$  for some sub-Chandrasekhar masses (see e.g. the evolution track of the RWD with  $M = 1.38M_\odot$  in the right panel of Fig. B.16) which raises the possibility that sub-Chandrasekhar WDs can experience, by angular momentum loss, not only the intuitively spin-down evolution, but also spin-up epochs.

### B.2.9. Astrophysical implications

It is appropriate to analyze the astrophysical consequences of the general relativistic RWDs presented in this work.

Most of the observed magnetic WDs are massive; for instance REJ 0317-853 with  $M \sim 1.35M_\odot$  and  $B \sim (1.7\text{--}6.6) \times 10^8$  G (see e.g. Barstow et al., 1995; Külebi et al., 2010b); PG 1658+441 with  $M \sim 1.31M_\odot$  and  $B \sim 2.3 \times 10^6$  G (see e.g. Liebert et al., 1983; Schmidt et al., 1992); and PG 1031+234 with the highest magnetic field  $\sim 10^9$  G (see e.g. Schmidt et al., 1986; Külebi et al., 2009). However, they are generally found to be slow rotators. It is worth mentioning that such a magnetic WDs can be indeed the result of the merger of double degenerate binaries; the misalignment of the final magnetic dipole moment of the newly born RWD with the rotation axis of the star depends on the difference of the masses of the WD components of the binary.

The precise computation of the evolution of the rotation period have to account for the actual value at each time of the moment of inertia and the equatorial and polar radii of the WD. Whether magnetic and gravitational radiation braking can explain or not the current relatively long rotation periods of some observed magnetic WDs is an important issue that deserves the appropriate attention and will be addressed elsewhere.

Magnetic braking of SCWDs has been recently invoked as a possible mechanism to explain the delayed time distribution of type Ia supernovae (SNe) (see Ilkov and Soker, 2012, for details): a type Ia SN explosion is delayed for a time typical of the spin-down time scale  $\tau_B$  due to magnetic braking, pro-

viding the result of the merging process of a WD binary system is a magnetic SCWD rather than a sub-Chandrasekhar one. The characteristic timescale  $\tau_B$  of SCWD has been estimated to be  $10^7 \lesssim \tau_B \lesssim 10^{10}$  yr for magnetic fields comprised in the range  $10^6 \lesssim B \lesssim 10^8$  G. A constant moment of inertia  $\sim 10^{49}$  g cm<sup>2</sup> and a fixed critical(maximum) rotation angular velocity

$$\Omega_{\text{crit}} \sim 0.7\Omega_K^{J=0} = 0.7\sqrt{\frac{GM^{J=0}}{R_{M^{J=0}}^3}}, \quad (\text{B.2.11})$$

have been adopted (Ilkov and Soker, 2012).

It is important to recall here that, as discussed in Sec. B.2.8, SCWDs spin-up by angular momentum loss, and therefore the reference to a “spin-down” time scale for them is just historical. SCWDs then evolve toward the mass-shedding limit, which determines in this case the critical angular velocity for rotational instability.

If we express  $\Omega_K^{J \neq 0}$  in terms of  $\Omega_K^{J=0}$  (see App. B.2.11), taking into account the values of  $j$  and  $q$  from the numerical integration, we find for RWDs that the Keplerian angular velocity can be written as

$$\Omega_K^{J \neq 0} = \sigma\Omega_K^{J=0}, \quad (\text{B.2.12})$$

where the coefficient  $\sigma$  varies in the interval [0.78,0.75] in the range of central densities  $[10^5, 10^{11}]$  g cm<sup>-3</sup>. It is important to mention that the above range of  $\sigma$  hold approximately the same independently on the chemical composition of the WD. However, the actual numerical value of the critical angular velocity,  $\Omega_K^{J \neq 0}$ , is different for different compositions owing to the dependence on  $(Z, A)$  of mass-radius relation of non-rotating WDs.

Furthermore, as we have shown, the evolution track followed by a SCWD depends strongly on the initial conditions of mass and angular momentum as well as on chemical composition, and evolution of the moment of inertia (see Fig. B.16 and Sec. B.2.8 for details). It is clear that the assumption of fixed moment of inertia  $I \sim 10^{49}$  g cm<sup>2</sup>, leads to a spin-down time scale depending only on the magnetic field strength. A detailed computation will lead to a strong dependence on the mass of the SCWD; resulting in a two-parameter family of delayed times  $\tau_B(M, B)$ . Detailed calculations of the lifetime of SCWDs braking-down due to magnetic dipole radiation are then needed to shed light on this important matter. Theoretical work along these lines is currently in progress and the results will be presented in a forthcoming publication.

Massive fast rotating and highly magnetized WDs have been proposed as an alternative scenario of Soft Gamma Ray Repeaters (SGRs) and Anomalous X-ray Pulsars (AXPs); see Malheiro et al. (2012) for details. Within such scenario, the range of minimum rotation periods of massive WDs found in this

work,  $0.3 \lesssim P_{min} \lesssim 2.2$  seconds, depending on the nuclear composition (see Table B.8), implies the rotational stability of SGRs and AXPs, which possess observed rotation periods  $2 \lesssim P \lesssim 12$  seconds. The relatively long minimum period of  $^{56}\text{Fe}$  RWDs  $\sim 2.2$  seconds, implies that RWDs describing SGRs and AXPs have to be composed of nuclear compositions lighter than  $^{56}\text{Fe}$ , e.g.  $^{12}\text{C}$  or  $^{16}\text{O}$ .

### B.2.10. Concluding remarks

We have calculated the properties of uniformly RWDs within the framework of GR using the Hartle formalism and our new EOS for cold WD matter based on the relativistic Feynman-Metropolis-Teller treatment (Rotondo et al., 2011c), which generalizes previous approaches including the EOS of Salpeter (1961a). A detailed comparison with RWDs described by the Chandrasekhar and the Salpeter EOS has been performed.

We constructed the region of stability of RWDs taking into account the mass-shedding limit, secular axisymmetric instability, inverse  $\beta$ -decay, and pycnonuclear reaction lifetimes. The latter have been computed using the updated theoretical models of Gasques et al. (2005); Yakovlev et al. (2006). We found that the minimum rotation periods for  $^4\text{He}$ ,  $^{12}\text{C}$ ,  $^{16}\text{O}$ , and  $^{56}\text{Fe}$  RWDs are  $\sim 0.3$ ,  $0.5$ ,  $0.7$  and  $2.2$  seconds, respectively (see Table B.8). For  $^{12}\text{C}$  WDs, the minimum period  $0.5$  seconds needs to be compared with the values  $P_{min}^{pyc} = 0.75$  and  $0.95$  seconds, obtained assuming as critical density the threshold for pycnonuclear reactions for lifetimes  $\tau_{pyc}^{C+C} = 0.1$  Myr and  $10$  Gyr, respectively. For the same chemical compositions, the maximum masses are  $\sim 1.500$ ,  $1.474$ ,  $1.467$ ,  $1.202 M_{\odot}$  (see Table B.7). These results and additional properties of RWDs can be found in Table B.6.

We have presented a new instability boundary of general relativistic SCWDs, over which they become axisymmetrically unstable. We have expressed the range of masses and rotation periods where this occurs through a fitting formula given by Eq. (B.2.6). A comparison with Newtonian RWDs in App. B.2.11 show to the conclusion that this new boundary of instability for uniformly rotating WDs is a general relativistic effect.

We showed that, by loosing angular momentum, sub-Chandrasekhar RWDs can experience both spin-up and spin-down epochs while, SCWDs, can only spin-up. These results are particularly important for the evolution of WDs whose masses approach, either from above or from below, the maximum non-rotating mass. The knowledge of the actual values of the mass, radii, and moment of inertia of massive RWDs are relevant for the computation of delay collapse times in the models of type Ia SN explosions. A careful analysis of all the possible instability boundaries as the one presented here have to be taken into account during the evolution of the WD at pre-SN stages.

We have indicated specific astrophysical systems where the results of this

work are relevant; for instance the long rotation periods of observed massive magnetic WDs; the delayed collapse of SCWDs as progenitors of type Ia SNe; and the alternative scenario for SGRs and AXPs based on massive RWDs.

### B.2.11. Supplementary information

#### The Hartle-Thorne solution and equatorial circular orbits

The HT metric given by Eq. (B.2.1) can be written in an analytic closed-form in the exterior vacuum case in terms of the total mass  $M$ , angular momentum  $J$ , and quadrupole moment  $Q$  of the rotating star. The angular velocity of local inertial frames  $\omega(r)$ , proportional to  $\Omega$ , and the functions  $h_0, h_2, m_0, m_2, k_2$ , proportional to  $\Omega^2$ , are derived from the Einstein equations (see Hartle, 1967; Hartle and Thorne, 1968, for details). Thus, the metric can be written as

$$\begin{aligned}
 ds^2 = & \left(1 - \frac{2M}{r}\right) \left[1 + 2k_1 P_2(\cos \theta) + 2 \left(1 - \frac{2M}{r}\right)^{-1} \frac{J^2}{r^4} (2 \cos^2 \theta - 1)\right] dt^2 \\
 & + \frac{4J}{r} \sin^2 \theta dt d\phi \\
 & - \left(1 - \frac{2M}{r}\right)^{-1} \left[1 - 2 \left(k_1 - \frac{6J^2}{r^4}\right) P_2(\cos \theta) - 2 \left(1 - \frac{2M}{r}\right)^{-1} \frac{J^2}{r^4}\right] dr^2 \\
 & - r^2 [1 - 2k_2 P_2(\cos \theta)] (d\theta^2 + \sin^2 \theta d\phi^2)
 \end{aligned} \tag{B.2.13}$$

where

$$\begin{aligned}
 k_1 &= \frac{J^2}{Mr^3} \left(1 + \frac{M}{r}\right) + \frac{5Q - J^2/M}{8M^3} Q_2^2 \left(\frac{r}{M} - 1\right), \\
 k_2 &= k_1 + \frac{J^2}{r^4} + \frac{5Q - J^2/M}{4M^2 r} \left(1 - \frac{2M}{r}\right)^{-1/2} Q_2^1 \left(\frac{r}{M} - 1\right),
 \end{aligned}$$

and

$$\begin{aligned}
 Q_2^1(x) &= (x^2 - 1)^{1/2} \left[ \frac{3x}{2} \ln \frac{x+1}{x-1} - \frac{3x^2 - 2}{x^2 - 1} \right], \\
 Q_2^2(x) &= (x^2 - 1) \left[ \frac{3}{2} \ln \frac{x+1}{x-1} - \frac{3x^3 - 5x}{(x^2 - 1)^2} \right],
 \end{aligned}$$

are the associated Legendre functions of the second kind, with  $x = r/M - 1$ , and  $P_2(\cos \theta) = (1/2)(3 \cos^2 \theta - 1)$  is the Legendre polynomial. The constants  $M, J$  and  $Q$  the total mass, angular momentum and mass quadrupole moment of the rotating object, respectively. This form of the metric corrects some misprints of the original paper by Hartle and Thorne (1968). The precise numerical values of  $M, J$  and  $Q$  are calculated from the matching procedure

of the exterior and interior metrics at the surface of the star.

The total mass of a rotating configuration is defined as  $M = M^{J \neq 0} = M^{J=0} + \delta M$ , where  $M^{J=0}$  is the mass of non-rotating configuration and  $\delta M$  is the change in mass of the rotating from the non-rotating configuration with the same central density. It should be stressed that in the terms involving  $J^2$  and  $Q$  the total mass  $M$  can be substituted by  $M^{J=0}$  since  $\delta M$  is already a second order term in the angular velocity.

The four-velocity  $u$  of a test particle on a circular orbit in equatorial plane of axisymmetric stationary spacetime can be parametrized by the constant angular velocity  $\Omega$  with respect to an observer at infinity

$$u = \Gamma[\partial_t + \Omega\partial_\phi], \quad (\text{B.2.14})$$

where  $\Gamma$  is a normalization factor which assures that  $u^\alpha u_\alpha = 1$ . From normalization and geodesics conditions we obtain the following expressions for  $\Gamma$  and  $\Omega = u^\phi/u^t$

$$\Gamma = \pm(g_{tt} + 2\Omega g_{t\phi} + \Omega^2 g_{\phi\phi})^{-1/2}, \quad (\text{B.2.15})$$

$$g_{tt,r} + 2\Omega g_{t\phi,r} + \Omega^2 g_{\phi\phi,r} = 0, \quad (\text{B.2.16})$$

hence,  $\Omega$ , the solution of (B.2.15), is given by

$$\Omega_{\pm orb}(r) = \frac{u^\phi}{u^t} = \frac{-g_{t\phi,r} \pm \sqrt{(g_{t\phi,r})^2 - g_{tt,r}g_{\phi\phi,r}}}{g_{\phi\phi,r}}, \quad (\text{B.2.17})$$

where  $(+/-)$  stands for co-rotating/counter-rotating orbits,  $u^\phi$  and  $u^t$  are the angular and time components of the four-velocity, and a colon stands for partial derivative with respect to the corresponding coordinate. In our case one needs to consider only co-rotating orbits (omitting the plus sign in  $\Omega_{+orb}(r) = \Omega_{orb}(r)$ ) to determine the mass shedding (Keplerian) angular velocity on the surface of the WD. For the Hartle-Thorne external solution Eq. (B.2.13) we have

$$\Omega_{orb}(r) = \sqrt{\frac{M}{r^3}} \left[ 1 - jF_1(r) + j^2F_2(r) + qF_3(r) \right], \quad (\text{B.2.18})$$

where  $j = J/M^2$  and  $q = Q/M^3$  are the dimensionless angular momentum

and quadrupole moment,

$$\begin{aligned}
 F_1 &= \left(\frac{M}{r}\right)^{3/2}, \\
 F_2 &= \frac{48M^7 - 80M^6r + 4M^5r^2 - 18M^4r^3 + 40M^3r^4 + 10M^2r^5 + 15Mr^6 - 15r^7}{16M^2r^4(r - 2M)} \\
 &\quad + F, \\
 F_3 &= \frac{6M^4 - 8M^3r - 2M^2r^2 - 3Mr^3 + 3r^4}{16M^2r(r - 2M)/5} - F, \\
 F &= \frac{15(r^3 - 2M^3)}{32M^3} \ln \frac{r}{r - 2M}.
 \end{aligned}$$

The mass shedding limiting angular velocity of a rotating star is the Keplerian angular velocity evaluated at the equator ( $r = R_{eq}$ ), i.e.

$$\Omega_K^{J \neq 0} = \Omega_{orb}(r = R_{eq}). \quad (\text{B.2.19})$$

In the static case i.e. when  $j = 0$  hence  $q = 0$  and  $\delta M = 0$  we have the well-known Schwarzschild solution and the orbital angular velocity for a test particle  $\Omega_{ms}^{J=0}$  on the surface ( $r = R$ ) of the WD is given by

$$\Omega_K^{J=0} = \sqrt{\frac{MJ=0}{R_{MJ=0}^3}}. \quad (\text{B.2.20})$$

We turn now to the weak field limit. Let us estimate the values of  $j$  and  $q$  recovering physical units with  $c$  and  $G$ . The dimensionless angular momentum is

$$j = \frac{cJ}{GM^2} = \frac{c}{G} \frac{\alpha MR^2 \Omega}{M^2} = \alpha \left(\frac{\Omega R}{c}\right) \left(\frac{GM}{c^2 R}\right)^{-1}, \quad (\text{B.2.21})$$

where we have used the fact that  $J = I\Omega$ , with  $I = \alpha MR^2$ , and  $\alpha \sim 0.1$  from our numerical integrations. For massive and fast rotating WDs we have  $(\Omega R)/c \sim 10^{-2}$  and  $(GM)/(c^2 R) \sim 10^{-3}$ , so  $j \sim 1$ .

The dimensionless quadrupole moment  $q$  is

$$q = \frac{c^4}{G^2} \frac{Q}{M^3} = \frac{c^4}{G^2} \frac{\beta MR^2}{M^3} = \beta \left(\frac{GM}{c^2 R}\right)^{-2}, \quad (\text{B.2.22})$$

where we have expressed the mass quadrupole moment  $Q$  in terms of mass and radius of the WD,  $Q = \beta MR^2$ , where  $\beta \sim 10^{-2}$ , so we have  $q \sim 10^4$ .

The large values of  $j$  and  $q$  might arise some suspicion on the products  $jF_1$ ,  $j^2F_2$  and  $qF_3$  as real correction factors in Eq. (B.2.18). It is easy to check this in the weak field limit  $M/r \ll 1$ , where the functions  $F_i$  can be expanded as a

power-series

$$\begin{aligned}
 F_1 &= \left(\frac{M}{r}\right)^{3/2}, \\
 F_2 &\approx \frac{1}{2}\left(\frac{M}{r}\right)^3 - \frac{117}{28}\left(\frac{M}{r}\right)^4 - 6\left(\frac{M}{r}\right)^5 - \dots, \\
 F_3 &\approx \frac{3}{4}\left(\frac{M}{r}\right)^2 + \frac{5}{4}\left(\frac{M}{r}\right)^3 + \frac{75}{28}\left(\frac{M}{r}\right)^4 + 6\left(\frac{M}{r}\right)^5 + \dots
 \end{aligned}$$

so evaluating at  $r = R$

$$jF_1 = \alpha \left(\frac{\Omega R}{c}\right) \left(\frac{GM}{c^2 R}\right)^{1/2}, \quad j^2 F_2 = \frac{\alpha}{2} \left(\frac{\Omega R}{c}\right) \left(\frac{GM}{c^2 R}\right)^2, \quad (\text{B.2.23})$$

so we finally have  $jF_1 \sim 10^{-9/2}$ ,  $j^2 F_2 \sim 10^{-9}$ , and  $qF_3 \sim 10^{-2}$ . We can therefore see that the products are indeed correction factors and, in addition, that effect due to the quadrupole deformation is larger than the frame-dragging effect.

### Pycnonuclear fusion reaction rates

The theoretical framework for the determination of the pycnonuclear reaction rates was developed by Salpeter and van Horn (1969). The number of reactions per unit volume per unit time can be written as

$$R_{pyc} = Z^4 A \rho S(E_p) 3.90 \times 10^{46} \lambda^{7/4} \exp(-2.638/\sqrt{\lambda}) \text{ cm}^{-3} \text{ s}^{-1} \quad (\text{B.2.24})$$

$$\lambda = \frac{1}{Z^2 A^{4/3}} \left( \frac{\rho}{1.3574 \times 10^{11} \text{ g cm}^{-3}} \right)^{1/3}, \quad (\text{B.2.25})$$

where  $S$  are astrophysical factors in units of Mev barns (1 barn =  $10^{-24} \text{ cm}^2$ ) that have to be evaluated at the energy  $E_p$  given by Eq. (B.2.4).

For the  $S$ -factors we adopt the results of Gasques et al. (2005) calculated with the NL2 nuclear model parameterization. For center of mass energies  $E \geq 19.8 \text{ MeV}$ , the  $S$ -factors can be fitted by

$$S(E) = 5.15 \times 10^{16} \exp \left[ -0.428E - \frac{3E^{0.308}}{1 + e^{0.613(8-E)}} \right] \text{ MeV barn}, \quad (\text{B.2.26})$$

which is appropriate for the ranges of the zero-point energies at high densities. For instance,  $^{12}\text{C}$  nuclei at  $\rho = 10^{10} \text{ g cm}^{-3}$  have a zero-point oscillation energy  $E_p \sim 34 \text{ keV}$ .

All the nuclei ( $Z, A$ ) at a given density  $\rho$  will fuse in a time  $\tau_{pyc}$  given by

$$\tau_{pyc} = \frac{n_N}{R_{pyc}} = \frac{\rho}{AM_u R_{pyc}}, \quad (\text{B.2.27})$$

where  $n_N = \rho / (AM_u)$  is the ion-density. Gasques et al. (2005) estimated that the  $S$ -factors (B.2.26) are uncertain within a factor  $\sim 3.5$ ; it is clear from the above equation that for a given lifetime  $\tau_{pyc}$  such uncertainties reflect also in the determination of the density threshold.

### Comparison with the Newtonian treatment and other works

We have constructed solutions of the Newtonian equilibrium equations for RWDs accurate up to order  $\Omega^2$ , following the procedure of Hartle (1967). In Fig. B.17 (left panel) we compare these Newtonian configurations with general relativistic RWDs for the Chandrasekhar EOS with  $\mu = 2$ . We can see clearly the differences between the two mass-density relations toward the high density region, as expected. A most remarkable difference is the existence of axisymmetric instability boundary in the general relativistic case, absent in its Newtonian counterpart.

Up to our knowledge, the only previous work on RWDs within GR is the one of Arutyunyan et al. (1971). A method to compute RWDs configurations accurate up to second order in  $\Omega$  was developed by two of the authors (see Sedrakyan and Chubaryan, 1968, for details), independently of the work of Hartle (1967). In (Arutyunyan et al., 1971), RWDs were computed for the Chandrasekhar EOS with  $\mu = 2$ .

In Fig. B.17 (right panel) we show the mass-central density relation obtained with their method with the ones constructed in this work for the same EOS. We note here that the results are different even at the level of static configurations, and since the methods are based on construction of rotating configurations from seed static ones, those differences extrapolate to the corresponding rotating objects. This fact is to be added to the possible additional difference arising from the different way of approaching the order  $\Omega^2$  in the approximation scheme. The differences between the two equilibrium configurations are evident.

Turning now to the problem of the maximum mass of a RWD, in Table B.9 we present the previous results obtained in Newtonian, Post-Newtonian approach and GR by several authors. Depending on their method, approach, treatment, theory and numerical code the authors showed different results. These maximum mass of RWDs are to be compared with the ones found in this work and presented in Table B.7 for the Chandrasekhar  $\mu = 2$ , Salpeter, and RFMT EOS.

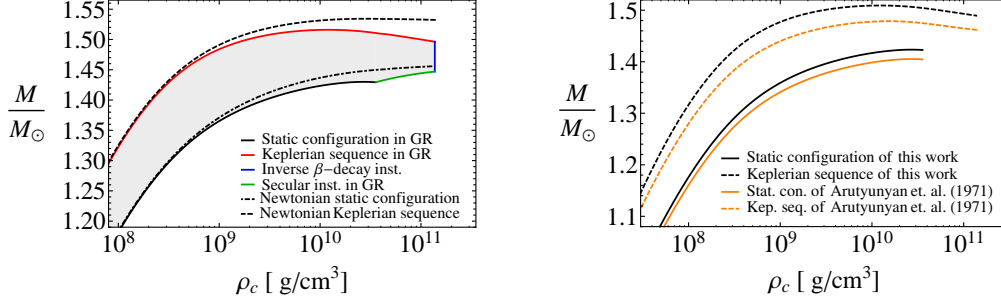


**Figure B.17.:** Left panel: Mass versus central density of Newtonian and general relativistic WDs for the Chandrasekhar EOS with  $\mu = 2$ . Both the non-rotating case and the Keplerian sequence are shown. We have stopped the density, just for sake of comparison, at the critical density for the onset of inverse  $\beta$ -decay of  ${}^4\text{He}$   $\rho = 1.39 \times 10^{11} \text{ g cm}^{-3}$ . Right panel: Mass versus central density relation for general relativistic WDs for the Chandrasekhar EOS with  $\mu = 2$  for the static and the Keplerian sequence in this work and the one of Arutyunyan et al. (1971).

Treatment/EOS	$M_{max}^{\neq 0}/M_\odot$	References
Newtonian/Chandrasekhar $\mu = 2$	1.474	Anand (1965)
Newtonian/Polytrope $n = 3$	1.487	Roxburgh (1965)
Post-Newtonian/Chandrasekhar $\mu = 2$	1.482	Roxburgh and Durney (1966)
GR/Chandrasekhar $\mu = 2$	1.478	Arutyunyan et al. (1971)

**Table B.9.:** Maximum rotating mass of WDs in literature.

### Accuracy of the Hartle's approach

In his classic work, Hartle (1967) described the slow rotation regime by requesting that fractional changes in pressure, energy density, and gravitational field due to the rotation of the star are all much smaller with respect to a non-rotating star with the same central density. From a dimensional analysis, such a condition implies

$$\Omega^2 \ll \left(\frac{c}{R}\right)^2 \frac{GM^{J=0}}{c^2 R}, \quad (\text{B.2.28})$$

where  $M^{J=0}$  is the mass of the unperturbed configuration and  $R$  its radius. The expression on the right is the only multiplicative combination of  $M$ ,  $R$ ,  $G$ , and  $c$ , and in the Newtonian limit coincides with the critical Keplerian angular velocity  $\Omega_K^{J=0}$  given by Eq. (B.2.20). For unperturbed configurations with  $(GM)/(c^2 R) < 1$ , the condition (B.2.28) implies  $\Omega R/c \ll 1$ . Namely, every particle must move at non-relativistic velocities if the perturbation to the original geometry have to be small in terms of percentage. Eq. (B.2.28) can be also written as

$$\Omega \ll \Omega_K^{J=0}, \quad (\text{B.2.29})$$

which is the reason why it is often believed that the slow rotation approximation is not suitable for the description of stars rotating at their mass-shedding value.

Let us discuss this point more carefully. It is clear that the request that the contribution of rotation to pressure, energy density, and gravitational field to be small can be summarized in a single expression, Eq. (B.2.28), since all of them are quantitatively given by the ratio between the rotational and the gravitational energy of the star. The rotational energy is  $T \sim MR^2\Omega^2$  and the gravitational energy is  $|W| \sim GM^2/R = (GM/c^2 R)Mc^2$ , hence the condition  $T/|W| \ll 1$  leads to Eq. (B.2.28) or (B.2.29). Now we will discuss the above condition for realistic values of the rotational and gravitational energy of a rotating star, abandoning the assumption of either fiducial or order of magnitude calculations. We show below that the actual limiting angular velocity on the right-hand-side of the condition (B.2.29) has to be higher than the Keplerian value.

We can write the gravitational binding energy of the star as  $|W| = \gamma GM^2/R$  and the rotational kinetic energy as  $T = (1/2)I\Omega^2 = (1/2)\alpha MR^2\Omega^2$ , where the constants  $\gamma$  and  $\alpha$  are structure constants that depends on the density and pressure distribution inside the star. According to the slow rotation approximation,  $T/|W| \ll 1$ , namely

$$\frac{T}{|W|} = \frac{\alpha MR^2\Omega^2/2}{\gamma GM^2/R} = \left(\frac{\alpha}{2\gamma}\right) \left(\frac{GM}{R^3}\right)^{-1} \Omega^2 = \left(\frac{\alpha}{2\gamma}\right) \left(\frac{\Omega}{\Omega_K^{J=0}}\right)^2 \ll 1, \quad (\text{B.2.30})$$

which can be rewritten in analogous form to Eq. B.2.29 as

$$\Omega \ll \sqrt{\frac{2\gamma}{\alpha}} \Omega_K^{J=0}. \quad (\text{B.2.31})$$

Now we check that the ratio of the structural constants is larger than unity. Let us first consider the simplest example of a constant density sphere. In this case  $\alpha = 2/5$  and  $\gamma = 3/5$ , so  $\sqrt{2\gamma/\alpha} \approx 1.73$ , and the condition (B.2.31) is  $\Omega \ll 1.73\Omega_K^{J=0}$ . If we consider now a more realistic density profile, for instance, a polytrope of index  $n = 3$ , we have (see e.g. Shapiro and Teukolsky, 1983a)

$$|W| = \frac{3}{5-n} \frac{GM^2}{R} = \frac{3}{2} \frac{GM^2}{R}, \quad T = \frac{1}{2} I \Omega^2 = \frac{1}{2} \frac{2}{3} M \langle r^2 \rangle \Omega^2 \quad (\text{B.2.32})$$

where  $\langle r^2 \rangle = 0.11303R^2$ . Therefore we have in this case  $\gamma = 3/2$  and  $\alpha = 0.075$ , and so Eq. (B.2.31) becomes  $\Omega \ll 6.32\Omega_K^{J=0}$ . This is not surprising since  $T/|W| \rightarrow 0.025$  when  $\Omega \rightarrow \Omega_K^{J=0}$ .

The above analysis has been done assuming spherical symmetry. When deviations from the spherical shape are taken into account, the ratio  $T/|W|$  turn to be even smaller than the previous estimates based on spherical polytropes. Since the equatorial radius satisfies  $R_{eq} > R$ , at mass-shedding we will have  $\Omega < \Omega_K^{J=0}$ . In fact, in the Roche model the mass-shedding angular velocity is  $\Omega_K^{J \neq 0} = (2/3)^{3/2} \Omega_K^{J=0} \approx 0.544\Omega_K^{J=0}$ , corresponding to a rotational to gravitational energy ratio  $T/|W| \approx 0.0074$  (see e.g. Shapiro and Teukolsky, 1983a).

In our RWDs we have obtained that the mass-shedding angular velocity satisfies  $\Omega_K^{J \neq 0} \approx 0.75\Omega_K^{J=0}$  at any density; see Eq. (B.2.12). Accordingly to this, we show in the left panel of Fig. B.18 the ratio  $T/|W|$  for RWDs as a function of the central density for the Keplerian sequence. For an increasing central density  $T/|W|$  decreases. On the right panel we have plotted the eccentricity versus the central density. For increasing central density the eccentricity decreases, so RWDs become less oblate at higher densities.

Now we turn to evaluate more specifically the deviations from the spherical symmetry. The expansion of the radial coordinate of a rotating configuration  $r(R, \theta)$  in powers of the angular velocity is written as (Hartle, 1967)

$$r = R + \zeta(R, \theta) + O(\Omega^4), \quad (\text{B.2.33})$$

where  $\zeta$  is the difference in the radial coordinate,  $r$ , between a point located at the polar angle  $\theta$  on the surface of constant density  $\rho(R)$  in the rotating configuration, and the point located at the same polar angle on the same constant density surface in the non-rotating configuration. In the slow ro-

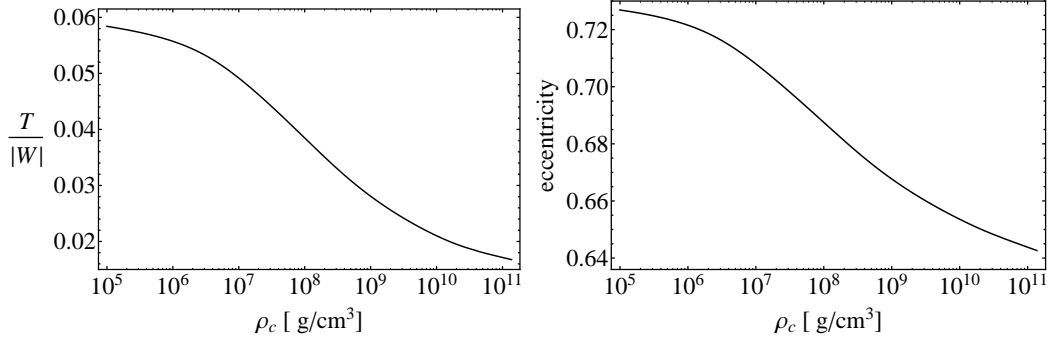


**Figure B.18.:** Left panel: rotational to gravitational energy ratio versus the central density for maximally rotating RWDs, calculated with the Chandrasekhar EOS  $\mu = 2$ . Right panel: the eccentricity versus the central density for the same sequence of RWDs.

tation regime, the fractional displacement of the surfaces of constant density due to the rotation have to be small, namely  $\xi(R, \theta)/R \ll 1$ , where  $\xi(R, \theta) = \xi_0(R) + \xi_2(R)P_2(\cos \theta)$  and  $\xi_0(R)$  and  $\xi_2(R)$  are function of  $R$  proportional to  $\Omega^2$ . On the right panel of Fig. B.19 the difference in the radial coordinate over static radius versus the central density is shown. Here we see the same tendency as in the case of the eccentricity, that these differences are decreasing with an increasing central density. On the left panel the rotation parameter  $\Omega R/c$  versus the central density is shown. Here, with an increasing central density the rotation parameter increases. Thus, for higher densities the system becomes less oblate, smaller in size with a larger rotation parameter i.e. higher angular velocity.

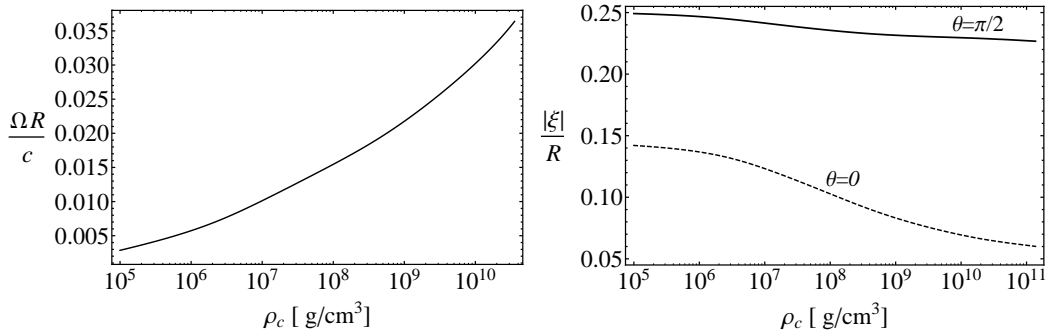


**Figure B.19.:** Left panel: the rotation parameter normalized to the speed of light versus the central density. Right panel: the difference in the radial coordinate over the static radius versus the central density. The solid curve corresponds to the difference between equatorial ( $\theta = \pi/2$ ) and static radii and the dashed curve corresponds to the difference between polar ( $\theta = 0$ ) and static radii.

In order to estimate the accuracy of the slow rotation approximation for RWDs, based on the above results, it is useful to compare all the above numbers with the known results for NSs. For instance, we notice that in NSs  $\Omega R/c \sim 10^{-1}$ ,  $\xi(R,0)/R \sim 10^{-2}$  and  $\xi(R, \pi/2)/R \sim 10^{-1}$  (see e.g. Berti et al., 2005), to be compared with the corresponding values of RWDs shown in Fig. B.19,  $\Omega R/c \lesssim 10^{-2}$ ,  $\xi(R,0)/R \sim 10^{-2}$  and  $\xi(R, \pi/2)/R \sim 10^{-1}$ . Weber and Glendenning (1992) calculate the accuracy of the Hartle's second order approximation and found that the mass of maximally rotating NSs is accurate within an error  $\lesssim 4\%$ ; Benhar et al. (2005a) found that the inclusion of third order expansion  $\Omega^3$  improved the mass-shedding limit numerical values in less than 1% for NSs obeying different EOS. On the other-hand, it is known that the ratio  $T/|W|$  in the case of NSs is as large as  $\sim 0.1$  in the Keplerian sequence (see e.g. Tables 1–5 of Berti and Stergioulas (2004)). Since RWDs have  $T/|W|$  and  $\Omega R/c$  smaller than NSs, and  $\delta R/R = \xi/R$  at least of the same order (see left panel of Fig. B.18), we expect that the description of the structure of RWDs up to the mass-shedding limit within the Hartle's approach to have at least the same accuracy as in the case of NSs.

## B.3. SGRs and AXPs as rotation powered massive white dwarfs

### B.3.1. Introduction

Soft Gamma Ray Repeaters (SGRs) and Anomalous X-ray Pulsars (AXPs) are a class of compact objects that show interesting observational properties (see e.g. Mereghetti, 2008a): rotational periods in the range  $P \sim (2-12)$  s, a narrow range with respect to the wide range of ordinary pulsars  $P \sim (0.001-10)$  s; spin-down rates  $\dot{P} \sim (10^{-13}-10^{-10})$ , larger than ordinary pulsars  $\dot{P} \sim 10^{-15}$ ; strong outburst of energies  $\sim (10^{41}-10^{43})$  erg, and for the case of SGRs, giant flares of even large energies  $\sim (10^{44}-10^{47})$  erg, not observed in ordinary pulsars.

The recent observation of SGR 0418+5729 with a rotational period of  $P = 9.08$  s, an upper limit of the first time derivative of the rotational period  $\dot{P} < 6.0 \times 10^{-15}$  (Rea et al., 2010), and an X-ray luminosity of  $L_X = 6.2 \times 10^{31}$  erg/s promises to be an authentic Rosetta Stone, a powerful discriminant for alternative models of SGRs and AXPs.

If described as a neutron star of  $M = 1.4M_\odot$ ,  $R = 10$  km and a moment of inertia  $I \approx 10^{45}$  g cm<sup>2</sup>, which we adopt hereafter as fiducial parameters, the loss of rotational energy of the neutron star

$$\dot{E}_{\text{rot}}^{\text{NS}} = -4\pi^2 I \frac{\dot{P}}{P^3} = -3.95 \times 10^{46} \frac{\dot{P}}{P^3} \text{ erg/s}, \quad (\text{B.3.1})$$

associated to its spin-down rate  $\dot{P}$ , cannot explain the X-ray luminosity of SGR 0418+5729, i.e.  $\dot{E}_{\text{rot}}^{\text{NS}} < L_X$ , excluding the possibility of identifying this source as an ordinary spin-down powered pulsar.

The magnetar model of SGRs and AXPs, based on a neutron star of fiducial parameters, needs a magnetic field larger than the critical field for vacuum polarization  $B_c = m_e^2 c^3 / (e\hbar) = 4.4 \times 10^{13}$  G in order to explain the observed X-ray luminosity in terms of the release of magnetic energy (see Duncan and Thompson, 1992; Thompson and Duncan, 1995, for details). However, the inferred upper limit of the surface magnetic field of SGR 0418+5729  $B < 7.5 \times 10^{12}$  G describing it as a neutron star (see Rea et al., 2010, for details), is well below the critical field challenging the power mechanism based on magnetic field decay purported in the magnetar scenario.

We show that the observed upper limit on the spin-down rate of SGR 0418+5729 is, instead, perfectly in line with a model based on a massive fast rotating highly magnetized white dwarf (see e.g. Paczynski, 1990) of mass  $M = 1.4M_\odot$ , radius  $R = 10^3$  km, and moment of inertia  $I \approx 10^{49}$  g cm<sup>2</sup>, which we adopt hereafter as fiducial white dwarf parameters. Such a configuration leads for SGR 0418+5729 to a magnetic field  $B < 7.5 \times 10^8$  G. The X-ray luminosity can then be expressed as originating from the loss of rota-

tional energy of the white dwarf leading to a theoretical prediction for the first time derivative of the rotational period

$$\frac{L_X P^3}{4\pi^2 I} \leq \dot{P}_{\text{SGR0418+5729}} < 6.0 \times 10^{-15}, \quad (\text{B.3.2})$$

where the lower limit is established by assuming that the observed X-ray luminosity of SGR 0418+5729 coincides with the rotational energy loss of the white dwarf. For this specific source, the lower limit of  $\dot{P}$  given by Eq. (B.3.2) is  $\dot{P}_{\text{SGR0418+5729}} \geq 1.18 \times 10^{-16}$ . This prediction is left to be verified by the dedicated scientific missions.

The assumption of massive fast rotating highly magnetized white dwarfs appears to be very appropriate since their observation has been solidly confirmed in the last years thanks to observational campaigns carried out by the X-ray Japanese satellite Suzaku (see e.g. Terada et al., 2008c; Terada, 2008; Terada et al., 2008d,b,a). The magnetic fields observed in white dwarfs are larger than  $10^6$  G all the way up to  $10^9$  G (see e.g. Angel et al., 1981; Ferrario et al., 1997; Nalezyty and Madej, 2004; Ferrario and Wickramasinghe, 2005; Terada et al., 2008c; Külebi et al., 2009). These observed massive fast rotating highly magnetized white dwarfs share common properties with SGRs/AXPs. The specific comparison between SGR 0418+5729 and the white dwarf AE Aquarii (Terada et al., 2008c) is given in Sec. B.3.4.

The aim of this article is to investigate the implications of the above considerations to all observed SGRs and AXPs. The article is organized as follows. In Sec. B.3.2 we summarize the main features of a model for SGRs and AXPs based on rotation powered white dwarfs while, in Sec. B.3.3, we recall the magnetar model. In Sec. B.3.4 we present the observations of massive fast rotating highly magnetized white dwarfs. The constraints on the rotation rate imposed by the rotational instabilities of fast rotating white dwarfs are discussed in Sec. B.3.5 and in Sec. B.3.6 we analyze the glitch-outburst connection in SGRs and AXPs. The magnetospheric emission from the white dwarf is discussed in Sec. B.3.7 and the possible connection between SGRs and AXPs with supernova remnants is presented in Sec. B.3.8. In Sec. B.3.9 we address the problem of fiducial parameters of both white dwarfs and neutron stars and, in Sec. B.3.10, we summarize conclusions and remarks.

### B.3.2. SGRs and AXPs within the white dwarf model

We first recall the pioneering works of Morini et al. (1988) and Paczynski (1990) on 1E 2259+586. This source is pulsating in the X-rays with a period  $P = 6.98$  s (Fahlman and Gregory, 1981), a spin-down rate of  $\dot{P} = 4.8 \times 10^{-13}$  (Davies et al., 1990) and X-ray luminosity  $L_X = 1.8 \times 10^{34}$  erg/s (Gregory and Fahlman, 1980; Hughes et al., 1981; Morini et al., 1988). Specially relevant in the case of 1E 2259+586 is also its position within the supernova remnant

G109.1-1.0 with age estimated  $t - t_0 = (12-17)$  kyr (Gregory and Fahlman, 1980; Hughes et al., 1981).

Paczynski developed for 1E 2259+586 a model based on a massive fast rotating highly magnetized white dwarf. The upper limit on the magnetic field (see e.g. Ferrari and Ruffini, 1969) obtained by requesting that the rotational energy loss due to the dipole field be smaller than the electromagnetic emission of the dipole, is given by

$$B = \left( \frac{3c^3}{8\pi^2} \frac{I}{R^6} P\dot{P} \right)^{1/2}, \quad (\text{B.3.3})$$

where  $P$  and  $\dot{P}$  are observed properties and the moment of inertia  $I$  and the radius  $R$  of the object are model dependent properties. For the aforementioned fiducial parameters of a fast rotating magnetized white dwarf, Eq. (B.3.3) becomes

$$B = 3.2 \times 10^{15} (P\dot{P})^{1/2} \text{ G}. \quad (\text{B.3.4})$$

The loss of rotational energy within this model is given by

$$\dot{E}_{\text{rot}}^{\text{WD}} = -4\pi^2 I \frac{\dot{P}}{P^3} = -3.95 \times 10^{50} \frac{\dot{P}}{P^3} \text{ erg/s}, \quad (\text{B.3.5})$$

which amply justifies the steady X-ray emission of 1E 2259+586 (see Table B.12).

A further development for the source 1E 2259+586, came from Usov (1994), who introduced the possibility in a white dwarf close to the critical mass limit, to observe sudden changes in the period of rotation, namely glitches.

When the rotation of the white dwarf slows down, centrifugal forces of the core decrease and gravity pulls it to a less oblate shape thereby stressing it. The release of such stresses leads to a sudden decrease of moment of inertia and correspondingly, by conservation of angular momentum

$$J = I\Omega = (I + \Delta I)(\Omega + \Delta\Omega) = \text{constant}, \quad (\text{B.3.6})$$

to a shortening of the rotational period

$$\frac{\Delta I}{I} = \frac{\Delta P}{P} = -\frac{\Delta\Omega}{\Omega}, \quad (\text{B.3.7})$$

leading to a gain of rotational energy in the spin-up process of the glitch

$$\Delta E_{\text{rot}}^{\text{WD}} = -\frac{2\pi^2 I \Delta P}{P^2} \frac{\Delta P}{P} = -1.98 \times 10^{50} \frac{\Delta P}{P^3} \text{ erg}, \quad (\text{B.3.8})$$

which is then released in the burst activity on the time scales from months to years (see e.g. Fig. B.20).

For the evolution of the period close to a glitch we follow the parameterization by Manchester and Taylor (1977). The angular velocity  $\Omega = 2\pi/P$ , since the glitch time  $t = t_g$ , until the complete or partial recovery, can be described as

$$\Omega = \Omega_0(t) + \Delta\Omega[1 - Q(1 - e^{-(t-t_g)/\tau_d})], \quad (\text{B.3.9})$$

where  $\Omega_0(t) = \Omega_0 + \dot{\Omega}(t - t_g)$  is the normal evolution of the frequency in absence of glitch, being  $\Omega_0$  the frequency prior to the glitch,  $\Delta\Omega = -2\pi\Delta P/P^2$  is the initial frequency jump, which can be decomposed in the persistent and decayed parts,  $\Delta\Omega_p$  and  $\Delta\Omega_d$  respectively,  $\tau_d$  is the timescale of the exponential decay of the frequency after the glitch and  $Q = \Delta\Omega_d/\Delta\Omega = 1 - \Delta\Omega_p/\Delta\Omega$  is the recovery fraction or ‘‘healing parameter’’. For full recovery we have  $Q = 1$ ,  $\Omega(t \gg \tau_d) = \Omega_0$ , and for zero recovery  $Q = 0$ ,  $\Omega(t \gg \tau_d) = \Omega_0(t) + \Delta\Omega$ . For simplicity we assume in the following and especially below in Sec. B.3.6, complete recovery  $Q = 1$ .

This mechanism in white dwarfs is similar, although simpler, than the one used to explain e.g. glitches in ordinary pulsars (see e.g. Baym and Pines, 1971; Shapiro and Teukolsky, 1983a). The essential difference is that neutron stars are composed by a superfluid core and a solid crust, being the latter the place where starquakes can originate leading to glitches. A two-component description is then needed, see e.g. Shapiro and Teukolsky (1983a). In the present case of a massive rotating white dwarf, such a two-component structure does not exist and the white dwarf behaves as a single solid system. What is important to stress is that the rotational energy released for  $Q \geq 1$  is largely sufficient for the explanation of the bursting phenomena, see Sec. B.3.6 for details.

The crystallization temperature of a white dwarf composed of nuclei ( $Z, A$ ) and mean density  $\bar{\rho}$  is given by (see e.g. Shapiro and Teukolsky, 1983a; Usov, 1994)

$$T_{\text{cry}} \simeq 2.28 \times 10^5 \frac{Z^2}{A^{1/3}} \left( \frac{\bar{\rho}}{10^6 \text{g/cm}^3} \right)^{1/3} \text{ K}. \quad (\text{B.3.10})$$

Thus, assuming an internal white dwarf temperature  $\sim 10^7$  K we find that the mean density for the crystallization of the white dwarf should be  $\sim 2.2 \times 10^7 \text{ g/cm}^3$  for  $^{12}\text{C}$ ,  $\sim 5.2 \times 10^6 \text{ g/cm}^3$  for  $^{16}\text{O}$  and  $\sim 1.25 \times 10^6 \text{ g/cm}^3$  for  $^{56}\text{Fe}$ . Very massive white dwarfs as the ones we are considering here have mean densities  $\sim 10^9 \text{ g/cm}^3$  and therefore a considerable fraction of their size should be in principle solid at these high temperatures (see also Althaus et al., 2005, 2007). It is worth to mention that, the phase separation of the constituents of CO white dwarfs, theoretically expected to occur in the crystallization process (see Garcia-Berro et al., 1988, for details), has been recently observationally confirmed solving the puzzle of the age discrepancy of the open cluster NGC 6791 (García-Berro et al., 2010a).

Under these physical conditions, starquakes leading to glitches in the white

dwarf may occur with a recurrence time (see e.g. Baym and Pines, 1971; Usov, 1994)

$$\delta t_q = \frac{2D^2}{B} \frac{|\Delta P|/P}{|\dot{E}_{\text{rot}}|}, \quad (\text{B.3.11})$$

where  $\dot{E}_{\text{rot}}$  is the loss of rotational energy (B.3.5),  $D = (3/25) GM_c^2/R_c$ ,  $B = 0.33 (4\pi/3) R_c^3 e^2 Z^2 [\bar{\rho}_c / (Am_p)]^{4/3}$ ,  $M_c$ ,  $R_c$  and  $\bar{\rho}_c$  are the mass, the radius and the mean density of the solid core, and  $m_p$  is the proton mass.

For the specific case of 1E 2259+586, Usov predicted the possible existence of changes of period  $\Delta P/P \approx -(1-3) \times 10^{-6}$  with a recurrence time between cracks  $\delta t_q \approx 7 \times 10^6 |\Delta P|/P \text{ yr} \approx$  a few times (1–10) yr. It is impressive that in 2002 indeed changes of the order of  $\Delta P/P \approx -4 \times 10^{-6}$  were observed in 1E 2259+586 (Kaspi et al., 2003; Woods et al., 2004) (see Fig. B.20 for details).

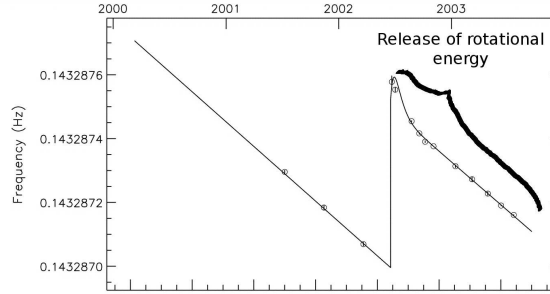


**Figure B.20.:** Timing analysis of the glitch of 1E 2259+586 on June 2002 (taken from Woods et al., 2004). The vertical axis shows the evolution of the spin frequency and the horizontal axis the date time. The observed fractional change of period is  $\Delta P/P = -\Delta\Omega/\Omega \sim -4 \times 10^{-6}$  and the observed energy released during the event is  $\sim 3 \times 10^{41}$  erg (Woods et al., 2004). Within the white dwarf model from such a  $\Delta P/P$  we obtain  $\Delta E_{\text{rot}}^{\text{WD}} \sim 1.7 \times 10^{43}$  erg as given by Eq. (B.3.8). We have modified the original figure (Woods et al., 2004) by indicating explicitly where the rotational energy is released after the spin-up, recovering its initial period prior to the glitch by the emission of a sequence of bursts on time scales from months to years (see e.g. Mereghetti, 2008a).

Our aim in the following is to show that this model can be also applied to the other SGRs and AXPs. Their entire energetics is explained by the rotational energy loss of fast rotating magnetized white dwarfs: 1) the X-ray luminosity is well below the rotational energy loss of the white dwarf (see Fig. B.21); 2) in all cases the large magnetic field is well below the critical field for vacuum polarization (see Fig. B.22 and Table B.12); 3) the energetics of all

the bursts can be simply related to the change of rotational energy implied by the observed change of rotational period (see Fig. B.23, Sec. B.3.5 and Table B.11).

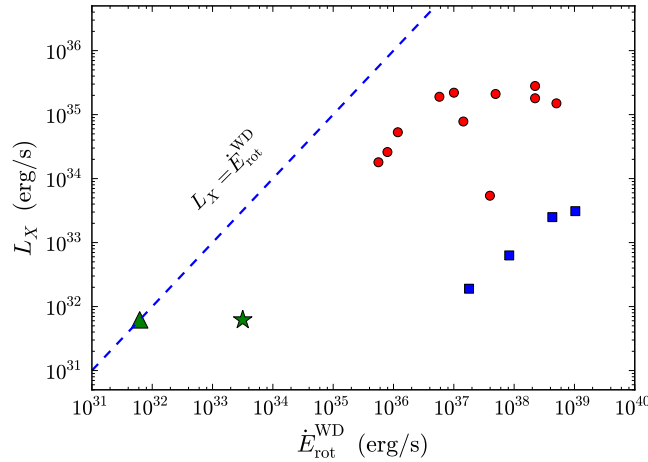


**Figure B.21.:** X-ray luminosity  $L_X$  versus the loss of rotational energy  $\dot{E}_{\text{rot}}$  describing SGRs and AXPs by rotation powered white dwarfs. The green star and the green triangle correspond to SGR 0418+5729 using respectively the upper and the lower limit of  $\dot{P}$  given by Eq. (B.3.2). The blue squares are the only four sources that satisfy  $L_X < \dot{E}_{\text{rot}}$  when described as neutron stars (see Fig. B.25 for details).

### B.3.3. SGRs and AXPs within the magnetar model

Let us turn to the alternative model commonly addressed as “magnetar” (see e.g. Duncan and Thompson, 1992; Thompson and Duncan, 1995) based on an ultramagnetized neutron star of  $M = 1.4M_{\odot}$  and  $R = 10$  km and then  $I \approx 10^{45}$  g cm<sup>2</sup> as the source of SGRs and AXPs. The limit of the magnetic field obtained from Eq. (B.3.3) becomes

$$B = 3.2 \times 10^{19} (P\dot{P})^{1/2} \text{ G}, \quad (\text{B.3.12})$$

which is four orders of magnitude larger than the surface magnetic field within the fast rotating magnetized white dwarf model (see Fig. B.24).

There are innumerable papers dedicated to this model and for a review covering more than 250 references on the subject see Mereghetti (2008a). The crucial point is that in this model there is no role of the rotational energy of the source: the X-ray luminosity is much bigger than the loss of rotational energy of the neutron star (see Fig. B.25).

Paradoxically, although the bursts appear to be correlated to the presence of glitches in the rotational period, the corresponding increase of change of

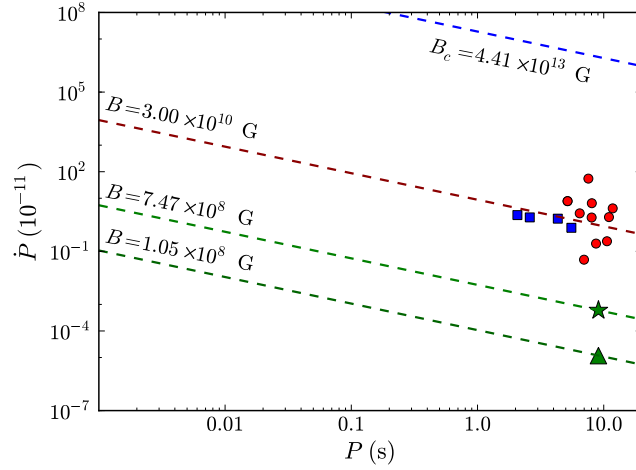


**Figure B.22.:**  $\dot{P}$ - $P$  diagram for all known SGRs and AXPs. The curves of constant magnetic field for white dwarfs given by Eq. (B.3.4) are shown. The blue dashed line corresponds to the critical magnetic field  $B_c = m_e^2 c^3 / (e\hbar)$ . The green star and the green triangle correspond to SGR 0418+5729 using respectively the upper and the lower limit of  $\dot{P}$  given by Eq. (B.3.2). The blue squares are the only four sources that satisfy  $L_X < \dot{E}_{\text{rot}}$  when described as rotation powered neutron stars (see Fig. B.25 for details).

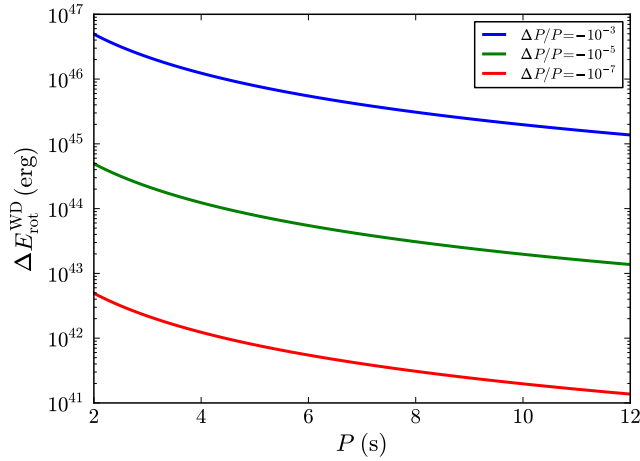


**Figure B.23.:** Change in the rotational energy of the white dwarf  $\Delta E_{\text{rot}}^{\text{WD}}$  given by Eq. (B.3.8) as a function of the rotational period  $P$  in seconds for selected fractional changes of period  $\Delta P/P$ .

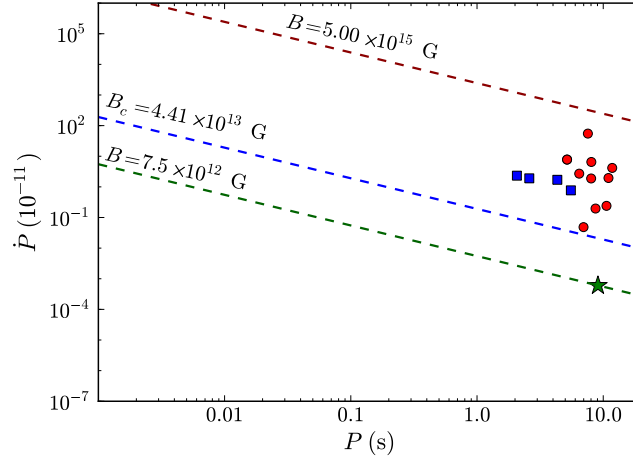


**Figure B.24.:**  $\dot{P}$ - $P$  diagram for all known SGRs and AXPs. The curves of constant magnetic field for neutron stars given by Eq. (B.3.12) are shown. The blue dashed line corresponds to the critical magnetic field  $B_c = m_e^2 c^3 / (e\hbar)$ . The green star corresponds to SGR 0418+5729 using the upper limit of  $\dot{P}$  given by Eq. (B.3.2). The blue squares are the only four sources that satisfy  $L_X < \dot{E}_{\text{rot}}$  when described as rotation powered neutron stars (see Fig. B.25 for details).

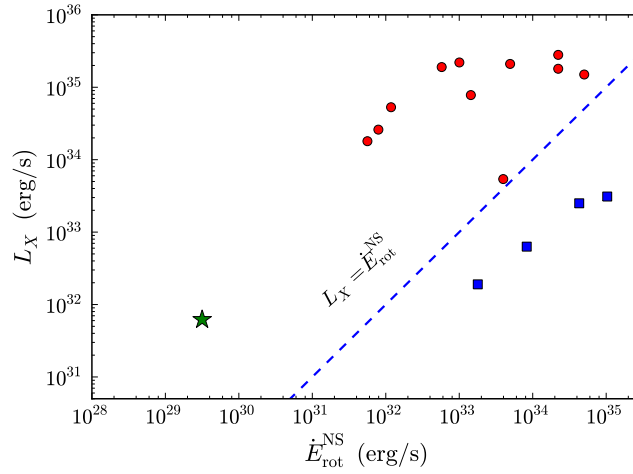


**Figure B.25.:** X-ray luminosity  $L_X$  versus the loss of rotational energy  $\dot{E}_{\text{rot}}$  describing SGRs and AXPs as neutron stars. The green star corresponds to SGR 0418+5729 using the upper limit of  $\dot{P}$  given by Eq. (B.3.2). The blue squares are the only four sources with  $L_X < \dot{E}_{\text{rot}}$ : 1E 1547.0-5408 with  $P = 2.07$  s and  $\dot{P} = 2.3 \times 10^{-11}$ ; SGR 1627-41 with  $P = 2.59$  s and  $\dot{P} = 1.9 \times 10^{-11}$ ; PSR J 1622-4950 with  $P = 4.33$  s and  $\dot{P} = 1.7 \times 10^{-11}$ ; and XTE J1810-197 with  $P = 5.54$  s and  $\dot{P} = 7.7 \times 10^{-12}$ .

rotational energy of the neutron star

$$\Delta E_{\text{rot}}^{\text{NS}} = -\frac{2\pi^2 I \Delta P}{P^2} = -1.98 \times 10^{46} \frac{\Delta P}{P^3} \text{ erg}, \quad (\text{B.3.13})$$

cannot explain the burst energetic  $\sim (10^{44}\text{--}10^{47})$  erg. This is a clear major difference between the two models based respectively on neutron stars and white dwarfs (see Figs. B.23 and B.26 for details).

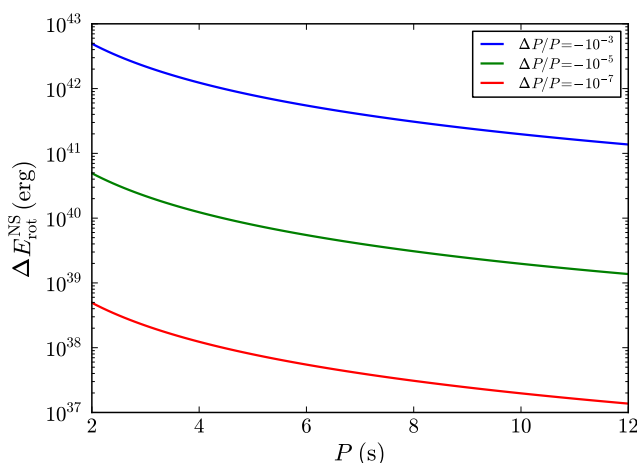


**Figure B.26.:** Change in the rotational energy of the neutron star  $\Delta E_{\text{rot}}^{\text{NS}}$  given by Eq. (B.3.13) as a function of the rotational period  $P$  in seconds for selected fractional changes of period  $\Delta P/P$ .

In magnetars, the value of the rotational period and its first time derivative are only used to establish an upper limit to the magnetic field of the neutron star. In view of the smallness of the moment of inertia of a neutron star with respect to the moment of inertia of a white dwarf, the magnetic field reaches in many cases outstandingly large values  $B \gg B_c \sim 4.4 \times 10^{13}$  G, from here the name magnetars (see Fig. B.24). The attempt has been proposed by Duncan and Thompson (1992) and Thompson and Duncan (1995) to assume a new energy source in physics and astrophysics: the magnetic energy in bulk. The role of thermonuclear energy has been well established by physics experiments on the ground as well as in astrophysics in the explanation of the energetics, life time, and build-up process of the nuclear elements in main sequence stars (see e.g. Bethe, 1968, and references therein); equally well established has been the role of rotational energy in pulsars (see e.g. Hewish, 1974; Bell and Hewish, 1967, and references therein); similarly well established has been the role of gravitational energy in accretion process into neutron stars and black holes and binary X-ray sources (see e.g. Giacconi, 2002; Giacconi and Ruffini, 1978 Reprinted 2010, and references therein). In the magnetars instead, it is introduced an alternative primary energy source

not yet tested neither in the laboratory (the case of magnetic monopoles) nor in astrophysics: a primary energy source due to overcritical magnetic fields.

The mostly qualitative considerations in the magnetar model can be summarized, see e.g. Ng et al. (2010): in the twisted magnetosphere model of magnetars (Thompson et al., 2002), the observed X-ray luminosity of a magnetar is determined both by its surface temperature and by magnetospheric currents, the latter due to the twisted dipolar field structure. The surface temperature in turn is determined by the energy output from within the star due to magnetic field decay, as well as on the nature of the atmosphere and the stellar magnetic field strength. This surface thermal emission is resonantly scattered by the current particles, thus resulting in an overall spectrum similar to a Comptonized blackbody (e.g. Lyutikov and Gavriil, 2006; Rea et al., 2008; Zane et al., 2009). In addition, the surface heating by return currents is believed to contribute substantially to  $L_X$ , at least at the same level as the thermal component induced from the interior field decay (Thompson et al., 2002). Magnetar outbursts in this picture occur with sudden increases in twist angle, consistent with the generic hardening of magnetar spectra during outbursts (e.g. Kaspi et al., 2003; Woods et al., 2004; Israel et al., 2007).

It is worth to recall that magnetic field configurations corresponding to a dipole twisted field have been routinely adopted in rotating neutron stars (see e.g. Cohen et al., 1973). Magnetic field annihilation and reconnection have been analogously adopted in solar physics (see e.g. Parker, 1957; Sweet, 1958) and also magnetic instabilities have been routinely studied in Tokamak (see e.g. Coppi et al., 1976). These effects certainly occur in magnetized white dwarfs. What is important to stress here is that in none of these systems the magnetic field has been assumed to be the primary energy source of the phenomena, unlike in magnetars.

It is appropriate to recall just a few of the difficulties of the magnetar model in fitting observations, in addition to the main one of SGR 0418+5729 addressed in this article. In particular, e.g.: (1) as recalled by S. Mereghetti 2008, “up to now, attempts to estimate the magnetic field strength through the measurement of cyclotron resonance features, as successfully done for accreting pulsars, have been inconclusive”; (2) the prediction of the high-energy gamma ray emission expected in the magnetars has been found to be inconsistent with the recent observation of the Fermi satellite (see e.g. Tong et al., 2010, 2011); (3) finally, it has been shown to be not viable the attempt to relate magnetars to the energy of the supernova remnants (see e.g. Allen and Horvath, 2004; Ferrario and Wickramasinghe, 2006; Vink and Kuiper, 2006; Vink, 2008) or to the formation of black holes (see e.g. Kasen and Bildsten (2010); Woosley (2010), see however e.g. Patnaude et al. (2009)) and of Gamma Ray Bursts (see e.g. Levan et al. (2006); Castro-Tirado et al. (2008); Stefanescu et al. (2008); Bernardini et al. (2009), see however e.g. Goldstein et al. (2011); Rea et al. (2011)).

In Table B.12 we compare and contrast the parameters of selected SGRs

and AXPs sources in the magnetar model and in the fast rotating highly magnetized white dwarf model: the larger radius of a white dwarf with respect to the radius of a neutron star of the same mass  $M = 1.4M_{\odot}$ , leads to the two models differing on the scale of mass density, moment of inertia, and rotational energy which imply a different scale for the surface magnetic fields, leading to a very different physical interpretation of the observations of SGRs and AXPs.

#### **B.3.4. Observations of massive fast rotating highly magnetized white dwarfs**

Some general considerations are appropriate. The white dwarf model appeals to standard and well tested aspects of physics and astrophysics. The observation of fast rotating white dwarfs with magnetic fields larger than  $10^6$  G all the way up to  $10^9$  G has been in the mean time solidly confirmed by observations (see e.g. Angel et al., 1981; Ferrario et al., 1997; Należyty and Madej, 2004; Ferrario and Wickramasinghe, 2005; Terada et al., 2008c). For a recent and extensive analysis of the magnetic field structure of highly magnetized white dwarfs see Külebi et al. (2009) and for a catalog of them see Külebi et al. (2010a) and also Kepler et al. (2010).

A specific example is the highly magnetized white dwarf AE Aquarii. The rotational period of this fast rotating magnetized white dwarf obtained from the sinusoidal pulsed flux in soft X-rays  $< 4$  keV (see e.g. Eracleous et al., 1991; Choi and Dotani, 2006) has been established to be  $P = 33$  s and it is spinning down at a rate  $\dot{P} = 5.64 \times 10^{-14}$ . The mass of the white dwarf is  $\sim M_{\odot}$  (de Jager et al., 1994) and the observed temperature is  $kT \sim 0.5$  keV. In addition to the soft X-ray component, hard X-ray pulsations were observed with the Japanese satellite Suzaku in October-November 2005 and October 2006. The luminosity of AE Aquarii  $\sim 10^{31}$  erg/s accounts for the 0.09% of the spin-down energy of the white dwarf (see Terada et al., 2008c, for details) and the inferred magnetic field of the source is  $B \sim 10^8$  G (Ikhsanov and Beskrovnaya, 2008).

This white dwarf is one of the most powerful particle accelerators: there is at least one event of detected TeV emission from this source during its optical flaring activity monitored between 1988 and 1992 (see e.g. Meintjes et al., 1992, 1993; de Jager et al., 1994; Ikhsanov and Biermann, 2006; Ikhsanov and Beskrovnaya, 2008; Kashiyama et al., 2011). In addition, it shows burst activity in X-rays (Terada et al., 2008c). Although AE Aquarii is a binary system with orbital period  $\sim 9.88$  hr (see de Jager et al., 1994, e.g.), very likely the power due to accretion of matter is inhibited by the fast rotation of the white dwarf (e.g. Itoh et al., 2006; Terada et al., 2008c).

Many of the observed physical properties of this white dwarf are very similar to the recently discovered SGR 0418+5729, as we explicitly show in Table

B.10.

	SGR 0418+5729	AE Aquarii
$P$ (s)	9.08	33.08
$\dot{P}$ ( $10^{-14}$ )	$< 0.6$	5.64
Age (Myr)	24	9.4
$L_X$ (erg/s)	$6.2 \times 10^{31}$	$\sim 10^{31}$
$kT$ (keV)	0.67	0.5
$B$ (G)	$< 7.45 \times 10^8$	$\sim 10^8$
Pulsed Fraction	0.3	$\sim 0.2-0.3$

**Table B.10.:** Comparison of the observational properties of SGR 0418+5729 and the white dwarf AE Aquarii. For SGR 0418+5729  $P$ ,  $\dot{P}$ , and  $L_X$  have been taken from Rea et al. (2010). The characteristic age is given by  $\text{Age} = P / (2\dot{P})$  and the surface magnetic field  $B$  is given by Eq. (B.3.4). The pulsed fraction of SGR 0418+5729 is taken from Esposito et al. (2010) and the one of the white dwarf AE Aquarii from Eracleous et al. (1991) and Choi and Dotani (2006).

Although very fast, AE Aquarii is not the fastest white dwarf observed. The rotational period obtained from the pulsed X-ray emission of RXJ 0648.0-4418, the white dwarf in the binary system HD49798/RXJ 0648.0-4418, is  $P = 13.2$  s (Israel et al., 1997). This white dwarf is one of the most massive white dwarfs with  $M = 1.28 \pm 0.05M_\odot$  (see Mereghetti et al., 2009, for details). Other very massive and highly magnetized white dwarfs are: REJ 0317-853 with  $M \sim 1.35M_\odot$  and  $B \sim (1.7-6.6) \times 10^8$  G (see e.g. Barstow et al., 1995; Külebi et al., 2010b); PG 1658+441 with  $M \sim 1.31M_\odot$  and  $B \sim 2.3 \times 10^6$  G (see e.g. Liebert et al., 1983; Schmidt et al., 1992); and PG 1031+234 with the highest magnetic field  $\sim 10^9$  G (see e.g. Schmidt et al., 1986; Külebi et al., 2009). It is interesting to note that the most highly magnetized white dwarfs are massive as well as isolated (see e.g. Należyty and Madej, 2004, for details).

### B.3.5. Rotational instability of white dwarfs

In order to be stable against secular instability of the MacClaurin versus the Jacobi ellipsoid (Ferrari and Ruffini, 1969), the minimal period of a white dwarf with the parameters discussed here is  $P_{\text{crit}} \sim 0.94$  s. For  $P \lesssim P_{\text{crit}}$  we would expect very significant emission of gravitational waves due to the transition from the triaxial Jacobi ellipsoids to the axially symmetric MacClaurin ellipsoids. This is well in agreement and explains the observed long periods of SGRs and AXPs  $\gtrsim 2$  s (see Fig. B.27). In the specific case of the source 1E 2259+586, assuming that the supernova remnant G109.1-1.0 and

1E 2259+586 are coeval, we obtain the initial rotational period of the white dwarf in the range  $0.94 \text{ s} < P_0 < 6.8 \text{ s}$  where, the lower limit, is given by the bifurcation point between MacClaurin spheroids and Jacobi ellipsoids (see e.g. Ferrari and Ruffini, 1969) and, the upper limit, is obtained for a constant value of  $\dot{P}$ . Describing today 1E 2259+586 by a MacClaurin spheroid, we obtain the ratio between the rotational energy and the gravitational energy  $E_{\text{rot}}/|E_{\text{grav}}| \sim 0.011$  (see Fig. B.27), well below the secular instability  $\sim 0.14$  and the dynamical instability  $\sim 0.25$  (see Chandrasekhar, 1969; Shapiro and Teukolsky, 1983a, for details).

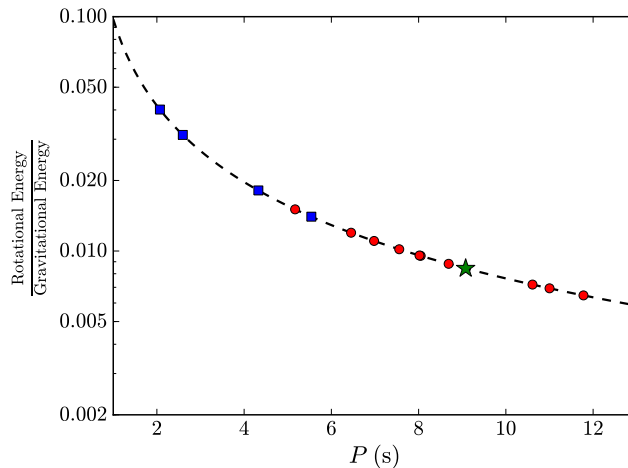


**Figure B.27.:** Ratio between the rotational energy and the gravitational energy of a MacClaurin spheroid of  $M = 1.4M_{\odot}$  and  $R = 10^3 \text{ km}$  as a function of its rotational period  $P$ . The rotational period between 2 and 12 s appears to be very appropriate for fast rotating white dwarfs. Fast rotating neutron stars present much shorter period in the millisecond region. We show on the curve the position of all known SGRs and AXPs. The green star corresponds to SGR 0418+5729. The blue squares are the only four sources that satisfy  $L_X < \dot{E}_{\text{rot}}$  when described as rotation powered neutron stars (see Fig. B.25 for details).

The above considerations add interest in the recent theoretical analysis of white dwarfs taking into account nuclear, weak and electromagnetic interactions within a general relativistic treatment (Rotondo et al., 2011b). A specially relevant result has been recently obtained (Boshkayev et al., 2013b) by analyzing a white dwarf endowed with mass, angular momentum, and quadrupole moment within the Hartle-Thorne formalism (Hartle, 1967; Hartle and Thorne, 1968). The rotating white dwarfs have been studied for the new equation of state given by Rotondo et al. (2011c) used for the construction of the non-rotating configurations by Rotondo et al. (2011b). The critical rotational periods for the onset of the axisymmetric, the mass-shedding and the inverse  $\beta$ -decay instabilities have been studied in detail. The exact value of the critical period of a white dwarf depends upon the central density of

the configuration; rotationally stable white dwarfs exist for rotational periods  $P > P_{\min}^{\text{WD}} \sim 0.3$  s. The shortest values for configurations supported by rotation with critical masses larger than the classical Chandrasekhar limit for non-rotating white dwarfs all the way up to  $M_{\max} \sim 1.5M_{\odot}$  (see Boshkayev et al., 2013b, for details).

Consequently, also the fastest sources e.g. 1E 1547.0-5408 with  $P = 2.07$  s, SGR 1627-41 with  $P = 2.59$  s, and PSR J 1622-4950 with  $P = 4.33$  s, can be safely described as massive fast rotating white dwarfs as shown in Fig. B.21.

### B.3.6. Glitches and outbursts in SGRs and AXPs

The energetic of the observed bursts within the white dwarf model of SGRs and AXPs can be fully explained by the observed change of period  $\Delta P < 0$  (glitches). In the case of the famous event of 5th March 1979 in the SGR 0526-66 ( $P = 8.05$  s), a fractional change of period of the white dwarf  $\Delta P/P \sim -10^{-4}$  (see Fig. B.23) would be sufficient to explain the energetics  $\sim 3.6 \times 10^{44}$  erg (Mereghetti, 2008a). Unfortunately, such a change of period could not be observed at the time (see e.g. Mazets et al., 1979), lacking the observations of the source prior to the event. Instead, in the case of the flares of 1E 2259+586 on June 2002 ( $P = 6.98$  s) and of 1E 1048.1-5937 ( $P = 6.45$  s) on March 2007, observational data are available. For 1E 2259+586, using the observed fractional change of period  $\Delta P/P \sim -4 \times 10^{-6}$  (Woods et al., 2004) (see also Fig. B.20), we obtain within the white dwarf model a change of rotational energy  $|\Delta E_{\text{rot}}^{\text{WD}}| \sim 1.7 \times 10^{43}$  erg, to be compared with the measured energy released during the event  $\sim 3 \times 10^{41}$  erg. For the glitch on the 26th March 2007 in 1E 1048.1-5937 with observed  $\Delta P/P \sim -1.63 \times 10^{-5}$ , we obtain  $|\Delta E_{\text{rot}}^{\text{WD}}| \sim 7.73 \times 10^{43}$  erg which is strikingly in agreement (and safely superior) with the observed energy released in the event  $4.3 \times 10^{42}$  erg (see e.g. Dib et al., 2009). In the case of super giant flares, there is no clear observational evidence of their association to glitches. However, changes in the moment of inertia of the white dwarf originating fractional changes of period of order  $\Delta P/P \sim -(10^{-5} - 10^{-3})$  (see Fig. B.23) could explain their large energetics ranging from  $10^{44}$  erg all the way up to  $10^{47}$  erg (see e.g. Mereghetti, 2008a). For the giant flare of SGR 1806-20 on 27th December 2004 (see e.g. Borkowski et al., 2004; Hurley et al., 2005) with observed energy  $\sim 10^{46}$  erg there is a gap of timing data of the source between October 2004 and March 2005 (see Mereghetti et al., 2005; Tiengo et al., 2005). The observed rotational period of SGR 1806-20 after March 2005 is not consistent with the expected rotational period obtained from the spin-down rate  $\dot{P} = 5.5 \times 10^{-10}$ ; instead, this is consistent with  $\dot{P} = 1.8 \times 10^{-10}$ . The change of rotational period has been attributed to “global reconfigurations of the neutron star magnetosphere” (see e.g. Tiengo et al., 2005). Within the white dwarf model, such a burst activity is consistent with a glitch with fractional change of period  $\sim -3 \times 10^{-3}$ . All

	SGR 0526-66	1E 2259+586	1E 1048.1-5937	SGR 1806-20
Date	March 1979	June 2002	March 2007	December 2004
Observed Energy (erg)	$3.6 \times 10^{44}$	$3 \times 10^{41}$	$4.2 \times 10^{42}$	$\sim 10^{46}$
$ \Delta P /P$	$1.2 \times 10^{-4}$ (predicted)	$4.24 \times 10^{-6}$ (observed)	$1.63 \times 10^{-5}$ (observed)	$3 \times 10^{-3}$ (predicted)
Predicted Energy (erg)	$3.6 \times 10^{44}$	$1.7 \times 10^{43}$	$7.7 \times 10^{43}$	$\sim 10^{46}$

**Table B.11.:** Glitches and Outbursts of some SGRs and AXPs within the white dwarf model. The predicted values of  $|\Delta P|/P$  are calculated with Eq. (B.3.8) assuming  $|\Delta E_{\text{rot}}^{\text{WD}}|$  equals the observed energy of the burst event. The predicted values of the energy released in the burst event is calculated with Eq. (B.3.8) using the observed fractional change of rotational period  $|\Delta P|/P$ .

the above discussion is summarized in Table B.11 and Figs. B.20 and B.23.

In all the above cases the gain of rotational energy in the glitch is much larger than the energy observed in the flaring activities following the glitches. This means that there is ample room to explain these glitch-outburst events in a large range of recovery fractions  $Q$ . It appears to be appropriate to systematically monitor the  $Q$  factors for all the glitches in SGRs and AXPs.

It is interesting that PSR J1846-0258,  $P = 0.3$  s, experienced in June 2006 a radiative event with estimated isotropic energy  $\sim (3.8\text{--}4.8) \times 10^{41}$  erg (Kumar and Safi-Harb, 2008). Assuming that such an event was triggered by a glitch in the neutron star one obtains an associated fractional change of period  $\Delta P/P \sim -(1.73\text{--}2.2) \times 10^{-6}$ , as given by Eq. (B.3.13). Indeed, as shown by Kuiper and Hermsen (2009), the outburst emission was accompanied by a large glitch  $\Delta P/P \sim -(2.0\text{--}4.4) \times 10^{-6}$  in perfect agreement with the theoretical prediction given by the loss of rotational power after the spin-up of the neutron star without advocate any magnetar phenomena. This fact reinforces the idea that PSR J1846-0258 is not a magnetar but an ordinary rotationally powered neutron star, also in line with the recent suggestions by Kuiper and Hermsen (2009) and Rea et al. (2010).

### B.3.7. Magnetosphere emission from white dwarfs

We return now to the structure of the magnetosphere of the white dwarf model for SGRs and AXPs. In order to have an agreement between the observed X-ray luminosity and the X-ray spectral distribution, it is necessary that only a part of the surface of the white dwarf has to be X-ray emitter.

We can define the dimensionless filling factor

$$\mathcal{R} = \frac{L_X}{4\pi R^2 \sigma T^4}, \quad (\text{B.3.14})$$

where  $\sigma$  is the Stefan-Boltzmann constant and  $T$  the temperature of the source. This factor gives an estimate of the effective area of X-ray emission and consequently information about the structure of the magnetic field from the surface of the object. It is interesting that this factor for the white dwarf is in

the range  $10^{-6}$ – $10^{-5}$  (see Table B.12), quite similar to the one of the Sun  $\mathcal{R}_{\odot} = L_{\odot}^X / (4\pi R_{\odot}^2 \sigma T_{\odot}^4) \approx (7.03 \times 10^{-8} - 1.2 \times 10^{-6})$  in the minimum  $L_{\odot}^X = 2.7 \times 10^{26}$  erg/s and in the maximum  $L_{\odot}^X = 4.7 \times 10^{27}$  erg/s of solar activity respectively (see e.g. Peres et al., 2000; Judge et al., 2003). This should be expected by the general argument of the conservation of flux in the transition from a highly magnetized main sequence star to a white dwarf. The magnetic field of the order of  $\sim 10^9$  G on the surface of these white dwarfs must clearly have a filamentary structure in the range  $\mathcal{R} \sim 10^{-6}$ – $10^{-5}$ .

In the specific case of SGR 0418+572 such an  $\mathcal{R}$  factor is  $\sim 10^{-9}$ , which is of the same order as the one of the white dwarf AE Aquarii, as can be seen from Table B.10 by comparing the values of  $L_X$  and  $KT$ , which are the quantities involved in Eq. (B.3.14).

At times the presence of an  $\mathcal{R}$  factor has been interpreted as originating from a spot-like radial emission of the radiation from the surface of the white dwarf. If one were to assume that the radiation occurs radially beamed and occurring just from the surface either of the neutron star or the white dwarf, a spot radiation would lead to a pulsed fraction of the emission flux determined by  $\sqrt{1/n \sum_{i=1}^n (y_i - \bar{y})^2} / \bar{y} \sim 1$ , where  $n$  is the number of phase bins per cycle,  $y_i$  is the number of counts in the  $i$ th phase bin and  $\bar{y}$  is the mean number of counts in the cycle (see e.g. Esposito et al., 2010, for details about this definition). This problem, which seems to be in contradiction with the observations of pulsed fractions  $< 1$  in SGRs and AXPs (see e.g. Esposito et al., 2010), would be equally severe both for neutron stars and white dwarfs (see e.g. Table B.10).

It is appropriate to recall that all the SGRs and AXPs within a rotating white dwarf model have magnetic fields in the range  $10^8 \text{ G} \lesssim B \lesssim 10^{11} \text{ G}$  (see Table B.12). It is quite natural to assume that the X-ray emission be linked to the presence of the magnetic field. It is worth to note that the modeling of the physics and the geometrical structure of the magnetic field and of the magnetospheres is a most active field of current research. As shown by Romani and Watters (2010), the morphology of the pulses as well as of the light curves strongly depend on many model parameters, e.g. special and general relativistic effects, the viewing angle, the magnetic moment-spin axis angle, the spin axis-line of sight angle, the specific location of the emission zone, and the adopted magnetospheric model including possible corrections due to deviations from a pure dipolar structure.

From the broad sinusoidal pulsed flux of SGRs/AXPs (see e.g. Mereghetti, 2008a), we know that the pulsed fraction is less than one and that the luminosity differs remarkably from a spiky one. We find then natural to assume that the emission comes from an area covering the white dwarf surface with a very marked filamentary structure. Similar considerations for neutron stars magnetospheres have been purported e.g. by Michel and Dessler (1981); Michel (1983) giving evidence of magnetospheric activity from the

pole all the way up to the equator; see also the most interesting case of the pair production activities in the magnetosphere of a rotating white dwarf considered for the transient radio source GCRT J1745–3009 by Zhang and Gil (2005). Moreover, such structures are regularly observed in the Sun and in the Earth Aurora. Explicit sinusoidal pulsed flux in soft X-rays ( $< 4$  keV) have been observed in AE Aquarii (see e.g. Eracleous et al., 1991; Choi and Dotani, 2006); and see also Fig. 6 in Mereghetti et al. (2011) for similar sinusoidal pulsed emission of the white dwarf RXJ 0648.0-4418 with rotational period  $P = 13.2$  s. For all the above sources, a filamentary structure of the magnetic field is clearly expected.

We do not discuss here the issue of the spectral features within the white dwarf model. The aim of this article is just to point out that all these problems can be address with merit starting from the rotational energy of a rotating white dwarf rather than the magnetic energy of a magnetar. The spectrum of the persistent emission of SGRs and AXPs for energies  $< 10$  keV is well fitted either by the superposition of a blackbody and a high energy tail or by a single blackbody or a double blackbody (see e.g. Mereghetti, 2008a). Such a spectral feature is clearly already evidenced for rotating white dwarfs; following the work of Terada et al. (2008c): in addition to the thermal modulation in the softer X-ray band, spiky pulsations like the ones of pulsars have been observed by the Suzaku satellite in the hard X-ray band of over 4 keV in the white dwarf AE Aquarii. The X-ray spectrum requires an additional hard X-ray component on the well-known thermal emissions with temperatures of 0.5 and 2.9 keV. Combined with results from timing analyses, spectral shapes and flux, it was there concluded that the hard X-ray pulsations should have a non-thermal origin, for example, possible Synchrotron emission with sub MeV electrons. The claim of the first discovery of a white dwarf equivalent to a neutron star pulsar was there made. In view of the possible evidence of very high energy emission in the TeV region observed during the optical flares of AE Aquarii (see e.g. de Jager et al., 1994; Ikhsanov and Biermann, 2006; Ikhsanov and Beskrovnaya, 2008; Terada et al., 2008c,d; Kashiyama et al., 2011, and references therein), it would be important to have observations by INTEGRAL and Fermi of rotating magnetized white dwarf in the 20-200 keV band in order to establish further analogies between fast rotating highly magnetized white dwarfs and magnetar candidates.

More specifically, for the source SGR 0418+5729 and its interpretation as a white dwarf, a crucial result has been recently obtained by Durant et al. (2011). We first recall the observed range of temperatures of massive isolated white dwarfs  $1.14 \times 10^4 \text{ K} \leq T \leq 5.52 \times 10^4 \text{ K}$ ; see Table 1 in (Ferrario et al., 2005). From the broad band Hubble Space Telescope imaging of the field of SGR 0418+5729, the upper limits of the black body surface temperature,  $T < 3.14 \times 10^4 \text{ K}$  and  $T < 1.18 \times 10^4 \text{ K}$  in the F110W and F606W filters, can be established for a radius  $R = 10^8 \text{ cm}$ . In this respect is also worth to recall the optical observations of AXP 4U0142+61 of Hulleman et al. (2000).

The photometric results of the field of 4U0142+61 at the 60-inch telescope on Palomar Mountain are in agreement with a  $1.3M_{\odot}$  white dwarf with a surface temperature  $\sim 4 \times 10^5$  K (see Hulleman et al., 2000, for details). These results are therefore fully consistent with the SGR/AXP white dwarf model, and follow-on missions of Hubble and VLT are strongly recommended.

### **B.3.8. The connection with supernova remnants**

We would like to address the special issue of the supernova remnants energetics and their association with SGRs and AXPs. A firm association between SGRs/AXPs and supernovae have been purported by Gaensler et al. (2001) in the cases 1E 1841–045 (SNR G27.4+0.0, Kes 73), AX J1845.0–0258 (SNR G29.6+0.1), and 1E 2259+586 (SNR G109.1–1.0, CTB 109). See also Gelfand and Gaensler (2007) for the possible association 1E 1547.0–5408 (SNR G327.24–0.13). What is of interest for us here is the special issue of the energetics of the supernova remnant and the present of an SGR or an AXP.

Paczynski, in the case of AXP 1E 2259+586, attempted to explain the supernova remnant by assuming a merger of a binary system of ordinary white dwarf of mass  $\sim (0.7–1)M_{\odot}$  based on models by Iben and Tutukov (1984) and Paczynski (1985) leading both to the formation of a fast rotating white dwarf and to the supernova remnant. Recent simulations of white dwarf-white dwarf mergers (see e.g. Pakmor et al., 2010) point that mergers of  $(0.8–0.9M_{\odot})$  produce supernova events generally not very efficient energetically, well below the observed explosion energy  $\sim 7.4 \times 10^{50}$  erg of the supernova remnant G109.1–1.0 associated to 1E 2259+586 (see e.g. Sasaki et al., 2004).

In the intervening years much more has been understood on the process of gravitational collapse and on the composition of the material surrounding neutron stars and black holes both from pulsar observations and Gamma Ray Bursts. Fascinating evidence for the presence of planets around pulsars in supernova remnants has been established (see e.g. Konacki et al., 1999; Hansen, 2002; Konacki and Wolszczan, 2003). Similarly, the presence of many body process of gravitational collapse has been evidenced for Gamma Ray Bursts (see e.g. Ruffini, 2009).

In view of this, we advance the possible scenario in which the SGRs/AXPs and the supernova remnant originate from a very close binary system composed of a white dwarf and a companion late evolved star, close to the process of gravitational collapse. The collapse of the companion star, either to a neutron star or to a black hole, leads to mass loss which can unbind the original binary system. Three possible cases can occur (see e.g. Ruffini, 1973): 1) if the loss of mass in the supernova explosion is  $M_{\text{loss}} < M/2$ , being  $M$  the total mass of the binary, the system holds bound; 2) if  $M_{\text{loss}} \sim M/2$  then the system becomes unbound and the white dwarf is expelled at nearly orbital motion velocity; and 3) if  $M_{\text{loss}} \gg M/2$  the white dwarf is kicked out with

very high runaway velocities. Only in the first case the object will lie at the center of the supernova remnant. For a review on the evolution of binary systems see Stairs (2004) and for a detailed treatment of the problem of runaway velocities from supernova explosions see Tauris and Bailes (1996); Tauris and Takens (1998). The white dwarf in this picture does not participate either to the gravitational collapse nor to the formation of the supernova remnant: it can have a period and a life time determine essentially by the prior evolution of the binary system. This explains the disagreement between the age of the supernova remnant and the characteristic age of the SGR/AXP when inferred by a neutron star model. In the case of large kick velocities the runaway white dwarf can collide with the surrounding material in the supernova remnant and very likely also with planets. Such collisions may well originate changes in the moment of inertia of the white dwarf, consequently in its rotational period, leading to glitches and burst activity.

In the above context it is appropriate to recall the pioneering work of Katz (1996) on explaining the super-Eddington luminosities in the flaring episodes of SGRs and AXPs as originating in accretion process of planetary fragments, in particular, the important role of magnetic confinement of an  $e^+e^-$  pair plasma. The model explains the observed self-absorbed thermal spectrum of flares and their nearly independence on their luminosity. Katz (1996) has shown that the infall of planetary fragments may lead to a continuous injection of energy to the magnetosphere which leads to magnetic confinement of the source if the magnetic field satisfies

$$B > \sqrt{\frac{2L}{cR^2}} = 2.6 \times 10^7 \sqrt{\frac{L_{41}}{R_8^2}} \text{ G}, \quad (\text{B.3.15})$$

where  $L_{41}$  is the luminosity in units of  $10^{41}$  erg/s and  $R_8$  is the radius of the source in units of  $10^8$  cm.

In the case when the radiation is not being continuously resupplied, but it is initially contained within the volume  $\sim 4\pi R^3/3$ , the minimum magnetic field for confinement is given by

$$B > \sqrt{\frac{6L\tau}{R^3}} = 2.45 \times 10^8 \sqrt{\frac{L_{41}\tau_{0.1}}{R_8^3}} \text{ G}, \quad (\text{B.3.16})$$

where  $\tau_{0.1}$  is the time  $\tau$  during which the source is radiating at a luminosity  $L$ , in units of 0.1 s. The fiducial values for  $L$  and for  $\tau$  has been chosen here to be typical of the bursting activity of SGRs/AXPs (see e.g. Mereghetti, 2008a). The above two bounds for the magnetic field are indeed in line with the surface magnetic fields obtained in this paper; see Fig. B.22 for details. Thus, the super-Eddington luminosities observed in the outbursts can be well explained within the white dwarf model and there is no need of introducing

the huge magnetic fields of the magnetar model (Paczynski, 1992; Thompson and Duncan, 1995).

### B.3.9. On the fiducial neutron star and white dwarf parameters in light of recent theoretical progress

Before concluding, we would like to introduce a word of caution on the fiducial values adopted both for the neutron star and the white dwarf in the above Sections. In the intervening years much more have been learned on the equation of state and on a more complex description of the structure parameters of both white dwarfs and neutron stars.

The equations of equilibrium of neutron stars, traditionally based on the Tolman-Oppenheimer-Volkoff equations, have been superseded by an alternative formulation based on the general relativistic Thomas-Fermi conditions of equilibrium within the Einstein-Maxwell equations Belvedere et al. (2012). Correspondingly, the above values of  $\sqrt{I/R^6}$  in Eq. (B.3.3) estimated in the fiducial parameters, leading to Eq. (B.3.12), can acquire in fact values in the range  $0.44 \lesssim \sqrt{I/R^6} / \sqrt{I_f/R_f^6} \lesssim 0.56$ , where the subscript ‘f’ stands for fiducial parameter. This range corresponds to the range of masses  $0.5 \lesssim M/M_\odot \lesssim 2.6$  (Belvedere et al., 2012). Correspondingly, the magnetic field is in the range  $0.44 \lesssim B/B_f^{\text{NS}} \lesssim 0.56$ , where  $B_f^{\text{NS}}$  is given by Eq. (B.3.12).

Similar considerations apply for the white dwarf case. General relativistic white dwarfs taking into account nuclear, weak and electromagnetic interactions have been recently constructed (Rotondo et al., 2011b) following the new equation of state for compressed nuclear matter given by Rotondo et al. (2011c). The case of rotating white dwarfs in general relativity has been studied by Boshkayev et al. (2013b). It has been found that white dwarfs can be as fast as  $P_{\text{min}}^{\text{WD}} \sim 0.3$  s and as massive as  $M_{\text{max}} \sim 1.5M_\odot$ ; see Sec. B.3.5 for details. For example, a white dwarf of  $M = 1.44M_\odot$  rotating with period  $P = 3.2$  s, will have an equatorial radius  $R_{\text{eq}} \sim 3604$  km, polar radius  $R_p \sim 2664$  km, and moment of inertia  $I \sim 2.9 \times 10^{49}$  g cm<sup>2</sup>. In this case we will have  $\sqrt{I/R^6} / \sqrt{I_f/R_f^6} \sim 0.01$  and therefore  $B/B_f^{\text{WD}} \sim 0.01$  where  $B_f^{\text{WD}}$  is given by Eq. (B.3.4).

This issue is particularly relevant to the study of the four sources in Fig. B.25. These sources can be definitely explained within a unified framework of rotating white dwarfs with all the other SGRs and AXPs. In view of the parameters recently obtained they may be also interpreted as regular neutron stars with a barely critical magnetic field. For these sources an option remain open for their interpretation as white dwarfs or neutron stars. A more refined analysis will clarify the correctness of the two possible interpretations both, in any case, alternative to the magnetar model.

### B.3.10. Conclusions and remarks

The recent observations of the source SGR 0418+5729 cast a firm separatrix in comparing and contrasting the two models for SGRs and AXPs based respectively on an ultramagnetized neutron star and on a white dwarf. The limit on the magnetic field derived in the case of a neutron star  $B = 7.5 \times 10^{12}$  G makes it not viable as an explanation based on the magnetar model both from a global energetic point of view and from the undercritical value of the magnetic field. In the white dwarf model, the picture is fully consistent. It is interesting that the rotational energy loss appears to approach the value of the observed X-ray luminosity with time (see Fig. B.28) as the magnetospheric activity settles down.

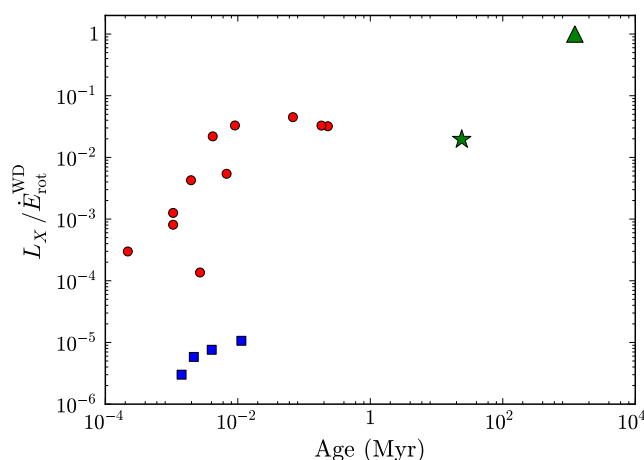


**Figure B.28.:** Ratio between the observed X-ray luminosity  $L_X$  and the loss of rotational energy  $\dot{E}_{rot}$  describing SGRs and AXPs by rotation powered white dwarfs. The green star and the green triangle correspond to SGR 0418+5729 using respectively the upper and the lower limit of  $\dot{P}$  given by Eq. (B.3.2). The blue squares are the only four sources that satisfy  $L_X < \dot{E}_{rot}$  when described as rotation powered neutron stars (see Fig. B.25 for details).

The description of SGR 0418+5729 as a white dwarf predicts the lower limit of the spin-down rate  $\dot{P}$  given by Eq. (B.3.2), the surface magnetic field is, accordingly to Eq. (B.3.4), constrained by  $1.05 \times 10^8 \text{ G} < B_{\text{SGR0418+5729}} < 7.47 \times 10^8 \text{ G}$  (see Fig. B.22). The campaign of observations launched by the Fermi and Agile satellites will address soon this issue and settle in the near future this theoretical prediction.

The characteristic changes of period  $\Delta P/P \sim -(10^{-7}-10^{-3})$  and the relating bursting activity  $\sim (10^{41}-10^{46})$  erg in SGRs and AXPs can be well explained in term of the rotational energy released after the glitch of the white dwarf. It is also appropriate to recall that fractional changes, on scales  $|\Delta P|/P \lesssim 10^{-6}$  are also observed in pulsars and routinely expressed in terms

of the release of rotational energy of the neutron star, without appealing to any magnetars phenomena; e.g. the glitch/outburst activity experienced in June 2006 by PSR J1846-0258 (see Sec. B.3.7) and the most recent event observed in the prototypical Crab pulsar B0531+21 in the Crab nebula (see e.g. Tavani, 2011; Fermi-LAT Collaboration, 2010).

The observation of massive fast rotating highly magnetized white dwarfs by dedicated missions as the one leadered by the X-ray Japanese satellite Suzaku (see e.g. Terada et al., 2008c) has led to the confirmation of the existence of white dwarfs sharing common properties with neutron star pulsars, hence their name white dwarf pulsars. The theoretical interpretation of the high-energy emission from white dwarf pulsars will certainly help to the understanding of the SGR and AXP phenomena (see e.g. Kashiyama et al., 2011).

We have given evidence that all SGRs and AXPs can be interpreted as rotating white dwarfs providing that the rotational period satisfies  $P > P_{\min}^{\text{WD}} \sim 0.3$  s. The white dwarf generate their energetics from the rotational energy and therefore there is no need to invoke the magnetic field decay of the magnetar model.

Concerning magnetized white dwarfs, the coupling between rotation and Rayleigh-Taylor instabilities arising from chemical separation upon crystallization may have an important role in the building of the magnetic field of the white dwarf.

	SGR 1806-20	SGR 0526-66	SGR 1900+14	SGR 0418+5729
$P$ (s)	7.56	8.05	5.17	9.08
$\dot{P}$ ( $10^{-11}$ )	54.9	6.5	7.78	$< 6.0 \times 10^{-4}$
Age (kyr)	2.22	1.97	1.05	$24.0 \times 10^3$
$L_X$ ( $10^{35}$ erg/s)	1.50	2.1	1.8	$6.2 \times 10^{-4}$
$kT$ (keV)	0.65	0.53	0.43	0.67
$\dot{E}_{\text{rot}}^{\text{WD}}$ ( $10^{37}$ erg/s)	50.24	4.92	22.24	$3.2 \times 10^{-4}$
$B_{\text{WD}}$ ( $10^9$ G)	206.10	73.18	64.16	0.75
$\mathcal{R}_{\text{WD}}$ ( $10^{-5}$ )	0.65	2.06	4.07	$2.4 \times 10^{-4}$
$\dot{E}_{\text{rot}}^{\text{NS}}$ ( $10^{35}$ erg/s)	0.502	0.05	0.22	$3.2 \times 10^{-6}$
$B_{\text{NS}}$ ( $10^{14}$ G)	20.61	7.32	6.42	0.075
$\mathcal{R}_{\text{NS}}$	0.065	0.21	0.41	$2.4 \times 10^{-5}$
	1E 1547-54	1E 1048-59	1E 1841-045	1E 2259+586
$P$ (s)	2.07	6.45	11.78	6.98
$\dot{P}$ ( $10^{-11}$ )	2.32	2.70	4.15	0.048
Age (kyr)	1.42	3.79	4.50	228.74
$L_X$ ( $10^{35}$ erg/s)	0.031	0.054	2.2	0.19
$kT$ (keV)	0.43	0.62	0.38	0.41
$\dot{E}_{\text{rot}}^{\text{WD}}$ ( $10^{37}$ erg/s)	103.29	3.97	1.01	0.056
$B_{\text{WD}}$ ( $10^9$ G)	22.17	42.22	70.71	5.88
$\mathcal{R}_{\text{WD}}$ ( $10^{-5}$ )	0.07	0.028	8.16	0.49
$\dot{E}_{\text{rot}}^{\text{NS}}$ ( $10^{35}$ erg/s)	1.03	0.040	0.010	$5.62 \times 10^{-4}$
$B_{\text{NS}}$ ( $10^{14}$ G)	2.22	4.22	7.07	0.59
$\mathcal{R}_{\text{NS}}$	0.007	0.0028	0.82	0.049

**Table B.12.:** SGRs and AXPs as white dwarfs and neutron stars. The rotational period  $P$ , the spin-down rate  $\dot{P}$ , the X-ray luminosity  $L_X$  and the temperature  $T$  have been taken from the McGill online catalog at [www.physics.mcgill.ca/~pulsar/magnetar/main.html](http://www.physics.mcgill.ca/~pulsar/magnetar/main.html). The characteristic age is given by  $\text{Age} = P/(2\dot{P})$ , the loss of rotational energy  $\dot{E}_{\text{rot}}$  is given by Eqs. (B.3.5) and Eq. (B.3.1) and the surface magnetic field is given by Eqs. (B.3.4) and (B.3.12) for white dwarfs and neutron stars respectively. The filling factor  $\mathcal{R}$  is given by Eq. (B.3.14).

## B.4. SGR 0418+5729 and Swift J1822.3-1606 as massive fast rotating highly magnetized white dwarfs

### B.4.1. Introduction

Soft Gamma Ray Repeaters (SGRs) and Anomalous X-ray Pulsars (AXPs) are a class of compact objects that show interesting observational properties (see e.g. Mereghetti, 2008a): rotational periods in the range  $P \sim (2-12)$  s, spin-down rates  $\dot{P} \sim (10^{-13}-10^{-10})$ , strong outburst of energies  $\sim (10^{41}-10^{43})$  erg, and in the case of SGRs, giant flares of even large energies  $\sim (10^{44}-10^{47})$  erg.

The most popular model for the description of SGRs and AXPs, the magnetar model, based on a neutron star of fiducial parameters  $M = 1.4M_{\odot}$ ,  $R = 10$  km and a moment of inertia  $I = 10^{45}$  g cm<sup>2</sup>, needs a neutron star magnetic field larger than the critical field for vacuum polarization  $B_c = m_e^2 c^3 / (e\hbar) = 4.4 \times 10^{13}$  G in order to explain the observed X-ray luminosity in terms of the release of magnetic energy (see Duncan and Thompson, 1992; Thompson and Duncan, 1995, for details). There exist in the literature other models based still on neutron stars but of ordinary fields  $B \sim 10^{12}$  G: these models involve either the generation of drift waves in the magnetosphere or the accretion of fallback material via a circumstellar disk (see Malov, 2010; Trümper et al., 2013, respectively, and references therein).

Turning to the experimental point of view, the observation of SGR 0418+5729 with a rotational period of  $P = 9.08$  s, an upper limit of the first time derivative of the rotational period  $\dot{P} < 6.0 \times 10^{-15}$  (Rea et al., 2010), and an X-ray luminosity of  $L_X = 6.2 \times 10^{31}$  erg s<sup>-1</sup> can be considered as the Rosetta Stone for alternative models of SGRs and AXPs. The inferred upper limit of the surface magnetic field of SGR 0418+5729  $B < 7.5 \times 10^{12}$  G describing it as a neutron star (see Rea et al., 2010, for details), is well below the critical field, which has challenged the power mechanism based on magnetic field decay in the magnetar scenario.

Alternatively, it has been recently pointed out how the pioneering works of Morini et al. (1988) and Paczynski (1990) on the description of 1E 2259+586 as a white dwarf can be indeed extended to all SGRs and AXPs. Such white dwarfs were assumed to have fiducial parameters  $M = 1.4M_{\odot}$ ,  $R = 10^3$  km,  $I = 10^{49}$  g cm<sup>2</sup>, and magnetic fields  $B \gtrsim 10^7$  G (see Malheiro et al., 2012, for details) inferred from the observed rotation periods and spindown rates.

It is remarkable that white dwarfs with large magnetic fields from  $10^7$  G all the way up to  $10^9$  G have been indeed observed; see e.g. Külebi et al. (2009), Külebi et al. (2010a), Kepler et al. (2010), and more recently Kepler et al. (2012). It is worth to mention also the fact that most of the observed magnetized white dwarfs are massive; see e.g. REJ 0317-853 with  $M \sim 1.35M_{\odot}$

and  $B \sim (1.7\text{--}6.6) \times 10^8$  G (see e.g. Barstow et al., 1995; Külebi et al., 2010b); PG 1658+441 with  $M \sim 1.31M_{\odot}$  and  $B \sim 2.3 \times 10^6$  G (see e.g. Liebert et al., 1983; Schmidt et al., 1992); and PG 1031+234 with the highest magnetic field  $\sim 10^9$  G (see e.g. Schmidt et al., 1986; Külebi et al., 2009).

The energetics of SGRs and AXPs including their steady emission, glitches, and their subsequent outburst activities have been shown to be powered by the rotational energy of the white dwarf (Malheiro et al., 2012). The occurrence of a glitch, the associated sudden shortening of the period, as well as the corresponding gain of rotational energy, can be explained by the release of gravitational energy associated with a sudden contraction and decrease of the moment of inertia of the uniformly rotating white dwarf, consistent with the conservation of their angular momentum.

Describing SGR 0418+5729 as a white dwarf, Malheiro et al. (2012) calculated an upper limit for the magnetic field  $B < 7.5 \times 10^8$  G and show that the X-ray luminosity observed from SGR 0418+5729 can be well explained as originating from the loss of rotational energy of the white dwarf leading to a theoretical prediction for the spindown rate

$$\frac{L_X P^3}{4\pi^2 I} = 1.18 \times 10^{-16} \leq \dot{P}_{\text{SGR0418+5729}} < 6.0 \times 10^{-15}, \quad (\text{B.4.1})$$

where the lower limit was established by assuming that the observed X-ray luminosity of SGR 0418+5729 coincides with the rotational energy loss of the white dwarf. As we will show below, these predictions can be still improved by considering realistic white dwarf parameters instead of fiducial values. It is important to mention at this point that, after the submission of this work, Rea et al. (2013) presented the X-ray timing analysis of the long term monitoring of SGR 0418+5729 with RXTE, SWIFT, Chandra, and XMM-Newton; which allowed the determination of the spin-down rate of SGR 0418+5729,  $\dot{P} = 4 \times 10^{-15}$ . These results confirm both our prediction given by Eq. (B.4.1) and the more stringent limits presented in this work in Sec. B.4.4 and given by Eq. (B.4.10), which being presented in advance to the observational results presented in (Rea et al., 2013), are to be considered as a predictions of the white dwarf model.

The situation has become even more striking considering the X-ray timing monitoring with Swift, RXTE, Suzaku, and XMM-Newton satellites of the recently discovered SGR Swift J1822.3-1606 (Rea et al., 2012). The rotation period  $P = 8.437$  s, and the spindown rate  $\dot{P} = 9.1 \times 10^{-14}$  have been obtained. Assuming a NS of fiducial parameters, a magnetic field  $B = 2.8 \times 10^{13}$  G is inferred, which is again in contradiction with a magnetar explanation for this source.

We recently computed (Boshkayev et al., 2013b) general relativistic uniformly rotating white dwarfs within the Hartle's formalism (Hartle, 1967). We used the relativistic Feynman-Metropolis-Teller equation of state (Ro-

tondo et al., 2011c), which generalizes the traditionally used equation of state of Salpeter (1961a). It has been there shown that rotating white dwarfs can be stable up to rotation periods close to 0.3 s (see Boshkayev et al. (2013b) and Sec. B.4.3 for details). This range of stable rotation periods for white dwarfs amply covers the observed rotation rates of SGRs and AXPs  $P \sim (2-12)$  s.

The aim of this work is to give a detailed description of the so-called *low magnetic field magnetars*, SGR 0418+5729 and Swift J1822.3-1606 as massive fast rotating highly magnetized white dwarfs. In addition to these two sources, we also present a similar analysis of the AXP prototype 1E 2259+586; which is the source on which Morini et al. (1988) and Paczynski (1990) proposed the idea of a description of AXPs based on white dwarfs. We thus extend the work of Malheiro et al. (2012) by using precise white dwarf parameters recently obtained by Boshkayev et al. (2013b) for general relativistic uniformly rotating white dwarfs. We present an analysis of the expected Optical and near-Infrared emission from these sources within the white dwarf model and confront the results with the observational data.

### B.4.2. Rotation powered white dwarfs

The loss of rotational energy associated with the spindown of the white dwarf is given by

$$|\dot{E}_{\text{rot}}| = 4\pi^2 I \frac{\dot{P}}{P^3} = 3.95 \times 10^{50} I_{49} \frac{\dot{P}}{P^3} \text{ ergs}^{-1}, \quad (\text{B.4.2})$$

where  $I_{49}$  is the moment of inertia of the white dwarf in units of  $10^{49}$  g cm<sup>2</sup>. This rotational energy loss amply justifies the steady X-ray emission of all SGRs and AXPs (see Malheiro et al., 2012, for details).

The upper limit on the magnetic field obtained by requesting that the rotational energy loss due to the dipole field be smaller than the electromagnetic emission of the magnetic dipole, is given by (see e.g. Ferrari and Ruffini, 1969)

$$B = \sqrt{\frac{3c^3}{8\pi^2} \frac{I}{\bar{R}^6} P \dot{P}} = 3.2 \times 10^{15} \sqrt{\frac{I_{49}}{\bar{R}_8^6} P \dot{P}} \text{ G}, \quad (\text{B.4.3})$$

where  $\bar{R}_8$  is the mean radius of the white dwarf in units of  $10^8$  cm. The mean radius is given by  $\bar{R} = (2R_{\text{eq}} + R_p)/3$  (see e.g. Hartle and Thorne, 1968) with  $R_{\text{eq}}$  and  $R_p$  the equatorial and polar radius of the star.

It is clear that the specific values of the rotational energy loss and the magnetic field depend on observed parameters, such as  $P$  and  $\dot{P}$ , as well as on model parameters, such as the mass, moment of inertia, and mean radius of the rotating white dwarf. It is worth mentioning that Eq. (B.4.3) gives information only on the dipole component of the magnetic field while there is the possibility that close to the star surface contributions from higher multipoles could be also important. As shown by Qadir et al. (1980), the presence of

higher electromagnetic multipoles increases the pulsar braking index to values larger than the traditional value  $n = 3$  of the magneto-dipole radiation.

### B.4.3. Structure and stability of rotating white dwarfs

The rotational stability of fast rotating white dwarfs was implicitly assumed by Malheiro et al. (2012). The crucial question of whether rotating white dwarfs can or not attain rotation periods as short as the ones observed in SGRs and AXPs has been recently addressed by Boshkayev et al. (2013b). The properties of uniformly rotating white dwarfs were computed within the framework of general relativity through the Hartle's formalism (Hartle, 1967). The equation of state for cold white dwarf matter is based on the relativistic Feynman-Metropolis-Teller treatment (Rotondo et al., 2011c), which generalizes the equation of state of Salpeter (1961a). The stability of rotating white dwarfs was analyzed taking into account the mass-shedding limit, inverse  $\beta$ -decay and pycnonuclear instabilities, as well as the secular axisymmetric instability, with the latter determined by the turning point method of Friedman et al. (1988); see Fig. B.29 and Boshkayev et al. (2013b), for details.

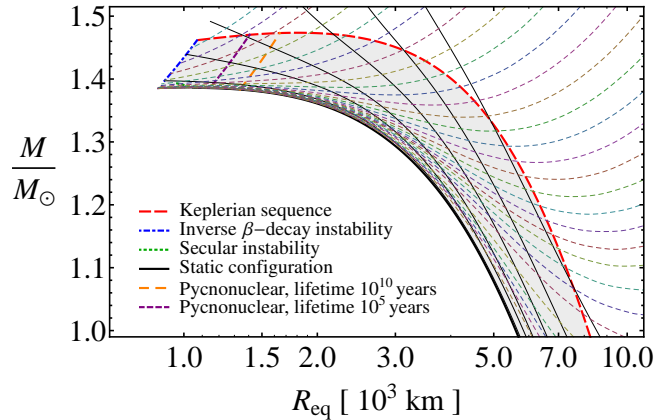


**Figure B.29.:** Mass versus equatorial radius of rotating  $^{12}\text{C}$  white dwarfs (Boshkayev et al., 2013b). The solid black curves correspond to  $J$ -constant sequences, where the static case  $J = 0$  the thickest one. The color thin-dashed curves correspond to  $P$ -constant sequences. The Keplerian sequence is the red thick dashed curve, the blue thick dotted-dashed curve is the inverse  $\beta$  instability boundary, and the green thick dotted curve is the axisymmetric instability line. The orange and purple dashed boundaries correspond to the pycnonuclear C+C fusion densities with reaction mean times  $\tau_{pyc} = 10$  Gyr and 0.1 Myr, respectively. The gray-shaded region is the stability region of rotating white dwarfs.

The minimum rotation period  $P_{\min}$  of white dwarfs is obtained for a configuration rotating at Keplerian angular velocity, at the critical inverse  $\beta$ -decay

density, namely this is the configuration lying at the crossing point between the mass-shedding and inverse  $\beta$ -decay boundaries. The numerical values of the minimum rotation period  $P_{\min} \approx (0.3, 0.5, 0.7, 2.2)$  s were found for Helium, Carbon, Oxygen, and Iron white dwarfs, respectively (Boshkayev et al., 2013b). As a byproduct, these values show that indeed all SGRs and AXPs can be described as rotating white dwarfs because their rotation periods are in the range  $2 \lesssim P \lesssim 12$  s.

The relatively long minimum period of rotating  $^{56}\text{Fe}$  white dwarfs,  $P_{\min} \approx 2.2$  s, lying just at the lower edge of the observed range of rotation periods of SGRs and AXPs, reveals crucial information on the chemical composition of SGRs and AXPs, namely they are very likely made of elements lighter than Iron, such as Carbon or Oxygen.

It can be seen from Fig. B.29 that every  $\Omega = 2\pi/P$  constant sequence intersects the stability region of general relativistic uniformly rotating white dwarfs ( $M$ - $R_{\text{eq}}$  curves inside the shaded region of Fig. B.29) in two points. These two points determine the minimum(maximum) mass  $M_{\min, \max}$  and maximum(minimum) equatorial radius  $R_{\text{eq}}^{\max, \min}$ , for the stability of a white dwarf rotating at the given angular velocity. Associated to the boundary values  $M_{\min, \max}$  and  $R_{\text{eq}}^{\max, \min}$ , we can obtain the corresponding bounds for the moment of inertia of the white dwarf,  $I_{\max, \min}$ , respectively.

We turn now to a specific analysis of the two sources, SGR 0418+5729 and SGR SGR 1822–1606.

#### B.4.4. SGR 0418+5729

##### Bounds on the white dwarf parameters

SGR 0418+5729 has a rotational period of  $P = 9.08$  s, and the upper limit of the spindown rate  $\dot{P} < 6.0 \times 10^{-15}$  was obtained by Rea et al. (2010). The corresponding rotation angular velocity of the source is  $\Omega = 2\pi/P = 0.69$  rad s $^{-1}$ . We show in Table B.13 bounds for the mass, equatorial radius, mean radius, and moment of inertia of SGR 0418+5729 obtained by the request of the rotational stability of the rotating white dwarf, as described in Section B.4.3, for selected chemical compositions. Hereafter we consider only general relativistic rotating Carbon white dwarfs.

##### Solidification and glitches

It has been shown by Malheiro et al. (2012) that the massive white dwarfs consistent with SGRs and AXPs possibly behave as solids since the internal temperature of the white dwarf ( $\sim 10^7$  K) is very likely lower than the crys-

B.4. SGR 0418+5729 and Swift J1822.3-1606 as massive fast rotating highly magnetized white dwarfs

Composition	$M_{\min}$	$M_{\max}$	$R_{\text{eq}}^{\min}$	$R_{\text{eq}}^{\max}$	$\bar{R}_{\min}$	$\bar{R}_{\max}$	$I_{48}^{\min}$	$I_{50}^{\max}$	$B_{\min}^{\text{upper}}$	$B_{\max}^{\text{upper}}$
Helium	1.18	1.41	1.16	6.88	1.15	6.24	3.59	1.48	1.18	2.90
Carbon	1.15	1.39	1.05	6.82	1.05	6.18	2.86	1.42	1.19	3.49
Oxygen	1.14	1.38	1.08	6.80	1.08	6.15	3.05	1.96	1.42	3.30
Iron	0.92	1.11	2.21	6.36	2.21	5.75	12.9	1.01	1.25	0.80

**Table B.13.:** Bounds on the properties of SGR 0418+5729. The masses  $M_{\min, \max}$  are in  $M_{\odot}$ , the equatorial  $R_{\text{eq}}^{\min, \max}$  and mean  $\bar{R}_{\min, \max}$  radii are in units of  $10^8$  cm, the moments of inertia  $I_{48}^{\min}$  and  $I_{50}^{\max}$  are in units of  $10^{48}$  g cm<sup>2</sup> and  $10^{50}$  g cm<sup>2</sup>, respectively. The magnetic fields  $B_{\min}^{\text{upper}}$  and  $B_{\max}^{\text{upper}}$  are in units of  $10^7$  G and  $10^8$  G, respectively.

tallization temperature (see e.g. Shapiro and Teukolsky, 1983a; Usov, 1994)

$$T_{\text{cry}} \simeq 2.3 \times 10^5 \frac{Z^2}{A^{1/3}} \left( \frac{\bar{\rho}}{10^6 \text{ g/cm}^3} \right)^{1/3} \text{ K}, \quad (\text{B.4.4})$$

where  $(Z, A)$  and  $\bar{\rho}$  denote the chemical composition and mean density, respectively.

This fact introduces the possibility in the white dwarf to observe sudden changes in the period of rotation, namely glitches. The expected theoretical values of the fractional change of periods of massive white dwarfs have been shown to be consistent with the values observed in many SGRs and AXPs (see Malheiro et al., 2012, for details).

From the bounds of  $M$  and  $R_{\text{eq}}$  we obtain that the mean density of SGR 0418+5729 must be in the range  $2.3 \times 10^6 \lesssim \bar{\rho} \lesssim 5.7 \times 10^8$  g cm<sup>3</sup>. Correspondingly, the crystallization temperature is comprised in the range  $4.8 \times 10^6$  K  $\lesssim T_{\text{cry}} \lesssim 3.0 \times 10^7$  K, where the lower and upper limits correspond to the configurations of minimum and maximum mass, respectively.

The crystallization temperature obtained here indicates that SGR 0418+5729 should behave as a rigid solid body and therefore glitches during the rotational energy loss, accompanied by radiative events, could happen. Starquakes leading to glitches in the white dwarf will occur with a recurrence time (see e.g. Baym and Pines, 1971; Usov, 1994; Malheiro et al., 2012)

$$\delta t_q = \frac{2\mathcal{D}^2}{\mathcal{B}} \frac{|\Delta P|/P}{|\dot{E}_{\text{rot}}|}, \quad (\text{B.4.5})$$

where

$$\mathcal{B} = 0.33 \frac{4\pi}{3} R_c^3 e^2 Z^2 \left( \frac{\bar{\rho}_c}{A m_p} \right)^{4/3}, \quad \mathcal{D} = \frac{3}{25} \frac{GM_c^2}{R_c},$$

with  $\dot{E}_{\text{rot}}$  the loss of rotational energy given by Eq. (B.4.2),  $M_c$ ,  $R_c$ , and  $\bar{\rho}_c$  are the mass, the radius and the mean density of the solid core, and  $m_p$  is the proton mass.

For the minimum and maximum mass configurations and the upper limit of the spindown rate  $\dot{P} < 6 \times 10^{-15}$ , we obtain a lower limit for recurrence time of starquakes

$$\delta t_q > \begin{cases} 4.2 \times 10^9 (|\Delta P|/P) \text{ yr}, & M = M_{\min} \\ 2.0 \times 10^{12} (|\Delta P|/P) \text{ yr}, & M = M_{\max} \end{cases}. \quad (\text{B.4.6})$$

For typical fractional change of periods  $|\Delta P|/P = 10^{-6}$ , observed in SGRs and AXPs, we obtain  $\delta t_q > 4 \times 10^3 \text{ yr}$  and  $\delta t_q > 2 \times 10^6 \text{ yr}$ , for  $M_{\min}$  and  $M_{\max}$  respectively. These very long starquake recurrent times are in agreement with the possibility that SGR 0418+5729 is an old white dwarf whose magnetospheric activity is settling down, in line with its relatively low spindown rate, magnetic field, and high efficiency parameter  $L_X/\dot{E}_{\text{rot}}$ , with respect to the values of other SGRs and AXPs (see e.g. Fig. 9 in Malheiro et al., 2012).

### Rotation power and magnetic field

Introducing the values of  $P$  and the upper limit  $\dot{P}$  into Eq. (B.4.2) we obtain an upper limit for the rotational energy loss

$$|\dot{E}_{\text{rot}}| < \begin{cases} 9.1 \times 10^{32} \text{ erg s}^{-1}, & M = M_{\max} \\ 4.5 \times 10^{34} \text{ erg s}^{-1}, & M = M_{\min} \end{cases}, \quad (\text{B.4.7})$$

which for any possible mass is larger than the observed X-ray luminosity of SGR 0418+5729,  $L_X = 6.2 \times 10^{31} \text{ erg s}^{-1}$ , assuming a distance of 2 kpc (Rea et al., 2010).

The corresponding upper limits on the magnetic field of SGR 0418+5729, obtained from Eq. (B.4.3) are (see also Table B.13)

$$B < B_{\min, \max}^{\text{upper}} = \begin{cases} 1.2 \times 10^7 \text{ G}, & M = M_{\min} \\ 3.5 \times 10^8 \text{ G}, & M = M_{\max} \end{cases}. \quad (\text{B.4.8})$$

It is worth noting that the above maximum possible value of the surface magnetic field of SGR 0418+5729 obtained for the maximum possible mass of a white dwarf with rotation period 9.08 s,  $B < 3.49 \times 10^8 \text{ G}$ , is even more stringent and improves the previously value given by Malheiro et al. (2012),  $B < 7.5 \times 10^8 \text{ G}$ , based on fiducial white dwarf parameters.

The presence of the magnetic field quantizes the electron spectrum and thus, their scattering with the photons, could generate absorption features in

the spectrum at frequencies of the order of

$$v_{cyc,e} = \frac{eB}{2\pi m_e c} = \begin{cases} 3.4 \times 10^{13} & \text{Hz, } M = M_{\min} \\ 9.8 \times 10^{14} & \text{Hz, } M = M_{\max} \end{cases}, \quad (\text{B.4.9})$$

corresponding to wavelengths 8.9 and 0.3  $\mu\text{m}$ , respectively.

### Prediction of the spindown rate

Assuming that the observed X-ray luminosity is lower than  $|\dot{E}_{\text{rot}}|$ , we obtain the lower limit for the spindown rate

$$\dot{P} > \frac{L_X P^3}{4\pi^2 I} = \begin{cases} 8.3 \times 10^{-18}, & M = M_{\min} \\ 4.1 \times 10^{-16}, & M = M_{\max} \end{cases}, \quad (\text{B.4.10})$$

which in the case of the white dwarf with the maximum possible mass is more stringent than the value reported by Malheiro et al. (2012),  $\dot{P} = 1.18 \times 10^{-16}$ , for a massive white dwarf of fiducial parameters.

### Optical spectrum and luminosity

Durant et al. (2011) observed SGR 0418+5729 with the two wide filters F606W and F110W of the Hubble Space Telescope within the positional error circle derived from Chandra observations of the field of SGR 0418+5729 (Rea et al., 2010). They derive the upper limits of the apparent magnitudes,  $m_{F606W} > 28.6$  and  $m_{F110W} > 27.4$  (Vega system). The approximate distance to the source is  $d = 2 \pm 0.5$  kpc (see Durant et al., 2011, for details). Assuming an interstellar extinction obtained from the  $N_H$  column absorption value observed in the X-ray data,  $A_V = 0.7$ , Durant et al. (2011) obtained the corresponding luminosity upper bounds  $L_{F606W} < 5 \times 10^{28}$  erg s $^{-1}$  and  $L_{F110W} < 6 \times 10^{28}$  erg s $^{-1}$ , respectively.

We use here a similar method, i.e. computing the interstellar extinction values for the V band from the  $N_H$  column absorption value observed in the X-ray data,  $N_H = 1.5 \times 10^{21}$  cm $^{-2}$  (Rea et al., 2010), and then using the empirical formula described in Predehl and Schmitt (1995). Then we have extrapolated the extinction to the other filters by using the method delineated in Cardelli et al. (1989). Since the F606W and the F110W are well approximated by the V and J band, we obtained for the extinction values  $A_{F606W} = 0.83$  and  $A_{F110W} = 0.235$  respectively. The corresponding luminosity upper bounds are, consequently,  $L_{F606W} < 6.82 \times 10^{28}$  erg s $^{-1}$  and  $L_{F110W} < 3.05 \times 10^{28}$  erg s $^{-1}$ .

An estimate of the effective surface temperature can be obtained by approx-

imating the spectral luminosity in these bands by the black body luminosity

$$L = 4\pi R^2 \sigma T^4, \quad (\text{B.4.11})$$

where  $\sigma = 5.67 \times 10^{-5} \text{ erg cm}^{-2} \text{ s}^{-1} \text{ K}^{-4}$  is the Stefan-Boltzmann constant. For a white dwarf of fiducial radius  $R = 10^8 \text{ cm}$ , the upper limits for the surface temperature,  $T < 9.6 \times 10^3 \text{ K}$  and  $T < 9.2 \times 10^3 \text{ K}$ , can be obtained for the F110W and F606W filters, replacing the upper limits for  $L_{F110W}$  and  $L_{F606W}$  in Eq. (B.4.11). These bounds of the surface temperature of the white dwarf can be improved by using the explicit dependence on the radius of the black body surface temperature for each filter. The black body flux at a given frequency  $\nu$ , in the source frame, is given by

$$\nu f_\nu = \pi \frac{2h}{c^2} \frac{\nu^4}{\exp[h\nu/(kT)] - 1}, \quad (\text{B.4.12})$$

where  $h$ ,  $k$ , and  $\nu$  are the Planck constant, the Boltzmann constant, and the spectral frequency respectively. From this expression we can obtain the temperature as a function of the frequency, the observed flux, the distance  $d$  and radius  $R$  of the black body source

$$T = \frac{h\nu}{k \ln \left( 1 + \frac{\pi 2h\nu^4 R^2}{c^2 d^2 F_{\nu,\text{obs}}} \right)}, \quad (\text{B.4.13})$$

where we have used the relation between the flux in the observed and source frames,  $F_{\nu,\text{obs}} = (R/d)^2 \nu f_\nu$ .

The observed fluxes, in units of  $\text{erg cm}^{-2} \text{ s}^{-1}$ , corrected for the extinction are given by

$$F_{\nu,\text{obs}}^{F606W} = 3.6 \times 10^{-20} \nu_{F606W} \times 10^{-0.4(m_{F606W} - A_{F606W})}, \quad (\text{B.4.14})$$

and

$$F_{\nu,\text{obs}}^{F110W} = 1.8 \times 10^{-20} \nu_{F110W} \times 10^{-0.4(m_{F110W} - A_{F110W})}, \quad (\text{B.4.15})$$

where  $\nu_{F606W} = 5.1 \times 10^{14} \text{ Hz}$  and  $\nu_{F110W} = 2.6 \times 10^{14} \text{ Hz}$  are the pivot frequencies of the F606W and F110W filters, respectively.

Introducing the upper limits of the apparent magnitudes of Durant et al. (2011) with the extinction values computed in this work, Eq. (B.4.13) gives the upper bounds on the temperature

$$T < \begin{cases} 1.3 \times 10^4 [\ln(1 + 0.44R_8^2)]^{-1} \text{ K}, & \text{F110W} \\ 2.4 \times 10^4 [\ln(1 + 6.35R_8^2)]^{-1} \text{ K}, & \text{F606W} \end{cases}, \quad (\text{B.4.16})$$

where  $R_8^2$  is the radius of the white dwarf in units of  $10^8 \text{ cm}$  and, following Durant et al. (2011), we have approximated the band integrated flux as  $\nu_c F_\nu$ ,

with  $\nu_c$  the pivot wavelength of the corresponding band filter.

In Fig. B.30, we show the constraints on the  $T$ - $R$  relation obtained from Eq. (B.4.16). We have used the range of radii defined by the minimum and maximum radius of SGR 0418+5729 inferred from the white dwarf stability analysis and summarized in Table B.13.

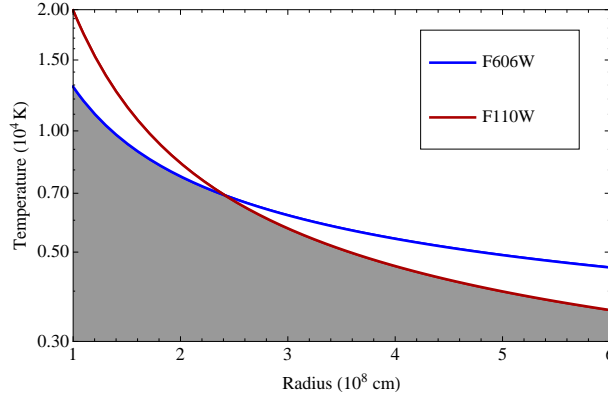


**Figure B.30.:** Temperature-Radius constraint given by Eq. (B.4.16). The gray region corresponds to the possible values for the temperature and the radius of the white dwarf. The range of radii correspond to the one defined by the minimum and maximum mean radius of SGR 0418+5729 inferred from the white dwarf stability analysis and summarized in Table B.13.

Malheiro et al. (2012) obtained for a white dwarf of fiducial parameters the upper limits for the white dwarf surface temperature,  $T < 3.14 \times 10^4$ . We now improve these bounds on the surface temperature using realistic white dwarf parameters. From the minimum and maximum values we have obtained for the mean radius of SGR 0418+5729 (see Table B.13) we obtain for the F110W filter

$$T_{F110W} < \begin{cases} 4.3 \times 10^3 & \text{K, } M = M_{\min} \\ 3.2 \times 10^4 & \text{K, } M = M_{\max} \end{cases}, \quad (\text{B.4.17})$$

and for the F606W filter

$$T_{F606W} < \begin{cases} 4.4 \times 10^3 & \text{K, } M = M_{\min} \\ 1.2 \times 10^4 & \text{K, } M = M_{\max} \end{cases}. \quad (\text{B.4.18})$$

It is clear that these constraints are in agreement with a model based on a massive fast rotating highly magnetic white dwarf for SGR 0418+5729. It is appropriate to recall in this respect some of the observed temperatures of massive isolated white dwarfs,  $1.14 \times 10^4 \text{ K} \leq T \leq 5.52 \times 10^4 \text{ K}$  as shown in the Table 1 in (Ferrario et al., 2005). It is also worth recalling the optical observations of 4U 0142+61 of Hulleman et al. (2000) where the photometric

results of the field of 4U 0142+61 at the 60-inch telescope on Palomar Mountain were found to be in agreement with a  $1.3M_{\odot}$  white dwarf with a surface temperature  $\sim 4 \times 10^5$  K (see Hulleman et al., 2000, for details).

We show in Fig. B.31 the expected optical magnitudes of a white dwarf with surface temperature  $T = 10^4$  K and radius  $R = 1.5 \times 10^8$  cm, located at a distance of 2 kpc. This radius corresponds to the upper limit given by the gray region shown in Fig. B.30, for this specific value of the temperature.

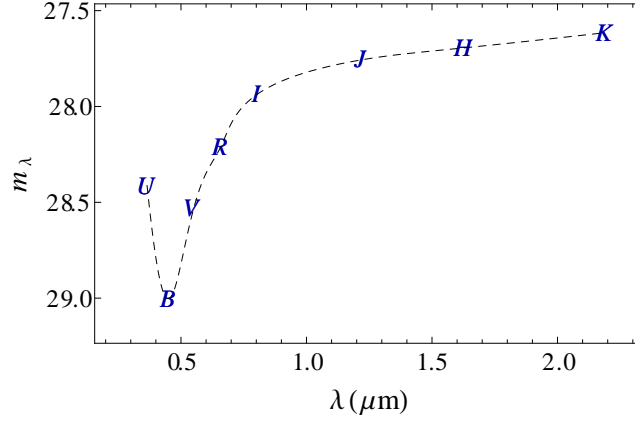


**Figure B.31.:** Expected optical magnitudes of SGR 0418+5729 obtained assuming a simple blackbody for the spectral emission from a white dwarf with surface temperature  $T = 10^4$  K and a radius of  $1.5 \times 10^8$  cm, according to the constraints shown in Fig. B.30.

### B.4.5. Swift J1822.3–1606

#### Bounds of the white dwarf parameters

Swift J1822.3–1606 (or SGR 1822–1606) was recently discovered in July 2011 by Swift Burst Alert Telescope (BAT). A recent X-ray timing monitoring with Swift, RXTE, Suzaku, and XMM-Newton satellites found that SGR 1822-1606 rotates with a period of  $P = 8.44$  s and slows down at a rate  $\dot{P} = 9.1 \times 10^{-14}$  (see Rea et al., 2012, for details). The corresponding rotation angular velocity of the source is  $\Omega = 2\pi/P = 0.74$  rad  $s^{-1}$ . Bounds for the mass, equatorial radius, and moment of inertia of SGR 0418+5729 obtained by the request of the rotational stability of the rotating white dwarf, as described in Section B.4.4, are shown in Table B.14.

#### Solidification and glitches

The mean density of SGR 1822–1606 is in the range  $2.7 \times 10^6 \lesssim \bar{\rho} \lesssim 5.7 \times 10^8$  g  $cm^3$ . The crystallization temperature for such a range following Eq. (B.4.4)

*B.4. SGR 0418+5729 and Swift J1822.3-1606 as massive fast rotating highly magnetized white dwarfs*

Composition	$M_{\min}$	$M_{\max}$	$R_{\text{eq}}^{\min}$	$R_{\text{eq}}^{\max}$	$\bar{R}_{\min}$	$\bar{R}_{\max}$	$I_{48}^{\min}$	$I_{50}^{\max}$	$B_{\min}$	$B_{\max}$
Helium	1.21	1.41	1.16	6.61	1.15	5.99	3.59	1.38	4.84	1.09
Carbon	1.17	1.39	1.05	6.55	1.05	5.93	2.86	1.32	4.87	1.31
Oxygen	1.16	1.38	1.08	6.53	1.08	5.91	3.05	1.83	5.80	1.24
Iron	0.95	1.11	2.21	6.11	2.20	5.53	12.9	0.94	5.09	0.30

**Table B.14.:** Bounds on the properties of Swift J1822.3–1606. The masses  $M_{\min, \max}$  are in  $M_{\odot}$ , the equatorial  $R_{\text{eq}}^{\min, \max}$  and mean  $\bar{R}_{\min, \max}$  radii area in units of  $10^8$  cm, the moments of inertia  $I_{48}^{\min}$  and  $I_{50}^{\max}$  are in units of  $10^{48}$  g cm<sup>2</sup> and  $10^{50}$  g cm<sup>2</sup>, respectively. The magnetic fields  $B_{\min}$  and  $B_{\max}$  are in units of  $10^7$  G and  $10^9$  G, respectively.

is then in the range  $5.0 \times 10^6$  K  $\lesssim T_{\text{cry}} \lesssim 3.0 \times 10^7$  K, which indicates that SGR 1822-1606 will likely behave as a rigid solid body.

For the minimum and maximum mass configurations and the spindown rate  $\dot{P} = 9.1 \times 10^{-14}$ , we obtain a lower limit for recurrence time of starquakes

$$\delta t_q > \begin{cases} 2.6 \times 10^8 (|\Delta P|/P) \text{ yr}, & M = M_{\min} \\ 1.1 \times 10^{11} (|\Delta P|/P) \text{ yr}, & M = M_{\max} \end{cases}, \quad (\text{B.4.19})$$

which for a typical fractional change of period  $|\Delta P|/P \sim 10^{-6}$  gives  $\delta t_q > 3 \times 10^2$  yr and  $\delta t_q > 10^5$  yr, for  $M_{\min}$  and  $M_{\max}$  respectively. The long recurrence time for starquakes obtained in this case, confirms the similarities between SGR 1822–1606 and SGR 0418+5729 as old objects with a settling down magnetospheric activity.

### Rotation power and magnetic field

Using the observed values of  $P$  and  $\dot{P}$ , we obtain from Eq. (B.4.2) a rotational energy loss

$$|\dot{E}_{\text{rot}}| \approx \begin{cases} 1.7 \times 10^{34} \text{ erg s}^{-1}, & M = M_{\max} \\ 7.9 \times 10^{35} \text{ erg s}^{-1}, & M = M_{\min} \end{cases}, \quad (\text{B.4.20})$$

which amply justifies the observed X-ray luminosity of SGR 1822–1606,  $L_X = 4 \times 10^{32}$  erg s<sup>-1</sup>, obtained assuming a distance of 5 kpc (see Rea et al., 2012, for details).

The surface magnetic field of SGR 1822.3–1606, as given by Eq. (B.4.3), is then between the values (see Table B.14)

$$B = \begin{cases} 4.9 \times 10^7 \text{ G}, & M = M_{\min} \\ 1.3 \times 10^9 \text{ G}, & M = M_{\max} \end{cases}. \quad (\text{B.4.21})$$

Corresponding to the above magnetic fields, the electron cyclotron fre-

quencies are

$$\nu_{cyc,e} = \frac{eB}{2\pi m_e c} = \begin{cases} 1.4 \times 10^{14} & \text{Hz, } M = M_{\min} \\ 3.6 \times 10^{15} & \text{Hz, } M = M_{\max} \end{cases}, \quad (\text{B.4.22})$$

that correspond to wavelengths 2.2 and 0.08  $\mu\text{m}$ , respectively.

### Optical spectrum and luminosity

Rea et al. (2012) observed the field of SGR 1822–1606 with the Gran Telescopio Canarias (GranTeCan) within the Swift-XRT position (Pagani et al., 2011). Three sources (S1, S2, and S3) were detected with the Sloan  $z$  filter with corresponding  $z$ -band magnitudes  $m_{z,S1} = 18.13 \pm 0.16$ ,  $m_{z,S2} = 20.05 \pm 0.04$ , and  $m_{z,S3} = 19.94 \pm 0.04$  (see Rea et al., 2012, for details). No additional objects were found to be consistent with the Swift-XRT position up to a magnitude  $m_z = 22.2 \pm 0.2$  ( $3\sigma$ ).

In addition, data from the UK Infrared Deep Sky Survey (UKIDSS) for the field of SGR 1822–1606 were found to be available, giving the magnitudes of the three aforementioned sources in the  $J$ ,  $H$ , and  $K$  bands;  $m_{J,i} = (13.92, 16.62, 16.43)$ ,  $m_{H,i} = (12.37, 15.75, 15.40)$ , and  $m_{K,i} = (11.62, 15.20, 14.88)$ , where the index  $i$  indicates the values for the sources S1, S2, and S3. In addition to S1, S2, and S3, no sources were detected within the consistent position up to the limiting magnitudes  $m_J = 19.3$ ,  $m_H = 18.3$ , and  $m_K = 17.3$  ( $5\sigma$ ).

We repeat the same analysis for SGR 0418+5729 to the case of SGR 1822–1606. We consider only the upper limits, since the three sources reported in Rea et al. (2012), S1, S2 and S3, are very luminous to be a white dwarf at the distance considered for the SGR,  $d \approx 5$  kpc. From the column density value,  $N_H = 7 \times 10^{21} \text{ cm}^{-2}$ , we obtain an extinction in the  $V$ -band of  $A_V = 3.89$ . From the Cardelli et al. (1989) relation we obtain the extinction values for the four bands considered,  $A_z = 1.86$ ,  $A_J = 1.10$ ,  $A_H = 0.74$  and  $A_K = 0.44$ . The extinction corrected upper limits do not put very strong constraints to the temperature and the radius of the white dwarf, due to the very large distance assumed for SGR 1822–1606. We show in Fig B.32 the expected extinction-corrected magnitudes for a white dwarf with a temperature  $T = 10^4$  K and a radius  $R = 1.5 \times 10^8$  cm at a distance of 5 kpc. We obtain a very deep value for the  $K$ -band of  $\approx 30$ . We conclude that, if SGR 1822–1606 is at the distance of 5 kpc assumed by Rea et al. (2012), it will be hard to detect the white dwarf. On the contrary, a possible detection would lead to a more precise determination of the distance.

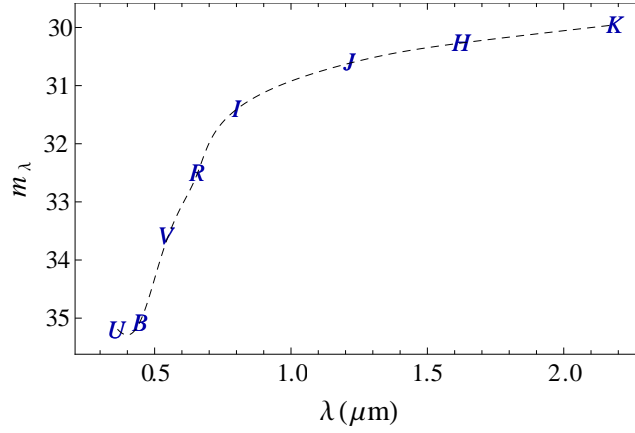


**Figure B.32.:** Expected optical magnitudes of SGR 1822–1606 assuming a blackbody spectral emission from a white dwarf with surface temperature  $T = 10^4$  K and a radius of  $1.5 \times 10^8$  cm.

### B.4.6. 1E 2259+586

#### Bounds of the white dwarf parameters

In addition to be considered as the AXP prototype, 1E 2259+586 is the source on which Morini et al. (1988) and Paczynski (1990) based their pioneering idea of describing AXPs as massive fast rotating and highly magnetized white dwarfs. This source is pulsating in X-rays with a period of  $P = 6.98$  s (Fahlman and Gregory, 1981), its spindown rate is  $\dot{P} = 4.8 \times 10^{-13}$  (Davies et al., 1990) and emits X-rays with a luminosity of  $L_X = 1.8 \times 10^{34}$  erg s $^{-1}$  (Gregory and Fahlman, 1980; Hughes et al., 1981; Morini et al., 1988). The corresponding rotation angular velocity of the source is  $\Omega = 2\pi/P = 0.90$  rad s $^{-1}$ . The obtained bounds for the mass, equatorial radius, and moment of inertia of 1E 2259+586 are shown in Table B.15.

Composition	$M_{\min}$	$M_{\max}$	$R_{\text{eq}}^{\min}$	$R_{\text{eq}}^{\max}$	$\bar{R}_{\min}$	$\bar{R}_{\max}$	$I_{48}^{\min}$	$I_{50}^{\max}$	$B_{\min}$	$B_{\max}$
Helium	1.28	1.41	1.15	5.94	1.15	5.39	3.56	1.12	1.26	2.30
Carbon	1.24	1.39	1.04	5.88	1.04	5.34	2.84	1.08	1.27	2.76
Oxygen	1.23	1.38	1.08	5.86	1.08	5.32	3.05	1.52	1.52	2.60
Iron	1.00	1.11	2.23	5.49	2.21	4.98	13.1	0.78	1.33	0.62

**Table B.15.:** Bounds on the properties of 1E 2259+586. The masses  $M_{\min, \max}$  are in  $M_{\odot}$ , the equatorial  $R_{\text{eq}}^{\min, \max}$  and mean  $\bar{R}_{\min, \max}$  radii area in units of  $10^8$  cm, the moments of inertia  $I_{48}^{\min}$  and  $I_{50}^{\max}$  are in units of  $10^{48}$  g cm $^2$  and  $10^{50}$  g cm $^2$ , respectively. The magnetic fields  $B_{\min}$  and  $B_{\max}$  are in units of  $10^8$  G and  $10^9$  G, respectively.

### Solidification and glitches

The mean density of SGR 1822–1606 is in the range  $3.9 \times 10^6 \lesssim \bar{\rho} \lesssim 5.9 \times 10^8$  g cm<sup>3</sup>. The crystallization temperature for such a range following Eq. (B.4.4) is then in the range  $5.7 \times 10^6$  K  $\lesssim T_{\text{cry}} \lesssim 3.0 \times 10^7$  K, which indicates that SGR 1822–1606 will likely behave as a rigid solid body.

For the minimum and maximum mass configurations and the spindown rate  $\dot{P} = 4.8 \times 10^{-13}$ , we obtain a lower limit for recurrence time of starquakes

$$\delta t_q > \begin{cases} 4.5 \times 10^7 (|\Delta P|/P) \text{ yr,} & M = M_{\text{min}} \\ 1.2 \times 10^{10} (|\Delta P|/P) \text{ yr,} & M = M_{\text{max}} \end{cases}, \quad (\text{B.4.23})$$

which for a typical fractional change of period  $|\Delta P|/P \sim 10^{-6}$  gives  $\delta t_q > 45$  yr and  $\delta t_q > 1.2 \times 10^4$  yr, for  $M_{\text{min}}$  and  $M_{\text{max}}$  respectively. This recurrence time for starquakes is much shorter than the ones of SGR 0418+5729 and SGR 1822–1606, indicating 1E 2259+586 as a very active source in which glitches and outburst activity, as the one observed in 2002 (Kaspi et al., 2003; Woods et al., 2004), can occur with relatively high frequency. It is interesting to note that even more frequent, with recurrence times of  $\lesssim 4$  yr, can be glitches of minor intensity  $|\Delta P|/P \lesssim 10^{-7}$ .

### Rotation power and magnetic field

Using the observed values of  $P$  and  $\dot{P}$ , we obtain from Eq. (B.4.2) a rotational energy loss

$$|\dot{E}_{\text{rot}}| \approx \begin{cases} 1.6 \times 10^{35} \text{ erg s}^{-1}, & M = M_{\text{max}} \\ 6.0 \times 10^{36} \text{ erg s}^{-1}, & M = M_{\text{min}} \end{cases}, \quad (\text{B.4.24})$$

much larger than the observed X-ray luminosity,  $L_X = 1.8 \times 10^{34}$  erg s<sup>-1</sup>, obtained assuming a distance of  $3.2 \pm 0.2$  kpc (see Kothes and Foster, 2012, for details).

The surface magnetic field of 1E 2259+586 inferred from Eq. (B.4.3) is (see Table B.15)

$$B = \begin{cases} 1.3 \times 10^8 \text{ G,} & M = M_{\text{min}} \\ 2.8 \times 10^9 \text{ G,} & M = M_{\text{max}} \end{cases}. \quad (\text{B.4.25})$$

Corresponding to the above magnetic fields, the electron cyclotron frequencies are

$$\nu_{\text{cyc},e} = \begin{cases} 3.6 \times 10^{14} \text{ Hz,} & M = M_{\text{min}} \\ 7.8 \times 10^{15} \text{ Hz,} & M = M_{\text{max}} \end{cases}, \quad (\text{B.4.26})$$

that correspond to wavelengths 0.8 and 0.04  $\mu\text{m}$ , respectively.

### Optical spectrum and luminosity

Using data from the Keck telescope, Hulleman et al. (2001) established a faint near-IR counterpart of 1E 2259+586 with a magnitude  $K_s = 21.7 \pm 0.2$ , consistent with the position given by Chandra. In addition, upper limits in the optical bands  $R = 26.4$ ,  $I = 25.6$ , and  $J = 23.8$ , were placed. From the column density obtained by Patel et al. (2001),  $N_H = 9.3 \pm 0.3 \times 10^{21} \text{ cm}^{-2}$ , and using again the empirical formula described of Predehl and Schmitt (1995), one obtains the absorption  $A_V = N_H / (1.79 \times 10^{21} \text{ cm}^{-2})$ , which Hulleman et al. (2001) used to obtain the extinction in the other bands  $A_R = 4.3$ ,  $A_I = 3.1$ ,  $A_J = 1.4$ ,  $A_K = 0.6$ .

It is known that the emission in the  $K$  band, the excess in the near-IR, is typically produced by the presence of a disk; see for instance (Hulleman et al., 2000) for the case of 4U 0142+61 and (Hulleman et al., 2001) for the present source 1E2259+586, although in the context of a fallback disk around a neutron star. We fit the spectrum of 1E 2259+586 as the sum of a black body component

$$F_{\text{BB}} = \pi \frac{2h}{c^2} \left( \frac{R_{\text{WD}}}{d} \right)^2 \frac{\nu^3}{e^{h\nu/(k_B T)} - 1}, \quad (\text{B.4.27})$$

where  $R_{\text{WD}}$  and  $T$  the radius and effective temperature of the white dwarf, and a passive flat, opaque dust disk (see e.g. Jura, 2003; Lorén-Aguilar et al., 2009)

$$F_{\text{disk}} = 12\pi^{1/3} \cos i \left( \frac{R_{\text{WD}}}{d} \right)^2 \left( \frac{2k_B T}{3h\nu} \right)^{8/3} \left( \frac{h\nu^3}{c^2} \right) \int_{x_{\text{in}}}^{x_{\text{out}}} \frac{x^{5/3}}{e^x - 1} dx, \quad (\text{B.4.28})$$

where  $i$  is the inclination angle of the disk, which we assume as zero degrees,  $x_{\text{in}} = h\nu/(k_B T_{\text{in}})$ ,  $x_{\text{out}} = h\nu/(k_B T_{\text{out}})$ , with  $T_{\text{in}}$  and  $T_{\text{out}}$  the temperatures of the disk at the inner and outer radii, respectively. These temperatures are related to the radii  $R_{\text{in}}$  and  $R_{\text{out}}$  of the disk through  $T_{\text{in,out}} = (2/3\pi)^{1/4} (R_{\text{WD}}/R_{\text{in,out}})^{3/4} T$ .

The total flux is then given by  $F_{\text{BB+disk}} = F_{\text{BB}} + F_{\text{disk}}$ . Since we have only one point from the observational data, the flux in the  $K_s$  band, it is difficult to place constraints on the spectrum parameters. However, we can use the fact that the emission has to respect the upper limits in the  $R$ ,  $I$ , and  $J$  bands. We have fixed the radius of the white dwarf as  $R_{\text{WD}} = 3 \times 10^8 \text{ cm}$ , a value in the interval of stability of Table B.15, and for the outer radius of the passive disk we give a typical value  $R_{\text{out}} = R_{\odot}$ . We found that good fitting values of the other parameters are  $T = 7.0 \times 10^4 \text{ K}$  and  $T_{\text{in}} = 2.0 \times 10^3 \text{ K}$ . We show in Fig. B.33 the observed spectrum of 1E 2259+586 in the IR, optical, and UV bands and the composite black body + disk model spectrum. The knowledge of more data besides the  $K_s$  band will lead to a definite determination of the parameter of the model and to the confirmation of the white dwarf nature of 1E 2259+586.

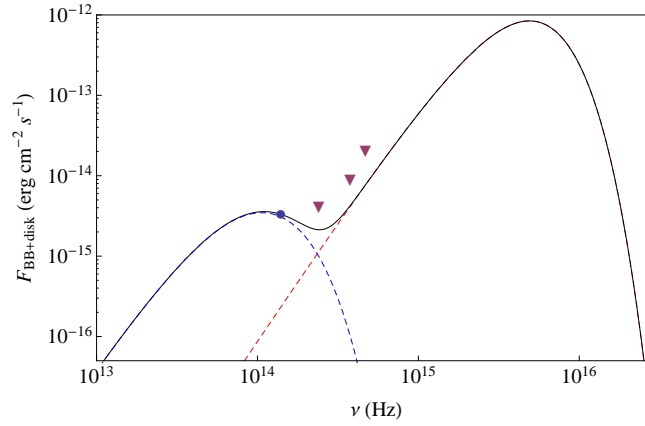


**Figure B.33.:** Observed and fitted spectrum of 1E 2259+586. The filled circle is the observed flux in the  $K_s$  band, and the triangles are the upper limits in the  $R$ ,  $I$ , and  $J$  bands. The parameters of the black body+disk spectrum are  $R_{\text{WD}} = 3.0 \times 10^8$  cm,  $T = 7.0 \times 10^4$  K,  $T_{\text{in}} = 2.0 \times 10^3$  K, and  $R_{\text{out}} = R_{\odot}$ . The blue-dashed curve is the contribution of the disk and the red-dashed curve is the contribution from a pure black body, the total spectrum is represented by the solid black curve.

It is worth to recall that the location of 1E 2259+586 appears to be associated to the supernova remnant G109.1–1.0 (CTB 109) whose age is estimated to be  $t - t_0 = (12\text{--}17)$  kyr (Gregory and Fahlman, 1980; Hughes et al., 1981). Paczynski (1990) proposed a merger of a binary of  $\sim (0.7\text{--}1)M_{\odot}$  white dwarfs that leads both to the formation of a fast rotating white dwarf and to the supernova remnant. Recent simulations of  $(0.8\text{--}0.9M_{\odot})$  white dwarf-white dwarf mergers (see e.g. Pakmor et al., 2010) point however to supernova events not very efficient energetically, below the observed explosion energy  $\sim 7.4 \times 10^{50}$  erg of G109.1–1.0 (see e.g. Sasaki et al., 2004). Another interesting possibility was advanced by Malheiro et al. (2012) that this system could be originated from a tight binary system composed of a white dwarf and a late evolved companion star, approaching the process of gravitational collapse. The collapse of the companion star, either to a neutron star or to a black hole, leads to mass loss which can unbind the original binary system. If the loss of mass in the supernova explosion is  $M_{\text{loss}} < M/2$  with  $M$  the total mass of the binary (see e.g. Ruffini, 1973), the system holds bound and therefore the object will lie close to the center of the supernova remnant. Both explanations are interesting and deserve further investigation. These two scenarios may well explain the presence of a disk of material around the white dwarf, either as material expelled from the white dwarf binary merger (see e.g. Lorén-Aguilar et al., 2009) in the scenario of Paczynski (1990), or as material coming from the supernova explosion and which is captured by the white dwarf in the scenario of Malheiro et al. (2012). As we have seen, the presence of such a disk explains the emission in the near-IR observed in sources such as 4U 0142+61

(see e.g. Hulleman et al., 2000) and in the present case of 1E 2259+586.

### **B.4.7. Concluding Remarks**

We have described SGR 0418+5729, Swift J1822.3-1606, and 1E 2259+586 as massive fast rotating highly magnetized white dwarfs. The reasons for the choice of these three sources are twofold: 1) the observations of SGR 0418+5729 (Rea et al., 2010),  $P = 9.08$  and  $\dot{P} < 6.0 \times 10^{-15}$ , and more recently the ones of Swift J1822.3-1606 (Rea et al., 2012),  $P = 8.44$  s and  $\dot{P} = 9.1 \times 10^{-14}$ , challenge the description of these sources as ultramagnetized neutron stars, as required by the magnetar model; 2) 1E 2259+586 is considered the AXP prototype with very good observational data including the best example of the glitch-outburst connection (see e.g. Woods et al., 2004) and, in addition, it represents a historical object being the one analyzed by Morini et al. (1988) and Paczynski (1990), where the canonical description based on white dwarfs was proposed.

We have shown that SGR 0418+5729 and Swift J1822.3-1606 are in full agreement with massive fast rotating highly magnetic white dwarfs. We have improved the white dwarf parameters given by Malheiro et al. (2012) for these sources and also for 1E 2259+586. From an analysis of the rotational stability of Boshkayev et al. (2013b), we have given bounds for the mass, radius, moment of inertia, and magnetic field of these sources; see Tables B.13, B.14, and B.15 for details.

We have improved the theoretical prediction of the lower limit for the spin-down rate of SGR 0418+5729, for which only the upper limit,  $\dot{P} < 6.0 \times 10^{-15}$ , is currently known (Rea et al., 2010). Based on a white dwarf of fiducial parameters, Malheiro et al. (2012) predicted for SGR 0418+5729 the lower limit  $\dot{P} > 1.18 \times 10^{-16}$ . Our present analysis based on realistic general relativistic rotating white dwarfs allows us to improve this prediction; see Eq. (B.4.10) in Sec. B.4.4 for the new numerical values. In the case of a white dwarf close to the critical mass, this new lower limit gives a very stringent constraint on the spindown rate of SGR 0418+5729,  $\dot{P} = 4 \times 10^{-16} < \dot{P} < 6 \times 10^{-15}$ , which we submit for observational verification. Indeed, after the submission of this work, Rea et al. (2013) reported the confirmation of the spin-down rate of SGR 0418+5729,  $\dot{P} = 4 \times 10^{-15}$ , at 3.5 sigma confidence level. This measurement fully confirms the results of Malheiro et al. (2012), see Eq. (B.4.1), as well as the more stringent constraints presented in this work, see Eq. (B.4.10), which being presented in advance to the observations have to be considered as predictions. This fact clearly represents an observational support for the white dwarf model of SGRs/AXPs.

In this line it is worth to mention the recent discussions on the high uncertainties and different results claimed by different authors on the value of the first period time derivative of Swift J1822.3-1606 (see Tong and Xu, 2012,

and references therein for details). Here we have used the value reported by Rea et al. (2012). However, it would be interesting also in this case to put a theoretical lower limit with the white dwarf mode. Using  $L_X = 4 \times 10^{32}$  erg s<sup>-1</sup> at a distance of 5 kpc (Rea et al., 2012), we obtain a lower limit  $\dot{P} \geq L_X P^3 / (4\pi^2 I) \approx 2.13 \times 10^{-15}$  for a <sup>12</sup>C white dwarf close to its maximum mass; see Table B.15. Indeed, this limit bounds from below all the observationally claimed spin-down rates for this source, known up to now.

We have given in Eqs. (B.4.9), (B.4.22), and (B.4.26) an additional prediction of the frequencies at which absorption features could be present in the spectrum of SGR 0418+5729, Swift J1822.3-1606, and 1E2259+586 respectively, as a result of the scattering of photons with electrons whose energy spectrum is quantized due to the magnetic field. The range we have obtained for such frequencies fall between the infrared and UV bands. In this line it is important to remark that magnetic fields in white dwarfs raging from 10<sup>7</sup> G up to 10<sup>9</sup> G are routinely observed; see e.g. Külebi et al. (2009), Külebi et al. (2010a), Kepler et al. (2010), and very recently Kepler et al. (2012) where from the Data Release 7 of the Sloan Digital Sky Survey, white dwarfs with magnetic fields in the range from around 10<sup>6</sup> G to 7.3 × 10<sup>8</sup> G has been found from the analysis of the Zeeman splitting of the Balmer absorption lines. Deep photometric and spectrometric observations in the range of cyclotron frequencies predicted in this work are therefore highly recommended to detect possible absorptions and line splitting features in the spectra of SGRs and AXPs.

We have presented the optical properties of SGR 0418+5729, Swift J1822.3-1606, and 1E 2259+586 as expected from a model based on white dwarfs. We have inferred the surface temperature and predicted the emission fluxes in the UV, Optical, and IR bands. We have shown that indeed the available observational data are consistent with a white dwarf model for these objects. In the particular case of 1E 2259+586 the observed excess in the near-IR is explained with the presence of a disk of dust around the white dwarf. Such a disk might be the result of material expelled during the merger of a white dwarf binary progenitor (Paczynski, 1990; Rueda et al., 2013) or as the result of material from the supernova explosion of an evolved star companion of the white dwarf in the binary scenario proposed by Malheiro et al. (2012) for the SGR/AXP-supernova connection.

It is important to discuss briefly the persistent X-ray emission of SGRs/AXPs. The time integrated X-ray spectrum is often well described by a composite black body + power-law model with temperatures of the order of  $k_B T_{BB} \sim 0.1$  keV (see e.g. Göhler et al., 2005). Such a black body component corresponds to temperatures  $T_{BB} \sim 10^6$  K, higher than the surface temperature of a white dwarf, as the ones predicted in this work. This clearly Spoints to an X-ray emission of magnetospheric origin and so this black body temperature of the X-ray spectrum is not to be associated with the white dwarf effective temperature (see e.g. Malheiro et al., 2012). A possible mechanism for the X-ray quiescent emission from a magnetized white dwarf was underlined by

Usov (1993): the reheating of the magnetosphere owing to the bombardment of the backward moving positrons created in the pair cascades formed in the interaction of the high-energy photons with the ultra-relativistic electrons. As shown by Usov (1993) in the specific case of 1E 2259+586, such a reheating of the polar caps is able to produce a stable X-ray luminosity  $L_X \sim 10^{35}$  erg s<sup>-1</sup>, in agreement with observations.

It is worth to mention that a well-known observational problem of SGRs and AXPs is the uncertainty in the estimation of the distances of the sources (see e.g. Kothes and Foster, 2012, for a critical discussion on the distance of 1E2259+586). These uncertainties strongly affect the estimates of the interstellar reddening  $A_V$ , which is crucial for the precise calculation of the source properties and therefore for a clear identification of the nature of the compact object. Deeper observations of Hubble and VLT are thus strongly recommended to establish the precise values of the luminosity in the Optical and in the near-IR bands, which will verify the white dwarf nature of SGRs and AXPs.

We encourage future observational campaigns from space and ground to verify all the predictions presented in this work.

## **B.5. A white dwarf merger as progenitor of the AXP 4U 0142+61?**

SGRs are sources of short ( $\sim 100$  ms), repeating bursts of soft  $\gamma$ -ray and X-ray radiation at irregular intervals, and share with AXPs several similarities, like rotation periods clustered between 2 and 12 s, and high magnetic fields. Their observed spindown rates range from  $\dot{P} \sim (10^{-15}$  to  $10^{-10})$ , and have typical X-ray luminosities in quiescent state  $L_X \sim 10^{35}$  ergs $^{-1}$ . Currently, it is widely accepted that these objects are magnetars (Duncan and Thompson, 1992; Thompson and Duncan, 1995), although there are competing scenarios that challenge this model — see, for instance, the excellent and recent review of Mereghetti (2008b), and references therein. Recently, Malheiro et al. (2012), following the pioneering works of Morini et al. (1988) and Paczynski (1990), have suggested an alternative model that could explain some properties of these sources. This model involves highly-magnetized white dwarfs. For this model to be viable the masses of the white dwarfs need to be rather large ( $M \gtrsim 1.2 M_\odot$ ), their magnetic fields should range from  $B \approx 10^7$  G all the way to  $10^{10}$  G, and the rotation periods should be rather small, of the order of a few seconds. The most apparent drawback of this scenario, namely the rotational stability of fast rotating white dwarfs, has been recently analyzed. Specifically, the crucial question of whether rotating white dwarfs can have rotation periods as short as the ones observed in AXPs has been recently addressed by Boshkayev et al. (2013b), who found that the minimum rotation period of typical carbon-oxygen white dwarfs is  $\sim 0.5$  s. Thus, since AXPs have rotation periods larger than this value they could be white dwarfs.

The existence of white dwarfs with magnetic fields ranging from  $10^7$  G up to  $10^9$  G is solidly confirmed by observations (Külebi et al., 2009). Observations show that most HFMDs are massive, and moreover, that none of them belongs to a non-interacting binary system, pointing towards a binary origin. However, although long-suspected (Wickramasinghe and Ferrario, 2000), it has only been recently shown that HFMDs might be the result of white dwarf mergers. SPH simulations of the coalescence process indicate that the result of the merger is a white dwarf that contains the mass of the undisrupted primary, surrounded by a hot corona made of about half of the mass of the disrupted secondary. In addition, a rapidly rotating Keplerian disk which contains the rest of the material of the secondary is also formed, as little mass is ejected from the system during the coalescence process. The rapidly-rotating hot corona is convective and an efficient  $\alpha\omega$  dynamo can produce magnetic fields of up to  $B \sim 10^{10}$  G (García-Berro et al., 2012).

In view of these considerations it is natural to ask ourselves if such binary mergers could also explain the properties of some AXPs. Here we explore such possibility for the specific case of the peculiar AXP 4U 0142+61. This AXP is by far the best observed source in the near-infrared (NIR), optical,

	Minimum	Maximum
$M (M_{\odot})$	1.16	1.39
$R_{\text{eq}} (10^8 \text{ cm})$	1.05	6.66
$\langle R \rangle (10^8 \text{ cm})$	1.05	6.03
$I (\text{g cm}^2)$	$2.9 \times 10^{48}$	$1.4 \times 10^{50}$

**Table B.16.:** Bounds for the mass, radius and moment of inertia of 4U 0142+61.

and ultraviolet (UV) bands and has two characteristics that make it a peculiar object. The first one is that 4U 0142+61 presents a confirmed infrared excess (Hulleman et al., 2000) that might be attributed to an accretion disk, whereas the second one is that it is too bright for its cooling age, thus challenging the conventional magnetar model. Here we show that the properties of this AXP can be well explained by a model in which the central compact remnant is a massive magnetized white dwarf resulting from the merger of two otherwise ordinary white dwarfs, surrounded by the heavy accretion disk produced during the merger.

### B.5.1. A model for 4U 0142+61

To start with, we compute the approximate mass and radius of 4U 0142+61. The stability of general relativistic uniformly rotating white dwarfs has been recently studied (Boshkayev et al., 2013b), and it has been shown that constant rotation period sequences intersect the stability region of white dwarfs in two points that determine lower and upper bounds for the mass, equatorial/polar radii and moment of inertia. In Table B.16 we show the bounds for 4U 0142+61. In this table  $\langle R \rangle = (2R_{\text{eq}} + R_{\text{p}})/3$  denotes the mean-radius, where  $R_{\text{eq}}$  and  $R_{\text{p}}$  are, respectively, the equatorial and polar radii.

#### IR, optical and UV photometry

We next fitted the spectrum of 4U 0142+61 as the sum of two components. The first one is a black body:

$$F_{\text{BB}} = \pi \frac{2h}{c^2} \left( \frac{R_{\text{WD}}}{d} \right)^2 \frac{\nu^3}{e^{h\nu/(k_{\text{B}}T_{\text{eff}})} - 1}, \quad (\text{B.5.1})$$

where  $R_{\text{WD}}$  and  $T_{\text{eff}}$  are, respectively, the radius and effective temperature of the white dwarf. As it will be shown in Sect. B.5.1, the system now behaves as an ejector, inhibiting the accretion of the disk material onto the central white dwarf. Thus, for the second component we adopted the black body disk model of Chiang and Goldreich (1997), which is more appropriate for

these systems (García-Berro et al., 2007):

$$F_{\text{disk}} = 12\pi^{1/3} \cos i \left( \frac{R_{\text{WD}}}{d} \right)^2 \left( \frac{2k_{\text{B}}T_{\text{eff}}}{3hv} \right)^{8/3} \left( \frac{hv^3}{c^2} \right) \times \int_{x_{\text{in}}}^{x_{\text{out}}} \frac{x^{5/3}}{e^x - 1} dx, \quad (\text{B.5.2})$$

where  $i$  is the inclination angle of the disk, which we assume to be face-on, and  $x = hv/(k_{\text{B}}T)$ . In this model the disk temperature  $T$  varies as  $r^{-3/4}$  (Chiang and Goldreich, 1997), with  $r$  the distance from the center of the white dwarf. It is worth mentioning that in previous studies of 4U 0142+61 (Hulleman et al., 2000; Wang et al., 2006) the irradiated disk model of Vrtilik et al. (1990) has been used instead, but this model is more appropriate for accreting sources.

We obtained that the spectrum best-fit parameters are:  $R_{\text{WD}} \approx 0.006 R_{\odot}$ ,  $T_{\text{eff}} \approx 1.31 \times 10^5$  K, inner and outer disk radii  $R_{\text{in}} = 0.97 R_{\odot}$ ,  $R_{\text{out}} = 51.1 R_{\odot}$  and correspondingly inner and outer disk temperatures  $T_{\text{in}} \approx 1950$  K and  $T_{\text{out}} \approx 100$  K, respectively. In Fig. B.34 we show the photometric data of 4U 0142+61 and our best-fit composite spectrum. The agreement of the composite spectrum with the observational data is quite good, taking into account that the high variability of the source in these bands can lead to changes in the optical fluxes of up to one order of magnitude (Durant and van Kerkwijk, 2006c). Thus, the white dwarf model is compatible with the observed photometry of 4U 0142+61, as it seems to occur for SGR 0418+5729, Swift J1822.3–1606, and 1E 2259+586 (Boshkayev et al., 2013a).

To check whether this is a realistic and consistent model for 4U 0142+61, we ran a SPH simulation of the merger of a  $0.6 + 1.0 M_{\odot}$  binary white dwarf, which results in a central remnant of  $\approx 1.1 M_{\odot}$ , with a radius  $R_{\text{WD}} \approx 0.006 R_{\odot}$ , in agreement with the photometric value. We recall that the central white dwarf will accrete some material from the surrounding disk (of mass  $M_{\text{disk}} \approx 0.5 M_{\odot}$ ) and, thus, will shrink a little. Moreover, the rotation period is  $P \approx 15.7$  s and the moment of inertia of the central white dwarf and the hot corona is  $I \approx 2.0 \times 10^{50}$  g cm<sup>2</sup>, which is slightly larger than our maximum estimate — see Table B.16. Furthermore, the magnetic field generated in the differentially-rotating hot corona produced in the aftermath of the merger amounts to  $B \sim 10^{10}$  G (García-Berro et al., 2012) which amply explains the magnetic field of 4U 0142+61, see Sect. B.5.1.

### The age and magnetic field of 4U 0142+61

The presence of a disk around the magnetized white dwarf plays a key role in the evolution of its rotation period. This results from a delicate interplay between the interaction of the disk with the magnetosphere of the star, and accretion of disk matter onto the surface of the white dwarf. A solution

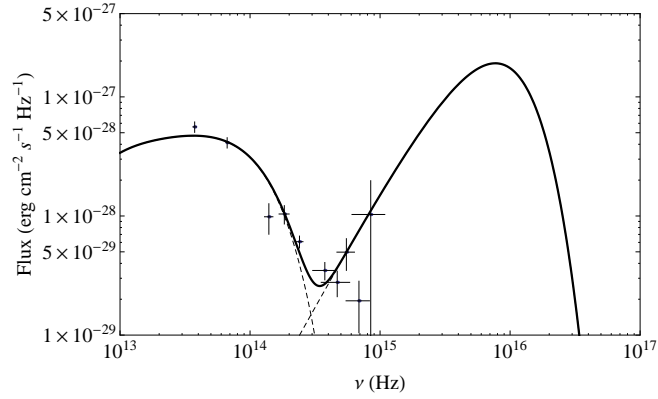


**Figure B.34.:** Observed and fitted spectrum of 4U 0142+61. Due to the high variability of the source in the optical bands we average all the existing data of the source in the different bands. All these data come from observations from 31 October 1994 up to 26 July 2005 (Hulleman et al., 2000, 2004; Dhillon et al., 2005; Morii et al., 2005; Durant and van Kerkwijk, 2006c; Morii et al., 2009). The result of the average is  $V = 25.66$ ,  $R = 25.25$ ,  $I = 23.76$ ,  $J = 22.04$ ,  $H = 20.70$ ,  $K = 19.97$ . There are upper limits in the  $U$  and  $B$  bands,  $U = 25.8$  (Dhillon et al., 2005) and  $B = 28.1$  (Hulleman et al., 2004), respectively. We also consider the observations of Wang et al. (2006) with the Spitzer/IRAC instrument at wavelengths  $4.5 \mu\text{m}$  and  $8.0 \mu\text{m}$ . The fluxes are  $36.3 \mu\text{Jy}$  and  $51.9 \mu\text{Jy}$ , respectively. We corrected the data for the interstellar extinction, using the estimated distance  $d = 3.6 \text{ kpc}$  (Durant and van Kerkwijk, 2006a) and an absorption in the  $V$  band  $A_V = 3.5$  (Durant and van Kerkwijk, 2006b). For the rest of the bands we used  $A_U = 1.569A_V$ ,  $A_B = 1.337A_V$ ,  $A_R = 0.751A_V$ ,  $A_I = 0.479A_V$ ,  $A_J = 1.569A_V$ ,  $A_H = 0.282A_V$ ,  $A_K = 0.114A_V$  (Cardelli et al., 1989). The extinction in the Spitzer/IRAC bands for  $A_K < 0.5$  are  $A_{4.5\mu\text{m}} = 0.26A_K$  and  $A_{8.0\mu\text{m}} = 0.21A_K$  (Chapman et al., 2009).

of the magneto-hydrodynamic equations including the explicit coupling of magnetosphere-disk system and the mass and angular momentum transfer from the disk to the star is not yet available. For this reason the torque acting on the star it is often followed using a phenomenological treatment. We adopt the model of Armitage and Clarke (1996), which assumes that the magnetic field lines threading the disk are closed. In this model the evolution of  $\omega$  is dictated by

$$\begin{aligned} \dot{\omega} = & - \frac{2B^2 \langle R \rangle^6 \omega^3}{3Ic^3} \sin^2 \theta + \frac{B^2 \langle R \rangle^6}{3I} \left[ \frac{1}{R_{\text{mag}}^3} - \frac{2}{(R_c R_{\text{mag}})^{3/2}} \right] \\ & + \frac{\dot{M} R_{\text{mag}}^2 \omega}{I}, \end{aligned} \quad (\text{B.5.3})$$

where  $\theta$  is the angle between the rotation axis and the magnetic dipole moment,  $R_{\text{mag}} = [B^2 \langle R \rangle^6 / (\dot{M} \sqrt{2GM})]^{2/7}$  is the magnetospheric radius (Chatterjee et al., 2000; Toropina et al., 2012; Matt et al., 2012; Rueda and Ruffini, 2012), and  $R_c = (GM/\omega^2)^{1/3}$  is the corotation radius. The first term in Eq. (B.5.3) describes the traditional magneto-dipole braking, the second one is the star-disk coupling, while the last one describes the angular momentum transfer from the disk to the white dwarf. We adopt an accretion rate corresponding to a Shakura-Sunyaev viscosity parameter  $\alpha_{\text{SS}} = 0.1$  (Cannizzo et al., 1990; Chatterjee et al., 2000; Ertan et al., 2009). Adopting a misalignment angle  $\theta = \pi/2$  and integrating Eq. (B.5.3) using the parameters resulting from our SPH simulation and it results that, for a wide range of magnetic field strengths, at early stages  $R_{\text{mag}} \approx R_{\text{WD}}$ . Thus, initially the star is spun-up due to the large accretion rates — see the insets of Fig. B.35. However, after  $\sim 1$  kyr, the inner radius of the disk — which is approximately given by the magnetospheric radius — becomes larger than the the light cylinder radius,  $R_{\text{lc}} = c/\omega$ . Hence, the disk cannot torque any longer the white dwarf, the rotation period reaches a minimum, and from this point on the disk and the star evolve independently, and accretion onto the magnetic poles stops. Thus, the star behaves as a normal pulsar, spinning-down by magneto-dipole radiation (Lamb et al., 1973; Chatterjee et al., 2000). The surface magnetic field needed to fit the observed values of  $P$  and  $\dot{P}$  when a mass  $M = 1.2 M_{\odot}$  is adopted is  $B \approx 2.3 \times 10^8$  G at an age  $\tau_{\text{sd}} = 64$  kyr — see Fig. B.35. This age estimate compares well with the spin-down characteristic age  $P/(2\dot{P}) \approx 68$  kyr. Moreover, the strength of the magnetic field can be compared with that directly derived using the traditional misaligned dipole expression

$$B = \sqrt{\frac{3c^3 I}{\langle R \rangle^6} \frac{P \dot{P}}{8\pi^2}}, \quad (\text{B.5.4})$$

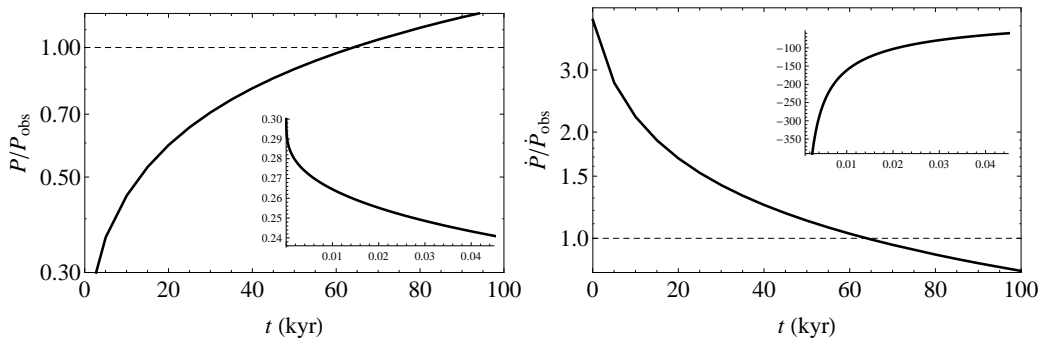


**Figure B.35.:** Time evolution of the period (left panel) and period derivative (right panel) of 4U 0142+61. The insets show to the early evolutionary phases of the system.

(Ferrari and Ruffini, 1969; Lamb et al., 1973) — which in our case is valid because  $R_{\text{in}} \approx R_{\odot}$  (see Sect. B.5.1) is larger than the radius of the light cylinder  $R_{\text{lc}} \approx 0.6 R_{\odot}$ . From the observed values  $P = 8.69$  s and  $\dot{P} = 2.03 \times 10^{-12}$  (Hulleman et al., 2000), we obtain  $B = 2.3 \times 10^8$  G for  $M_{\text{min}}$ , and  $6.2 \times 10^9$  G for  $M_{\text{max}}$ , in agreement with the result obtained integrating Eq. (B.5.3). Additionally, there are other indications that the magnetic field derived in this way is sound. In particular, the spectrum of 4U 0142+61 exhibits a significant drop-off between the  $B$  and  $V$  bands, at a frequency  $\nu \approx 10^{15}$  Hz, see Fig. B.34. Hulleman et al. (2004) concluded that this feature is not due to variability and, moreover, they advanced that it is consistent with the electron cyclotron emission of a magnetic field  $B \sim 10^8$  G. Adopting the minimum and maximum masses derived from our model we obtain electron cyclotron frequencies  $\nu_{\text{cyc}} = eB/(2\pi m_e c) = 6.3 \times 10^{14}$  Hz and  $1.7 \times 10^{16}$  Hz, which correspond to wavelengths that fall between the NIR and the UV, 0.5 and 176  $\mu\text{m}$ , respectively. This suggests that the magnetic field must be closer to the lower value, and therefore that the corresponding mass should be  $\sim 1.2 M_{\odot}$ . Actually, it is interesting to realize that although the mass of the remnant of the coalescence is slightly smaller than our fiducial mass for 4U 0142+61 —  $\sim 1.1$  and  $\sim 1.2 M_{\odot}$ , respectively — the mass accreted during the spin-up phase is  $M_{\text{acc}} \sim 0.05 M_{\odot}$ , in good agreement with the mass derived from the photometric solution. It could be argued that this is the maximum possible accreted mass, since during these early stages super-Eddington accretion rates are needed to accrete all the material inflowing from the disk. Nevertheless, during the very early stages after the merger the temperature of the coalesced system is very high, and the emission of neutrinos is not negligible (García-Berro et al., 2012).

We now compute the cooling age of 4U 0142+61, and compare it with the spin-down age. As the hot, convective corona resulting from the merger is very short-lived (García-Berro et al., 2012) the evolution of the surface luminosity of the white dwarf can be estimated using Mestel’s cooling law (Mes-

tel, 1952):

$$\tau_{\text{cool}} = \frac{1}{\langle A \rangle} \left( \frac{bMZ^{2/5}}{L_{\text{WD}}} \right)^{1/x} - 0.1, \quad (\text{B.5.5})$$

where  $\langle A \rangle$  is the average atomic weight of the core of the white dwarf,  $Z$  is the metallicity of its envelope,  $x = 1.4$ ,  $b = 635$  (Hurley and Shara, 2003), and the rest of the symbols have their usual meaning. Adopting a carbon-oxygen core and  $Z \approx 0.001$ , which is a reasonable value (Althaus et al., 2010a), we obtain a cooling age  $\tau_{\text{cool}} \approx 64$  kyr, in good agreement with the spin-down age.

### X-ray luminosity

For a distance  $d = 3.6$  kpc, Durant and van Kerkwijk (2006a) estimated an isotropic X-ray luminosity  $L_X = 4\pi d^2 f_X^{\text{unabs}} \approx 1.3 \times 10^{35}$  erg s $^{-1}$ , using the unabsorbed X-ray flux  $f_X^{\text{unabs}} = 8.3 \times 10^{-11}$  erg s $^{-1}$  cm $^{-2}$  obtained by Patel et al. (2003). We use the result of the latest observations of 4U 0142+61 with the EPIC cameras onboard *XMM-Newton*,  $f_X^{\text{unabs}} = 7.2 \times 10^{-11}$  erg s $^{-1}$  cm $^{-2}$  (Göhler et al., 2005), obtaining  $L_X \approx 1.1 \times 10^{35}$  erg s $^{-1}$  when the same distance is adopted. The loss of rotational energy associated with the spin-down of 4U 0142+61,  $\dot{E}_{\text{rot}} = -4\pi^2 I \dot{P} / P^3$  gives  $|\dot{E}_{\text{rot}}| = 1.7 \times 10^{37}$  erg s $^{-1}$  for  $M_{\text{min}}$  and  $3.4 \times 10^{35}$  erg s $^{-1}$  for  $M_{\text{max}}$ , that cover the estimated X-ray luminosity.

The time integrated X-ray spectrum of 4U 0142+61 is well described by a black body and a power-law model with  $k_B T_{\text{BB}} = 0.4$  keV and photon index  $\Gamma = 3.62$  (Göhler et al., 2005). The black body component corresponds to a temperature  $T_{\text{BB}} \sim 4.6 \times 10^6$  K, which is higher than the surface temperature of a hot white dwarf. However, these systems may have coronal temperatures much higher than that of the surface (Malheiro et al., 2012), and thus the X-ray emission would be of magnetospheric origin. Because the inner radius of the disk is larger than the radius of the light cylinder  $R_{\text{lc}}$  (see Sect. B.5.1) the mechanisms producing such radiation are similar to those of pulsars. In particular, a possible mechanism was delineated by Usov (1993), who showed that reheating of the magnetosphere by the bombardment of positrons moving backward to the surface of the star can produce large X-ray luminosities. Positrons are produced the interaction of high-energy photons with ultra-relativistic electrons, resulting in the creation of electron-positron pairs. Following closely the calculations of Usov (1993) we computed the theoretically expected X-ray luminosity of 4U 0142+61. We found that the reheating of polar caps produces a persistent X-ray luminosity  $L_X \sim 2 \times 10^{35}$  erg s $^{-1}$ , in agreement with observations. Nonetheless, there are other possibilities. If the conventional magnetar interpretation is adopted, the X-ray luminosity would be due to the neutron star. Alternatively, it could also be due to ongoing accretion from a fossil disk onto the neutron star (Alpar, 2001). In such cases

the white dwarf product of the merger would have accreted enough material to undergo accretion induced collapse to a neutron star.

### **B.5.2. Conclusions**

We studied the possibility that the peculiar AXP 4U 0141+61 is a massive, fast-rotating, highly magnetized white dwarf, and we explored the viability of this object being the result of the coalescence of a binary white dwarf. Specifically, from its observed rotational velocity we first derived bounds for the mass, radius, and moment of inertia. Afterwards, we fitted the IR, optical, and UV data of 4U 0142+61 with a composite spectrum made of two components, a black body and a dust disk, finding a good agreement with the observations. Moreover, we showed that the characteristics of the disk are consistent with the results of a SPH simulation of the merger of a  $0.6 + 1.0 M_{\odot}$  binary system. We then estimated the age and the magnetic field of this AXP. Adopting the results of our SPH simulation we obtained a magnetic field  $B = 2.3 \times 10^8$  G, and a post-merger age  $\approx 64$  kyr. The cyclotron frequency of this magnetic field  $\nu_{\text{cyc}} \sim 6 \times 10^{14}$  Hz would explain an absorption feature observed in the spectrum of 4U 0142+61 at  $\nu \sim 10^{15}$  Hz. Furthermore, our age estimate is in excellent agreement with the white dwarf cooling age. We also showed that the X-ray luminosity of 4U 0142+61 can be well explained by the rotational energy loss, and we inferred a theoretical estimate  $L_X \approx 2 \times 10^{35}$  erg s $^{-1}$ , which agrees with the observed value,  $L_X \approx 1.09 \times 10^{35}$  erg s $^{-1}$ . All these findings may support the hypothesis that the peculiar AXP 4U 0141+61 was originated in a white dwarf binary merger.

## B.6. Finite temperature effects on the mass-radius relation of white dwarfs

General relativistic effects are important in the high density branch of white dwarfs; for instance they lead to the gravitational collapse of the star prior to the trigger of the inverse  $\beta$  decay instability in  $^{12}\text{C}$  white dwarfs Rotondo et al. (2011b). We here construct the mass-radius relation of white dwarfs in their entire range of stability, so we use the equations of hydrostatic equilibrium within the framework of general relativity. Assuming the spherically symmetric metric

$$ds^2 = e^{\nu(r)}c^2dt^2 - e^{\lambda(r)}dr^2 - r^2d\theta^2 - r^2\sin^2\theta d\varphi^2, \quad (\text{B.6.1})$$

the equations of equilibrium can be written in the Tolman-Oppenheimer-Volkoff form

$$\frac{dv(r)}{dr} = \frac{2G}{c^2} \frac{4\pi r^3 P(r) / c^2 + M(r)}{r^2 \left[ 1 - \frac{2GM(r)}{c^2 r} \right]}, \quad (\text{B.6.2})$$

$$\frac{dM(r)}{dr} = 4\pi r^2 \frac{\mathcal{E}(r)}{c^2}, \quad (\text{B.6.3})$$

$$\frac{dP(r)}{dr} = -\frac{1}{2} \frac{dv(r)}{dr} [\mathcal{E}(r) + P(r)], \quad (\text{B.6.4})$$

where we have introduced the mass enclosed at the distance  $r$  through  $e^{-\lambda(r)} = 1 - 2GM(r)/(c^2 r)$ ,  $\mathcal{E}(r) = c^2 \rho(r)$  is the energy-density and  $P(r)$  is the total pressure, given in App. A.3.

These equations can be integrated for a wide range of central densities, temperatures, and for selected chemical compositions, for instance  $^4\text{He}$ ,  $^{12}\text{C}$ ,  $^{16}\text{O}$ , and  $^{56}\text{Fe}$ . In Figs. B.36 and B.37, we show in particular the mass-central density and mass-radius relations of  $^4\text{He}$  white dwarfs in the range of densities and radii where finite temperature effects are more important.

The minima in these plots mark the transition from the ideal to the degenerate behavior of the electron gas: from left to right in the  $M - \rho_c$  relation and from left to right in the  $M - R$  relation. Thus these minima can be used to give an estimate of the minimum mass that a star should have to be able to burn stably a given chemical composition since the condition of a stable burning requires that the gas be non-degenerate. Consequently, stable burning requires that the star lies on the branch of solutions on the left-hand side of the minimum of the  $M - \rho_c$  diagram or on the right-hand side of the minimum of the  $M - R$  diagram. For instance, helium burning is triggered at a temperature  $T_{\text{He+He}} \approx 10^8$  K, so we can obtain from the solutions shown in Fig. B.36 that the minimum mass for stable helium burning is  $M_{\text{min}}^{\text{He+He}} \approx 0.51 M_{\odot}$ . The corresponding radius and density of this configura-

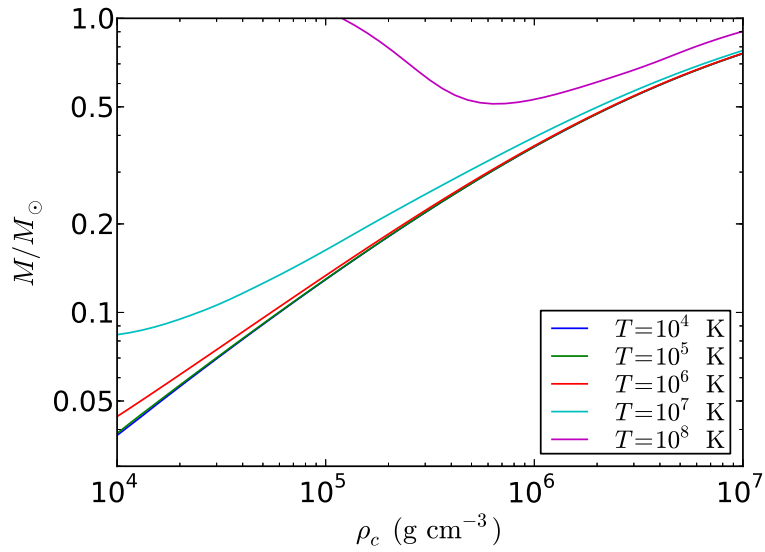


**Figure B.36.:** Total mass versus radius for  ${}^4\text{He}$  white dwarfs for selected temperatures from  $T = 10^4$  K to  $T = 10^8$  K.

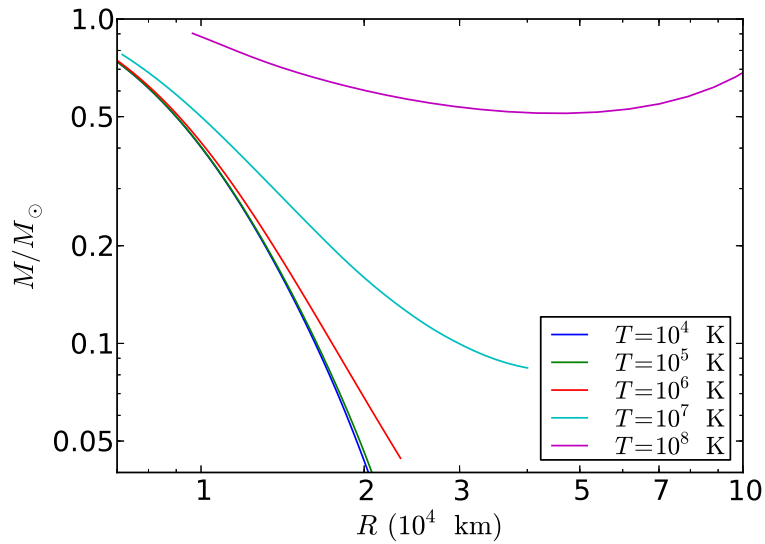


**Figure B.37.:** Total mass versus central density for  ${}^4\text{He}$  white dwarfs for selected temperatures from  $T = 10^4$  K to  $T = 10^8$  K.

tion is  $4.54 \times 10^9 \text{ cm} \approx 0.065 R_{\odot}$  and  $6.59 \times 10^5 \text{ g cm}^{-3}$ , respectively. A similar analysis can be done for the other compositions.

### B.6.1. The ultra low-mass white dwarf companion of PSR J1738+0333

It is clear that the effects of the temperature are particularly important at low densities, and hence for low-mass white dwarfs. We analyze here the specific case of the white dwarf companion of the millisecond pulsar PSR J1738+0333. We refer to Antoniadis et al. (2012), for details on the observations and technical aspects of the derivation of the binary parameters.

Antoniadis et al. (2012) obtained with the the Goodman High Throughput Spectrograph instrument of the Southern Astrophysical Research Telescope (SOAR) at Cerro Pachón, Chile, a photometric radius of the white dwarf,  $R_{\text{WD}} = 0.042 \pm 0.004 R_{\odot}$ . On the other hand, the analysis of the white dwarf atmosphere spectrum with the models of Ref. Koester (2008) led to an effective surface temperature,  $T_{\text{eff}} = 9130 \pm 150 \text{ K}$ , and a logarithm of the surface gravity,  $\log(g) = \log(GM_{\text{WD}}/R_{\text{WD}}^2) = 6.55 \pm 0.1$ . Using the evolutionary mass-radius relation of Painei et al. (2000), the mass of the white dwarf was estimated in Ref. Antoniadis et al. (2012) to be  $M_{\text{WD}} = 0.181_{-0.005}^{+0.007} M_{\odot}$ , and a corresponding radius  $R_{\text{WD}} = 0.037_{-0.003}^{+0.004} R_{\odot}$ , in agreement with the photometric value.

A first attempt to obtain the mass of the white dwarf can be done directly from the observed data by combining the spectral and photometric analysis. Assuming the photometric radius as the star radius the mass of the white dwarf would be  $M_{\text{WD}} = gR_{\text{WD}}^2/G \approx 0.23 M_{\odot}$ , using the central values of  $R_{\text{WD}}$  and  $g$ , which is roughly consistent with the mass derived from the mass-radius relation of Ref. Painei et al. (2000).

In order to compare our mass-radius relation at finite temperatures with the above results and infer the internal temperature of the white dwarf, we plotted in Figs. B.38 and B.39 our theoretical surface gravity-mass and radius relations for  $^4\text{He}$  white dwarfs, together with the above observational constraints.

An inspection of Fig. B.38 does not give us any information on the possible internal temperature of the white dwarf since, in principle, we do not have any a priori information on the mass. However, from Fig. B.39 we clearly identify that the interior temperature of the white dwarf core should be  $T \approx 2\text{--}3 \times 10^7 \text{ K}$ .

In Fig. B.40 we plot the mass-radius relation for  $^4\text{He}$  white dwarfs with the observational constraints of the companion of PSR J1738+0333. We can now compare our results with an estimate obtained for instance using the relation found by Koester in Ref. Koester (1976) between the central and surface temperatures of the white dwarf,  $T_{\text{eff}}^4/g = 2.05 \times 10^{-10} T_c^{2.56}$ . Using the value

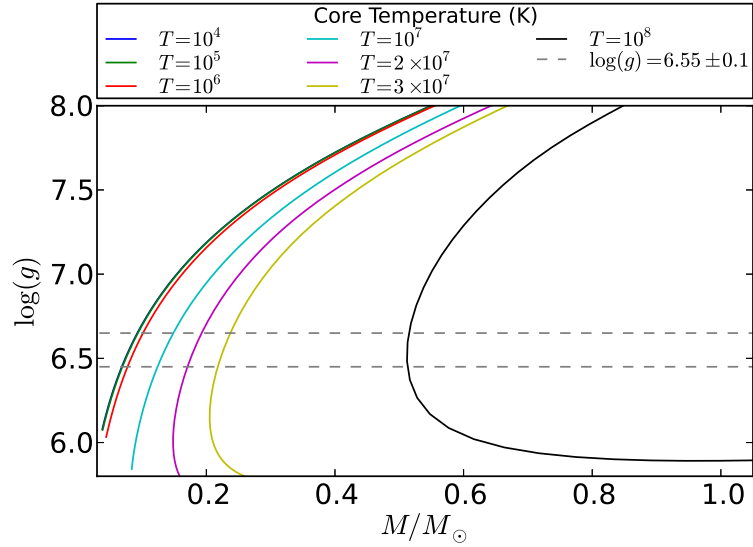


**Figure B.38.:** Logarithm of the surface gravity,  $\log(g) = \log(GM_{\text{WD}}/R_{\text{WD}}^2)$ , as a function of the mass for  ${}^4\text{He}$  white dwarfs for selected interior temperatures from  $T = 10^4$  K to  $T = 10^8$  K. The horizontal dashed lines indicate the maximum and minimum best-fit values  $\log(g) = 6.55 \pm 0.1$ .

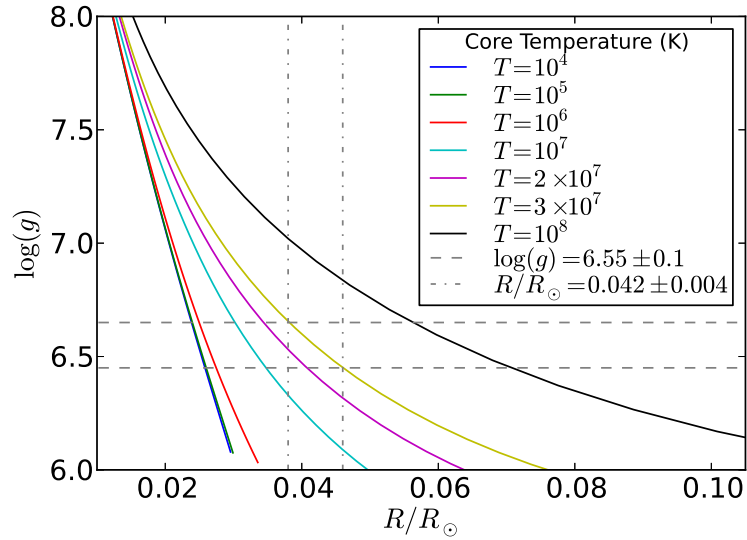


**Figure B.39.:** Logarithm of the surface gravity,  $\log(g) = \log(GM_{\text{WD}}/R_{\text{WD}}^2)$ , as a function of the radius for  ${}^4\text{He}$  white dwarfs for selected interior temperatures from  $T = 10^4$  K to  $T = 10^8$  K. The horizontal dashed and dot-dashed lines indicate the maximum and minimum best-fit values of the surface gravity,  $\log(g) = 6.55 \pm 0.1$  and photometric radii  $R_{\text{WD}} = 0.042 \pm 0.004R_{\odot}$ , respectively.

$T_{\text{eff}} = 9130$  K and  $\log(g) = 6.55$ , this relation gives  $T_c \approx 2.6 \times 10^7$  K, in full agreement with our inference. In this estimate we have neglected the contribution of the thickness of the envelope to the total surface radius of the white dwarf. However, this approximation does not introduce a large error since the envelope would be in this case at most  $\sim 10^{-2} R_{\text{WD}}$  thick.

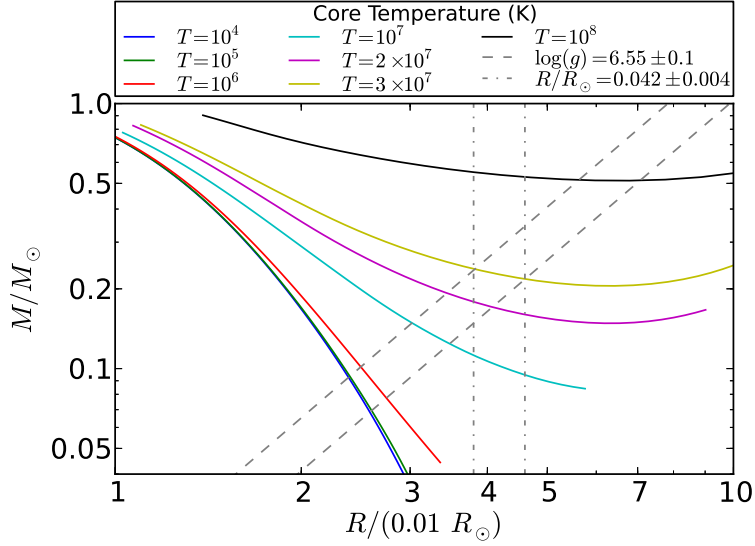


**Figure B.40.:** Logarithm of the surface gravity  $\log(g) = \log(GM_{\text{WD}}/R_{\text{WD}}^2)$  as a function of the radius for  ${}^4\text{He}$  white dwarfs for selected interior temperatures from  $T = 10^4$  K to  $T = 10^8$  K. The dashed and dot-dashed lines indicate the maximum and minimum best-fit values of the surface gravity,  $\log(g) = 6.55 \pm 0.1$  and photometric radii  $R_{\text{WD}} = 0.042 \pm 0.004 R_{\odot}$ , respectively.

### B.6.2. Discussion

Deviations from the degenerate equation of state have been shown to occur in the regions of interest of low-mass white dwarfs and in the outermost layers of neutron star crusts. Ultra-low mass white dwarfs,  $M_{\text{WD}} \sim 0.2 M_{\odot}$  Antoniadis et al. (2013a, 2012), have been found in binary systems with neutron stars companions. These objects have central densities  $\lesssim 10^6$  g cm $^{-3}$ , where the degenerate approximation breaks down and so thermal effects cannot be neglected. We have analyzed here the specific case of PSR J1738+0333, whose mass and radius was estimated in Antoniadis et al. (2012) using the evolutionary mass-radius relation of Painei et al. Painei et al. (2000). They obtained  $M_{\text{WD}} = 0.181^{+0.007}_{-0.005} M_{\odot}$ ,  $R_{\text{WD}} = 0.037^{+0.004}_{-0.003} R_{\odot}$ , in agreement with the spectrometric and photometric data. We inferred for this object an internal temperature  $T \approx 2\text{--}3 \times 10^7$  K, and a mass  $M_{\text{WD}} \approx 0.2 M_{\odot}$  assuming for instance the photometric radius,  $R = 0.042 R_{\odot}$ , as the star radius. We checked also

our result using the relation by Koester Koester (1976) between the internal and surface white dwarf temperatures,  $T_{\text{eff}}^4/g = 2.05 \times 10^{-10} T_c^{2.56}$ . Using the surface temperature and the logarithm of the surface gravity obtained from the spectral analysis,  $T_{\text{eff}} = 9130$  K and  $\log(g) = 6.55$ , this relation gives  $T_c \approx 2.6 \times 10^7$  K, in full agreement with our results.

## B.7. Dynamical instability of white dwarfs and breaking of spherical symmetry under the presence of extreme magnetic fields

It has been recently purported that the presence of a extremely large uniform magnetic field of order  $10^{18}$  G in the interior of a white dwarf, increases the maximum mass of the star from the traditional Chandrasekhar value,  $\approx 1.44 M_{\odot}$ , to a new upper bound  $\approx 2.58 M_{\odot}$ . Such a much larger limit would make these astrophysical objects viable candidates for the explanation of the superluminous population of type Ia supernovae. We show that the new mass limit was obtained neglecting several macro and micro physical aspects such as gravitational, dynamical stability, breaking of spherical symmetry, general relativity, inverse  $\beta$  decay, and pycnonuclear fusion reactions. These effects are relevant for the self-consistent description of the structure and assessment of stability of these objects. When accounted for, they lead to the conclusion that the existence of such ultramagnetized white dwarfs in nature is very unlikely due to violation of minimal requests of stability, and therefore the canonical Chandrasekhar mass limit of white dwarfs has to be still applied.

### B.7.1. Introduction

It has been proposed that the light curves of some peculiar superluminous Ia supernovae could be explained by white dwarf progenitors whose masses are larger than the traditional Chandrasekhar limit,

$$M_{\text{Ch}} = 2.015 \frac{\sqrt{3\pi}}{2} \frac{m_{\text{Pl}}^3}{(\mu_e m_H)^2} \approx 1.44 M_{\odot}, \quad (\text{B.7.1})$$

where  $\mu_e \approx 2$  is the mean molecular weight per electron,  $m_H$  the mass of hydrogen atom, and  $m_{\text{Pl}} = \sqrt{\hbar c / G}$  is the Planck mass. These objects are called super-Chandrasekhar white dwarfs. The higher binding energy of these objects could then explained both the low kinetic energies and high luminosity observed in these supernovae Howell et al. (2006). In this scenario, such white dwarfs do need a gravitational mass in the range  $(2.1\text{--}2.8) M_{\odot}$ , depending on the amount of nickel needed to successfully explain the supernovae Howell et al. (2006); Hicken et al. (2007); Yamanaka et al. (2009); Scalzo et al. (2010); Silverman et al. (2011); Taubenberger et al. (2011).

Upasana & Banibrata Das and Mukhopadhyay (2013) recently purported that the effects of a quantizing strong and uniform magnetic field on the equation of state of a white dwarf, would increase its critical mass up to a new value  $M_{\text{max}} \approx 2.58 M_{\odot}$ , significantly higher than the Chandrasekhar limit (B.7.1), thus becoming a viable candidate progenitor of superluminous type

Ia supernovae. This a new mass limit would be reached for extremely large magnetic fields of the order of  $10^{18}$  G.

However, as we show in this Letter the existence of such ultramagnetized white dwarfs in nature is quite dubious, since the approach followed in Das and Mukhopadhyay (2013) for the construction of the configurations ignores several macro and micro physical effects and instabilities needed for a complete and accurate description of a magnetized white dwarf. We show that indeed all these ignored effects make improbable that a white dwarf could reach such a hypothetical extreme state either in single or binary evolution.

### B.7.2. Ultramagnetized white dwarfs

In a recent work, Upasana & Banibrata Das and Mukhopadhyay (2013) studied the effects of extreme magnetic field in the mass and radius of white dwarfs. The equation of state of a degenerate electron gas in presence of a magnetic field  $B$  directed along the  $z$ -axis, in the limit  $B \rightarrow \infty$  when all electrons are constrained to the lowest Landau level, obeys a polytrope-like for  $P = K_m \rho^2$ , where

$$K_m = \frac{m_e c^2 \pi^2 \lambda_e^3}{(\mu_e m_H)^2 B_D}, \quad (\text{B.7.2})$$

with  $\lambda_e$  the electron Compton wavelength, and  $B_D = B/B_c$  the magnetic field in units of the critical field  $B_c = m_e^2 c^3 / (e \hbar) = 4.41 \times 10^{13}$  G. For obtaining the above expression, in Ref. Das and Mukhopadhyay (2013) the density of the system was assumed to be given by  $\rho = \mu_e m_H n_e$ , so determined only by the nuclei component, where  $n_e$  is the electron number density.

Then, Lane-Emden solution of Newtonian self-gravitating polytropes of index  $n = 1$  was used to obtain the mass of an ultramagnetized white dwarf

$$M = 4\pi^2 \rho_c \left( \frac{K_m}{2\pi G} \right)^{3/2}, \quad (\text{B.7.3})$$

and the corresponding radius

$$R = \sqrt{\frac{\pi K_m}{2G}}, \quad (\text{B.7.4})$$

where  $\rho_c$  is the central density.

In the present limit of one Landau level with high electron Fermi energies  $E_e^F, E_e^F = E_{\max}^F \gg m_e c^2$ , with

$$E_{\max}^F = m_e c^2 \sqrt{1 + 2B_D} \approx m_e c^2 \sqrt{2B_D} \quad (\text{B.7.5})$$

the maximum possible value of  $E_e^F$ ,  $\rho_c$  becomes Das and Mukhopadhyay

(2013)

$$\rho_c = \frac{\pi M}{4R^3} = \frac{\mu_e m_H}{\sqrt{2}\pi^2 \lambda_e^3} B_D^{3/2}. \quad (\text{B.7.6})$$

Introducing Eq. (B.7.6) into Eq. (B.7.3), Upasana & Banibrata Das and Mukhopadhyay (2013) obtained the mass limit of ultramagnetized white dwarfs

$$M_{\text{max}} = \pi^{3/2} \frac{m_{\text{Pl}}^3}{(\mu_e m_H)^2} \approx 2.58 M_{\odot}, \quad (\text{B.7.7})$$

when  $\rho_c \rightarrow \infty$  and  $R \rightarrow 0$ . This upper bound is larger than the canonical Chandrasekhar limit given by Eq. (B.7.1).

We reproduce in Fig. B.41 the evolutionary track of the white dwarf proposed in Das and Mukhopadhyay (2013). The magnetic field along the curve is increasing as a consequence of accretion of matter onto the star. It can be seen in the plot how the star reaches the maximum mass limit (B.7.7) while reducing its radius.

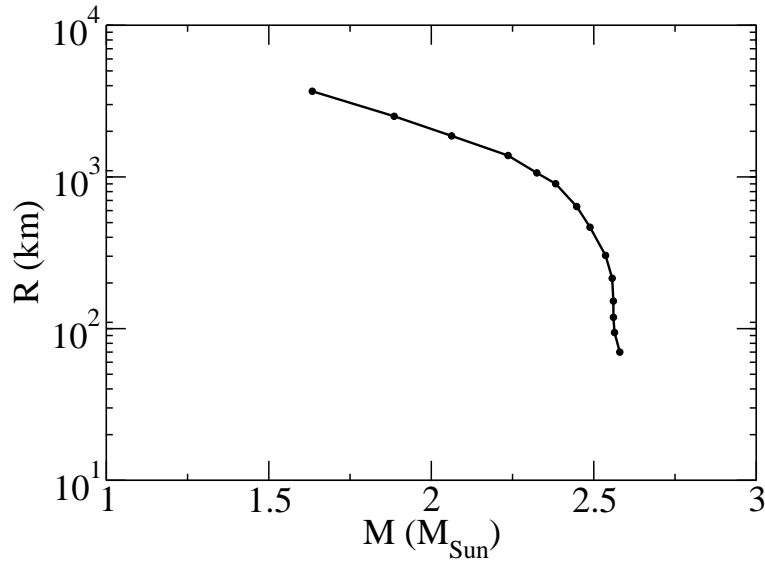


**Figure B.41.:** Mass-radius relation of magnetized white dwarfs - the curve represents the evolutionary track of the white dwarf with the increase of the uniform magnetic field inside the star obtained in Ref. Das and Mukhopadhyay (2013).

Already at this point it is possible to identify some of the assumptions in the model of Ref. Das and Mukhopadhyay (2013) that led to the above results, and which we show below are incorrect and/or unjustified, invalidating their final conclusions. 1) The equation of state assumed in the limit of very intense magnetic fields,  $B \rightarrow \infty$ ; 2) a uniform magnetic field is adopted; 3) the huge magnetic fields and the obtained mass-radius relation explicitly violate even the absolute upper limit to the magnetic field imposed by the Virial theorem;

4) dynamical instabilities due to quadrupole deformation are not taken into account either; 5) spherical symmetry is assumed for all values of the magnetic field; 6) the role of the magnetic field in the hydrostatic equilibrium equations is neglected; 7) general relativistic effects are ignored even if the final configuration is almost as compact as a neutron star and the magnetic energy is larger than the matter energy-density; 8) microphysical effects such as inverse  $\beta$  decay and pycnonuclear fusion reactions, important in a regime where the electrons are highly relativistic,  $E_e^F \gg m_e c^2$ , are neglected; and 9) the magnetic field, the density, and the electron Fermi energy are assumed to increase with time inside the star as a consequence of a continuous accretion process onto the white dwarf.

### B.7.3. Equation of state and virial theorem violation

Being much lighter, the electrons in the white dwarf interior are more easily disturbed by a magnetic field than the ions. Eventually, the electron gas might become quantized in Landau levels, providing the magnetic field is larger than the critical field  $B_c$ . However, for “moderate” values of the field, i.e.  $B \sim B_c$ , the equation of state deviates still very little from the unmagnetized one. Thus, appreciable effects are seen only when the electrons occupy only the lower Landau levels, which is possible for  $B_D \sim [E_{\max}^F / (m_e c^2)]^2$ . Since the electrons in massive white dwarfs are ultrarelativistic with Fermi energies  $E_e^F \gtrsim 10 m_e c^2$ , it implies the necessity of magnetic fields  $B_D \gtrsim 10^2$  or  $B \gtrsim 4 \times 10^{15}$  G, in order to have not negligible magnetic field effects. It can be checked from the virial theorem that such large magnetic fields cannot develop in the interior of the white dwarf since they violate the absolute upper bound imposed by the virial theorem applied to a white dwarf which is approaching the Chandrasekhar mass limit.

The limiting field can be computed following the argument by Chandrasekhar & Fermi in their seminal paper Chandrasekhar and Fermi (1953). There exists a magnetic field limit,  $B_{\max}$ , above which an equilibrium configuration is impossible because the electromagnetic energy,  $W_B$ , exceeds the gravitational energy,  $W_G$ , therefore becoming gravitationally unbound. If one includes the forces derived from the magnetic field, one can write the virial scalar relation for an equilibrium configuration as as Chandrasekhar and Fermi (1953)

$$3\Pi + W_B + W_G = 0, \quad (\text{B.7.8})$$

where  $\Pi = \int P dV$ , with  $P$  the pressure of the system,  $W_B$  the positive magnetic energy, and  $W_G$  the negative gravitational potential energy. The quantity  $\Pi$  satisfies  $\Pi = (\gamma - 1)U$  for a polytrope,  $P = K\rho^\gamma$ , where  $U$  is the total kinetic energy of particles. Since the total energy of the configuration can be written as  $E = U + W_B + W_G$ , then one can eliminate  $U$  from Eq. (B.7.8) to

obtain

$$E = -\frac{3\gamma - 4}{3(\gamma - 1)}(|W_G| - W_B), \quad (\text{B.7.9})$$

and therefore the necessary condition for the stability of the star,  $E < 0$ , is given by

$$(3\gamma - 4)|W_G| \left(1 - \frac{W_B}{|W_G|}\right) > 0. \quad (\text{B.7.10})$$

From this expression we can recover, in absence of magnetic field ( $W_B = 0$ ), the known condition for bound unmagnetized polytropes  $\gamma < 4/3$ , or  $n < 3$  in terms of the polytrope index  $n$  defined by  $\gamma = 1 + 1/n$ .

The presence of a magnetic field weakens the stability, and as shown in Eq. (B.7.10), no matter the value of  $\gamma$ , the star becomes gravitationally unbound when the magnetic energy exceeds the gravitational one; i.e.  $W_B > |W_G|$ . This condition clearly implies an upper bound for the magnetic field, obtained for  $W_B = |W_G|$ . In order to determine such limit we first obtain an expression for the magnetic energy of the star, which considering a constant magnetic field can be written as

$$W_B = \frac{B^2}{8\pi} \frac{4\pi R^3}{3} = \frac{B^2 R^3}{6}. \quad (\text{B.7.11})$$

As we discussed above, the equation of state assumes a polytrope-like for with  $\gamma = 2$  or  $n = 1$  under extreme magnetic fields, such that only one Landau level is populated and  $E_F \gg m_e c^2$  Das and Mukhopadhyay (2013). Thus, the gravitational energy density of the spherical star configuration is (see e.g. Shapiro and Teukolsky (1983a))

$$W_G = -\frac{3}{5-n} \frac{GM^2}{R} = -\frac{3}{4} \frac{GM^2}{R}, \quad (\text{B.7.12})$$

where  $M$  and  $R$  are the mass and star radius, respectively, and  $G$  is the Newton gravitational constant. Using Eqs. (B.7.11) and (B.7.12), and expressing  $M$  and  $R$  in units of solar mass and solar radius, we find that the maximum value of magnetic field  $B_{\max}$  is given by

$$B_{\max} = 2.24 \times 10^8 \frac{M}{M_\odot} \left(\frac{R_\odot}{R}\right)^2. \quad (\text{B.7.13})$$

In the case of a Chandrasekhar white dwarf with the maximum mass  $M = 1.44M_\odot$  and a radius of 3000 km, consistent with the recent calculation of massive white dwarfs Boshkayev et al. (2013b), we obtain  $B_{\max} \sim 1.7 \times 10^{13}$  G. This value is clearly lower than the critical field  $B_c = 4.4 \times 10^{13}$  G.

Since the Fermi energy of the electrons is of the order of  $10m_e c^2$  at the high densities of massive white dwarfs approaching the maximum mass, the

above conclusions, reached on the basis on a classic analysis, hold approximately up to magnetic fields of the order of  $10^{15}$  G, from which the magnetic field start to modify appreciably the equation of state of the ultrarelativistic electrons.

In order to quantify how strong is the violation of the virial theorem produced by the magnetic fields used in Das and Mukhopadhyay (2013), we choose three star configurations whose values of  $M$  and  $R$  lie in the region of high mass configuration,  $M > 2M_{\odot}$  (see red points in Fig. B.42). Using the approximation of Eq. (B.7.6), we obtain the corresponding constant magnetic field  $B$  of these stars configurations. We compare these values of  $B$  with the maximum value,  $B_{\max}$ , allowed by the virial theorem (B.7.13). In Fig. B.42 we show that such extreme magnetic fields with  $B > B_{\max}$  and the magnetized white dwarfs of Table B.17 are in the instability region, violating the virial theorem. In Table B.17 we show also for these configurations the magnetic energy  $W_B$  given by Eq. (B.7.11), and the magnitude of the gravitational energy  $|W_G|$ . These results indicate that the magnetic field obtained in Ref. Das and Mukhopadhyay (2013), are at least one order of magnitude larger than the maximum magnetic field allowed,  $B_{\max}$ . As a consequence, for the three star configurations,  $W_B/|W_G| \sim 250$  well above the stability condition which requires  $W_B/|W_G| \sim 1$ . Thus, these white dwarf are unstable and unbound.

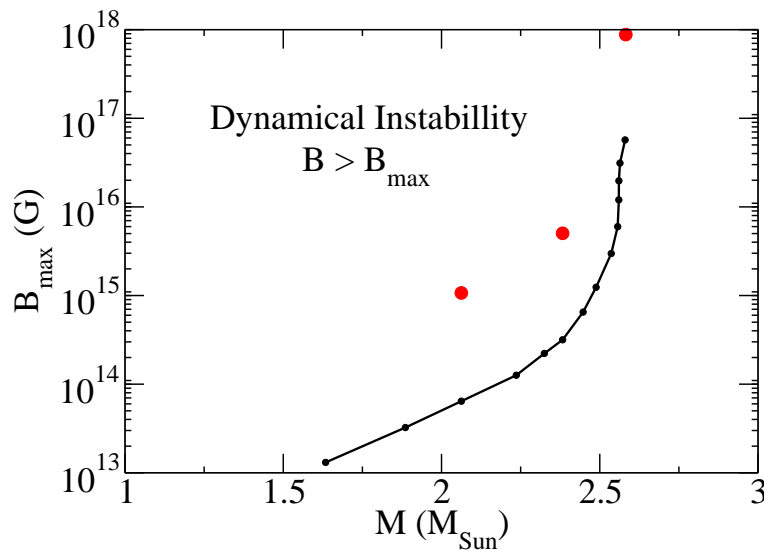


**Figure B.42.:** (Color online) Maximum magnetic field  $B_{\max}$  as a function of the star mass. We show the three values of the magnetic field of Table 1 that are above the  $B_{\max}$  line, in the dynamical instability region.

The repulsive magnetic force due to a possible variable magnetic field, as discussed in Ref. Malheiro et al. (2007), was not considered. Furthermore, a uniform magnetic field in the  $z$ -direction inside the star, yields a dipole exter-

nal field Chandrasekhar and Fermi (1953). In this case, even if the magnetic fields are continuous at the star surface, their derivatives are not, producing a repulsive magnetic force at the surface. This force will push against the attractive gravitational force such that for a large magnetic field, the magnetic force will overcome the gravitational one, destabilizing the star. This physical situation is exactly the same expressed in the virial theorem condition for the star stability ( $W_B < |W_G|$ ) discussed above.

Ostriker & Hartwick Ostriker and Hartwick (1968) analyzed the effect of magnetic fields in white dwarfs, and concluded that they lead to stars with larger masses but also larger radii. One of the main consequences of the increasing magnetic field is that even a small ratio of magnetic to gravitational energy will produce an appreciable increase in the radii of magnetized white dwarfs. Consequently, it leads to a reduction of the central density, even for small mass changes. This conclusions were also confirmed in Ref. Suh and Mathews (2000), where the effect of magnetic fields in the mass-radius relation for magnetic white dwarfs were also investigated. Thus, the very compact magnetized white dwarf configuration obtained in Ref. Das and Mukhopadhyay (2013), in which large magnetic field implies large mass and *small* radius, are possible only because the effect of the repulsive magnetic force (Lorentz force) has not been properly considered.

Since in Ref. Das and Mukhopadhyay (2013) it is considered the influence of a very large constant magnetic fields in the star mass and radius, assuming values for the magnetic field larger than the above limits, we conclude that these extremely magnetized white dwarfs must be unstable and unbound. The limiting magnetic field values shown in Table B.17 are clearly obtained with the radii given in Ref. Das and Mukhopadhyay (2013), which are much smaller than the self-consistent solution of the equilibrium equations would give. Since the maximum magnetic field depends on  $R^{-2}$ , see Eq. (B.7.13), the real maximum possible field would actually be smaller than the one computed here.

#### B.7.4. Breaking of spherical symmetry and quadrupole instability

It was shown by Chandrasekhar & Fermi Chandrasekhar and Fermi (1953) that the figure of equilibrium of an incompressible fluid sphere with an internal uniform magnetic field that matches an external dipole field, is not represented by a sphere. The star becomes oblate by contracting along the axis of symmetry, namely along the direction of the magnetic field. Thus, we consider the fluid sphere to be deformed in such a way that the equation of the bounding surface is given by

$$r(\mu) = R + \epsilon P_l(\mu), \quad (\text{B.7.14})$$

where  $\mu = \cos \theta$ , with  $\theta$  the polar angle, and  $P_l(\mu)$  denotes the Legendre polynomial of order  $l$ . It is easy to see that the deviation from the spherical configuration is given by the term  $P_l(\mu)$ , thus in Ref. Chandrasekhar and Fermi (1953), such a perturbation was called “ $P_l$ - deformation”. The quantity  $\epsilon$  satisfies  $\epsilon \ll R$  and measures the deviations from a spherical configuration. The polar and equatorial radii are  $R_p = R + \epsilon P_l(1)$  and  $R_{\text{eq}} = R + \epsilon P_l(0)$  respectively, thus  $\epsilon = -(2/3)(R_{\text{eq}} - R_p)$  and therefore  $\epsilon/R = -(2/3)(R_{\text{eq}} - R_p)/R$ , for the axisymmetric deformed configuration with  $l = 2$ .

It was shown in Chandrasekhar and Fermi (1953) that such an axisymmetrically deformed object is favorable energetically with respect to the spherical star. Thus, the star becomes unstable and proceeds to collapse along the magnetic field axis, turning into an oblate spheroidal shape with  $\epsilon < 0$ . The contraction continues until the configuration reaches a value of  $\epsilon/R$  given by

$$\frac{\epsilon}{R} = -\frac{15 B^2 R^4}{8 GM^2}. \quad (\text{B.7.15})$$

Using the expression for  $B_{\text{max}}$  given by Eq. (B.7.13), one obtains

$$\frac{\epsilon}{R} = -\frac{135}{16} \left( \frac{B}{B_{\text{max}}} \right)^2 \simeq -8.4 \left( \frac{B}{B_{\text{max}}} \right)^2. \quad (\text{B.7.16})$$

Therefore, when the internal magnetic field is close to the limit set by the virial theorem, the star deviates to a highly oblate shape.

We show in the last column of Table B.17, the “ $P_l$ - deformation”,  $\epsilon/R$ . The results show that  $|\epsilon/R| \gtrsim 2 \times 10^3$ , which implies that the star has a highly oblate shape and thus the spherical symmetry is strongly broken. Therefore, in order to account for the deformation caused by the presence of a magnetic field, a more consistent calculation considering cylindrical symmetry, as in Chandrasekhar and Fermi (1953); Ostriker and Hartwick (1968), is mandatory.

### B.7.5. Microscopic instabilities

It is known that at sufficiently high densities in the interior of white dwarfs, the inverse  $\beta$  decay or electron capture process becomes energetically favorable, and therefore a nucleus  $(Z, A)$  transforms into a different nucleus  $(Z - 1, A)$  by capturing energetic electrons. Such a process destabilizes the star since the electrons are the main responsible for the pressure in a white dwarf Harrison et al. (1958, 1965); Shapiro and Teukolsky (1983a). The process sets in when the electron chemical potential reaches the threshold energy,  $\epsilon_Z^\beta$ , given by the difference of the nuclear binding energy between the initial and final nucleus. For helium, carbon, oxygen, and iron,  $\epsilon_Z^\beta$  is approximately

20.6, 13.4, 10.4, and 3.7 MeV (see e.g. Shapiro and Teukolsky (1983a)). For unmagnetized general relativistic white dwarfs, this occurs at a critical density  $\rho_{\text{crit}}^{\beta} \approx 1.4 \times 10^{11}$ ,  $4.0 \times 10^{10}$ ,  $1.9 \times 10^{10}$ , and  $1.2 \times 10^9$  g cm<sup>-3</sup>, respectively for the same chemical compositions (see Table II in Rotondo et al. (2011b)).

This instability was recently analyzed in Ref. Chamel et al. (2013) for the ultramagnetized white dwarfs discussed here. Using Eq. (B.7.5), it can be seen that the electron capture process limits the magnetic field to values lower than

$$B_D^{\beta} = \frac{1}{2} \left( \frac{\epsilon_Z^{\beta}}{m_e c^2} \right)^2 \approx 812.6, 342.3, 207.9, 26.2, \quad (\text{B.7.17})$$

or  $B \approx 3.6 \times 10^{16}$ ,  $1.5 \times 10^{16}$ ,  $9.1 \times 10^{15}$ , and  $1.1 \times 10^{15}$  G, where we have used the previously mentioned values of  $\epsilon_Z^{\beta}$  for helium, carbon, oxygen, and iron, respectively. The electron capture in this case is shown to occur even at critical central densities lower than in the unmagnetized case. The values of the critical densities are  $\rho_{\text{crit}}^{\beta} \approx 9.6 \times 10^{10}$ ,  $9.6 \times 10^{10}$ ,  $1.2 \times 10^{10}$ , and  $6.0 \times 10^8$  g cm<sup>-3</sup>, respectively for helium, carbon, oxygen, and iron. These densities are obtained by introducing the limiting values of Eq. (B.7.17) into Eq. (B.7.6). The above densities are much smaller than the densities of the massive ultramagnetized white dwarfs considered in Ref. Das and Mukhopadhyay (2013); configurations approaching the maximum mass given by Eq. (B.7.7) have magnetic fields with  $B_D \gtrsim 10^4$  and therefore central densities  $\rho_c \gtrsim 4 \times 10^{12}$  g cm<sup>-3</sup>. These densities are even higher than the neutron drip density,  $\rho_{\text{drip}} \approx 4.3 \times 10^{11}$  g cm<sup>-3</sup>, at which the less bound neutrons in nuclei start to drip out forming a Fermi gas Baym et al. (1971a). The neutron drip process will then start when  $\rho_c = \rho_{\text{drip}}$  where  $\rho_c$  is given by Eq. (B.7.6). For a carbon composition it occurs for a magnetic field  $B_D \approx 531$ , or  $B \approx 2.3 \times 10^{16}$  G Chamel et al. (2013).

Pycnonuclear fusion reactions might establish a more stringent limit with respect to the inverse  $\beta$  decay in an ultramagnetized white dwarf Chamel et al. (2013). Carbon fusion leads to <sup>24</sup>Mg, which undergoes electron capture, thus inverse  $\beta$  decay instability, at a density of approximately  $\rho_{\text{crit,Mg}}^{\beta} \approx 3 \times 10^9$  g cm<sup>-3</sup>. Therefore, if C+C fusion occurs at rates highly enough at densities  $\rho_{\text{crit,Mg}}^{\beta}$  to produce appreciable amounts of <sup>24</sup>Mg in times shorter than a Hubble time, then this process imposes a more tight constraint to the density of the white dwarf. Based on the up-to-date astrophysical S-factors computed in Ref. Gasques et al. (2005), we recently obtained in Boshkayev et al. (2013b) the pycnonuclear carbon fusion in white dwarfs. We found for instance that, C+C fusion occurs at a timescale of 0.1 Myr at a density  $\rho_{\text{pyc}}^{\text{C+C}} \approx 1.6 \times 10^{10}$  g cm<sup>-3</sup>. Using Eq. (B.7.6), we infer that such a density is reached for a magnetic field  $B_D \approx 246.6$ , or  $B \approx 1.1 \times 10^{16}$  G. Longer reaction times implies lower densities and thus lower magnetic fields.

The above limits to the magnetic field obtained from microscopic instability processes are, however, still higher than the maximal values allowed by the virial theorem. Thus, the macroscopic dynamical instabilities sets in before both electron captures and pycnonuclear reactions.

### B.7.6. General relativistic effects

We now turn to show that for ultra high magnetic fields as the ones considered in Das and Mukhopadhyay (2013), general relativistic effects are relevant; therefore a Newtonian treatment of the equations of equilibrium is not appropriate. First we can calculate the contribution to the star mass owing to ultra high magnetic fields, as the ones considered in Das and Mukhopadhyay (2013). This can be approximately obtained by estimating the magnetic energy stored in the volume of the white dwarf given by Eq. (B.7.11). This gives for the maximum white dwarf mass in Das and Mukhopadhyay (2013), obtained for a magnetic field  $B \approx 10^{18}$  G, a contribution  $m_B = W_B/c^2 \approx 24.7 M_\odot$ . This value is approximately one order of magnitude larger than the mass computed in Das and Mukhopadhyay (2013), which implies a total star mass of  $\approx 27.3 M_\odot$ , instead of  $2.6 M_\odot$ . However, as we have shown such a large magnetic fields cannot be reached in the star; thus the real configurations of equilibrium likely have a magnetic field energy-density much smaller than the matter energy-density, implying that the unmagnetized maximum mass, the Chandrasekhar mass (B.7.1), still applies.

On the other hand, as we have seen when the maximum mass (B.7.7) is approached for magnetic fields  $B_D \gtrsim 10^4$ , the central density of the system is  $\rho_c \gtrsim 4 \times 10^{12}$  g cm<sup>-3</sup>. In particular, the maximum mass configuration would have a radius  $R \approx 70$  km and thus a central density  $\rho_c \approx 1.2 \times 10^{13}$  g cm<sup>-3</sup>, just one order of magnitude less than the nuclear saturation density. These values imply that the mass, radius, and density of the ultramagnetized objects considered in Das and Mukhopadhyay (2013) are much more similar to the parameters of neutron star rather than to the ones of white dwarfs. Thus, it is natural to ask whether the compactness of the star,  $\mathcal{C} = GM/(c^2R)$ , is such to require a full general relativistic treatment. For the above star parameters close to the maximum mass configuration, we see that  $\mathcal{C} \approx 0.05$ , a value in clear contrast with a Newtonian treatment of the equilibrium equations.

In this line, our previous results of Ref. Rotondo et al. (2011b) become relevant. We found there that, in the case of carbon white dwarfs, general relativistic instability sets in at a density  $\rho_{\text{crit}} \approx 2 \times 10^{10}$  g cm<sup>-3</sup>, prior to the inverse  $\beta$  decay instability. Such a density is much lower than the densities of the ultramagnetized white dwarfs of Ref. Das and Mukhopadhyay (2013).

$M (M_{\odot})$	$R \text{ (km)}$	$B \text{ (G)}$	$B_{\text{max}} \text{ (G)}$	$W_B (\times 10^{51} \text{erg})$	$ W_G  (\times 10^{51} \text{erg})$	$W_B/ W_G $	$m_B (M_{\odot})$	$\epsilon/R$
2.58	$7.02 \times 10^1$	$8.80 \times 10^{17}$	$5.67 \times 10^{16}$	$4.43 \times 10^4$	$1.88 \times 10^2$	235	24.71	-2008.34
2.38	$9.60 \times 10^2$	$4.44 \times 10^{15}$	$2.79 \times 10^{14}$	$2.90 \times 10^3$	$1.17 \times 10^1$	248	1.62	-2119.34
2.06	$1.86 \times 10^3$	$1.07 \times 10^{15}$	$6.42 \times 10^{13}$	$1.23 \times 10^3$	4.52	273	0.69	-2333.49

**Table B.17.:** Mass-Radius configurations of magnetized white dwarfs of Ref. Das and Mukhopadhyay (2013) with the correspondent magnetic field  $B$ , the maximum virial magnetic field  $B_{\text{max}}$ , magnetic energy  $W_B$  and gravitational  $W_G$ , the ratio of them  $W_B/|W_G|$ , the magnetic mass in units of solar mass  $m_B$ , and the values of eccentricity in units of the spherical star radius  $\epsilon/R$ .

### **B.7.7. Evolutionary path**

As a possible mechanism of formation of ultramagnetized white dwarfs, in Ref. Das and Mukhopadhyay (2013) it was proposed that the star by accretion could increase continuously its central density and magnetic field. However, as we have shown it is unlikely that such an accretion could bring the white dwarf to such extreme regimes without passing through all the instability channels analyzed in this work; most likely a continuous increase of the central density by accretion leads to the triggering of the white dwarf gravitational collapse to a neutron star, or to explosive burning processes leading to ordinary type Ia supernovae.

### **B.7.8. Conclusions**

We have shown that the ultramagnetized,  $B \gtrsim 10^{15}$  G, massive,  $M \gtrsim 2M_{\odot}$ , white dwarfs introduced in Das and Mukhopadhyay (2013) are unlikely to exist in nature since they are subjected to several macro and micro instabilities which would make a white dwarf either to collapse or to explode much prior to the reaching of such a hypothetical structure. The construction of equilibrium configurations of a magnetized compact star needs the inclusion of several effects not accounted for in Ref. Das and Mukhopadhyay (2013), and therefore the acceptance of such ultramagnetized white dwarfs as possible astrophysical objects has to be considered with most caution.



# C. Neutron Stars Physics and Astrophysics

## C.1. Self-gravitating system of degenerate neutrons, protons and electrons in beta equilibrium

### C.1.1. Introduction

The insurgence of critical electric fields in the process of gravitational collapse leading to vacuum polarization process (Ruffini et al., 2010b) has convinced us of the necessity of critically reexamining the gravitational and electro-dynamical properties in neutron stars. In this light we have recently generalized the Feynman, Metropolis and Teller treatment of compressed atoms to the relativistic regimes (Rotondo et al., 2011c). We have so enforced, self-consistently in a relativistic Thomas-Fermi equation, the  $\beta$  equilibrium condition extending the works of Popov (1971b), Zeldovich and Popov (1972), Migdal et al. (1976, 1977), Ferreira et al. (1980) and Ruffini and Stella (1981) for heavy nuclei. Thanks to the existence of scaling laws (see Rotondo et al. (2011c) and Ruffini (2008b)) this treatment has been extrapolated to compressed nuclear matter cores of stellar dimensions with mass numbers  $A \simeq (m_{\text{Planck}}/m_n)^3 \sim 10^{57}$  or  $M_{\text{core}} \sim M_{\odot}$ . Such configurations fulfill global but not local charge neutrality. They have electric fields on the core surface, increasing for decreasing values of the electron Fermi energy  $E_e^F$  reaching values much larger than the critical value  $E_c = m_e^2 c^3 / (e\hbar)$ , for  $E_e^F = 0$ . The assumption of constant distribution of protons at nuclear densities simulates, in such a treatment, the confinement due to the strong interactions in the case of nuclei and heavy nuclei and due to both the gravitational field and the strong interactions in the case of nuclear matter cores of stellar sizes.

In this work we introduce explicitly the effects of gravitation by considering a general relativistic system of degenerate fermions composed of neutrons, protons and electrons in  $\beta$ -equilibrium: this is the simplest nontrivial system in which new electro-dynamical and general relativistic properties of the equilibrium configuration can be clearly and rigorously illustrated. We first prove that the condition of local charge neutrality can never be implemented since it violates necessary conditions of equilibrium at the micro-

physical scale. We then prove the existence of a solution with global, but not local, charge neutrality. Such a solution accounts for essential gravito-electrodynamical effects. First we recall the constancy of the general relativistic Fermi energy of each specie pioneered by Klein (1949). We subsequently introduce the general relativistic Thomas-Fermi equations for the three fermion species fulfilling relativistic quantum statistics, governed by the Einstein-Maxwell equations. The solution of this system of equations presents a formidable mathematical challenge in theoretical physics. The traditional difficulties encountered in proving the existence and unicity of the solution of the Thomas-Fermi equation are here enhanced by the necessity of solving the general relativistic Thomas-Fermi equation coupled with the Einstein-Maxwell system of equations. We present the general solution for the equilibrium configuration, from the center of the star all the way to the border, giving the details of the gravitational field, of the electro-dynamical field as well as of the conserved quantities.

We illustrate such a solution by selecting a central density  $\rho(0) = 3.94\rho_{\text{nuc}}$ , where  $\rho_{\text{nuc}} \simeq 2.7 \times 10^{14} \text{ g cm}^{-3}$  is the nuclear density. We point out the existence near the boundary of the core in the equilibrium configuration of three different radii, in decreasing order:  $R_e$  corresponding to the vanishing of the Fermi momentum of the electron component;  $P_e^F = 0$ ,  $R_p$  corresponding to the vanishing of the Fermi momentum of the proton component;  $P_p^F = 0$  and  $R_n$  corresponding to the radius at which the Fermi momentum of neutrons vanishes:  $P_n^F = 0$ . We then give explicit expressions for the proton versus electron density ratio and the proton versus neutron density ratio for any value of the radial coordinate as well as for the electric potential at the center of the configuration. A novel situation occurs: the description of the pressure and density is not anylonger a local one. Their determination needs prior knowledge of the global electro-dynamical and gravitational potentials on the entire system as well as of the radii  $R_n$ ,  $R_p$  and  $R_e$ . This is a necessary outcome of the self-consistent solution of the eigenfunction within general relativistic Thomas-Fermi equation in the Einstein-Maxwell background. As expected from the considerations in Rotondo et al. (2011c), the electric potential at the center of the configuration fulfills  $eV(0) \simeq m_\pi c^2$  and the gravitational potential  $1 - e^{v(0)/2} \simeq m_\pi/m_p$ . The implementation of the constancy of the general relativistic Fermi energy of each particle species and the consequent system of equations illustrated here is the simplest possible example admitting a rigorous nontrivial solution. It will necessarily apply in the case of additional particle species and of the inclusion of nuclear interactions: in this cases however it is not sufficient and the contribution of nuclear fields must be taken into due account.

### C.1.2. The impossibility of a solution with local charge neutrality

We consider the equilibrium configurations of a degenerate gas of neutrons, protons and electrons with total matter energy density and total matter pressure

$$\mathcal{E} = \sum_{i=n,p,e} \frac{2}{(2\pi\hbar)^3} \int_0^{P_i^F} \epsilon_i(p) 4\pi p^2 dp, \quad (\text{C.1.1})$$

$$P = \sum_{i=n,p,e} \frac{1}{3} \frac{2}{(2\pi\hbar)^3} \int_0^{P_i^F} \frac{p^2}{\epsilon_i(p)} 4\pi p^2 dp, \quad (\text{C.1.2})$$

where  $\epsilon_i(p) = \sqrt{c^2 p^2 + m_i^2 c^4}$  is the relativistic single particle energy. In addition, we require the condition of  $\beta$ -equilibrium between neutrons, protons and electrons

$$\mu_n = \mu_p + \mu_e, \quad (\text{C.1.3})$$

where  $P_i^F$  denotes the Fermi momentum and  $\mu_i = \partial\mathcal{E}/\partial n_i = \sqrt{c^2 (P_i^F)^2 + m_i^2 c^4}$  is the free-chemical potential of particle-species with number density  $n_i = (P_i^F)^3 / (3\pi^2 \hbar^3)$ . We now introduce the extension to general relativity of the Thomas-Fermi equilibrium condition on the generalized Fermi energy  $E_e^F$  of the electron component

$$E_e^F = e^{\nu/2} \mu_e - m_e c^2 - eV = \text{constant}, \quad (\text{C.1.4})$$

where  $e$  is the fundamental charge,  $V$  is the Coulomb potential of the configuration and we have introduced the metric

$$ds^2 = e^{\nu(r)} c^2 dt^2 - e^{\lambda(r)} dr^2 - r^2 d\theta^2 - r^2 \sin^2 \theta d\varphi^2, \quad (\text{C.1.5})$$

for a spherically symmetric non-rotating neutron star. The metric function  $\lambda$  is related to the mass  $M(r)$  and the electric field  $E(r) = -e^{-(\nu+\lambda)/2} V'$  (a prime stands for radial derivative) through

$$e^{-\lambda} = 1 - \frac{2GM(r)}{c^2 r} + \frac{G}{c^4} r^2 E^2(r). \quad (\text{C.1.6})$$

Thus the equations for the neutron star equilibrium configuration consist of the following Einstein-Maxwell equations and general relativistic Thomas-

Fermi equation

$$M' = 4\pi r^2 \frac{\mathcal{E}}{c^2} - \frac{4\pi r^3}{c^2} e^{-\nu/2} \hat{V}' (n_p - n_e), \quad (\text{C.1.7})$$

$$\nu' = \frac{2G}{c^2} \frac{4\pi r^3 P/c^2 + M - r^3 E^2/c^2}{r^2 \left(1 - \frac{2GM}{c^2 r} + \frac{Gr^2 E^2}{c^4}\right)}, \quad (\text{C.1.8})$$

$$P' + \frac{\nu'}{2} (\mathcal{E} + P) = -(P^{\text{em}})' - \frac{4P^{\text{em}}}{r}, \quad (\text{C.1.9})$$

$$\hat{V}'' + \frac{2}{r} \hat{V}' \left[1 - \frac{r(\nu' + \lambda')}{4}\right] = -4\pi\alpha\hbar c e^{\nu/2} e^\lambda \left\{ n_p - \frac{e^{-3\nu/2}}{3\pi^2} [\hat{V}^2 + 2m_e c^2 \hat{V} - m_e^2 c^4 (e^\nu - 1)]^{3/2} \right\}, \quad (\text{C.1.10})$$

where  $\alpha$  denotes the fine structure constant,  $\hat{V} = E_e^F + eV$ ,  $P^{\text{em}} = -E^2/(8\pi)$  and we have used Eq. (C.1.4) to obtain Eq. (C.1.10).

It can be demonstrated that the assumption of the equilibrium condition (C.1.4) together with the  $\beta$ -equilibrium condition (C.1.3) and the hydrostatic equilibrium (C.1.9) is enough to guarantee the constancy of the generalized Fermi energy

$$E_i^F = e^{\nu/2} \mu_i - m_i c^2 + q_i V, \quad i = n, p, e, \quad (\text{C.1.11})$$

for all particle species separately. Here  $q_i$  denotes the particle unit charge of the  $i$ -species. Indeed, as shown by Olson and Bailyn (1975, 1978), when the fermion nature of the constituents and their degeneracy is taken into account, in the configuration of minimum energy the generalized Fermi energies  $E_i^F$  defined by (C.1.11) must be constant over the entire configuration. These minimum energy conditions generalize the equilibrium conditions of Klein (1949) and of Kodama and Yamada (1972) to the case of degenerate multi-component fluids with particle species with non-zero unit charge.

If one were to assume, as often done in literature, the local charge neutrality condition  $n_e(r) = n_p(r)$  instead of assuming the equilibrium condition (C.1.4), this would lead to  $V = 0$  identically (since there will be no electric fields generated by the neutral matter distribution) implying via Eqs. (C.1.3) and (C.1.9)

$$\begin{aligned} E_e^F + E_p^F &= e^{\nu/2} (\mu_e + \mu_p) - (m_e + m_p) c^2 = E_n^F \\ &+ (m_n - m_e - m_p) c^2 = \text{constant}. \end{aligned} \quad (\text{C.1.12})$$

Thus the neutron Fermi energy would be constant throughout the configuration as well as the sum of the proton and electron Fermi energies but not

the individual Fermi energies of each component. In Fig. C.1 we show the results of the Einstein equations for a selected value of the central density of a system of degenerate neutrons, protons, and electrons in  $\beta$ -equilibrium under the constraint of local charge neutrality. In particular, we have plotted the Fermi energy of the particle species in units of the pion rest-energy. It can be seen that indeed the Fermi energies of the protons and electrons are not constant throughout the configuration which would lead to microscopic instability. This proves the impossibility of having a self-consistent configuration fulfilling the condition of local charge neutrality for our system. This result is complementary to the conclusion of Eq. (4.6) of Olson and Bailyn (1975) who found that, at zero temperature, only a dust solution with zero particle kinetic energy can satisfy the condition of local charge neutrality and such a configuration is clearly unacceptable for an equilibrium state of a self-gravitating system.

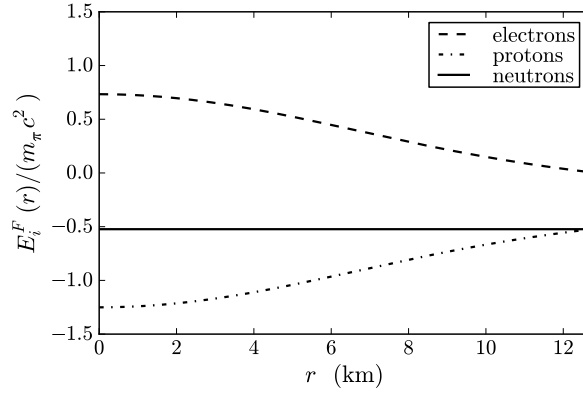


**Figure C.1.:** Fermi energies for neutrons, protons and electrons in units of the pion rest-energy for a locally neutral configuration with central density  $\rho(0) = 3.94\rho_{\text{nuc}}$ , where  $\rho_{\text{nuc}} = 2.7 \times 10^{14} \text{ g cm}^{-3}$  denotes the nuclear density.

### C.1.3. The solution with global charge neutrality

We turn now to describe the equilibrium configurations fulfilling only global charge neutrality. We solve self-consistently Eqs. (C.1.7) and (C.1.8) for the metric, Eq. (C.1.9) for the hydrostatic equilibrium of the three degenerate fermions and, in addition, we impose Eq. (C.1.3) for the  $\beta$ -equilibrium. The crucial equation relating the proton and the electron distributions is then given by the general relativistic Thomas-Fermi equation (C.1.10). The boundary conditions are: for Eq. (C.1.7) the regularity at the origin:  $M(0) = 0$ , for Eq. (C.1.9) a given value of the central density, and for Eq. (C.1.10) the regularity at the origin  $n_e(0) = n_p(0)$ , and a second condition at infinity which

results in an eigenvalue problem determined by imposing the global charge neutrality conditions

$$\hat{V}(R_e) = E_e^F, \quad \hat{V}'(R_e) = 0, \quad (\text{C.1.13})$$

at the radius  $R_e$  of the electron distribution defined by

$$P_e^F(R_e) = 0, \quad (\text{C.1.14})$$

from which follows

$$\begin{aligned} E_e^F &= m_e c^2 e^{\nu(R_e)/2} - m_e c^2 \\ &= m_e c^2 \sqrt{1 - \frac{2GM(R_e)}{c^2 R_e}} - m_e c^2. \end{aligned} \quad (\text{C.1.15})$$

Then the eigenvalue problem consists in determining the gravitational potential and the Coulomb potential at the center of the configuration that satisfy the conditions (C.1.13)–(C.1.15) at the boundary.

#### C.1.4. Numerical integration of the equilibrium equations

The solution for the particle densities, the gravitational potential, the Coulomb potential and the electric field are shown in Fig. (C.2) for a configuration with central density  $\rho(0) = 3.94\rho_{\text{nuc}}$ . In order to compare our results with those obtained in the case of nuclear matter cores of stellar dimensions Rotondo et al. (2011c) as well as to analyze the gravito-electrodynamical stability of the configuration we have plotted the electric potential in units of the pion rest-energy and the gravitational potential in units of the pion-to-proton mass ratio. One particular interesting new feature is the approach to the boundary of the configuration: three different radii are present corresponding to distinct radii at which the individual particle Fermi pressure vanishes. The radius  $R_e$  for the electron component corresponding to  $P_e^F(R_e) = 0$ , the radius  $R_p$  for the proton component corresponding to  $P_p^F(R_p) = 0$  and the radius  $R_n$  for the neutron component corresponding to  $P_n^F(R_n) = 0$ .

The smallest radius  $R_n$  is due to the threshold energy for  $\beta$ -decay which occurs at a density  $\sim 10^7 \text{ g cm}^{-3}$ . The radius  $R_p$  is larger than  $R_n$  because the proton mass is slightly smaller than the neutron mass. Instead,  $R_e > R_p$  due to a combined effect of the difference between the proton and electron masses and the implementation of the global charge neutrality condition through the Thomas-Fermi equilibrium conditions.

For the configuration of Fig. C.2 we found  $R_n \simeq 12.735 \text{ km}$ ,  $R_p \simeq 12.863 \text{ km}$  and  $R_e \simeq R_p + 10^3 \lambda_e$  where  $\lambda_e = \hbar / (m_e c)$  denotes the electron Compton wavelength. We find that the electron component follows closely the pro-

ton component up to the radius  $R_p$  and neutralizes the configuration at  $R_e$  without having a net charge, contrary to the results e.g in Olson and Baily (1978).

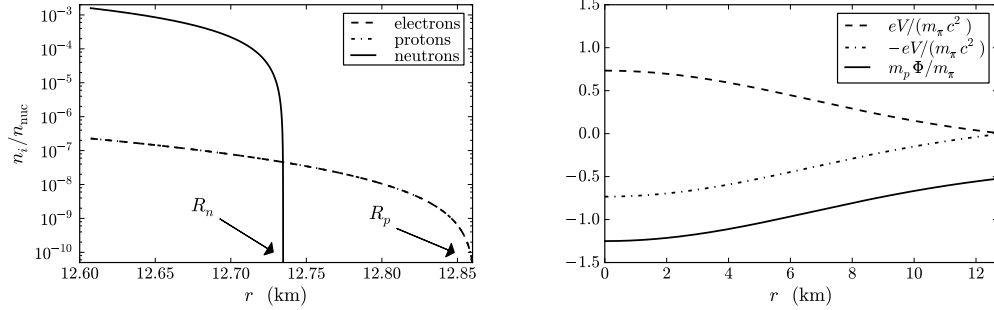


**Figure C.2.:** Top panel: particle number density of neutrons, protons, and electrons approaching the boundary of the configuration in units of the nuclear density  $n_{\text{nuc}} \simeq 1.6 \times 10^{38} \text{ cm}^{-3}$ . Bottom panel: proton and electron Coulomb potentials in units of the pion rest-energy  $eV/(m_{\pi}c^2)$  and  $-eV/(m_{\pi}c^2)$  respectively and the proton gravitational potential in units of the pion mass  $m_p\Phi/m_{\pi}$  where  $\Phi = (e^{\nu/2} - 1)$ .

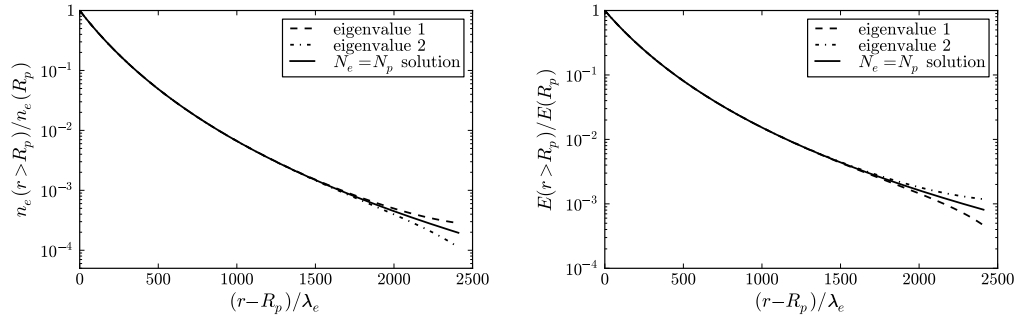


**Figure C.3.:** Top panel: electron number density for  $r \geq R_p$  normalized to its value at  $r = R_p$ . Bottom panel: electric field for  $r \geq R_p$  normalized to its value at  $r = R_p$ . We have shown also the behavior of the solution of the general relativistic Thomas-Fermi equation (C.1.10) for two different eigenvalues close to the one which gives the globally neutral configuration.

It can be seen from Fig. C.2 that the negative proton gravitational potential energy is indeed always larger than the positive proton electric potential energy. Therefore the configuration is stable against Coulomb repulsion. This confirms the results in the simplified case analyzed by Rotondo et al. (2011c).

From Eq. (C.1.11) and the relation between Fermi momentum and the particle density  $P_i^F = (3\pi^2\hbar^3 n_i)^{1/3}$ , we obtain the proton-to-electron and proton-to-neutron ratio for any value of the radial coordinate

$$\frac{n_p(r)}{n_e(r)} = \left[ \frac{f^2(r)\mu_e^2(r) - m_p^2 c^4}{\mu_e^2(r) - m_e^2 c^4} \right]^{3/2}, \quad (\text{C.1.16})$$

$$\frac{n_p(r)}{n_n(r)} = \left[ \frac{g^2(r)\mu_n^2(r) - m_p^2 c^4}{\mu_n^2(r) - m_n^2 c^4} \right]^{3/2}, \quad (\text{C.1.17})$$

where  $f(r) = (E_p^F + m_p c^2 - eV)/(E_e^F + m_e c^2 + eV)$ ,  $g(r) = (E_p^F + m_p c^2 - eV)/(E_n^F + m_n c^2)$  and the constant values of the generalized Fermi energies are given by

$$E_n^F = m_n c^2 e^{\nu(R_n)/2} - m_n c^2, \quad (\text{C.1.18})$$

$$E_p^F = m_p c^2 e^{\nu(R_p)/2} - m_p c^2 + eV(R_p), \quad (\text{C.1.19})$$

$$E_e^F = m_e c^2 e^{\nu(R_e)/2} - m_e c^2. \quad (\text{C.1.20})$$

A novel situation occurs: the determination of the quantities (C.1.16) and (C.1.18) necessarily require the prior knowledge of the global electro-dynamical and gravitational potential from the center of the configuration all the way out to the boundary defined by the radii  $R_e$ ,  $R_p$  and  $R_n$ . This necessity is an outcome of the solution for the eigenfunction of the general relativistic Thomas-Fermi equation (C.1.10).

From the regularity condition at the center of the star  $n_e(0) = n_p(0)$  together with Eq. (C.1.16) we obtain the Coulomb potential at the center of the configuration

$$eV(0) = \frac{(m_p - m_e)c^2}{2} \left[ 1 + \frac{E_p^F - E_e^F}{(m_p - m_e)c^2} - \frac{(m_p + m_e)c^2}{E_n^F + m_n c^2} e^{\nu(0)} \right] \quad (\text{C.1.21})$$

which after some algebraic manipulation and defining the central density in units of the nuclear density  $\eta = \rho(0)/\rho_{\text{nuc}}$  can be estimated as

$$\begin{aligned} eV(0) &\simeq \frac{1}{2} \left[ m_p c^2 e^{\nu(R_p)/2} - m_e c^2 e^{\nu(R_e)/2} - \frac{m_n c^2 e^{\nu(R_n)/2}}{1 + [P_n^F(0)/(m_n c)]^2} \right] \\ &\simeq \frac{1}{2} \left[ \frac{(3\pi^2 \eta / 2)^{2/3} m_p}{(3\pi^2 \eta / 2)^{2/3} m_\pi + m_n^2 / m_\pi} \right] m_\pi c^2, \end{aligned} \quad (\text{C.1.22})$$

where we have approximated the gravitational potential at the boundary as  $e^{\nu(R_e)/2} \simeq e^{\nu(R_p)/2} \simeq e^{\nu(R_n)/2} \simeq 1$ . Then for configurations with central den-

sities larger than the nuclear density we necessarily have  $eV(0) \gtrsim 0.35m_\pi c^2$ . In particular, for the configuration we have exemplified with  $\eta = 3.94$  in Fig. C.2, from the above expression (C.1.22) we obtain  $eV(0) \simeq 0.85m_\pi c^2$ . This value of the central potential agrees with the one obtained in the simplified case of nuclear matter cores with constant proton density (Rotondo et al., 2011c).

### **C.1.5. Conclusions**

We have proved in the first part of this letter that the treatment generally used for the description of neutron stars adopting the condition of local charge neutrality, is not consistent with the Einstein-Maxwell equations and micro-physical conditions of equilibrium consistent with quantum statistics (see Fig. C.1). We have shown how to construct a self-consistent solution for a general relativistic system of degenerate neutrons, protons and electrons in  $\beta$ -equilibrium fulfilling global but not local charge neutrality.

Although the mass-radius relation in the simple example considered here in our new treatment, differs slightly from the one of the traditional approaches, the differences in the electrodynamic structure are clearly very large. As is well-known these effects can lead to important astrophysical consequences on the physics of the gravitational collapse of a neutron star to a black hole Ruffini et al. (2010b).

Having established in the simplest possible example the new set of Einstein-Maxwell and general relativistic Thomas-Fermi equations, we now proceed to extend this approach when strong interactions are present Rueda et al. (2011). The contribution of the strong fields to the energy-momentum tensor, to the four-vector current and consequently to the Einstein-Maxwell equations have to be taken into account. Clearly in this more general case, the conditions introduced in this letter have to be still fulfilled: the  $r$ -independence of the generalized Fermi energy of electrons and the fulfillment of the general relativistic Thomas-Fermi equation Rueda et al. (2011). In addition, the generalized Fermi energy of protons and neutrons will depend on the nuclear interaction fields. The fluid of neutrons, protons and electrons in this more general case does not extend all the way to the neutron star surface but is confined to the neutron star core endowed with overcritical electric fields, in precise analogy with the case of the compressed nuclear matter core of stellar dimension described in Rotondo et al. (2011c).

## C.2. The Klein first integrals in an equilibrium system with electromagnetic, weak, strong and gravitational interactions

### C.2.1. Introduction

The unsolved problems of supernovae theories as well as the necessity of processes leading to electrodynamical phenomena during the gravitational collapse to a black hole (Ruffini et al., 2010b) lead to the necessity of critically reexamining the current treatment of neutron stars. In a series of articles (see Rotondo et al. (2011c,d)), we have recently developed the first steps towards a new consistent treatment for the description of neutron stars, well beyond the traditional Tolman-Oppenheimer-Volkoff equations.

First we have generalized the treatment of compressed atoms of Feynman, Metropolis and Teller to the relativistic regimes (see Rotondo et al. (2011c) for details). There, it has been enforced self-consistently in a relativistic Thomas-Fermi equation, the condition of  $\beta$ -equilibrium extending the works of Popov (1971b), Zeldovich and Popov (1972), Migdal et al. (1976, 1977), Ferreira et al. (1980) and Ruffini and Stella (1981) for heavy nuclei. Then, through the using of scaling laws, following Ruffini (2008b); Popov (2010), this treatment was extrapolated to compressed nuclear matter cores at nuclear and supranuclear densities. Such cores have stellar dimensions and mass numbers  $A \simeq (m_{\text{Planck}}/m_n)^3 \sim 10^{57}$  or  $M_{\text{core}} \sim M_{\odot}$ . In addition, they fulfill global but not local charge neutrality having electric fields on the core surface, increasing for decreasing values of the electron Fermi energy  $E_e^F$  reaching values much larger than the critical value  $E_c = m_e^2 c^3 / (e\hbar)$ , for  $E_e^F = 0$ . The assumption of constant distribution of protons at nuclear densities simulates, in such a treatment, the confinement due to the strong interactions in the case of nuclei and heavy nuclei and due to both the gravitational field and strong interactions in the case of nuclear matter cores of stellar sizes at nuclear and supranuclear densities.

In a subsequent work Rotondo et al. (2011d), we have generalized the above approach explicitly including the effects of the gravitational field by considering the most simplified nontrivial but rigorous treatment of a general relativistic system of neutrons, protons and electrons in  $\beta$ -equilibrium. It has been there proved that the traditional treatment for the description of neutron stars adopting the condition of local charge neutrality is not consistent with the Einstein-Maxwell equations and with microphysical conditions of equilibrium within quantum statistics. The role of the constancy of the general relativistic Fermi energy of each particle species pioneered by Klein (1949) has been there emphasized and, the full system of equilibrium equations consisting of the Einstein-Maxwell and general relativistic Thomas-Fermi equations has been formulated. The corresponding solution of such a system of

equations has been there given in the simplest possible example of a configuration of neutrons, protons and electrons in  $\beta$ -equilibrium with electromagnetic, weak and gravitational interactions. New electrodynamic and general relativistic properties of the equilibrium configurations have been there illustrated.

The aim of this work is to make an essential new step: we further proceed to the description of a system of neutrons, protons and electrons fulfilling strong, electromagnetic, weak and gravitational interactions. The essential role of the Klein first integrals is evidenced and their theoretical formulation is presented in the Einstein-Maxwell background. For the sake of generality the treatment is performed in the most general case in which finite temperature effects are also taking into account. We adopt throughout the work natural units  $\hbar = c = 1$ .

### C.2.2. The Constitutive General Relativistic Equations

The densities in the core of a neutron star exceed the nuclear density  $\rho_{\text{nuc}} \sim 2.7 \times 10^{14} \text{ g/cm}^3$  and may reach densities of order  $\sim 10^{17} \text{ g/cm}^3$  at the verge of the gravitational collapse of the neutron star to a black hole. There is therefore the need of a consistent relativistic theory for the description of the interactions between the matter constituents. In particular, approaches for the nuclear interaction between nucleons based on phenomenological potentials and non-relativistic many-body theory become inapplicable (see Bowers et al. (1973b,a)).

A self-consistent relativistic and well-tested model for the nuclear interactions is the Walecka model (see Duerr (1956); Walecka (1974) for details). This model share common features with the model adopted by Bowers et al. in (Bowers et al., 1973b,a); in both of them the nucleons interact through a Yukawa coupling and the flat spacetime has been considered to construct the equation of state of nuclear matter. The technique of constructing the equation of state assuming flat spacetime has been generally used since, as pointed out in Bowers et al. (1973b,a), as long as  $\rho < 10^{49} \text{ g/cm}^3$  the gravitational contributions to interactions between particles are negligible. However, when we turn to neutron star configurations at nuclear and supranuclear densities, it has been shown in Rotondo et al. (2011d) how the solution of the Einstein-Maxwell system of equations is mandatory.

In the often called extended version of the Walecka model, the strong interaction between nucleons is described by the exchange of three virtual mesons:  $\sigma$  is an isoscalar meson field providing the attractive long-range part of the nuclear force;  $\omega$  is a massive vector field that models the repulsive short range and;  $\rho$  is the massive isovector field that takes account surface as well as isospin effects of nuclei (see also Boguta and Bodmer (1977); Ring (1996)).

The total Lagrangian density of the system is given by

$$\mathcal{L} = \mathcal{L}_g + \mathcal{L}_f + \mathcal{L}_\sigma + \mathcal{L}_\omega + \mathcal{L}_\rho + \mathcal{L}_\gamma + \mathcal{L}_{\text{int}}, \quad (\text{C.2.1})$$

where the Lagrangian densities for the free-fields are

$$\mathcal{L}_g = -\frac{R}{16\pi G}, \quad (\text{C.2.2})$$

$$\mathcal{L}_\gamma = -\frac{1}{4}F_{\mu\nu}F^{\mu\nu}, \quad (\text{C.2.3})$$

$$\mathcal{L}_\sigma = \frac{1}{2}\nabla_\mu\sigma\nabla^\mu\sigma - U(\sigma), \quad (\text{C.2.4})$$

$$\mathcal{L}_\omega = -\frac{1}{4}\Omega_{\mu\nu}\Omega^{\mu\nu} + \frac{1}{2}m_\omega^2\omega_\mu\omega^\mu, \quad (\text{C.2.5})$$

$$\mathcal{L}_\rho = -\frac{1}{4}\mathcal{R}_{\mu\nu}\mathcal{R}^{\mu\nu} + \frac{1}{2}m_\rho^2\rho_\mu\rho^\mu, \quad (\text{C.2.6})$$

where  $\Omega_{\mu\nu} \equiv \partial_\mu\omega_\nu - \partial_\nu\omega_\mu$ ,  $\mathcal{R}_{\mu\nu} \equiv \partial_\mu\rho_\nu - \partial_\nu\rho_\mu$ ,  $F_{\mu\nu} \equiv \partial_\mu A_\nu - \partial_\nu A_\mu$  are the field strength tensors for the  $\omega^\mu$ ,  $\rho$  and  $A^\mu$  fields respectively,  $\nabla_\mu$  stands for covariant derivative and  $R$  is the Ricci scalar. We adopt the Lorenz gauge for the fields  $A_\mu$ ,  $\omega_\mu$ , and  $\rho_\mu$ . The self-interaction scalar field potential  $U(\sigma)$  is a quartic-order polynom for a renormalizable theory (see e.g. Lee and Wick (1974)). The specific functional form of  $U(\sigma)$  is not relevant for the scope of this work, thus we will not adopt any particular form of it hereafter.

The Lagrangian density for the three fermion species is

$$\mathcal{L}_f = \sum_{i=e,N} \bar{\psi}_i (i\gamma^\mu D_\mu - m_i) \psi_i, \quad (\text{C.2.7})$$

where  $\psi_N$  is the nucleon isospin doublet,  $\psi_e$  is the electronic singlet,  $m_i$  states for the mass of each particle-specie and  $D_\mu = \partial_\mu + \Gamma_\mu$ , being  $\Gamma_\mu$  the Dirac spin connections that satisfy the commutation relation

$$[\gamma_\mu, \Gamma_\nu] = \partial_\nu\gamma_\mu - \Gamma_{\mu\nu}^\alpha\gamma_\alpha, \quad (\text{C.2.8})$$

where  $\Gamma_{\mu\nu}^\alpha$  denotes the Christoffel symbols.

The interacting part of the Lagrangian density is, in the minimal coupling assumption, given by

$$\mathcal{L}_{\text{int}} = -g_\sigma\sigma\bar{\psi}_N\psi_N - g_\omega\omega_\mu J_\omega^\mu - g_\rho\rho_\mu J_\rho^\mu + eA_\mu J_{\gamma,e}^\mu - eA_\mu J_{\gamma,N}^\mu, \quad (\text{C.2.9})$$

where the conserved currents are

$$J_\omega^\mu = \bar{\psi}_N \gamma^\mu \psi_N, \quad (\text{C.2.10})$$

$$J_\rho^\mu = \bar{\psi}_N \tau_3 \gamma^\mu \psi_N, \quad (\text{C.2.11})$$

$$J_{\gamma,e}^\mu = \bar{\psi}_e \gamma^\mu \psi_e, \quad (\text{C.2.12})$$

$$J_{\gamma,N}^\mu = \bar{\psi}_N \left( \frac{1 + \tau_3}{2} \right) \gamma^\mu \psi_N. \quad (\text{C.2.13})$$

The coupling constants of the  $\sigma$ ,  $\omega$  and  $\rho$ -fields are  $g_\sigma$ ,  $g_\omega$  and  $g_\rho$ , and  $e$  is the fundamental electric charge. The Dirac matrices  $\gamma^\mu$  and the isospin Pauli matrices satisfy the Dirac algebra in curved spacetime (see e.g. Lee and Pang (1987))

$$\{\gamma^\mu, \gamma^\nu\} = 2g^{\mu\nu}, \quad (\text{C.2.14})$$

$$\{\gamma_\mu, \gamma_\nu\} = 2g_{\mu\nu}, \quad (\text{C.2.15})$$

$$\{\gamma^\mu, \gamma_\nu\} = 2\delta_\nu^\mu, \quad (\text{C.2.16})$$

$$[\tau_i, \tau_j] = 2i\epsilon_{ijk}\tau^k. \quad (\text{C.2.17})$$

The Einstein-Maxwell-Dirac system of equations is then given by

$$G_{\mu\nu} + 8\pi G T_{\mu\nu} = 0, \quad (\text{C.2.18})$$

$$\nabla_\mu F^{\mu\nu} - e J_{ch}^\nu = 0, \quad (\text{C.2.19})$$

$$\nabla_\mu \Omega^{\mu\nu} + m_\omega^2 \omega^\nu - g_\omega J_\omega^\nu = 0, \quad (\text{C.2.20})$$

$$\nabla_\mu \mathcal{R}^{\mu\nu} + m_\rho^2 \rho^\nu - g_\rho J_\rho^\nu = 0, \quad (\text{C.2.21})$$

$$\nabla_\mu \nabla^\mu \sigma + \partial_\sigma U(\sigma) + g_s n_s = 0, \quad (\text{C.2.22})$$

$$[\gamma_\mu (iD^\mu - V_N^\mu) - \tilde{m}_N] \psi_N = 0, \quad (\text{C.2.23})$$

$$[\gamma_\mu (iD^\mu + eA^\mu) - m_e] \psi_e = 0, \quad (\text{C.2.24})$$

where the scalar density  $n_s = \bar{\psi}_N \psi_N$ , the nucleon effective mass  $\tilde{m}_N \equiv m_N + g_\sigma \sigma$ , and

$$V_N^\mu \equiv g_\omega \omega^\mu + g_\rho \tau \rho^\mu + e \left( \frac{1 + \tau_3}{2} \right) A^\mu, \quad (\text{C.2.25})$$

is the effective four potential of nucleons. The energy-momentum tensor of free-fields and free-fermions  $T^{\mu\nu}$  of the system (C.2.3)–(C.2.6) is

$$T^{\mu\nu} = T_f^{\mu\nu} + T_\gamma^{\mu\nu} + T_\sigma^{\mu\nu} + T_\omega^{\mu\nu} + T_\rho^{\mu\nu}, \quad (\text{C.2.26})$$

where

$$T_\gamma^{\mu\nu} = -F_\alpha^\mu F^{\alpha\nu} - \frac{1}{4}g^{\mu\nu}F_{\alpha\beta}F^{\alpha\beta}, \quad (\text{C.2.27})$$

$$T_\sigma^{\mu\nu} = \nabla^\mu \nabla^\nu \sigma - g^{\mu\nu} \left[ \frac{1}{2} \nabla_\sigma \sigma \nabla^\sigma \sigma - U(\sigma) \right], \quad (\text{C.2.28})$$

$$T_\omega^{\mu\nu} = -\Omega_\alpha^\mu \Omega^{\alpha\nu} - \frac{1}{4}g^{\mu\nu} \Omega_{\alpha\beta} \Omega^{\alpha\beta} + m_\omega^2 \left( \omega^\mu \omega^\nu - \frac{1}{2}g^{\mu\nu} \omega_\alpha \omega^\alpha \right) \quad (\text{C.2.29})$$

$$T_\rho^{\mu\nu} = -\mathcal{R}_\alpha^\mu \mathcal{R}^{\alpha\nu} - \frac{1}{4}g^{\mu\nu} \mathcal{R}_{\alpha\beta} \mathcal{R}^{\alpha\beta} + m_\rho^2 \left( \mathcal{R}^\mu \mathcal{R}^\nu - \frac{1}{2}g^{\mu\nu} \mathcal{R}_\alpha \omega^\alpha \right), \quad (\text{C.2.30})$$

are the contribution due to free-fields and  $T_f^{\mu\nu}$  is the contribution of free-fermions which we discuss below.

### C.2.3. The Thermodynamic Laws and the Field Equations in the Spherically Symmetric Case

We first introduce the non-rotating spherically symmetric spacetime metric

$$ds^2 = e^{\nu(r)} dt^2 - e^{\lambda(r)} dr^2 - r^2 d\theta^2 - r^2 \sin^2 \theta d\varphi^2, \quad (\text{C.2.31})$$

where the  $\nu(r)$  and  $\lambda(r)$  are only functions of the radial coordinate  $r$ .

For very large number of fermions, we can adopt the mean-field approximation in which fermion-field operators are replaced by their expectation values (see e.g. Walecka (1974) for details).

We write the nucleon doublet and the electronic spinor as  $\psi_i = \psi_i(k)e^{-ik_\mu x^\mu}$  in the phase-space. Suppose that neutrons, protons and electrons, and the corresponding antiparticles, are in thermodynamic equilibrium with a finite temperature  $T$ . The occupation fermion-number operators of the “ $k$ ”-state,  $N_i(k) = \psi_i^\dagger(k)\psi_i(k)$  with  $i = e, p, n$ , are replaced by their Fermi-distributions

$$f_i^\pm(k) = \langle \psi_i^\pm(k)^\dagger \psi_i^\pm(k) \rangle = \left[ \exp \left( \frac{\epsilon_i(k) \mp \mu_i}{k_B T} \right) + 1 \right]^{-1}, \quad (\text{C.2.32})$$

where  $k_B$  is the Boltzmann constant,  $\mu_i$  and  $\epsilon_i(k) = \sqrt{k^2 + \tilde{m}_i^2}$  denote the single-particle chemical potential and energy-spectrum (we recall that for electrons  $\tilde{m}_e = m_e$ ). The sign ‘+’ correspond to particles and ‘-’ to antiparticles. We do not consider “real” bosons to be present in the system; the only distribution functions involved in the computation are due to fermions and antifermions and therefore phenomena as Bose-Einstein condensation does not occur within this theory (see e.g. Bowers et al. (1973b) for details).

It is worth to recall that all the thermodynamic quantities, e.g.  $k, \epsilon, T \dots$ , are written here in the local frame which is related to the coordinate frame by the

Lorentz “boost”

$$\Lambda_\alpha^{(a)} = (u_\alpha, \chi_\alpha, \Theta_\alpha, \Phi_\alpha), \quad (\text{C.2.33})$$

where  $u_\alpha = e^{v/2}\delta_\alpha^0$ ,  $\chi_\alpha = e^{\lambda/2}\delta_\alpha^1$ ,  $\Theta_\alpha = r\delta_\alpha^2$ , and  $\Phi_\alpha = r\sin\theta\delta_\alpha^3$ , being  $\delta_\beta^\alpha$  the usual Kronecker delta symbol.

The number-density  $n_i$  of the  $i$ -specie, taking into account the antiparticle contribution is, within the mean-field approximation, given by

$$n_i = \frac{2}{(2\pi)^3} \int d^3k [f_i^+(k) - f_i^-(k)]. \quad (\text{C.2.34})$$

The contribution of free-fermions and antifermions to the energy-momentum tensor can be then written in the perfect fluid form (see e.g. Ruffini and Bonazzola (1969))

$$T_f^{\mu\nu} = (\mathcal{E} + \mathcal{P})u^\mu u^\nu - \mathcal{P}g^{\mu\nu}, \quad (\text{C.2.35})$$

where  $u^\mu$  is the four-velocity of the fluid which satisfies  $u^\mu u_\mu = 1$ , and the energy-density  $\mathcal{E}$  and the pressure  $\mathcal{P}$  are given by

$$\mathcal{E} = \sum_{i=n,p,e} \mathcal{E}_i, \quad \mathcal{P} = \sum_{i=n,p,e} \mathcal{P}_i, \quad (\text{C.2.36})$$

being  $\mathcal{E}_i$  and  $\mathcal{P}_i$  the single fermion-antifermion fluid contributions

$$\mathcal{E}_i = \frac{2}{(2\pi)^3} \int d^3k \epsilon_i(k) [f_i^+(k) + f_i^-(k)], \quad (\text{C.2.37})$$

$$\mathcal{P}_i = \frac{1}{3} \frac{2}{(2\pi)^3} \int d^3k \frac{k^2}{\epsilon_i(k)} [f_i^+(k) + f_i^-(k)]. \quad (\text{C.2.38})$$

The equation of state (C.2.36)–(C.2.38) satisfies the thermodynamic law

$$\mathcal{E} + \mathcal{P} - T\mathcal{S} = \sum_{i=n,p,e} n_i \mu_i, \quad (\text{C.2.39})$$

where  $\mathcal{S} = S/V$  is the entropy per unit volume (entropy density) and  $\mu_i = \partial\mathcal{E}/\partial n_i$  is the free-chemical potential of the  $i$ -specie. At zero-temperature  $T = 0$ ,  $\mu_i = \sqrt{(K_i^F)^2 + \tilde{m}_i^2}$  and  $n_i = (K_i^F)^3/(3\pi^2)$ , where  $K_i^F$  denotes the Fermi momentum of the  $i$ -specie.

The scalar density  $n_s$ , within the mean-field approximation, is given by the following expectation value

$$n_s = \langle \bar{\psi}_N \psi_N \rangle = \frac{2}{(2\pi)^3} \sum_{i=n,p} \int d^3k \frac{\tilde{m}_N}{\epsilon_i(k)} [f_i^+(k) + f_i^-(k)]. \quad (\text{C.2.40})$$

In the static case, only the temporal components of the covariant currents survive, i.e.  $\langle \bar{\psi}(x) \gamma^i \psi(x) \rangle = 0$ . Thus, by taking the expectation values of

Eqs. (C.2.10)–(C.2.13), we obtain the non-vanishing components of the currents

$$J_0^{ch} = n_{ch}u_0 = (n_p - n_e)u_0, \quad (\text{C.2.41})$$

$$J_0^\omega = n_b u_0 = (n_n + n_p)u_0, \quad (\text{C.2.42})$$

$$J_0^\rho = n_3 u_0 = (n_p - n_n)u_0, \quad (\text{C.2.43})$$

where  $n_b$ ,  $n_p$ ,  $n_n$  and  $n_e$  are the baryon, proton, neutron and electron number densities which are functions only of the spatial coordinates, and  $u_0 = \sqrt{g_{00}} = e^{v/2}$ .

Making a variation of Eq. (C.2.39) and using Eqs. (C.2.36)–(C.2.38) and (C.2.40), we obtain the generalized Gibbs-Duhem relation

$$d\mathcal{P} = \sum_{i=n,p,e} n_i d\mu_i - g_\sigma n_s d\sigma + \mathcal{S} dT, \quad (\text{C.2.44})$$

which can be rewritten as

$$d\mathcal{P} = \sum_{i=n,p,e} n_i d\mu_i - g_\sigma n_s d\sigma + \left( \mathcal{E} + \mathcal{P} - \sum_{i=n,p,e} n_i \mu_i \right) \frac{dT}{T}, \quad (\text{C.2.45})$$

where we have used Eq. (C.2.39) to eliminate  $\mathcal{S}$ , and we have used the relation between the scalar density and the fluid energy-density  $n_s = \partial\mathcal{E}/\partial\tilde{m}_N$ , which follows from Eqs. (C.2.36)–(C.2.38) and (C.2.40).

Thus, the Einstein-Maxwell equations (C.2.18–C.2.22) become

$$e^{-\lambda(r)} \left( \frac{1}{r^2} - \frac{1}{r} \frac{d\lambda}{dr} \right) - \frac{1}{r^2} = -8\pi G T_0^0, \quad (\text{C.2.46})$$

$$e^{-\lambda(r)} \left( \frac{1}{r^2} + \frac{1}{r} \frac{dv}{dr} \right) - \frac{1}{r^2} = -8\pi G T_1^1, \quad (\text{C.2.47})$$

$$e^{-\lambda(r)} \left[ \frac{1}{2} \left( \frac{dv}{dr} - \frac{d\lambda}{dr} \right) \left( \frac{1}{r} + \frac{1}{2} \frac{dv}{dr} \right) + \frac{1}{2} \frac{d^2 v}{dr^2} \right] = -8\pi G T_3^3, \quad (\text{C.2.48})$$

$$\frac{d^2 V}{dr^2} + \frac{dV}{dr} \left[ \frac{2}{r} - \frac{1}{2} \left( \frac{dv}{dr} + \frac{d\lambda}{dr} \right) \right] = -e^\lambda e J_{ch}^0, \quad (\text{C.2.49})$$

$$\frac{d^2 \sigma}{dr^2} + \frac{d\sigma}{dr} \left[ \frac{2}{r} - \frac{1}{2} \left( \frac{dv}{dr} + \frac{d\lambda}{dr} \right) \right] = e^\lambda [\partial_\sigma U(\sigma) + g_s n_s], \quad (\text{C.2.50})$$

$$\frac{d^2 \omega}{dr^2} + \frac{d\omega}{dr} \left[ \frac{2}{r} - \frac{1}{2} \left( \frac{dv}{dr} + \frac{d\lambda}{dr} \right) \right] = -e^\lambda [g_\omega J_\omega^0 - m_\omega^2 \omega], \quad (\text{C.2.51})$$

$$\frac{d^2 \rho}{dr^2} + \frac{d\rho}{dr} \left[ \frac{2}{r} - \frac{1}{2} \left( \frac{dv}{dr} + \frac{d\lambda}{dr} \right) \right] = -e^\lambda [g_\rho J_\rho^0 - m_\rho^2 \rho], \quad (\text{C.2.52})$$

where we have introduced the notation  $\omega_0 = \omega$ ,  $\rho_0 = \rho$ , and  $A_0 = V$ . The

metric function  $\lambda$  is related to the mass  $M(r)$  and the electric field  $E(r) = -e^{-(\nu+\lambda)/2}V'$  through

$$e^{-\lambda(r)} = 1 - \frac{2GM(r)}{r} + Gr^2E^2(r) = 1 - \frac{2GM(r)}{r} + \frac{GQ^2(r)}{r^2}, \quad (\text{C.2.53})$$

where we have introduced also the conserved charge  $Q(r) = r^2E(r)$ .

An important equation, although not independent of the Einstein-Maxwell equations (C.2.46)–(C.2.52), is given the energy-momentum conservation law

$$\nabla_\mu T^{\mu\nu} = -g_\omega J_\mu^\omega \Omega^{\mu\nu} - g_\rho J_\mu^\rho \mathcal{R}^{\mu\nu} + e J_\mu^{ch} F^{\mu\nu}, \quad (\text{C.2.54})$$

from which we have

$$\frac{d\mathcal{P}}{dr} = -\frac{(\mathcal{E} + \mathcal{P})}{2} \frac{d\nu}{dr} - g_\sigma n_s \frac{d\sigma}{dr} - g_\omega J_\omega^0 \frac{d\omega}{dr} - g_\rho J_\rho^0 \frac{d\rho}{dr} - e J_{ch}^0 \frac{dV}{dr}, \quad (\text{C.2.55})$$

where we have used the energy-momentum tensor  $T^{\mu\nu}$  given by Eq. (C.2.26).

#### C.2.4. Constancy of the Klein potentials and beta equilibrium

Introducing the nucleon doublet and the electronic spinor in the wave-form  $\psi_i = \psi_i(k)e^{-ik_\mu x^\mu}$  in phase-space, the Dirac equations (C.2.24) become

$$(\gamma_\mu \mathcal{K}_i^\mu - \tilde{m}_i) \psi_i(k) = 0, \quad (\text{C.2.56})$$

where

$$\mathcal{K}_i^\mu \equiv k^\mu - V_i^\mu, \quad V_e^\mu = -eA^\mu. \quad (\text{C.2.57})$$

In the mean-field approximation, making the quadrature of Dirac operators in Eq. (C.2.56) and averaging over all states “ $k$ ”, we obtain the generalized chemical potentials or, for short Klein potentials for electrons  $E_e$ , neutrons  $E_n$  and protons  $E_p$

$$E_e = \sqrt{g_{00}}\mu_e - eV = e^{v/2}\mu_e - eV, \quad (\text{C.2.58})$$

$$E_p = \sqrt{g_{00}}\mu_p + g_\omega\omega + g_\rho\rho + eV = e^{v/2}\mu_p + g_\omega\omega + g_\rho\rho + eV, \quad (\text{C.2.59})$$

$$E_n = \sqrt{g_{00}}\mu_n + g_\omega\omega - g_\rho\rho = e^{v/2}\mu_n + g_\omega\omega - g_\rho\rho, \quad (\text{C.2.60})$$

where we have used Eqs. (C.2.14)–(C.2.17) and Eqs. (C.2.32), (C.2.34), (C.2.36)–(C.2.38). In the zero-temperature case, they are generalized Fermi energies for electrons  $E_e = E_e^F$ , neutrons  $E_n = E_n^F$  and protons  $E_p = E_p^F$ .

Using the equations of motion for the fields  $\rho$ ,  $\omega$  and  $\sigma$ , and using the generalized Gibbs-Duhem relation (C.2.45), the energy-momentum conservation

equation (C.2.55) can be rewritten as

$$e^{\nu/2} \sum_{i=n,p,e} n_i \left( d\mu_i - \frac{dT}{T} \mu_i \right) + (\mathcal{E} + \mathcal{P}) e^{\nu/2} \left( \frac{dT}{T} + \frac{1}{2} d\nu \right) + g_\omega n_b d\omega + g_\rho n_3 d\rho + en_{ch} dV = 0. \quad (\text{C.2.61})$$

The isothermal Tolman condition (Tolman, 1930) (see also Klein (1949)) demands the constancy of the gravitationally red-shifted temperature

$$\frac{dT}{T} + \frac{1}{2} d\nu = 0, \quad \text{or} \quad e^{\nu/2} T = \text{constant}. \quad (\text{C.2.62})$$

Such a condition can be used into Eq. (C.2.61) to obtain

$$\sum_{i=n,p,e} n_i d(e^{\nu/2} \mu_i) + g_\omega n_b d\omega + g_\rho n_3 d\rho + en_{ch} dV = 0. \quad (\text{C.2.63})$$

Moreover, using the expressions (C.2.58)–(C.2.59) of the generalized chemical potentials, Eq. (C.2.63) can be rewritten as

$$\sum_{i=n,p,e} n_i dE_i = 0, \quad (\text{C.2.64})$$

which leads for independent and non-zero particle number densities  $n_i \neq 0$  to the constancy of the Klein potentials (C.2.58)–(C.2.60) for each particle-species, i.e.

$$E_e = e^{\nu/2} \mu_e - eV = \text{constant}, \quad (\text{C.2.65})$$

$$E_p = e^{\nu/2} \mu_p + \mathcal{V}_p = \text{constant}, \quad (\text{C.2.66})$$

$$E_n = e^{\nu/2} \mu_n + \mathcal{V}_n = \text{constant}, \quad (\text{C.2.67})$$

where

$$\mathcal{V}_p = g_\omega \omega + g_\rho \rho + eV, \quad (\text{C.2.68})$$

$$\mathcal{V}_n = g_\omega \omega - g_\rho \rho. \quad (\text{C.2.69})$$

In the case of nuclear matter in  $\beta$ -equilibrium (assuming not trapped neutrinos), the values of the constant Klein potentials (C.2.65)–(C.2.67) are linked by the condition

$$E_n = E_p + E_e, \quad (\text{C.2.70})$$

which can be rewritten explicitly in terms of the chemical potentials as

$$\mu_n = \mu_p + \mu_e + 2g_\rho \rho e^{-\nu/2}. \quad (\text{C.2.71})$$

### **C.2.5. Concluding Remarks**

We have presented the self-consistent equations of equilibrium at finite temperatures for a system of neutrons, protons and electrons in  $\beta$ -equilibrium within general relativity including quantum statistics, electro-weak, and strong interactions. In the mean-field approximation, we obtained the generalized particle chemical potentials from the Dirac equations for nucleons and electrons.

From the Einstein-Maxwell equations, the thermodynamic laws and energy-momentum conservation, we obtain the constancy of the Klein potential of each particle-specie and of the gravitationally red-shifted temperature throughout the configuration, i.e. the first Klein integrals and the Tolman isothermal condition respectively. In the non-interacting degenerate case, following a minimization energy procedure, it was demonstrated that the thermodynamic equilibrium condition of constancy of the generalized particle Fermi energy of all particle species holds (see Olson and Baily (1975)). Such a procedure can be straightforwardly applied to the present case, being the final result given by the equilibrium conditions (C.2.65) and (C.2.66).

The precise values of such constants are linked, in the case of nuclear matter in  $\beta$ -equilibrium, by Eq. (C.2.70), and their full determination needs the inclusion of additional constraints to the system, e.g. global charge neutrality (see e.g. Rotondo et al. (2011d)).

The correct implementation of such generalized Thomas-Fermi equilibrium conditions needs the self-consistent solution of the global problem of equilibrium of the configuration following from the solution of the Einstein-Maxwell equations (C.2.46), (C.2.47), (C.2.49)–(C.2.53), the general relativistic thermodynamic equilibrium conditions (C.2.62), (C.2.65) and (C.2.66), together with the constraints, e.g.  $\beta$ -equilibrium and global charge neutrality.

Thus, the full system of Einstein-Maxwell-Thomas-Fermi equations can be

rewritten in the form

$$e^{-\lambda(r)} \left( \frac{1}{r^2} - \frac{1}{r} \frac{d\lambda}{dr} \right) - \frac{1}{r^2} = -8\pi GT_0^0, \quad (\text{C.2.72})$$

$$e^{-\lambda(r)} \left( \frac{1}{r^2} + \frac{1}{r} \frac{dv}{dr} \right) - \frac{1}{r^2} = -8\pi GT_1^1, \quad (\text{C.2.73})$$

$$V'' + \frac{2}{r} V' \left[ 1 - \frac{r(v' + \lambda')}{4} \right] = -4\pi e e^{v/2} e^\lambda (n_p - n_e), \quad (\text{C.2.74})$$

$$\frac{d^2\sigma}{dr^2} + \frac{d\sigma}{dr} \left[ \frac{2}{r} - \frac{1}{2} \left( \frac{dv}{dr} + \frac{d\lambda}{dr} \right) \right] = e^\lambda [\partial_\sigma U(\sigma) + g_s n_s], \quad (\text{C.2.75})$$

$$\frac{d^2\omega}{dr^2} + \frac{d\omega}{dr} \left[ \frac{2}{r} - \frac{1}{2} \left( \frac{dv}{dr} + \frac{d\lambda}{dr} \right) \right] = -e^\lambda [g_\omega J_\omega^0 - m_\omega^2 \omega], \quad (\text{C.2.76})$$

$$\frac{d^2\rho}{dr^2} + \frac{d\rho}{dr} \left[ \frac{2}{r} - \frac{1}{2} \left( \frac{dv}{dr} + \frac{d\lambda}{dr} \right) \right] = -e^\lambda [g_\rho J_\rho^0 - m_\rho^2 \rho], \quad (\text{C.2.77})$$

$$E_e = e^{v/2} \mu_e - eV = \text{constant}, \quad (\text{C.2.78})$$

$$E_p = e^{v/2} \mu_p + \mathcal{V}_p = \text{constant}, \quad (\text{C.2.79})$$

$$E_n = e^{v/2} \mu_n + \mathcal{V}_n = \text{constant}, \quad (\text{C.2.80})$$

$$e^{v/2} T = \text{constant}, \quad (\text{C.2.81})$$

where the constants  $E_n$ ,  $E_p$  and  $E_e$  are linked by Eq. (C.2.70) and  $\mathcal{V}_{p,n}$  is given by Eq. (C.2.68). In particular, in the degenerate case  $T = 0$ , Eq. (C.2.74) becomes

$$\hat{V}'' + \frac{2}{r} \hat{V}' \left[ 1 - \frac{r(v' + \lambda')}{4} \right] = -4\pi\alpha e^{v/2} e^\lambda \left\{ n_p - \frac{e^{-3v/2}}{3\pi^2} [\hat{V}^2 + 2m_e \hat{V} - m_e^2 (e^v - 1)]^{3/2} \right\}, \quad (\text{C.2.82})$$

where  $\hat{V} \equiv eV + E_e$  and we have used Eq. (C.2.78) into Eq. (C.2.74). This equation is the general relativistic extension of the relativistic Thomas-Fermi equation recently introduced in Rotondo et al. (2011c) for the study of compressed atoms. In addition, Eq. (C.2.82) has been recently used to obtain the globally neutral configurations in the simpler case of degenerate neutrons, protons and electrons in  $\beta$ -equilibrium (Rotondo et al., 2011d).

## C.3. The constitutive equations of a self-gravitating system of neutrons, protons and electrons

### C.3.1. Introduction

We have recently introduced a new approach which thanks to the existence of scaling laws can apply to compressed atoms as well as to massive nuclear matter cores of stellar dimensions (Rotondo et al., 2011c). This approach concerning the compressed atom has already given a new contribution in the study of white dwarfs. It represents the first self-consistent calculation taking into due account the electromagnetic contribution in a relativistic treatment of the Thomas-Fermi equation, within global formulation of the equilibrium of white dwarfs in general relativity (Rotondo et al., 2011b).

The application of the above results (Rotondo et al., 2011c,b) to the case of neutron stars is much more complex and it has been approached stepwise. As a first step we have considered the application of this novel approach to the case of a system of neutrons, protons, and electrons in  $\beta$ -equilibrium at zero temperatures within general relativity (Rotondo et al., 2011d). These results are shortly recalled in Sec. C.3.2. The essential role of the generalized Fermi energy of particles (the Klein potentials) and their constancy on the entire equilibrium configuration has been outlined. The existence of an electric potential over the entire configuration has been evidenced.

We have there proved, for the case of this simplified example where strong interactions are neglected, that the traditional approach of describing the system imposing the condition of local charge neutrality and solving the corresponding TOV equations (see e.g. Shapiro and Teukolsky (1983a)) is conceptually inconsistent. We have then substitute the condition of local charge neutrality with the condition of global charge neutrality and derived the correct system of equations within the Einstein-Maxwell-Thomas-Fermi system. The boundary conditions are also different from a traditional Cauchy data with the values of the functions and first derivatives at the center into a boundary condition at the center and delicate eigenvalue problem at the boundary determining the condition of charge neutrality at the border; see Sec. C.3.2. The conceptual differences and the alternative mathematical equations of the two approaches, the ones imposing local versus global charge neutrality, lead to the presence of additional electro-dynamical global structures. However, in the specific simple example considered in Rotondo et al. (2011d), they do not give significant quantitative differences in the mass-radius relation for the equilibrium configurations. A very different situation occurs when strong interactions are also taken into account.

Interestingly, these results should have been expected on the ground of some classical works dating back to Rosseland (1924) about the gravito-polarization

in self-gravitating ideal Boltzmann electron-ion plasma. We indeed show that our general relativistic equations for the case of global charge neutrality in the Newtonian regime reproduce the Rosseland result. The work of Rosseland has attracted in time additional attention and has been generalized to the case of multicomponent systems; see e.g. Iosilevskiy (2009) and also in the case of general relativity the important results (Klein, 1949; Kodama and Yamada, 1972; Olson and Baily, 1975).

In order to transfer these results in the treatment of realistic neutron stars, the introduction of strong interactions is clearly necessary. We have recently generalized our treatment to the case of strong interactions in Rueda et al. (2011). There the major aim has been to prove the constancy of the Klein potentials in the case in which the nuclear interactions are described by a Lagrangian including in addition to the gravitational, electromagnetic, and weak interactions, also the presence of  $\sigma$ ,  $\omega$ , and  $\rho$  virtual mesons that mediate the nuclear interactions. These results are shortly summarized for completeness in Sec. C.3.3.

It is clear that neutron stars are not at zero temperatures but have temperatures which in the case of the Crab pulsar are  $T \sim 10^6$  K, see e.g. Tennant et al. (2001); Weisskopf et al. (2004). It has been pointed out to us that the thermal energy expected in a neutron star is much larger than the Coulomb energy obtained e.g. in Rotondo et al. (2011d). Before proceeding further in this research we have to prove that these gravito-polarization effect do survive in the presence of a system at  $T \neq 0$ . In any way, the study of the equilibrium of a system of neutrons, protons, and electrons including all the interactions need to be generalized to the case of finite temperatures. This treatment is here presented in Sec. C.3.4. The constancy of the Klein potentials in this more general case is presented in Sec. C.3.5 where it is also explicitly shown how the thermal effects do not modify the existence of gravito-polarization. The generality of the formalism here introduced allows to approach as well the classical Boltzmann limit consistently.

we have finally outlined in the conclusions how this theoretical formulation is now sufficient to approach the problem of the possible existence of overcritical fields at the interface between the the core and the crust of the neutron star.

### C.3.2. Einstein-Maxwell-Thomas-Fermi equations in the degenerate case

Following Rotondo et al. (2011d), we consider the equilibrium configurations of a degenerate gas of neutrons, protons and electrons with total matter en-

ergy density and total matter pressure

$$\mathcal{E} = \sum_{i=n,p,e} \frac{2}{(2\pi\hbar)^3} \int_0^{P_i^F} \epsilon_i(p) 4\pi p^2 dp, \quad (\text{C.3.1})$$

$$P = \sum_{i=n,p,e} \frac{1}{3} \frac{2}{(2\pi\hbar)^3} \int_0^{P_i^F} \frac{p^2}{\epsilon_i(p)} 4\pi p^2 dp, \quad (\text{C.3.2})$$

where  $\epsilon_i(p) = \sqrt{c^2 p^2 + m_i^2 c^4}$  is the relativistic single particle energy and  $P_i^F$  denote the Fermi momentum, related to the particle number density  $n_i$  by  $n_i = (P_i^F)^3 / (3\pi^2 \hbar^3)$ .

Introducing the metric for a spherically symmetric non-rotating configuration

$$ds^2 = e^{\nu(r)} c^2 dt^2 - e^{\lambda(r)} dr^2 - r^2 d\theta^2 - r^2 \sin^2 \theta d\varphi^2, \quad (\text{C.3.3})$$

the full system of equations composed by the Einstein-Maxwell-Thomas-Fermi equations can be written as (see Rotondo et al. (2011d) for details)

$$M' = 4\pi r^2 \frac{\mathcal{E}}{c^2} - \frac{4\pi r^3}{c^2} e^{-\nu/2} \hat{V}' \left\{ n_p - \frac{e^{-3\nu/2}}{3\pi^2} [\hat{V}^2 + 2m_e c^2 \hat{V} - m_e^2 c^4 (e^\nu - 1)]^{3/2} \right\}, \quad (\text{C.3.4})$$

$$\nu' = \frac{2G}{c^2} \frac{4\pi r^3 P / c^2 + M - r^3 E^2 / c^2}{r^2 \left( 1 - \frac{2GM}{c^2 r} + \frac{Gr^2 E^2}{c^4} \right)}, \quad (\text{C.3.5})$$

$$E_e^F = e^{\nu/2} \mu_e - m_e c^2 - eV = \text{constant}, \quad (\text{C.3.6})$$

$$E_p^F = e^{\nu/2} \mu_p - m_p c^2 + eV = \text{constant}, \quad (\text{C.3.7})$$

$$E_n^F = E_e^F + E_p^F - (m_n - m_e - m_p) c^2, \quad (\text{C.3.8})$$

$$\hat{V}'' + \frac{2}{r} \hat{V}' \left[ 1 - \frac{r(\nu' + \lambda')}{4} \right] = -4\pi \alpha \hbar c e^{\nu/2} e^\lambda \left\{ n_p - \frac{e^{-3\nu/2}}{3\pi^2} [\hat{V}^2 + 2m_e c^2 \hat{V} - m_e^2 c^4 (e^\nu - 1)]^{3/2} \right\}, \quad (\text{C.3.9})$$

where a prime stands for radial derivative, Eqs. (C.3.6)–(C.3.7) are the extension to general relativity of the Thomas-Fermi equilibrium condition on the generalized Fermi energies of electrons and protons, Eq. (C.3.8) is the condition of  $\beta$ -equilibrium between neutrons, protons, and electrons. We recall that from Eqs. (C.3.6)–(C.3.8) it follows also the constancy of the generalized neutron Fermi energy. The Eq. (C.3.9) is the general relativistic extension of the relativistic Thomas-Fermi equation recently introduced in the rel-

ativistic Feynman-Metropolis-Teller treatment for the study of compressed atoms (Rotondo et al., 2011c). In the above equations  $e$  is the fundamental charge,  $\alpha$  is the fine structure constant,  $V$  is the Coulomb potential,  $\mu_i = \partial\mathcal{E}/\partial n_i = \sqrt{c^2(P_i^F)^2 + m_i^2 c^4}$  is the free-chemical potential of particle-species,  $\lambda(r)$  is the metric function related to the mass  $M(r)$  and the electric field  $E(r) = -e^{-(\nu+\lambda)/2} V'$  through

$$e^{-\lambda} = 1 - \frac{2GM(r)}{c^2 r} + \frac{G}{c^4} r^2 E^2(r). \quad (\text{C.3.10})$$

and  $\hat{V} = E_e^F + eV$ .

As shown in Rotondo et al. (2011d), the condition of local charge neutrality  $n_e(r) = n_p(r)$  often adopted in literature is not consistent with Eqs. (C.3.6) and (C.3.7), see Fig. 1 of Rotondo et al. (2011d) for details. Therefore, we consider equilibrium configurations fulfilling only global charge neutrality. We solve self-consistently Eq. (C.3.4) and (C.3.5) for the metric, Eqs. (C.3.6)–(C.3.8) for the equilibrium of the three degenerate fermion species and for the  $\beta$ -equilibrium. The crucial equation relating the proton and the electron distributions is then given by the general relativistic Thomas-Fermi equation (C.3.9). The boundary conditions are: for Eq. (C.3.4) the regularity at the origin:  $M(0) = 0$ , for Eqs. (C.3.6)–(C.3.8) a given value of the central density, and for Eq. (C.3.9) the regularity at the origin  $n_e(0) = n_p(0)$ , and a second condition at infinity which results in an eigenvalue problem determined by imposing the global charge neutrality conditions

$$\hat{V}(R_e) = E_e^F, \quad \hat{V}'(R_e) = 0, \quad (\text{C.3.11})$$

at the radius  $R_e$  of the electron distribution defined by

$$P_e^F(R_e) = 0, \quad (\text{C.3.12})$$

from which follows

$$\begin{aligned} E_e^F &= m_e c^2 e^{\nu(R_e)/2} - m_e c^2 \\ &= m_e c^2 \sqrt{1 - \frac{2GM(R_e)}{c^2 R_e}} - m_e c^2. \end{aligned} \quad (\text{C.3.13})$$

The eigenvalue problem consists in determining the gravitational potential and the Coulomb potential at the center of the configuration that satisfy the conditions (C.3.11)–(C.3.13) at the boundary. In Fig. 2 of Rotondo et al. (2011d) we have shown the solution for the density, the gravitational potential and electric potential for a configuration with central density  $\rho(0) = 3.94\rho_{\text{nuc}}$ , where  $\rho_{\text{nuc}} \sim 2.7 \times 10^{14} \text{ g/cm}^3$ .

A particular interesting new feature is the approach to the boundary of the

configuration where three different radii are present corresponding to distinct radii at which the individual particle Fermi pressures vanish. The radius  $R_e$  for the electron component corresponding to  $P_e^F(R_e) = 0$ , the radius  $R_p$  for the proton component corresponding to  $P_p^F(R_p) = 0$  and the radius  $R_n$  for the neutron component corresponding to  $P_n^F(R_n) = 0$ . For a configuration with the aforementioned central density we found, for instance,  $R_n \simeq 12.735$  km,  $R_p \simeq 12.863$  km and  $R_e \simeq R_p + 10^3 \lambda_e$  where  $\lambda_e = \hbar/(m_e c)$  denotes the electron Compton wavelength (see Figs. 2 and 3 of Rotondo et al. (2011d), for details). The occurrence of the radius  $R_n$  is due to the threshold energy for inverse  $\beta$ -decay equilibrium between free neutrons, protons, and electrons, at around  $\rho \sim 10^7$  (see e.g. Shapiro and Teukolsky (1983a)). The electron component follows closely the proton component up to the radius  $R_p$  where the proton density drops to zero. The “proton skin”,  $R_p - R_n \sim 0.1$  km, can be understood as being due to the difference between the proton and the neutron mass. The charge difference leads to gravitational and Coulomb forces acting on protons and only gravitational force on neutrons. The electron component then fully neutralizes the positive charge at  $R_e$  leading to a global configuration without net charge, contrary to the results presented e.g. in Olson and Bailyn (1978).

It can be seen from Fig. 2 in Rotondo et al. (2011d) that the depth of the Coulomb potential is of the order of  $\lesssim m_\pi c^2$ . In Fig. C.4 we have plotted the Coulomb potential and the corresponding electric field of the configuration studied here and in Rotondo et al. (2011d). A Coulomb potential  $\sim m_\pi c^2/e$  decreasing in a typical macroscopic neutron star radius  $R \sim \lambda_\pi(m_{\text{Planck}}/m_p)$  creates an electric field  $\sim (m_p/m_{\text{Planck}})(m_\pi/m_e)^2 E_c \sim 10^{-14} E_c$ , being  $E_c = m_e^2 c^3/(e\hbar)$  the critical electric field for vacuum polarization.

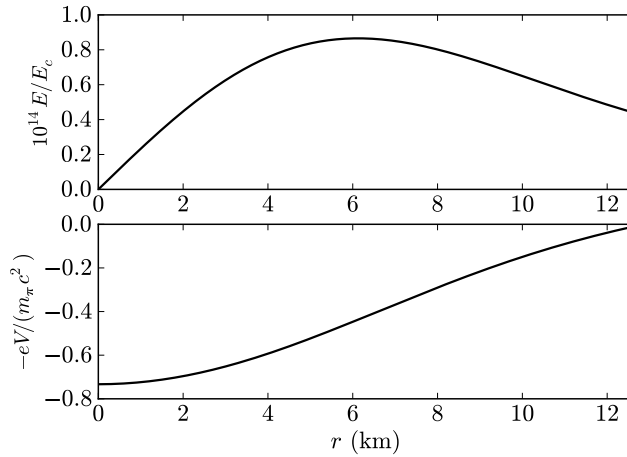


**Figure C.4.:** Electric field and electron Coulomb potential energy of the configuration of neutrons, protons, and electrons in  $\beta$ -equilibrium studied here and in Rotondo et al. (2011d).

### C.3.3. Newtonian limit

Despite the fact that the strong gravitational field of neutron stars requires a general relativistic treatment, it is interesting to explore the Newtonian limit of all the above considerations. This can help to elucidate if the gravito-electromagnetic effects we have found are of general relativistic nature or to prove their validity in a Newtonian regime.

The Newtonian limit of the equilibrium equations can be obtained by the weak-field non-relativistic limit. We expand the gravitational potential at first-order  $e^{v/2} \approx 1 + \Phi/c^2$ , where  $\Phi$  is the Newtonian gravitational potential. In the non-relativistic mechanics limit  $c \rightarrow \infty$ , the particle chemical potential becomes  $\mu_i \rightarrow \tilde{\mu}_i + m_i c^2$ , where  $\tilde{\mu}_i = (P_i^F)^2 / (2m_i)$  denotes the non-relativistic free-chemical potential. Applying these considerations, the electron and proton equilibrium law (C.3.6) becomes

$$E_p^{F,\text{Newt}} = \tilde{\mu}_p + m_p \Phi + eV = \text{constant}, \quad (\text{C.3.14})$$

$$E_e^{F,\text{Newt}} = \tilde{\mu}_e + m_e \Phi - eV = \text{constant}, \quad (\text{C.3.15})$$

which is the classical condition of thermodynamic equilibrium of a fluid of charged particles in presence of external gravitational and electrostatic fields.

The condition of  $\beta$ -equilibrium is, in this case, given by

$$E_n^{F,\text{Newt}} = E_p^{F,\text{Newt}} + E_e^{F,\text{Newt}}, \quad (\text{C.3.16})$$

which links the constants  $E_p^{F,\text{Newt}}$  and  $E_e^{F,\text{Newt}}$  to the constant neutron Fermi energy  $E_n^{F,\text{Newt}}$ .

From the constancy of the proton and electron Fermi energies it follows the relation

$$\tilde{\mu}_p - \tilde{\mu}_e + (m_p - m_e)\Phi + 2eV = \text{constant}, \quad (\text{C.3.17})$$

which in the case of an ideal electron-ion gas becomes the Rosseland relation of equilibrium (see Eq. 7 in Rosseland (1924)). It is interesting to obtain from the above equation an estimate of the Coulomb potential well inside the configuration. Evaluating Eq. (C.3.17) at the radius of the configuration where the particle free chemical potentials go to zero, we obtain an estimate of the ratio of the Coulomb potential energy and the gravitational energy close to the surface of the configuration

$$\frac{eV(R)}{\Phi(R)} \sim -\frac{m_p - m_e}{2}. \quad (\text{C.3.18})$$

Assuming that the system is at nuclear density,  $\rho \sim m_p / \lambda_\pi^3$  where  $\lambda_\pi = \hbar / (m_\pi c)$  is the pion Compton wavelength, the mass and the radius of the configuration are roughly given by  $M \sim m_{\text{Planck}}^3 / m_p^2$  and  $R \sim \lambda_\pi (m_{\text{Planck}} / m_p)$

and therefore the gravitational potential will be  $\Phi(R) = -GM/R \sim (m_\pi/m_p)c^2$ . Consequently, the Coulomb potential energy close to the border is approximately  $eV(R) \sim m_\pi c^2/2$ . Assuming a constant charge density approximation, the Coulomb potential energy at the center of the configuration is 3/2 times its value at the surface, thus we obtain approximately

$$eV(0) \sim \frac{3}{4}m_\pi c^2, \quad (\text{C.3.19})$$

which is in full agreement with both with the numerical results and with the general relativistic formulas given by Eqs. (21) and (22) of Rotondo et al. (2011d). This numerical value is also in line with the Coulomb potential well obtained from the idealized treatment presented in Ruffini (2008b); Popov (2010); Rotondo et al. (2011e,c).

In the weak-field non-relativistic limit, the Einstein-Maxwell equations (C.3.4)–(C.3.9) become

$$M' = 4\pi r^2 \rho(r), \quad (\text{C.3.20})$$

$$\Phi' = \frac{GM}{r^2}, \quad (\text{C.3.21})$$

$$P' = -\frac{GM}{r^2} \rho - \left[ n_p - \frac{(2m_e)^{3/2}}{3\pi^2 \hbar^3} (\hat{V} - m_e \Phi)^{3/2} \right] \hat{V}', \quad (\text{C.3.22})$$

$$\hat{V}'' + \frac{2}{r} \hat{V}' = -4\pi e^2 \left[ n_p - \frac{(2m_e)^{3/2}}{3\pi^2 \hbar^3} (\hat{V} - m_e \Phi)^{3/2} \right], \quad (\text{C.3.23})$$

where  $\rho$  in this case is the rest-mass density

$$\rho = \sum_{i=n,p,e} m_i n_i. \quad (\text{C.3.24})$$

The solution of Eqs. (C.3.14), (C.3.20)–(C.3.23) together with the  $\beta$ -equilibrium condition (C.3.16) leads to qualitatively similar electro-dynamical properties as the one obtained in the general relativistic case. In Fig. C.5 we show the electric field in the region  $r < R_n$  ( $R_n^{\text{Newt}} < R_n^{\text{GR}}$ ) both for the Newtonian as well as for the General Relativistic configuration for the given central density  $\rho(0) = 3.94\rho_{\text{nuc}}$ . From the quantitative point of view, the electric field of the Newtonian configuration is larger than the electric field of the general relativistic configuration.

### C.3.4. Introducing strong interactions

It is clear now that if one considers a fluid of only neutrons, protons, and electrons in  $\beta$ -equilibrium neglecting the effects of the strong interactions and

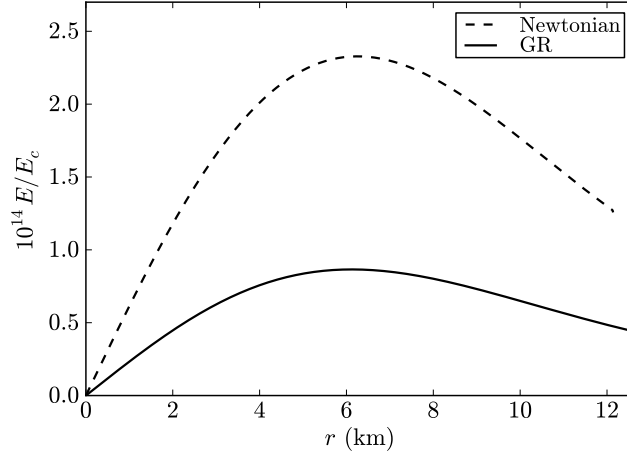


**Figure C.5.:** Electric field (multiplied by  $10^{14}$ ) in units of the critical field  $E_c = m_e^2 c^3 / (e \hbar) \sim 10^{16}$  Volt/cm in the region  $r < R_n$  both for the Newtonian and the General Relativistic configurations. The central density of both systems is  $\rho(0) = 3.94 \rho_{\text{nuc}}$  where  $\rho_{\text{nuc}} = 2.7 \times 10^{14}$  g cm<sup>-3</sup> is the nuclear density.

the presence of a crust, then the electromagnetic structure is the one shown in Figs. C.4 and C.5.

The effect of having different radii  $R_n$ ,  $R_p$ , and  $R_e$  needs to be also studied in the more general case when strong interactions and the presence of the crust of the neutron star are included. The complete study of such a problem must to be necessarily done within a fully relativistic approach taking into account the strong, weak, electromagnetic, and gravitational interactions.

Indeed, in the mean time we have given an essential step forward in Rueda et al. (2011) by formulating such a treatment. The nuclear interactions have been there included through the Walecka model (see Duerr (1956); Walecka (1974) for details, and Bowers et al. (1973b,a) for a similar theory) in which nucleons interact by Yukawa-like couplings. The strong interaction between nucleons is thus described by the exchange of three virtual mesons: an isoscalar meson field  $\sigma$  providing the attractive long-range part of the nuclear force; the massive vector field  $\omega_\mu$  that models the repulsive short range and; the massive isovector field  $\rho_\mu$  which takes account of the isospin effects of nuclei (see also Boguta and Bodmer (1977); Ring (1996)).

As shown in Rueda et al. (2011), the more general Einstein-Maxwell-Thomas-Fermi equations including strong interactions which generalizes Eqs. (C.3.65)–

(C.3.71) can be written as (in units with  $\hbar = c = 1$ )

$$e^{-\lambda(r)} \left( \frac{1}{r^2} - \frac{\lambda'}{r} \right) - \frac{1}{r^2} = -8\pi G T_0^0, \quad (\text{C.3.25})$$

$$e^{-\lambda(r)} \left( \frac{1}{r^2} + \frac{\nu'}{r} \right) - \frac{1}{r^2} = -8\pi G T_1^1, \quad (\text{C.3.26})$$

$$\nabla^\mu \nabla_\mu V = -4\pi e^\lambda e J_0^{ch}, \quad (\text{C.3.27})$$

$$\nabla^\mu \nabla_\mu \sigma = e^\lambda [\partial_\sigma U(\sigma) + g_\sigma n_s], \quad (\text{C.3.28})$$

$$\nabla^\mu \nabla_\mu \omega = -e^\lambda (g_\omega J_\omega^0 - m_\omega^2 \omega), \quad (\text{C.3.29})$$

$$\nabla^\mu \nabla_\mu \rho = -e^\lambda (g_\rho J_\rho^0 - m_\rho^2 \rho), \quad (\text{C.3.30})$$

$$E_e = e^{\nu/2} \mu_e - eV = \text{constant}, \quad (\text{C.3.31})$$

$$E_p = e^{\nu/2} \mu_p + \mathcal{V}_p = \text{constant}, \quad (\text{C.3.32})$$

$$E_n = e^{\nu/2} \mu_n + \mathcal{V}_n = \text{constant}, \quad (\text{C.3.33})$$

$$e^{\nu/2} T = \text{constant}, \quad (\text{C.3.34})$$

where  $\nabla^\mu \nabla_\mu = d^2/dr^2 + [2/r - (1/2)(\nu' + \lambda')]d/dr$ , being  $\nabla^\mu$  the covariant derivative and

$$\mathcal{V}_p = g_\omega \omega + g_\rho \rho + eV, \quad (\text{C.3.35})$$

$$\mathcal{V}_n = g_\omega \omega - g_\rho \rho, \quad (\text{C.3.36})$$

are the effective potentials of nucleons, being  $V \equiv A_0$ ,  $\omega \equiv \omega_0$ ,  $\rho \equiv \omega_0$  the time components of the electromagnetic and the meson potentials, and  $g_\sigma$ ,  $g_\omega$ ,  $g_\rho$  denote the coupling constants between the nucleons and the massive mesons. The self-interaction scalar field potential  $U(\sigma)$  can be in general a quartic-order polynom for a renormalizable theory (see e.g. Lee and Wick (1974)).

The scalar density is given by  $n_s = \partial \mathcal{E} / \partial \tilde{m}_N$  where  $\tilde{m}_N = m_N + g_\sigma \sigma$  is the effective nucleon mass. The only non-vanishing components of the currents are

$$J_0^{ch} = (n_p - n_e) u_0, \quad (\text{C.3.37})$$

$$J_0^\omega = (n_n + n_p) u_0, \quad (\text{C.3.38})$$

$$J_0^\rho = (n_p - n_n) u_0, \quad (\text{C.3.39})$$

where  $u_0 = \sqrt{g_{00}} = e^{\nu/2}$  is the covariant time component of the four-velocity of the fluid.

The function  $\lambda(r)$  satisfies also in this case Eq. (C.3.10) and the energy-momentum tensor is

$$T^{\mu\nu} = T_f^{\mu\nu} + T_\gamma^{\mu\nu} + T_\sigma^{\mu\nu} + T_\omega^{\mu\nu} + T_\rho^{\mu\nu}, \quad (\text{C.3.40})$$

where

$$T_\gamma^{\mu\nu} = -\frac{1}{4\pi} \left( F_\alpha^\mu F^{\alpha\nu} + \frac{1}{4} g^{\mu\nu} F_{\alpha\beta} F^{\alpha\beta} \right), \quad (\text{C.3.41})$$

$$T_\sigma^{\mu\nu} = \nabla^\mu \nabla^\nu \sigma - g^{\mu\nu} \left[ \frac{1}{2} \nabla_\sigma \sigma \nabla^\sigma \sigma - U(\sigma) \right], \quad (\text{C.3.42})$$

$$\begin{aligned} T_\omega^{\mu\nu} &= -\Omega_\alpha^\mu \Omega^{\alpha\nu} - \frac{1}{4} g^{\mu\nu} \Omega_{\alpha\beta} \Omega^{\alpha\beta} \\ &+ m_\omega^2 \left( \omega^\mu \omega^\nu - \frac{1}{2} g^{\mu\nu} \omega_\alpha \omega^\alpha \right), \end{aligned} \quad (\text{C.3.43})$$

$$\begin{aligned} T_\rho^{\mu\nu} &= -\mathcal{R}_\alpha^\mu \mathcal{R}^{\alpha\nu} - \frac{1}{4} g^{\mu\nu} \mathcal{R}_{\alpha\beta} \mathcal{R}^{\alpha\beta} \\ &+ m_\rho^2 \left( \mathcal{R}^\mu \mathcal{R}^\nu - \frac{1}{2} g^{\mu\nu} \mathcal{R}_\alpha \mathcal{R}^\alpha \right), \end{aligned} \quad (\text{C.3.44})$$

$$T_f^{\mu\nu} = (\mathcal{E} + P) u^\mu u^\nu - P g^{\mu\nu}, \quad (\text{C.3.45})$$

where  $\Omega_{\mu\nu} \equiv \partial_\mu \omega_\nu - \partial_\nu \omega_\mu$ ,  $\mathcal{R}_{\mu\nu} \equiv \partial_\mu \rho_\nu - \partial_\nu \rho_\mu$ ,  $F_{\mu\nu} \equiv \partial_\mu A_\nu - \partial_\nu A_\mu$  are the field strength tensors for the  $\omega^\mu$ ,  $\rho^\mu$  and  $A^\mu$  fields respectively.

The equilibrium conditions of the constancy of the Klein potentials of the particles throughout the configuration is expressed by Eqs. (C.3.31)–(C.3.33) and Eq. (C.3.34) is the Tolman isothermality condition analogous to Eq. (C.3.71).

There are additional contributions of the strong interaction to the nuclear symmetry energy given within this theory mainly by the  $\rho$ -meson. Such contributions change the proton skin structure  $R_p > R_n$  shown in this work to a “neutron skin” effect  $R_n > R_p$  in the core-crust boundary layer at nuclear density Belvedere et al. (2012), in close analogy to the neutron skin observed in neutron rich nuclei, see e.g. Tamii et al. (2011).

### C.3.5. Finite temperature effects

The above results have been obtained within the zero temperature approximation. Temperatures of the order of  $\sim 10^6$  K are expected to exist at the surface of old neutron stars (Tennant et al., 2001; Weisskopf et al., 2004), or temperatures of  $10^8 - 10^9$  K could, in principle, exist in neutron star interiors. We are going to show that these thermal effects do not affect the considerations on gravito-polarization here introduced. For neutron stars, the Fermi temperature

$$T_i^F = \frac{\mu_i - m_i c^2}{k}, \quad (\text{C.3.46})$$

where  $k$  is the Boltzmann constant, can be as large as  $\sim 10^{12}$  K for electrons,  $\sim 10^{11}$  K for protons and  $\sim 10^{13}$  K for neutrons for typical central densities of neutron stars. This means that neutron stars interiors are, at a high degree of

accuracy, degenerate systems. However, the total thermal energy of a neutron star  $E_{\text{th}} \sim 10^{48} T_9^2$  erg (see e.g. Yakovlev and Pethick (2004a)) where  $T_9$  is the temperature in units of  $10^9$  K, is much larger than the Coulomb energy  $E_C \sim (1/6)R^3 E^2 \sim 10^{16}$  erg, where  $E$  is the internal electric field here considered (see Figs. C.4 and C.5) and  $R$  is the radius of the configuration. It can be then of interest to ask the question if our electro-dynamical structure will still occur in presence of thermal effects.

In this more general case, the equation of state given by Eqs. (C.3.1) and (C.3.2), is replaced by

$$\mathcal{E} = \sum_{i=n,p,e} \frac{2}{(2\pi\hbar)^3} \int_0^\infty \tilde{\epsilon}_i(p) f_i(p) 4\pi p^2 dp, \quad (\text{C.3.47})$$

$$P = \sum_{i=n,p,e} \frac{1}{3} \frac{2}{(2\pi\hbar)^3} \int_0^\infty \frac{p^2 f_i(p)}{\tilde{\epsilon}_i(p) + m_i c^2} 4\pi p^2 dp, \quad (\text{C.3.48})$$

where

$$f_i(p) = \frac{1}{\exp[(\tilde{\epsilon}_i(p) - \tilde{\mu}_i)/(kT)] + 1}, \quad (\text{C.3.49})$$

is the Fermi-Dirac fermion distribution function which gives the particle number density  $n_i$

$$n_i = \frac{2}{(2\pi\hbar)^3} \int_0^\infty f_i(p) 4\pi p^2 dp, \quad (\text{C.3.50})$$

where  $\tilde{\epsilon}_i(p) = \epsilon_i(p) - m_i c^2 = \sqrt{c^2 p^2 + m_i^2 c^4} - m_i c^2$  and  $\tilde{\mu}_i$  are the free single particle energy and the free particle chemical potential with the particle rest mass-energy  $m_i c^2$  subtracted off.

### **Tolman isothermality and conserved Klein potentials**

We turn now to demonstrate the constancy of the Klein potentials and the constancy of the gravitationally red-shifted temperature throughout the configuration.

The equation of state (C.3.47)–(C.3.48) satisfies the thermodynamic law

$$\mathcal{E} + P - Ts = \sum_{i=n,p,e} n_i \mu_i, \quad (\text{C.3.51})$$

where  $s = S/V$  is the entropy per unit volume and  $\mu_i = \partial\mathcal{E}/\partial n_i$  is the free-chemical potential of the  $i$ -specie. At zero-temperature  $T = 0$ ,  $\mu_i = \sqrt{(cP_i^F)^2 + \tilde{m}_i^2 c^4}$  and  $n_i = (P_i^F)^3 / (3\pi^2 \hbar^3)$ , where  $P_i^F$  denotes the Fermi momentum of the  $i$ -specie.

From Eq. (C.3.51) follows the Gibbs-Duhem relation

$$dP = \sum_{i=n,p,e} n_i d\mu_i + s dT, \quad (\text{C.3.52})$$

which can be rewritten as

$$dP = \sum_{i=n,p,e} n_i d\mu_i + \left( \varepsilon + P - \sum_{i=n,p,e} n_i \mu_i \right) \frac{dT}{T}. \quad (\text{C.3.53})$$

Using the Gibbs-Duhem relation (C.3.53) the energy-momentum conservation equation (see Rotondo et al. (2011d) for details)

$$e^{v/2} dP + e^{v/2} \frac{dv}{2} (\varepsilon + P) + e dV (n_p - n_e) = 0, \quad (\text{C.3.54})$$

can be rewritten as

$$\begin{aligned} e^{v/2} \sum_{i=n,p,e} n_i \left( d\mu_i - \frac{dT}{T} \mu_i \right) + (\varepsilon + P) e^{v/2} \left( \frac{dT}{T} \right. \\ \left. + \frac{1}{2} dv \right) + e (n_p - n_e) dV = 0. \end{aligned} \quad (\text{C.3.55})$$

The Tolman isothermal condition (Tolman, 1930) (see also Klein (1949)) demands the constancy of the gravitationally red-shifted temperature

$$\frac{dT}{T} + \frac{1}{2} dv = 0, \quad \text{or} \quad T_\infty = e^{v/2} T = \text{constant}, \quad (\text{C.3.56})$$

which can be used into Eq. (C.3.55) to obtain

$$\sum_{i=n,p,e} n_i d(e^{v/2} \mu_i) + e (n_p - n_e) dV = 0. \quad (\text{C.3.57})$$

We now introduce the generalized chemical potentials, or Klein potentials, for electrons  $E_e$ , protons  $E_p$  and neutrons  $E_n$

$$E_e = e^{v/2} \mu_e - m_e c^2 - eV, \quad (\text{C.3.58})$$

$$E_p = e^{v/2} \mu_p - m_p c^2 + eV, \quad (\text{C.3.59})$$

$$E_n = e^{v/2} \mu_n - m_n c^2, \quad (\text{C.3.60})$$

which in the zero temperature limit are the generalized Fermi energies for electrons  $E_e = E_e^F$ , neutrons  $E_n = E_n^F$  and protons  $E_p = E_p^F$  introduced in Sec. II (see Eq. (C.3.6)). Using Eqs. (C.3.58), (C.3.59) and (C.3.60), Eq. (C.3.57)

becomes

$$\sum_{i=n,p,e} n_i dE_i = 0, \quad (\text{C.3.61})$$

which leads for independent and non-zero particle number densities  $n_i \neq 0$  to the constancy of the Klein potentials (C.3.58)–(C.3.60) for each particle-species, i.e.

$$E_e = e^{v/2} \mu_e - m_e c^2 - eV = \text{constant}, \quad (\text{C.3.62})$$

$$E_p = e^{v/2} \mu_p - m_p c^2 + eV = \text{constant}, \quad (\text{C.3.63})$$

$$E_n = e^{v/2} \mu_n - m_n c^2 = \text{constant}. \quad (\text{C.3.64})$$

In the zero temperature limit the constancy of the Klein potential of each particle-specie becomes the constancy of the generalized Fermi energies introduced in Sec. C.3.2 (see Eqs. (C.3.6)–(C.3.8)). This is a crucial point because, as discussed in Rotondo et al. (2011d), the constancy of the generalized Fermi energies proves the impossibility of having a self-consistent configuration fulfilling the condition of local charge neutrality and  $\beta$ -equilibrium (see e.g. Fig. 1 of Rotondo et al. (2011d)). Further, as shown in Rueda et al. (2011), the constancy of the Klein potentials holds in the more general case when the strong interactions between nucleons are taken into account.

Therefore, introducing the new dimensionless variables  $\eta_i = \tilde{\mu}_i / (kT)$  and  $\beta_i = kT / (m_i c^2)$ , the new set of Einstein-Maxwell-Thomas-Fermi equations generalizing the system (C.3.4)–(C.3.9) to the case of finite temperatures is

$$M' = 4\pi r^2 \frac{\mathcal{E}}{c^2} - \frac{4\pi r^3}{c^2} e^{-v/2} \hat{V}' (n_p - n_e), \quad (\text{C.3.65})$$

$$v' = \frac{2G}{c^2} \frac{4\pi r^3 P / c^2 + M - r^3 E^2 / c^2}{r^2 \left( 1 - \frac{2GM}{c^2 r} + \frac{Gr^2 E^2}{c^4} \right)}, \quad (\text{C.3.66})$$

$$\begin{aligned} E_e &= m_e c^2 e^{v/2} (1 + \beta_e \eta_e) - m_e c^2 - eV \\ &= \text{constant}, \end{aligned} \quad (\text{C.3.67})$$

$$\begin{aligned} E_p &= m_p c^2 e^{v/2} (1 + \beta_p \eta_p) - m_p c^2 + eV \\ &= \text{constant}, \end{aligned} \quad (\text{C.3.68})$$

$$E_n = E_e + E_p - (m_n - m_e - m_p) c^2, \quad (\text{C.3.69})$$

$$\begin{aligned} \hat{V}'' + \frac{2}{r} \hat{V}' \left[ 1 - \frac{r(v' + \lambda')}{4} \right] &= -4\pi \alpha \hbar c e^{v/2} e^\lambda (n_p \\ &- n_e), \end{aligned} \quad (\text{C.3.70})$$

$$e^{v/2} \beta_i = \text{constant}, \quad i = n, p, e, \quad (\text{C.3.71})$$

where Eq. (C.3.69) is the condition of  $\beta$ -equilibrium between neutrons, pro-

tons and electrons, and the number density of the  $i$ -specie is given by

$$n_i = \frac{2^{1/2} m_i^3 c^3}{\pi^2 \hbar^3} \beta_i^{3/2} (F_{1/2}^i + \beta_i F_{3/2}^i), \quad (\text{C.3.72})$$

where we have introduced the relativistic Fermi-Dirac integrals of order  $j$

$$F_j^i = F_j(\eta_i, \beta_i) = \int_0^\infty \frac{x^j \left(1 + \frac{1}{2} \beta_i x\right)^{1/2}}{1 + e^{x - \eta_i}} dx. \quad (\text{C.3.73})$$

The above formulation generalizes to the case of finite temperatures the Einstein-Maxwell-Thomas-Fermi equations obtained in Rotondo et al. (2011d) and recalled here in Sec. C.3.2. This formulation can be also straightforwardly done in the presence of strong interactions generalizing the formulation of Sec. C.3.4 (see Rueda et al. (2011) for details).

### Numerical results

We have integrated numerically the system of equations (C.3.65)–(C.3.71) for given temperatures  $T_\infty \neq 0$ . As expected, the results are both qualitatively and quantitatively similar to the ones obtained with the degenerate approximation. The largest difference we found is at the surface boundary of the configuration, where, due to the low density of the system, finite temperature effects are more effective. As an example, we compare in Fig. C.6 the electron density for  $r > R_p$  in the degenerate and in the non-degenerate case for  $T_\infty = 2.3 \times 10^5$  K. For distances  $r < R_p$  the results are essentially the same as in the degenerate case. In the region  $r \ll R_n$  at large densities  $> \rho_{\text{nuc}} = 2.7 \times 10^{14}$  g/cm<sup>3</sup>, the electro-dynamical properties of the configuration i.e. Coulomb potential and electric field remain unperturbed even for very large temperatures  $T_\infty \sim 10^{11}$  K. This is due to the fact that thermal effects are largely compensated by the gravitational potential as given by Eq. (C.3.56); the Coulomb interaction is not involved in this balance and is not affected by the thermal energy.

It is worth to mention that from general computations of the heating and cooling mechanisms it turns out that neutron star interiors are highly isothermal (in the sense of Tolman) due to the high thermal conductivity of degenerate particles (Yakovlev and Pethick, 2004a). In real neutron stars, the fluid of neutrons, protons and electrons in  $\beta$ -equilibrium studied in this work does not extend all the way to the neutron star surface but is confined to the neutron star core surrounded by the neutron star crust. In this more general case, the surface structure shown in Fig. C.6 is replaced by the crust composed of nuclei and degenerate electrons. The condition of isothermality breaks down in the surface non-degenerate layers of the star due to existence of high temperature gradients (see e.g. Yakovlev and Pethick (2004a), for details).

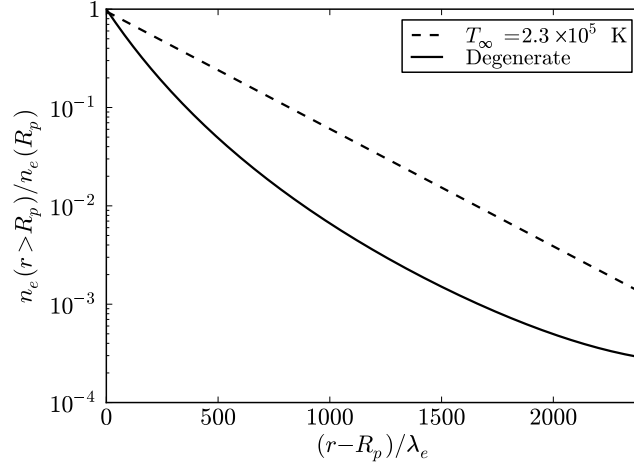


**Figure C.6.:** Electron number density for  $r \geq R_p$  normalized to its value at  $r = R_p$  both for  $T = 0$  K (degenerate case) and for a finite temperature of  $T_\infty = 2.3 \times 10^5$  K.

### C.3.6. Concluding Remarks

In this work we have addressed three additional aspects of the description of a self-gravitating system of neutrons, protons and electrons in  $\beta$ -equilibrium:

1) We have first recall the formulation of the constitutive Einstein-Maxwell-Thomas-Fermi equations and their solution in the simple case of self-gravitating neutrons, protons, and electrons in  $\beta$ -equilibrium. The properties of the electromagnetic structure of the configuration shown in Rotondo et al. (2011d) have been also recalled; the Coulomb potential energy inside the configuration is  $eV \sim m_\pi c^2$  and the electric field  $E \sim (m_p/m_{\text{Planck}})(m_\pi/m_e)^2 E_c$  and explicitly given in Fig. C.4.

2) We have presented the Newtonian limit of the treatment (Rotondo et al., 2011d) by taking the weak field approximation and the non-relativistic  $c \rightarrow \infty$  limit of the general relativistic Thomas-Fermi and Einstein-Maxwell equations (C.3.4)–(C.3.9). The numerical integration of the Newtonian equations shows that the gravito-electrodynamic structure evidenced in Rotondo et al. (2011d) (see also Sec. C.3.2) is already present in the Newtonian regime. We have also shown how our equations fulfill the Rosseland relation of equilibrium (Rosseland, 1924) for an electron-ion ideal gas in the case of a Newtonian gravitational field, see Eqs. (C.3.17)–(C.3.18), Eqs. (C.3.20)–(C.3.23), and Eqs. (C.3.4)–(C.3.9). The differences in the electromagnetic structure between the Newtonian and the general relativistic treatments are very large (see Fig. C.5).

3) We have recalled in Sec. C.3.4 the extension of the Einstein-Maxwell-Thomas-Fermi equations (C.3.4–C.3.9) to the case when strong interactions between nucleons are taking into account by introducing the presence of  $\sigma$ ,

$\omega$  and  $\rho$  virtual mesons which mediate nuclear interactions in a Yukawa-like fashion, following (Rueda et al., 2011), see Eqs. (C.3.25–C.3.34).

4) We have then extended all our previous works to the case of finite temperatures enforcing the Tolman “isothermal” condition in general relativity. We have reached a fundamental conclusion: although the thermal energy stored in old neutron stars with surface temperatures  $\sim 10^6$  K (Tennant et al., 2001; Weisskopf et al., 2004) is much larger than the internal Coulomb energy (see Sec. C.3.4), still the electromagnetic structure (see Fig. C.5) is unaffected by the presence of the thermal component. Physically this effect is due to the very large Fermi energy of the neutrons  $\sim 1$  GeV, of the protons  $\sim 10$  MeV and of the electrons  $\sim 0.1$  GeV, as can be seen from Eq. (C.3.46). In the general relativistic “isothermal” system there exists a temperature gradient, compensated by the variation of the gravitational potential as dictated by the Tolman condition given by Eq. (C.3.56). The Coulomb interaction is not involved in the balance between the thermal and the gravitational energies and is not affected by the presence of large thermal energies.

We recalled that a surface structure characterized by the presence of three different radii, one for each particle specie, emerges when global Coulomb effects are taken into due account. The radius  $R_e$  in the case  $T \neq 0$  is larger with respect to the one obtained in the degenerate approximation (see Fig. C.6). However, in realistic neutron stars the surface structure of Fig. C.6 is replaced by the surface layers composed of nuclei and non-degenerate electrons where isothermality breaks down due to existence of high temperature gradients (Yakovlev and Pethick, 2004a).

As a by product, we have given the explicit demonstration of the constancy throughout the configuration of the Klein potentials of each species in the more general case of finite temperatures. This generalizes the condition of the constancy of the general relativistic Fermi energies derived in the special case  $T = 0$  in Rotondo et al. (2011d).

The above results are relevant to the extension to thermal effects of the relativistic Feynman-Metropolis-Teller treatment of compressed atoms (Rotondo et al., 2011c), recently applied to the construction of general relativistic white dwarf equilibrium configurations (Rotondo et al., 2011b). They are therefore relevant for the description of the neutron star crust as well as of hot white dwarfs.

The study of the Thomas-Fermi equation within the Einstein-Maxwell system of equations responds to a precise request of consistency of a theoretical treatment. As evidenced in Rotondo et al. (2011d) it overcomes the conceptual difficulties of the Tolman-Oppenheimer-Volkoff treatment. Nevertheless, the two treatments when applied to the case of neutrons, protons, and electrons in  $\beta$ -equilibrium do not give quantitative appreciable differences in the masses and radii of the equilibrium configurations. It becomes therefore natural to ask under which physical conditions the gravito-polarization effects become quantitatively relevant.

When strong interactions are considered (Rueda et al., 2011) a new situation occurs. The neutron star core necessarily presents a sharp boundary surrounded by a crust of nuclei and electrons described by the generalized Feynman-Metropolis-Teller treatment presented in Rotondo et al. (2011c). Under these conditions, the entire theoretical treatment presented in this work and in Rotondo et al. (2011d); Rueda et al. (2011) are not optional and become a necessity.

The presence of a Coulomb potential affects the structure of the phase-transition leading to the occurrence of overcritical electric fields through core-crust boundary interface. Similar electrostatic effects are expected to occur at the interlayer boundaries within the crust of a neutron star where changes of the nucleus charge  $Z$  and mass number  $A$  of the composing nuclei occur (see e.g. Haensel and Pichon (1994)), as well as at the surface of quark stars (Alcock et al., 1986; Stejner and Madsen, 2005), at the transition from the hadronic phase to the color flavor locked phase in hybrid stars (Alford et al., 2001) and in liquid white dwarfs where it may cause sedimentation of heavy nuclei (Bildsten and Hall, 2001; Althaus et al., 2010b; García-Berro et al., 2010b).

In Fig. C.7 we show the expected behavior of the Coulomb potential as modeled in the heuristic simplified approach (Ruffini, 2008b; Popov, 2010; Rotondo et al., 2011e). If the electron Coulomb potential  $-eV \sim m_\pi c^2$  suffers a sharp increasing in a scale typical of the electron screening length  $\sim \lambda_e = \hbar/(m_e c)$ , it will create an electric field of order  $\sim (m_\pi/m_e)^2 E_c \sim 10^3 E_c$ .

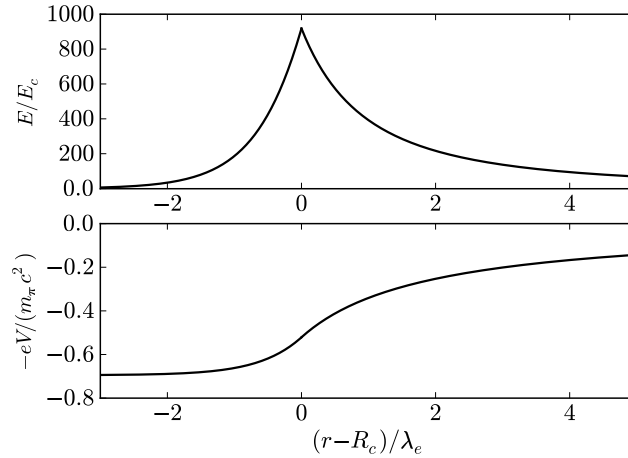


**Figure C.7.:** Expected enhancement of the electric field at a sharp increasing of the electron Coulomb potential  $-eV$  e.g. at a phase transition from the core to the crust in a neutron star as modeled in the simplified approach (Ruffini, 2008b; Popov, 2010; Rotondo et al., 2011e). Here  $R_c$  denotes the core radius.

A key result in the present work is that the gravito-polarization effects survive at finite temperatures and we can therefore proceed to the study of

neutron star configurations through the theoretical framework formulated in Rueda et al. (2011) and recalled in Sec. C.3.4. It is now possible to confirm if the phase-transition at the boundary of the neutron star core follows the idealization advanced in Ruffini (2008b); Popov (2010); Rotondo et al. (2011e) and shown in Fig. C.7. It is clear that the formation of overcritical fields is of great astrophysical interest. The mass and thickness of the neutron star crust in the two alternative treatments are markedly different. The continuity of the generalized Klein potentials, at the boundary of the core, plays a crucial role in the determination of the mass and thickness of the crust (Belvedere et al., 2012). The process of gravitational collapse of a core endowed with electromagnetic structure leads to signatures and energetics markedly different from the ones of a core endowed uniquely of gravitational interactions (Ruffini et al., 2003b,a; Ruffini and Xue, 2008; Ruffini et al., 2010b).

## **C.4. Neutron stars fulfilling all fundamental interactions**

### **C.4.1. Introduction**

It is well known that the classic works of Tolman (1939) and of Oppenheimer and Volkoff (1939), for short TOV, addresses the problem of neutron star equilibrium configurations composed only of neutrons. For the more general case when protons and electrons are also considered, in all of the scientific literature on neutron stars it is assumed that the condition of local charge neutrality applies identically to all points of the equilibrium configuration (see e.g. Haensel et al. (2007)). Consequently, the corresponding solutions in this more general case of a non-rotating neutron star, are systematically obtained also on the base of the TOV equations. We have recently shown the the condition of local charge neutrality is

In general, the formulation of the equilibrium of systems composed by different particle species must be established within the framework of statistical physics of multicomponent systems. Thermodynamic equilibrium of these systems is warranted by demanding the constancy throughout the configuration of the generalized chemical potentials, often called “electro-chemical”, of each of the components of the system; see e.g. Klein (1949); Kodama and Yamada (1972); Olson and Bailyn (1975). Such generalized potentials include not only the contribution due to kinetic energy but also the contribution due to the potential fields, e.g. gravitational and electromagnetic potential energies per particle, and in the case of rotating stars also the centrifugal potential. For such systems in presence of gravitational and Coulomb fields, global electric polarization effects at macroscopic scales occur. The balance of the gravitational and electric forces acting on ions and electrons in ideal electron-ion plasma leading to the occurrence of gravito-polarization was pointed out in the classic work of Rosseland (1924).

If one turns to consider the gravito-polarization effects in neutron stars, the corresponding theoretical treatment acquires remarkable conceptual and theoretical complexity, since it must be necessarily formulated consistently within the Einstein-Maxwell system of equations. Klein (1949) first introduced the constancy of the general relativistic chemical potential of particles, hereafter “Klein potentials”, in the study of the thermodynamic equilibrium of a self-gravitating one-component fluid of neutral particles throughout the configuration within the framework of general relativity. The extension of the Klein’s work to the case of neutral multicomponent degenerate fluids can be found in Kodama and Yamada (1972) and to the case of multi-component degenerate fluid of charged particles in Olson and Bailyn (1975).

Using the concept of Klein potentials, we have recently proved the impossibility of imposing the condition of local charge neutrality in the simplest case

of a self-gravitating system of degenerate neutrons, protons and electrons in  $\beta$ -equilibrium Rotondo et al. (2011d): it has been shown that the consistent treatment of the above system implies the solution of the general relativistic Thomas-Fermi equations, coupled with the Einstein-Maxwell ones, being the TOV equations thus superseded.

We have recently formulated the theory of a system of neutrons, protons and electrons fulfilling strong, electromagnetic, weak and gravitational interactions (Rueda et al., 2011). The role of the Klein first integrals has been again evidenced and their theoretical formulation in the Einstein-Maxwell background and in the most general case of finite temperature has been there presented, generalizing the previous results for the “non-interacting” case (Rotondo et al., 2011d). The strong interactions, modeled by a relativistic nuclear theory, are there described by the introduction of the  $\sigma$ ,  $\omega$  and  $\rho$  virtual mesons (Duerr, 1956; Walecka, 1974; Bowers et al., 1973b,a) (see Subsec. C.4.2 for details).

In this work we construct for the first time the equilibrium configurations of non-rotating neutron stars following the new approach (Rotondo et al., 2011d; Rueda et al., 2011). The full set of the Einstein-Maxwell-Thomas-Fermi equations is solved numerically for zero temperatures and for selected parameterizations of the nuclear model.

## C.4.2. The Constitutive Relativistic Equations

### Core Equations

It has been clearly recognized that, since neutron stars cores may reach density of order  $\sim 10^{16}$ – $10^{17}$  g/cm<sup>3</sup>, much larger than the nuclear density  $\rho_{\text{nuc}} \sim 2.7 \times 10^{14}$  g/cm<sup>3</sup>, approaches for the nuclear interaction between nucleons based on phenomenological potentials and non-relativistic many-body theories become inapplicable (see Bowers et al. (1973b,a)). A self-consistent relativistic and well-tested model for the nuclear interactions has been formulated in Duerr (1956); Walecka (1974); Bowers et al. (1973b,a). Within this model the nucleons interact with  $\sigma$ ,  $\omega$  and  $\rho$  mesons through Yukawa-like couplings and assuming flat spacetime the equation of state of nuclear matter has been determined. However, it has been clearly stated in Rotondo et al. (2011d); Rueda et al. (2011) that, when we turn into a neutron star configuration at nuclear and supranuclear, the global description of the Einstein-Maxwell-Thomas-Fermi equations is mandatory. Associated to this system of equations there is a sophisticated eigenvalue problem, especially the one for the general relativistic Thomas-Fermi equation is necessary in order to fulfill the global charge neutrality of the system and to consistently describe the confinement of the ultrarelativistic electrons.

The strong interactions between nucleons are described by the exchange of three virtual mesons:  $\sigma$  is an isoscalar meson field providing the attractive

long-range part of the nuclear force;  $\omega$  is a massive vector field that models the repulsive short range and;  $\rho$  is the massive isovector field that takes account surface as well as isospin effects of nuclei (see also Boguta and Bodmer (1977); Ring (1996)).

The total Lagrangian density of the system is given by

$$\mathcal{L} = \mathcal{L}_g + \mathcal{L}_f + \mathcal{L}_\sigma + \mathcal{L}_\omega + \mathcal{L}_\rho + \mathcal{L}_\gamma + \mathcal{L}_{\text{int}}, \quad (\text{C.4.1})$$

where the Lagrangian densities for the free-fields are

$$\mathcal{L}_g = -\frac{R}{16\pi G}, \quad (\text{C.4.2})$$

$$\mathcal{L}_\gamma = -\frac{1}{16\pi} F_{\mu\nu} F^{\mu\nu}, \quad (\text{C.4.3})$$

$$\mathcal{L}_\sigma = \frac{1}{2} \nabla_\mu \sigma \nabla^\mu \sigma - U(\sigma), \quad (\text{C.4.4})$$

$$\mathcal{L}_\omega = -\frac{1}{4} \Omega_{\mu\nu} \Omega^{\mu\nu} + \frac{1}{2} m_\omega^2 \omega_\mu \omega^\mu, \quad (\text{C.4.5})$$

$$\mathcal{L}_\rho = -\frac{1}{4} \mathcal{R}_{\mu\nu} \mathcal{R}^{\mu\nu} + \frac{1}{2} m_\rho^2 \rho_\mu \rho^\mu, \quad (\text{C.4.6})$$

where  $\Omega_{\mu\nu} \equiv \partial_\mu \omega_\nu - \partial_\nu \omega_\mu$ ,  $\mathcal{R}_{\mu\nu} \equiv \partial_\mu \rho_\nu - \partial_\nu \rho_\mu$ ,  $F_{\mu\nu} \equiv \partial_\mu A_\nu - \partial_\nu A_\mu$  are the field strength tensors for the  $\omega^\mu$ ,  $\rho$  and  $A^\mu$  fields respectively,  $\nabla_\mu$  stands for covariant derivative and  $R$  is the Ricci scalar. We adopt the Lorenz gauge for the fields  $A_\mu$ ,  $\omega_\mu$ , and  $\rho_\mu$ . The self-interaction scalar field potential  $U(\sigma)$  is a quartic-order polynom for a renormalizable theory (see e.g. Lee and Wick (1974)).

The Lagrangian density for the three fermion species is

$$\mathcal{L}_f = \sum_{i=e,N} \bar{\psi}_i (i\gamma^\mu D_\mu - m_i) \psi_i, \quad (\text{C.4.7})$$

where  $\psi_N$  is the nucleon isospin doublet,  $\psi_e$  is the electronic singlet,  $m_i$  states for the mass of each particle-specie and  $D_\mu = \partial_\mu + \Gamma_\mu$ , being  $\Gamma_\mu$  the Dirac spin connections.

The interacting part of the Lagrangian density is, in the minimal coupling assumption, given by

$$\begin{aligned} \mathcal{L}_{\text{int}} &= -g_\sigma \sigma \bar{\psi}_N \psi_N - g_\omega \omega_\mu J_\omega^\mu - g_\rho \rho_\mu J_\rho^\mu \\ &+ e A_\mu J_{\gamma,e}^\mu - e A_\mu J_{\gamma,N}^\mu, \end{aligned} \quad (\text{C.4.8})$$

where the conserved currents are

$$J_\omega^\mu = \bar{\psi}_N \gamma^\mu \psi_N, \quad (\text{C.4.9})$$

$$J_\rho^\mu = \bar{\psi}_N \tau_3 \gamma^\mu \psi_N, \quad (\text{C.4.10})$$

$$J_{\gamma,e}^\mu = \bar{\psi}_e \gamma^\mu \psi_e, \quad (\text{C.4.11})$$

$$J_{\gamma,N}^\mu = \bar{\psi}_N \left( \frac{1 + \tau_3}{2} \right) \gamma^\mu \psi_N. \quad (\text{C.4.12})$$

The coupling constants of the  $\sigma$ ,  $\omega$  and  $\rho$ -fields are  $g_\sigma$ ,  $g_\omega$  and  $g_\rho$ , and  $e$  is the fundamental electric charge. The Dirac matrices  $\gamma^\mu$  and the isospin Pauli matrices satisfy the Dirac algebra in curved spacetime (see e.g. Lee and Pang (1987) for details).

We first introduce the non-rotating spherically symmetric spacetime metric

$$ds^2 = e^{\nu(r)} dt^2 - e^{\lambda(r)} dr^2 - r^2 d\theta^2 - r^2 \sin^2 \theta d\varphi^2, \quad (\text{C.4.13})$$

where the  $\nu(r)$  and  $\lambda(r)$  are only functions of the radial coordinate  $r$ .

For very large number of fermions, we adopt the mean-field approximation in which fermion-field operators are replaced by their expectation values (see Ruffini and Bonazzola (1969) for details). Within this approximation, the full system of general relativistic equations can be written in the form

$$e^{-\lambda(r)} \left( \frac{1}{r^2} - \frac{1}{r} \frac{d\lambda}{dr} \right) - \frac{1}{r^2} = -8\pi G T_0^0, \quad (\text{C.4.14})$$

$$e^{-\lambda(r)} \left( \frac{1}{r^2} + \frac{1}{r} \frac{d\nu}{dr} \right) - \frac{1}{r^2} = -8\pi G T_1^1, \quad (\text{C.4.15})$$

$$V'' + \frac{2}{r} V' \left[ 1 - \frac{r(\nu' + \lambda')}{4} \right] = -4\pi e e^{\nu/2} e^\lambda (n_p - n_e), \quad (\text{C.4.16})$$

$$\frac{d^2\sigma}{dr^2} + \frac{d\sigma}{dr} \left[ \frac{2}{r} - \frac{1}{2} \left( \frac{d\nu}{dr} + \frac{d\lambda}{dr} \right) \right] = e^\lambda [\partial_\sigma U(\sigma) + g_s n_s], \quad (\text{C.4.17})$$

$$\frac{d^2\omega}{dr^2} + \frac{d\omega}{dr} \left[ \frac{2}{r} - \frac{1}{2} \left( \frac{d\nu}{dr} + \frac{d\lambda}{dr} \right) \right] = -e^\lambda (g_\omega J_\omega^0 - m_\omega^2 \omega), \quad (\text{C.4.18})$$

$$\frac{d^2\rho}{dr^2} + \frac{d\rho}{dr} \left[ \frac{2}{r} - \frac{1}{2} \left( \frac{d\nu}{dr} + \frac{d\lambda}{dr} \right) \right] = -e^\lambda (g_\rho J_\rho^0 - m_\rho^2 \rho), \quad (\text{C.4.19})$$

$$E_e^F = e^{\nu/2} \mu_e - eV = \text{constant}, \quad (\text{C.4.20})$$

$$E_p^F = e^{\nu/2} \mu_p + \mathcal{V}_p = \text{constant}, \quad (\text{C.4.21})$$

$$E_n^F = e^{\nu/2} \mu_n + \mathcal{V}_n = \text{constant}, \quad (\text{C.4.22})$$

where we have introduced the notation  $\omega_0 = \omega$ ,  $\rho_0 = \rho$ , and  $A_0 = V$  for the temporal components of the meson-fields. Here  $\mu_i = \partial\mathcal{E}/\partial n_i = \sqrt{(P_i^F)^2 + \tilde{m}_i^2}$

and  $n_i = (P_i^F)^3 / (3\pi^2)$  are the free-chemical potential and number density of the  $i$ -specie with Fermi momentum  $P_i^F$ . The particle effective mass is  $\tilde{m}_N = m_N + g_s\sigma$  and  $\tilde{m}_e = m_e$  and the effective potentials  $\mathcal{V}_{p,n}$  are given by

$$\mathcal{V}_p = g_\omega\omega + g_\rho\rho + eV, \quad (\text{C.4.23})$$

$$\mathcal{V}_n = g_\omega\omega - g_\rho\rho. \quad (\text{C.4.24})$$

The constancy of the generalized Fermi energies  $E_n^F$ ,  $E_p^F$  and  $E_e^F$ , the Klein potentials, derives from the thermodynamic equilibrium conditions given by the statistical physics of multicomponent systems, applied to a system of degenerate neutrons, protons, and electrons within the framework of general relativity (see Rueda et al. (2011) for details). These constants are linked by the  $\beta$ -equilibrium between the matter constituents

$$E_n^F = E_p^F + E_e^F. \quad (\text{C.4.25})$$

The electron density  $n_e$  is, via Eq. (C.4.20), given by

$$n_e = \frac{e^{-3\nu/2}}{3\pi^2} [\hat{V}^2 + 2m_e\hat{V} - m_e^2(e^\nu - 1)]^{3/2}, \quad (\text{C.4.26})$$

where  $\hat{V} \equiv eV + E_e^F$ . Substituting Eq.( C.4.26) into Eq. (C.4.16) one obtains the general relativistic extension of the relativistic Thomas-Fermi equation recently introduced for the study of compressed atoms (Rotondo et al., 2011c,b). This system of equations has to be solved with the boundary condition of global neutrality; see Rotondo et al. (2011d); Rueda et al. (2011) and below for details.

The scalar density  $n_s$ , within the mean-field approximation, is given by the following expectation value

$$n_s = \langle \bar{\psi}_N \psi_N \rangle = \frac{2}{(2\pi)^3} \sum_{i=n,p} \int d^3k \frac{\tilde{m}_N}{\epsilon_i(p)}, \quad (\text{C.4.27})$$

where  $\epsilon_i(p) = \sqrt{p^2 + \tilde{m}_i^2}$  is the single particle energy.

In the static case, only the temporal components of the covariant currents survive, i.e.  $\langle \bar{\psi}(x)\gamma^i\psi(x) \rangle = 0$ . Thus, by taking the expectation values of Eqs. (C.2.10)–(C.2.13), we obtain the non-vanishing components of the currents

$$J_0^{ch} = n_{ch}u_0 = (n_p - n_e)u_0, \quad (\text{C.4.28})$$

$$J_0^\omega = n_b u_0 = (n_n + n_p)u_0, \quad (\text{C.4.29})$$

$$J_0^\rho = n_3 u_0 = (n_p - n_n)u_0, \quad (\text{C.4.30})$$

where  $n_b = n_p + n_n$  is the baryon number density and  $u_0 = \sqrt{g_{00}} = e^{v/2}$  is the covariant temporal component of the four-velocity of the fluid, which satisfies  $u^\mu u_\mu = 1$ .

The metric function  $\lambda$  is related to the mass  $M(r)$  and the electric field  $E(r) = -e^{-(v+\lambda)/2} V'$  through

$$\begin{aligned} e^{-\lambda(r)} &= 1 - \frac{2GM(r)}{r} + Gr^2 E^2(r) \\ &= 1 - \frac{2GM(r)}{r} + \frac{GQ^2(r)}{r^2}, \end{aligned} \quad (\text{C.4.31})$$

being  $Q(r)$  the conserved charge, related to the electric field by  $Q(r) = r^2 E(r)$ .

The energy-momentum tensor of free-fields and free-fermions  $T^{\mu\nu}$  of the system is

$$T^{\mu\nu} = T_f^{\mu\nu} + T_\gamma^{\mu\nu} + T_\sigma^{\mu\nu} + T_\omega^{\mu\nu} + T_\rho^{\mu\nu}, \quad (\text{C.4.32})$$

where

$$T_\gamma^{\mu\nu} = -\frac{1}{4\pi} \left( F_\alpha^\mu F^{\alpha\nu} + \frac{1}{4} g^{\mu\nu} F_{\alpha\beta} F^{\alpha\beta} \right), \quad (\text{C.4.33})$$

$$T_\sigma^{\mu\nu} = \nabla^\mu \nabla^\nu \sigma - g^{\mu\nu} \left[ \frac{1}{2} \nabla_\sigma \sigma \nabla^\sigma \sigma - U(\sigma) \right], \quad (\text{C.4.34})$$

$$\begin{aligned} T_\omega^{\mu\nu} &= -\Omega_\alpha^\mu \Omega^{\alpha\nu} - \frac{1}{4} g^{\mu\nu} \Omega_{\alpha\beta} \Omega^{\alpha\beta} \\ &+ m_\omega^2 \left( \omega^\mu \omega^\nu - \frac{1}{2} g^{\mu\nu} \omega_\alpha \omega^\alpha \right), \end{aligned} \quad (\text{C.4.35})$$

$$\begin{aligned} T_\rho^{\mu\nu} &= -\mathcal{R}_\alpha^\mu \mathcal{R}^{\alpha\nu} - \frac{1}{4} g^{\mu\nu} \mathcal{R}_{\alpha\beta} \mathcal{R}^{\alpha\beta} \\ &+ m_\rho^2 \left( \mathcal{R}^\mu \mathcal{R}^\nu - \frac{1}{2} g^{\mu\nu} \mathcal{R}_\alpha \mathcal{R}^\alpha \right), \end{aligned} \quad (\text{C.4.36})$$

$$T_f^{\mu\nu} = (\mathcal{E} + \mathcal{P}) u^\mu u^\nu - \mathcal{P} g^{\mu\nu}, \quad (\text{C.4.37})$$

where the energy-density  $\mathcal{E}$  and the pressure  $\mathcal{P}$  are given by

$$\mathcal{E} = \sum_{i=n,p,e} \mathcal{E}_i, \quad \mathcal{P} = \sum_{i=n,p,e} \mathcal{P}_i, \quad (\text{C.4.38})$$

being  $\mathcal{E}_i$  and  $\mathcal{P}_i$  the single fermion fluid contributions

$$\mathcal{E}_i = \frac{2}{(2\pi)^3} \int_0^{P_i^F} \epsilon_i(p) 4\pi p^2 dp, \quad (\text{C.4.39})$$

$$\mathcal{P}_i = \frac{1}{3} \frac{2}{(2\pi)^3} \int_0^{P_i^F} \frac{p^2}{\epsilon_i(p)} 4\pi p^2 dp. \quad (\text{C.4.40})$$

It is worth to recall that the equation of state (C.4.38)–(C.4.40) satisfies the thermodynamic law

$$\mathcal{E} + \mathcal{P} = \sum_{i=n,p,e} n_i \mu_i. \quad (\text{C.4.41})$$

The parameters of the nuclear model, namely the coupling constants  $g_s$ ,  $g_\omega$  and  $g_\rho$ , and the meson masses  $m_\sigma$ ,  $m_\omega$  and  $m_\rho$  are usually fixed by fitting experimental properties of nuclei, e.g. saturation density, binding energy per nucleon (or experimental masses), symmetry energy, surface energy, and nuclear incompressibility. In Table C.1 we present selected fits of the nuclear parameters. In particular, we show the following parameter sets: NL3 (Lalazisis et al., 1997), NL-SH (Sharma et al., 1993), TM1 (Sugahara and Toki, 1994), and TM2 (Hirata et al., 1995).

	NL3	NL-SH	TM1	TM2
$m_\sigma$ (MeV)	508.194	526.059	511.198	526.443
$m_\omega$ (MeV)	782.501	783.000	783.000	783.000
$m_\rho$ (MeV)	763.000	763.000	770.000	770.000
$g_s$	10.2170	10.4440	10.0289	11.4694
$g_\omega$	12.8680	12.9450	12.6139	14.6377
$g_\rho$	4.4740	4.3830	4.6322	4.6783
$g_2$ (fm <sup>-1</sup> )	-10.4310	-6.9099	-7.2325	-4.4440
$g_3$	-28.8850	-15.8337	0.6183	4.6076
$c_3$	0.0000	0.0000	71.3075	84.5318

**Table C.1.:** Selected parameter sets of the  $\sigma$ - $\omega$ - $\rho$  model.

The constants  $g_2$  and  $g_3$  are the third and fourth order constants of the self-scalar interaction as given by the scalar self-interaction potential

$$U(\sigma) = \frac{1}{2}m_\sigma^2\sigma^2 + \frac{1}{3}g_2\sigma^3 + \frac{1}{4}g_3\sigma^4. \quad (\text{C.4.42})$$

The non-zero constant  $c_3$  that appears in the TM1 and TM2 models corresponds to the self-coupling constant of the non-linear vector self-coupling  $\frac{1}{4}c_3(\omega_\mu\omega^\mu)^2$ . We have not include such a self-coupling vector interaction in the general formulation presented above. However, we show also here the results of the integration when such a self-interaction is taken into account and we refer to Sugahara and Toki (1994); Hirata et al. (1995) for details about the motivations of including that contribution.

The numerical integration of the core equations can be started given a central density and the regularity conditions at the origin; see below Sec. C.4.3 for details. At nuclear density the phase-transition to the “solid” crust takes place. Thus, the radius of the core  $R_{\text{core}}$  is given by  $\mathcal{E}(r = R_{\text{core}})/c^2 = \rho_{\text{nuc}}$ . These equations must be solved with the boundary conditions given by the

fulfillment of the condition of global charge neutrality and the continuity of the Klein potentials of particles between the core and the crust.

### Core-crust transition layer equations

In the core-crust interface, the mean-field approximation for the meson-fields is not valid any longer and thus a full numerical integration of the meson-field equations of motion, taking into account all gradient terms, must be performed. We expect the core-crust transition boundary-layer to be a region with characteristic length scale of the order of the electron Compton wavelength  $\sim \lambda_e = \hbar/(m_e c) \sim 100$  fm corresponding to the electron screening scale. Then, in the core-crust transition layer, the system of equations (C.4.14)–(C.4.22) reduces to

$$V'' + \frac{2}{r}V' = -e^{\lambda_{\text{core}}} e J_{ch}^0, \quad (\text{C.4.43})$$

$$\sigma'' + \frac{2}{r}\sigma' = e^{\lambda_{\text{core}}} [\partial_\sigma U(\sigma) + g_s n_s], \quad (\text{C.4.44})$$

$$\omega'' + \frac{2}{r}\omega' = -e^{\lambda_{\text{core}}} [g_\omega J_\omega^0 - m_\omega^2 \omega], \quad (\text{C.4.45})$$

$$\rho'' + \frac{2}{r}\rho' = -e^{\lambda_{\text{core}}} [g_\rho J_\rho^0 - m_\rho^2 \rho], \quad (\text{C.4.46})$$

$$e^{\nu_{\text{core}}/2} \mu_e - eV = \text{constant}, \quad (\text{C.4.47})$$

$$e^{\nu_{\text{core}}/2} \mu_p + eV + g_\omega \omega + g_\rho \rho = \text{constant}, \quad (\text{C.4.48})$$

$$\mu_n = \mu_p + \mu_e + 2 g_\rho \rho e^{-\nu_{\text{core}}/2}, \quad (\text{C.4.49})$$

due to the fact that the metric functions are essentially constant on the core-crust transition layer and thus we can take their values at the core-radius  $e^{\nu_{\text{core}}} \equiv e^{\nu(R_{\text{core}})}$  and  $e^{\lambda_{\text{core}}} \equiv e^{\lambda(R_{\text{core}})}$ .

The system of equations of the transition layer has a stiff nature due to the existence of two different scale lengths. The first one is associated with the nuclear interactions  $\sim \lambda_\pi = \hbar/(m_\pi c) \sim 1.5$  fm and the second one is due to the aforementioned screening length  $\sim \lambda_e = \hbar/(m_e c) \sim 100$  fm. Thus, the numerical integration of Eqs. (C.4.43)–(C.4.49) has been performed subdividing the core-crust transition layer in the following three regions: (I) a mean-field-like region where all the fields vary slowly with length scale  $\sim \lambda_e$ , (II) a strongly interacting region of scale  $\sim \lambda_\pi$  where the surface tension due to nuclear interactions dominate producing a sudden decrease of the proton and the neutron densities and, (III) a Thomas-Fermi-like region of scale  $\sim \lambda_e$  where only a layer of opposite charge made of electrons is present producing the total screening of the positively charged core. The results of the numerical integration of the equilibrium equations are shown in Fig. C.8-C.9 for the NL3-model.

We have integrated numerically Eqs. (C.4.14)–(C.4.22) for the models listed in Table C.1. The boundary conditions for the numerical integration are fixed through the following procedure. We start assuming a value for the central baryon number density  $n_b(0) = n_n(0) + n_p(0)$ . From the regularity conditions at the origin we have  $e^{-\lambda(0)} = 1$  and  $n_e(0) = n_p(0)$ .

The metric function  $\nu$  at the origin can be chosen arbitrarily, e.g.  $\nu(0) = 0$ , due to the fact that the system of equations remain invariant under the shift  $\nu \rightarrow \nu + \text{constant}$ . The right value of  $\nu$  is obtained once the end of the integration of the core has been accomplished and duly matched to the crust, by fulfilling the following identity at the surface of the neutron star,

$$e^{\nu(R)} = e^{-\lambda(R)} = 1 - \frac{2GM(R)}{c^2R}, \quad (\text{C.4.50})$$

being  $M(R)$  and  $R$  the total mass and radius of the star. Then, taking into account the above conditions, we solve the system (C.4.17)–(C.4.22) at the origin for the other unknowns  $\sigma(0), \omega(0), \rho(0), n_n(0), n_p(0), n_e(0)$ .

The initial conditions for the numerical integration of the core-crust transition layer equations are determined by the final values given by the numerical integration of the core equations, i.e. we take the values of all the variables at the core-radius  $R_{\text{core}}$ .

In the region I the effect of the Coulomb interaction is clear: on the proton-profile we can see a bump due to Coulomb repulsion while the electron-profile decreases as expected. Such a Coulomb effect is indirectly felt also by the neutrons due to the coupled nature of the system of equations. However, the neutron-bump is much smaller than the one of protons and it is not appreciable in Fig. C.8-C.9 due to the plot-scale. In the region II we see clearly the effect of the surface tension due to nuclear interaction which produces a sharp decrease of the neutron and proton profiles in a characteristic scale  $\sim \lambda_\pi$ . In addition, it can be seen a neutron skin effect, analogous to the one observed in heavy nuclei, which makes the scale of the neutron density falloff slightly larger with respect to the proton one, in close analogy to the neutron skin effect observed in neutron rich nuclei, see e.g. Tamii et al. (2011). The region III is characterized by a smooth decreasing of the electron density which resembles the behavior of the electrons surrounding a nucleus in the Thomas-Fermi model.

The matching to the crust must be done at the radius  $R_{\text{core}} + \delta R$  where full charge neutrality is reached. The thickness of the core-crust transition boundary layer  $\delta R$  as well as the value of the electron density at the edge of the crust,  $R_{\text{core}} + \delta R$ , depends on the nuclear parameters, especially on the nuclear surface tension.

The equilibrium conditions given by the constancy of the Klein potentials (C.4.20)–(C.4.22) throughout the configuration, impose in the transition layer

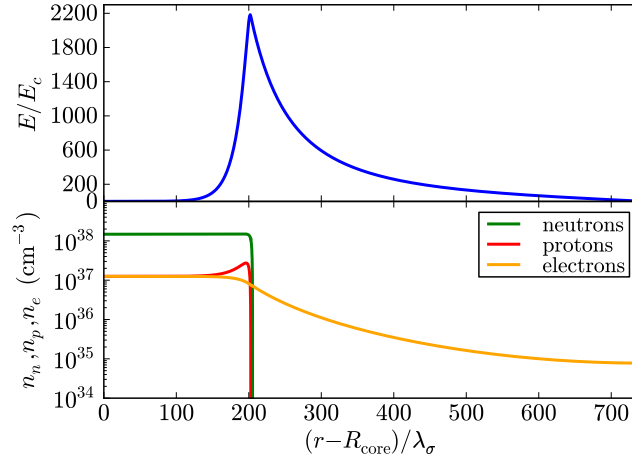


**Figure C.8.:** Upper panel: electric field in the core-crust transition layer in units of the critical field  $E_c$ . Lower panel: particle density profiles in the core-crust boundary interface in units of  $\text{cm}^{-3}$ . Here we use the NL3-model of Table C.1 and  $\lambda_\sigma = \hbar/(m_\sigma c) \sim 0.4$  fm denotes the sigma-meson Compton wavelength. The density at the edge of the crust in this example is  $\rho_{\text{crust}} = \rho_{\text{drip}} = 4.3 \times 10^{11}$  g/cm<sup>3</sup>.

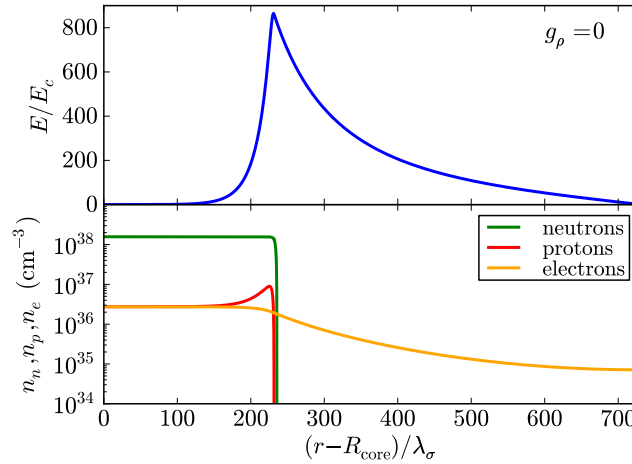


**Figure C.9.:** The same as Fig. C.8, but setting  $g_\rho = 0$  in order to see the effects of the  $\rho$ -meson with respect to the case  $g_\rho \neq 0$ .

the following continuity condition

$$e^{V_{\text{core}}/2} \mu_e^{\text{core}} - eV^{\text{core}} = e^{V_{\text{crust}}/2} \mu_e^{\text{crust}}. \quad (\text{C.4.51})$$

where  $\mu_e^{\text{core}} = \mu_e(R_{\text{core}})$ ,  $eV^{\text{core}} = eV(R_{\text{core}})$ , and  $\mu_e^{\text{crust}} = \mu_e(R_{\text{core}} + \delta R)$ , and  $e^{V_{\text{crust}}} \simeq e^{V_{\text{core}}}$ .

The electron chemical potential and the density decrease, in the boundary interface, until values  $\mu_e^{\text{crust}} < \mu_e^{\text{core}}$  and  $\rho_{\text{crust}} < \rho_{\text{core}}$ . For each central density, an entire family of core-crust interface boundaries and, correspondingly, an entire family of crusts with different mass and thickness, exist. The configuration with  $\rho_{\text{crust}} = \rho_{\text{drip}} \sim 4.3 \times 10^{11} \text{ g/cm}^3$  separates neutron stars with and without inner crust. In the so-called inner crust, the neutrons dripped from the nuclei in the crust form a fluid that coexist with the nuclei lattice and the degenerate electrons (Baym et al., 1971a). The presence of the neutron fluid in the crust changes the nuclear surface tension at the core radius, in close analogy to the reduction of the surface tension of the nuclei in the crust due to the presence of the dripped neutrons, see e.g. Baym et al. (1971a) for details. This reduction of the nuclear tension is not taken into account in the nuclear parameters which are obtained to fit the properties of bare nuclei, see Table C.1. Thus we present here the results for configurations  $\rho_{\text{crust}} \leq \rho_{\text{drip}}$ , i.e for neutron stars possessing only outer crust. The construction of configurations with  $\rho_{\text{crust}} > \rho_{\text{drip}}$  needs to be studied in more detail and will be the subject of a forthcoming work.

In Figs. C.8 and C.9, we show the core-crust transition layer for the NL3 model of Table C.1 with and without the presence of the  $\rho$ -meson respectively. The presence of the  $\rho$ -meson is responsible for the nuclear asymmetry within this nuclear model. The relevance of the nuclear symmetry energy on the structure of nuclei and neutron stars is continuously stressed in literature; see e.g. M  ther et al. (1987); Kubis (2007); Sharma and Pal (2009); Hebeler et al. (2010); Loan et al. (2011). The precise value of the nuclear symmetry energy plays here a crucial in determining the precise value of the  $\rho$ -meson coupling which, in the present case, is essential in the determination of the intensity of the electric field in the core-crust boundary interface; as can be seen from the comparison of Figs. C.8 and C.9.

### Crust equations

Turning now to the crust, it is clear from our recent treatment of white dwarfs (Rotondo et al., 2011b) that also this problem can be solved by the adoption of Wigner-Seitz cells and from the relativistic Feynman-Metropolis-Teller (RFMT) approach (Rotondo et al., 2011c) it follows that the crust is clearly

neutral. Thus, the structure equations to be integrated are the TOV equations

$$\frac{d\mathcal{P}}{dr} = -\frac{G(\mathcal{E} + \mathcal{P})(M + 4\pi r^3 \mathcal{P})}{r^2(1 - \frac{2GM}{r})}, \quad (\text{C.4.52})$$

$$\frac{dM}{dr} = 4\pi r^2 \mathcal{E}, \quad (\text{C.4.53})$$

where  $M = M(r)$  is the mass enclosed at the radius  $r$ .

The effects of the Coulomb interaction in “solid”-like electron-ion systems appears only at the microscopic level e.g. Debye-Hueckel screening in classical systems (Debye and Hueckerl, 1923) and Thomas-Fermi screening in the degenerate case (Mott, 1936). In order to analyze the effects of the microscopic screening on the structure of the configuration we will consider two equations of state for the crust: the locally neutral case or uniform approximation (see e.g. Chandrasekhar (1931b)) and, for simplicity, instead of using the RFMT EoS (Rotondo et al., 2011c), we use as second EoS the one due to Baym, Pethick and Sutherland (BPS) (Baym et al., 1971a), which is by far the most used equation of state in literature for the description of the neutron star crust (see e.g. Haensel et al. (2007)).

In the uniform approximation, both the degenerate electrons and the nucleons distribution are considered constant inside each cell of volume  $V_{\text{ws}}$ . This kind of configuration can be obtained only imposing microscopically the condition of local charge neutrality

$$n_e = \frac{Z}{V_{\text{ws}}}. \quad (\text{C.4.54})$$

The total pressure of the system is assumed to be entirely due to the electrons, i.e.

$$\mathcal{P} = \mathcal{P}_e = \frac{2}{3(2\pi\hbar)^3} \int_0^{p_e^{\text{F}}} \frac{c^2 p^2 4\pi p^2}{\sqrt{c^2 p^2 + m_e^2 c^4}} dp, \quad (\text{C.4.55})$$

and the total energy-density due to the nuclei, i.e.  $\mathcal{E} = (A/Z)m_N n_e$ , where  $m_N$  is the nucleon mass.

We turn now to the BPS equation of state. The first correction to the uniform model, corresponds to abandon the assumption of the electron-nucleon fluid through the so-called “lattice” model which introduces the concept of Wigner-Seitz cell: each cell of radius  $R_{\text{ws}}$  contains a point-like nucleus of charge  $+Ze$  with  $A$  nucleons surrounded by a uniformly distributed cloud of  $Z$  fully-degenerate electrons.

The sequence of the equilibrium nuclides present at each density in the BPS equation of state is obtained by looking for the nuclear composition that minimizes the energy per nucleon for each fixed nuclear composition  $(Z, A)$  (see Table C.2 and Baym et al. (1971a) for details). The pressure  $\mathcal{P}$  and the

energy-density  $\mathcal{E}$  of the system are, within this model, given by

$$\mathcal{P} = \mathcal{P}_e + \frac{1}{3}W_L n_N, \quad (\text{C.4.56})$$

$$\frac{\mathcal{E}}{n_b} = \frac{W_N + W_L}{A} + \frac{\mathcal{E}_e(n_b Z/A)}{n_b}, \quad (\text{C.4.57})$$

where the electron energy-density is given by

$$\mathcal{E}_e = \frac{2}{(2\pi)^3} \int_0^{p_e^F} \sqrt{p^2 + m_e^2} 4\pi p^2 dp, \quad (\text{C.4.58})$$

and  $W_N(A, Z)$  is the total energy of an isolated nucleus given by the semi-empirical formula

$$W_N = m_n c^2 (A - Z) + m_p c^2 Z - bA, \quad (\text{C.4.59})$$

with  $b$  being the Myers and Swiatecki binding energy per nucleon (Myers, 1966). The lattice energy per nucleus  $W_L$  is given by

$$W_L = -\frac{1.819620Z^2 e^2}{a}, \quad (\text{C.4.60})$$

where the lattice constant  $a$  is related to the nucleon density  $n_N$  by  $n_N a^3 = 2$ .

### C.4.3. Neutron star structure

In the traditional TOV treatment the density and the pressure are a priori assumed to be continuous as well as the local charge neutrality of the system. The distinguishing feature of our new solution is that the Klein potentials are constant throughout the three regions; the core, the crust and the transition interface boundary. An overcritical electric field is formed and consequently a discontinuity in density is found with a continuous total pressure including the surface tension of the boundary. In Figs. C.10 and C.11, we compare and contrast the density profiles of configurations obtained from the traditional TOV treatment and with the treatment presented here.

In Figs. C.12–C.18 we show the results of the numerical integration of the system of the general relativistic constitutive equations of the configuration from the center all the way up to the surface with the appropriate boundary conditions between the involved phases. In particular, we have plotted the mass-radius relation as well as the compactness of the neutron stars obtained with the models listed in Table C.1.

It is worth to note that the inclusion of the Coulomb interaction and in particular the presence of the negative lattice energy  $W_L$  results in a decreasing of the pressure of the cells. Such an effect, as shown in Fig. C.15–C.18, leads

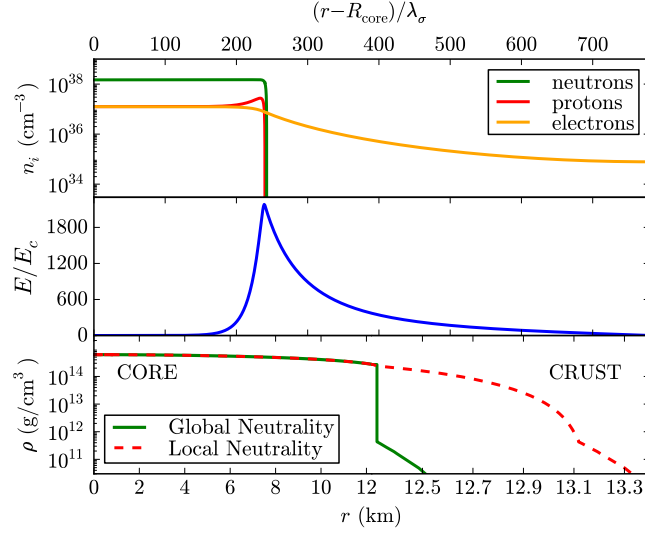


**Figure C.10.:** Upper panel: electric field in the core-crust transition layer, in units of the critical field  $E_c$ . Middle panel: particle density profiles in the core-crust boundary interface, in units of  $\text{cm}^{-3}$ . Lower panel: density profile inside a neutron star with central density  $\rho(0) \sim 5\rho_{\text{nuc}}$ . We compare and contrast the structural differences between the solution obtained from the traditional TOV equations (locally neutral case) and the globally neutral solution presented here. We use here the NL3 nuclear parametrization of Table C.1 and  $\lambda_\sigma = \hbar/(m_\sigma c) \sim 0.4$  fm, denotes the sigma-meson Compton wavelength. In this example the density at the edge of the crust is  $\rho_{\text{crust}} = \rho_{\text{drip}} = 4.3 \times 10^{11} \text{ g/cm}^3$ .

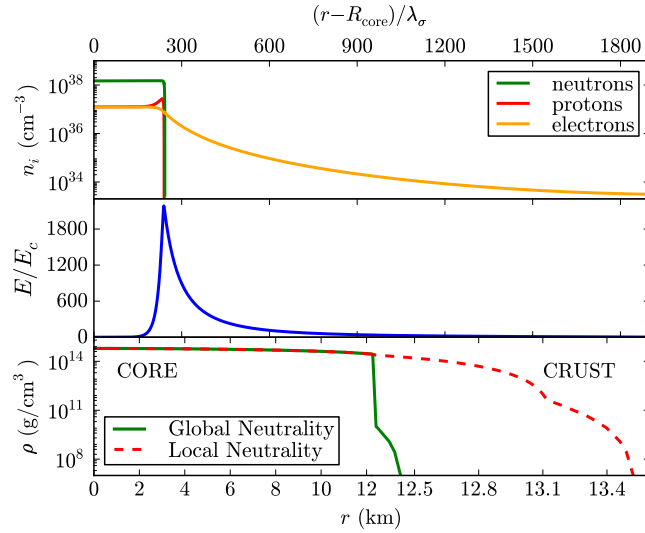


**Figure C.11.:** Same as Fig. C.10. In this example the density at the edge of the crust is  $\rho_{\text{crust}} = 10^{10} \text{ g/cm}^3$ .

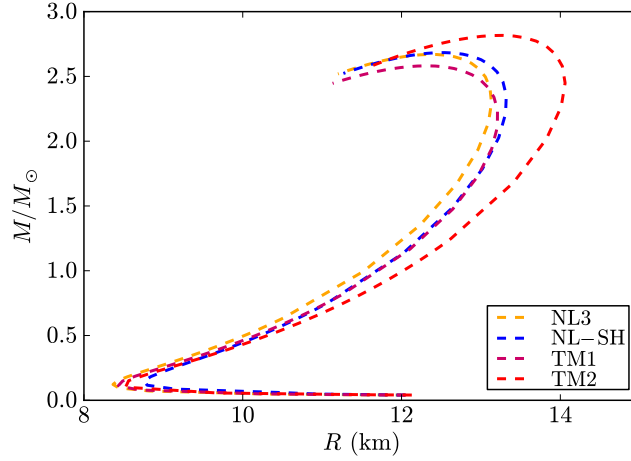


**Figure C.12.:** Mass-Radius relation for the neutron stars obtained with the nuclear models listed in Table C.1. In the crust we have used the BPS equation of state. The mass is given in solar masses and the radius in km.

to a decreasing of the mass and the thickness of the crust with respect to the uniform-approximation case where no Coulomb interactions are taken into account.

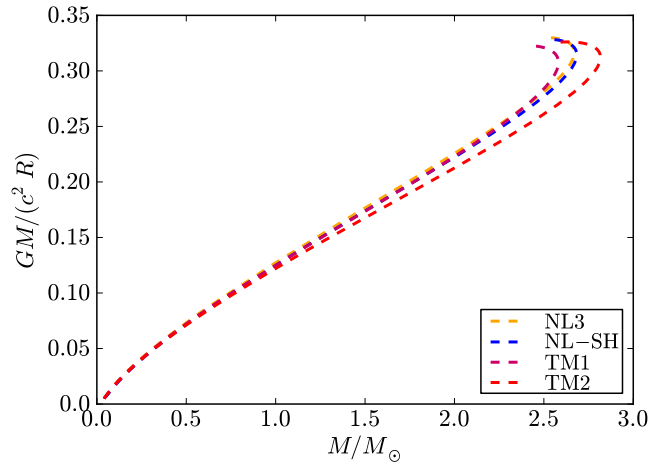


**Figure C.13.:** Compactness of the star  $GM/(c^2 R)$  as a function of the star mass  $M$ . In the crust we have used the BPS equation of state and the nuclear models are in Table C.1.

Comparing the mass and the thickness of the crust obtained with these two different EoS, we obtain systematically crusts with smaller mass and larger thickness when Coulomb interactions are taken into account. This results are in line with the recent results in Rotondo et al. (2011b), where the mass-radius relation of white-dwarfs has been calculated using an EoS based on the relativistic Feynman-Metropolis-Teller model for compressed atoms (Rotondo

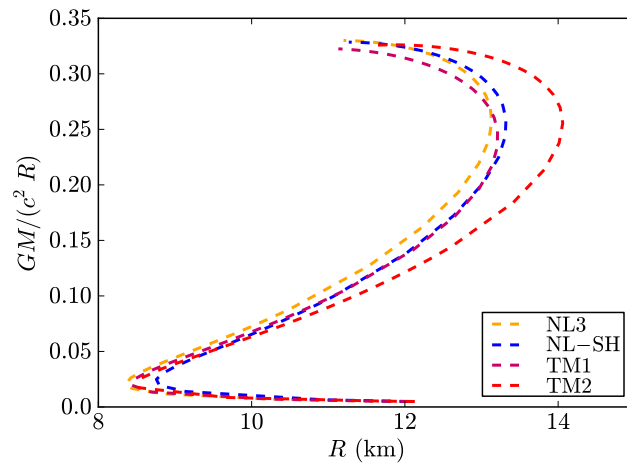


**Figure C.14.:** Compactness of the star  $GM/(c^2 R)$  as a function of the star radius  $R$ . In the crust we have used the BPS equation of state and the nuclear models are in Table C.1.

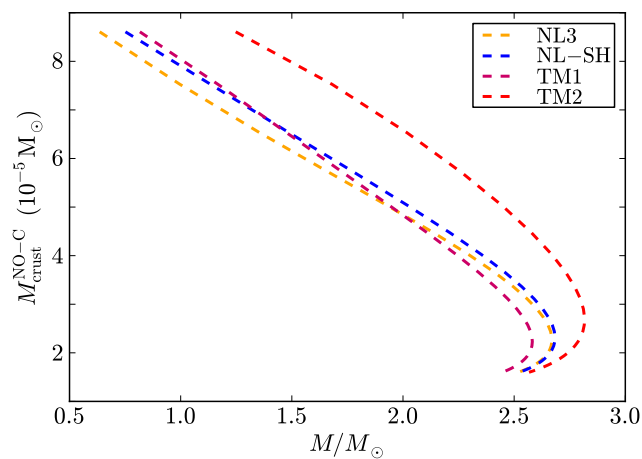


**Figure C.15.:** Mass of the crust as a function of the compactness for the crust EoS without Coulomb interactions.

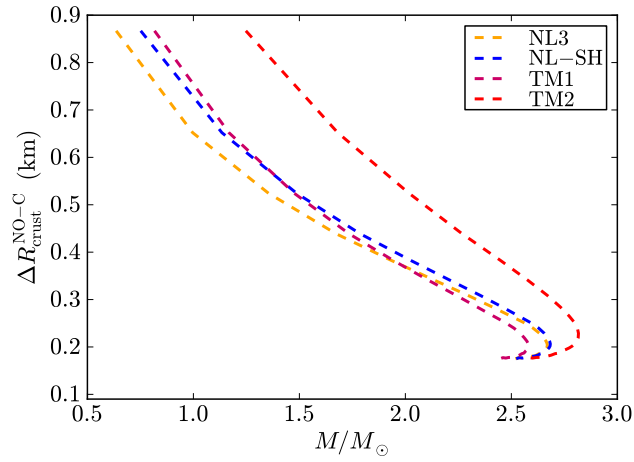


**Figure C.16.:** Crust-thickness as a function of the compactness for the crust EoS without Coulomb interactions.

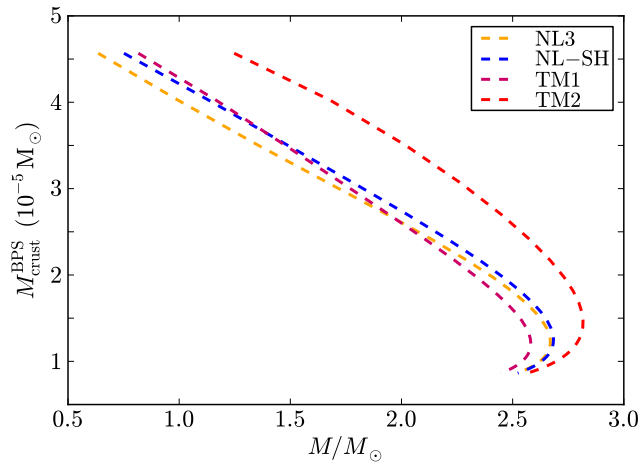


**Figure C.17.:** Crust mass as a function of the compactness for crust with the BPS EoS.

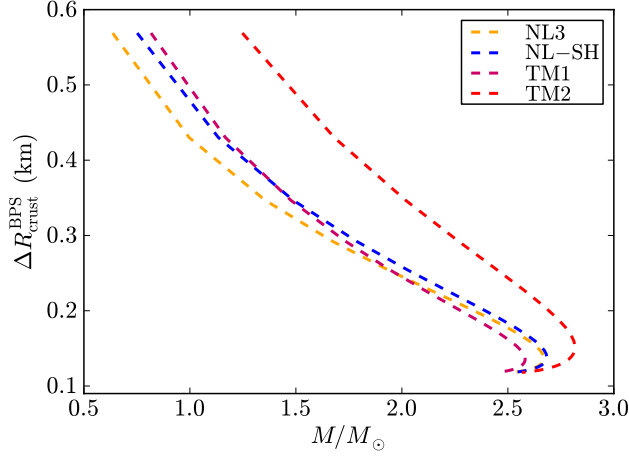


**Figure C.18.:** Crust thickness as a function of the compactness for crust with the BPS EoS.

et al., 2011c).

In the case of the BPS EoS, the average nuclear composition in the outer crust, namely the average charge to mass ratio of nuclei  $Z/A$ , is obtained by calculating the contribution of each nuclear composition present to the mass of the crust. We exemplified the analysis for two different cores:  $M_{\text{core}} = 2.56M_{\odot}$ ,  $R_{\text{core}} = 12.79$  km;  $M_{\text{core}} = 1.35M_{\odot}$ ,  $R_{\text{core}} = 11.76$  km. The relative abundance of each nuclide within the crust of the star can be obtained as

$$\text{R.A.} = \frac{1}{M_{\text{crust}}^{\text{BPS}}} \int_{\Delta r} 4\pi r^2 \varepsilon dr, \quad (\text{C.4.61})$$

where the integration is carried out in the layer of thickness  $\Delta r$  where the particular nuclide is present; see C.2 and Fig. C.19. Our results are in agreement with the analysis on the neutron star crust composition obtained in Goriely et al. (2011a,b). In both cases we obtain as average nuclear composition  $^{105}_{35}\text{Br}$ . The corresponding crusts with fixed nuclear composition  $^{105}_{35}\text{Br}$  for the two chosen cores are calculated neglecting Coulomb interactions (i.e. using the first EoS). The mass and the thickness of these crusts with fixed  $^{105}_{35}\text{Br}$  are different with respect to the ones obtained using the full BPS EoS, leading to such average nuclear composition. For the two selected examples we obtain that the mass and the thickness of the crust with average  $^{105}_{35}\text{Br}$  are, respectively, 18% larger and 5% smaller with respect to the ones obtained with the corresponding BPS EoS. This result shows how small microscopic effects due to the Coulomb interaction in the crust of the neutron star leads to quantitative not negligible effects on the macroscopic structure of the configuration.

Equilibrium Nuclei Below Neutron Drip						
Nucleus	Z	$\rho_{max}(\text{g cm}^{-3})$	$\Delta R_1$ (km)	R.A.1(%)	$\Delta R_2$ (km)	R.A.2(%)
$^{56}\text{Fe}$	26	$8.1 \times 10^6$	0.0165	$7.56652 \times 10^{-7}$	0.0064	$6.96927 \times 10^{-7}$
$^{62}\text{Ni}$	28	$2.7 \times 10^8$	0.0310	0.00010	0.0121	0.00009
$^{64}\text{Ni}$	28	$1.2 \times 10^9$	0.0364	0.00057	0.0141	0.00054
$^{84}\text{Se}$	34	$8.2 \times 10^9$	0.0046	0.00722	0.0017	0.00683
$^{82}\text{Ge}$	32	$2.2 \times 10^{10}$	0.0100	0.02071	0.0039	0.01983
$^{80}\text{Zn}$	38	$4.8 \times 10^{10}$	0.1085	0.04521	0.0416	0.04384
$^{78}\text{Ni}$	28	$1.6 \times 10^{11}$	0.0531	0.25635	0.0203	0.25305
$^{76}\text{Fe}$	26	$1.8 \times 10^{11}$	0.0569	0.04193	0.0215	0.04183
$^{124}\text{Mo}$	42	$1.9 \times 10^{11}$	0.0715	0.02078	0.0268	0.02076
$^{122}\text{Zr}$	40	$2.7 \times 10^{11}$	0.0341	0.20730	0.0127	0.20811
$^{120}\text{Sr}$	38	$3.7 \times 10^{11}$	0.0389	0.23898	0.0145	0.24167
$^{118}\text{Kr}$	36	$4.3 \times 10^{11}$	0.0101	0.16081	0.0038	0.16344

**Table C.2.:**  $\rho_{max}$  is the maximum density at which the nuclide is present;  $\Delta R_1$ ,  $\Delta R_2$  and R.A.1(%), R.A.2(%) are respectively the thickness of the layer where a given nuclide is present and their relative abundances in the outer crust for two different cases:  $M_{\text{core}} = 2.56M_{\odot}$ ,  $R_{\text{core}} = 12.79$  km;  $M_{\text{core}} = 1.35M_{\odot}$ ,  $R_{\text{core}} = 11.76$  km.

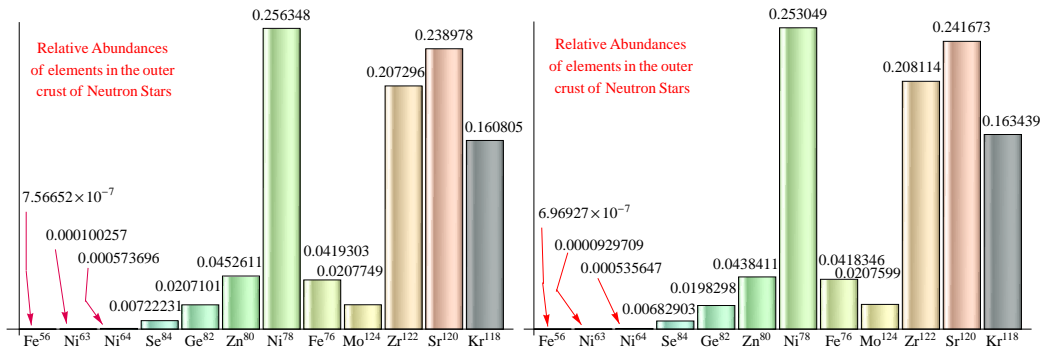


**Figure C.19.:** Relative abundances of chemical elements in the crust for the two cores analyzed in Table C.2

#### C.4.4. Observational constraints on the mass-radius relation

It has been recently pointed out that the most up-to-date stringent constraints to the mass-radius relation of neutron stars are provided by the largest mass, the largest radius, the highest rotational frequency, and the maximum surface gravity, observed for pulsars (Trümper, 2011).

So far, the highest neutron star mass measured with a high level of experimental confidence is the mass of the 3.15 millisecond pulsar PSR J1614-2230,  $M = 1.97 \pm 0.04 M_{\odot}$ , obtained from the Shapiro time delay and the Keplerian orbital parameters of the binary system (Demorest et al., 2010a). The fitting of the thermonuclear burst oscillation light curves from the accreting millisecond pulsar XTE J1814-338 weakly constrain the mass-radius relation imposing an upper limit to the surface gravity of the neutron star,  $GM/(c^2 R) < 0.24$  (Bhattacharyya et al., 2005). A lower limit of the radius of RX J1856-3754, as seen by an observer at infinity  $R_{\infty} = R[1 - 2GM/(c^2 R)]^{-1/2} > 16.8$  km, has been obtained from the fit of the optical and X-ray spectra of the source (Trümper et al., 2004); it gives the constraint  $2GM/c^2 > R - R^3/(R_{\infty}^{\min})^2$ , being  $R_{\infty}^{\min} = 16.8$  km. Assuming a neutron star of  $M = 1.4 M_{\odot}$  to fit the Chandra data of the low-mass X-ray binary X7, it turns out that the radius of the star satisfies  $R = 14.5_{-1.6}^{+1.8}$  km, at 90% confidence level, corresponding to  $R_{\infty} = [15.64, 18.86]$  km, respectively (see Heinke et al. (2006) for details). The maximum rotation rate of a neutron star taking into account both the effects of general relativity and deformations has been found to be  $\nu_{\max} = 1045(M/M_{\odot})^{1/2}(10 \text{ km}/R)^{3/2}$  Hz, largely independent of the equation of state (Lattimer and Prakash, 2004a). The fastest observed pulsar is PSR J1748-2246ad with a rotation frequency of 716 Hz (Hessels et al., 2006a), which results in the constraint  $M \geq 0.47(R/10 \text{ km})^3 M_{\odot}$ . In Fig. C.20 we show all these constraints and the mass-radius relation presented in this work.

As discussed by J. E. Trümper in Trümper (2011), the above constraints strongly favor stiff equations of state which provide high maximum masses for neutron stars. In addition, putting all of them together, the radius of a canonical neutron star of mass  $M = 1.4 M_{\odot}$  is highly constrained to the range  $R \gtrsim 12$  km disfavoring, at the same time, the strange quark hypothesis for these specific objects. It is clear from Fig. C.20 that the mass-radius relation presented here is consistent with all the observation constraints, for all the nuclear parametrizations of Table C.1. We present in Table C.3, the radii predicted by our mass-radius relation for a canonical neutron star of  $M = 1.4 M_{\odot}$  as well as for the millisecond pulsar PSR J1614-2230,  $M = 1.97 \pm 0.04 M_{\odot}$ .

#### C.4.5. Comparison with the traditional TOV treatment

In the traditional TOV treatment local charge neutrality as well as the continuity of the pressure and the density in the core-crust transition are assumed. This leads to explicit violation of the constancy of the Klein poten-

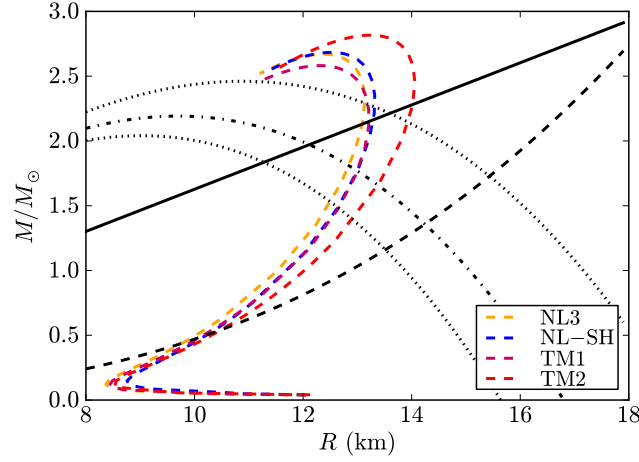


**Figure C.20.:** Constraints on the mass-radius relation given by J. E. Trümper in Trümper (2011) and the theoretical mass-radius relation presented in this work in Fig. C.12. The solid line is the upper limit of the surface gravity of XTE J1814-338, the dotted-dashed curve corresponds to the lower limit to the radius of RX J1856-3754, the dashed line is the constraint imposed by the fastest spinning pulsar PSR J1748-2246ad, and the dotted curves are the 90% confidence level contours of constant  $R_\infty$  of the neutron star in the low-mass X-ray binary X7. Any mass-radius relation should pass through the area delimited by the solid, the dashed and the dotted lines and, in addition, it must have a maximum mass larger than the mass of PSR J1614-2230,  $M = 1.97 \pm 0.04M_\odot$ .

$M(M_\odot)$	$R_{\text{NL3}}$	$R_{\text{NL-SH}}$	$R_{\text{TM1}}$	$R_{\text{TM2}}$
1.40	12.31	12.47	12.53	12.93
1.93	12.96	13.14	13.13	13.73
2.01	13.02	13.20	13.17	13.82

**Table C.3.:** Radii (in km) predicted by the nuclear parametrizations NL3, NL-Sh, TM1 and TM2 of Table C.1, for a canonical neutron star of  $M = 1.4M_\odot$  and for the millisecond pulsar PSR J1614-2230,  $M = 1.97 \pm 0.04M_\odot$ .

tials throughout the configuration (see e.g. Rotondo et al. (2011d)). In such a case there is a smooth transition from the core to the crust without any density discontinuity and therefore the density at the edge of the crust is  $\sim \rho_{\text{nuc}} \sim 2.7 \times 10^{14} \text{ g/cm}^3$ . The so-called inner crust in those configurations extends in the range of densities  $\rho_{\text{drip}} \lesssim \rho \lesssim \rho_{\text{nuc}}$  while, at densities  $\rho \lesssim \rho_{\text{drip}}$ , there is the so-called outer crust.

Due to the continuity of the Klein potentials in the transition from the core to the crust, there is a decrease of the Coulomb potential from  $\sim m_{\pi}c^2/e$  at the core radius  $R_{\text{core}}$  down to zero at the edge of the neutral crust. Correspondingly, the electron chemical potential decreases from its value at the core radius until a value approximately given by  $\mu_e^{\text{crust}} \sim \mu_e^{\text{drip}} \sim 26 \text{ MeV}$  (see Fig. C.8-C.9). Therefore, no crusts with densities larger than the neutron drip density  $\rho_{\text{drip}} \sim 4.3 \times 10^{11} \text{ g/cm}^3$  exist, leading to crusts made only of outer crust.

In Figs. C.21 and C.22 we compare and contrast the mass and the thickness of the crust as obtained from the traditional TOV treatment with the new configurations presented here.

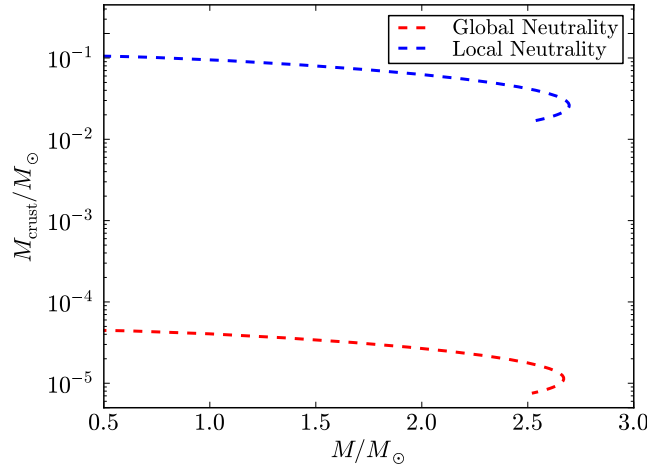


**Figure C.21.:** Mass of the crust given by the traditional locally neutral Tolman-Oppenheimer-Volkoff treatment and by the new globally neutral equilibrium configurations presented in this work. We use here the NL3 nuclear model, see Table C.1.

The markedly differences both in mass and thickness of the crusts (see Figs. C.21 and C.22) obtained from the traditional Tolman-Oppenheimer-Volkoff approach and the new equilibrium configurations presented here, leads to a very different mass-radius relations which we compare and contrast in Fig. C.23.

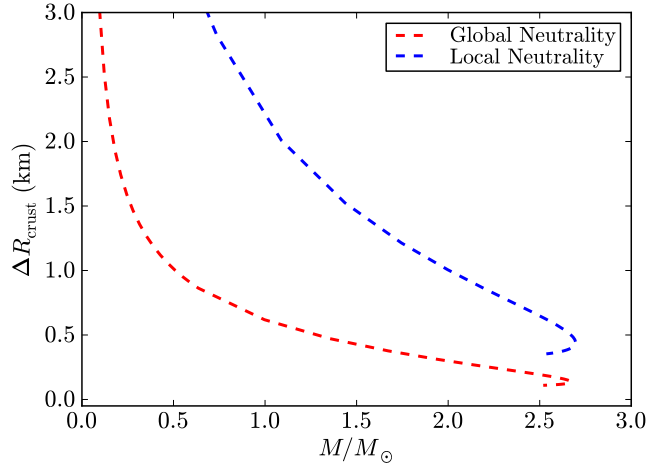


**Figure C.22.:** Thickness of the crust given by the traditional locally neutral Tolman-Oppenheimer-Volkoff treatment and by the new globally neutral equilibrium configurations presented in this work<sup>3</sup>. We use here the NL3 nuclear model, see Table C.1.

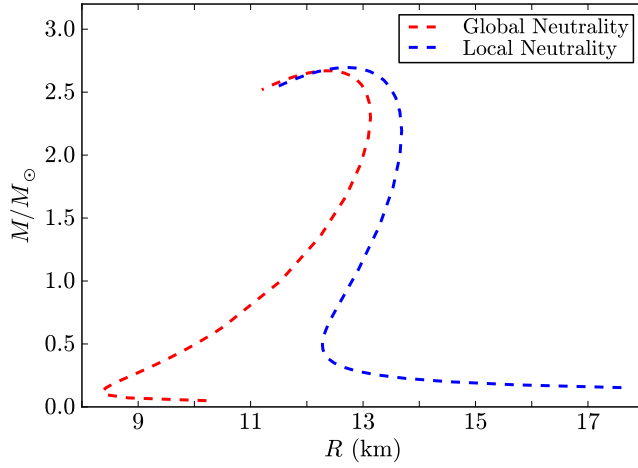


**Figure C.23.:** Mass-Radius relation obtained with the traditional locally neutral TOV treatment and with the new globally neutral equilibrium configurations presented here. We use here the NL3 nuclear model, see Table C.1.

### C.4.6. Concluding Remarks

We have formulated the equations of equilibrium of neutron stars based on our recent works (Rueda et al., 2011; Rotondo et al., 2011c,b,d). The strong, weak, electromagnetic, and gravitational interactions are taken into due account within the framework of general relativity. In particular, the strong interactions between nucleons is described by the exchange of the  $\sigma$ ,  $\omega$ , and  $\rho$  mesons. The equilibrium conditions are given by the set of Einstein-Maxwell-Thomas-Fermi equations and by the constancy of the general relativistic Fermi energies of particles, the Klein potentials, throughout the configuration.

We have solved these equilibrium equations numerically, in the case of zero temperatures, for the nuclear parameter sets NL3 (Lalazissis et al., 1997), NL-SH (Sharma et al., 1993), TM1 (Sugahara and Toki, 1994), and TM2 (Hirata et al., 1995); see Table C.1 for details.

A new structure of the star is found: the positively charged core at supranuclear densities is surrounded by an electronic distribution of thickness  $\gtrsim \hbar/(m_e c) \sim 10^2 \hbar/(m_\pi c)$  of opposite charge and, at lower densities, a neutral ordinary crust.

In the core interior the Coulomb potential well is  $\sim m_\pi c^2/e$  and correspondingly the electric field is  $\sim (m_p/m_{\text{Planck}})(m_\pi/m_e)^2 E_c \sim 10^{-14} E_c$ . Due to the equilibrium condition given by the constancy of the Klein potentials, there is a discontinuity in the density at the transition from the core to the crust, and correspondingly an overcritical electric field  $\sim (m_\pi/m_e)^2 E_c$  develops in the boundary interface; see Fig. C.8–C.9.

The continuity of the Klein potentials at the core-crust boundary interface leads to a decreasing of the electron chemical potential and density, until values  $\mu_e^{\text{crust}} < \mu_e^{\text{core}}$  and  $\rho_{\text{crust}} < \rho_{\text{core}}$  at the edge of the crust, where global charge neutrality is achieved. For each central density, an entire family of core-crust interface boundaries and, correspondingly, an entire family of crusts with different mass and thickness, exist. The larger  $\rho_{\text{crust}}$ , the smaller the thickness of the interface, the peak of the electric field, and the larger the mass and the thickness of the crust. The configuration with  $\rho_{\text{crust}} = \rho_{\text{drip}} \sim 4.3 \times 10^{11} \text{ g/cm}^3$  separates neutron stars with and without inner crust. The neutron stars with  $\rho_{\text{crust}} > \rho_{\text{drip}}$  deserve a further analysis in order to account for the reduction of the nuclear tension at the core-crust transition due to the presence of dripped neutrons from the nuclei in the crust.

All the above new features lead to crusts with masses and thickness smaller than the ones obtained from the traditional TOV treatment, and we have shown specifically neutron stars with  $\rho_{\text{crust}} = \rho_{\text{drip}}$ ; see Figs. C.21–C.22. The mass-radius relation obtained in this case have been compared and contrasted with the one obtained from the locally neutral TOV approach; see Fig. C.23. We have shown that our mass-radius relation is in line with observations, based on the recent work by J. E. Trümper (Trümper, 2011); see Fig. C.20 for details.

The electromagnetic structure of the neutron star presented here is of clear astrophysical relevance. The process of gravitational collapse of a core endowed with electromagnetic structure leads to signatures and energetics very different from the ones of a core endowed uniquely of gravitational interactions; see e.g. Ruffini et al. (2003b,a); Ruffini and Xue (2008); Ruffini et al. (2010b).

It is clear that the release of gravitational energy in the process of gravitational collapse of the core, following the classic work of Gamow and Schoenberg (1941), is carried away by neutrinos. The additional nuclear and electromagnetic energy  $\sim 10^{51}$  erg of the collapsing core introduced in this work are expected to be carried away by electron-positron plasma created in the overcritical electromagnetic field in the collapsing core.

## C.5. Uniformly rotating neutron stars

### C.5.1. Introduction

We have recently shown (Rotondo et al., 2011d; Rueda et al., 2011; Belvedere et al., 2012) that the Tolman-Oppenheimer-Volkoff (TOV) equations (Tolman, 1939; Oppenheimer and Volkoff, 1939), traditionally used to describe the neutron star equilibrium configurations, are superseded once the strong, weak, electromagnetic and gravitational interactions are taken into account. Instead, the Einstein-Maxwell system of equations coupled with the general relativistic Thomas-Fermi equations have to be used, namely what we called the EMTF system of equations. While in the TOV approach the condition of local charge neutrality,  $n_e(r) = n_p(r)$  is imposed (see e.g. Haensel et al. (2007) and references therein), the EMTF approach requests the less stringent condition of global charge neutrality, namely

$$\int \rho_{\text{ch}} d^3r = \int e[n_p(r) - n_e(r)] d^3r = 0, \quad (\text{C.5.1})$$

where  $\rho_{\text{ch}}$  is the charge density,  $e$  is the fundamental electric charge, and the integral is carried out on the entire volume of the system.

The Lagrangian density taking into account all the interactions include the free-fields terms  $\mathcal{L}_g$ ,  $\mathcal{L}_\gamma$ ,  $\mathcal{L}_\sigma$ ,  $\mathcal{L}_\omega$ ,  $\mathcal{L}_\rho$  (respectively for the gravitational, the electromagnetic, and the three mesonic fields), the three fermion species (electrons, protons and neutrons) term  $\mathcal{L}_f$  and the interacting part in the minimal coupling assumption,  $\mathcal{L}_{\text{int}}$  (Rueda et al., 2011; Belvedere et al., 2012):

$$\mathcal{L} = \mathcal{L}_g + \mathcal{L}_f + \mathcal{L}_\sigma + \mathcal{L}_\omega + \mathcal{L}_\rho + \mathcal{L}_\gamma + \mathcal{L}_{\text{int}}, \quad (\text{C.5.2})$$

where<sup>1</sup>

$$\begin{aligned} \mathcal{L}_g &= -\frac{R}{16\pi}, \quad \mathcal{L}_f = \sum_{i=e,N} \bar{\psi}_i (i\gamma^\mu D_\mu - m_i) \psi_i, \\ \mathcal{L}_\sigma &= \frac{\nabla_\mu \sigma \nabla^\mu \sigma}{2} - U(\sigma), \quad \mathcal{L}_\omega = -\frac{\Omega_{\mu\nu} \Omega^{\mu\nu}}{4} + \frac{m_\omega^2 \omega_\mu \omega^\mu}{2}, \\ \mathcal{L}_\rho &= -\frac{\mathcal{R}_{\mu\nu} \mathcal{R}^{\mu\nu}}{4} + \frac{m_\rho^2 \rho_\mu \rho^\mu}{2}, \quad \mathcal{L}_\gamma = -\frac{F_{\mu\nu} F^{\mu\nu}}{16\pi}, \\ \mathcal{L}_{\text{int}} &= -g_\sigma \sigma \bar{\psi}_N \psi_N - g_\omega \omega_\mu J_\omega^\mu - g_\rho \rho_\mu J_\rho^\mu + e A_\mu J_{\gamma,e}^\mu \\ &\quad - e A_\mu J_{\gamma,N}^\mu, \end{aligned}$$

where the description of the strong interactions between the nucleons is made through the  $\sigma$ - $\omega$ - $\rho$  nuclear model in the version of Boguta & Bodmer Boguta

---

<sup>1</sup>We use spacetime metric signature  $(+, -, -, -)$  and geometric units  $G = c = 1$  unless otherwise specified.

and Bodmer (1977). Thus  $\Omega_{\mu\nu} \equiv \partial_\mu\omega_\nu - \partial_\nu\omega_\mu$ ,  $\mathcal{R}_{\mu\nu} \equiv \partial_\mu\rho_\nu - \partial_\nu\rho_\mu$ ,  $F_{\mu\nu} \equiv \partial_\mu A_\nu - \partial_\nu A_\mu$  are the field strength tensors for the  $\omega^\mu$ ,  $\rho$  and  $A^\mu$  fields respectively,  $\nabla_\mu$  stands for covariant derivative and  $R$  is the Ricci scalar. We adopt the Lorenz gauge for the fields  $A_\mu$ ,  $\omega_\mu$ , and  $\rho_\mu$ . The self-interaction scalar field potential is  $U(\sigma)$ ,  $\psi_N$  is the nucleon isospin doublet,  $\psi_e$  is the electronic singlet,  $m_i$  states for the mass of each particle-specie and  $D_\mu = \partial_\mu + \Gamma_\mu$ , being  $\Gamma_\mu$  the Dirac spin connections. The conserved currents are  $J_\omega^\mu = \bar{\psi}_N\gamma^\mu\psi_N$ ,  $J_\rho^\mu = \bar{\psi}_N\tau_3\gamma^\mu\psi_N$ ,  $J_{\gamma,e}^\mu = \bar{\psi}_e\gamma^\mu\psi_e$ , and  $J_{\gamma,N}^\mu = \bar{\psi}_N(1/2)(1 + \tau_3)\gamma^\mu\psi_N$ , being  $\tau_3$  the particle isospin.

The nuclear model is fixed once the values of the coupling constants and the masses of the three mesons are fixed: for instance in the NL3 parameter set Lalazissis et al. (1997) used in Belvedere et al. (2012) and in this work we have  $m_\sigma = 508.193$  MeV,  $m_\omega = 782.501$  MeV,  $m_\rho = 763.000$  MeV,  $g_\sigma = 10.2170$ ,  $g_\omega = 12.8680$ ,  $g_\rho = 4.4740$ , plus two constants that give the strength of the self-scalar interactions,  $g_2 = -10.4310$  fm $^{-1}$  and  $g_3 = -28.8850$ .

From the equations of motion of the above Lagrangian we obtain the EMTF equations (see Rueda et al. (2011); Belvedere et al. (2012), for details). The solution of the EMTF coupled differential equations leads to a new structure of the star, as shown in Fig C.24: a positively charged core at supranuclear densities,  $\rho > \rho_{\text{nuc}} \sim 2.7 \times 10^{14}$  g cm $^{-3}$ , surrounded by an electron distribution of thickness  $\gtrsim \hbar/(m_e c)$  and, at lower densities  $\rho < \rho_{\text{nuc}}$ , a neutral ordinary crust.

The thermodynamic equilibrium is ensured by the constancy of the particle Klein potentials Klein (1949) generalized to the presence of electrostatic and strong fields (Rotondo et al., 2011d; Rueda et al., 2011; Belvedere et al., 2012)

$$\frac{1}{u^t} [\mu_i + (q_i A_\alpha + g_\omega \omega_\alpha + g_\rho \tau_{3,i} \rho_\alpha) u^\alpha] = \text{constant}, \quad (\text{C.5.3})$$

where the subscript  $i$  stands for each kind of particle,  $\mu_i$  is the particle chemical potential, and  $q_i$  is the particle electric charge. In the static case only the time components of the vector fields,  $A_0$ ,  $\omega_0$ ,  $\rho_0$  are present. In the above equation  $u^t = (g_{tt})^{-1/2}$  is the time component of the fluid four-velocity which satisfies  $u_\alpha u^\alpha = 1$ ;  $g_{tt}$  is the t-t component of the spherically symmetric metric

$$ds^2 = e^\nu dt^2 - e^\lambda dr^2 - dr^2 - r^2(d\theta^2 + \sin^2\theta d\phi^2). \quad (\text{C.5.4})$$

The equilibrium conditions (C.5.3) lead to a discontinuity in the density at the core-crust transition and, correspondingly, an overcritical electric field  $\sim (m_\pi/m_e)^2 E_c$ , where  $E_c = m_\pi^2 c^3 / (e\hbar) \sim 1.3 \times 10^{16}$  Volt cm $^{-1}$ , appears in the core-crust boundary interface. The constancy of the Klein potentials is necessary to fulfill the requirement of thermodynamical equilibrium, together with the constancy of the gravitationally red-shifted temperature (Tolman condi-

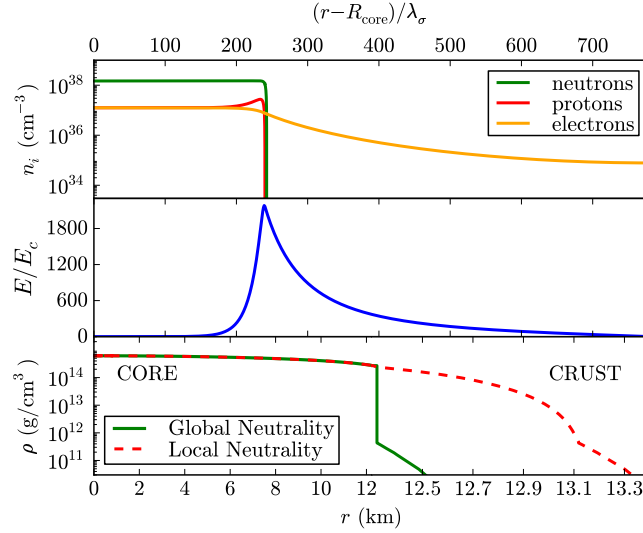


**Figure C.24.:** In the top and center panels we show the neutron, proton, electron densities and the electric field in units of the critical electric field  $E_c$  in the core-crust transition layer, whereas in the bottom panel we show a specific example of a density profile inside a neutron star. In this plot we have used for the globally neutral case a density at the edge of the crust equal to the neutron drip density,  $\rho_{\text{drip}} \sim 4.3 \times 10^{11} \text{ g cm}^{-3}$ .

tion) Tolman (1930); Klein (1949), if finite temperatures are considered (see e.g. Rueda et al. (2011)). In particular, the continuity of the electron Klein potential leads to a decreasing of the electron chemical potential  $\mu_e$  and density at the core-crust boundary interface. They reach values  $\mu_e^{\text{crust}} < \mu_e^{\text{core}}$  and  $\rho_{\text{crust}} < \rho_{\text{core}}$  at the edge of the crust, where global charge neutrality is achieved.

As we have shown in (Belvedere et al., 2012), the solution of this new set of equilibrium equations leads to neutron star crusts with smaller mass and thinner thickness, and consequently to a new mass-radius relation which markedly differs from the one given by the solution of the TOV equations in the case of local charge neutrality; see Fig. C.25.

We extend in this work the previous results to the case when the neutron star is rotating as a rigid body. To this aim we use the Hartle's approach (Hartle, 1967) which solves the Einstein equations accurately up to second order approximation in the angular velocity of the star,  $\Omega$  (see next section C.5.2 for details).

In this rotating case, the condition of the constancy of the particle Klein potential has the same form as Eq. (C.5.3), but the fluid inside the star now moves with a four-velocity of a rigid rotating body,  $u^\alpha = (u^t, 0, 0, u^\phi)$ , with

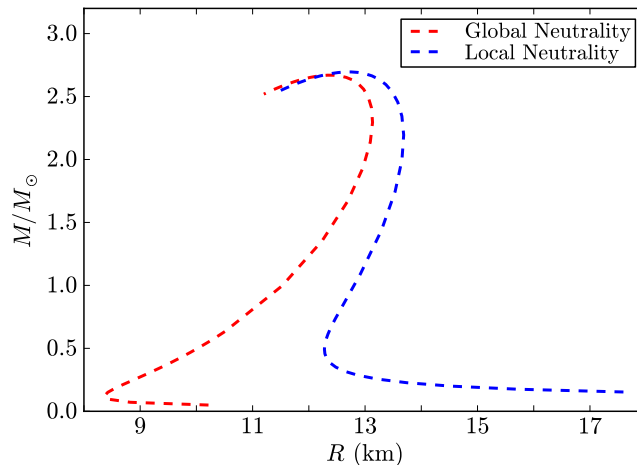


**Figure C.25.:** Neutron star mass-radius relation in the static (non-rotating) case for both global and local charge neutrality configurations (see Belvedere et al. (2012), for details). In this plot we have used for the globally neutral case a density at the edge of the crust equal to the neutron drip density,  $\rho_{\text{drip}} \sim 4.3 \times 10^{11} \text{ g cm}^{-3}$ .

(see Hartle and Sharp (1967) and C.5.10, for details)

$$u^t = (g_{tt} + 2\Omega g_{t\phi} + \Omega^2 g_{\phi\phi})^{-1/2}, \quad u^\phi = \Omega u^t, \quad (\text{C.5.5})$$

where  $\phi$  is the azimuthal angular coordinate with respect to which the metric is symmetric, namely the metric is independent of  $\phi$  (axial symmetry). The metric functions  $g_{\alpha\beta}$  are now given by Eq. (C.5.6) below. It is then clear that in a frame comoving with the rotating star,  $u^t = (g_{tt})^{-1/2}$ , and the Klein equilibrium condition becomes the same as Eq. (C.5.3), as expected.

We applied the Hartle's formalism to the seed static solution obtained from the integration of the EMTF equations (Belvedere et al., 2012). For the construction of the new mass-radius relation we take into account the Keplerian mass-shedding limit and the secular axisymmetric instability (see section C.5.3). We compute in section C.5.4 the mass  $M$ , polar  $R_p$  and equatorial  $R_{\text{eq}}$  radii, angular momentum  $J$ , eccentricity  $\epsilon$ , and quadrupole moment  $Q$ , as a function of the central density and the rotation angular velocity  $\Omega$  of the stable neutron star. Based on the criteria of equilibrium we calculate the maximum stable neutron star mass and from the gravitational binding energy of the configurations establish the minimum mass under which the neutron star becomes gravitationally unbound. We compare and contrast the results for both globally and locally neutral rotating neutron stars. Observational constraints on the mass-radius relation are discussed in section C.5.8. We finally summarize the results in section C.5.9.

### C.5.2. Hartle's slow rotation approximation

In his pioneering work, Hartle (1967) computed the equilibrium equations of slowly rotating stars in the context of General Relativity. The solutions of the Einstein equations are obtained through a perturbative method, expanding the metric functions up to the second order in the angular velocity  $\Omega$ . Under this assumption the structure of compact objects can be approximately described by the total mass  $M$ , angular momentum  $J$  and quadrupole moment  $Q$ . The slow rotation regime implies that the perturbations owing to the rotation are relatively small with respect to the known non-rotating geometry. The interior solution is derived by solving numerically a system of ordinary differential equations for the perturbation functions. The exterior solution for the vacuum surrounding the star, can be written analytically in terms of  $M$ ,  $J$ , and  $Q$  (see Hartle (1967); Hartle and Thorne (1968) for details). The numerical values for all the physical quantities are derived by matching the interior and the exterior solution on the border of the star.

The spacetime metric for the rotating configuration up to the second order of  $\Omega$  is given by (Hartle, 1967)

$$ds^2 = e^\nu (1 + 2h) dt^2 - e^\lambda \left[ 1 + \frac{2m}{r - 2M^{J=0}} \right] dr^2 - r^2 (1 + 2k) \left[ d\theta^2 + \sin^2 \theta (d\phi - \omega dt)^2 \right], \quad (\text{C.5.6})$$

where  $\nu = \nu(r)$ ,  $\lambda = \lambda(r)$ , and  $M^{J=0} = M^{J=0}(r)$  are the metric functions and mass profiles of the corresponding seed non-rotating star with the same central density as the rotating one; see Eq. (C.5.4). The functions  $h = h(r, \theta)$ ,  $m = m(r, \theta)$ ,  $k = k(r, \theta)$  and the fluid angular velocity in the local inertial frame,  $\omega = \omega(r)$ , have to be calculated from the Einstein equations. Expanding up to the second order the metric in spherical harmonics we have

$$h(r, \theta) = h_0(r) + h_2(r)P_2(\cos \theta), \quad (\text{C.5.7})$$

$$m(r, \theta) = m_0(r) + m_2(r)P_2(\cos \theta), \quad (\text{C.5.8})$$

$$k(r, \theta) = k_0(r) + k_2(r)P_2(\cos \theta), \quad (\text{C.5.9})$$

where  $P_2(\cos \theta)$  is the Legendre polynomial of second order. Because the metric does not change under transformations of the type  $r \rightarrow f(r)$ , we can assume  $k_0(r) = 0$ .

The functions  $h = h(r, \theta)$ ,  $m = m(r, \theta)$ ,  $k = k(r, \theta)$  have analytic form in the exterior(vacuum) spacetime and they can be found in C.5.10. From the matching condition between the interior and exterior metrics, the mass, angular momentum, and quadrupole moment can be computed.

First the angular momentum is computed. It is introduced the angular velocity of the fluid relative to the local inertial frame,  $\bar{\omega}(r) = \Omega - \omega(r)$ . It

can be shown from the Einstein equations at first order in  $\Omega$  that  $\bar{\omega}$  satisfies the differential equation

$$\frac{1}{r^4} \frac{d}{dr} \left( r^4 j \frac{d\bar{\omega}}{dr} \right) + \frac{4}{r} \frac{dj}{dr} \bar{\omega} = 0, \quad (\text{C.5.10})$$

where  $j(r) = e^{-(\nu+\lambda)/2}$  with  $\nu$  and  $\lambda$  the metric functions of the seed non-rotating solution (C.5.4).

From the matching equations, the angular momentum of the star results to be given by

$$J = \frac{1}{6} R^4 \left( \frac{d\bar{\omega}}{dr} \right)_{r=R}, \quad (\text{C.5.11})$$

so the angular velocity  $\Omega$  is related to the angular momentum as

$$\Omega = \bar{\omega}(R) + \frac{2J}{R^3}. \quad (\text{C.5.12})$$

The total mass of the rotating star,  $M$ , is given by

$$M = M_{J=0} + \delta M, \quad \delta M = m_0(R) + J^2/R^3, \quad (\text{C.5.13})$$

where  $\delta M$  is the contribution to the mass owing to rotation. The first order perturbation function  $m_0$  is computed from the solution of the differential equation

$$\frac{dm_0}{dr} = 4\pi r^2 \frac{d\mathcal{E}}{dP} (\mathcal{E} + P) p_0^* + \frac{1}{12} j^2 r^4 \left( \frac{d\bar{\omega}}{dr} \right)^2 - \frac{1}{3} \frac{dj^2}{dr} r^3 \bar{\omega}^2, \quad (\text{C.5.14})$$

$$\begin{aligned} \frac{dp_0^*}{dr} = & -\frac{m_0(1 + 8\pi r^2 P)}{(r - 2M)^2} - \frac{4\pi r^2 (\mathcal{E} + P)}{(r - 2M)} p_0^* + \frac{1}{12} \frac{j^2 r^4}{(r - 2M)} \left( \frac{d\bar{\omega}}{dr} \right)^2 \\ & + \frac{1}{3} \frac{d}{dr} \left( \frac{r^3 j^2 \bar{\omega}^2}{r - 2M} \right). \end{aligned} \quad (\text{C.5.15})$$

where  $\mathcal{E}$  and  $P$  are the total energy-density and pressure.

Turning to the quadrupole moment of the neutron star, it is given by

$$Q = \frac{J^2}{M} + \frac{8}{5} \mathcal{K} M^3, \quad (\text{C.5.16})$$

where  $\mathcal{K}$  is a constant of integration. This constant is fixed from the matching

of the second order function  $h_2$  obtained in the interior from

$$\frac{dk_2}{dr} = -\frac{dh_2}{dr} - h_2 \frac{dv}{dr} + \left( \frac{1}{r} + \frac{1}{2} \frac{dv}{dr} \right) \left[ -\frac{1}{3} r^3 \bar{\omega}^2 \frac{dj^2}{dr} \right. \quad (\text{C.5.17})$$

$$\left. + \frac{1}{6} r^4 j^2 \left( \frac{d\bar{\omega}}{dr} \right)^2 \right], \quad (\text{C.5.18})$$

$$\begin{aligned} \frac{dh_2}{dr} = h_2 \left\{ -\frac{dv}{dr} + \frac{r}{r-2M} \left( \frac{dv}{dr} \right)^{-1} \left[ 8\pi(\mathcal{E} + P) \right. \right. \\ \left. \left. - \frac{4M}{r^3} \right] \right\} - \frac{4(k_2 + h_2)}{r(r-2M)} \left( \frac{dv}{dr} \right)^{-1} \\ + \frac{1}{6} \left[ \frac{r}{2} \frac{dv}{dr} - \frac{1}{r-2M} \left( \frac{dv}{dr} \right)^{-1} \right] r^3 j^2 \left( \frac{d\bar{\omega}}{dr} \right)^2 \\ - \frac{1}{3} \left[ \frac{r}{2} \frac{dv}{dr} + \frac{1}{r-2M} \left( \frac{dv}{dr} \right)^{-1} \right] r^2 \bar{\omega}^2 \frac{dj^2}{dr}, \quad (\text{C.5.19}) \end{aligned}$$

with its exterior counterpart (see Hartle (1967) and C.5.10).

It is worth to underline that the influence of the induced magnetic field owing to the rotation of the charged core of the neutron star in the globally neutral case is negligible (Boshkayev et al., 2012b). In fact, for a rotating neutron star of period  $P = 10$  ms and radius  $R \sim 10$  km, the radial component of the magnetic field  $B_r$  in the core interior has its maximum at the poles with a value  $B_r \sim 2.9 \times 10^{-16} B_c$ , where  $B_c = m_e^2 c^3 / (e \hbar) \approx 4.4 \times 10^{13}$  G is the critical magnetic field for vacuum polarization. The angular component of the magnetic field  $B_\theta$ , instead, has its maximum value at the equator and, as for the radial component, it is very low in the interior of the neutron star core, i.e.  $|B_\theta| \sim 2.9 \times 10^{-16} B_c$ . In the case of a sharp core-crust transition as the one studied in (Belvedere et al., 2012) and shown in Fig. C.24, this component will grow in the transition layer to values of the order of  $|B_\theta| \sim 10^2 B_c$  (see Boshkayev et al. (2012b), for further details). However, since we are here interested in the macroscopic properties of the neutron star, we can ignore at first approximation the presence of the electromagnetic magnetic field in the macroscopic regions where they are indeed very small, and safely apply the original Hartle's formulation without any generalization to the electromagnetic case.

### C.5.3. Stability of uniformly rotating neutron stars

#### Secular axisymmetric instability

In a sequence of increasing central density in the  $M$ - $\rho_c$  curve,  $\rho_c \equiv \rho(0)$ , the maximum mass of a non-rotating neutron star is defined as the first maximum of such a curve, namely the point where  $\partial M / \partial \rho_c = 0$ . This derivative

defines the secular instability point, and, if the perturbation obeys the same EOS as the equilibrium configuration, it coincides also with the dynamical instability point (see e.g. Shapiro and Teukolsky (1983a)). In the rotating case, the situation becomes more complicated and in order to find the axisymmetric dynamical instability points, the perturbed solutions with zero frequency modes (the so-called neutral frequency line) have to be calculated. However Friedman et al. (1988), following the works of Sorkin (1981, 1982), described a turning-point method to obtain the points at which secular instability is reached by uniformly rotating stars. In a constant angular momentum sequence, the turning point is located in the maximum of the mass-central density relation, namely the onset of secular axisymmetric instability is given by

$$\left[ \frac{\partial M(\rho_c, J)}{\partial \rho_c} \right]_{J=\text{constant}} = 0, \quad (\text{C.5.20})$$

and once the secular instability sets in, the star evolves quasi-stationarily until it reaches a point of dynamical instability where gravitational collapse sets in (Stergioulas, 2003).

The above equation defines an upper limit for the mass at a given  $J$  for a uniformly rotating star, however this criterion is a sufficient but not necessary condition for the instability. This means that all the configurations with the given angular momentum  $J$  on the right side of the turning point defined by Eq. (C.5.20) are secularly unstable, but it does not imply that the configurations on the left side of it are stable. An example of dynamically unstable configurations on the left side of the turning-point limiting boundary in neutron stars was recently shown in (Takami et al., 2011), for a specific EOS.

### Keplerian mass-shedding instability

The maximum velocity for a particle to remain in equilibrium on the equator of a star, kept bound by the balance between gravitational and centrifugal force, is the Keplerian velocity of a free particle computed at the same location. As shown, for instance in (Stergioulas, 2003), a star rotating at Keplerian rate becomes unstable due to the loss of mass from its surface. The mass shedding limiting angular velocity of a rotating star is the Keplerian angular velocity evaluated at the equator,  $r = R_{\text{eq}}$ , i.e.  $\Omega_K^{J \neq 0} = \Omega_K(r = R_{\text{eq}})$ . Friedman et al. (1986b) introduced a method to obtain the maximum possible angular velocity of the star before reaching the mass-shedding limit; however Torok et al. (2008) and Bini et al. (2013), demonstrated a simpler way to compute the Keplerian angular velocity of a rotating star. They showed that the mass-shedding angular velocity,  $\Omega_K^{J \neq 0}$ , can be computed as the orbital angular velocity of a test particle in the external field of the star and corotating with it on its equatorial plane at the distance  $r = R_{\text{eq}}$ . For the Hartle external

solution, this is given by

$$\Omega_K^{J \neq 0}(r) = \sqrt{\frac{M}{r^3}} \left[ 1 - jF_1(r) + j^2F_2(r) + qF_3(r) \right], \quad (\text{C.5.21})$$

where  $j = J/M^2$  and  $q = Q/M^3$  are the dimensionless angular momentum and quadrupole moment. Further details and the analytical expression of the functions  $F_i$  can be found in C.5.10.

### Gravitational binding energy

Besides the above stability requirements, one should check that the neutron star is gravitationally bound. In the non-rotating case, the binding energy of the star can be computed as

$$W_{J=0} = M_{J=0} - M_{\text{rest}}^{J=0}, \quad M_{\text{rest}}^{J=0} = m_b A_{J=0}, \quad (\text{C.5.22})$$

where  $M_{\text{rest}}^{J=0}$  is the rest-mass of the star,  $m_b$  is the rest-mass per baryon, and  $A_{J=0}$  is the total number of baryons inside the star. So the non-rotating star is considered bound if  $W_{J=0} < 0$ .

In the slow rotation approximation the total binding energy is given by (see Eqs. (114–115) of Hartle (1967))

$$W_{J \neq 0} = W_{J=0} + \delta W, \quad \delta W = \frac{J^2}{R^3} - \int_0^R 4\pi r^2 B(r) dr, \quad (\text{C.5.23})$$

where

$$\begin{aligned} B(r) = & (\mathcal{E} + P)p_0^* \left\{ \frac{d\mathcal{E}}{dP} \left[ \left(1 - \frac{2M}{r}\right)^{-1/2} - 1 \right] \right. \\ & \left. - \frac{du}{dP} \left(1 - \frac{2M}{r}\right)^{-1/2} \right\} + (\mathcal{E} - u) \left(1 - \frac{2M}{r}\right)^{-3/2} \left[ \frac{m_0}{r} \right. \\ & \left. + \frac{1}{3} j^2 r^2 \bar{\omega}^2 \right] - \frac{1}{4\pi r^2} \left[ \frac{1}{12} j^2 r^4 \left( \frac{d\bar{\omega}}{dr} \right)^2 - \frac{1}{3} \frac{dj^2}{dr} r^3 \bar{\omega}^2 \right], \end{aligned} \quad (\text{C.5.24})$$

where  $u = \mathcal{E} - m_b n_b$  is the internal energy of the star, with  $n_b$  the baryon number density.

We will therefore request that the binding energy be negative, namely  $W_{J \neq 0} < 0$ . As we will show below in Sec. C.5.5 this condition leads to a minimum mass for the neutron star under which the star becomes gravitationally unbound.

### C.5.4. Structure of uniformly rotating neutron stars

In this section we show the results of the integration of the Hartle equations for the globally and locally charge neutrality neutron stars constructed in (Belvedere et al., 2012); see e.g. Fig. C.24. Following Belvedere et al. (2012), we adopt, as an example, globally neutral neutron stars with a density at the edge of the crust equal to the neutron drip density, namely  $\rho_{\text{crust}} = \rho_{\text{drip}} \approx 4.3 \times 10^{11} \text{ g cm}^{-3}$ .

#### Secular instability boundary

In Fig. C.26 we show the mass-central density curve for globally neutral neutron stars in the region close to the axisymmetric stability boundaries. Specifically we show some  $J$ -constant sequences to show that indeed along each of these curves there exist a maximum mass point (turning point). The line joining all the turning points defines the secular instability limit. In Fig. C.26 the axisymmetric stable zone is on the left side of the instability line.

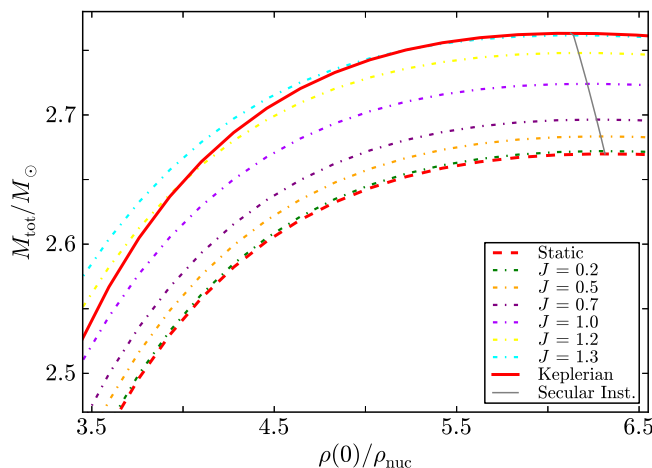


**Figure C.26.:** Total mass versus central density of globally neutral neutron stars. The continuous line represents the configuration with Keplerian angular velocity, the dashed line represents the static configuration, the dotted-dashed lines represent the  $J$ -constant sequences (in units of  $10^{11} \text{ cm}^2$ ). The gray line joins all the turning points of the  $J$ -constant sequences, so it defines the secular instability boundary.

Clearly we can transform the mass-central density relation in a mass-radius relation. In Fig. C.27 we show the mass versus the equatorial radius of the neutron star that correspond to the range of densities of Fig. C.26. In this plot the stable zone is on the right side of the instability line.

We can construct a fitting curve joining the turning points of the  $J$ -constant sequences line which determines the secular axisymmetric instability bound-

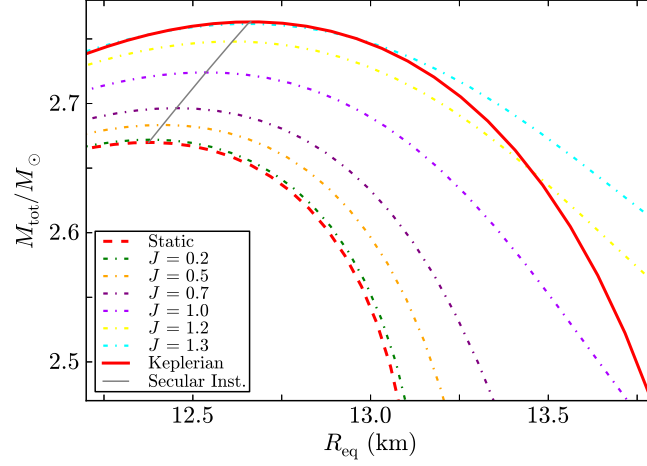


**Figure C.27.:** Total mass versus equatorial radius of globally neutral neutron stars. The continuous line represents the configuration with Keplerian angular velocity, the dashed line represents the static configuration, the dotted-dashed lines represent the  $J$ -constant sequences (in units of  $10^{11} \text{ cm}^2$ ). The gray curve joins all the turning points of the  $J$ -constant sequences, so it defines the secular instability boundary.

ary. Defining  $m_{\text{max},0} \equiv M_{\text{max}}^{J=0}/M_{\odot}$  as the maximum stable mass (in solar mass units) of the non-rotating neutron star constructed with the same EOS and  $R_{\text{eq},10}$  as the equatorial radius in units of 10 km, we find that for globally neutral configurations the instability line can be fitted by the function

$$\left[ \frac{M(R_{\text{eq}})}{M_{\odot}} \right]_{\text{GCN}} = 21.22 - 6.68 m_{\text{max},0}^{\text{GCN}} - \frac{9.29 - 3.36 m_{\text{max},0}^{\text{GCN}}}{0.12 R_{\text{eq},10}^{6.08}}, \quad (\text{C.5.25})$$

in the appropriate range of radii,  $1.24 \lesssim R_{\text{eq},10} \lesssim 1.27$ , and  $m_{\text{max},0}^{\text{GCN}} \approx 2.67$ .

The turning points of locally neutral configurations in the mass-central density plane are shown in Fig. C.28. the corresponding mass-equatorial radius plane is plotted in Fig. C.29.

As for globally neutral neutron stars, the secular instability line can be fitted with some function that in this case reads

$$\left[ \frac{M(R_{\text{eq}})}{M_{\odot}} \right]_{\text{LCN}} = 20.51 - 6.35 m_{\text{max},0}^{\text{LCN}} - \frac{4.13 - 1.48 m_{\text{max},0}^{\text{LCN}}}{0.051 R_{\text{eq},10}^{5.71}}, \quad (\text{C.5.26})$$

where now  $1.27 \lesssim R_{\text{eq},10} \lesssim 1.30$ , and  $m_{\text{max},0}^{\text{LCN}} \approx 2.70$ .

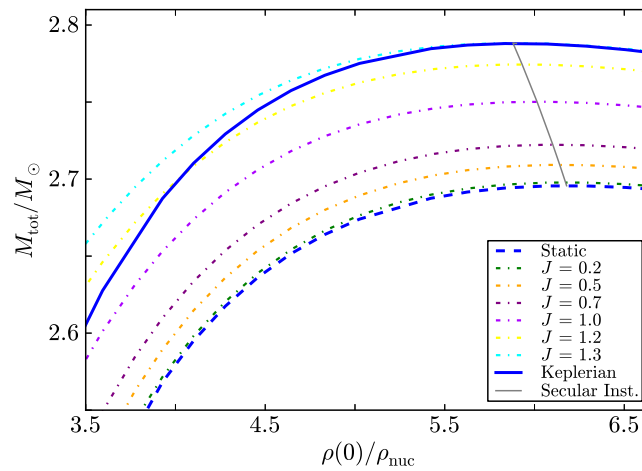


**Figure C.28.:** Total mass versus central density of locally neutral neutron stars. The continuous line represents the configuration with Keplerian angular velocity, the dashed line represents the static configuration, the dotted-dashed lines represent the  $J$ -constant sequences (in units of  $10^{11} \text{ cm}^2$ ). The gray line joins all the turning points of the  $J$ -constant sequences, so it defines the secular instability boundary.

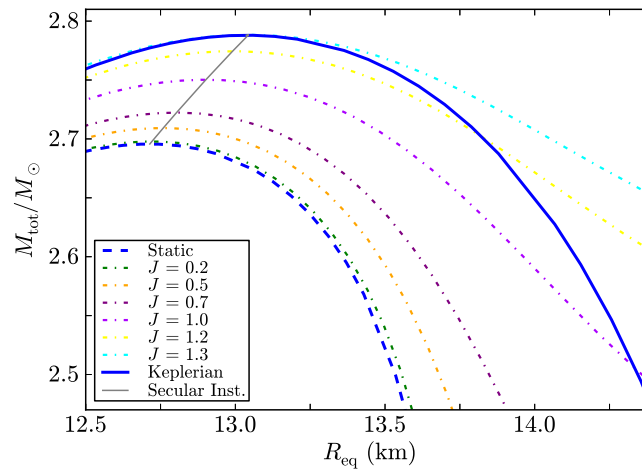


**Figure C.29.:** Total mass versus equatorial radius of locally neutral neutron stars. The continuous line represents the configuration with Keplerian angular velocity, the dashed line represents the static configuration, the dotted-dashed lines represent the  $J$ -constant sequences (in units of  $10^{11} \text{ cm}^2$ ). The gray curve joins all the turning points of the  $J$ -constant sequences, so it defines the secular instability boundary.

### Keplerian mass-shedding sequence

We turn now to analyze in detail the behavior of the different properties of the neutron star along the Keplerian mass-shedding sequence. For the sake of reference we have indicated in the following plots stars with the selected masses  $M \approx [1, 1.4, 2.04, 2.5] M_{\odot}$ . The cyan star indicates the fastest observed pulsar, PSR J1748–2446ad Hessels et al. (2006a), with a rotation frequency of  $f \approx 716$  Hz. The gray filled circles indicate the last stable configuration of the Keplerian sequence, namely the point where the Keplerian and the secular stability boundaries cross each other.

**Maximum mass and rotation frequency** The total mass of the rotating star is computed from Eq. (C.5.13). In Fig. C.30 is shown the total mass of the neutron star as a function of the rotation frequency for the Keplerian sequence. It is clear that for a given mass, the rotational frequency is higher for a globally neutral neutron star with respect to the locally neutral one.

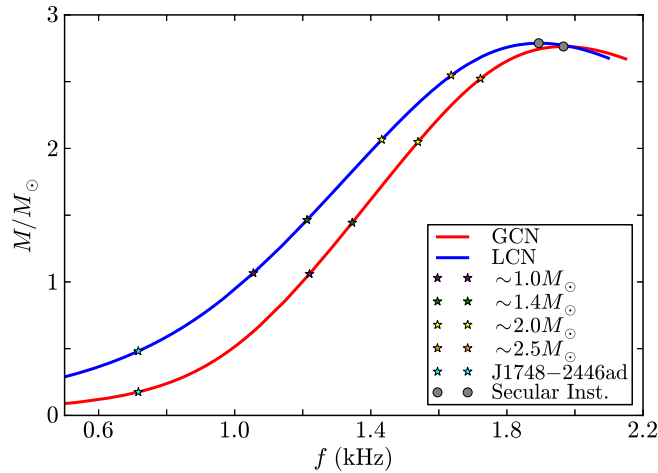


**Figure C.30.:** Total mass versus rotational Keplerian frequency both for the global (red) and local (blue) charge neutrality cases.

The maximum neutron star mass is obtained at the crossing point between the secular instability and the Keplerian limit. For the global charge neutrality case we obtain  $M^{J \neq 0} \approx 2.76 M_{\odot}$  with a corresponding equatorial radius  $R_{\text{eq}} \approx 12.66$  km. This implies an increase in mass and radius of 3.37% and 2.26% respectively with respect to the non-rotating maximum mass configuration,  $M_{\text{max}}^{J=0} \approx 2.67 M_{\odot}$  and  $R \approx 12.38$  km, obtained in (Belvedere et al., 2012). For the local charge neutrality configurations, the maximum mass of rotating neutron stars is  $M^{J \neq 0} \approx 2.79 M_{\odot}$  and the corresponding  $R_{\text{eq}} \approx 13.04$  km. Thus, for this case the increase with respect the maximum mass of non-rotating neutron stars is 3.33% and 2.6% in radius; we recall that for

this nuclear EOS the critical mass and corresponding radius of locally neutral neutron stars are  $M_{\max}^{J=0} \approx 2.7 M_{\odot}$  and  $R \approx 12.71$  km.

These maximum mass configurations have at the same time the maximum possible rotation rates. In the global charge neutrality we obtain  $f_{\max}^{\text{GCN}} \approx 1.97$  kHz or equivalently a minimum rotation period  $P_{\min}^{\text{GCN}} \approx 0.51$  ms. For locally neutral neutron stars we obtain  $f_{\max}^{\text{LCN}} \approx 1.89$  kHz, or  $P_{\min}^{\text{GCN}} \approx 0.53$  ms.

**Minimum mass and rotation frequency** We compute now the gravitational binding energy of the neutron star from Eq. (C.5.23) as a function of the central density and angular velocity. We make this for central densities higher than the nuclear density, thus we impose the neutron star to have a supranuclear hadronic core. In Fig. C.31 we plot the binding energy  $W$  of the neutron star as a function of the neutron star mass along the Keplerian sequence. For the sake of comparison we show also the binding energy of the non-rotating configurations.

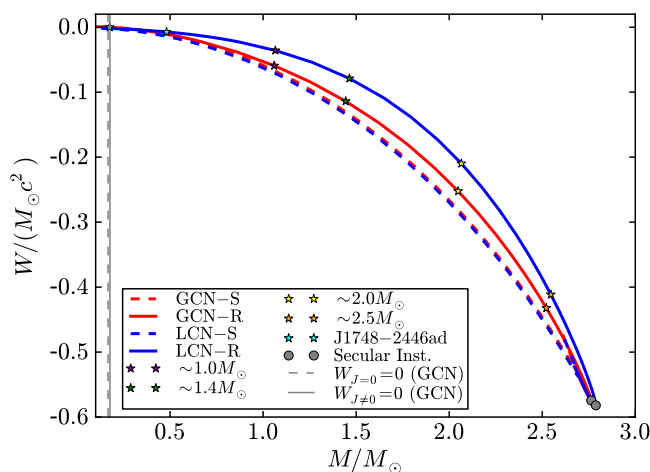


**Figure C.31.:** Neutron star binding energy versus total mass along the the Keplerian sequence both for the global (red) and local (blue) charge neutrality.

We found that the globally neutral neutron stars studied here are bound up to some minimum mass at which the gravitational binding energy vanishes. For the static and Keplerian configurations we find that  $W_{J=0} = 0$ , and  $W_{J \neq 0} = 0$  respectively at

$$M_{\min}^{J=0} \approx 0.17 M_{\odot}, \quad M_{\min}^{J \neq 0} \approx 0.18 M_{\odot}, \quad (\text{C.5.27})$$

while in the local charge neutrality case all the configurations are bound for the present EOS (see Fig. C.31).

The corresponding plot of  $W$  as a function of the central density is shown in Fig. C.32.

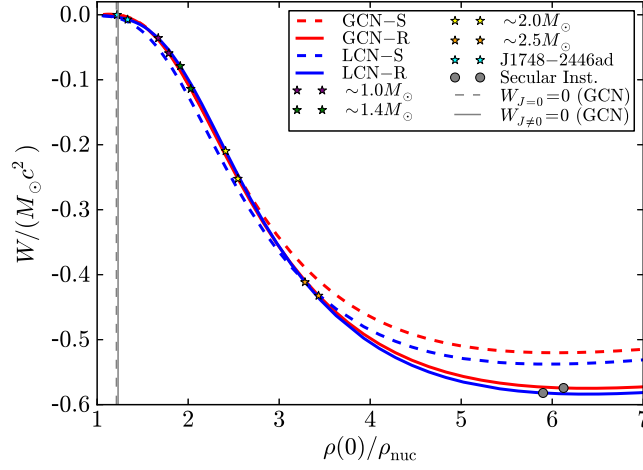


**Figure C.32.:** Neutron star binding energy versus central density along the Keplerian sequence both for the global (red) and local (blue) charge neutrality.

Interestingly, the rotation frequency of the configuration with the minimum mass,  $M_{\min}^{J \neq 0} \approx 0.18 M_{\odot}$ , has a rotation frequency

$$f_{\min} = f(M_{\min}^{J \neq 0}) \approx 0.72 \text{ kHz} , \quad (\text{C.5.28})$$

that is the minimum rotation rate that globally neutral configurations can have along the Keplerian sequence in order to be gravitationally bound. The above value is slightly higher than the frequency of the fastest observed pulsar, PSR J1748–2446ad, which has a frequency of 716 Hz Hessels et al. (2006a). This implies that PSR J1748–2446ad cannot be rotating at the Keplerian rate. Details can be seen in Fig. C.33 where we show the dependence of  $W$  on the rotation frequency.

### C.5.5. Neutron star mass-radius relation

We summarize now the above results in form of a new mass-radius relation of uniformly rotating neutron stars, including the Keplerian and secular instability boundary limits. In Fig. C.34 we show a summary plot of the equilibrium configurations of rotating neutron stars. In particular we show the total mass versus the equatorial radius: the dashed lines represent the static (non-rotating,  $J = 0$ ) sequences, while the solid lines represent the corresponding Keplerian mass-shedding sequences. The secular instability boundaries are plotted in pink-red and light blue color for the global and local charge neutrality cases, respectively.

It can be seen that due to the deformation for a given mass the radius of the rotating case is larger than the static one, and similarly the mass of the

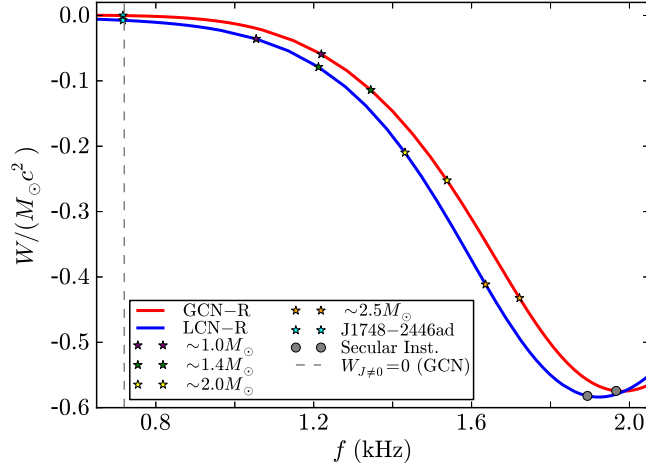


**Figure C.33.:** Neutron star binding energy versus frequency for the Keplerian sequence both for the global (red) and local (blue) charge neutrality neutron stars.

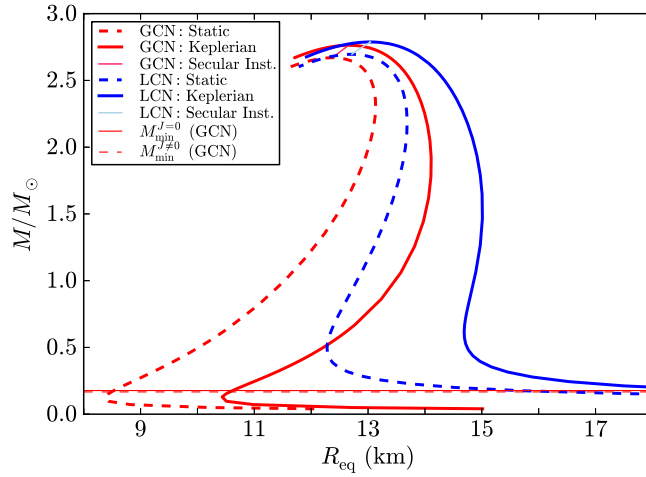


**Figure C.34.:** Total mass versus total equatorial radius for the global (red) and local (blue) charge neutrality cases. The dashed curves represent the static configurations, while the solid lines are the uniformly rotating neutron stars. The pink-red and light-blue color lines define the secular instability boundary for the globally and locally neutral cases, namely the lines given by Eqs. (C.5.25) and (C.5.25), respectively.

rotating star is larger than the corresponding static one. It can be also seen that the configurations obeying global charge neutrality are more compact with respect to the ones satisfying local charge neutrality.

### C.5.6. Deformation of the neutron star

In this section we explore the deformation properties of the neutron star. The behavior of the eccentricity, the rotational to gravitational energy ratio, as well as the quadrupole moment, are investigated as a function of the mass, density, and rotation frequency of the neutron star.

#### Eccentricity

A measurement of the level of deformation of the neutron star can be estimated with the eccentricity

$$\epsilon = \sqrt{1 - \left(\frac{R_p}{R_{\text{eq}}}\right)^2}, \quad (\text{C.5.29})$$

where  $R_p$  and  $R_{\text{eq}}$  are the polar and equatorial radii of the configuration. Thus,  $\epsilon = 0$  defines the spherical limit and  $0 < \epsilon < 1$  correspond to oblate configurations.

In Fig. C.35, we show the behavior of the total eccentricity (C.5.29), as a function of the neutron star frequency.

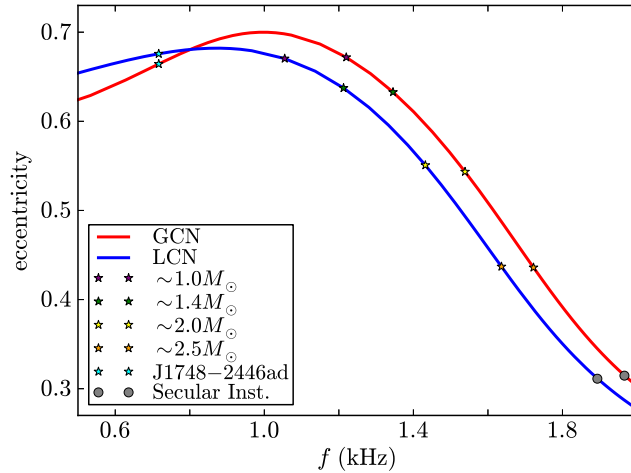


**Figure C.35.:** Eccentricity (C.5.29) versus frequency for the Keplerian sequence both for the global (red) and local (blue) charge neutrality cases.

We can see that in general the globally neutral neutron star has an eccentricity larger than the one of the locally neutral configuration for almost the entire range of frequencies and the corresponding central densities, except for the low frequencies  $f \lesssim 0.8$  kHz and central densities  $\rho(0) \lesssim 1.3\rho_{\text{nuc}}$ ; see also Fig. C.36. Starting from low values of the frequency  $f$  and central density  $\rho(0)$ , the neutron stars increase their oblateness, and after reaching the maximum value of the eccentricity, the compactness increases and the configurations tend to a more spherical shape.

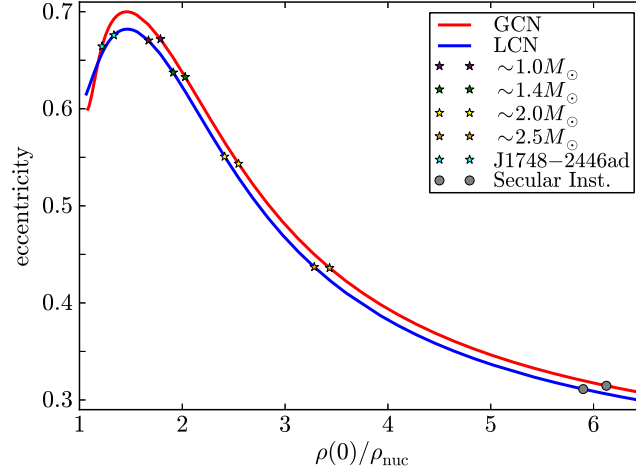


**Figure C.36.:** Eccentricity (C.5.29) versus central density for the Keplerian sequence both for the global (red) and local (blue) charge neutrality cases.

### Rotational to gravitational energy ratio

Other property of the star related to the centrifugal deformation of the star is the ratio between the gravitational energy and the rotational energy of the star. The former is given by Eq. (C.5.23) where as the latter is

$$T = \frac{1}{2} I \Omega^2, \quad (\text{C.5.30})$$

where  $I$  is the neutron star moment of inertia, which can be computed from the relation

$$I = \frac{J}{\Omega}, \quad (\text{C.5.31})$$

with  $J$  the angular momentum given by Eq. (C.5.11) and the angular velocity by Eq. (C.5.12). Since  $J$  is a first-order quantity and so proportional to  $\Omega$ , the moment of inertia given by Eq. (C.5.31) does not depend on the angular velocity. This implies that  $I$  corresponds to the moment of inertia of the non-rotating unperturbed seed object. Thus, in order to account for both frame dragging and quadrupole deformation effects, the perturbation has to be extended to  $\mathcal{O}(\Omega^3)$ .

In Figs. C.37 and C.38 we show the behavior of the total momentum of inertia, i.e.  $I = I_{\text{core}} + I_{\text{crust}}$ , with respect to the total mass and central density for both globally and locally neutral non-rotating neutron stars.

We can see from Figs. C.37 and C.38 that the total moment of inertia is quite similar for both global and local charge neutrality cases. This is due to the fact that the globally neutral configurations differ from the locally ones mostly in the structure of the crust, which however contributes much less than the neutron star core to the total moment of inertia (see below in section

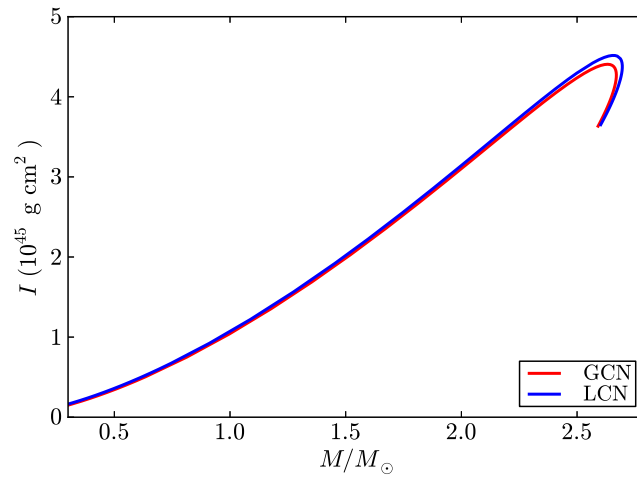


**Figure C.37.:** Total moment of inertia versus total mass both for globally (red) and locally (blue) neutral non-rotating neutron stars.

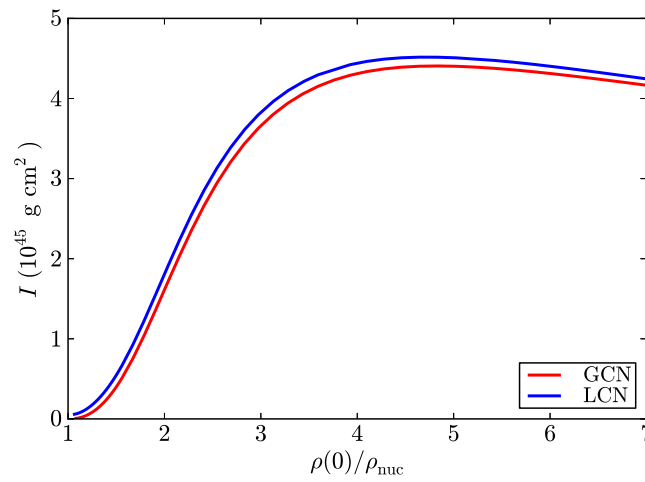


**Figure C.38.:** Total moment of inertia versus central density for globally (red) and locally (blue) neutral non-rotating neutron stars.

C.5.7).

We show in Fig. C.39 the ratio  $T/|W|$  as a function of the mass of the neutron stars along the Keplerian sequence. In Fig. C.39 instead we plot the dependence of the ratio on the central density and in Fig. C.41 on the Keplerian frequency.

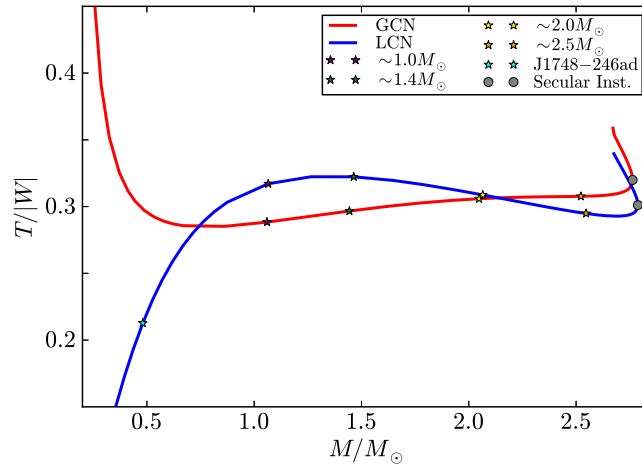


**Figure C.39.:** Rotational to gravitational binding energy ratio versus total mass along the the Keplerian sequence both for the global (red) and local (blue) charge neutrality.

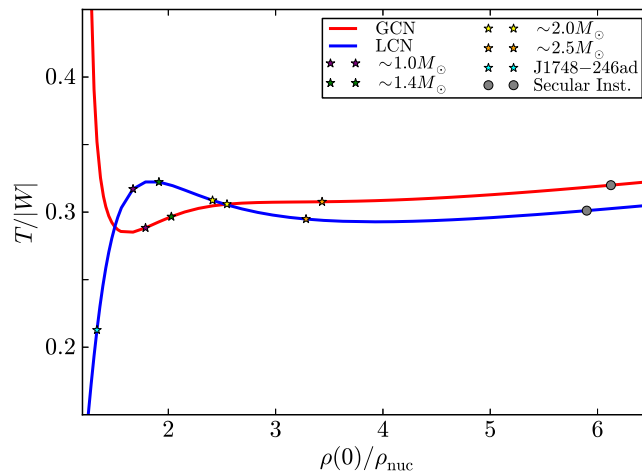


**Figure C.40.:** Rotational to gravitational binding energy ratio versus central density along the the Keplerian sequence both for the global (red) and local (blue) charge neutrality.

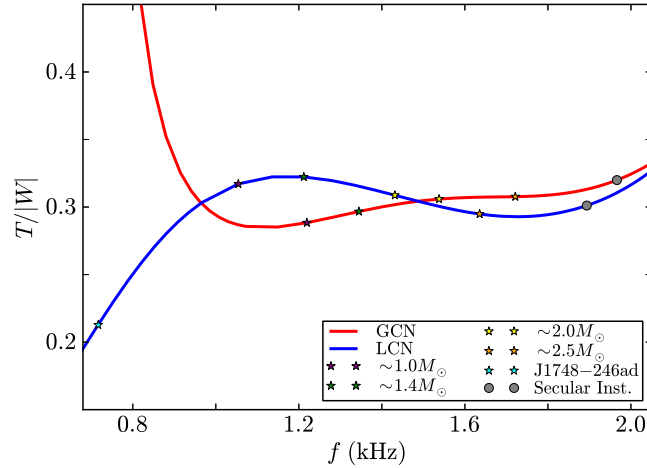


**Figure C.41.:** Rotational to gravitational binding energy ratio versus frequency along the Keplerian sequence both for the global (red) and local (blue) charge neutrality cases.

### Quadrupole moment

In Figs. C.42 and C.43 we show the quadrupole moment,  $Q$  given by Eq. (C.5.16), as a function of the total mass and central density for both globally and locally neutral neutron stars along the Keplerian sequence. The dependence of  $Q$  on the rotation frequency is shown in Fig. C.44. We have normalized the quadrupole moment  $Q$  to the quantity  $MR^2$  of the non-rotating configuration with the same central density.

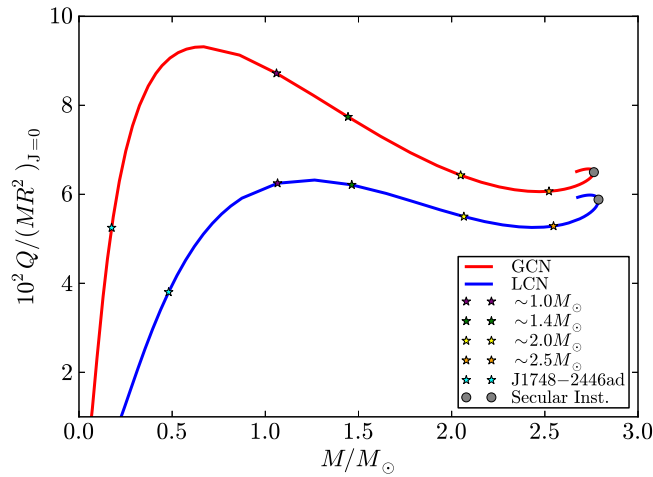


**Figure C.42.:** Total quadrupole moment versus total mass along the Keplerian sequence both for the global (red) and local (blue) charge neutrality cases. The quadrupole moment  $Q$  is here in units of the quantity  $MR^2$  of the non-rotating configuration with the same central density.

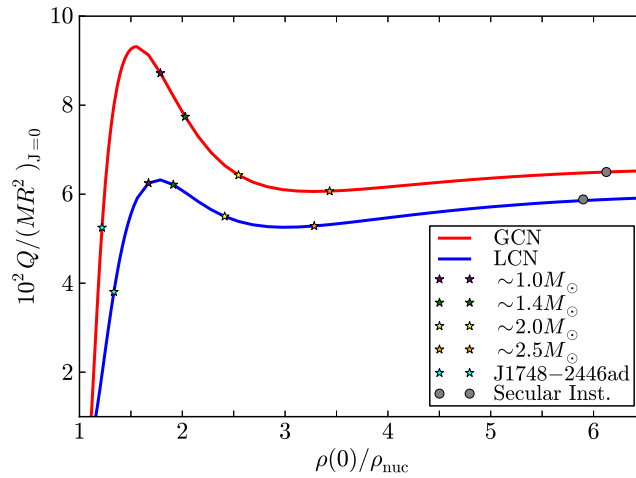


**Figure C.43.:** Total quadrupole moment versus central density along the Keplerian sequence both for the global (red) and local (blue) charge neutrality cases. The quadrupole moment  $Q$  is here in units of the quantity  $MR^2$  of the non-rotating configuration with the same central density.

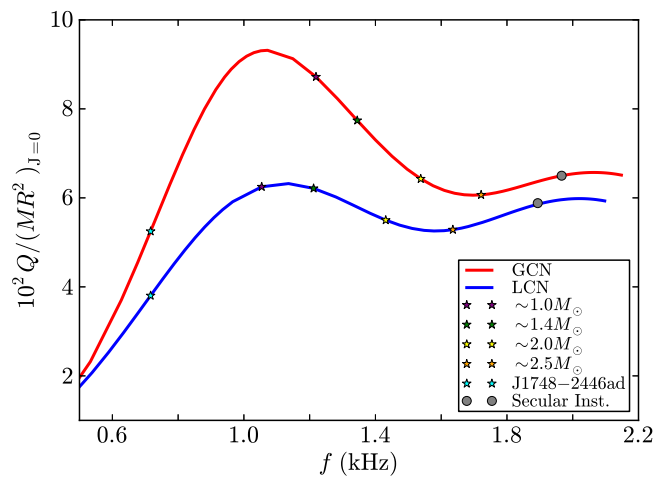


**Figure C.44.:** Total quadrupole moment versus frequency along the Keplerian sequence both for the global (red) and local (blue) charge neutrality cases. The quadrupole moment  $Q$  is here in units of the quantity  $MR^2$  of the non-rotating configuration with the same central density.

### C.5.7. Core and crust moment of inertia

In order to study the single contribution of the core and the crust to the moment of inertia of the neutron star, we shall use the integral expression for the moment of inertia. Multiplying Eq. (C.5.10) by  $r^3$  and making the integral of it we obtain<sup>2</sup>

$$I(r) = -\frac{2}{3} \int_0^r r^3 \frac{dj}{dr} \frac{\bar{\omega}(r)}{\Omega} dr = \frac{8\pi}{3} \int_0^r r^4 (\varepsilon + P) e^{(\lambda-\nu)/2} \frac{\bar{\omega}(r)}{\Omega} dr, \quad (\text{C.5.32})$$

where the integration is carried out in the region of interest. Thus, the contribution of the core,  $I_{\text{core}}$ , is obtained integrating from the origin up to the radius of the core, and the contribution of the crust,  $I_{\text{crust}}$ , integrating from the core to the total radius of the neutron star.

We show in Figs. C.45 and C.46 the ratio between the moment of inertia of the crust and the one of the core as a function of the total mass and central density, respectively, for both the globally and locally neutral configurations.

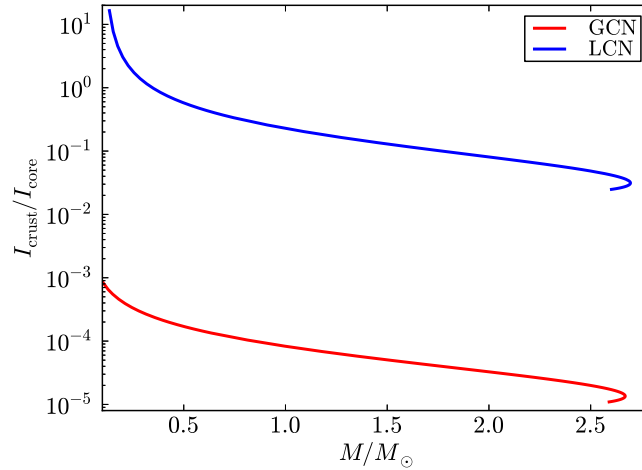


**Figure C.45.:** Crust to core moment of inertia ratio versus the total mass of both globally and locally neutral non-rotating neutron stars.

### C.5.8. Observational constraints

In Fig. C.47 we show the above mass-radius relations together with the most recent and stringent constraints indicated by Trümper (2011):

1. *The largest mass.* Until 2013 it was given by the mass of the 3.15 millisecond pulsar PSR J1614-2230  $M = 1.97 \pm 0.04 M_{\odot}$  Demorest et al. (2010a), however the recent reported mass  $2.01 \pm 0.04 M_{\odot}$  for the neutron star in

<sup>2</sup>It is clear that this expression approaches, in the weak field limit, the classic Newtonian expression  $I_{\text{Newtonian}} = (8\pi/3) \int r^4 \rho dr$  where  $\rho$  is the mass-density (Hartle, 1967).

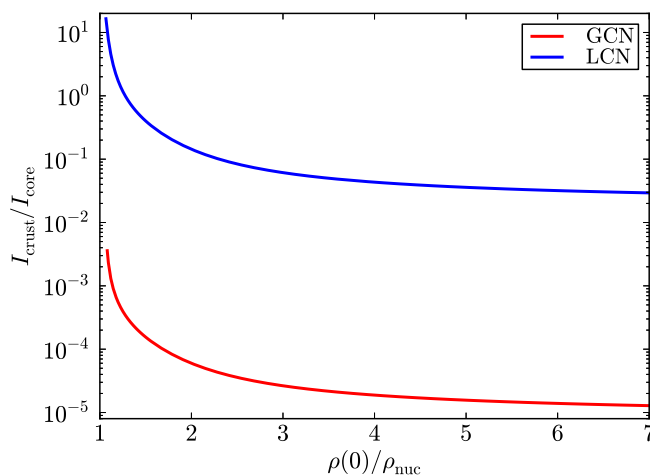


**Figure C.46.:** Crust to core moment of inertia ratio versus the central density both globally and locally neutral non-rotating neutron stars.

the relativistic binary PSR J0348+0432 (Antoniadis et al., 2013b) puts an even more stringent request to the nuclear EOS. Thus, the maximum mass of the neutron star has to be larger than the mass of PSR J0348+0432, this constraint is represented by the orange-color stars in Fig. C.47.

2. *The largest radius.* It is given by the lower limit to the radius of RX J1856-3754. The lower limit to the radius as seen by an observer at infinity is  $R_\infty = R[1 - 2GM/(c^2R)]^{-1/2} > 16.8$  km, as given by the fit of the optical and X-ray spectra of the source Trümper et al. (2004); so in the mass-radius relation this constraint reads  $2GM/c^2 > R - R^3/(R_\infty^{\min})^2$ , with  $R_\infty^{\min} = 16.8$  km. We represent this constraint with the dotted-dashed curve in Fig. C.47.
3. *The maximum surface gravity.* Using a neutron star of  $M = 1.4M_\odot$  to fit the Chandra data of the low-mass X-ray binary X7, it turns out that the radius of the star satisfies at 90% confidence level,  $R = 14.5^{+1.8}_{-1.6}$  km, which gives  $R_\infty = [15.64, 18.86]$  km, respectively Heinke et al. (2006). Using the same formula as before,  $2GM/c^2 > R - R^3/(R_\infty^{\min})^2$ , we obtain the dotted curves shown in Fig. C.47.
4. *The highest rotation frequency.* Given by the frequency of PSR J1748-2446ad, 716 Hz Hessels et al. (2006a). We constructed the constant frequency sequence  $f = 716$  Hz for both globally (dashed pink) and locally (dashed light blue) neutral neutron stars and indicated with a cyan-color star the point where these curves cross the corresponding Keplerian sequence (see Fig. C.47).

It is worth to analyze with some detail the latter constraint given by the highest measured rotation rate of a pulsar. Lattimer and Prakash (2004a) claimed that the Keplerian frequency of a neutron star, taking into account the effects of general relativity and deformation can be computed independently on the EOS, with the simple formula

$$f_K^{\text{LP}} = 1045 \left( \frac{M}{M_\odot} \right)^{1/2} \left( \frac{10 \text{ km}}{R} \right)^{3/2} \text{ Hz}, \quad (\text{C.5.33})$$

where  $M$  and  $R$  are the mass and radius of the non-rotating neutron star. This formula in principle should be valid for neutron star masses not very close to the maximum stable mass Lattimer and Prakash (2004a).

The Eq. (C.5.33) is often used to impose a constraint to the neutron star mass-radius relation by replacing  $f_K^{\text{LP}}$  with the frequency 716 Hz of PSR J1748–2446ad (see e.g. Trümper (2011)), namely

$$M = \left( \frac{716}{1045} \right)^2 \left( \frac{R}{10 \text{ km}} \right)^3 M_\odot \approx 0.47 \left( \frac{R}{10 \text{ km}} \right)^3 M_\odot. \quad (\text{C.5.34})$$

This constraint is represented by the gray dashed curve in Fig. C.47. One should therefore expect the dashed curve to pass over the cyan-color stars, which represent the actual position of PSR J1748-2446ad assuming it is at the Keplerian limit. It is clear that Eq. (C.5.34) is very far from representing correctly the real position of the star on the Keplerian curve, and this happens for both globally and locally neutral neutron stars.

Specifically, we obtained that if PSR J1748-2446ad is rotating at the Keplerian rate, it should have a mass and equatorial radius of  $0.17 M_\odot$  and 10.61 km for the globally neutral neutron star. As we have shown the minimum mass on the Keplerian sequence is  $M_{\text{min}} = 0.18 M_\odot$ , see Eq. (C.5.27), which implies that PSR J1748–2446ad actually does not impose any constraint to this mass-radius relation. The frequency of PSR J1748–2446ad is just too low to be on the Keplerian sequence and be bound. For the locally neutral configuration we found  $0.48 M_\odot$  and 14.8 km, respectively for mass and equatorial radius; we can see from Fig. C.47 that instead Eq. (C.5.34) would predict for the same radius a mass  $M \sim 1.5 M_\odot$ .

The reason for this result is as follows. Eq. (C.5.21) can be written in terms of the non-rotating mass and radius of the neutron star as

$$\Omega_K^{J \neq 0} = \beta \sqrt{\frac{GM^{J=0}}{R^3}}, \quad (\text{C.5.35})$$

where  $\beta$  is some coefficient to be determined. We find that  $\beta$  has a non-trivial dependence on the central density of the star, in fact ranging from 0.72 to 0.91 for central densities from  $1.08\rho_{\text{nuc}}$  to  $10.56\rho_{\text{nuc}}$ , both for global and local

$M(M_{\odot})$	$R^{J=0}$	$R_{\text{eq}}^{J \neq 0}$
1.40	12.313	13.943
1.93	12.959	14.109
1.97	12.991	14.104
2.01	13.020	14.097
2.05	13.046	14.087

**Table C.4.:** Radii (in km) for a canonical neutron star of  $M = 1.4M_{\odot}$  and for PSR J1614–2230 Demorest et al. (2010a),  $M = 1.97 \pm 0.04M_{\odot}$ , and PSR J0348+0432 (Antoniadis et al., 2013b),  $M = 2.01 \pm 0.04M_{\odot}$ . These configurations are computed under the constraint of global charge neutrality and for a density at the edge of the crust equal to the neutron drip density. The nuclear parameterizations NL3 has been used.

charge neutrality. This dependence is caused by the effects of general relativity, the angular momentum, and the quadrupole deformation mostly owing to the presence of the factor  $[1 - jF_1(r) + j^2F_2(r) + qF_3(r)]$  in Eq. (C.5.21). Thus, we have found that Eq. (C.5.33) and consequently Eq. (C.5.34) are not applicable, in general.

Similarly to what presented in (Rueda et al., 2011) for the static neutron stars and introduced by Trümper (2011), the above observational constraints show a preference on stiff EOS that provide highest maximum masses for neutron stars. Taking into account the above constraints, the radius of a canonical neutron star of mass  $M = 1.4M_{\odot}$  is strongly constrained to  $R \geq 12$  km, disfavoring at the same time strange quark matter stars. It is evident from Fig. C.47 that mass-radius relations for both the static and the rotating case presented here, are consistent with all the observational constraints. In Table C.4 we show the radii predicted by our mass-radius relation both for the static and the rotating case for a canonical neutron star as well as for the most massive neutron stars discovered, namely, the millisecond pulsar PSR J1614–2230 Demorest et al. (2010a),  $M = 1.97 \pm 0.04M_{\odot}$ , and the most recent PSR J0348+0432,  $M = 2.01 \pm 0.04M_{\odot}$  (Antoniadis et al., 2013b).

### C.5.9. Concluding remarks

We have constructed equilibrium configurations of uniformly rotating neutron stars in both the global charge neutrality and local charge neutrality cases, generalizing our previous work (Belvedere et al., 2012). To do this we have applied the Hartle’s method to the seed static solution obtained from the integration of the Einstein-Maxwell-Thomas-Fermi equations (Belvedere et al., 2012). We calculated the mass, angular momentum, quadrupole moment, polar and equatorial radii and eccentricity, as functions of the central density and the rotation angular velocity of the neutron star.

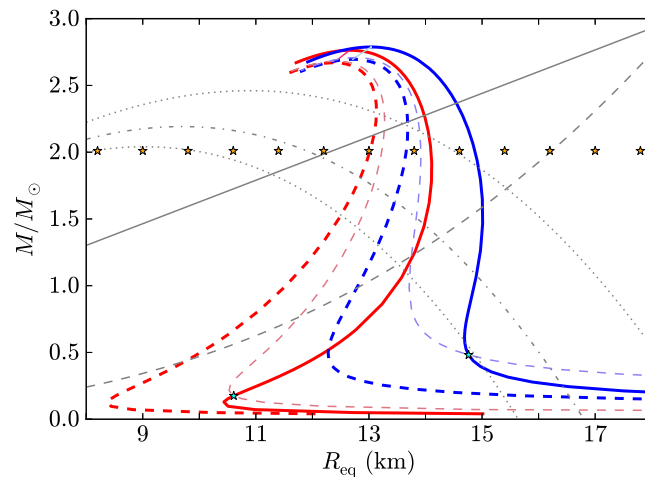


**Figure C.47.:** Observational constraints on the mass-radius relation given by Trümper (2011) and the theoretical mass-radius relation presented in this work in Fig. C.34. The red lines represent the configuration with global charge neutrality, while the blue lines represent the configuration with local charge neutrality. The pink-red line and the light-blue line represent the secular axisymmetric stability boundaries for the globally neutral and the locally neutral case, respectively. The red and blue solid lines represent the Keplerian sequences and the red and blue dashed lines represent the static cases presented in (Belvedere et al., 2012).

	Global Neutrality	Local Neutrality
$M_{\max}^{J=0}(M_{\odot})$	2.67	2.69
$M_{\max}^{J\neq 0}(M_{\odot})$	2.76	2.79
$f_{\max}$ (kHz)	1.97	1.89
$P_{\min}$ (ms)	0.51	0.53
$M_{\min}^{J=0}(M_{\odot})$	0.17	–
$M_{\min}^{J\neq 0}(M_{\odot})$	0.18	–
$f_{\min}^K$ (kHz)	0.20	–

**Table C.5.:** Maximum mass, maximum frequency, minimum period, minimum mass of globally and locally neutral neutron stars.

The Keplerian mass-shedding limit and the secular axisymmetric instability have been analyzed for the construction of the region of stability of rotating neutron stars. We have given fitting curves of the secular instability boundary in Eqs. (C.5.25) and (C.5.26) for global and local charge neutrality, respectively. With this analysis we have established in section C.5.4 the maximum mass and maximum rotation frequency of the neutron star. We computed in section C.5.4 the gravitational binding energy of the configurations as a function of the central density and rotation rate. We did this for central densities higher than the nuclear one, so imposing that the neutron star has a supranuclear hadronic core. We found that there is a minimum mass under which the neutron star becomes gravitationally unbound. To this configuration it is associated a minimum frequency with which the star should rotate; see Eq. (C.5.28). We gave these values in particular for the Keplerian sequence. We found that locally neutral neutron stars with supranuclear cores remained always bound for the present EOS. In Table C.5 we summarize all these results.

We finally analyzed in section C.5.8 the current observational constraints on the mass-radius relation of neutron stars. We found that the formula given by Lattimer and Prakash (2004a), see Eqs. (C.5.33) and (C.5.34), to compute the Keplerian limit of a neutron star of given mass and radius is not valid in general. Assuming that PSR J1748–2446ad rotates at the Keplerian rate we obtained that it should have a mass of  $0.17 M_{\odot}$  and an equatorial radius of 10.61 km, for the global charge neutrality case. For locally neutral configurations, we obtained  $0.48 M_{\odot}$  and 14.8 km, respectively for mass and equatorial radius. Instead, Eq. (C.5.34) would predict for the same radius a mass  $M \sim 1.5 M_{\odot}$  (see Fig. C.47).

This implies that PSR J1748–32446ad does not constrain the mass-radius relation since it cannot rotate with the Keplerian angular velocity, otherwise it would not be gravitationally bound. On the other hand, if its frequency of 716 Hz were lower but close to the Keplerian one, it would imply that PSR J1748–32446ad is the less massive neutron star ever observed. Although

locally neutral neutron stars hold bound along the entire Keplerian sequence, we have shown that PSR J1748–2446ad represents a much weaker constraint to their mass-radius relation to what previously thought.

It would be interesting to analyze the generality of the above results since the most recent measurement of the mass PSR J0348+0432,  $M = 2.01 \pm 0.04M_{\odot}$  (Antoniadis et al., 2013b), favors stiff nuclear EOS as the one used here.

## C.5.10. Supplementary material

### The Hartle solution and equatorial circular orbits

**The Hartle-Thorne vacuum solution** It is possible to write the Hartle-Thorne metric given by eq. C.5.6 in an analytic closed-form in the exterior vacuum case as function of the total mass  $M$ , angular momentum  $J$ , and quadrupole moment  $Q$  of the rotating star. The angular velocity of local inertial frames  $\omega(r)$ , proportional to  $\Omega$ , and the functions  $h_0, h_2, m_0, m_2, k_2$ , proportional to  $\Omega^2$ , are derived from the Einstein equations (see Hartle, 1967; Hartle and Thorne, 1968, for details). Following this prescriptions the eq. C.5.6 become:

$$\begin{aligned}
 ds^2 = & \left(1 - \frac{2M}{r}\right) \left[1 + 2k_1 P_2(\cos \theta) \right. \\
 & + 2 \left(1 - \frac{2M}{r}\right)^{-1} \frac{J^2}{r^4} (2 \cos^2 \theta - 1) \left. \right] dt^2 \\
 & + \frac{4J}{r} \sin^2 \theta dt d\phi - \left(1 - \frac{2M}{r}\right)^{-1} \\
 & \times \left[1 - 2 \left(k_1 - \frac{6J^2}{r^4}\right) P_2(\cos \theta) \right. \\
 & - 2 \left(1 - \frac{2M}{r}\right)^{-1} \frac{J^2}{r^4} \left. \right] dr^2 \\
 & - r^2 [1 - 2k_2 P_2(\cos \theta)] (d\theta^2 + \sin^2 \theta d\phi^2), \tag{C.5.36}
 \end{aligned}$$

where

$$\begin{aligned}
 k_1 &= \frac{J^2}{Mr^3} \left(1 + \frac{M}{r}\right) + \frac{5Q - J^2/M}{8M^3} Q_2^2(x), \\
 k_2 &= k_1 + \frac{J^2}{r^4} + \frac{5}{4} \frac{Q - J^2/M}{M^2 r \sqrt{1 - 2M/r}} Q_2^1(x),
 \end{aligned}$$

and

$$Q_2^1(x) = (x^2 - 1)^{1/2} \left[ \frac{3x}{2} \ln \left( \frac{x+1}{x-1} \right) - \frac{3x^2 - 2}{x^2 - 1} \right],$$

$$Q_2^2(x) = (x^2 - 1) \left[ \frac{3}{2} \ln \left( \frac{x+1}{x-1} \right) - \frac{3x^3 - 5x}{(x^2 - 1)^2} \right],$$

are the associated Legendre functions of the second kind, being  $P_2(\cos \theta) = (1/2)(3 \cos^2 \theta - 1)$  the Legendre polynomial, and where it has been effectuated the re-scaling  $x = r/M - 1$ . The constants  $M$ ,  $J$  and  $Q$  are the total mass, angular momentum and mass quadrupole moment of the rotating object, respectively. This form of the metric corrects some misprints of the original paper by Hartle and Thorne (1968) (see also Berti et al. (2005) and Boshkayev et al. (2012a)). To obtain the exact numerical values of  $M$ ,  $J$  and  $Q$ , the exterior and interior metrics have to be matched at the surface of the star. It is worthy underline that in the terms involving  $J^2$  and  $Q$ , the total mass  $M$  can be substituted by  $M^{J=0}$  since  $\delta M$  is already a second order term in the angular velocity.

**Angular velocity of equatorial circular orbits** It is possible to obtain the analytical expression for the angular velocity  $\Omega$  given by Eq. (C.5.21) with respect to an observer at infinity, taking into account the parameterization of the four-velocity  $u$  of a test particle on a circular orbit in equatorial plane of axisymmetric stationary spacetime, regarding as parameter the angular velocity  $\Omega$  itself:

$$u = \Gamma[\partial_t + \Omega\partial_\phi], \quad (\text{C.5.37})$$

where  $\Gamma$  is a normalization factor such that  $u^\alpha u_\alpha = 1$ . Normalizing and applying the geodesics conditions we get the following expressions for  $\Gamma$  and  $\Omega = u^\phi/u^t$

$$\Gamma = \pm(g_{tt} + 2\Omega g_{t\phi} + \Omega^2 g_{\phi\phi})^{-1/2}, \quad (\text{C.5.38})$$

$$g_{tt,r} + 2\Omega g_{t\phi,r} + \Omega^2 g_{\phi\phi,r} = 0. \quad (\text{C.5.39})$$

Thus, the solution of Eq. (C.5.38) can be written as

$$\Omega_{\text{orb}}^\pm(r) = \frac{u^\phi}{u^t} = \frac{-g_{t\phi,r} \pm \sqrt{(g_{t\phi,r})^2 - g_{tt,r}g_{\phi\phi,r}}}{g_{\phi\phi,r}}, \quad (\text{C.5.40})$$

where  $+/-$  stands for co-rotating/counter-rotating orbits,  $u^\phi$  and  $u^t$  are the angular and time components of the four-velocity respectively, and a colon stands for partial derivative with respect to the corresponding coordinate. To determine the mass shedding angular velocity (the Keplerian angular velocity) of the neutron stars, we need to consider only the co-rotating orbit, so

from here and thereafter we take into account only the plus sign in Eq. (C.5.38) and we write  $\Omega_{\text{orb}}^+(r) = \Omega_{\text{orb}}(r)$ .

For the Hartle external solution given by Eq. (C.5.36) we obtain Eq. (C.5.21) with

$$\begin{aligned}
 F_1 &= \left(\frac{M}{r}\right)^{3/2}, & F &= \frac{15(r^3 - 2M^3)}{32M^3} \ln \frac{r}{r - 2M}, \\
 F_2 &= \frac{48M^7 - 80M^6r + 4M^5r^2 - 18M^4r^3}{16M^2r^4(r - 2M)} \\
 &\quad + \frac{40M^3r^4 + 10M^2r^5 + 15Mr^6 - 15r^7}{16M^2r^4(r - 2M)} + F, \\
 F_3 &= \frac{6M^4 - 8M^3r - 2M^2r^2 - 3Mr^3 + 3r^4}{16M^2r(r - 2M)/5} - F.
 \end{aligned}$$

The maximum angular velocity possible for a rotating star at the mass-shedding limit is the Keplerian angular velocity evaluated at the equator ( $r = R_{\text{eq}}$ ), i.e.

$$\Omega_K^{J \neq 0} = \Omega_{\text{orb}}(r = R_{\text{eq}}). \quad (\text{C.5.41})$$

In the static case i.e. when  $j = 0$  hence  $q = 0$  and  $\delta M = 0$  we have the well-known Schwarzschild solution and the orbital angular velocity for a test particle  $\Omega_K^{J=0}$  on the surface ( $r = R$ ) of the neutron star is given by

$$\Omega_K^{J=0} = \sqrt{\frac{M^{J=0}}{R_{M^{J=0}}^3}}. \quad (\text{C.5.42})$$

## C.6. On the surface tension of neutron star matter

### C.6.1. Introduction

The relativistic mean field theory (RMFT) of nuclear matter and Thomas-Fermi model have attracted great attention during the last few decades. The simplest relativistic model of nuclear matter that accounts for the saturation properties of symmetric nuclear matter includes one scalar field which gives the attractive long-range part of the nuclear force and one vector field which gives the repulsive short-range; these two meson fields interact with nucleons through Yukawa couplings. This so-called  $\sigma$ - $\omega$  model has been considered by Duerr (1956), Miller and Green (1972), and later by Walecka (1974). The relevance of such interactions and relativistic effects in the determination of the equation of state and in the properties of nuclear matter such as compressibility and the nucleon effective mass was clearly pointed out in (Miller and Green, 1972; Boguta and Rafelski, 1977; Boguta and Bodmer, 1977). In (Lee and Wick, 1974; Lee, 1975; Lee and Margulies, 1975), Lee and collaborators considered a model with only one scalar field with self-interaction up to quartic order based on the  $\sigma$ -model. They introduced the repulsive contribution of nuclear force through a *hard-sphere* model that artificially increases the nucleon Fermi momentum, emulating the effect of a massive vector field coupled to nucleons. The importance of allowing scalar meson self-interactions (cubic and quartic terms in the scalar field potential) as adjustable parameters to reproduce physical nuclear properties and not due to renormalization (see e.g. Walecka, 1974) was stressed in (Boguta and Bodmer, 1977; Boguta and Stocker, 1983; Boguta and Moszkowski, 1983; Boguta, 1989). As recognized in (Boguta and Bodmer, 1977), it is necessary to introduce additional isovector fields to obtain the agreement with the empirical symmetry energy of nuclear matter at the saturation density. The model contained Dirac nucleons together with a self-interacting scalar  $\sigma$  and a vector meson  $\omega$  as well as an isovector meson  $\rho$  has been widely used to the end.

With a very limited number of parameters, the RMFT has been shown to be able to give a quantitative description of a variety of nuclear properties (Serot, 1992; Ring, 1996; Bender et al., 2003). Recently, taking into account the electromagnetic and weak interactions, the RMFT with the Thomas-Fermi approximation has gained remarkable successes in understanding the inhomogeneous structures and properties of low-density nuclear matter which is realized in the supernovae core or in the crust of neutron stars (see e.g. Maruyama et al., 2005; Avancini et al., 2008; Okamoto et al., 2012; Grill et al., 2012). The surface properties of nuclear matter such as surface tension and curvature energy play an important role in the description of these structures and also in other phenomena, for instance saddle-point configurations in nuclear fission, fragment distributions in heavy-ion collisions, and phase transition between different phases of nuclear matter.

The nuclear surface properties at saturation density have been analyzed for a long time in the semi-infinite nuclear matter model using RMFT or effective field theory (Furnstahl et al., 1996, 1997, 1998; Serot and Walecka, 1997) with the Thomas-Fermi approximation or Hartree-Fock approximation (Boguta and Bodmer, 1977; Brack et al., 1985; Sharma et al., 1991; von-Eiff et al., 1994b,a, 1995; Centelles et al., 1998; del Estal et al., 1999; Patra et al., 2002; Danielewicz and Lee, 2009). In the supranuclear regime realized in the interior of neutron stars, there is the possibility that phase transition occurs from hadronic to pion and kaon condensed phase as well as to quark matter phase (see e.g. Glendenning, 1992, 2001; Glendenning and Schaffner-Bielich, 1999). The surface tension of the transition layer between the hadronic and kaon condensed or quark matter phases has been calculated in the semi-infinite matter model and the surface tension plays an important role for the structure of the phase transition region (Christiansen et al., 2000; Alford et al., 2001). In the low-density (density smaller than the saturation density) case, as pointed out in (Ravenhall et al., 1983), the shape of constituent nuclei is expected to change from spherical droplet to the so-called nuclear pasta structures such as cylindrical rod, slab, cylindrical tube, and spherical bubble. The surface tensions of nuclear pasta structures have been investigated and it has pointed out that the pasta phase strongly depends on the value of the surface tension (Maruyama et al., 2005; Avancini et al., 2008; Grill et al., 2012).

The importance of the extension of the Thomas-Fermi approximation to general relativistic systems such as neutron stars was emphasized in (Rotonondo et al., 2011d). We showed there that the traditionally imposed condition of local charge neutrality is not consistent with the field equations and microphysical equilibrium for a system of neutrons, protons, and electrons in  $\beta$ -equilibrium and obeying relativistic quantum statistics. Thus, only the condition of global but not local charge neutrality can be imposed. This leads to the appearance of gravito-polarization in the cores of neutron stars. The generalization of such a work to the case where the strong interactions between nucleons are accounted for was presented in (Rueda et al., 2011). Both the Thomas-Fermi approximation and RMFT were used. It was shown that the Einstein-Maxwell-Thomas-Fermi system of equations within RMFT supersede the traditional Tolman-Oppenheimer-Volkoff (Tolman, 1939; Oppenheimer and Volkoff, 1939) equations used for the construction of neutron star configurations.

Realistic neutron star configurations including all the interactions between particles and the presence of a crust below nuclear density, were constructed in (Belvedere et al., 2012) by solving numerically the Einstein-Maxwell-Thomas-Fermi equations fulfilling the condition of global charge neutrality. As pointed out in (Belvedere et al., 2012), the self-consistent solution of these new equations of equilibrium leads to the existence of a transition layer between the core and the crust of the star. This is markedly different from the neutron star structure obtained from the solution of the TOV equations imposing local

charge neutrality (Haensel et al., 2007), leading to a new mass-radius relation of neutron stars. Such core-crust transition layer occurs near the nuclear saturation density. The core (bulk region) inside this transition layer is a hadronic phase and the crust outside this transition is composed by the nuclei lattice and the ocean of relativistic degenerate electrons and possibly neutrons at densities below nuclear saturation and larger than the estimated neutron drip value  $\sim 4.3 \times 10^{11} \text{ g cm}^{-3}$ . Inside the transition region it is developed a very strong electric field overwhelming the critical value for vacuum break-down  $E_c = m_e^2 c^3 / (e\hbar)$ , where  $m_e$  is the electron rest-mass. The  $e^+e^-$  pair creation out from vacuum is however forbidden in the system due to the Pauli blocking of degenerate electrons.

In this article we study the detailed structure of this transition layer formed near the nuclear saturation density. We calculate all the contributions to the surface tension as well as the electrostatic energy stored in this core-crust layer. We analyze the stability of these systems under the Bohr-Wheeler fission mechanism (Bohr and Wheeler, 1939). We analyze the role of the electron contribution and compare and contrast the surface energy of these neutron stars with the phenomenological results in nuclear physics for both ordinary and superheavy nuclei.

The article is organized as follows. In Sec. C.6.2, we study the surface structure and the surface tension as well as the Coulomb energy for neutron star matter without the influence of the gravitational field. We formulate in Sec. C.6.2 the relativistic equations for a system of neutrons, protons and electrons fulfilling strong and electromagnetic interactions as well as  $\beta$ -equilibrium. In Sec. C.6.2, we use the semi-infinite matter model (Baym et al., 1971a) to formulate the equations governing the surface tension for the transition layer of this system when the electron density is nearly equal to the proton density in the core bulk region. In Sec. C.6.2, we calculate the surface structure and solve these equations to obtain the surface tension and the Coulomb energy at the nuclear saturation density and neglecting the presence of the crust. Then we study in Sec. C.6.2 the dependence of the surface tension and the Coulomb energy on the baryon number density. In Sec. C.6.2, we study the influence of fermion densities in the outside region (crust) on the surface tension and the Coulomb energy. In Sec. C.6.3, we study the structure and the surface tension as well as the Coulomb energy for the core-crust transition region in the presence of the gravitational field within the framework of general relativity. We present the set of general relativistic equations in Sec. C.6.3. Then in Sec. C.6.3, we calculate the surface tension for the transition layer with these equations including the presence of the gravitational interactions. In Sec. C.6.4, we calculate the surface tension and the Coulomb energy for the transition layer of the system when the electron density is smaller than the proton density in the bulk region and compare the results with known phenomenological results in nuclear physics. We finally summarize and conclude in Sec. C.6.5. We use units with  $\hbar = c = 1$  throughout

the article.

## C.6.2. Surface properties for neutron star matter without gravitational interaction

### Relativistic equations of motion

As described in (Belvedere et al., 2012), the system we consider is composed of degenerate neutrons, protons, and electrons fulfilling global charge neutrality and  $\beta$ -equilibrium. To describe the nuclear interactions, here we employ the RMFT with the Thomas-Fermi approximation. We adopt the phenomenological nuclear model of Boguta and Bodmer (1977).

Taking into account the strong, electromagnetic, and weak interactions, the total Lagrangian density of the system is given by

$$\mathcal{L} = \mathcal{L}_f + \mathcal{L}_\sigma + \mathcal{L}_\omega + \mathcal{L}_\rho + \mathcal{L}_\gamma + \mathcal{L}_{int}, \quad (\text{C.6.1})$$

where the Lagrangian densities for the free-fields are

$$\mathcal{L}_\gamma = -\frac{1}{16\pi} F_{\mu\nu} F^{\mu\nu}, \quad (\text{C.6.2})$$

$$\mathcal{L}_\sigma = \frac{1}{2} \nabla_\mu \sigma \nabla^\mu \sigma - U(\sigma), \quad (\text{C.6.3})$$

$$\mathcal{L}_\omega = -\frac{1}{4} \Omega_{\mu\nu} \Omega^{\mu\nu} + \frac{1}{2} m_\omega^2 \omega_\mu \omega^\mu, \quad (\text{C.6.4})$$

$$\mathcal{L}_\rho = -\frac{1}{4} \mathcal{R}_{\mu\nu} \mathcal{R}^{\mu\nu} + \frac{1}{2} m_\rho^2 \rho_\mu \rho^\mu, \quad (\text{C.6.5})$$

where  $\Omega_{\mu\nu} \equiv \partial_\mu \omega_\nu - \partial_\nu \omega_\mu$ ,  $\mathcal{R}_{\mu\nu} \equiv \partial_\mu \rho_\nu - \partial_\nu \rho_\mu$ ,  $F_{\mu\nu} \equiv \partial_\mu A_\nu - \partial_\nu A_\mu$  are the field strength tensors for the vector meson field  $\omega$ , isovector meson field  $\rho$ , and electromagnetic field  $A$  respectively,  $\nabla_\mu$  stands for covariant derivative. The Lorenz gauge is adopted for the fields  $A_\mu$ ,  $\omega_\mu$ , and  $\rho_\mu$ .

The Lagrangian density for the three fermion species is

$$\mathcal{L}_f = \sum_{i=e,N} \bar{\psi}_i (i\gamma^\mu \partial_\mu - m_i) \psi_i, \quad (\text{C.6.6})$$

where  $\psi_N$  is the nucleon isospin doublet,  $\psi_e$  is the electronic singlet, and  $m_i$  stands for the rest-mass of each  $i$ -fermion specie.

The scalar self-interaction potential is

$$U(\sigma) = \frac{1}{2} m_\sigma^2 \sigma^2 + \frac{1}{3} g_2 \sigma^3 + \frac{1}{4} g_3 \sigma^4. \quad (\text{C.6.7})$$

The interacting part of the Lagrangian density is given by

$$\mathcal{L}_{int} = -g_\sigma \sigma \bar{\psi}_N \psi_N - g_\omega \omega_\mu J_\omega^\mu - g_\rho \rho_\mu J_\rho^\mu + e A_\mu J_{\gamma,e}^\mu - e A_\mu J_{\gamma,N}^\mu, \quad (\text{C.6.8})$$

where the conserved currents are

$$J_\omega^\mu = \bar{\psi}_N \gamma^\mu \psi_N, \quad (\text{C.6.9})$$

$$J_\rho^\mu = \bar{\psi}_N \tau_3 \gamma^\mu \psi_N, \quad (\text{C.6.10})$$

$$J_{\gamma,e}^\mu = \bar{\psi}_e \gamma^\mu \psi_e, \quad (\text{C.6.11})$$

$$J_{\gamma,N}^\mu = \bar{\psi}_N \left( \frac{1 + \tau_3}{2} \right) \gamma^\mu \psi_N, \quad (\text{C.6.12})$$

with  $g_\sigma$ ,  $g_\omega$ , and  $g_\rho$  the coupling constants of the  $\sigma$ ,  $\omega$  and  $\rho$  fields, and  $e$  is the fundamental electric charge.  $\tau_3$  is the third component of the isospin Pauli matrices.

Within the Thomas-Fermi approximation, the position-dependent equations of motion for this system are given by

$$\nabla^2 V = -4\pi e(n_p - n_e), \quad (\text{C.6.13})$$

$$\nabla^2 \sigma = \partial_\sigma U(\sigma) + g_s n_s, \quad (\text{C.6.14})$$

$$\nabla^2 \omega = -(g_\omega J_0^\omega - m_\omega^2 \omega), \quad (\text{C.6.15})$$

$$\nabla^2 \rho = -(g_\rho J_0^\rho - m_\rho^2 \rho), \quad (\text{C.6.16})$$

$$E_e^F = \mu_e - eV = \text{constant}, \quad (\text{C.6.17})$$

$$E_p^F = \mu_p + g_\omega \omega + g_\rho \rho + eV = \text{constant}, \quad (\text{C.6.18})$$

$$E_n^F = \mu_n + g_\omega \omega - g_\rho \rho = \text{constant}, \quad (\text{C.6.19})$$

where the notation  $\omega_0 \equiv \omega$ ,  $\rho_0 \equiv \rho$ , and  $A_0 \equiv V$  for the time components of the meson fields have been introduced. Here  $\mu_i = \sqrt{(P_i^F)^2 + \tilde{m}_i^2}$  and  $n_i = (P_i^F)^3 / (3\pi^2)$  are the free chemical potential and number density of the  $i$ -specie with Fermi momentum  $P_i^F$ . The particle effective masses are  $\tilde{m}_N = m_N + g_s \sigma$  and  $\tilde{m}_e = m_e$ .

The generalized chemical potential of electrons, protons, and neutrons,  $E_e^F$ ,  $E_p^F$ , and  $E_n^F$ , derived from the thermodynamic equilibrium conditions given by the statistical physics of multicomponent systems, are linked by the  $\beta$ -equilibrium (Boguta, 1981) of protons, neutrons, and electrons

$$E_n^F = E_p^F + E_e^F. \quad (\text{C.6.20})$$

The scalar density  $n_s$  is given by the expectation value

$$n_s = \langle \bar{\psi}_N \psi_N \rangle = \frac{2}{(2\pi)^3} \sum_{i=n,p} \int_0^{P_i^F} d^3k \frac{\tilde{m}_N}{\epsilon_i(k)}, \quad (\text{C.6.21})$$

where  $\epsilon_i(k) = \sqrt{k^2 + \tilde{m}_i^2}$  is the single particle energy. In the static case, only the time components of the covariant currents survive, i.e.  $\langle \bar{\psi}(x) \gamma^i \psi(x) \rangle = 0$ . The nonvanishing components of the currents are

$$J_0^{ch} = n_p - n_e, \quad (\text{C.6.22})$$

$$J_0^\omega = n_b = n_n + n_p, \quad (\text{C.6.23})$$

$$J_0^\rho = n_p - n_n, \quad (\text{C.6.24})$$

here  $n_b = n_p + n_n$  is the baryon number density.

For the system of static uniform matter in its ground state, the source currents  $\bar{\psi}\psi$  and  $\bar{\psi}\gamma^\mu\psi$  are position-independent. The derivative terms in Eqs. (C.6.14)-(C.6.16) are zero. As a consequence, equations (C.6.14)-(C.6.16) reduce to the simpler form

$$\partial_\sigma U(\sigma) + g_s n_s = 0, \quad (\text{C.6.25})$$

$$-(g_\omega J_0^\omega - m_\omega^2 \omega) = 0, \quad (\text{C.6.26})$$

$$-(g_\rho J_0^\rho - m_\rho^2 \rho) = 0. \quad (\text{C.6.27})$$

### Surface tension for semi-infinite matter

As shown in (Belvedere et al., 2012), in the bulk hadronic phase of neutron star cores, the charge separation is very small, so the electron density  $n_{eb}$  is nearly equal to the proton density  $n_{pb}$ . For the system with  $n_{eb} \simeq n_{pb}$  in the bulk region and obeying global charge neutrality, we can apply the semi-infinite matter model to calculate the surface tension. We construct the surface tension for the transition layer of this system following the method of Baym et al. (1971a) (BBP).

In the semi-infinite matter model, one assumes a plane surface (with small thickness compared with the bulk region size) perpendicular to the  $z$ -axis separating two semi-infinite regions, represented here by the inside core bulk and the outside crust. The number density of the  $i$ -specie ( $i = n, p, e$ ) fermion  $n_i(\vec{r})$  approaches the bulk density of the  $i$ -specie fermion  $n_{ib}$  as the position  $z \rightarrow -\infty$ , and approaches the density in the outside region of the  $i$ -specie fermion  $n_{io}$  as the  $z \rightarrow +\infty$ . The semi-infinite matter is a one-dimensional system, namely there is only  $z$ -dependence. To construct the surface tension, one imagines a reference system with a sharp surface at  $z = a_i$  at which fermion densities and meson fields fall discontinuously from the bulk region

to the outside region. Following Baym et al. (1971a), the location of the reference surface for the  $i$ -specie fermion is defined by the condition that the reference system has the same number of the  $i$ -specie fermion as the original system

$$\int_{z=-\infty}^{a_i} d^3r [n_i(\vec{r}) - n_{ib}] + \int_{z=a_i}^{\infty} d^3r [n_i(\vec{r}) - n_{io}] = 0; \quad i = n, p, e. \quad (\text{C.6.28})$$

Apply the definition of reference surface in Eq. (C.6.28) to neutron, proton, and electron yields slightly different reference surface.

Similar to the definition of reference surface for fermion, we define the location of the reference surfaces for meson fields by

$$\int_{z=-\infty}^{a_i} d^3r [F_i(\vec{r}) - F_{ib}] + \int_{z=a_i}^{\infty} d^3r [F_i(\vec{r}) - F_{io}] = 0; \quad i = \sigma, \omega, \rho, \quad (\text{C.6.29})$$

where  $F_i(\vec{r})$  is the time component of the  $i$ -specie meson field,  $F_{ib}$  is the time component of the  $i$ -specie meson field in the bulk region, and  $F_{io}$  is the time component of the  $i$ -specie meson field in the outside region.

Thus, the total surface tension can be written as the sum of three contributions

$$\sigma_t = \sigma_N + \sigma_e + \sigma_C, \quad (\text{C.6.30})$$

where we have introduced the nuclear surface tension following the method of BBP (Baym et al., 1971a),

$$\sigma_N = \sum_{i=n,p,\sigma,\omega,\rho} \left\{ \int_{-\infty}^{a_i} [\epsilon_i(z) - \epsilon_{ib}] dz + \int_{a_i}^{\infty} [\epsilon_i(z) - \epsilon_{io}] dz \right\}, \quad (\text{C.6.31})$$

the electron surface tension

$$\sigma_e = \left\{ \int_{-\infty}^{a_e} [\epsilon_e(z) - \epsilon_{eb}] dz + \int_{a_e}^{\infty} [\epsilon_e(z) - \epsilon_{eo}] dz \right\}, \quad (\text{C.6.32})$$

and the surface tension for the electric field as

$$\sigma_C = \int_{-\infty}^{\infty} \epsilon_E(z) dz, \quad (\text{C.6.33})$$

with  $\epsilon_i(z)$  the energy density of the  $i$ -specie fermion or meson field,  $\epsilon_{ib}$  is the energy density of the  $i$ -specie fermion or meson field in the bulk region,  $\epsilon_{io}$  is the energy density of the  $i$ -specie fermion or meson field in the outside region, and  $\epsilon_E(z) = E^2/(8\pi)$  is the electrostatic energy density.

It is important to remark here that owing to the small charge separation present in the system in the core bulk region, we can assume that the electric field only exists in the transition layer surface. Thus we can consider the

electrostatic energy as a surface property of the system, hence contributing to the surface energy. This is a major difference between the present system and an ordinary nucleus where the electrostatic energy is a volume property.

The relation between the surface energy and Coulomb energy is very important for a nucleus. As shown by Bohr and Wheeler (1939) when the condition

$$E_{coul} > 2E_{sur} \quad (\text{C.6.34})$$

satisfies, the nucleus becomes unstable against nuclear fission, here  $E_{coul}$  is the Coulomb energy of the nucleus and  $E_{sur}$  is the surface energy of the nucleus. It is important to recall that the idealized picture of the deformed nucleus of Bohr and Wheeler is represented by two positively charged spheres joined by a nuclear attraction neck. It is thus the interplay of the Coulomb and nuclear surface energies that determines the lower energy state. Following this argument one could think that since we are treating here a globally neutral system such an instability mechanism is absent. However, the condition (C.6.34) can be also obtained by requesting that a uniformly charged spheroid constructed from an axially symmetric deformation at constant volume of a uniformly charged sphere, be energetically favorable. From a careful look at the derivation of Eq. (C.6.34), it can be seen that this result follows from the fact that Coulomb energy of the unperturbed system (the sphere) depends on the radius as  $E_{coul} \propto R^{-1}$ . Such an inverse radius dependence holds also in the case of a uniformly charged shell, and also in the case of the globally neutral massive nuclear density cores studied in (Rotondo et al., 2011e,c); which fully reflect the properties of the system studied in this work. We then expect that the Bohr-Wheeler condition of instability against fission given by Eq. (C.6.34) applies also to our system. Clearly such a condition is obtained keeping the system at nuclear density and neglecting the the extra binding effect of gravity.

In thermodynamics, the surface tension is related to the mechanical work needed to increase a surface area,

$$dW = \sigma dS, \quad (\text{C.6.35})$$

here  $\sigma$  is the surface tension,  $dS$  is the variation of the surface area, and  $dW$  is the mechanical work needed to increase the surface area of the system. In this point of view, a system with a positive surface tension has an attractive nature, and a system with a negative surface tension has a repulsive nature.

The Eqs. (C.6.30)–(C.6.33) show that the surface tension mainly depends on the fermion density and meson field profiles and the energy densities of fermions and meson fields. For semi-infinite matter, the system is only z-

dependence and Eqs. (C.6.13)–(C.6.16) become

$$\frac{d^2V}{dz^2} = -4\pi e(n_p - n_e), \quad (\text{C.6.36})$$

$$\frac{d^2\sigma}{dz^2} = \partial_\sigma U(\sigma) + g_s n_s, \quad (\text{C.6.37})$$

$$\frac{d^2\omega}{dz^2} = -(g_\omega J_0^\omega - m_\omega^2 \omega), \quad (\text{C.6.38})$$

$$\frac{d^2\rho}{dz^2} = -(g_\rho J_0^\rho - m_\rho^2 \rho). \quad (\text{C.6.39})$$

The energy density of the  $i$ -specie fermion is given by

$$\begin{aligned} \epsilon_i(z) = & \frac{1}{8\pi^2} \left\{ P_i^F \sqrt{(P_i^F)^2 + \tilde{m}_i^2} [2(P_i^F)^2 + \tilde{m}_i^2] \right. \\ & \left. - \tilde{m}_i^4 \ln \frac{P_i^F + \sqrt{(P_i^F)^2 + \tilde{m}_i^2}}{\tilde{m}_i} \right\}, \end{aligned} \quad (\text{C.6.40})$$

and the energy densities of the meson fields are

$$\epsilon_\sigma(z) = \frac{1}{2} \left( \frac{d\sigma}{dz} \right)^2 + U(\sigma), \quad (\text{C.6.41})$$

$$\epsilon_\omega(z) = \frac{1}{2} \left( \frac{d\omega}{dz} \right)^2 + \frac{1}{2} m_\omega^2 \omega^2, \quad (\text{C.6.42})$$

$$\epsilon_\rho(z) = \frac{1}{2} \left( \frac{d\rho}{dz} \right)^2 + \frac{1}{2} m_\rho^2 \rho^2, \quad (\text{C.6.43})$$

$$\epsilon_E(z) = \frac{1}{8\pi} \left( \frac{dV}{dz} \right)^2. \quad (\text{C.6.44})$$

We can solve Eqs. (C.6.36)–(C.6.39) and Eqs. (C.6.17)–(C.6.19) to obtain the fermion density and meson field profiles. This system of equations can be numerically solved with appropriate boundary conditions.

The parameters of the nuclear model, namely the coupling constants  $g_\sigma$ ,  $g_\omega$ , and  $g_\rho$ , the meson masses  $m_\sigma$ ,  $m_\omega$ , and  $m_\rho$ , and the third and fourth order constants of the self-scalar interaction  $g_2$  and  $g_3$  are fixed by fitting experimental properties of nuclei, such as saturation density, binding energy per nucleon, symmetry energy, surface energy, and nuclear incompressibility. We here use the parameters of the NL3 parameterization (Lalazissis et al., 1997), shown in Table C.6.

	NL3		NL3
$m_\sigma$ (MeV)	508.194	$g_\omega$	12.8680
$m_\omega$ (MeV)	782.501	$g_\rho$	4.4740
$m_\rho$ (MeV)	763.000	$g_2$ (fm <sup>-1</sup> )	-10.4310
$g_\sigma$	10.2170	$g_3$	-28.8850

**Table C.6.:** The parameters of the nuclear model from NL3.

### Surface structure and surface tension at the nuclear saturation density

The boundary conditions for the numerical integration are fixed through the following procedure. We start assuming that the bulk region is formed by uniform matter, so we can apply Eqs. (C.6.25)–(C.6.27) to the bulk core. We assume the baryon number density of the bulk region to be the nuclear saturation density,  $n_{bb} = n_{nb} + n_{pb} = n_{nucl} = 0.16 \text{ fm}^{-3}$ .

First we will compute the surface properties in the case when the fermion densities and meson fields to be zero in the outside region, namely neglecting the influence of the outside crust region. We have also in the bulk core the condition  $n_{pb} \simeq n_{eb}$ . Taking into account the above conditions, we can solve the equations (C.6.25)–(C.6.27) together with the  $\beta$ -equilibrium (C.6.20) in the bulk region to obtain  $\sigma_b$ ,  $\omega_b$ ,  $\rho_b$ ,  $n_{nb}$ ,  $n_{pb}$ , and  $n_{eb}$ . Using this bulk region values as boundary conditions, we solve Eqs. (C.6.36)–(C.6.39) and Eqs. (C.6.17)–(C.6.19) in the surface region. The results are shown in Fig. C.48. Since the fermion densities tend to be zero in the outside region, the thickness of the surface region for electrons should be infinite. However we just show the results up to a very small electron density here, due to the plot-scale and the accuracy of the numerical calculation.

There exist two scale lengths in this system, one is related to the nuclear interactions ( $\sim \lambda_\pi = \hbar/(m_\pi c) \sim 1.5 \text{ fm}$ ) and another one is related to the electron screening ( $\sim \lambda_e = \hbar/(m_e c) \sim 100 \text{ fm}$ ). It is shown in Fig. C.48 that the transition layer can be divided by three regions due to the existence of these two different scale lengths. (I) due to the electromagnetic interaction, all the fields vary slowly with the length scale  $\sim \lambda_e$ . In this region the effect of the Coulomb interaction is clear: on the proton density profile we can see a bump due to Coulomb repulsion while the electron density profile decreases. The neutrons also feels this Coulomb effect indirectly due to the coupled nature of the system of equations. But this effect is much smaller than the effect on protons and it is not appreciable in Fig. C.48 due to the plot-scale. (II) due to the nuclear interactions, a sharp decrease of the proton and neutron densities happens in the length scale  $\lambda_\pi$ . It can be seen a neutron skin effect, which makes the scale of the neutron density falloff slightly larger with respect to the proton one, in analogy to the one observed in heavy nuclei and in neutron rich nuclei (Tamii et al., 2011). (III) the electron density decreases smoothly

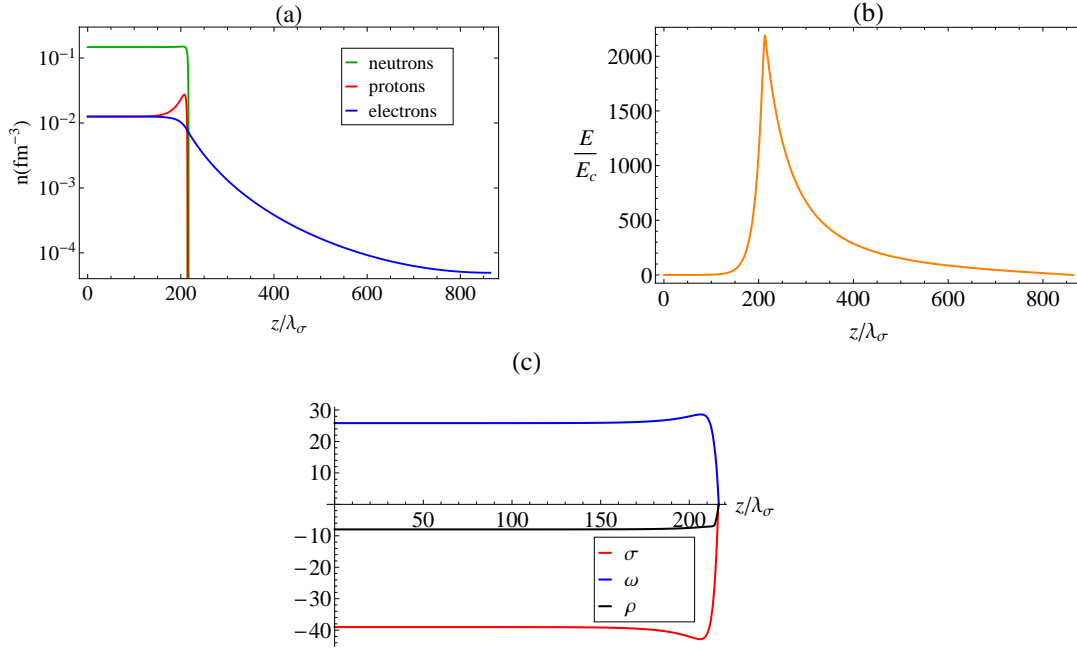


**Figure C.48.:** (a): fermion density profiles in units of  $\text{fm}^{-3}$ . (b): electric field in units of the critical field  $E_c = m_e^2 c^3 / (e\hbar)$ . (c): meson fields  $\sigma$ ,  $\omega$ , and  $\rho$  in the unit of MeV. Here the baryon number density of the bulk region is the nuclear saturation value, and the fermion densities and meson fields tend to be zero in the outside region.  $\lambda_\sigma = \hbar / (m_\sigma c) \sim 0.4$  fm is the Compton wavelength of the  $\sigma$  meson.

in the length scale  $\lambda_e$  and this produces the total screening of the positively charged core. As shown in Fig. C.48, we can obtain an electric field that is larger than critical field in the surface region. However, no  $e^+e^-$  pair can be produced in this region due to the Pauli blocking owing to the presence of degenerate electrons.

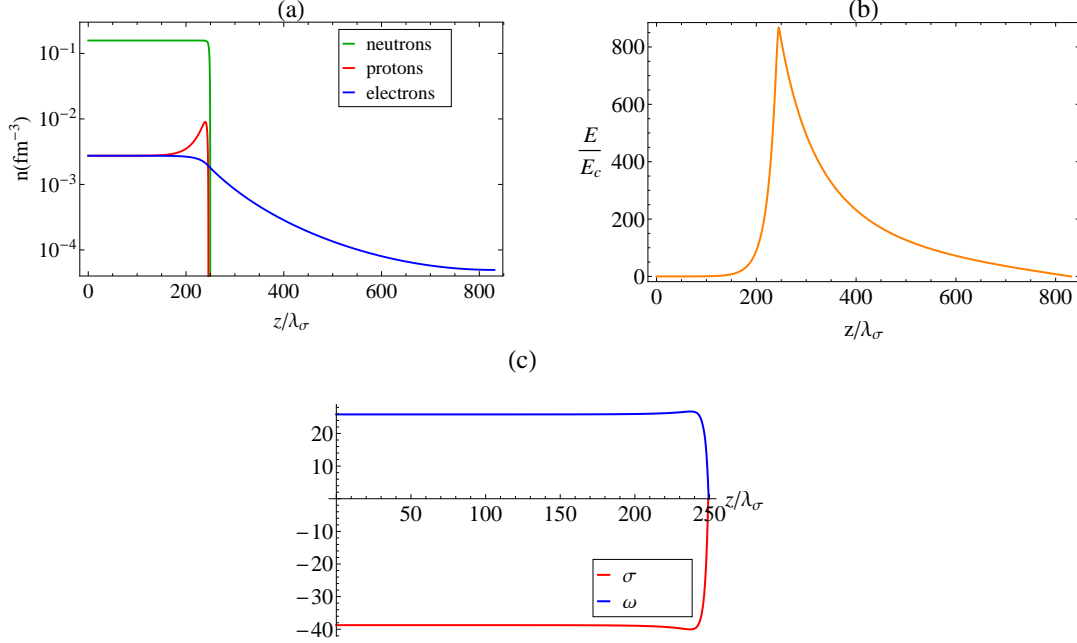


**Figure C.49.:** (a): fermion density profiles in units of  $\text{fm}^{-3}$ . (b): electric field in units of the critical field  $E_c$ . (c): meson fields  $\sigma$  and  $\omega$  in the unit of MeV. Here the baryon number density of the bulk region is the nuclear saturation density, the fermion densities and meson fields tend to be zero in the outside region, and  $\rho$  meson is not included in the calculation.

In order to study the effect of the  $\rho$  meson, we solve Eqs. (C.6.36)–(C.6.39) and Eqs. (C.6.17)–(C.6.19) without the presence of the  $\rho$  meson. The results are shown in Fig. C.49. The fermion density and meson field profiles are similar to those in the case with the presence of the  $\rho$  meson, as shown in Figs. C.48 and C.49. Due to the absence of the  $\rho$  meson, the proton (and hence the electron) to neutron density ratio decreases, so if the baryon density is the same it causes a lowering of the electric field intensity.

Using the definitions in Eqs. (C.6.30)–(C.6.33), we can calculate the surface tensions for this transition layer. The results are shown in Table C.7. The presence of  $\rho$  decreases the total surface tension  $\sigma_t$  but increases the Coulomb energy, and so  $\sigma_C$ . We can see that the difference of the surface tension for nucleons  $\sigma_N$  in the presence and absence of the  $\rho$  meson is relatively small with respect to the changes on the electron component and the electric field. We can explain this small difference from the fact that although the  $\rho$  meson increases the proton to neutron density ratio, in neutron stars

	$\sigma_t$	$\sigma_N$	$\sigma_e$	$\sigma_C$
$\sigma \omega$	6.28	7.07	-1.72	0.92
$\sigma \omega \rho$	3.10	7.30	-8.34	4.14

**Table C.7.:** Total and specific surface tensions in  $\text{MeV fm}^{-2}$  of semi-infinite matter with and without the presence of the  $\rho$  meson. Here the baryon number density in the bulk region is set to the nuclear saturation value and the fermion densities and meson fields tend to be zero in the outside region.

the  $\beta$ -equilibrium in presence of degenerate electrons leads to a high isospin asymmetry  $1 - 2Z/A \approx 1$ , hence the system is still dominated by the neutron component, as we show below.

It is interesting to compare the above results with the ones in (Alford et al., 2001) where the surface tension of the interface between quark matter in color-flavor-locked (CFL) phase and ordinary hadronic phase. The surface tension was obtained as the sum of two contributions: (I) the first due to the QCD-scale interface, which they treated as infinitely sharp and estimated based on dimensional analysis,  $\sigma_{QCD} \sim 300 \text{ MeV fm}^{-2}$ ; (II) a surface tension  $\sigma_{\text{boundarylayer}} \approx 420 \text{ MeV fm}^{-2}$  associated to the electron screening length and computed from the particle number density profiles similarly as here. Thus, they obtained a total surface tension  $\sigma_{\text{sur}} = \sigma_{QCD} + \sigma_{\text{boundarylayer}} \approx 720 \text{ MeV fm}^{-2}$ . The difference between our result in Table C.7 and the result in (Alford et al., 2001) is mainly due to the fact that the CFL-hadronic interface occurs in the inner core of the neutron star at baryon densities much higher than the nuclear saturation value separating the core and the crust.

In order to understand where the surface tension comes from, we calculate the contribution of each fermion and meson field to the surface tension as

$$\sigma_n = \int_{-\infty}^{a_n} [\epsilon_n(z) - \epsilon_{nb}] dz + \int_{a_n}^{\infty} [\epsilon_n(z) - \epsilon_{no}] dz, \quad (\text{C.6.45})$$

$$\sigma_p = \int_{-\infty}^{a_p} [\epsilon_p(z) - \epsilon_{pb}] dz + \int_{a_p}^{\infty} [\epsilon_p(z) - \epsilon_{po}] dz, \quad (\text{C.6.46})$$

$$\sigma_e = \int_{-\infty}^{a_e} [\epsilon_e(z) - \epsilon_{eb}] dz + \int_{a_e}^{\infty} [\epsilon_e(z) - \epsilon_{eo}] dz, \quad (\text{C.6.47})$$

$$\sigma_\sigma = \int_{-\infty}^{a_\sigma} [\epsilon_\sigma(z) - \epsilon_{\sigma b}] dz + \int_{a_\sigma}^{\infty} [\epsilon_\sigma(z) - \epsilon_{\sigma o}] dz, \quad (\text{C.6.48})$$

$$\sigma_\omega = \int_{-\infty}^{a_\omega} [\epsilon_\omega(z) - \epsilon_{\omega b}] dz + \int_{a_\omega}^{\infty} [\epsilon_\omega(z) - \epsilon_{\omega o}] dz, \quad (\text{C.6.49})$$

$$\sigma_\rho = \int_{-\infty}^{a_\rho} [\epsilon_\rho(z) - \epsilon_{\rho b}] dz + \int_{a_\rho}^{\infty} [\epsilon_\rho(z) - \epsilon_{\rho o}] dz. \quad (\text{C.6.50})$$

The results are shown in Table C.8. For sake of comparison we also show the

results in the case of ordinary nuclear matter, namely for a system without the presence of electrons. As shown in Eqs. (C.6.45)–(C.6.50), the contribution of each fermion and meson field to the surface tension strongly depends on the profile and the energy density of the fermion and meson field. As shown in Figs. C.48 and C.49, comparing to the profiles in the case without the presence of the  $\rho$  meson, the presence of the  $\rho$  meson leads to larger proton and electron densities, and a larger bump of proton density happens. This effect is felt indirectly by neutrons (although much less strong), due to the coupled nature of the system of equations (C.6.36)–(C.6.39) and (C.6.17)–(C.6.19). There is no such a bump of the profiles in the case of normal nuclear matter. Comparing the results of the three cases in Table C.8, the effect of the bump of proton density on the surface tension is significant. The bump on the profiles decreases the value of the surface tension for fermions and increases the one for bosons. These results provide an evidence of large effect of electromagnetic interaction and electrons on the proton and neutron density profiles, and therefore on the global value of the surface energy of the system.

	$\sigma_n$	$\sigma_p$	$\sigma_e$	$\sigma_\sigma$	$\sigma_\omega$	$\sigma_\rho$
$n p e \sigma \omega$	3.54	−0.36	−1.72	3.16	0.73	
$n p e \sigma \omega \rho$	−27.35	−5.19	−8.34	22.20	19.93	−2.28
$n p \sigma \omega \rho$	19.43	12.23		−16.08	−13.83	−0.04

**Table C.8.:** Contribution of each fermion and meson field to the surface tension, in  $\text{MeV fm}^{-2}$ . First row: semi-infinite matter without the presence of the  $\rho$  meson. Second row: semi-infinite matter with the presence of the  $\rho$  meson. Third row: normal nuclear matter (without the presence of electrons). Here the baryon number density in the bulk region is the nuclear saturation density, and the fermion densities and meson fields tend to be zero in the outside region.

### Influence of baryon number density on the surface tension

In order to study the dependence of the surface tension on the baryon number density, we calculate the surface tensions for different  $n_{bb}$  following the similar procedure in Sec. C.6.2. The results are shown in Fig. C.50. From the results, the total surface tension can be fitted by

$$\sigma_{t,fit} = 1.05 + 2.02 \left( \frac{n_{bb}}{n_{nucl}} \right)^{3.33} \left( \text{MeV fm}^{-2} \right), \quad (\text{C.6.51})$$

the surface tension for electric field can be fitted by

$$\sigma_{C,fit} = -0.37 + 4.50 \left( \frac{n_{bb}}{n_{nucl}} \right)^2 \left( \text{MeV fm}^{-2} \right), \quad (\text{C.6.52})$$

and the surface tension for nucleons can be fitted by

$$\sigma_{N,fit} = 0.95 + 6.33 \left( \frac{n_{bb}}{n_{nucl}} \right)^{2.91} \left( \text{MeV fm}^{-2} \right). \quad (\text{C.6.53})$$

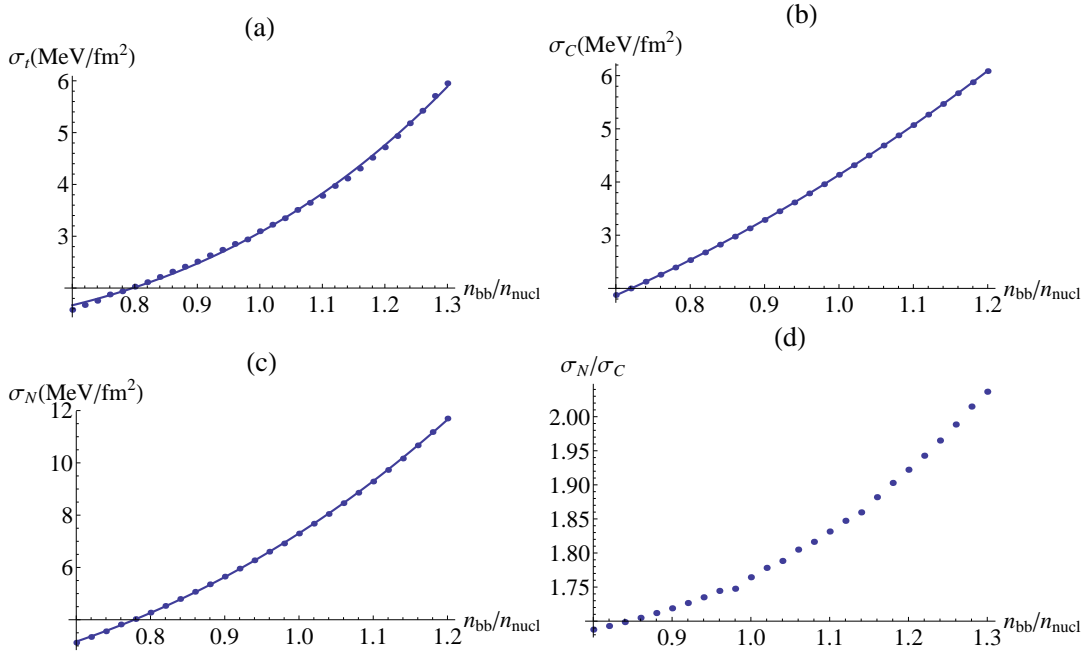


**Figure C.50.:** The dependence of the surface tension of semi-infinite matter on the baryon number density in the bulk region. Here the fermion densities and meson fields tend to be zero in the outside region. (a): the total surface tension  $\sigma_t$ , compared with the fit given in Eq. (C.6.51). (b): surface tension for electric field  $\sigma_C$ , compared with the fit given in Eq. (C.6.52). (c): surface tension for nucleons  $\sigma_N$ , compared with the fit given in Eq. (C.6.53). (d): ratio of surface tension for nucleons and the surface tension for electric field  $\sigma_N/\sigma_C$ .

As shown by Baym et al. (1971a), the phenomenological surface tension for nucleons within the Thomas-Fermi approximation can be written as

$$\sigma_{sur}^{BBP} = B(W_o - W_i)^{\frac{1}{2}}(n_i - n_o)^{\frac{3}{2}}, \quad (\text{C.6.54})$$

where  $B$  is a constant,  $W_o$  and  $W_i$  are the binding energy per nucleon in the outside and inside bulk regions,  $n_o$  and  $n_i$  are the nucleon number density

in the outside and inside bulk regions. In the case of this section, we set the fermions densities and meson fields to be zero in the outside region, i.e.  $n_o = W_o = 0$ . Since the fractional concentration of protons in the system we consider here is small, the binding energy per nucleon is (Baym et al., 1971a)

$$W(k, x) = W(k, 0) + f(x) \approx 19.74k^2 - k^3 \frac{40.4 - 1.088k^3}{1 + 2.545k} + f(x), \quad (\text{C.6.55})$$

where  $k$  is defined by  $n = 2k^3/(3\pi^2)$ , with  $n$  the nucleon number density, and  $x$  is the fractional concentration of protons. The function  $f(x)$  is a small correction to  $W(k, 0)$  since  $x$  is small in our system. From Eq. (C.6.55), one can estimate that the leading term in the binding energy  $W_i$  is the kinetic term, proportional to  $k^2$ , i.e.  $W_i \propto k^2 \propto n_{bb}^{2/3}$ . Thus one can estimate that  $\sigma_{sur}^{BBP} \propto n_{bb}^{11/6}$  in the BBP phenomenological result Baym et al. (1971a), where the effect of electromagnetic interaction on the profile of fermion density is neglected. This BBP phenomenological result is different from our result in Eq. (C.6.53). This is due to the fact that the electromagnetic interaction and the presence of electron change the proton and neutron density profiles.

For  $\sigma_C$ , as shown in Eq. (C.6.52) the surface tension for electric field is proportional to the square of the baryon number density. This results can be understood as follows. The Thomas-Fermi equilibrium condition for electrons given by Eq. (C.6.17) tell us that the Coulomb potential in the bulk core is proportional to the bulk electron chemical potential, so  $V_b \propto \mu_{eb}$ , and since the electrons are ultra-relativistic at these densities we have  $V_c \propto P_{eb}^F \propto n_{eb}^{1/3}$ . The thickness of the layer is of order  $\Delta r \sim n_{eb}^{-1/3}$  and so the electric field scales as  $E \sim -\Delta V/\Delta r \sim V_b/\Delta r \propto n_{eb}^{2/3}$ . Thus the contribution of the Coulomb energy to the surface tension satisfies  $\sigma_C \propto E^2 \Delta r \propto n_{eb}$  and since in the bulk core we have  $n_{eb} \simeq n_{pb}$  we obtain  $\sigma_C \propto n_{eb} = y n_{bb}$ , where  $y = n_{pb}/n_{bb}$  is the proton fraction in the bulk region. In neutron stars the  $\beta$ -equilibrium between neutrons, protons and electrons leads to a highly nuclear isospin asymmetry ( $y \ll 1$ ), and since the nucleons are approximately non-relativistic and the electrons ultra-relativistic around nuclear saturation density, it can be estimated from Eq. (C.6.20) that the proton fraction is proportional to the baryon density, i.e.  $y \propto n_{bb}$ , and therefore we finally obtain our final result  $\sigma_C \propto n_{bb}^2$ .

In Fig. C.50 we show also the nuclear to Coulomb surface tension ratio  $\sigma_N/\sigma_C$ . We find that this ratio is larger than unity for all baryon number densities we considered. This would in principle imply that the system is stable with respect to the Bohr-Wheeler condition (C.6.34) as we have previously discussed.

It is also worth to mention that the result that  $\sigma_N/\sigma_C > 1$  for every nucleon density in our system can be explained as the result of the penetration of the relativistic electrons into the nucleus (see Rotondo et al., 2011e,c, for details). This is allowed for a configurations with sufficiently large sizes  $r_0 A^{1/3} >$

$\hbar/(m_e c)$  or mass numbers  $A > \hbar^3/(r_0 m_e c)^3 \sim 10^7$ , where  $r_0 \approx 1.2$  fm. For systems with much larger mass numbers as neutron stars  $A_{NS} \sim 10^{57}$  the penetration of electrons is such that they nearly neutralize the system and the electric field becomes appreciable only near the core surface (Rotondo et al., 2011e,c).

However the transition layer could be unbound if the gravitational binding energy of the shell to the core is smaller than its electrostatic energy. An approximate computation of the stability of the transition layer in the above sense can be found in (Rotondo et al., 2011e), where it was shown within Newtonian gravity that the layer is gravitational bound providing the system has a number of baryons  $A \gtrsim 0.004(Z/A)^{1/2}(m_{Pl}/m_N)^3 \sim 10^{55}(Z/A)^{1/2}$  or a mass  $M = m_N A \gtrsim 0.01(Z/A)^{1/2}M_\odot$ , where  $m_N$  and  $m_{Pl} = (\hbar c/G)^{1/2}$  are the nucleon and Planck mass. It is clear that this stability requirement implies a lower limit for our globally neutral neutron stars. It would be interesting to perform a detailed calculation taking into account the effects of general relativity as well as of the magnetic field on the transition surface induced by rotation (see e.g. Boshkayev et al., 2012b) and the centrifugal potential acting on the shell. However such calculation is out of the scope of this work and will be presented elsewhere.

### Influence of fermion densities in the outside region on the surface tension

As described in (Belvedere et al., 2012) the generalized fermion chemical potentials have to match, at the end of the core-crust transition boundary layer, their corresponding values at the edge of the crust (outside region), i.e. they must satisfy a condition of continuity. This implies a non-zero particle density as matching value. The thickness of the core-crust transition boundary layer as well as the value of the electron density at the edge of the crust  $n_e^{crust}$  depend on the nuclear parameters (Belvedere et al., 2012), especially on the nuclear surface tension. So it is important to study the surface structure for different fermion densities in the outside region. The crust is composed by a nuclei lattice in a background of degenerate electrons, whose density at the edge of the crust is denoted here as  $n_e^{crust}$ . There are in addition free neutrons in the crust when the density of the crust  $\rho_{crust}$  is higher than the neutron-drip value  $\rho_{drip} \sim 4.3 \times 10^{11} \text{ g cm}^{-3}$  (Baym et al., 1971a). So when the density of the crust  $\rho_{crust}$  is smaller than the neutron-drip value, i.e.  $\rho_{crust} < \rho_{drip}$ , we set the proton and neutron densities as zero in the outside region while the electron density must to match the value  $n_e^{crust}$ . In the cases when  $\rho_{crust} > \rho_{drip}$  both neutrons and electrons have to match their corresponding crust values at the end of the core-crust transition layer. As shown by Baym et al. (1971a) there is no proton-drip at any density of interest in these systems and therefore we keep zero as outside proton density value. In order to set the matching density values for electrons and neutrons we use the relation of the free neutron and electron densities of Baym et al. (1971a). At the neutron-drip point the

electron Fermi momentum is around  $P_{eo}^F \approx 26$  MeV or  $P_{eo}^F / P_{eb}^F \approx 0.18$ .

Following a similar procedure as in Sec. C.6.2, we obtain the fermion density and meson field profiles in this case and calculate its surface tension. The results of the dependence of the surface tension on the outside electron densities and the density of the crust are shown in Fig. C.51.

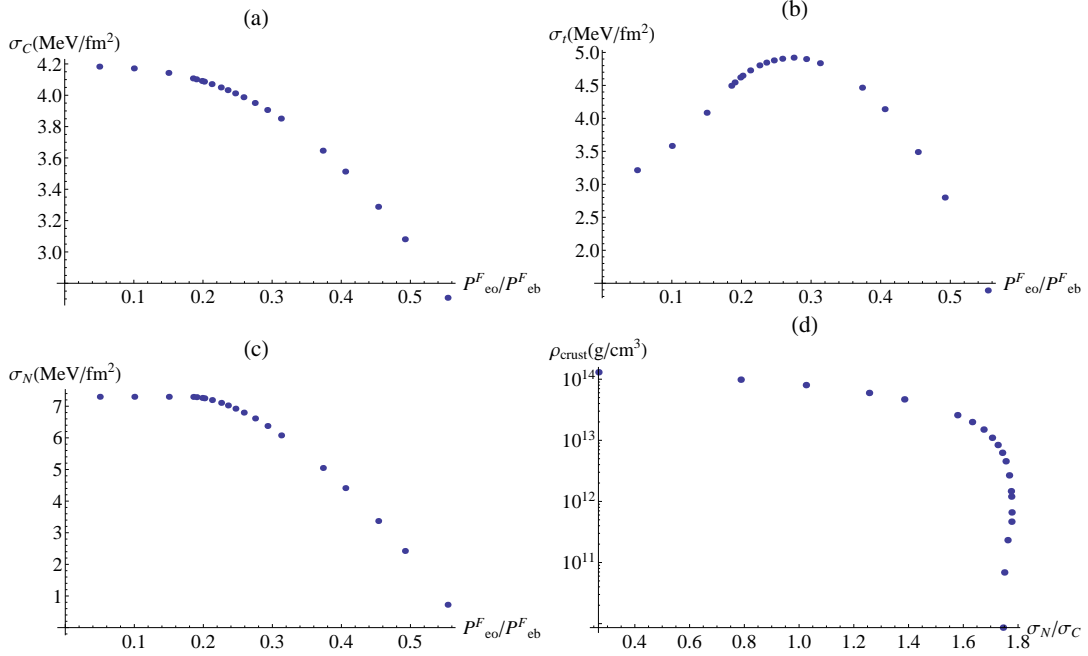


**Figure C.51.:** Dependence of the surface tension of semi-infinite matter on the fermion densities in the outside region and the density of the crust. Here the baryon number density of the bulk region is the nuclear saturation density. (a) surface tension for electric field  $\sigma_C$ . (b): the total surface tension  $\sigma_t$ . (c): the surface tension for nucleons  $\sigma_N$ . (d): ratio of the surface tension for nucleons and the surface tension for electric field  $\sigma_N / \sigma_C$ , respect to the density of the crust  $\rho_{crust}$ . The neutron-drip point  $\rho_{drip} \sim 4.3 \times 10^{11}$  g cm<sup>-3</sup> is around  $P_{eo}^F / P_{eb}^F \approx 0.18$ .

The results of Fig. C.51 show that the Bohr-Wheeler condition (C.6.34) for the instability is reached at a crust density  $\rho_{crust}^{crit} \sim 1.2 \times 10^{14}$  g cm<sup>-3</sup>, so the system becomes unstable against fission when  $\rho_{crust} > \rho_{crust}^{crit}$ ; imposing a physical upper limit to the density at the edge of the crust. It becomes interesting to include the binding effect of gravity and any other attractive contribution that strengthen the stability of the system; which will be analyzed elsewhere. It is interesting that this upper limit on the crust density implies a lower limit to the maximum electric field in the core-crust transition region, limiting at the same time to approach a state of quasi-local charge neutrality of the neutron star.

As shown in Fig. C.51, the surface tension for electric field decreases as in-

creasing the electron number density in the outside region. The reason is that the increasing electron number density in the outside region (Belvedere et al., 2012) causes a decreasing of the thickness of the interface and of the proton and electron density difference, i.e. the surface charge density decreases.

It is shown in Fig. C.51 that the dependence of the surface tension for nucleons  $\sigma_N$  on the electron number density in the outside region is weak before the neutron-drip point. The influence of electron density in the outside region on the surface structure of nucleons is small in this case. After the neutron-drip point, the free neutrons in the outside region lower the surface tension significantly, as expected in the BBP phenomenological result (Baym et al., 1971a). In addition, as shown in Fig. C.51, the total surface tension  $\sigma_t$  first increases and then decreases as increasing the fermion densities in the outside region. This is due to the combination of the following two effects. (I) as shown in Table C.8, the contribution of electrons to the total surface tension is negative. When increasing the electron density in the outside region, the effect of electrons on the surface tension becomes weaker. This increases the total surface tension. (II) After the neutron-drip point, the surface tension for nucleons  $\sigma_N$  is lowered significantly by the free neutrons in the outside region.

### C.6.3. Surface properties for neutron star matter with gravitational interaction

#### Relativistic equations

Here we add the gravitational interaction to the system we studied above. Taking into account the strong, electromagnetic, weak and gravitational interactions, the total Lagrangian density of the system is given by

$$\mathcal{L}^G = \mathcal{L}_g + \mathcal{L}_f^G + \mathcal{L}_\sigma + \mathcal{L}_\omega + \mathcal{L}_\rho + \mathcal{L}_\gamma + \mathcal{L}_{int}. \quad (\text{C.6.56})$$

Here the Lagrangian densities for the gravity is

$$\mathcal{L}_g = -\frac{R}{16\pi G}, \quad (\text{C.6.57})$$

where  $G$  is the gravitational constant, and  $R$  is the Ricci scalar. The Lagrangian density for the three fermion species in the gravity field is

$$\mathcal{L}_f^G = \sum_{i=e,N} \bar{\psi}_i (i\gamma^\mu D_\mu - m_i) \psi_i, \quad (\text{C.6.58})$$

where  $D_\mu = \partial_\mu + \Gamma_\mu$ , being  $\Gamma_\mu$  the Dirac spin connections. The other parts of the Lagrangian density in Eq. (C.6.56) have the same formulations as given in Sec. C.6.2.

We introduce the non-rotating spherically symmetric spacetime metric

$$ds^2 = e^{\nu(r)} dt^2 - e^{\lambda(r)} dr^2 - r^2 d\theta^2 - r^2 \sin^2 \theta d\varphi^2, \quad (\text{C.6.59})$$

where the  $\nu(r)$  and  $\lambda(r)$  are only functions of the radial coordinate  $r$ .

Within the Thomas-Fermi approximation and mean-field approximation, we can get the full system of general relativistic equations. We are here interested in the core-crust transition layer, which as we have shown happens in a tiny region (Belvedere et al., 2012) with a characteristic length scale  $\sim \lambda_e = \hbar/(m_e c) \sim 100$  fm. Correspondingly, the metric functions are essentially constant in this region. Thus in the core-crust transition layer the system of equations can be written as

$$\frac{d^2 V}{dr^2} + \frac{2}{r} \frac{dV}{dr} = -4\pi e e^{\nu_{core}/2} e^{\lambda_{core}} (n_p - n_e), \quad (\text{C.6.60})$$

$$\frac{d^2 \sigma}{dr^2} + \frac{2}{r} \frac{d\sigma}{dr} = e^{\lambda_{core}} [\partial_\sigma U(\sigma) + g_s n_s], \quad (\text{C.6.61})$$

$$\frac{d^2 \omega}{dr^2} + \frac{2}{r} \frac{d\omega}{dr} = -e^{\lambda_{core}} (g_\omega J_0^{\omega G} - m_\omega^2 \omega), \quad (\text{C.6.62})$$

$$\frac{d^2 \rho}{dr^2} + \frac{2}{r} \frac{d\rho}{dr} = -e^{\lambda_{core}} (g_\rho J_0^{\rho G} - m_\rho^2 \rho), \quad (\text{C.6.63})$$

$$E_e^{FG} = e^{\nu_{core}/2} \mu_e - eV = \text{constant}, \quad (\text{C.6.64})$$

$$E_p^{FG} = e^{\nu_{core}/2} \mu_p + g_\omega \omega + g_\rho \rho + eV = \text{constant}, \quad (\text{C.6.65})$$

$$E_n^{FG} = e^{\nu_{core}/2} \mu_n + g_\omega \omega - g_\rho \rho = \text{constant}, \quad (\text{C.6.66})$$

where the notation is the same as in Sec. C.6.2. In addition,  $e^{\nu_{core}} \equiv e^{\nu(r_{core})}$  and  $e^{\lambda_{core}} \equiv e^{\lambda(r_{core})}$  are the metric functions evaluated at the core radius  $r_{core}$ . The generalized Fermi energies  $E_e^{FG}$ ,  $E_p^{FG}$ , and  $E_n^{FG}$  (so-called the Klein potentials (Rueda et al., 2011)) are linked by the  $\beta$ -equilibrium of protons, neutrons, and electrons

$$E_n^{FG} = E_p^{FG} + E_e^{FG}. \quad (\text{C.6.67})$$

Within the mean-field approximation and Thomas-Fermi approximation, the scalar density  $n_s$  is the same as in the case without gravitational interaction given by Eq. (C.6.21) and the non-vanishing components of the currents are

$$J_0^{chG} = e^{\nu_{core}/2} (n_p - n_e), \quad (\text{C.6.68})$$

$$J_0^{\omega G} = e^{\nu_{core}/2} (n_n + n_p), \quad (\text{C.6.69})$$

$$J_0^{\rho G} = e^{\nu_{core}/2} (n_p - n_n). \quad (\text{C.6.70})$$

### Surface tension for semi-infinite matter

Since the core-crust transition layer has a characteristic length scale of the order of the electron Compton wavelength, this is very small compared to the radius of neutron stars. So it is a good approximation to use the semi-infinite matter model to construct the surface tension for the system with the electron density  $n_{eb}$  is approximately equal to proton density  $n_{pb}$  in bulk region.

We follow the same procedure described in Sec. C.6.2 to construct the surface tension. We assume a surface with small thickness separating two semi-infinite regions (bulk region and outside region). Also we imagine a reference system with a sharp surface at the position  $a_i$  at which the matter and meson fields fall discontinuously from the bulk region to the outside region. Following the definition of fermion number in curved space-time Eq. (C.6.59) (see e.g. Lee and Pang, 1987), the  $i$ -specie fermion number  $N_i$  is given by

$$N_i = 4\pi \int e^{\lambda/2} r^2 n_i(r) dr. \quad (\text{C.6.71})$$

Since the metric functions are constant in the surface region we consider as described in Sec. C.6.3, and the size of the surface region is very small compared to the radius of neutron stars, we can treat  $e^{\lambda/2} r^2$  as a constant in the integral, the location of the reference surfaces of fermions and meson fields have the similar expressions in Eq. (C.6.28) and Eq. (C.6.29)

$$\int_{-\infty}^{a_i} dr [n_i(r) - n_{ib}] + \int_{a_i}^{\infty} dr [n_i(r) - n_{io}] = 0; \quad i = n, p, e, \quad (\text{C.6.72})$$

$$\int_{-\infty}^{a_i} dr [F_i(r) - F_{ib}] + \int_{a_i}^{\infty} dr [F_i(r) - F_{io}] = 0; \quad i = \sigma, \omega, \rho, \quad (\text{C.6.73})$$

where  $n_i(r)$  is the number density of the  $i$ -specie fermion, and  $F_i(r)$  is the time component of the  $i$ -specie meson field.

The energy associated to the density  $\epsilon(r) = T_0^0$ , where  $T_\beta^\alpha$  is the energy-momentum tensor of the system, can be calculated in the spherically symmetric metric by (see e.g. Lee and Pang, 1987)

$$E = 4\pi \int e^{(v+\lambda)/2} r^2 \epsilon(r) dr. \quad (\text{C.6.74})$$

So we can calculate the total surface tension by

$$\begin{aligned} \sigma_t^G = & \sum_{i=n,p,e,\sigma,\omega,\rho} e^{(v_{core}+\lambda_{core})/2} \left\{ \int_{-\infty}^{a_i} [\epsilon_i^G(r) - \epsilon_{ib}^G] dr + \int_{a_i}^{\infty} [\epsilon_i^G(r) - \epsilon_{io}^G] dr \right\} \\ & + e^{(v_{core}+\lambda_{core})/2} \int_{-\infty}^{\infty} \epsilon_E^G(r) dr, \end{aligned} \quad (\text{C.6.75})$$

where  $\epsilon_i^G(r)$  is the energy density of the  $i$ -specie fermion or meson field,  $\epsilon_{ib}^G$  is the energy density of the  $i$ -specie fermion or meson field in the bulk region,  $\epsilon_{io}^G$  is the energy density of the  $i$ -specie fermion or meson field in the outside region, and  $\epsilon_E(r)^G$  is the energy density of the electric field.

For later discussions, we define the surface tension for nucleons as

$$\sigma_N^G = \sum_{i=n,p,\sigma,\omega,\rho} e^{(v_{core}+\lambda_{core})/2} \left\{ \int_{-\infty}^{a_i} [\epsilon_i^G(r) - \epsilon_{ib}^G] dr + \int_{a_i}^{\infty} [\epsilon_i^G(r) - \epsilon_{io}^G] dr \right\}, \quad (C.6.76)$$

and the surface tension for electric field as

$$\sigma_C^G = e^{(v_{core}+\lambda_{core})/2} \int_{-\infty}^{\infty} \epsilon_E^G(r) dr. \quad (C.6.77)$$

The energy density of the  $i$ -specie fermion  $\epsilon_i^G(r)$  has the same formulation as Eq. (C.6.40), and the energy densities of the meson fields are (see e.g. Lee and Pang, 1987)

$$\epsilon_\sigma^G(r) = \frac{1}{2} e^{-\lambda_{core}} \left( \frac{d\sigma}{dr} \right)^2 + U(\sigma), \quad (C.6.78)$$

$$\epsilon_\omega^G(r) = \frac{1}{2} e^{-(\lambda_{core}+v_{core})} \left( \frac{d\omega}{dr} \right)^2 + \frac{1}{2} e^{-v_{core}} m_\omega^2 \omega^2, \quad (C.6.79)$$

$$\epsilon_\rho^G(r) = \frac{1}{2} e^{-(\lambda_{core}+v_{core})} \left( \frac{d\rho}{dr} \right)^2 + \frac{1}{2} e^{-v_{core}} m_\rho^2 \rho^2, \quad (C.6.80)$$

$$\epsilon_E^G(r) = e^{-(\lambda_{core}+v_{core})} \frac{1}{8\pi} \left( \frac{dV}{dr} \right)^2. \quad (C.6.81)$$

As described in (Belvedere et al., 2012), fields vary slowly in the core of neutron stars, so it is a good approximation to treat the bulk region as the uniform matter. For the uniform matter, the equations (C.6.61)-(C.6.63) reduce to

$$0 = \partial_\sigma U(\sigma) + g_s n_s, \quad (C.6.82)$$

$$0 = g_\omega J_0^{\omega G} - m_\omega^2 \omega, \quad (C.6.83)$$

$$0 = g_\rho J_0^{\rho G} - m_\rho^2 \rho. \quad (C.6.84)$$

Following the similar procedure in Sec. C.6.2, we solve the Eqs. (C.6.60)-(C.6.66) to obtain the fermion density and meson field profiles. We assume the baryon number density in the bulk region to be the nuclear saturation density,  $n_{bb} = n_{nb} + n_{pb} = n_{nucl} = 0.16 \text{ fm}^{-3}$ . We have again assumed  $n_{pb} \simeq n_{eb}$  in the bulk (core) region, and we set the fermion densities and meson fields to be zero in the outside region for sake of comparison with the

previous results of Fig. C.48. At the core-radius (in this case the surface) of the neutron star, the metric functions have to match the Schwarzschild solution due to the global neutrality condition, so at the border of the star we have

$$e^{V_{core}} = e^{-\lambda_{core}} = 1 - \frac{2GM(r_{core})}{r_{core}}, \quad (\text{C.6.85})$$

with  $M(r_{core})$  the total mass of the star. The results of the solution are shown in Fig. C.52 for the case  $e^{\lambda_{core}} = e^{-V_{core}} = 1.5$ .

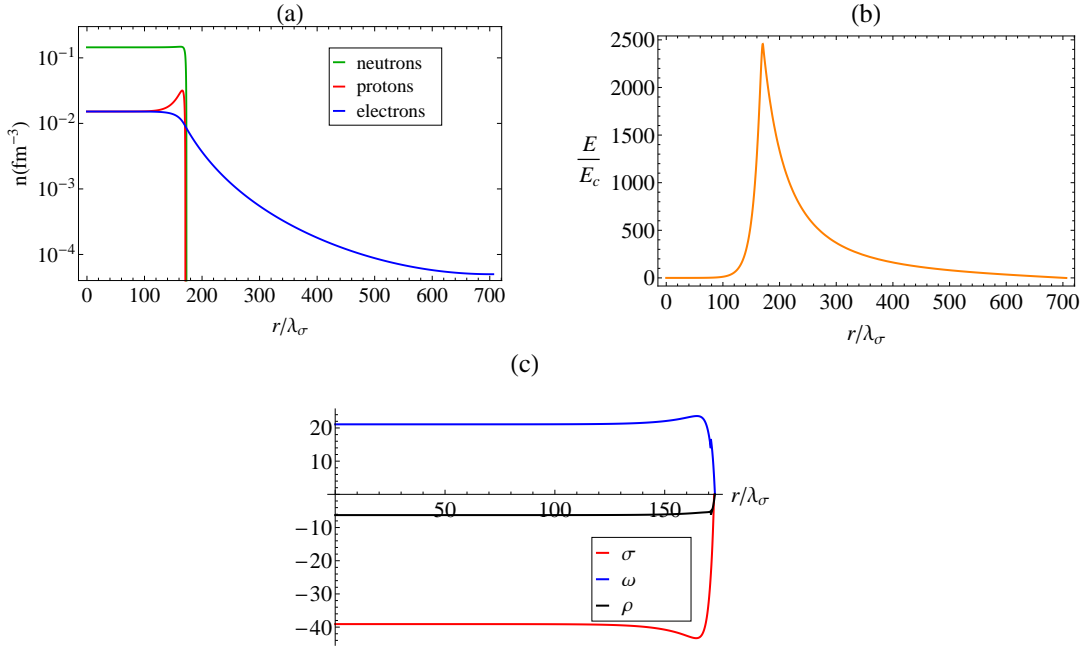


**Figure C.52.:** (a): fermion density profiles in units of  $\text{fm}^{-3}$ . (b): electric field in units of the critical field  $E_c$ . (c): meson fields  $\sigma$ ,  $\omega$ , and  $\rho$  in the unit of MeV. Here we set  $e^{\lambda_{core}} = e^{-V_{core}} = 1.5$ , the baryon number density in the bulk region is the nuclear saturation density, and the fermion densities and meson fields tend to be zero in the outside region.

In curved spacetime, the electric field is given by (see e.g. Belvedere et al., 2012)

$$|E| = e^{-(\lambda_{core} + V_{core})/2} \frac{dV}{dr}. \quad (\text{C.6.86})$$

Comparing to the results shown in Fig. C.48, the fermion density and meson field profiles are similar to their counterparts in the case without the gravitational field. In Fig. C.52 we see a larger proton density, a smaller neutron density, and a smaller size of the core-crust transition layer leading to a larger maximum of the electric field, comparing to Fig. C.48.

Using the definitions in Eqs. (C.6.75)-(C.6.77), we obtain the surface tensions for the transition layer of this system. Fig. C.53 shows the results of the

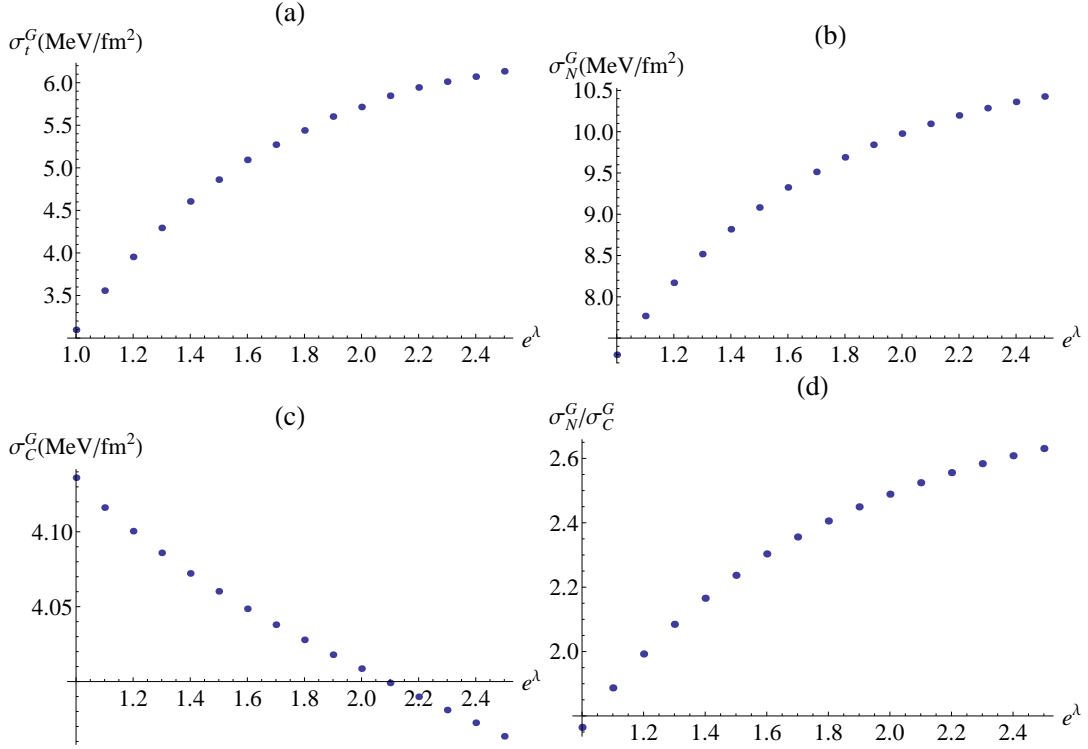


**Figure C.53.:** The dependence of the surface tension of semi-infinite matter on the value of metric  $e^{\lambda_{core}}$ . (a): the total surface tension  $\sigma_t^G$ . (b): surface tension for nucleons  $\sigma_N^G$ . (c): surface tension for electric field  $\sigma_C^G$ . (d): ratio of surface tension for nucleons and the surface tension for electric field  $\sigma_N^G/\sigma_C^G$ . Here the baryon number density in the bulk region is the nuclear saturation density, and the fermion densities and meson fields tend to be zero in the outside region.

dependence of the surface tension on the value of metric  $e^{\lambda_{core}}$ . As shown in Fig. C.53, the total surface tension and the surface tension for nucleons increase as increasing the value of the metric  $e^{\lambda_{core}}$ . As described in Sec. C.6.2, the surface tension mainly depends on the profiles of the fermion and meson densities and energy densities. There are two effects which influence on the characters of the total surface tension and the surface tension for nucleons. First, as we have seen the presence of gravitational field changes the fermion density and meson field profiles. Second, the difference between the proton density and the neutron density becomes smaller when the value of the metric  $e^{\lambda_{core}}$  increases; lowering the isospin asymmetry of the system. The combination of these two effects leads to the characters of the total surface tension and the surface tension for nucleons shown in Fig. C.53. In addition, as shown in Fig. C.53, the change of the value of the surface tension for electric field when increasing the value of  $e^{\lambda_{core}}$  is small. That is due to the balance of the following two effects: (I) the electric field in the surface region becomes larger (see Fig. C.52); (II) the thickness of the surface becomes smaller, and then the Coulomb energy distributes in a smaller region. It can be also checked from Fig. C.52 how in the limit  $e^{\lambda_{core}} \rightarrow 1$  all quantities tend to the values found in Sec. C.6.2 in the flat case.

#### C.6.4. Surface tension for the system with small electron density

Now we turn to consider a system with the electron density in the bulk region smaller than the proton one, i.e.  $n_{eb} < n_{bp}$ , to study the effects of electrons on the surface structure and surface tension. In this section we did not take into account the gravitational field. In order to construct the surface tension, we consider this system as a superheavy nucleus whose nucleon number is so large that electrons can penetrate inside the nucleus. We adopt this superheavy nucleus as a spherical droplet, so we have spherical symmetry in this system. We assume a spherical surface (the size of the system we consider here is larger than ordinary nuclei, so the curvature energy here is small compared to the surface energy) with small thickness separating one finite region (inside the nuclear region) and one semi-infinite region (outside region). The number density of the  $i$ -specie fermion  $n_i(r)$  approaches the density of the  $i$ -specie fermion  $n_{ib}$  in the origin as the position  $r \rightarrow 0$ , and approaches the density in the outside region of the  $i$ -specie fermion  $n_{io}$  as the  $r \rightarrow +\infty$ . To construct the surface tension, as in the case of the semi-infinite matter model, we imagine a reference system with a sharp surface at radius  $r_i$  at which the matter and meson fields fall discontinuously from the bulk region to the outside region. Following the similar method of Baym et al. (1971a), the location of the reference surface for the  $i$ -specie fermion is defined by the condition that the reference system has the same number of  $i$ -specie fermion

as the original system

$$4\pi \int_0^{r_i} r^2 dr [n_i(r) - n_{ib}] + 4\pi \int_{r_i}^{\infty} r^2 dr [n_i(r) - n_{io}] = 0; \quad i = n, p, e. \quad (\text{C.6.87})$$

Similar to definition of reference surface for fermions, the location of the reference surfaces for meson fields are defined by

$$4\pi \int_0^{r_i} r^2 dr [F_i(r) - F_{ib}] + 4\pi \int_{r_i}^{\infty} r^2 dr [F_i(r) - F_{io}] = 0; \quad i = \sigma, \omega, \rho, \quad (\text{C.6.88})$$

where  $F_i(r)$  is the time component of the  $i$ -specie meson field,  $F_{ib}$  is the time component of the  $i$ -specie meson field in the inside region, and  $F_{io}$  is the time component of the  $i$ -specie meson field in the outside region.

Similar to the way of Baym et al. (1971a), the surface energy can be computed as the total energy subtracting off the bulk energy,

$$E_{sur} = \sum_{i=n,p,\sigma,\omega,\rho} \left\{ 4\pi \int_0^{r_i} r^2 [\epsilon_i(r) - \epsilon_{ib}] dr + 4\pi \int_{r_i}^{\infty} r^2 [\epsilon_i(r) - \epsilon_{io}] dr \right\}, \quad (\text{C.6.89})$$

and the Coulomb energy is

$$E_{coul} = 4\pi \int_0^{\infty} r^2 \epsilon_E(r) dr, \quad (\text{C.6.90})$$

where  $\epsilon_i(r)$  is the energy density of the  $i$ -specie fermion or meson field,  $\epsilon_{ib}$  is the energy density of the  $i$ -specie fermion or meson field in the center of the system,  $\epsilon_{io}$  is the energy density of the  $i$ -specie fermion or meson field in the outside region, and  $\epsilon_E(r)$  is the energy density of the electric field. The surface tension for nucleons is given as the surface energy per unit area,

$$\sigma_{Ns} = \frac{E_{sur}}{4\pi r_n^2}, \quad (\text{C.6.91})$$

and similarly we obtain the Coulomb energy per unit area

$$\sigma_{Cs} = \frac{E_{coul}}{4\pi r_n^2}, \quad (\text{C.6.92})$$

where  $r_n$  is the reference radius of neutrons defined by Eq. (C.6.87). Since the neutron number is much larger than the proton number in the system, so it is reasonable to set the radius of neutrons to be the radius of nucleus to estimate the surface tension; this is consistent with the existence of the neutrons halo or neutron skin effect.

For this spherical system, the equations (C.6.13)-(C.6.16) become

$$\frac{d^2V}{dr^2} + \frac{2}{r} \frac{dV}{dr} = -4\pi e(n_p - n_e), \quad (\text{C.6.93})$$

$$\frac{d^2\sigma}{dr^2} + \frac{2}{r} \frac{d\sigma}{dr} = \partial_\sigma U(\sigma) + g_s n_s, \quad (\text{C.6.94})$$

$$\frac{d^2\omega}{dr^2} + \frac{2}{r} \frac{d\omega}{dr} = -(g_\omega J_0^\omega - m_\omega^2 \omega), \quad (\text{C.6.95})$$

$$\frac{d^2\rho}{dr^2} + \frac{2}{r} \frac{d\rho}{dr} = -(g_\rho J_0^\rho - m_\rho^2 \rho). \quad (\text{C.6.96})$$

The energy density of the i-specie fermion  $\epsilon_i(r)$  has the same formulation as Eq. (C.6.40), and the energy densities of the meson fields in this spherical system are

$$\epsilon_\sigma(r) = \frac{1}{2} \left( \frac{d\sigma}{dr} \right)^2 + U(\sigma), \quad (\text{C.6.97})$$

$$\epsilon_\omega(r) = \frac{1}{2} \left( \frac{d\omega}{dr} \right)^2 + \frac{1}{2} m_\omega^2 \omega^2, \quad (\text{C.6.98})$$

$$\epsilon_\rho(r) = \frac{1}{2} \left( \frac{d\rho}{dr} \right)^2 + \frac{1}{2} m_\rho^2 \rho^2, \quad (\text{C.6.99})$$

$$\epsilon_E(r) = \frac{1}{8\pi} \left( \frac{dV}{dr} \right)^2. \quad (\text{C.6.100})$$

Following the similar procedure in Sec. C.6.2, we solve the equations (C.6.93)-(C.6.96) and (C.6.17)-(C.6.19) to obtain the fermion density and meson field profiles. We assume the baryon number density in the region near the center to be the nuclear saturation density,  $n_{bb} = n_{nb} + n_{pb} = n_{nucl} = 0.16 \text{ fm}^{-3}$ , and we set a small electron density  $n_{eb} = y_e n_{pb}$  in the region near the center with electron fraction  $y_e < 1$ . We set the fermion densities and meson fields to be zero in the outside region. The results of the solution are shown in Fig. C.54 for the case  $P_e^F = 0.95 P_p^F$  in the region near the center of the system, and in Fig. C.55 for the case  $P_e^F = 0.5 P_p^F$  in the region near the center of the system.

As shown in Fig. C.54, when the difference between the electron and proton density in the region near the center of the system ( $n_{pb} - n_{eb}$ ) is small, the fermion density and meson field profiles are similar to their counterparts in the case of semi-infinite matter (electron density nearly equal to the proton density in the bulk region  $n_{eb} \simeq n_{pb}$ ). Comparing to the results in the case of semi-infinite matter in Fig. C.48, the bump of the proton profile is larger in this case, as expected from the fact that the internal electric field is less screened in this case than when  $n_{eb} \simeq n_{pb}$ . We can also see how the fermion and meson field profiles change for increasing charge separations  $n_{pb} - n_{eb}$ .

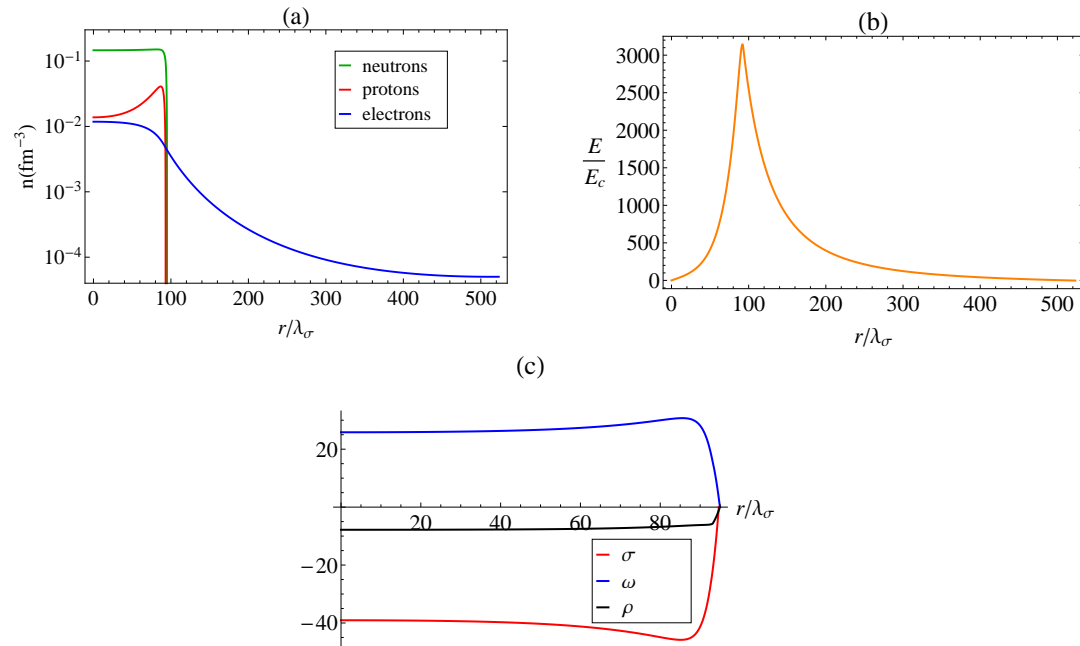


**Figure C.54.:** (a): fermion density profiles in units of  $\text{fm}^{-3}$ . (b): electric field in units of the critical field  $E_c$ . (c): meson fields  $\sigma$ ,  $\omega$ , and  $\rho$  in the unit of MeV. Here we set  $P_e^F = 0.95P_p^F$  in the region near the center of the system, the baryon number density in the region near the center is the nuclear saturation density, and the fermion densities and meson fields tend to be zero in the outside region.

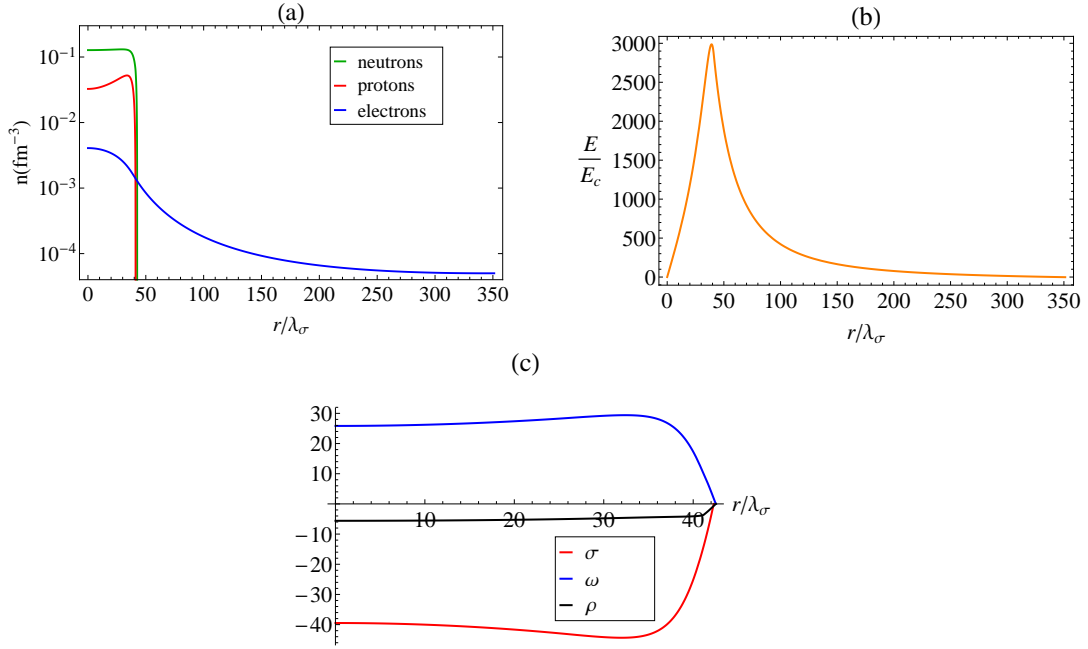


**Figure C.55.:** (a): fermion density profiles in units of  $\text{fm}^{-3}$ . (b): electric field in units of the critical field  $E_c$ . (c): meson fields  $\sigma$ ,  $\omega$ , and  $\rho$  in the unit of MeV. Here we set  $P_e^F = 0.5P_p^F$  in the region near the center of the system, the baryon number density in the region near the center is the nuclear saturation density, and the fermions densities and meson fields tend to be zero in the outside region.

Using the definitions in Eqs. (C.6.91) and (C.6.92), we obtain the surface tensions for the transition layer of this system. The results of the dependence of the surface tension on the ratio of the electron Fermi momentum and the proton Fermi momentum in the region near the center of the system ( $P_{eb}^F/P_{pb}^F$ ) are shown in Fig. C.56. From the results, the system is stable with respect to the Bohr-Wheeler condition Eq. (C.6.34) of the stability, in all ratios  $P_{eb}^F/P_{pb}^F$  we considered. As shown in Fig. C.56, the surface tension for nucleons first increases and then decreases when the difference between the electron and proton density increases, and the surface tension tends to the phenomenological result ( $\sim 1 \text{ MeV fm}^{-2}$ ) in nuclear physics without the presence of electrons in the inside bulk region (Baym et al., 1971a). There are two effects which influence on the surface tension for nucleons: (I) for  $n_{eb} < n_{pb}$  the bump of the proton profile around the nuclear surface enhances as shown in Figs. C.54–C.55, and (II) the higher the difference  $n_{pb} - n_{eb}$  the lower the nuclear asymmetry. As a consequence, the total energy of the system decreases. The combination of these two effects leads to the results of the surface tension for nucleons shown in Fig. C.56.

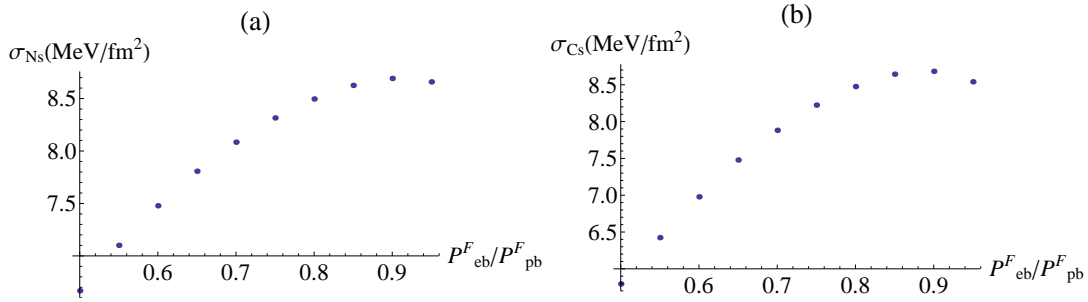


**Figure C.56.:** The dependence of the surface tension on the ratio  $P_{eb}^F/P_{pb}^F$ .  $P_{eb}^F$  is the Fermi momentum of electrons in the region near the center of the system, and  $P_{pb}^F$  is the Fermi momentum of protons in the region near the center of the system. The baryon number density in the region near the center is the nuclear saturation density, and the fermion densities and meson fields tend to be zero in the outside region. (a): surface tension for nucleons,  $\sigma_{Ns}$ . (b): Coulomb energy per unit area,  $\sigma_{Cs}$ .

### C.6.5. Summary

Taking into account strong, weak, electromagnetic, and gravitational interactions, and fulfilling the global charge neutrality of the system, a transition layer will happen between the core and crust of neutron stars (Belvedere et al., 2012). This is different from the results from traditional TOV equations imposing local charge neutrality. This core-crust transition layer happens at the saturation density of nuclear matter. In this article, using RMFT

together with the Thomas-Fermi approximation, we give a detailed description of the structure of this transition layer. We computed the surface tension and Coulomb energy of the transition shell and analyze the role of each fermion component and meson fields in the determination of the properties of this core-crust transition layer.

Following the method of Baym et al. (1971a), we applied the semi-infinite matter model to construct the surface tension for the transition layer of this system with the electron density is approximately equal to the proton density in the bulk region. The results show that, in the surface region, a proton bump appears due to Coulomb repulsion. The neutron skin effect and electron screening effect are described in detail. We calculated the surface tension and the Coulomb energy for the transition layer of this system for different baryon number densities near the nuclear saturation density. The results show that the total surface tension as well as surface tension for electric field and the surface tension for nucleons are proportional to some power-law function of the baryon number density in the bulk region; see Eqs. (C.6.51), (C.6.53) and (C.6.52). The difference between the surface energy of this neutron star matter and the phenomenological results (Baym et al., 1971a) in nuclear physics has been analyzed. We also studied the surface structure for different fermion densities in the outside region, namely for different densities of the neutron star crust.

We presented this analysis both in flat and curved spacetime. In the latter case we treated the system in the background of non-rotating spherically symmetric case as in (Belvedere et al., 2012). Since the length scale (the order of the electron Compton wavelength) of the core-crust transition layer is much smaller than the radius of neutron stars, we used the semi-infinite matter model as an approximation to construct the surface tension for the transition layer of this system with the electron density is approximately equal to the proton density in the bulk region. The results show that the fermion density and meson field profiles are similar to the case without the presence of gravitational field, although some quantitative differences appear. We show that the total surface tension and the surface tension for nucleons increase as increasing the value of the metric function  $e^{\lambda_{core}}$ .

We then calculated the surface tension and the Coulomb energy for the transition layer of the system with the electron density is smaller than the proton density in the bulk region using the spherical droplet model. We show how the surface tension and the electrostatic energy per unit area are drastically affected by the increasing proton repulsion and decreasing nuclear asymmetry with a decreasing electron to proton density ratio (see Figs. C.54, C.55 and C.56).

We studied the instability against Bohr-Wheeler surface deformation for all the systems. We find that the instability sets in at a critical density of the crust  $\rho_{crust}^{crit} \sim 1.2 \times 10^{14} \text{ g cm}^{-3}$ . This implies a lower limit to the maximum electric field of the core-crust transition region and makes inaccessible a state

of quasi-local charge neutrality for the neutron star, which will in principle be reached when the limit  $\rho_{crust} = \rho_{core} \approx \rho_{nuc}$ , is approached.

The results of this work open the way to more general studies relevant for the analysis of the stability of neutron stars and the core-crust transition surface. Some of the effects that need to be addressed for the stability of the shell include gravitational binding, centrifugal repulsion, magnetic field induced by rotating electric field and hence magnetic dipole-dipole interactions. It would be interesting to perform a similar analysis for the case of strange stars both bare and in presence of outer crust.

As pointed out in (Sotani et al., 2012), the frequencies of shear oscillations due to the hadron-quark mixed phase in neutron stars depend strongly on the surface tension of the hadron-quark interface. It would be interesting to perform a analysis for the dependence of the surface waves on the surface tension of the core-crust transition surface.

## C.7. On the cooling of globally neutral neutron stars

In our previous work Belvedere et al. (2012), we developed a new model of neutron star fulfilling global and not local charge neutrality. We showed that the equilibrium equations of this new treatment supersede the traditional ones based on the Tolman-Oppenheimer-Volkoff (TOV) system of equations, which obeys local charge neutrality. The new coupled system equations, what we called Einstein-Maxwell-Thomas-Fermi (EMTF) equations, introduces self-consistently the presence of the electromagnetic interactions in addition to the nuclear, weak, and gravitational interactions within the framework of general relativity. The weak interactions are accounted for by requesting the  $\beta$ -stability, and the strong interactions are modeled via the  $\sigma$ - $\omega$ - $\rho$  nuclear model, where  $\sigma$ ,  $\omega$  and  $\rho$  are the mediator massive vector mesons. In this work we use the NL3 parameterization of this nuclear model (see Ref. Belvedere et al. (2012) for more details). In the supranuclear core is composed by a degenerate gas of neutrons, protons, and electrons in  $\beta$ -equilibrium. The crust in its outer region  $\rho \leq \rho_{\text{drip}} \approx 4.3 \times 10^{11} \text{ g cm}^{-3}$  is composed ions and electrons and in its inner region, at  $\rho_{\text{drip}} < \rho < \rho_{\text{nuc}}$ , where  $\rho_{\text{nuc}} \approx 2.7 \times 10^{14} \text{ g cm}^{-3}$  is the nuclear saturation density, there is an additional component of free neutrons dripped out from nuclei.

The solution of the EMTF equations of equilibrium leads to a new structure of the neutron stars very different from the traditional configurations obtained through the TOV equations: the core is positively charged as a consequence of the balance between gravitational and Coulomb forces that results in the appearance of a Coulomb potential energy  $eV \sim m_{\pi}c^2$  deep. The core-crust transition starts at  $\rho = \rho_{\text{nuc}}$ . The transition is marked by the existence of a thin,  $\Delta r \sim \text{few hundreds fm}$ , electron layer fully screening the core charge. In this transition layer the electric field becomes overcritical,  $E \sim m_{\pi}^2 c^3 / (e\hbar)$ , and the particle densities decrease until the base of the crust, which is reached when global charge neutrality is achieved. Consequently, the core is matched to the crust at a density  $\rho_{\text{crust}} \leq \rho_{\text{nuc}}$ . In the limit  $\rho_{\text{crust}} \rightarrow \rho_{\text{nuc}}$ , both  $\Delta r$  and  $E$  of the transition layer vanish, and the solution approaches the one given by local charge neutrality (see Figs. 3 and 5 in Belvedere et al. (2012)).

Configurations with  $\rho_{\text{crust}} > \rho_{\text{drip}}$  possess both inner and outer crust while in the cases with  $\rho_{\text{crust}} \leq \rho_{\text{drip}}$  the neutron star have only outer crust. All the above features lead to a new mass-radius relation of neutron stars; see Belvedere et al. (2012) and Fig. C.57.

The aim of this work is to compute the thermal evolution of globally neutral neutron stars. Here we focus on the cooling curves in the stage of evolution where the thermal structure of the neutron star can be considered as formed by a large isothermal core and an insulating thin radiative envelope at the bottom layers. As we will see, this stage of the evolution is appropriate

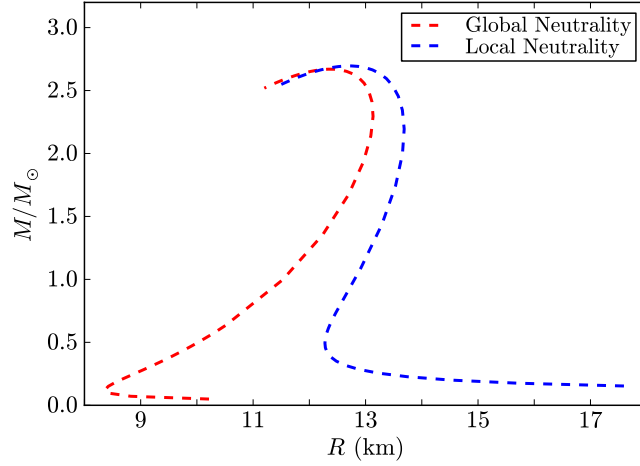


**Figure C.57.:** Mass-radius relation obtained with the traditional locally neutral TOV treatment case and the global charge neutrality configurations, with  $\rho_{\text{crust}} = \rho_{\text{drip}}$  Belvedere et al. (2012). Configurations lying between the red and blue curves possess inner crust.

to describe the thermal evolution of the isolated neutron stars for which observational data is available. We use geometric units  $G = c = 1$  throughout.

### C.7.1. Thermal evolution equations

The general relativistic equations of thermal evolution are energy balance and the energy transport equations which for a spherically symmetric star read

$$\frac{\partial(Le^\nu)}{\partial r} = -\frac{4\pi r^2}{\sqrt{1-2m/r}} \left[ \epsilon_\nu e^\nu + c_\nu \frac{\partial(Te^{\nu/2})}{\partial t} \right], \quad (\text{C.7.1})$$

$$\frac{Le^\nu}{4\pi r^2 \kappa} = \sqrt{1-2m/r} \frac{\partial(Te^{\nu/2})}{\partial r}, \quad (\text{C.7.2})$$

where  $\epsilon_\nu$  is the neutrino emissivity,  $c_\nu$  is the heat capacity per unit volume,  $\kappa$  is the thermal conductivity,  $T(r, t)$  is the interior temperature,  $L(r, t)$  is the radiation luminosity,  $m$  is the mass enclosed within a radius  $r$ , and  $\nu = \ln g_{00}$ , with  $g_{00}$  the 0–0 component of the metric.

We have two boundary conditions required by the equations C.7.1 and C.7.2, one for the center  $L(r = 0) = 0$  and another one for the surface  $T(r = R) = T_s$  Yakovlev and Pethick (2004b).

We included all the relevant processes of neutrino emission: in the core we consider the direct and modified Urca processes, neutron-neutron (nn), proton-proton (pp) and neutron-proton (np) Bremsstrahlung. In the crust we have plasmon decay,  $e^-e^+$  pair annihilation, electron-nucleus and nucleon-nucleon Bremsstrahlung. The heat capacity is due to by electrons, protons and neu-

trons in the core and by electrons and ions in the crust. The thermal conductivity in the core is given mainly by electrons and neutrons and in the crust is the result of the scattering of electrons with atomic nuclei Gnedin et al. (2001).

### C.7.2. General relativistic isothermality

Most of the available observational data on the surface temperature of isolated neutron stars correspond to middle-ages,  $t \sim 10^4$ – $10^6$  yr, see e.g. Yakovlev and Pethick (2004b). By that times, the neutron star has already passed the thermal relaxation phase following the neutron star birth. In such a phase the crust stays hotter than the core and so heat flows from the crust to the core as a cooling wave that expands from the center outward. The thermal relaxation epoch ends when this cooling wave reaches the surface. The temperature gradient between the core and the crust vanishes and the thermal structure of the neutron star can be described as formed by an isothermal core and a thin insulating envelope without any sink of energy and from where photons scape. The isothermal core extends from the center up to a boundary layer at density  $\rho_b \approx 10^{10}$  g cm<sup>-3</sup> Gudmundsson et al. (1983), and the envelope is found at the lower density layers and where large temperature gradients exist.

In the isothermal core, the energy balance and transport equations (C.7.1) and (C.7.2) become

$$\epsilon_\nu e^\nu + c_\nu \frac{\partial(Te^{\nu/2})}{\partial t} = 0, \quad \frac{\partial e^{\nu/2} T}{\partial r} = 0. \quad (\text{C.7.3})$$

### C.7.3. Occurrence of the direct Urca process

The direct Urca process,  $n \rightarrow p + e + \bar{\nu}_e$  and  $p + e \rightarrow n + \nu_e$ , is possible in neutron star cores only if the fraction of particles involved in the reaction are such that the energy and momentum can be conserved simultaneously. The process is then possible if the triangle inequality,  $P_n^F < P_p^F + P_e^F$ , is satisfied, where  $P_{n,p,e}^F$  are the Fermi momenta of neutrons, protons, and electrons, respectively.

We computed the region in the core of the globally neutral neutron stars shown in Fig. C.57 where the direct Urca process occurs. In Fig. C.58 we show the size and mass fraction of the neutron star core where the process occurs as a function of the total mass of the star.

### C.7.4. Cooling curves

The thermal relaxation epoch in which the isothermal core with temperature  $T_b$  is developed is of the order of  $\Delta t \lesssim 100$  yr (see e.g. Gnedin et al. (2001)),

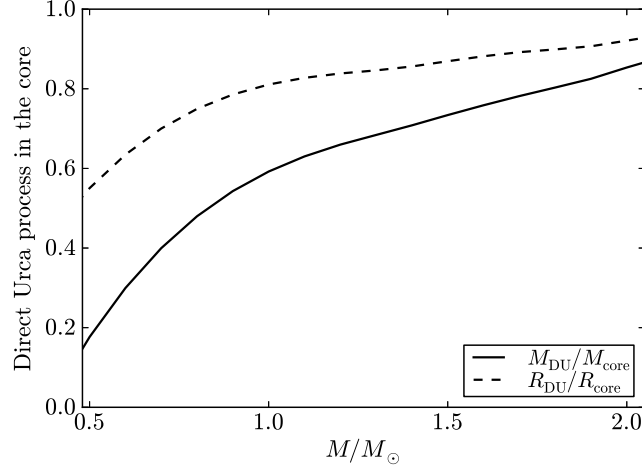


**Figure C.58.:** Fraction of the mass and size of the core of a globally neutral neutron star where the direct Urca process occurs.

a time well within the ages of the observed isolated neutron stars,  $t \sim 10^4$ – $10^6$  yr. Therefore, lacking observational data at the early phases, we can start our thermal evolution from the point where the star already has reached the isothermality, so without need considering the relaxation phase.

We computed the cooling curves by integrating numerically Eq. (C.7.3) with initial condition the temperature  $T_b$ . The surface temperature is calculated using the results by Gudmundsson et al. (1983), which obtained a relation between the surface temperature  $T_s$  and  $T_b$ ,

$$T_b = 1.288 \times 10^8 \left( \frac{T_{s6}^4}{g_{s14}} \right)^{0.455} \text{ K}, \quad (\text{C.7.4})$$

where  $T_{s6}$  is the surface temperature in units of  $10^6$  K and  $g_{s14}$  is the surface gravity,  $g = (GM/R^2)\sqrt{1 - 2M/R}$ , in units of  $10^{14} \text{ cm s}^{-2}$ , with  $M$  and  $R$  the total mass and radius of the neutron star.

In the following we show our results for the surface temperature as observed at infinity,

$$T_s^\infty = e^{\nu(R)/2} T_s = \sqrt{1 - \frac{2M}{R}} T_s. \quad (\text{C.7.5})$$

In Fig. C.59 we show the surface temperature  $T_s$  as a function of the time  $t$  for a global neutrality neutron star with and without considering the occurrence of the direct Urca process in the core. It can be seen that when active, the direct Urca reactions make the star to cool faster with respect to the case when they are absent. The reason for this is that this process has  $\epsilon_\nu \propto T^6$  while the other processes have  $\epsilon_\nu \propto T^8$ , which leads via Eq. (C.7.3) to  $T \propto t^{-1/4}$  and  $\propto t^{-1/6}$  respectively.

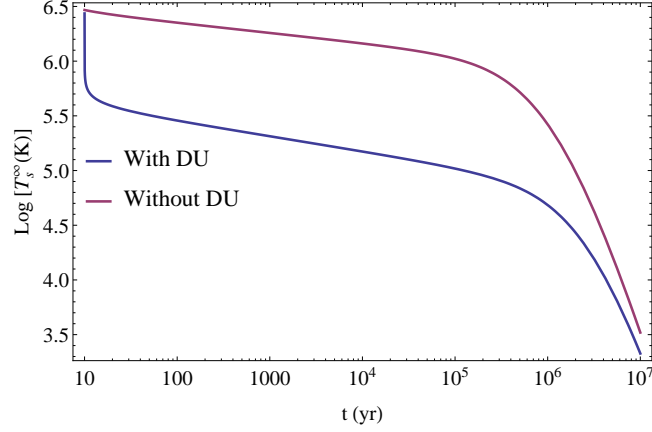


**Figure C.59.:** Surface temperature at infinity  $T_s^\infty$  as a function of time  $t$  in yr with (blue curve) and without (red curve) considering Direct Urca process (DU).

We show in Fig. C.60 the cooling curves for selected neutron star masses, for  $1.4 M_\odot$  and  $2.0 M_\odot$ , at the same central temperature, while Fig. C.61 shows the evolution of a neutron star with  $1.4 M_\odot$  for two different central temperature,  $T = 3 \times 10^9$  K and  $T = 5 \times 10^9$  K. We contrast our theoretical curves with some isolated neutron stars observational data taken from Ref. Yakovlev and Pethick (2004b).

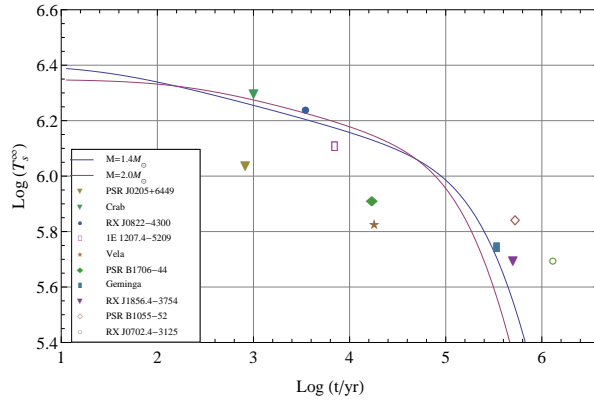


**Figure C.60.:** Surface temperature at infinity  $T_s^\infty$  as a function of time  $t$  in yr for two neutron star with selected masses,  $1.4 M_\odot$  and  $2.0 M_\odot$ , at the same central temperature  $T = 3 \times 10^9$  K.

### C.7.5. Conclusions

We calculated the thermal evolution of globally neutral neutron stars in the isothermal stage of their evolution, which follows the thermal relaxation phase.

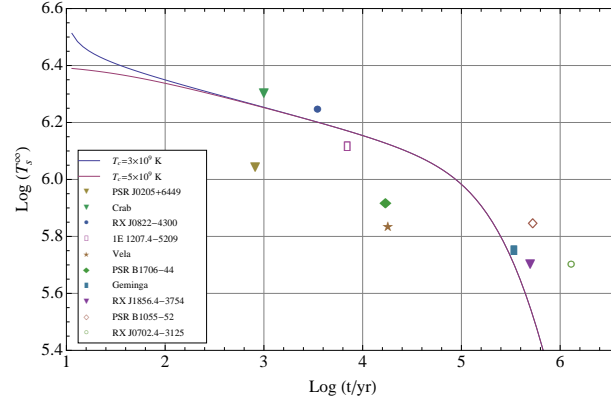


**Figure C.61.:** Surface temperature at infinity  $T_s^\infty$  as a function of time  $t$  for neutron star with selected central temperatures  $T = 3 \times 10^9$  K and  $T = 5 \times 10^9$  K, and mass  $1.4 M_\odot$ .

We contrast the cooling curves with some observational data of middle-ages isolated neutron stars. We computed the fraction of the core where the direct Urca process is active for the case of the NL3 parameterization of the  $\sigma$ - $\omega$ - $\rho$  nuclear model. This work is a first step towards the full calculation of the thermal evolution considering the early phases where the star is far from isothermality, which reveals crucial information from the properties of the crust of the neutron star.

## C.8. Thermal evolution of neutron stars: global and local charge neutrality cases

In recent works Rotondo et al. (2011d); Rueda et al. (2011); Belvedere et al. (2012), we developed a new model of neutron star fulfilling global but not local charge neutrality. We showed that the equilibrium equations of this new treatment supersede the traditional ones based on the Tolman-Oppenheimer-Volkoff (TOV) system of equations, which obeys local charge neutrality. The new coupled system equations, what we called Einstein-Maxwell-Thomas-Fermi (EMTF) equations, introduces self-consistently the presence of the electromagnetic interactions in addition to the nuclear, weak, and gravitational interactions within the framework of general relativity. The weak interactions are accounted for by requesting the  $\beta$ -stability, and the strong interactions are modeled via the  $\sigma$ - $\omega$ - $\rho$  nuclear model, where  $\sigma$ ,  $\omega$  and  $\rho$  are the mediator massive vector mesons. In this work we use the NL3 parameterization of this nuclear model (see Ref. Belvedere et al. (2012) for more details). In the supranuclear core is composed by a degenerate gas of neutrons, protons, and electrons in  $\beta$ -equilibrium. The crust in its outer region  $\rho \leq \rho_{\text{drip}} \approx 4.3 \times 10^{11} \text{ g cm}^{-3}$  is composed ions and electrons and in its inner region, at  $\rho_{\text{drip}} < \rho < \rho_{\text{nuc}}$ , where  $\rho_{\text{nuc}} \approx 2.7 \times 10^{14} \text{ g cm}^{-3}$  is the nuclear saturation density, there is an additional component of free neutrons dripped out from nuclei.

The solution of the EMTF equations of equilibrium leads to a new structure of the neutron stars very different from the traditional configurations obtained through the TOV equations (see Fig. C.62): the core is positively charged as a consequence of the balance between gravitational and Coulomb forces that results in the appearance of a Coulomb potential energy  $eV \sim m_{\pi}c^2$  deep. The core-crust transition starts at  $\rho = \rho_{\text{nuc}}$ . The transition is marked by the existence of a thin,  $\Delta r \sim \text{few hundreds fm}$ , electron layer fully screening the core charge. In this transition layer the electric field becomes overcritical,  $E \sim m_{\pi}^2c^3/(e\hbar)$ , and the particle densities decrease until the base of the crust, which is reached when global charge neutrality is achieved. Consequently, the core is matched to the crust at a density  $\rho_{\text{crust}} \leq \rho_{\text{nuc}}$ .

Configurations with  $\rho_{\text{crust}} > \rho_{\text{drip}}$  possess both inner and outer crust while in the cases with  $\rho_{\text{crust}} \leq \rho_{\text{drip}}$  the neutron star have only outer crust. In the limit  $\rho_{\text{crust}} \rightarrow \rho_{\text{nuc}}$ , both  $\Delta r$  and  $E$  of the transition layer vanish, and the solution approaches the one given by local charge neutrality (see Figs. 3 and 5 in Belvedere et al. (2012)). All the above features lead to a new mass-radius relation of neutron stars; see Belvedere et al. (2012) and Fig. C.63.

The aim of this work is to compute the thermal evolution of globally neutral neutron stars with and without inner crust, all the way up to approach the limit when  $\rho_{\text{crust}} \leq \rho_{\text{nuc}}$ , which corresponds to TOV-like solutions satisfying local charge neutrality. We use geometric units  $G = c = 1$  throughout.

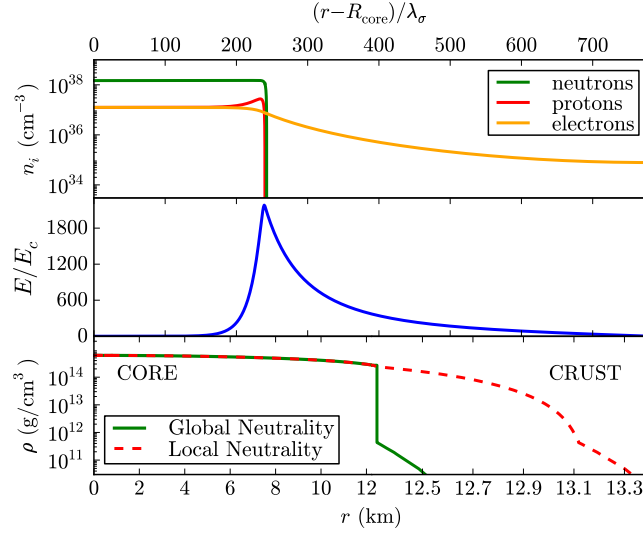


**Figure C.62.:** In the top and center panels we show the neutron, proton, electron densities and the electric field in units of the critical electric field  $E_c$  in the core-crust transition layer, whereas in the bottom panel we show a specific example of a density profile inside a neutron star. In this plot we have used for the globally neutral case a density at the edge of the crust equal to the neutron drip density,  $\rho_{\text{drip}} \approx 4.3 \times 10^{11} \text{ g cm}^{-3}$ .  $\lambda_\sigma = \hbar/(m_\sigma c) \sim 0.4 \text{ fm}$  denotes the  $\sigma$ -meson Compton wavelength.

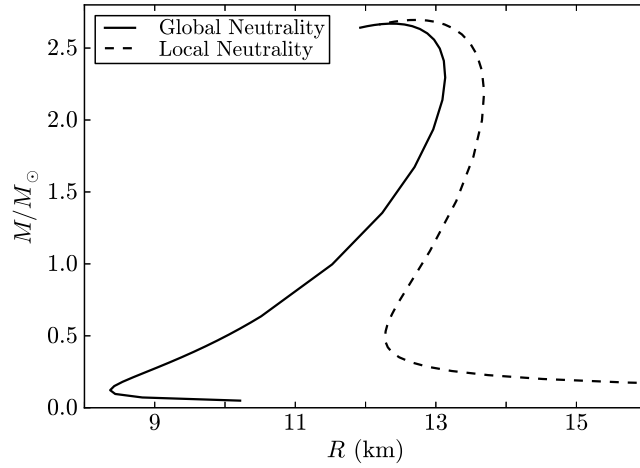


**Figure C.63.:** Mass-radius relation obtained with the traditional locally neutral TOV treatment case and the global charge neutrality configurations, with  $\rho_{\text{crust}} = \rho_{\text{drip}}$  Belvedere et al. (2012). Configurations lying between the solid and dashed curves have  $\rho_{\text{crust}} > \rho_{\text{drip}}$  and so they possess inner crust.

### C.8.1. Thermal evolution equations

For a spherically symmetric spacetime appropriate for non-rotating neutron stars

$$ds^2 = e^{\nu(r)} dt^2 - e^{\lambda(r)} dr^2 - r^2 d\theta^2 - r^2 \sin^2 \theta d\varphi^2, \quad (\text{C.8.1})$$

the general relativistic equations of energy balance and energy transport for the description of the thermal evolution read (see e.g. Thorne (1977))

$$\frac{\partial(Le^\nu)}{\partial r} = -\frac{4\pi r^2}{\sqrt{1-2m/r}} \left[ \epsilon_\nu e^\nu + c_\nu \frac{\partial(Te^{\nu/2})}{\partial t} \right], \quad (\text{C.8.2})$$

$$\frac{Le^\nu}{4\pi r^2 \kappa} = \sqrt{1-2m/r} \frac{\partial(Te^{\nu/2})}{\partial r}. \quad (\text{C.8.3})$$

Eqs. (C.8.2–C.8.3) depend on the structure of the star through the variables  $r$ ,  $\rho(r)$ ,  $m(r)$ , and  $\nu(r)$  that represent the radial distance, the energy density, the mass function, and the general relativistic gravitational potential, respectively. The thermal variables are represented by the interior temperature  $T(r, t)$ , the radiation luminosity  $L(r, t)$ , neutrino emissivity  $\epsilon_\nu(r, T)$ , thermal conductivity  $\kappa(r, T)$  and specific heat per unit volume  $c_\nu(r, T)$ .

The boundary conditions of Eqs. (C.8.2–C.8.3) are determined by the luminosity at the center and at the surface. The luminosity vanishes at the stellar center, i.e.  $L(r = 0) = 0$ , since at this point the heat flux is zero. At the surface, the luminosity is defined by the relationship between the mantle temperature, which we denote to as  $T_b$ , and the temperature outside of the star,  $T(r = R) = T_s$ .

We included all the relevant process of neutrino emission: in the core we consider the direct and modified Urca processes, neutron-neutron (nn), proton-proton (pp) and neutron-proton (np) Bremsstrahlung. In the crust we have plasmon decay,  $e^- e^+$  pair annihilation, electron-nucleus and nucleon-nucleon Bremsstrahlung. The heat capacity is due to by electrons, protons and neutrons in the core and by electrons and ions in the crust. The thermal conductivity in the core is given mainly by electrons and neutrons and in the crust is the result of the scattering of electrons with atomic nuclei Gnedin et al. (2001).

### C.8.2. Cooling curves and relaxation time

The thermal relaxation epoch in which the isothermal core with temperature  $T_b$  is developed is of the order of  $\Delta t \lesssim 100$  yr (see e.g. Gnedin et al. (2001)), a time well within the ages of the observed isolated neutron stars,  $t \sim 10^4$ – $10^6$  yr. Therefore, lacking observational data at the early phases, we can start our thermal evolution from the point where the star already has reached the isothermality, so without need considering the relaxation phase.

We computed the cooling curves by integrating numerically Eqs. (C.8.2–

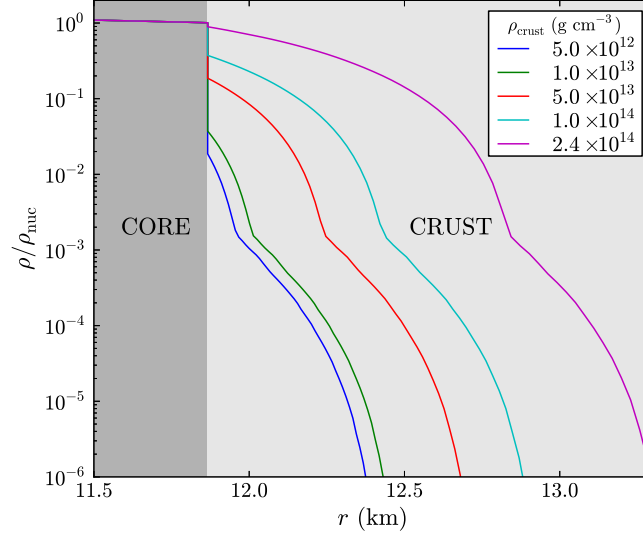


**Figure C.64.:** Density profiles of globally neutral neutron star with mass  $M \approx 1.4 M_{\odot}$  for selected values of the density at the base of the crust,  $\rho_{\text{crust}}$ . Notice that the transition to the crust occurs at the nuclear saturation density,  $\rho_{\text{nuc}}$ .

C.8.3). The surface temperature is calculated using the results by Gudmundsson et al. (1983), which obtained a relation between the surface temperature  $T_s$  and  $T_b$ ,

$$T_b = 1.288 \times 10^8 \left( \frac{T_{s6}^4}{g_{s14}} \right)^{0.455} \text{ K}, \quad (\text{C.8.4})$$

where  $T_{s6}$  is the surface temperature in units of  $10^6$  K and  $g_{s14}$  is the surface gravity,  $g = (GM/R^2)\sqrt{1 - 2M/R}$ , in units of  $10^{14} \text{ cm s}^{-2}$ , with  $M$  and  $R$  the total mass and radius of the neutron star.

In the following we show our results for the surface temperature as observed at infinity,  $T_s^{\infty} = e^{\nu(R)/2} T_s$  where  $e^{\nu(R)/2} = \sqrt{1 - 2M/R}$ . We computed the full cooling curves for a globally neutral neutron star with mass  $1.4 M_{\odot}$  for selected values of  $\rho_{\text{crust}}$ .

In Fig. C.65 we show the surface temperature at infinity,  $T_s^{\infty}$ , as a function of time  $t$  in yr for the neutron star configurations shown in Fig. C.64. In Fig. C.66 we show the temperature at the base of the crust as a function of  $t$  for the same configurations. The Fig. C.67 is an enlargement of Fig. C.65 around the temperature drop at the end of the thermal relaxation phase.

We can see in this figure that the time to the temperature drop is different for the star with densities higher and lower than  $5 \times 10^{13} \text{ g cm}^{-3}$ . For stars with  $\rho \lesssim 5 \times 10^{13} \text{ g cm}^{-3}$ , the thicker the crust the shorter relaxation time, while for  $\rho > 5 \times 10^{13} \text{ g cm}^{-3}$ , the thicker the crust the longer the relaxation time. The latter behavior is in agreement with the results by Lattimer et al. (1994), while the former is in clear contrast. The reason for this is that in

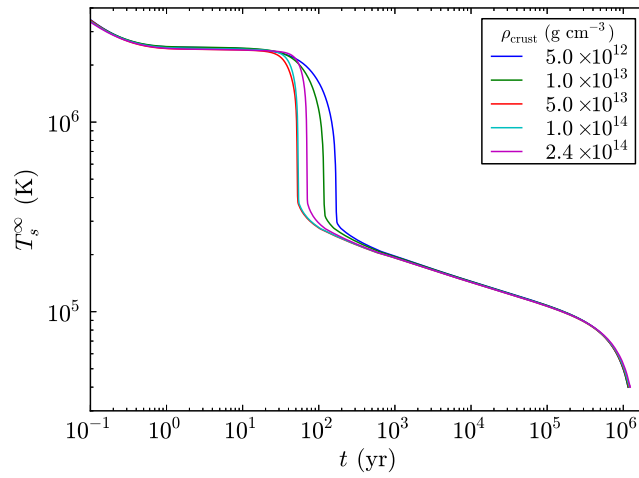


**Figure C.65.:** Surface temperature at infinity  $T_s^\infty$  as a function of time  $t$  in yr for the neutron star configurations shown in Fig. C.64.

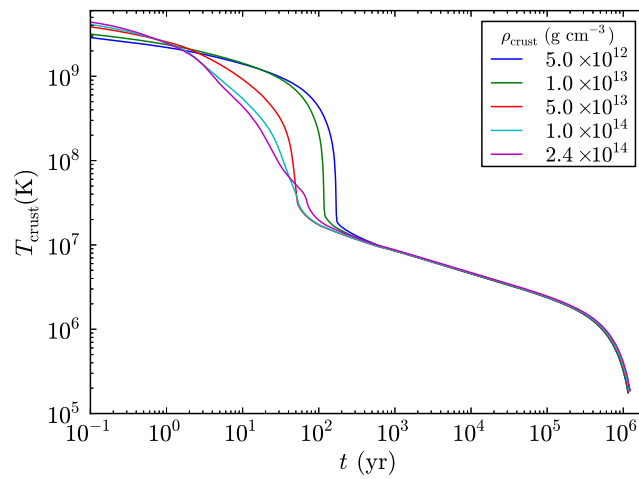


**Figure C.66.:** Temperature at the base of the crust as a function of time  $t$  in yr for the neutron star configurations shown in Fig. C.64.

a very thin crust with a small or absent inner crust, some neutrino emission processes are blocked. This leads to a crust that is kept hotter for longer times.

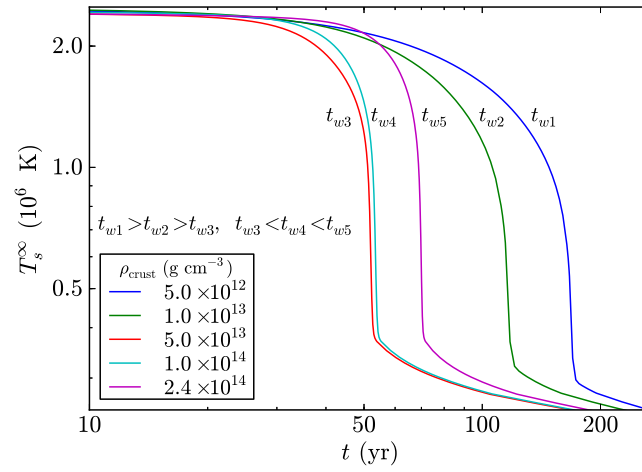


**Figure C.67.:** Enlargement of the evolution of the surface temperature around its drop at the end of the thermal relaxation phase, for the neutron stars shown in Fig. C.64.

## C.9. Realistic versus fiducial parameters of rotating neutron stars

We have recently shown in (Rotondo et al., 2011d; Rueda et al., 2011; Belvedere et al., 2012), both for the static and the rotating case, how the traditional approach to study the equilibrium configurations for neutron stars, based on the solution of the Tolman-Oppenheimer-Volkoff (TOV) system of equations (Oppenheimer and Volkoff, 1939; Tolman, 1939), has to be superseded once the weak, strong, gravitational and electromagnetic interactions are taken into account. The TOV equations must be then replaced by the Einstein-Maxwell system of equations coupled to the general relativistic Thomas-Fermi equations of equilibrium, giving raise to the what we have called the Einstein-Maxwell-Thomas-Fermi (EMTF) equations.

While in the TOV approach the condition of local charge neutrality,  $n_e(r) = n_p(r)$ , is applied, in the EMTF model the condition of global charge neutrality,  $N_e = N_p$ , is imposed, where  $n_i$  and  $N_i$  are the number density and total number of particles of the  $i$ -specie, respectively. The thermodynamic equilibrium of the star is ensured by the constancy of the generalized chemical potentials (Klein potentials) of each system species along the whole configuration (Klein, 1949; Rotondo et al., 2011d; Rueda et al., 2011) as well as of the gravitationally redshifted temperature if finite temperatures are considered (Tolman, 1930). To introduce the strong interactions we follow the  $\sigma$ - $\omega$ - $\rho$  nuclear model within relativistic mean field theory á la Boguta & Bodmer (Boguta and Bodmer, 1977), while the weak interactions are modeled via  $\beta$ -equilibrium. The nuclear model is fixed once the values of the coupling constants and the masses of the three mesons are fixed: in this work, as in the previous ones (Belvedere et al., 2012, 2013), we follow the so-called NL3 parameter set (Lalazissis et al., 1997), with  $m_\sigma=508.194$  MeV,  $m_\omega=782.501$  MeV,  $m_\rho=763.000$  MeV,  $g_\sigma=10.2170$ ,  $g_\omega=12.8680$ ,  $g_\rho=4.4740$ , plus two constants that give the strength of the self-scalar interactions,  $g_2 = -10.4310 \text{ fm}^{-1}$  and  $g_3 = -28.8850$ .

The solution of the EMTF equations of equilibrium leads to a new structure of the neutron stars markedly different from the traditional configurations obtained through the TOV equations, as shown in Fig C.68: from the supranuclear central density up to the nuclear density  $\rho_{\text{nuc}} \approx 2.7 \times 10^{14} \text{ g cm}^{-3}$ , we find the neutron star core, which is composed by a degenerate gas of neutrons, protons, and electrons in  $\beta$ -equilibrium, and is positively charged. The core is surrounded by an electron layer a few hundreds fermi thick that fully screens its charge. In this core-crust transition layer the electric field reaches values as large as  $E \sim (m_\pi/m_e)^2 E_c$ , where  $E_c = m_e^2 c^3 / (e\hbar) \approx 1.3 \times 10^{16} \text{ Volt cm}^{-1}$  is the critical field for vacuum polarization. The  $e^+e^-$  pair creation is however inhibited by Pauli blocking. In this layer the particle densities decrease until the point where global charge neutrality is reached

and the crust is found. Consequently, the core is matched to the crust via this interface at a density  $\rho_{\text{crust}} \leq \rho_{\text{nuc}}$ . In the limit  $\rho_{\text{crust}} \rightarrow \rho_{\text{nuc}}$ , the thickness of the transition layer as well as the electric field inside it vanish, and the solution approaches the one given by local charge neutrality (see Figs. 3 and 5 in Belvedere et al. (2012)). The crust in its outer region  $\rho \leq \rho_{\text{drip}} \approx 4.3 \times 10^{11} \text{ g cm}^{-3}$  is composed by white dwarf-like material (ions and electrons), following for instance the BPS equation of state (EOS) (Baym et al., 1971b). In its inner region, at densities  $\rho > \rho_{\text{drip}}$ , free neutrons are present and the EOS follows for instance the BBP description (Baym et al., 1971b). Configurations with  $\rho_{\text{crust}} > \rho_{\text{drip}}$  possess both inner and outer crust while in the cases with  $\rho_{\text{crust}} \leq \rho_{\text{drip}}$  the neutron star have only outer crust. As shown by Belvedere et al. (2012), all the above new features lead to a new mass-radius relation of static neutron stars.

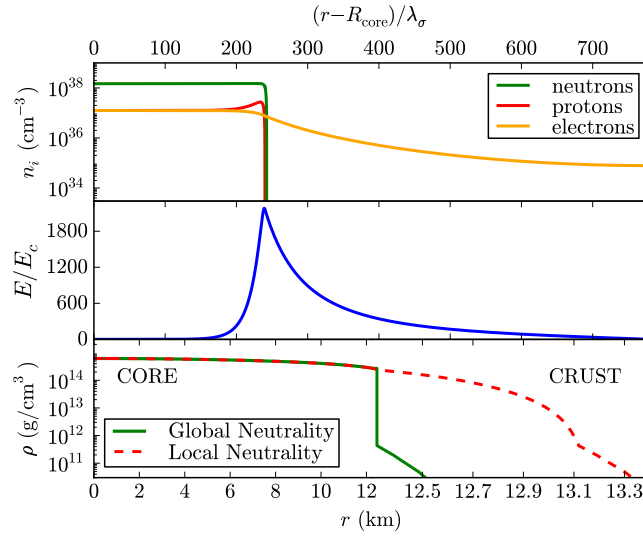


**Figure C.68.:** In the top and center panels we show the neutron, proton, electron densities and the electric field in units of the critical electric field  $E_c$  in the core-crust transition layer, whereas in the bottom panel we show a specific example of a density profile inside a neutron star. In this plot we have used for the globally neutral case a density at the edge of the crust equal to the neutron drip density,  $\rho_{\text{drip}} \approx 4.3 \times 10^{11} \text{ g cm}^{-3}$ , and  $\lambda_\sigma = \hbar/(m_\sigma c) \sim 0.4 \text{ fm}$  denotes the  $\sigma$ -meson Compton wavelength.

The static case has been recently extended to the rotating one in (Belvedere et al., 2013), assuming the neutron star as a rotating rigid body within the Hartle formalism (Hartle, 1967). In this method the Einstein equations are computed perturbatively by expanding the metric functions with respect to the star rotation angular velocity,  $\Omega$ , up to second order. We refer to (Belvedere et al., 2013) and references therein for further technical details.

In Fig. C.69 we show the mass-radius relation that results from the integra-

tion of the EMTF equations for the equilibrium configurations of static and rotating neutron stars. The dashed lines represent the non-rotating, ( $J = 0$ ), sequences, while the solid lines represent the corresponding Keplerian sequences. The pink-red and light blue lines represent the secular instability boundaries for the global and local charge neutrality cases respectively. Once the secular instability line is crossed, the star evolves quasi-stationarily until it reaches a dynamically unstable point and the gravitational collapse get started (Stergioulas, 2003). The horizontal thin red lines give the minimum mass for the static (solid line) and rotating (dashed line) sequences for the global charge neutrality case. This minimum mass limits are defined by change on sign of the gravitational binding energy  $W$  of the star, namely by the condition  $W=0$ . We did not find any minimum mass limit for the local charge neutrality case.

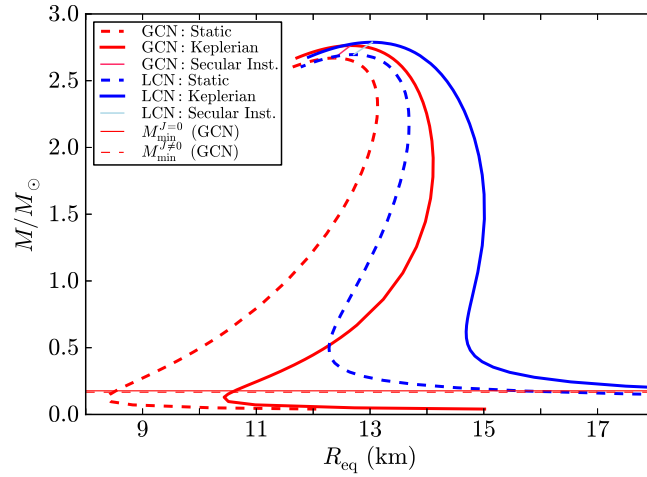


**Figure C.69.:** Total mass versus total equatorial radius for the global (red) and local (blue) charge neutrality cases. The dashed curves represent the static configurations, while the solid lines are the uniformly rotating neutron stars. The pink-red and light-blue color lines define the secular instability boundary for the globally and locally neutral cases respectively. The horizontal thin red lines define the minimum mass in the GCN case.

From all the above we can see that in the intervening years from the seminal work of Oppenheimer and Volkoff (1939) on neutron stars, much more has been learned concerning the EOS including the nuclear interactions, and on a more complex description of the structure parameters and stability of both static and rotating neutron stars. In spite of this fact, it is common in the pulsar literature to infer neutron star astrophysical observables such as surface magnetic field and luminosity by adopting as fiducial structure parameters for the mass, radius, and moment of inertia,  $M = 1.4 M_\odot$ ,  $R = 10$  km,  $I = 10^{45}$  g cm<sup>2</sup>, respectively. However, it is clear that both different theoretical models or, for a fixed model, different structure parameters by vary-

ing central density and/or rotation frequency, can give rise to quite different quantitative estimates of the astrophysical quantities.

In this line, we would like to introduce a word of caution also on the use of some analytic formulas existing in the literature for the determination of the maximum rotation frequency (see e.g. Lattimer and Prakash, 2004a) and of the moment of inertia (see e.g. Ravenhall and Pethick, 1994; Lattimer and Schutz, 2005) of a neutron star.

This work is organized as follows. In section C.9.1 we briefly summarize the perturbative method followed to solve the Einstein equations in the rotating case, recalling the quantities involved in our analysis, namely the angular velocity of the star  $\Omega$ , the moment of inertia  $I$  and the variation on mass due to the rotation. Moreover we discuss the validity of our method in describing the moment of inertia obtained through the Hartle's formalism.

In section C.9.2 we construct the Keplerian sequence of globally and locally neutral neutron stars. We compare qualitatively and quantitatively our results with the approximate analytic formula given by Lattimer and Prakash (2004a). We analyze specifically the case of the fastest observed pulsar PSR J1748–2446ad (Hessels et al., 2006a) with a frequency of 716 Hz, which is often used in the literature to constraint the mass-radius relation and so the EOS of neutron stars (see e.g. Trümper, 2011).

In section C.9.3 we calculate the moment of inertia of globally and locally neutral neutron stars and compare and contrast the results with the approximate formulas given by Ravenhall and Pethick (1994) and also Lattimer and Schutz (2005) for the moment of inertia as a function of the star compactness.

Turning to the astrophysical observables of pulsars, in section C.9.4, we analyze the estimates of the magnetic field and radiation efficiency of the high-magnetic field pulsars class. We compare and contrast the values of realistic neutron star configurations with the ones derived using the above fiducial parameters, with which fields larger than the quantum critical value for vacuum breakdown,  $B_c = m_e^2 c^2 / (e \hbar) \approx 4.4 \times 10^{13}$  G, are obtained (see e.g. Ng and Kaspi, 2011).

We use geometric units with  $G = c = 1$  throughout unless otherwise specified.

### C.9.1. Neutron star's quantities

In 1967 Hartle showed in his trailblazing work (Hartle, 1967), that the equilibrium equations for a slowly rotating star can be obtained through an expansion of the metric functions up to some order in the angular velocity  $\Omega$ . In particular, he shown that conducting the expansion up to the second order, it is possible to describe the structure of a compact star by its total mass  $M$ , angular momentum  $J$  and quadrupole moment  $Q$ . To obtain such quantities, the interior and the exterior solutions has to be matched at the border

of the star. More in detail, the interior solution is derived through a numerical solving of a system of ordinary differential equations for the perturbation functions, while the exterior solution, for the vacuum surrounding the star, can be written in an analytical form in terms of  $M$ ,  $J$ , and  $Q$  (Hartle, 1967; Hartle and Thorne, 1968).

Up to the second order in  $\Omega$ , the spacetime metric for the rotating configuration is given by (Hartle, 1967):

$$ds^2 = e^\nu (1 + 2h) dt^2 - e^\lambda \left[ 1 + \frac{2m}{r - 2M_0} \right] dr^2 - r^2 (1 + 2k) \left[ d\theta^2 + \sin^2 \theta (d\phi - \omega dt)^2 \right], \quad (\text{C.9.1})$$

where  $\nu = \nu(r)$ ,  $\lambda = \lambda(r)$ , and  $M_0 = M_0(r)$  are the metric functions and mass profiles of the corresponding seed static star with the same central density as the rotating one. The functions  $h = h(r, \theta)$ ,  $m = m(r, \theta)$ ,  $k = k(r, \theta)$  and the fluid angular velocity in the local inertial frame,  $\omega = \omega(r)$ , have to be calculated from the Einstein equations. The functions  $h = h(r, \theta)$ ,  $m = m(r, \theta)$ ,  $k = k(r, \theta)$  have analytic form in the exterior (vacuum) spacetime (Belvedere et al., 2013).

Through an expansion up to the first order in  $\Omega$  and the matching between the interior and exterior solutions, it is possible to obtain the angular momentum  $J$  of the star as well as the total mass  $M$ . The former is given by:

$$J = \frac{1}{6} R^4 \left( \frac{d\bar{\omega}}{dr} \right)_{r=R}, \quad (\text{C.9.2})$$

related to the angular velocity  $\Omega$  by

$$\Omega = \bar{\omega}(R) + \frac{2J}{R^3}, \quad (\text{C.9.3})$$

where  $R$  is the total radius of the non-rotating star and  $\bar{\omega}(r) = \Omega - \omega(r)$  is the angular velocity of the fluid relative to the local inertial frame, being  $\omega$  the fluid angular velocity in the local inertial frame. The latter is given by:

$$M = M_0 + \delta M, \quad \delta M = m_0(R) + J^2/R^3, \quad (\text{C.9.4})$$

where  $M_0$  is the mass of the non-rotating star and  $\delta M$  is the contribution to the mass due to the rotation, while  $m_0$  with its connected quantity  $p_0^*$  are two second order functions related to the pressure perturbation, computed

by solving the coupled differential equations:

$$\begin{aligned} \frac{dm_0}{dr} &= 4\pi r^2 \frac{d\varepsilon}{dP} (\varepsilon + P) p_0^* + \frac{1}{12} j^2 r^4 \left( \frac{d\bar{\omega}}{dr} \right)^2 \\ &\quad - \frac{1}{3} \frac{dj^2}{dr} r^3 \bar{\omega}^2, \end{aligned} \quad (\text{C.9.5})$$

$$\begin{aligned} \frac{dp_0^*}{dr} &= -\frac{m_0(1 + 8\pi r^2 P)}{(r - 2M_0)^2} - \frac{4\pi r^2 (\varepsilon + P)}{(r - 2M_0)} p_0^* \\ &\quad + \frac{1}{12} \frac{j^2 r^4}{(r - 2M_0)} \left( \frac{d\bar{\omega}}{dr} \right)^2 + \frac{1}{3} \frac{d}{dr} \left( \frac{r^3 j^2 \bar{\omega}^2}{r - 2M_0} \right), \end{aligned} \quad (\text{C.9.6})$$

where  $\varepsilon$  and  $P$  are the total energy-density and pressure.

The moment of inertia can be computed from the relation

$$I = \frac{J}{\Omega}, \quad (\text{C.9.7})$$

which tell us that, since  $J$  a first-order quantity, i.e. proportional to  $\Omega$ , this moment of inertia given by Eq. (C.9.7) does not depend on the angular velocity and so it does not take into account deviations from spherical symmetry. Thus, it represents the moment of inertia of the non-rotating unperturbed spherical object; contributions of the angular velocity and deformation are accounted for only in an expansion up to the third order in  $\Omega$ .

Indeed, owing to the high density of neutron stars, most of the observed pulsars are accurately described by a perturbed spherical geometry and the accuracy of the moment of inertia of the non-rotating star is a good approximation for the actual value of the rotating object. The accuracy of the approximation increases for stiffer EOS (see Benhar et al., 2005b, for details), as it is the case of the EOS obtained from  $\sigma$ - $\omega$ - $\rho$  relativistic nuclear mean field models (Boguta and Bodmer, 1977) such as the one used in this work.

### C.9.2. Accuracy of approximate analytic formulas for the Keplerian sequence

It has been obtained by Lattimer and Prakash (2004a) that the numerical value of the Keplerian frequency, namely the maximum rotation frequency, of a neutron star accounting for the effects of general relativity, deformation, and independent on the EOS, can be well fitted from the simple formula

$$f_K^{\text{L\&P}} = \frac{\Omega_K^{\text{L\&P}}}{2\pi} = 1045 \left( \frac{M_0}{M_\odot} \right)^{1/2} \left( \frac{10 \text{ km}}{R} \right)^{3/2} \text{ Hz}, \quad (\text{C.9.8})$$

providing the neutron star mass is not very close to the maximum stable value.

The Eq. (C.9.8) is often used to impose a constraint to the neutron star mass-radius relation (see e.g. Trümper, 2011), by replacing  $f_K^{\text{LP}}$  with the frequency of the fastest observed pulsar PSR J1748–2446ad (Hessels et al., 2006a), 716 Hz. Specifically, by doing this it can be obtained either an upper bound to the radius or a lower bound to the mass:

$$M_0 \geq \left( \frac{716}{1045} \right)^2 \left( \frac{R}{10 \text{ km}} \right)^3 M_\odot \approx 0.47 \left( \frac{R}{10 \text{ km}} \right)^3 M_\odot. \quad (\text{C.9.9})$$

In Fig. C.70 we show the approximate constraint given by Eq. (C.9.9) represented by the gray dot-dashed curve together with the Keplerian sequence of globally and locally neutral neutron stars obtained in this work. We have also constructed the constant frequency sequence for fastest observed pulsar PSR J1748–2446ad with  $f = 716$  Hz. The crossing point of this constant frequency curve with the Keplerian one is represented by a cyan-color star.

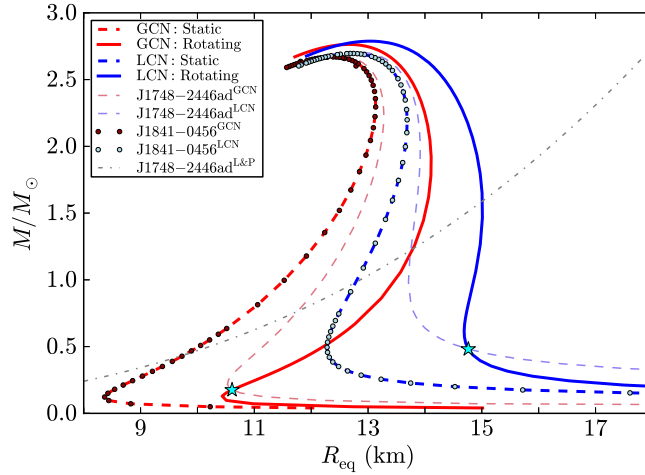


**Figure C.70.:** Gray dot-dashed line: constraint on the mass-radius relation given by Eq. C.9.9, as shown in (Trümper, 2011). Light-red and light-blue dashed lines: mass-radius relation for a constant rotational frequency  $f = 716$  Hz, for the global and local charge neutrality respectively. The two cyan-color stars at the bottom of the plot represent the pulsar PSR J1748-2446ad for our new configuration and the traditional one, both along the Keplerian sequence.

One should therefore expect that, if accurate, the dot-dashed curve passes over (or close to) the two cyan-color stars at the bottom of Fig. C.70. It is clear that Eq. (C.9.9) is very far from representing correctly the position of a star on the Keplerian sequence, and this inconsistency is equally severe for both globally and locally neutral neutron stars. Quantitatively, we can see that

Eq. (C.9.9) would predict for the same radius a much larger mass, namely  $M \approx 0.56 M_\odot$  in the globally neutral case and  $M \approx 1.5 M_\odot$  in the locally neutral one; see Fig. C.70.

The reason of the discrepancy between Eq. (C.5.33) and the real results, is as follows. The maximum Keplerian velocity can be written in terms of the non-rotating mass and radius of the neutron star as (see Belvedere et al., 2013)

$$\Omega_K^{J \neq 0} = \mathcal{C} \sqrt{\frac{M_0}{R^3}}, \quad (\text{C.9.10})$$

or in terms of rotation frequency

$$f_K = \mathcal{C} \times 1833 \left( \frac{M_0}{M_\odot} \right)^{1/2} \left( \frac{10 \text{ km}}{R} \right)^{3/2} \text{ Hz}, \quad (\text{C.9.11})$$

where  $\rho_c \equiv \rho(0)$  is the central density, and  $\mathcal{C}$  is a coefficient given by

$$\mathcal{C} = \sqrt{\frac{1 + \delta M/M_0}{(1 + \delta R/R)^3}} \left[ 1 - jF_1(r) + j^2F_2(r) + qF_3(r) \right]. \quad (\text{C.9.12})$$

Here  $\delta R$  is the contribution to the radius due to rotation,  $j = J/M_0^2$  and  $q = Q/M_0^3$  are the dimensionless angular momentum and quadrupole moment. The functions  $F_i$  can be found in Appendix A of (Belvedere et al., 2013), and the quadrupole moment  $Q$  is given by

$$Q = \frac{J^2}{M_0} + \frac{8}{5} \mathcal{K} M_0^3, \quad (\text{C.9.13})$$

where  $\mathcal{K}$  is a constant of integration fixed from the matching of the function  $h_2$  between the interior and exterior spacetimes, being  $h_2$  the second order function of the expansion of  $h = h(r, \theta)$ ; see Hartle (1967) and Appendix A in (Belvedere et al., 2013).

In Fig. C.71 we plot the dependence of the coefficient  $\mathcal{C}$  in Eq. (C.9.10) as a function of the static neutron star mass,  $M_0$ . In contrast to the constancy of such a coefficient in the approximate analytic formula (C.5.33), we find that  $\mathcal{C}$  has a non-trivial dependence on the central density (or the mass) of the star. Indeed, we obtain  $0.720 \lesssim \mathcal{C}_{\text{GCN}} \lesssim 0.912$  and  $0.750 \lesssim \mathcal{C}_{\text{LCN}} \lesssim 0.916$  for the global and local charge neutrality cases, respectively (see Fig. C.71). This dependence is caused by the effects of general relativity, the angular momentum, the quadrupole deformation, and the specific EOS used. Therefore, the Eqs. (C.5.33) and (C.9.9) are, in general, not applicable for all neutron star models.

We show in Fig. C.72 the accuracy of the approximate analytic formula for the Keplerian sequence given by Eq. (C.5.33) with respect to the actual value obtained from our numerical integrations,  $1 - f_K^{\text{L\&P}}/f_K$ , where  $f_K$  is obtained

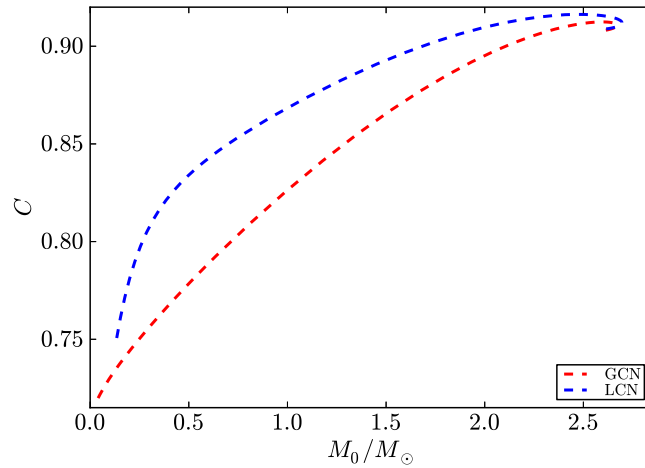


**Figure C.71.:** Coefficient  $\mathcal{C}$  in Eq. (C.9.10) as a function of the mass of the non-rotating neutron star for both global and local charge neutrality.

via Eqs. (C.9.11) and (C.9.12).

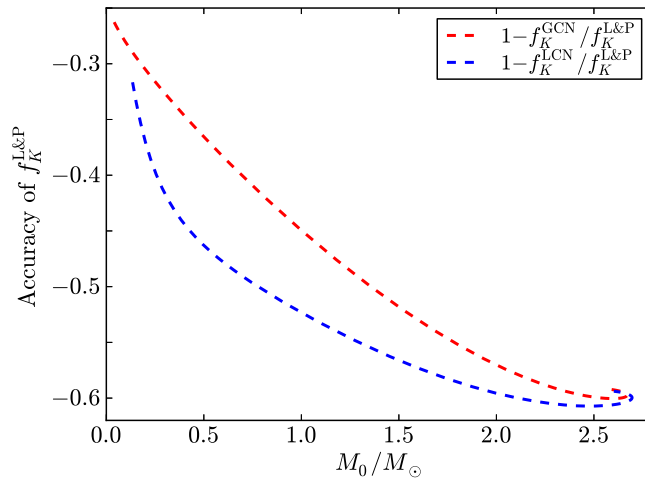


**Figure C.72.:** Accuracy of the approximate formula (C.5.33) by Lattimer and Prakash (2004a) with respect to the numerical values obtained from Eqs. (C.9.11) and (C.9.12) for both global (red dashed) and local (blue dashed) charge neutrality cases, as a function of the non-rotating neutron star mass,  $M_0$ .

### C.9.3. Accuracy of approximate analytic formulas for the moment of inertia

It has been claimed in the literature the possibility of constructing model-independent approximate analytic formulas to compute the moment of iner-

tia of a neutron star as a function of its compactness,  $GM_0/(c^2R)$ .

Ravenhall and Pethick (1994) for instance obtained that, within 10% of accuracy, the moment of inertia for a large variety of the EOS existing at the time is fitted by the formula

$$\frac{I}{M_0R^2} = 0.21 \left( 1 - 2 \frac{GM_0}{c^2R} \right)^{-1}, \quad (\text{C.9.14})$$

except for those configurations with masses  $M_0 \lesssim M_\odot$ .

Lattimer and Schutz (2005) calculated the moment of inertia for several hadronic EOS and concluded that  $I/(M_0R^2)$  follows approximately the following universal expression

$$\frac{I}{M_0R^2} = (0.237 \pm 0.008) \left[ 1 + 2.84 \frac{GM_0}{c^2R} + 18.9 \left( \frac{GM_0}{c^2R} \right)^4 \right], \quad (\text{C.9.15})$$

for EOS that leads to maximum masses larger than  $1.6M_\odot$  and for values  $M_0/R \gtrsim 0.07 M_\odot/\text{km}$  and  $M \geq M_\odot$ .

In Fig. C.73 we compare the approximate formulas (C.9.14) and (C.9.15) with the actual behavior of  $I/(M_0R^2)$  as a function of the neutron star compactness.

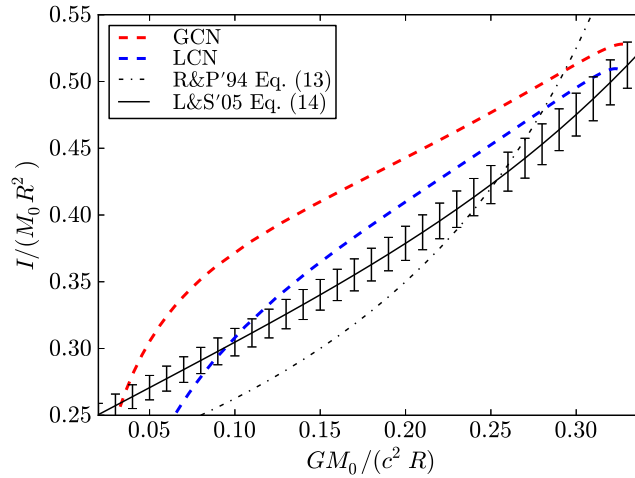


**Figure C.73.:** Comparison between the approximate formulas (C.9.15) and (C.9.14) by Lattimer and Schutz (2005) and Ravenhall and Pethick (1994), respectively, with the real behavior of  $I/(M_0R^2)$  as a function of the compactness parameter of the neutron star,  $GM_0/(c^2R)$ . We have also plotted the errors of the formula (C.9.15) as calculated by Lattimer and Schutz (2005).

We show in Fig. (C.74) the accuracy of the approximate formulas (C.9.14)

and (C.9.15) with respect to the numerical values obtained from Eq. (C.5.31) for both globally and locally neutral neutron stars. Namely we plot as a function of the compactness the value of  $1 - I_{\text{GCN}}/I_{\text{R\&P,L\&P}}$  and  $1 - I_{\text{LCN}}/I_{\text{R\&P,L\&P}}$ .

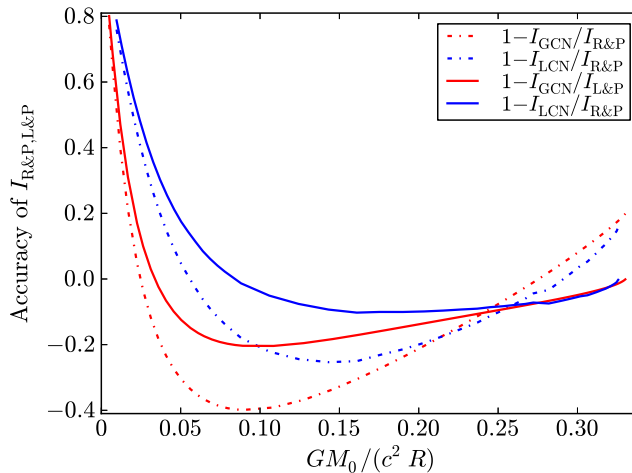


**Figure C.74.:** Accuracy of the approximate formulas (C.9.15) and (C.9.14) by Lattimer and Schutz (2005) and Ravenhall and Pethick (1994), respectively, with respect to the numerical values obtained from Eq. (C.5.31) for both globally and locally neutral neutron stars, as a function of the compactness,  $GM_0/(c^2R)$ .

We can see the performance of the above approximate formulas is in general not accurate. The accuracy improves with increasing compactness and in particular for configurations very close to the one of maximum mass. However, it is clear that the above approximate formulas cannot be considered as good approximations for the moment of inertia of any neutron star since the qualitative and quantitative behavior of it depends very strongly on the nuclear EOS. As we have shown here, these particular descriptions fail in the case of stiff EOS as the ones given by relativistic nuclear mean field theory models.

#### C.9.4. Implications on the magnetic-dipole model of pulsars

The upper limit on the magnetic field of a pulsar (see e.g. (Ferrari and Ruffini, 1969)), obtained by requesting that the rotational energy loss due to the dipole field be smaller than the electromagnetic emission of the dipole, is given by

$$B = \left( \frac{3c^3}{8\pi^2} \frac{I}{R^6} P\dot{P} \right)^{1/2}, \quad (\text{C.9.16})$$

where  $P$  and  $\dot{P}$  are the rotational period and the spin-down rate of the pulsar which are observational properties, and the moment of inertia  $I$  and the radius  $R$  of the object are model dependent properties. For the often used in literature, fiducial parameters of the canonical neutron star  $M = 1.4M_{\odot}$ ,  $R = 10$  km, and moment of inertia  $I = 10^{45}$  g cm<sup>2</sup>, Eq. (C.9.16) becomes

$$B_f = 3.2 \times 10^{19} (P\dot{P})^{1/2} \text{ G}. \quad (\text{C.9.17})$$

The loss of rotational energy within this model is given by

$$\dot{E}_{\text{rot}} = -4\pi^2 I \frac{\dot{P}}{P^3}, \quad (\text{C.9.18})$$

which in the case of fiducial neutron star parameters becomes

$$\dot{E}_{\text{rot}}^f = -3.95 \times 10^{46} \frac{\dot{P}}{P^3} \text{ erg s}^{-1}. \quad (\text{C.9.19})$$

There is an interesting family of pulsars known as high-magnetic field pulsars characterized by surface magnetic fields, inferred from their period and spin-down rates thorough Eq. (C.9.17), close or in some cases even larger than the quantum critical field (see e.g. Ng and Kaspi, 2011; Zhu et al., 2011, and Table C.9 for details):

$$B_c = \frac{m_e^2 c^2}{e\hbar} = 4.41 \times 10^{13} \text{ G}. \quad (\text{C.9.20})$$

Pulsar	$B_f/B_c$	$L_X$ ( $10^{33}$ erg s <sup>-1</sup> )	$P$ (s)	$\dot{P}$ ( $10^{-12}$ )
J1846–0258	1.11	25-28, 120-170	0.326	7.083
J1819–1458	1.13	1.8 – 2.4	4.263	0.575
J1734–3333	1.18	0.1 – 3.4	1.169	2.279
J1814–1744	1.24	< 43	1.169	2.279
J1718–3718	1.67	0.14 – 2.6	3.378	1.598
J1847–0130	2.13	< 34	6.707	1.275

**Table C.9.:** Magnetic fields of the overcritical high-magnetic field pulsars obtained assuming fiducial neutron star parameters,  $R = 10$  km and  $I = 10^{45}$  g cm<sup>2</sup>, respectively, namely using Eq. (B.3.12). See Zhu et al. (2011); Ng and Kaspi (2011) for additional details of these pulsars.

Due to this fact, it has been suggested the possibility that this family of pulsars can be the missing link, i.e. transition objects, between rotation powered pulsars and the so-called magnetars: neutron stars powered by the decay of overcritical magnetic fields. In principle this would lead to a large unseen population of magnetars in a quiescence state which could be disguised as

radio pulsars (see e.g. Zhu et al., 2011, for details). However, as we shall show below, these conclusions might be premature since the magnetic fields, inferred using a neutron star of fiducial parameters, are in general overestimated. In particular, they could be in some cases larger by almost an order of magnitude when compared with the magnetic field obtained from Eq. (B.4.3) using realistic mass-radius relations and the corresponding general relativistic moment of inertia.

In Fig. C.75 we show the ratio between the magnetic field obtained via Eq. (C.9.16) using the realistic mass-radius relations of globally and locally neutral neutron stars used in this work and the one obtained with fiducial parameters given by Eq. (C.9.17), which we denote to as  $B_f$ . We did this for both static and maximally rotating (Keplerian sequence) neutron stars. For the rotating stars we substitute the radius  $R$  in Eq. (C.9.16) by the mean-radius,  $\langle R \rangle = (2R_{\text{eq}} + R_p)/3$ , where  $R_{\text{eq}}$  and  $R_p$  are, respectively, the equatorial and polar radii.

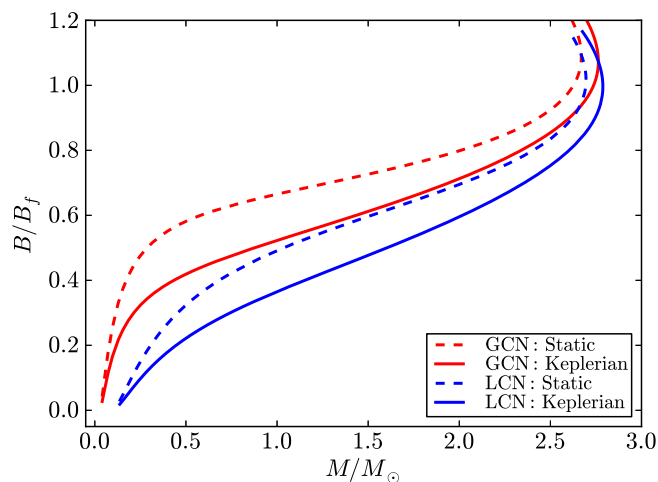


**Figure C.75.:** Ratio between the magnetic field given by Eq. (C.9.16) obtained with the realistic mass-radius relations of globally and locally neutral neutron stars of this work and the one obtained with fiducial parameters, given by Eq. (C.9.17). The stars

We can see from this figure that the inferred magnetic field decreases with the neutron star mass. Therefore, the configurations of maximum and minimum mass give us respectively upper and lower limits to the magnetic field.

In Fig. C.76 we have plotted the magnetic fields inferred for the high-magnetic field pulsars of Table C.9 within the static approximation, namely using the radius of the non-rotating configurations. This is in principle a good approximation for this family of pulsars since their rotation periods are well far the millisecond region, where appreciable deviations from spherical symmetry are expected. As can be noticed from Fig. C.75, the non-rotating approximation give us an upper limit to the magnetic field with respect to

the value obtained from the actual rotating configuration.

We find that, in the global neutrality case, PSR J1847–0130 and PSR J1718–3718 are under-critical up to a mass  $M_0 \approx 0.25 M_\odot$ , and  $M_0 \approx 0.65 M_\odot$ , respectively, while the other pulsars are under-critical up to masses  $M_0 \approx 2.3$ – $2.5 M_\odot$ . In the local charge neutrality case, PSR J1847–0130 and PSR J1718–3718 are under-critical up to a mass  $M_0 \approx 0.9 M_\odot$  and  $M_0 \approx 1.5 M_\odot$  respectively, while the other sources up to masses  $M_0 \approx 2.5$ – $2.7 M_\odot$ .

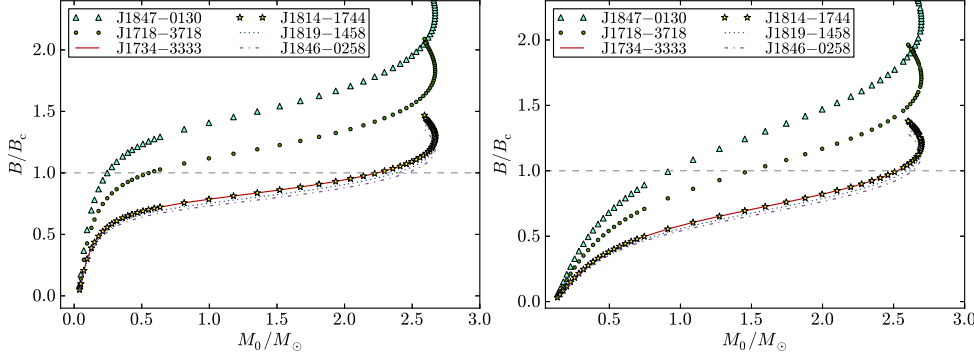


**Figure C.76.:** Magnetic field  $B$  in the dipole approximation, in units of critical magnetic field  $B_c$ , as function of the mass (in solar masses) for static neutron stars in the global (left panel) and local (right panel) charge neutrality cases. We show the high-magnetic field pulsar of Table C.9 for which overcritical values ( $B/B_c > 1$ ) are obtained using fiducial neutron star parameters.

We turn now to the efficiency of pulsars in converting rotational energy into electromagnetic radiation. In Fig. C.77 we show the X-ray luminosity to rotation energy loss ratio,  $L_X/\dot{E}_{\text{rot}}$  as a function of the neutron star mass, for both global and local charge neutrality.

In the global charge neutrality case, we have  $L_X < \dot{E}_{\text{rot}}$  for PSR J1718–3718 for  $M_0 \gtrsim 1.2 M_\odot$  and for the entire range of masses if we adopt as  $L_X$  the observational upper or lower limit, respectively; PSR J1814–1744 for  $M_0 \gtrsim 0.8 M_\odot$  assuming  $L_X$  as given by its upper limit, and the rest of objects in the entire range of stable masses with the only exception of PSR J1847–0130 and PSR J1819–1458, for which no range of masses with  $L_X < \dot{E}_{\text{rot}}$  can be obtained. Analogous conclusions are found for the case of local charge neutrality.

For PSR J1847–0130 it is only known an upper limit for  $L_X$ , so there is still room for solutions with  $L_X < \dot{E}_{\text{rot}}$  if future observations lead to an observed value smaller than this present upper limit. In this line, the only object with  $L_X > \dot{E}_{\text{rot}}$  for any mass is PSR J1819–1458. For this particular object there is still the possibility of being a rotation powered neutron star since the currently used value of the distance to the source, 3.6 kpc, inferred from its dispersion measure, is poorly accurate with a considerable uncertainty of at least 25% (see McLaughlin et al., 2007, for details). It is also worth to note that the

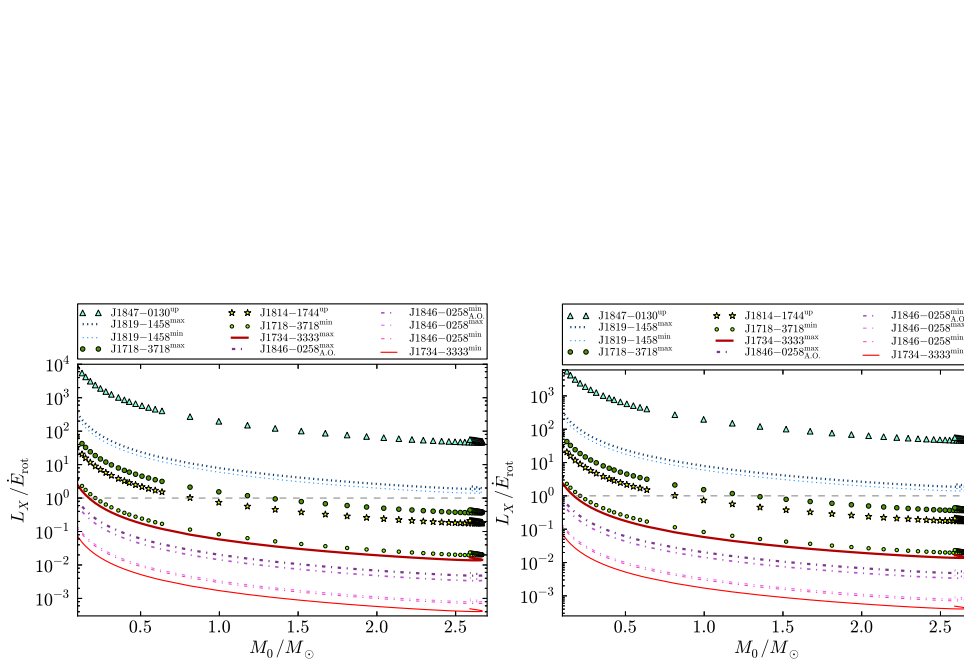


**Figure C.77.:** Ratio between the observed X-ray luminosity  $L_X$  and the loss of rotational energy  $\dot{E}_{rot}$  versus total mass of the rotating neutron star, in units of  $M_\odot$ . Are drawn the high-B pulsar from the work by Ng and Kaspi (2011) for which a magnetic field higher than the critical field  $B_c$  is inferred, once the fiducial value for the moment of inertia  $I = 10^{45}$  g cm<sup>2</sup> is taken into account (see Table C.9). Pulsars with luminosity  $L_X$  defined by an upper limit are labeled with “up”, for pulsars with luminosity  $L_X$  not well established we have assumed the existent lower limits (label “min”) and upper limits (label “max”) on it. The values for the pulsar PSR J1846-0258 are divided in prior the 2006 outburst and after the 2006 outburst (label “A.O.”). Left plot: global charge neutrality. Right plot: local charge neutrality. The magnetic fields shown are referred to the high-magnetic field pulsars of Table C.9.

rotation energy loss, see Eq. (C.9.18), depends on the neutron star structure only through the moment of inertia, which can be very different for different nuclear EOS and/or owing to the improved value for rotating objects, obtained for instance with a third-order series expansion in  $\Omega$ , which is larger than the non-rotating value used here (see e.g. Fig. 5 in Benhar et al., 2005b).

### C.9.5. Conclusions

We have constructed equilibrium configurations of uniformly rotating neutron stars in the globally and locally neutral pictures. We calculated the neutron star parameters from the numerical integration of the general relativistic equations of equilibrium and compared and contrasted them with the traditionally adopted fiducial values. We showed that the sequence of maximally rotating neutron stars cannot be fitted by some existent approximate analytic formulas in the literature (Lattimer and Prakash, 2004a). A similar conclusion was reached for the moment of inertia of the configurations, as compared with the formulas given by Ravenhall and Pethick (1994) and Lattimer and Schutz (2005).

We then explored the consequences of our results on the astrophysics of pulsars. We showed that the magnetic field inferred from the magnetic-dipole formula can be overestimated up to one order of magnitude if fiducial parameters are adopted. We analyzed in addition the specific case of the high-magnetic field pulsar class, for which overcritical magnetic fields have been obtained in the literature with the use of fiducial neutron star parameters. We found that, instead, the magnetic field of all the high-magnetic field pulsars turn to be under-critical for appropriate values of the neutron star mass. This nontrivial dependence of the inferred magnetic field on the neutron star mass in addition to the dependence on  $P$  and  $\dot{P}$ , namely  $B = B(I(M_0), R(M_0), P, \dot{P})$ , leads to the impossibility of accommodating the pulsars in a typical  $\dot{P} - P$  diagram together with a priori fixed values of the magnetic field; see Fig. C.76.

We finally showed that the X-ray luminosity of these pulsars can be well explained via the loss of rotational energy and therefore they fall into the family of ordinary rotation powered pulsars. The only possible exceptions were found to be PSR J1847–0130 and PSR J1819–1458, which however present still observational uncertainties in the determination of their distances and/or luminosities, which leave still room for a possible explanation in terms of spin-down power. We also discussed the possible effects of different nuclear models as well as the improved values of the moment of inertia given by further expansion orders of the slow rotation approximation or full numerical integration of the equilibrium equations in the rotating case.

# D. Neutron Stars Physics with Gamma-Ray Bursts

## D.1. Cooling of young neutron stars in GRBs associated to Supernovae

### D.1.1. Introduction

The investigation of the thermal evolution of neutron stars is a powerful tool to probe the inner composition of these objects. The cooling of neutron stars has been investigated by many authors, where many different microscopic models were assumed (see Schaab et al., 1996; Page et al., 2004, 2006, 2009; Blaschke et al., 2000; Grigorian et al., 2005; Blaschke et al., 2006; Negreiros et al., 2010). Most of the research on the thermal evolution of compact stars focus on objects with ages greater than 10-100 years, which is comprehensible if one consider that the thermal data, currently available to us, is for pulsars with estimated ages of or greater than 330 years (Page et al., 2004, 2009). In this letter we discuss the thermal evolution of young neutron stars, in the little explored time window that spans from ages greater than 1 minute (just after the proto-neutron star regime (Prakash et al., 2001)) to ages  $\leq 10$ -100 years, when the neutron star becomes isothermal (see Gnedin et al., 2001, for details).

We discuss the possibility that the late X-ray emission (URCA hereafter <sup>1</sup>) following a few GRBs associated with SNe; e.g. URCA-1 in GRB980425-SN1998bw (Ruffini et al., 2004; Frascetti et al., 2005; Bernardini et al., 2008), URCA-2 in GRB030329-SN2003dh (Bernardini et al., 2004, 2005b), and URCA-3 in the system GRB031203-SN2003lw (Bernardini et al., 2005a; Ruffini et al., 2007a, 2008b) (see Fig. D.3 for details), might actually be originated by young ( $t \sim 1$  minute-(10-100) years), hot ( $T \sim 10^7$ - $10^8$  K) neutron stars, that are remnants of the SN (Ruffini et al., 2007a) and which we have here called neo-neutron stars. Relevant also are the observations of the isolated Type

---

<sup>1</sup>The name URCA-1 and URCA-2 mentioned here were given to these sources when presented for the first time at the MG10 meeting held in Rio de Janeiro in the town of URCA. The location of the MG10 meeting was very close to the "Cassino da URCA" where George Gamow and Mario Schoenberg conceived the process of neutrino emission for the cooling process of neutron stars which also took the name from the town of URCA, the URCA process (see e.g detailed history in Ruffini et al., 2005; Gamow, 1970)

Ic Supernova SN 1994I (Immler et al., 2002) and SN 2002ap (Soria et al., 2004) which present late emissions similar to the ones observed in URCA-1, URCA-2, and URCA-3.

In this letter we propose a revision of the boundary conditions usually employed in the thermal cooling theory of neutron stars, in order to match the proper conditions of the atmosphere at young ages. We also discuss the importance of the thermal processes taking place in the crust, which also have important effects on the initial stages of thermal evolution. We stress that we are not calling into question the validity of the current treatment of the atmosphere of compact stars but, instead, we point out the need of extending them to appropriately describe the conditions of neo-neutron stars.

### **D.1.2. Cooling of Young, Hot Neutron Stars**

There are three important ingredients that govern the thermal evolution of a compact star, these are: 1) the microscopic input, that accounts for the neutrino emissivities, specific heat and thermal conductivity; 2) the macroscopic structure of the star, namely its mass, radius, pressure profile, crust size, etc.; and 3) the boundary condition at the surface of the star, that provides a relationship between the mantle temperature and that of the atmosphere, the latter being what we ultimately observe. These ingredients have been extensively studied, and a comprehensive review can be found in Page et al. (2006). As discussed in Gnedin et al. (2001), during the initial stages of thermal evolution (ages  $\leq 10 - 100$  years), the core and the crust of the neutron star are thermally decoupled. This is due to the fact that the high density core is emitting neutrinos at a much higher rate than the crust, which causes it to cool down more quickly. This effectively means, that initially the neutron star is cooling “inside out”, with the core colder than the outer layers. This scenario is schematically depicted in Figure D.1.

The dominant neutrino emission processes in the crust are given by the Bremsstrahlung, plasmon decay, and electron-positron annihilation processes. Following the footsteps of Gnedin et al. (2001), we calculate the thermal evolution of neutron stars, by adding artificially a phenomenological source of heat (see details in Sec. D.1.4). This allow us to estimate how much heat is needed, so that the thermal evolution of a neo-neutron star matches the X-ray light curve of late emission of GRB-SN.

After this initial core-crust decoupled state, the “cooling wave” originated in the core reaches the crust, and the object becomes isothermal. The time scale of this process is between 10–100 years, depending on the properties of the crust (Gnedin et al., 2001). This means that during the initial stages of thermal evolution the crust shields the core, and all the information we might obtain at this stage, refers only to the crust and to the atmosphere of the star. This raises another issue, that concerns the atmosphere of the star. The ther-

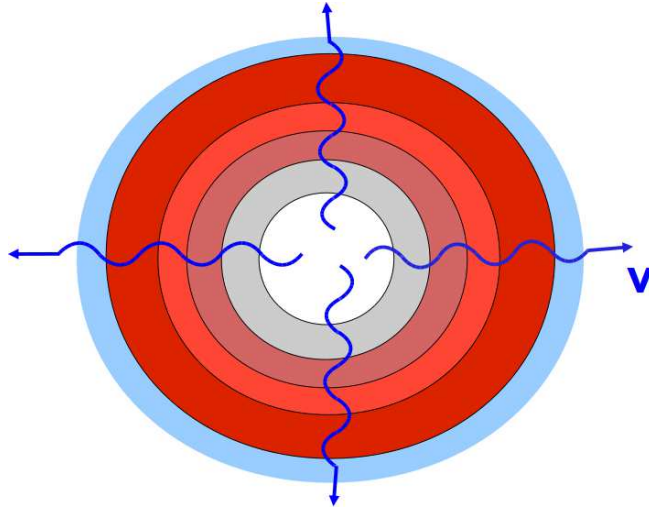


**Figure D.1.:** Schematic representation of the cooling of a young neutron star. Due to stronger neutrino emissivities, the core of the star cools down more quickly than the crust, causing the star to cool inside out. Darker and lighter areas represent higher and lower temperatures respectively.

mal connection between the mantle and the atmosphere is what defines the photon luminosity, which is what we observe. Therefore, the appropriate description of the atmosphere is key to the correct understanding of the thermal evolution of neutron stars. In the usual approach, the thermal relaxation-time of the atmosphere is assumed to be much smaller than that of the neutron star, furthermore neutrino emissions from the atmosphere are also considered negligible (see Gudmundsson et al., 1983). Under these assumptions, and assuming a plane-parallel approximation (which is reasonable since the atmosphere is  $\sim 100$  m thick), one can get a relationship between the temperature of the mantle  $T_b$  and the temperature of atmosphere  $T_e$ , or equivalently the luminosity  $L_e$ . Gudmundsson et al. (1983) have originally found a  $T_b$ - $T_e$  relationship that depends on the surface gravity of the neutron star. This relationship was further developed by Potekhin et al. (1997), to account for the possibility of mass accreted in the initial stages, and of magnetic fields effects. As pointed out by Gudmundsson et al. (1983), such assumptions for the atmosphere of the star are only valid for objects older than a few 10 years, when the temperature, for densities below  $10^{10}$  g/cm<sup>3</sup>, has dropped below  $10^9$ K. In fact, we see that the current boundary conditions yields temperatures  $\sim 10^7$  K ( $L \sim 10^{37}$  erg/s, equivalently) for young neutron stars (age  $< 1$ -10 years). This should raise some suspicion since proto-neutron stars studies (see Prakash et al., 2001, and references therein), indicate that neutron stars just after this regime have temperatures  $\sim 10^{10}$ - $10^{11}$  K.

The properties of the atmosphere of a sufficiently hot, nascent neutron star should differ significantly from those considered in Gudmundsson et al.

(1983) and Potekhin et al. (1997). Especially since at hot temperatures ( $T \gtrsim 10^9$  K) the atmosphere might not be transparent to neutrinos, and thus the neutrino transport equations have to be considered. The coupled equations of neutrino and photon transport, in the atmosphere of a neutron star, were solved by Salpeter and Shapiro (1981), and Duncan et al. (1986). In these works the authors have performed detailed calculations of the atmosphere properties of hot neutron stars. They have found the following photon luminosity, as observed at infinity,

$$L_{\infty} = 50 \times t^{-7/12} \times (T_{10})^{7/4} \times (R_{10})^{17/9} \times \left(\frac{M}{M_{\odot}}\right)^{-1} \times L_E, \quad (\text{D.1.1})$$

where  $t$  is time in seconds,  $T_{10}$  is the initial temperature in units of 10 MeV,  $R_{10}$  is the neutron star radius in units of 10 km,  $M$  is the neutron star mass, and  $L_E \sim 2.0 \times 10^{38}$  erg/s is the Eddington luminosity. Duncan et al. (1986) found that the above expression should be valid for at least the initial 100 s. In Fig. D.2 we can see how the luminosity of the star changes for the first 100 s, for stars with different initial temperatures.

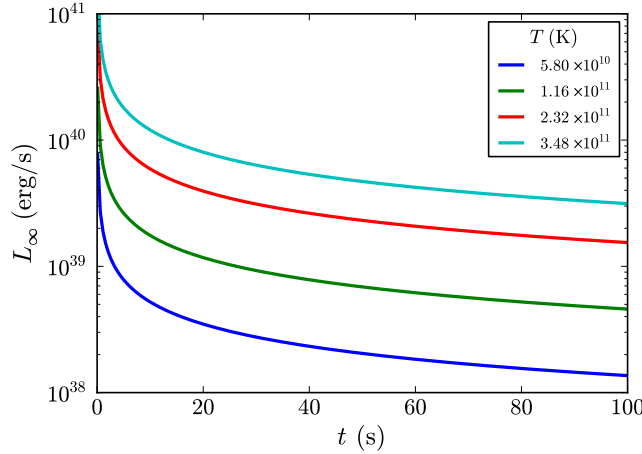


**Figure D.2.:** Luminosity of a hot nascent neutron star as observed at infinity given by Eq. (D.1.1) during the initial 100 s (Duncan et al., 1986), with the initial temperatures indicated. The neutron star is assumed to have a mass of  $1.4M_{\odot}$ , and a radius of 13 km.

According to these results, during the initial 100 s, the photon luminosity emerging from the atmosphere will be higher than the Eddington luminosity. This implies that there will be mass loss, due to neutrino-driven winds from the young atmosphere. As shown by Duncan et al. (1986), the total mass loss only becomes appreciable for neutron stars with large radii and high initial temperatures. For a typical neutron star with the canonical mass of  $1.4M_{\odot}$ , a radius of 13 km and initial temperature of  $\sim 10^{11}$  K, the total mass loss was estimated to be  $\sim 6.2 \times 10^{-6}M_{\odot}$ .

In addition to the high luminosities associated to the atmosphere of young neutron stars, one need also to consider fallback onto the surface of the neutron star. Potekhin et al. (1997) discussed how fallback, at earlier stages of evolution, would modify the properties of the atmosphere, and hence of the boundary conditions. Once more however, in this investigation, such a fallback is assumed to have happened at early times and the modified boundary conditions are only valid if the fallback has already ceased. Chevalier (1989) has studied the fallback onto young neutron stars, and found that while there is an envelope, a luminosity near the Eddington limit should be present. Furthermore, the authors have found that in this case the energy from the envelope can be radiated away in a time of  $\sim 1$  year. This timescale however, might be lengthened if effects of rotation are accounted during the fallback. In addition to that, Turolla et al. (1994) have discussed the possibility of “hot solutions” for the atmosphere of neutron stars undergoing spherical accretion. It was shown that for  $L \geq 10^{-2}L_E$  the temperature at the atmosphere of a neutron star might be  $\sim 10^9$ – $10^{11}$  K.

### **D.1.3. Late X-Ray Emission in GRBs associated to Supernovae: URCA**

It seems clear to us that, after the analysis of the scenario described above, we must extend the current model for the boundary conditions used in cooling calculations, to include the effects of a high temperature atmosphere, with possibly super-Eddington luminosity. Up until this point however, little attention has been given to the thermal evolution of young neutron stars, mainly due to the absence of observational data of neutron stars with ages  $< 330$  years. It has been recently proposed (Ruffini et al., 2007a) that the long lasting X-ray emission called there URCA (see Fig. D.3) of a few GRBs associated to SNe; URCA-1 in GRB980425-SN1998bw, URCA-2 in GRB030329-SN2003dh, and URCA-3 in GRB031203-SN2003lw, might actually be originated in the compact star remnant of the SN: a neo-neutron star. In this scenario the GRB is described as the core collapse of a massive star, whose remnant is a black hole. This massive star is supposed to be in a binary system, whose companion is on the verge of going supernova. The GRB triggers the supernova explosion in the companion star, which in turns leaves behind a neutron star (Ruffini et al., 2001). An alternative scenario has been recently suggested in which the so-called GRB is actually not a GRB but the observed X-ray emission originates from a collapsing core: a proto-neutron star leading directly to a SN explosion. This concept is is very similar to the one of a proto-black hole introduced in Ruffini et al. (2011, 2010a); Izzo et al. (2011), where the emission from the collapsing core is clearly well distinguished from the GRB. In that case the collapsing core leads to the formation of the black hole while in the present case it leads to the formation of a neutron star.

Both scenarios lead to the formation of a neo-neutron star and they are supported by the observation of Supernova 1979C (Patnaude et al., 2011), where a similar X-ray light curve also followed the supernova. In Fig. D.3 we show the X-ray light curve associated with the URCAs.

From Fig. D.3 we can see that the X-ray luminosities of these sources are of the same magnitude as that expected for neo-neutron stars, as discussed above. In Table D.1 we summarize the representative parameters of the four GRB-SN systems, including the very large kinetic energy observed in all SNe (Mazzali, 2006). We have also included the association GRB060218-SN2006aj (see Dainotti et al., 2007, 2010, for details). It must be noted that similar prolonged X-ray emission has been observed also in connection with other Type Ic SN not associated with GRBs, like e.g. SN1994I (Immler et al., 2002) and SN2002ap (Soria et al., 2004) (see Fig. D.4 for details).

GRB	$E_{e^\pm}^{tot}$ (erg)	$E_{SN}^{bolom}$ (erg) <sup>a</sup>	$E_{SN}^{kin}$ (erg) <sup>b</sup>	$E_{URCA}$ (erg) <sup>c</sup>	$\frac{E_{e^\pm}^{tot}}{E_{URCA}}$	$\frac{E_{SN}^{kin}}{E_{URCA}}$	$R_{NS}$ (km) <sup>d</sup>	$z^e$
980425	$1.2 \times 10^{48}$	$2.3 \times 10^{49}$	$1.0 \times 10^{52}$	$3 \times 10^{48}$	0.4	$1.7 \times 10^4$	8	0.0085
030329	$2.1 \times 10^{52}$	$1.8 \times 10^{49}$	$8.0 \times 10^{51}$	$3 \times 10^{49}$	$6 \times 10^2$	$1.2 \times 10^3$	14	0.1685
031203	$1.8 \times 10^{50}$	$3.1 \times 10^{49}$	$1.5 \times 10^{52}$	$2 \times 10^{49}$	8.2	$3.0 \times 10^3$	20	0.105
060218	$1.8 \times 10^{50}$	$9.2 \times 10^{48}$	$2.0 \times 10^{51}$	?	?	?	?	0.033

**Table D.1.:** a) see Kaneko et al. (2007); b) Mazzali, P., private communication at MG11 meeting in Berlin, July 2006, Iwamoto et al. (1998); c) evaluated fitting the URCAs with a power law followed by an exponentially decaying part; d) evaluated assuming a mass of the neutron star  $M = 1.5M_\odot$  and  $T \sim 5\text{--}7$  keV in the source rest frame; e) see Galama et al. (1998); Greiner et al. (2003); Prochaska et al. (2004); Mirabal et al. (2006). Here  $E_{e^\pm}^{tot}$  is the total energy of GRB,  $E_{SN}^{bolom}$  and  $E_{SN}^{kin}$  are the bolometric and the kinetic energy of the SN,  $E_{URCA}$  is the energy of the late X-ray emission URCA (see Fig. D.3),  $R_{NS}$  is the radius of the neutron star and  $z$  is the redshift of the event.

#### D.1.4. Neo-Neutron Star Luminosity and the URCAs

Another important ingredient for the cooling of young neutron stars are the crust properties. As illustrated in Fig. D.1, due to the stronger neutrino emission from the core, during the initial stages the core and crust are thermally decoupled. For that reason, the initial stages of the thermal evolution reflects the properties of the crust, while the core remains invisible. Thus the proper description of the crust structure and composition, is also fundamental for understanding the initial thermal evolution stages of a neutron star. We now briefly discuss the current understanding of the crustal processes and how such might be related with the data available from the URCAs.

There are several active emission mechanisms in the neutron star crust, e.g.  $e$ -Ion Bremsstrahlung, plasmon decay,  $e^+e^-$  annihilation,  $e-e$  and  $n-n$  Bremsstrahlung, synchrotron emission, as well as Cooper pair processes for

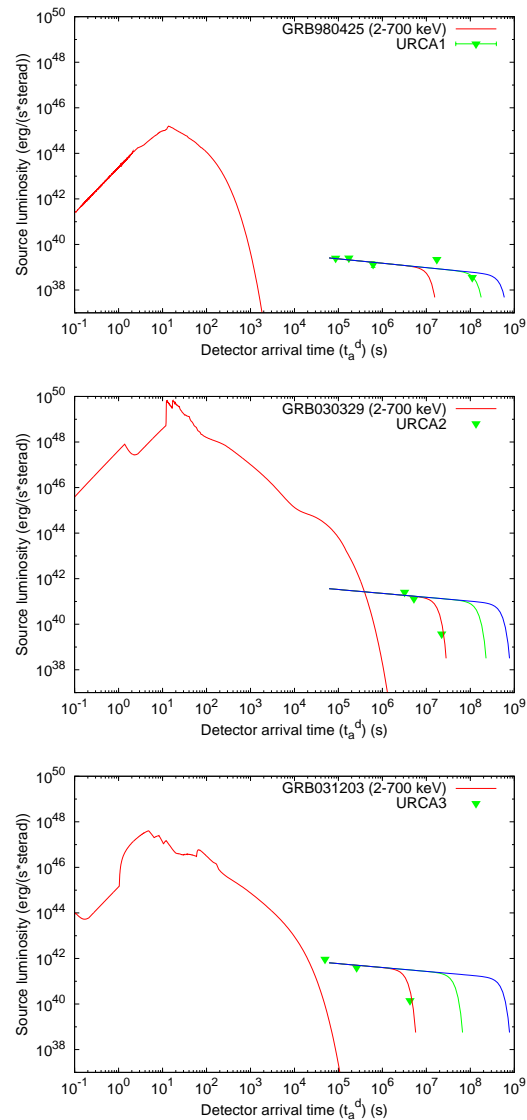


**Figure D.3.:** Synthetic light curves of GRB980425 (A) (Ruffini et al., 2004; Fraschetti et al., 2005; Bernardini et al., 2008) , GRB030329 (B) (Bernardini et al., 2004, 2005b) and GRB031203 (C) (Bernardini et al., 2005a; Ruffini et al., 2007a, 2008b) . The solid curves represent the hard X-ray emission (10-200 keV range) and the triangles are 2-10 keV flux points. The optical luminosities of the SNe accompanying these GRBs are also reported with crosses (see Ruffini et al., 2007a, for details). The curves fitting the late X-ray luminosity (URCAs) are qualitative cooling curves based on Canuto (1978); see also Ruffini et al. (2004, 2007a, 2008b); Bernardini et al. (2004, 2005a,b, 2008); Fraschetti et al. (2005), for details.

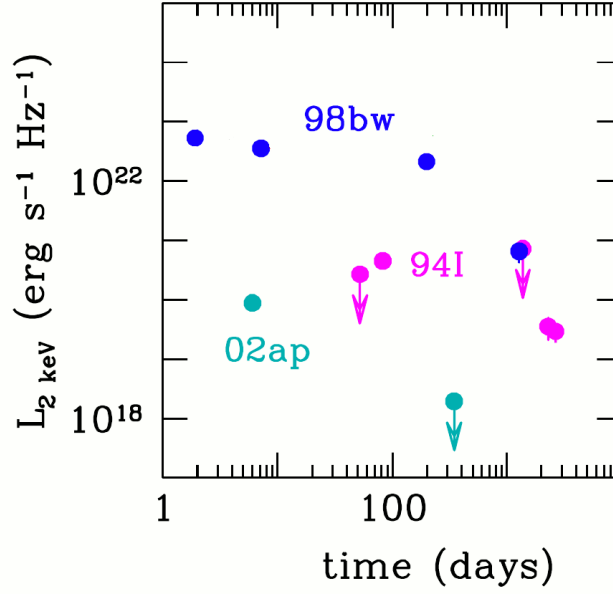


**Figure D.4.:** X-ray light curves of the counterparts of GRB980425-SN1998bw and of two Type Ic SNe not accompanied by GRBs: SN1994I (“normal”) and SN2002ap (broad-lined). The data are from Pian et al. (2000); Immler et al. (2002); Kouveliotou et al. (2004); Soria et al. (2004).

temperatures smaller than the critical temperature for superfluidity  $T_{\text{crit}}$ . However, as shown by Yakovlev et al. (2001), for temperatures above  $10^8$  K, which is the regime we are interested, the first three processes are the dominant ones. For instance, synchrotron emission channels might become slightly relevant, but only for  $T < 10^8$  K and for very high magnetic fields  $> 10^{14}$  G. The Cooper pair mechanism, possibly important for objects of a few hundred years old like Cas A (see e.g. Page et al., 2011; Shternin et al., 2011, for details), is irrelevant in the present case since we are dealing with neutron star ages  $< 10$  years and thus temperatures well above  $T_{\text{crit}}$ .

At temperatures  $T \sim 3 \times 10^9$  K, we can write for the most important emission processes in the crust

$$\epsilon_B \sim 10^{21} \text{erg s}^{-1} \text{cm}^{-3}, \quad (\text{D.1.2})$$

$$\epsilon_P \sim 10^{22} \text{erg s}^{-1} \text{cm}^{-3}, \quad (\text{D.1.3})$$

$$\epsilon_{ep} \sim 10^{19} \text{erg s}^{-1} \text{cm}^{-3}, \quad (\text{D.1.4})$$

where  $\epsilon_i$  denotes the emissivity and the indexes  $B$ ,  $P$ ,  $ep$  denote the following processes: Bremsstrahlung, plasmon decay, and pair annihilation, respectively.

In order to estimate the amount of heat needed to match the theoretical thermal evolution of a neo-neutron star to the light curve of the URCA we

have added a phenomenological source of heat parametrized by

$$H = H_0 e^{-t/\tau_s}, \quad (\text{D.1.5})$$

with  $H_0$  being the magnitude of the heat source, and  $\tau_s$  being the time scale in which it is active. For our calculations we set  $\tau_s = 1$  year.

In addition, we have introduced a phenomenological boundary condition for the early stages of evolution of the surface temperature  $T_s$  that follows the form  $T_s = T_x g_{14}^{1/4} T_8^{0.55}$  K, where  $T_x = 0.87 \times 10^6 + (T_0 - 0.87 \times 10^6) e^{-t/\tau_s}$  K,  $T_8$  is the mantle temperature  $T_b$  in units of  $10^8$  K,  $T_0$  is the initial temperature of the atmosphere, and  $g_{14}$  is the surface acceleration of gravity in units of  $10^{14}$  cm/s<sup>2</sup>. With this new boundary condition we can mimic the high temperature of the atmosphere for young neutron stars by setting the temperature at early times to a higher value and, for times greater than  $\tau_s$ , it asymptotically goes to its traditional value  $\sim 0.87 \times 10^6$  K.

In Fig. D.5 we show the cooling curves of neo-neutron stars resulting from the presence of the heating source given by Eq. (D.1.5), in addition to the traditional cooling processes of neutron stars. The cooling curves are obtained self-consistently by solving the full, general relativistic, energy transport and balance equations with no approximations as described in Schaab et al. (1996); Page et al. (2006); Negreiros et al. (2010). We show also the observed data for the X-ray light curve associated with the URCA. This allow us to identify the key factor leading to the matching of the neo-neutron star luminosity with the X-ray emission of the URCA.

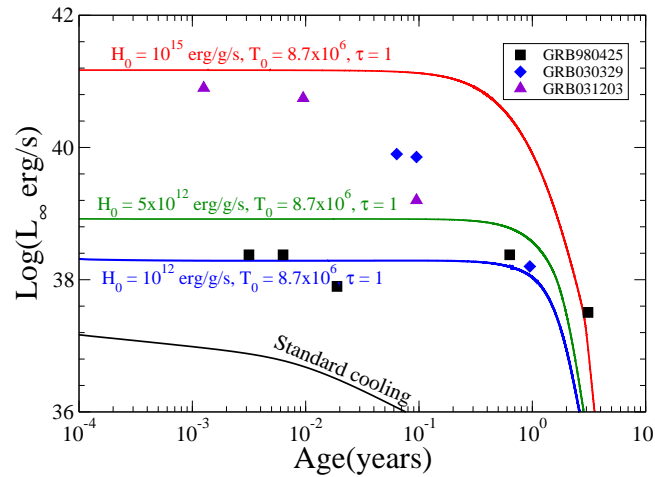


**Figure D.5.:** Thermal evolution of neo-neutron stars for selected values of the heating source  $H_0 = [10^{12}, 5 \times 10^{12}, 10^{15}]$  erg/g/s and for an initial temperature of the atmosphere  $T_0 = 8.7 \times 10^6$  K. The observed data represents the X-ray light curve associated with the URCA.

### **D.1.5. Discussion and Conclusions**

The major role played by the neutrino emissions from the crust of a neo-neutron star at the initial stages of the object is illustrated by Fig. D.5. In addition, by calibrating our additional heating source at early times to  $H_0 \sim 10^{12}$ – $10^{15}$  erg/g/s, we find a striking agreement of the luminosity obtained from the cooling of a neo-neutron stars with the prolonged ( $t = 10^8$ – $10^9$  s) X-ray emission observed in GRB associated with Supernova (see Fig. D.5 for details). This could indicate that something might be missing in our current understanding of the crust of neutron stars. It might be that, as is the case for the atmosphere, we need to further develop our current models for the crust, as to describe properly the properties of neo-neutron stars. The traditional thermal processes taking place in the crust might be enhanced by the extreme high temperature conditions of neo-neutron star and, additional heating processes not yet studied within this context could also take place under such conditions and deserve further analysis.

Particularly interesting in this respect are the processes of  $e^+e^-$  pair creation expected to occur in the interphase between the core and the crust during the neutron star formation leading to the appearance of critical fields (see Ruffini et al., 2007c; Ruffini, 2008a; Rueda et al., 2010a,b; Popov, 2010; Ruffini et al., 2010b; Rotondo et al., 2011c,d,e,a; Rueda et al., 2011, for details)

It is also worth to mention that the additional heating source needed at early times,  $H_0 \sim 10^{12}$ – $10^{15}$  erg/g/s (or  $H_0 \sim 10^{-6}$ – $10^{-3}$  MeV/Nucleon/s), is in striking agreement with the heat released from nuclear fusion reactions, radiative neutron captures and photodisintegrations in the early stages of neutron star mergers found by Goriely et al. (2011a,b). Fission as well as  $\beta$ -decays have been also there included; i.e neutron-induced fission, spontaneous fission,  $\beta$ -delayed fission, photofission, as well as  $\beta$ -delayed neutron emission.

All this suggests the exciting possibility that we are, for the first time, observing a nascent hot neutron star. This possibility alone warrants further studies on this subject, so we might obtain a more concrete picture of the thermal evolution of neo-neutron stars. A proposal has been recently submitted by E. Pian et al. to the Chandra satellite to observe if a similar prolonged X-ray emission exists also in GRB100316D associated with SN2010bh (Pian et al., 2011). We encourage also dedicated observations of isolated SN in view of the similarities between URCA-1–URCA-3 and the Type Ic Supernova SN 1994I (Immler et al., 2002) and SN 2002ap (Soria et al., 2004).

## D.2. Gravitational Waves versus Electromagnetic Emission in Gamma-Ray Bursts

The recent progress in the understanding the physical nature of neutron star equilibrium configurations and the first observational evidence of a genuinely Short Gamma-Ray Burst, GRB 090227B, allows to give an estimate of the gravitational waves versus electromagnetic emission in a Gamma-Ray Burst.

### D.2.1. Global versus local charge neutrality

We first recall that we have recently proved Belvedere et al. (2012); Rueda et al. (2011); Rotondo et al. (2011d) how the consistent treatment of neutron star equilibrium configurations, taking into account the strong, weak, electromagnetic, and gravitational interactions, implies the solution of the general relativistic Thomas-Fermi equations, coupled with the Einstein-Maxwell system of equations. This new set of equations supersedes the traditional Tolman-Oppenheimer-Volkoff (TOV) equations, which imply the condition of local charge neutrality throughout the configuration (Tolman, 1939; Oppenheimer and Volkoff, 1939).

The solution of the Einstein-Maxwell-Thomas-Fermi coupled differential equations leads to a new structure of the star (Belvedere et al., 2012): the positively charged core at supranuclear densities,  $\rho > \rho_{\text{nuc}} \sim 2.7 \times 10^{14} \text{ g cm}^{-3}$ , is surrounded by an electron distribution of thickness  $\gtrsim \hbar / (m_e c)$  and, at lower densities  $\rho < \rho_{\text{nuc}}$ , a neutral ordinary crust. The equilibrium condition given by the constancy of the particle Klein potentials leads to a discontinuity in the density at the core-crust transition and, correspondingly, an overcritical electric field  $\sim (m_\pi / m_e)^2 E_c$ , where  $E_c = m_e^2 c^3 / (e \hbar) \sim 1.3 \times 10^{16} \text{ Volt/cm}$ , develops in the boundary interface; see Fig. D.6. In particular, the continuity of the electron Klein potential leads to a decreasing of the electron chemical potential  $\mu_e$  and density at the core-crust boundary interface. They reach values  $\mu_e^{\text{crust}} < \mu_e^{\text{core}}$  and  $\rho_{\text{crust}} < \rho_{\text{core}}$  at the edge of the crust, where global charge neutrality is achieved (see Fig. D.6). We shall adopt some features of these neutron stars computed using the NL3 parameterization Lalazissis et al. (1997) of the phenomenological  $\sigma$ - $\omega$ - $\rho$  nuclear model; we refer to Belvedere et al. (2012) for details.

For each central density there exists an entire family of core-crust interface boundaries and, correspondingly, a family of crusts with different mass  $M_{\text{crust}}$  and thickness  $\Delta R_{\text{crust}}$ . The larger  $\rho_{\text{crust}}$ , the smaller the thickness of the core-crust interface, the peak of the electric field, and the larger the  $M_{\text{crust}}$  and  $\Delta R_{\text{crust}}$ . The configuration with  $\rho_{\text{crust}} = \rho_{\text{drip}} \sim 4.3 \times 10^{11} \text{ g/cm}^3$  separates neutron stars with and without inner crust. All the above new features lead to crusts with masses and thickness smaller than the ones obtained from the traditional TOV treatment. The mass-radius relation obtained in this case

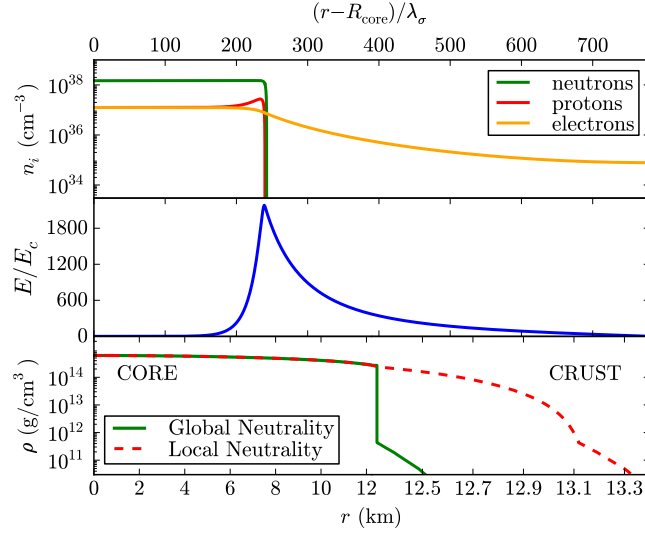


**Figure D.6.:** Upper panel: particle density profiles in the core-crust boundary interface, in units of  $\text{cm}^{-3}$ . Middle panel: electric field in the core-crust transition layer, in units of the critical field  $E_c$ . Lower panel: density profile inside a neutron star with central density  $\rho(0) \sim 5\rho_{\text{nuc}}$ . We show here the differences between the solution obtained from the TOV equations (locally neutral case) and the globally neutral solution presented in Belvedere et al. (2012). In this example the density at the edge of the crust is  $\rho_{\text{crust}} = \rho_{\text{drip}} = 4.3 \times 10^{11} \text{ g/cm}^3$  and  $\lambda_\sigma = \hbar/(m_\sigma c) \sim 0.4 \text{ fm}$  denotes the  $\sigma$ -meson Compton wavelength.

have been compared and contrasted with the one obtained from the locally neutral TOV approach; see Fig. D.7 and Belvedere et al. (2012) for details.

In Fig. D.7 we show how our new neutron star theory is in agreement with the most up-to-date stringent observational constraints to the mass-radius relation of neutron stars, that are provided by the largest mass, the largest radius, the highest rotational frequency, and the maximum surface gravity, observed from pulsars Trümper (2011). They are imposed by the mass of PSR J1614-2230  $M = 1.97 \pm 0.04 M_{\odot}$  Demorest et al. (2010a), the lower limit to the radius of RX J1856-3754 Trümper et al. (2004) (dotted-dashed curve), the 716 Hz PSR J1748-2246ad Hessels et al. (2006a) (dashed curve), and the surface gravity of the neutron star in the Low Mass X-Ray Binary X7 from which 90% confidence level contours of constant  $R_{\infty}$  can be extracted Heinke et al. (2006) (dotted curves); see Belvedere et al. (2012) for further details.

The above constraints strongly favor stiff nuclear equations of state such as the ones obtained from relativistic mean field models, which provide high maximum masses for neutron stars Trümper (2011). In addition, the radius of a canonical neutron star of mass  $M = 1.4 M_{\odot}$  is highly constrained to the range  $R \gtrsim 12$  km, ruling out a strange quark hypothesis for these objects. Our new neutron star mass-radius relation fully agrees with all the above requirements, for instance, we find that a canonical neutron star with  $M = 1.40 M_{\odot}$  has a radius  $R = 12.31$  km, for the NL3 parameterization of the nuclear EoS (see Belvedere et al., 2012, for details).

## D.2.2. GRB 090227B

We now turn to the observations of GRB 090227B (see Muccino et al., 2013, for details). The progress obtained from the Fermi-GBM and Konus-Wind satellites has been used to identify the new class of genuinely short GRBs: short bursts with the same inner engine of the long GRBs but endowed with a severely low value of the baryon load,  $B \equiv M_B c^2 / E_{tot}^{GRB} \lesssim 5 \times 10^{-5}$ , where  $M_B$  is the mass of the baryons engulfed by the expanding ultrarelativistic  $e^+e^-$  plasma of energy  $E_{tot}^{GRB}$ . The emission from these GRBs mainly consists in a first emission, the peak GRB (P-GRB), followed by a softer emission squeezed on the first one. The typical separation between the two components is expected to be shorter than 1–10 ms.

A special case is GRB 090227B. From the 16 ms time-binned light curves a significant thermal emission in the first 96 ms, which has been identified with the P-GRB, has been found Muccino et al. (2013). The subsequent emission is identified with the extended afterglow. The P-GRB of 090227B has the highest temperature ever observed,  $k_B T = 517$  keV, where  $k_B$  is the Boltzmann constant. The results of the fit of the light curve and spectrum of GRB 090227B are summarized in Table D.2. In particular we show the total energy emitted  $E_{tot}^{GRB}$ , Baryon load  $B$ , Lorentz factor at transparency  $\Gamma_{tr}$ , cosmologi-

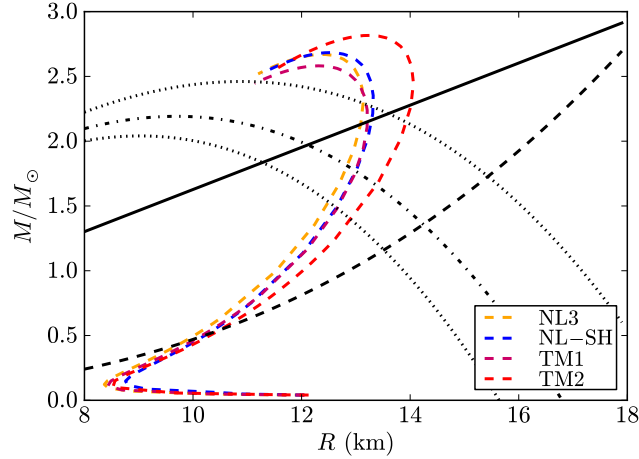


**Figure D.7.:** Constraints on the neutron star mass-radius relation (see Trümper, 2011, and references therein). We compare and contrast the theoretical  $M$ - $R$  relation of globally neutral neutron stars Belvedere et al. (2012) (blue curve) obtained from the solution of the Einstein-Maxwell-Thomas-Fermi equations and locally neutral neutron stars (red curve) obtained by solving the TOV equations. Any mass-radius relation have a maximum mass larger than  $M = 1.97 \pm 0.04M_{\odot}$  and should pass through the area delimited by the solid, dotted-dashed, dashed, and dotted curves.

cal redshift  $z$ , intrinsic duration of the GRB emission  $\Delta t$ , and average density of the CircumBurst Medium (CBM)  $\langle n_{CBM} \rangle$ ; we refer to Muccino et al. (2013) for further details.

The above quantitative results lead to the conclusion that the progenitor of GRB 090227B is a neutron star binary: (1) the natal kicks velocities imparted to a neutron star binary at birth can be even larger than  $200 \text{ km s}^{-1}$  and therefore a binary system can runaway to the halo of its host galaxy, clearly pointing to a very low average number density of the CBM; (2) the very large total energy, which we can indeed infer in view of the absence of beaming, and the very short time scale of emission point again to a neutron star binary; (3) as we shall show below the very small value of the baryon load is strikingly consistent with two neutron stars having small crusts, in line with the recent neutron star theory Belvedere et al. (2012).

### D.2.3. Inference of neutron star binary parameters

We now infer the binary component parameters. It is clear that the merging of two neutron stars will lead to a GRB if the total mass of the binary satisfies

$$M_1 + M_2 \gtrsim M_{\text{crit}} = 2.67M_{\odot}, \quad (\text{D.2.1})$$

$E_{tot}^{GRB}$ (erg)	$2.83 \times 10^{53}$
$B$	$4.13 \times 10^{-5}$
$\Gamma_{tr}$	$1.44 \times 10^4$
$z$	1.61
$\Delta t$ (s)	0.35
$\langle n_{CBM} \rangle$ (cm $^{-3}$ )	$1.9 \times 10^{-5}$

**Table D.2.:** Properties of GRB 090227B:  $E_{tot}^{GRB}$  is the total energy emitted in the GRB,  $B$  is the Baryon load,  $\Gamma_{tr}$  is the Lorentz factor at transparency, the cosmological redshift is denoted by  $z$ , the intrinsic duration of the GRB is  $\Delta t$ , and the average density of the CBM is  $\langle n_{CBM} \rangle$ . We refer to Muccino et al. (2013) for additional details.

where  $M_{crit}$  is the critical mass over which a neutron star undergoes gravitational collapse to a black hole. The numerical value reported in Eq. (D.2.1) has been taken from Belvedere et al. (2012).

Assuming for simplicity a binary with twin components  $M_1 = M_2 = M$ , we obtain masses  $M = 1.335M_{\odot}$  and correspondingly radii  $R_1 = R_2 = 12.24$  km (see Fig. D.7 and Belvedere et al. (2012)). The mass of the corresponding crust of each component is  $M_{crust} \sim 3.6 \times 10^{-5}M_{\odot}$  and the thickness of the crust is  $\Delta R_{crust} \sim 0.47$  km.

The location of the binary in the very low interstellar density medium of galactic halos makes possible to probe the neutron star theory and equation of state through the knowledge of the baryon load  $B$  inferred from the fitting of the GRB light curve and spectrum. The baryonic matter which the GRB interact with is in these systems provided by the material of the neutron star crusts ejected during the binary coalescence. Thus, a theoretical expectation of the baryon load  $B$  left in a binary neutron star merger is

$$B = \frac{\eta M_{crust} c^2}{E_{tot}^{GRB}}, \quad (D.2.2)$$

where  $\eta$  is the fraction of the crustal mass ejected. Here we are assuming that the mass ejected during the merger comes from the outer layers of the neutron star, namely from the crust of the star.

In Fig. D.8 we have plotted the theoretical baryon load given by Eq. (D.2.2) for GRB 090227B, namely using  $E_{tot}^{GRB} = 2.83 \times 10^{53}$  erg, as a function of the mass  $M$  of the globally and locally neutral neutron stars shown in Fig. D.7.

The agreement of the observed baryon load of GRB 090227B (see Table D.2 and Muccino et al. (2013)) with the low mass of the crust obtained from the globally neutral neutron stars of Belvedere et al. (2012) is evident (see Fig. D.8). It can be compared and contrasted with the ones obtained enforcing the local charge neutrality condition. For the specific binary neutron star

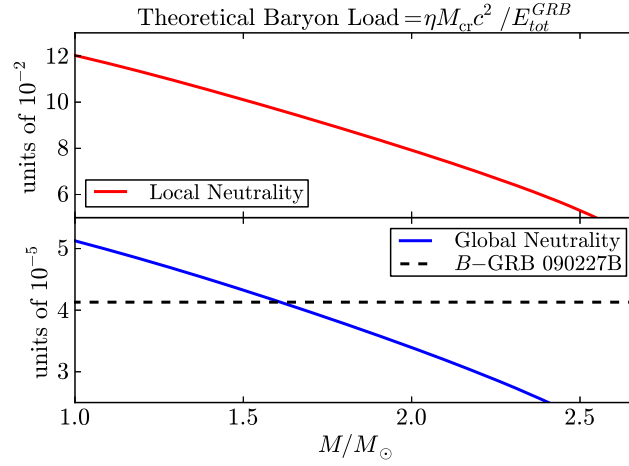


**Figure D.8.:** Baryon load expected to be left by a binary neutron star merger, given by Eq. (D.2.2) for  $\eta = 1$ , as a function of the total mass  $M$  of globally (lower panel, units  $10^{-5}$ ) and locally neutral (upper panel, units  $10^{-2}$ ) neutron stars, for the case of GRB 090227B. We have indicated the observed baryon load of GRB 090227B,  $B = 4.13 \times 10^{-5}$ ; see Table D.2 and Muccino et al. (2013).

system studied here we obtain a theoretical prediction of the baryon load from Eq. (D.2.2) with  $\eta = 1$ ,  $B \sim 7.6 \times 10^{-5}$ , or a mass of the baryons  $M_B = E_{\text{crust}}^B / c^2 \sim 1.2 \times 10^{-5} M_{\odot}$ , to be confronted with the one obtained from the fitting procedure of GRB 090227B,  $B \sim 4.13 \times 10^{-5}$ , corresponding to  $M_B = B E_{\text{tot}}^{\text{GRB}} / c^2 \sim 0.7 \times 10^{-5} M_{\odot}$ . The above theoretical predictions of the neutron star crust mass  $M_{\text{crust}}$  and consequently the value of  $E_{\text{crust}}^B$  and  $B$  have been inferred for a crust with a density at its edge equal to the neutron drip density  $\rho_{\text{drip}} \sim 4.3 \times 10^{11} \text{ g cm}^{-3}$ . Neutron star crusts with densities  $\rho < \rho_{\text{drip}}$  are predicted by the new neutron star theory Belvedere et al. (2012), there is still room for smaller values of the baryonic matter ejected in a binary process, and consequently to still shorter genuinely short GRBs.

The mass-energy of the baryon ejecta obtained from the estimate (D.2.2) gives for locally neutral neutron stars values  $10^2$ – $10^3$  bigger than the ones analyzed before (see Fig. D.8), due to the more massive crusts obtained from the TOV-like treatment (see Belvedere et al., 2012, for details). It implies that Eq. (D.2.2) gives in such a case  $M_B \sim 10^{-3}$ – $10^{-2} M_{\odot}$ , in line with previous results obtained from the numerical simulation of the dynamical evolution of neutron star binaries (see e.g. Ruffert and Janka, 2001; Goriely et al., 2011b), where locally neutral neutron stars are employed.

### D.2.4. Gravitational wave emission

The emission of gravitational waves signals from binaries system are the most expected signals to be detect by the interferometers called Advanced LIGO<sup>2</sup>-VIRGO<sup>3</sup> and they have been planned for to be operational in a few years with a improved sensitivity approximately a factor of 10 better than the first generation of detectors. The connexion between short gamma-ray signals and gravitational waves signals as a coincidence of the same event would allow us in principle to understand more about the origin of short GRBs (see Kobayashi and Mészáros (2003), and references therein).

We use here the adiabatic approximation to estimate the gravitational wave emission from the binary neutrons star. We used the above values of the neutron star binary progenitor estimated for the short GRB 090227B at a cosmological redshift  $z = 1.61$  Muccino et al. (2013). We assume for simplicity a circular orbit  $r$  (separation between the two neutron star centers) and the emission in the spiral phase until the both stars *touch* each other at a distance,  $r = R_1 + R_2 = 24.48$  km, from the radial coordinate origin.

#### Classical Dynamics

The orbital angular velocity of the binary with components  $(M_1, R_1)$  and  $(M_2, R_2)$  orbiting each other in a circular orbit of radius  $r$ , is given by

$$\omega = \sqrt{\frac{G(M_1 + M_2)}{r^3}}, \quad (\text{D.2.3})$$

and its total binding energy is

$$E_b = -\frac{1}{2} \frac{GM_1M_2}{r}. \quad (\text{D.2.4})$$

The leading term driving the loss of binding energy via gravitational wave emission is given by

$$-\frac{dE_b}{dt} = \frac{32}{5} \frac{G^4}{c^5} \frac{(M_1 + M_2)(M_1M_2)^2}{r^5}, \quad (\text{D.2.5})$$

which leads to a decreasing of the separation  $r$  with time and consequently a shortening of the orbital period  $P = 2\pi/\omega$  dictated by (Landau and Lifshitz, 1980)

$$\frac{1}{P} \frac{dP}{dt} = \frac{3}{2} \frac{1}{r} \frac{dr}{dt} = -\frac{3}{2} \frac{1}{E_b} \frac{dE_b}{dt}. \quad (\text{D.2.6})$$

The loss of orbital binding energy by emission of gravitational waves from

<sup>2</sup><http://www.advancedligo.mit.edu>

<sup>3</sup><http://www.cascina.virgo.inft.it>

the neutron star system in spiral phase for non-relativistic and point-like particles can be written as a function of the gravitational waves frequency  $f$  as

$$\frac{dE_b}{df} = -\frac{1}{3}(\pi G)^{2/3}\mathcal{M}^{5/3}f^{-1/3}, \quad (\text{D.2.7})$$

where  $\mathcal{M} = (M_1 M_2)^{3/5} / (M_1 + M_2)^{1/5}$  is the called chirp mass.

### Effective one-body dynamics

The effective one-body (EOB) formalism (Damour and Nagar, 2010) maps the conservative dynamics of a binary system of non spinning objects onto the geodesic dynamics of one body of reduced mass  $\mu = M_1 M_2 / M$ , with  $M = M_1 + M_2$  the total binary mass. The effective metric is a modified Schwarzschild metric given by

$$ds^2 = -A(r)dt^2 + B(r)dr^2 + r^2(d\theta^2 + \sin^2\theta d\phi^2) \quad (\text{D.2.8})$$

where  $r = GM/R$  and the radial potential is given by,

$$A(u; v) = P_5^1[1 - 2u + 2vu^3 + a_4vu^4 + a_5vu^5], \quad (\text{D.2.9})$$

with  $u = 1/r$ ,  $v = M_1 M_2 / (M_1 + M_2)^2$  is the symmetric mass ratio (see Fig. D.9),  $P_n^m$  denotes the Padè approximant Damour and Nagar (2009) or order  $(n, m)$  and the values of the 3 and 4 post-Newtonian (PN)-level coefficients are  $a_4 = 94/3 - (41/32)\pi^2$  and  $a_5(v) = a_5^{c0} + va_5^{c1}$  (see Bini and Damour (2013), for details).

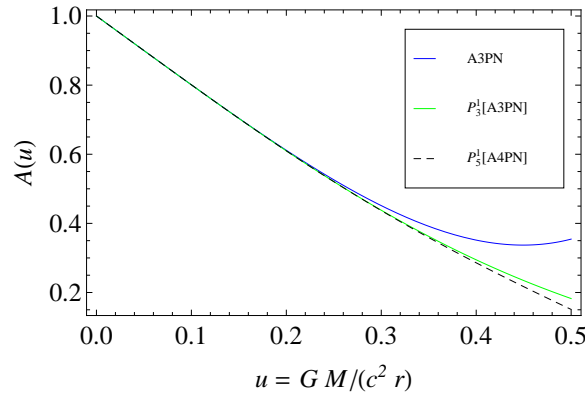


**Figure D.9.:** Comparison between the EOB radial potential as a function of the  $u$ -parameter for the cases:  $A(u; \circ) = 3\text{PN}$  (blue line),  $P_3^1[A(u; \circ) = 3\text{PN}]$  (green line) and  $P_5^1[A(u; \circ) = 4\text{PN}]$  (dashed-black line), where the  $P_n^m[\cdot]$  is the Padè approximant.

The EOB Hamiltonian is

$$H = M\sqrt{1 + 2\nu(\hat{H}_{\text{eff}} - 1)}, \quad (\text{D.2.10})$$

and effective Hamiltonian is described by

$$\hat{H}_{\text{eff}}^2 = A(u) + p_\phi^2 B(u), \quad (\text{D.2.11})$$

where  $B(u) = u^2 A(u)$  and the angular momentum for the circular orbit is given by

$$p_\phi^2 = -\frac{A'(u)}{[u^2 A(u)]'}. \quad (\text{D.2.12})$$

We need to write  $\hat{H}_{\text{eff}}$  as a function of the orbital frequency  $\Omega$  for which we need to write the  $u$ -parameter as a function of  $\Omega$ . This is obtained from the angular Hamilton equation of motion in the circular case

$$GM\Omega(u) = \frac{1}{u} \frac{\partial H}{\partial p_\phi} = \frac{MA(u)p_\phi(u)u^2}{H\hat{H}_{\text{eff}}}, \quad (\text{D.2.13})$$

which we can solve numerically (see e.g. Fig. D.10).

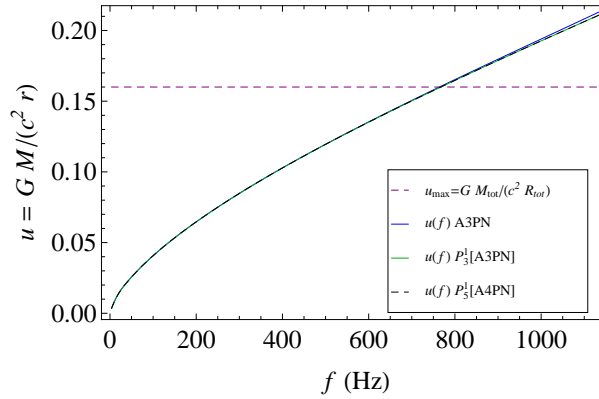


**Figure D.10.:** The  $u$  parameter as a function of the source frequency obtained from Eq. D.2.13 in the case of a symmetric binary,  $M_1 = M_2$ , so  $\nu = 1/4$ .

The binding energy as a function of the orbital frequency (see Fig. D.11) is,

$$E_b(\Omega) = H - M = M[\sqrt{1 + 2\nu(\hat{H}_{\text{eff}} - 1)} - 1], \quad (\text{D.2.14})$$

and the gravitational energy spectrum is obtained through the derivative  $dE_b/d\Omega$ .

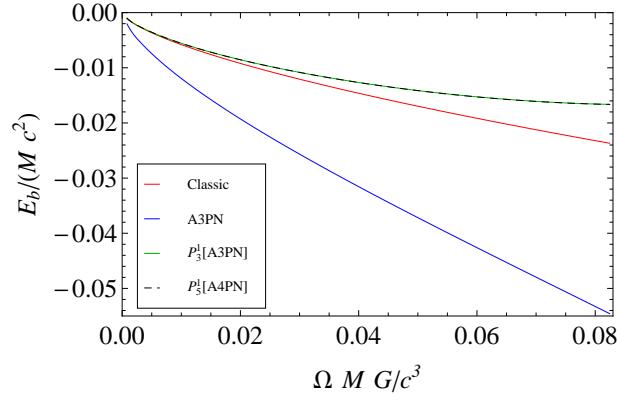


**Figure D.11.:** Comparison of the EOB binding energies using the radial potential  $A(u; \circ) = 3\text{PN}$ ,  $P_3^1[A(u; \circ) = 3\text{PN}]$  and  $P_5^1[A(u; \circ) = 4\text{PN}]$ .

### Signal-to-noise ratio

The signal-to-noise ratio (SNR) is defined by

$$\rho^2 = 4 \int_0^\infty \frac{|\tilde{h}(f)|}{S_h(f)} df, \quad (\text{D.2.15})$$

where  $\tilde{h}(f)$  is the Fourier transform of  $h(t)$  and  $S_h(f)$  is the noise spectral density of the detector.

The response of the detector is defined as  $R = h(t) + n(t)$ , where the signal is

$$h(t) = F_+ h_+ + F_\times h_\times \quad (\text{D.2.16})$$

and  $n(t)$  is the noise. The  $F_{+, \times}$  are the called beam patterns and depend on the detector, and the functions  $h_{+, \times}$  are the polarizations of the gravitational wave, which depend on the source (see e.g. Thorne (1987), for details).

The average of the square SNR  $\langle \rho^2 \rangle$  over all orientations and directions to the source, depends on the energy spectrum  $dE_b/df$  of the emitted gravitational waves (see Flanagan and Hughes (1998), for details),

$$\langle \rho^2 \rangle = \frac{2(1+z)^2}{5\pi^2 d_L^2} \int_{f_{\min}}^{f_{\max}} \frac{1}{f_d^2 S_h(f_d)} \frac{dE_b}{df} [(1+z)f_d] df_d, \quad (\text{D.2.17})$$

where  $z$  is the cosmological redshift,  $d_L$  is the luminosity distance,  $f_d = f/(1+z)$  is the gravitational wave frequency at the detector,  $f = \Omega/\pi$  is the frequency in the source frame,  $\Omega$  is the orbital frequency, the minimal bandwidth frequency of the detector is  $f_{\min}$ , and  $f_{\max} = f_c/(1+z)$  is the maximal bandwidth frequency where  $f_c$  is the binary contact frequency.

The characteristic gravitational waves amplitude is defined using the Fourier transform of the gravitational wave signal  $h(t)$ ,  $h_c(f) = f|\tilde{h}(f)|$  and is given

by,

$$h_c^2(f) = \frac{2(1+z)^2}{\pi^2 d_L^2} \frac{dE_b}{df} [(1+z)f_d], \quad (\text{D.2.18})$$

Note that this definition of the  $h_c(f)$  is as a function of the gravitational waves energy spectrum (see e.g. Flanagan and Hughes (1998); Kobayashi and Mészáros (2003), for details).

The gravitational waves emission dominates the energy loss during the spiraling phase while the electromagnetic radiation dominates from the coalescence with the final emission of a short GRB if the total mass of the binary exceeds the critical mass for neutron star gravitational collapse. Thus, an upper limit for the gravitational wave emission radiated away can be obtained from the energy difference between the initial binary at time  $t_0 = 0$  with separation  $r_0$  and energy  $E_0$ , and the binary at time  $t_f$  and separation  $r_f = R_1 + R_2$ , with energy  $E_f$ , when the two components *touch* each other.

An absolute upper limit, for the gravitational wave energy emission,  $\Delta E_{\text{GW}}^{\text{max}}$ , can be therefore determined by the assumption of an infinite initial separation  $r_0 \rightarrow \infty$ , i.e.

$$\Delta E_{\text{GW}}^{\text{max}} = |E_b(t_f) - E_b(t_0)|. \quad (\text{D.2.19})$$

For the neutron star binary discussed in this work for GRB 090227B, we obtain the absolute upper bound shown in Table D.3. The gravitational wave energy emission  $\Delta E_{\text{GW}}^{\text{max}}$  which in the case of the genuinely short GRB 090227B is one order of magnitude smaller than the emitted electromagnetic energy  $E_{\text{tot}}^{\text{GRB}} = 2.83 \times 10^{53}$  erg (see Table D.2).

Classical	EOB A3PN	EOB $P_5^1$ [A3PN]	EOB $P_5^1$ [A4PN]
$9.6 \times 10^{52}$	$9.68 \times 10^{52}$	$7.41 \times 10^{52}$	$7.42 \times 10^{52}$

**Table D.3.:** Upper limit for the total gravitational waves emission,  $\Delta E_{\text{GW}}^{\text{max}}$ , in erg.

It is also worth mentioning that indeed this numerical value for  $\Delta E_{\text{GW}}^{\text{max}}$  limits from above the results of full numerical integrations of the gravitational wave radiation emitted in the neutron star binaries during the entire process of spiraling and merging (see e.g. Ruffert and Janka (2001)).

In Figs. D.12 and D.13 we show the characteristic gravitational wave amplitude as a function of the energy spectrum  $dE_b/df$  for both cases, the non-relativistic point-like particles, Eq. D.2.7, and for the EOB formalism, see Eq. (D.2.13). In the same plot is possible to compare the amplitude  $h_c(f)$  in [*strain*/ $\sqrt{\text{Hz}}$ ] units with the the noise density spectrum  $S_h(f)$  of the Advanced LIGO interferometer.

The difference between Figs. D.12 and D.13 is because the first one was calculated using the estimated redshift of GRB 090227B,  $z = 1.61$ , while in Fig. D.13, we show the results for a hypothetical redshift  $z = 0.08$ , at which

such a short GRB would be detected by Advanced Ligo with a signal-to-noise ratio SNR=5.

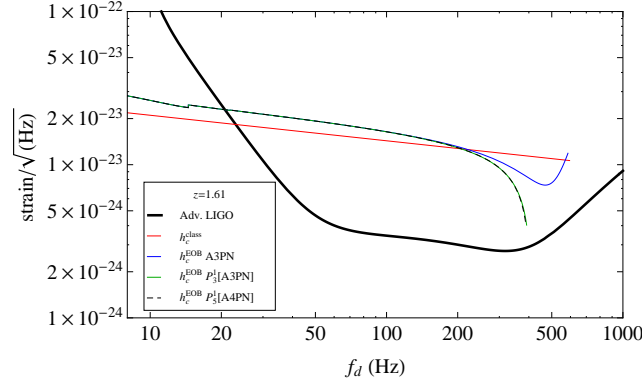


**Figure D.12.:** The characteristic gravitational waves amplitude, Eq.(D.2.18), was calculated using the progenitor’s values of the short GRB 090227B, a cosmological redshift  $z = 1.61$ , and the  $h_c(f)$  as a function of the gravitational wave energy spectrum  $dE_b/df$  for both cases, the non-relativistic point-like particles D.2.7 (red line) and the EOB formalism, see Eq. (D.2.13). The radial potential  $A(u; \nu)$  was calculated using post-Newtonian approximation (PN). The blue line is  $A(u; \nu) = 3PN$ , using the Padè approximant we calculated the  $P_3^1[A(u; \nu) = 3PN]$  (green line) and the  $P_5^1[A(u; \nu) = 4PN]$  (dashed-black line). The  $S_h(f)$  is the noise spectral density of Advanced LIGO.

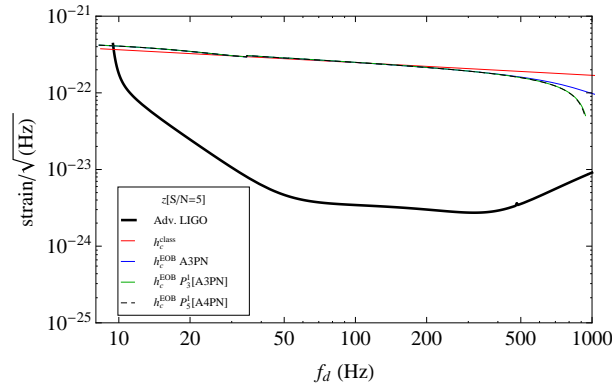


**Figure D.13.:** We estimated the signal-to-noise (SNR) and we found the redshift  $z = 0.08$  for a gravitational wave detection with SNR=5 by Advanced LIGO. We calculated the characteristic gravitational wave amplitude  $h_c(f) = \sqrt{f S_h(f)}$  for the classical case (red line) and for the EOB formalism. The blue line is  $A(u; \nu) = 3PN$ , using the Padè approximant we calculated the  $P_3^1[A(u; \nu) = 3PN]$  (green line) and the  $P_5^1[A(u; \nu) = 4PN]$  (dashed-black line). The  $S_h(f)$  is the noise spectral density of Advanced LIGO.

Additional contributions to the gravitational wave power due to higher multipole moments of the components such as angular momentum  $J$  and quadrupole moment  $Q$  (deformation) are conceptually relevant corrections to the above formulas (see e.g. Ryan (1995) and references therein, for details); however they are quantitatively negligible for the present purpose. For instance, the first correction due to the spin angular momentum  $J$  of the neutron star components is given by  $-11/4 j\omega M$  in geometric units, where  $j = cJ/(GM^2)$  is the dimensionless angular momentum parameter. This correction is only of order  $10^{-2}$  for a binary orbit of very high angular frequency  $\sim$  kHz and for neutron stars with  $M = 1.335M_\odot$  and  $j = 0.4$ . We recall that the fastest observed pulsar, PSR J1748-2246ad, has a rotation frequency of 716 Hz Hessels et al. (2006a), which gives  $j \sim 0.51 I_{45}/(M_0/M_\odot)^2 = 0.26 I_{45}$  with the latter value for a canonical NS of  $M = 1.4M_\odot$ ,  $I_{45}$  is the moment of inertia in units of  $10^{45}$  g cm<sup>2</sup>. The first correction due to the quadrupole deformation multipole moment  $Q$  of the neutron star, given by  $-2 Q\omega^{4/3}M^{-5/3}$ , is of order  $10^{-3}$  for the same parameters with  $Q \sim 4 \times 10^{43}$  g cm<sup>2</sup>  $\sim 3$  km<sup>3</sup>, the latter value in geometric units.

### D.2.5. Conclusions

We showed that the observations of the genuinely short GRB 090227B lead to crucial information on the binary neutron star progenitor. The data obtained from the electromagnetic spectrum allows to probe crucial aspects of the correct theory of neutron stars and their equation of state. The baryon load parameter  $B$  obtained from the analysis of GRB 090227B, leads to a most remarkable agreement of the baryonic matter expected to be ejected in a neutron star binary merger and validate the choice of the parameters of the binary components,  $M_1 = M_2 = 1.34M_\odot$ , and  $R_1 = R_2 = 12.24$  km. This represents a test of the actual neutron star parameters described by the recent developed self-consistent theory of neutron stars Belvedere et al. (2012) that takes into account the strong, weak, electromagnetic and gravitational interactions within general relativity.

We computed the dynamics of the neutron star binary progenitor prior to the merger and emission of the GRB. We compare and contrast the classic description of the dynamics with the more general one given by the framework of the effective one-body formalism, which we use up to 4-PN order. We estimate the detectability of GRB 090227B by the Advanced LIGO interferometer, by computing the signal-to-noise ratio up to the contact point of the binary components, for the theoretically inferred cosmological redshift,  $z = 1.61$  (Muccino et al., 2013). We also estimate the redshift at which Advanced LIGO would detect this GRB with a signal-to-noise ratio equal to five; we obtained  $z \approx 0.08$ . From the dynamics, we then estimated the total energy release in form of gravitational waves (see Table D.3). From this, we

concluded that the emission of electromagnetic radiation in a GRB by a binary neutron star system is at least one order of magnitude larger than the gravitational wave emission.

# E. Exact Solutions of the Einstein-Maxwell equations in Astrophysics

## E.1. On the relativistic precession and oscillation frequencies of test particles around rapidly rotating compact stars

### E.1.1. Introduction

One of the greatest challenges of the general theory of relativity has been the construction of solutions to the Einstein-Maxwell field equations representing the gravitational field of compact stars such as neutron stars (NSs). Stationary axially symmetric spacetimes satisfy basic properties one expects for rotating objects, namely time symmetry and reflection symmetry with respect to the rotation axis (see e.g. Pachón and Sanabria-Gómez, 2006). The simplest stationary axially symmetric exact exterior vacuum solution describing a rotating configuration is the well-known Kerr metric (Kerr, 1963). The Kerr metric is fully described by two free parameters: the mass  $M$  and the angular momentum  $J$  of the object. However, it is known from numerical models that the quadrupole moment of rotating NSs deviates considerably from the one given by the Kerr solution  $Q_{\text{Kerr}} = -J^2/(Mc^2)$  (see e.g. Laarakkers and Poisson, 1999, for details).

In the mean time, a considerable number of analytic exterior solutions with a more complex multipolar structure than the one of the Kerr solution have been developed (see e.g. Manko et al., 1995, 2000; Stephani et al., 2003). Whether analytic exterior solutions are accurate or not to describe the gravitational field of compact stars is an interesting and very active topic of research (see e.g. Stute and Camenzind, 2002; Berti and Stergioulas, 2004; Pachón et al., 2006, and references therein).

The accuracy of analytic solutions to describe the exterior geometry of a realistic rotating compact star has been tested by comparing physical properties, e.g. the radius of the Innermost Stable Circular Orbit (ISCO) on the equatorial plane and the gravitational redshift (see Sibgatullin and Sunyaev, 1998; Berti and Stergioulas, 2004; Pachón et al., 2006, for details). In order

to do such a comparison, the free parameters (i.e. the lowest multipole moments) of the analytic exterior spacetime, are fixed to the corresponding lowest multipole moments given by numerical interior solutions of the Einstein equations, for NS realistic models (see e.g. Berti and Stergioulas, 2004).

Following such a procedure, the solution of Manko et al. (2000) has been compared by Stute and Camenzind (2002) and by Berti and Stergioulas (2004) with the numerical solutions for NSs calculated by Cook et al. (1994) and with those derived by Berti and Stergioulas (2004), respectively. However, being a generalization of the solution of Tomimatsu and Sato (1972), it cannot describe slowly rotating compact stars (see e.g. Berti and Stergioulas, 2004), but the dynamics of astrophysical objects with anisotropic stresses (see Dubeibe et al., 2007, for details).

Following a similar procedure, based on tests of the ISCOs radii on the equatorial plane of the rotating neutron stars obtained by Berti and Stergioulas (2004), it has been shown that the six-parametric solution of Pachón et al. (2006) (hereafter PRS solution, see Sec. E.1.2 for details) is more accurate than the model of Manko et al. (2000). In addition, being a generalization of the Kerr solution, this solution can be used for arbitrary rotation rates.

Besides the ISCOs radii, there are additional physical properties that can be computed with analytic and numerical models and thus useful to compare and contrast the accuracy of analytic exact models. The aim of this work is to analyze the properties of orbital frequencies of neutral test particles in the PRS and in the Kerr geometries with especial focus on the Keplerian  $\nu_K$ , frame-dragging (Lense-Thirring)  $\nu_{LT}$ , as well as the precession(oscillation) frequencies of the radial and vertical motions,  $\nu_\rho^P(\nu_\rho^{OS})$  and  $\nu_z^P(\nu_z^{OS})$ , respectively.

The relevance of these frequencies relies on the fact that they are often invoked to explain the Quasi-Periodic Oscillations (QPOs) observed in some relativistic astrophysical systems such as Low Mass X-ray Binaries (LMXBs), binary systems harboring either a NS or a black hole (BH) accreting matter from a companion star. For instance, within the Relativistic Precession Model (RPM) introduced by Stella and Vietri (1998); Morsink and Stella (1999); Stella et al. (1999); Stella and Vietri (1999), the kHz QPOs are interpreted as a direct manifestation of the modes of relativistic epicyclic motion of blobs arising at various radii  $r$  in the inner parts of the accretion disk around the compact object (see Sec. E.1.6, for details).

In addition to the RPM, the Keplerian, precession and oscillation frequencies are used in other QPO theoretical models (see e.g. Lin et al., 2011, for a recent comparison of the existing models). Due to the influence of general relativistic effects in the determination of such frequencies, an observational confirmation of any of the models might lead to an outstanding test of general relativity in the strong field regime. In this line, it is of interest to compare and contrast the orbital frequencies given by the Kerr solution and by the PRS solution (see Sec. E.1.3), which help to establish the differences between pos-

sible BH and NS signatures. We emphasize in this work the major role of the quadrupole moment as well as of the octupole moment of the object, whose possible measurement can be used as a tool to test the no-hair theorem of BHs (see e.g. Johannsen and Psaltis, 2011). In the case of NSs, the interpretation of QPOs as the manifestation of orbital motion frequencies might lead to crucial information of the NS parameters such as mass, angular momentum (see e.g. Stella and Vietri, 1998; Török et al., 2010), and quadrupole moment (see e.g. Morsink and Stella, 1999). These parameters reveal, at the same time, invaluable information about the EoS of nuclear matter.

The work is organized as follows. In Sec. E.1.2 we recall the properties of the PRS solution. The computation of the orbital frequencies as well as the comparison of their features in the Kerr and in the PRS spacetimes, is shown in Sec. E.1.3. In Sec. E.1.4 we study the accuracy of the analytic formulas of the periastron and nodal frequencies derived by Ryan (1995) for stationary axially symmetric spacetimes. In Sections 5 and 6 we discuss the accuracy of the PRS solution in describing the frequencies of realistic NS models and its relevance in the Relativistic Precession Model, respectively. The conclusions of this work and a discussion on possible additional effects to be accounted for in the determination of the orbital frequencies, e.g. the effect of magnetic dipole moment, are outlined in Sec. E.1.7.

### **E.1.2. The PRS analytic exact solution**

We first recall the PRS analytic model (Pachón et al., 2006), for the exterior gravitational field of a compact object<sup>1</sup>. In the stationary axisymmetric case, the simplest form of the metric can be written as (Papapetrou, 1953)

$$ds^2 = -f(dt - \omega d\phi)^2 + f^{-1} \left[ e^{2\gamma}(d\rho^2 + dz^2) + \rho^2 d\phi^2 \right], \quad (\text{E.1.1})$$

where  $f$ ,  $\omega$  and  $\gamma$  are functions of the quasi-cylindrical Weyl coordinates  $(\rho, z)$ . Thus, the components of the metric tensor  $g_{\mu\nu}$  are

$$g_{\phi\phi} = \frac{\rho^2}{f(\rho, z)} - f(\rho, z)\omega(\rho, z)^2, g_{tt} = -f(\rho, z), \quad (\text{E.1.2})$$

$$g_{t\phi} = f(\rho, z)\omega(\rho, z), g_{zz} = g_{\rho\rho} = \frac{e^{2\gamma(\rho, z)}}{f(\rho, z)} = \frac{1}{g^{zz}} = \frac{1}{g^{\rho\rho}}. \quad (\text{E.1.3})$$

Using the above line element, the Einstein-Maxwell equations can be reformulated, via Ernst's procedure in terms of two complex potentials  $\mathcal{E}(\rho, z)$  and  $\Phi(\rho, z)$  (Ernst, 1968a,b). By means of Sibgatullin's integral method (Sib-

---

<sup>1</sup>Mathematica 8.0 scripts with the solution, some limiting cases as well as the the calculations presented in this paper are available at <http://www.chem.utoronto.ca/~lpachon/scripts/nstars>

gatullin, 1991; Manko and Sibgatullin, 1993) this system of equations can be solved via

$$\mathcal{E}(z, \rho) = \int_{-1}^1 \frac{d\sigma}{\pi} \frac{e(\xi)\mu(\sigma)}{\sqrt{1-\sigma^2}}, \quad \Phi(z, \rho) = \int_{-1}^1 \frac{d\sigma}{\pi} \frac{f(\xi)\mu(\sigma)}{\sqrt{1-\sigma^2}}, \quad (\text{E.1.4})$$

where  $e(z) := \mathcal{E}(z, \rho = 0)$  and  $f(z) := \Phi(z, \rho = 0)$ . The unknown function  $\mu(\sigma)$  must satisfy the singular integral equation

$$\int_{-1}^1 \frac{\mu(\sigma)[e(\xi) + \bar{e}(\eta) + 2f(\xi)\bar{f}(\eta)]d\sigma}{(\sigma - \tau)\sqrt{1-\sigma^2}} = 0 \quad (\text{E.1.5})$$

and the normalizing condition

$$\int_{-1}^1 \frac{\mu(\sigma)d\sigma}{\sqrt{1-\sigma^2}} = \pi, \quad (\text{E.1.6})$$

where  $\xi = z + i\rho\sigma$ ,  $\eta = z + i\rho\tau$ ,  $\rho$  and  $z$  being the Weyl-Papapetrou quasi-cylindrical coordinates,  $\sigma, \tau \in [-1, 1]$ ,  $\bar{e}(\eta) := \overline{e(\bar{\eta})}$ ,  $\bar{f}(\eta) := \overline{f(\bar{\eta})}$  and the overbar stands for complex conjugation. In (Pachón et al., 2006), the Ernst potentials were chosen as

$$e(z) = \frac{z^3 - z^2(m + ia) - kz + is}{z^3 + z^2(m - ia) - kz + is}, \quad f(z) = \frac{qz^2 + i\mu z}{z^3 + z^2(m - ia) - kz + is}. \quad (\text{E.1.7})$$

We calculate the multipole moments following the procedure of Hoense-laers and Perjés (1990). We denote the mass multipoles by  $M_i$  while, the current (rotation) multipoles, by  $S_i$ . The electric multipoles are denoted by  $Q_i$  and the magnetic ones by  $\mathcal{B}_i$ . Thus, for the PRS solution we have

$$\begin{aligned} M_0 &= m, & M_2 &= mk - ma^2, & \dots \\ S_1 &= ma, & S_3 &= -ma^3 + 2mak - ms, & \dots \end{aligned} \quad (\text{E.1.8})$$

$$\begin{aligned} Q_0 &= q, & Q_2 &= -a^2q - a\mu + kq, & \dots \\ \mathcal{B}_1 &= \mu + aq, & \mathcal{B}_3 &= -a^2\mu + \mu k - a^3q + 2akq - qs, & \dots \end{aligned} \quad (\text{E.1.9})$$

This allows us to identify  $m$  as the total mass,  $a$  as the total angular momentum per unit mass ( $a = J/m$ , being  $J$  the total angular momentum); while  $k$ ,  $s$ ,  $q$  and  $\mu$  are associated to the mass-quadrupole moment  $M_2$ , current octupole  $S_3$ , electric charge and magnetic dipole, respectively.

The potentials (E.1.7) can be written in an alternative way, we mean

$$e(z) = 1 + \sum_{i=3}^3 \frac{e_i}{z - \beta_i}, \quad f(z) = \sum_{i=3}^3 \frac{f_i}{z - \beta_i}, \quad (\text{E.1.10})$$

with  $(i, k \neq j)$

$$e_j = (-1)^j \frac{2m\beta_j^2}{(\beta_j - \beta_k)(\beta_j - \beta_i)}, \quad f_j = (-1)^{j+1} \frac{i\mu + d\beta_j}{(\beta_j - \beta_k)(\beta_j - \beta_i)}. \quad (\text{E.1.11})$$

Then, using Eqs. (E.1.4) and (E.1.7), we obtain the Ernst potentials

$$\mathcal{E} = \frac{A + B}{A - B}, \quad \Phi = \frac{C}{A - B}, \quad (\text{E.1.12})$$

and the metric functions in the whole spacetime

$$f = \frac{A\bar{A} - B\bar{B} + C\bar{C}}{(A - B)(\bar{A} - \bar{B})}, \quad e^{2\gamma} = \frac{A\bar{A} - B\bar{B} + C\bar{C}}{K\bar{K} \prod_{n=1}^6 r_n}, \quad (\text{E.1.13})$$

$$\omega = \frac{\text{Im}[(A + B)\bar{H} - (\bar{A} + \bar{B})G - C\bar{I}]}{A\bar{A} - B\bar{B} + C\bar{C}}, \quad (\text{E.1.14})$$

where the functions  $A, B, C, H, G, K,$  and  $I$  can be found in the Appendix E.1.8.

The PRS electrovacuum exact solution belongs to the extended  $N$ -soliton solution of the Einstein-Maxwell equations derived by Ruiz et al. (1995), in the particular case  $N = 3$ . In addition, the functional form of the metric functions resembles the one derived previously by Bretón et al. (1999). Besides the limiting cases discussed in Pachón et al. (2006) it is worth mentioning that, in the vacuum case  $q = 0$  and  $\mu = 0$ , for  $s = 0$  this solution reduces to the solution of Manko et al. (1995) under the same physical conditions, namely  $q = 0$ ,  $c = 0$  and  $b = 0$  in Manko et al. (1995).

### **E.1.3. Orbital Motion Frequencies on the Equatorial Plane**

Although for the case of compact stars contributions from the magnetic field could be relevant (see e.g. Bakala et al., 2010; Sanabria-Gómez et al., 2010; Bakala et al., 2012), we focus in this work on the frequencies of neutral particles orbiting a neutral compact object. We calculate here the Keplerian  $\nu_K = \Omega_K/(2\pi)$ , frame-dragging (Lense-Thirring)  $\nu_{LT} = \Omega_{LT}/(2\pi)$ , radial oscillation and precession,  $\nu_\rho^{\text{OS}} = \Omega_\rho^{\text{OS}}/(2\pi)$  and  $\nu_\rho^{\text{P}} = \Omega_\rho^{\text{P}}/(2\pi)$ , and vertical oscillation and precession frequencies,  $\nu_z^{\text{OS}} = \Omega_z^{\text{OS}}/(2\pi)$  and  $\nu_\rho^{\text{P}} = \Omega_\rho^{\text{P}}/(2\pi)$ , respectively.

The geodesic motion of test particles along the radial coordinate, on the equatorial plane  $z = 0$ , is governed by the effective potential (see e.g. Ryan, 1995)

$$V(\rho) = 1 - \frac{E^2 g_{\phi\phi} + 2ELg_{t\phi} + L^2 g_{tt}}{g_{t\phi}^2 - g_{tt}g_{\phi\phi}}, \quad (\text{E.1.15})$$

where, for circular orbits, the energy  $E$  and angular momentum  $L$  are determined by the conditions  $V = 0$  and  $dV/d\rho = 0$  (see Eqs. E.1.18–E.1.19). The frequencies at the ISCO's location (determined by the additional condition  $d^2V/d\rho^2 = 0$ ) are of particular interest. Thus, before starting the discussion of the frequencies, it is important to explore the ISCO parametric dependence. We report here, as standard in the literature, the *physical* ISCO radius given by  $\sqrt{g_{\phi\phi}}$  evaluated at the root of Eq. (E.1.15) that gives the coordinate ISCO radius. In the upper panel of Fig. E.1 we plotted contours of constant ISCO radii as a function of the dimensionless angular momentum parameter  $j = J/M_0^2$  and the star quadrupole moment  $M_2$ , for the PRS solution. The use of the dimensionless parameter  $j$  in the horizontal axis allows to, qualitatively, relate deviations of the contour lines from vertical lines to the influence of the quadrupole moment. We can see that the ISCO radius decreases for increasing  $j$  and decreasing  $M_2$ . A quantitative measurement of this influence could be derived from the effective slope of the contour lines. We are interested in the comparison with the Kerr geometry, so in the lower panel, we plotted contours of constant ratio  $r_{\text{ISCO,PRS}}/r_{\text{ISCO,Kerr}}$  as a function of  $j$  and the difference between the quadrupole moment of the PRS solution  $M_{2,\text{PRS}}$  and the Kerr quadrupole  $M_{2,\text{Kerr}} = -ma^2$ , i.e.  $M_{2,\text{PRS}} - M_{2,\text{Kerr}} = M_{2,\text{PRS}} + ma^2 = mk$ , see Eq. (E.1.8). Deviations from the Kerr geometry are evident. Negative values of the angular momentum correspond to the radii of the counter-rotating orbits obtained here through the change  $g_{t\phi} \rightarrow -g_{t\phi}$  (see discussion below).

We stress that the accuracy of the PRS solution for describing the ISCO radius of *realistic* NSs was already shown to be higher with respect to other analytic models (see Pachón et al., 2006, for details). In Table E.1 we compare the ISCO radius for two rapidly rotating NS, models 20 and 26, of Table VI of Pappas and Apostolatos (2012) for the EoS L. The lowest multipole moments of the analytic models are fixed to the numerical values obtained by Pappas and Apostolatos (2012). In the case of the Kerr solution, only  $M_0$  and  $J$  can be fixed, while  $M_2$ , and  $S_3$  have values that depend on  $M_0$  and  $J$  and therefore cannot be fixed. For the PRS solution with  $s = 0$ ,  $M_0$ ,  $J$  and  $M_2$  can be fixed while  $S_3$  remains induced by the lower moments. We present also the ISCO radius obtained by fixing  $M_0$ ,  $J$ ,  $M_2$ , as well as  $S_3$  in the PRS analytic exact model.

In Figs. E.1–E.6, we have fixed as an example  $M_0 = m = 1.88M_\odot = 2.78 \text{ km}$ , and  $s = 0$ . We recall that the quadrupole moment in the geometric units used here ( $\text{km}^3$ ) is related to the one in CGS units by  $M_2^{\text{CGS}} = (10^{15}c^2/G)M_2^{\text{geo}} = 1.35 \times 10^{43}(M_2^{\text{geo}}/\text{km}^3) \text{ g cm}^2$ , and the mass of the Sun is

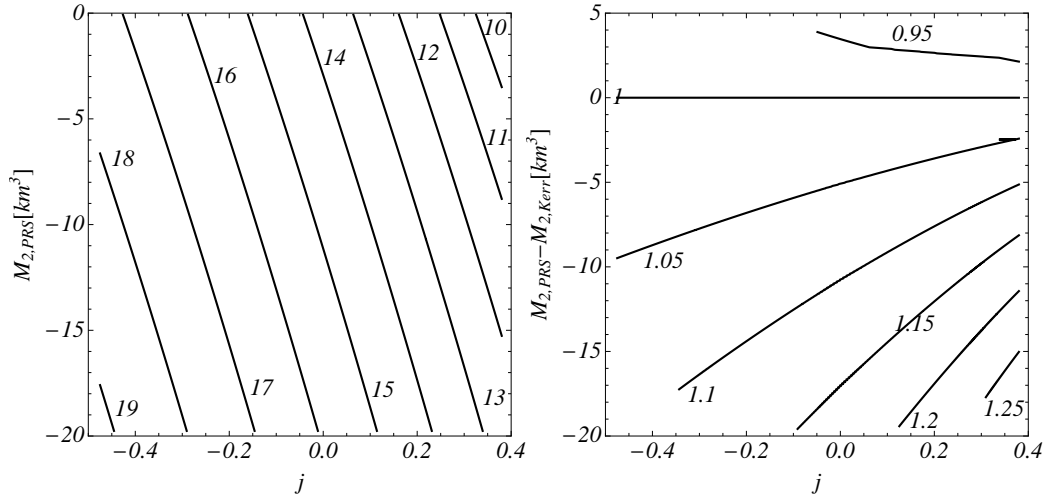


**Figure E.1.:** Left panel: Contours of constant ISCO radius as a function of the dimensionless angular momentum parameter  $j = J/M_0^2$  and the quadrupole moment  $M_2$  for the PRS solution, for a compact object with mass  $M_0 = m = 1.88M_\odot = 2.78$  km. Contours are labeled by the corresponding the value of the ISCO radius in km. Negative values of  $j$  depict the counter-rotating case and negative values of the quadrupole moment  $M_2$  correspond to oblate configurations. The values of  $M_2$  are in the range  $0 \leq M_2 \leq 20$  km<sup>3</sup> that corresponds in CGS units to  $0 \leq M_2 \leq -2.7 \times 10^{44}$  g cm<sup>2</sup>, which covers the typical range of fast rotating NSs. Right panel: Contours of constant ratio  $r_{\text{ISCO,PRS}}/r_{\text{ISCO,Kerr}}$  as a function of  $j$  and the difference  $M_{2,\text{PRS}} - M_{2,\text{Kerr}}$ . The quadrupole moment difference is comprised in the range  $-2.7 \times 10^{44} \leq M_2 \leq 6.8 \times 10^{43}$  g cm<sup>2</sup>.

	$R_N$ [km]	$R_{SS}$ [km]	$R_{\text{Kerr}}$ [km]	$R_{\text{PRS},s=0}$ [km]	$R_{\text{PRS}}$ [km]
M20	19.81	13.39	16.14	19.28	18.99
M26	19.87	17.16	15.94	19.65	19.54

**Table E.1.:** Comparison of the ISCO radius for the selected NS models 20 and 26 of Table VI of Pappas and Apostolatos (2012) for the EoS L. Model 20:  $M_0 = 4.167$  km ( $2.82M_\odot$ ),  $j = J/M_0^2 = 0.70$ ,  $M_2 = -79.8$  km<sup>3</sup> ( $-1.08 \times 10^{45}$  g cm<sup>2</sup>) and  $S_3 = -401.0$  km<sup>4</sup>. Model 26:  $M_0 = 4.36$  km ( $2.95M_\odot$ ),  $j = J/M_0^2 = 0.56$ ,  $M_2 = -45.2$  km<sup>3</sup> ( $-6.10 \times 10^{44}$  g cm<sup>2</sup>) and  $S_3 = -170.0$  km<sup>4</sup>. The subscript N stands for the numerical calculation of Pappas and Apostolatos (2012) and SS stands for the Shibata and Sasaki (1998) approximated ISCO radius expression.

$M_{\odot}^{\text{geo}} = 1.477 \text{ km}$ . The dimensionless angular momentum  $j$  is obtained from the CGS values of  $J$  and  $M_0$  as  $j = cJ / (GM_0^2)$ .

It is appropriate to compare the range of values of  $j = J/M_0^2$  and  $M_2$  used in Figs. E.1–E.6 with typical values of a NS. For the used mass  $M_0 = 1.88M_{\odot}$ , Morsink and Stella (1999) obtained a quadrupole moment  $M_2 = -5.3 \times 10^{43} \text{ g cm}^2 = 3.93 \text{ km}^3$ , with the latter value in geometric units, for a NS of angular rotation frequency  $\nu_s = 290 \text{ Hz}$  (rotation period of 3.45 milliseconds), corresponding to a dimensionless angular momentum  $j = J/M_0^2 = 0.19$ , for the EoS L. For a fixed mass the quadrupole moment is an increasing function of  $j$  because an increasing of the angular momentum at fixed mass results in an increasing of the oblateness (eccentricity) of the star, and so the quadrupole moment. Based on this fact, it is clear that not all the pairs of quadrupole and angular momentum pairs depicted in, e.g., Fig. E.1 are physically realizable. The maximum rotation rate of a neutron star taking into account both the effects of general relativity and deformations has been found to be  $\nu_{s,\text{max}} = 1045(M_0/M_{\odot})^{1/2}(10 \text{ km}/R)^{3/2} \text{ Hz}$ , largely independent on the EoS (see Lattimer and Prakash, 2004b, for details). Corresponding to this maximum rotation rate, the angular momentum is  $J_{\text{max}} = 2\pi\nu_{s,\text{max}}I \sim 6.56 \times 10^{48} I_{45} \text{ g cm}^2 \text{ s}^{-1}$ , and  $j_{\text{max}} = GJ_{\text{max}}/(cM_0^2) \sim 0.74I_{45}/(M_0/M_{\odot})^2$ , where  $I_{45}$  is the moment of inertia of the NS in units of  $10^{45} \text{ g cm}^2$ . The fastest observed pulsar is PSR J1748-2246ad with a rotation frequency of 716 Hz (Hessels et al., 2006b), which constrains the mass of the NS to  $M_0 \geq 0.47(R/10 \text{ km})^3 M_{\odot}$ , and  $j \sim 0.51I_{45}/(M_0/M_{\odot})^2$ , which becomes  $j \sim 0.26I_{45}$  for a canonical NS of  $M_0 = 1.4M_{\odot}$ .

### Keplerian Frequency

Now we turn into the frequencies analysis. For stationary axially symmetric spacetimes, the frequency of Keplerian orbits is given by (see e.g. Ryan, 1995)

$$\Omega_{\text{K}} = \frac{-g_{t\phi,\rho} \pm \sqrt{g_{t\phi,\rho}^2 - g_{\phi\phi,\rho}g_{tt,\rho}}}{g_{\phi\phi,\rho}}, \quad (\text{E.1.16})$$

where a colon stands for partial derivative with respect to the indicated coordinate and '+' and '-' stands for corotating and counter-rotating orbits, respectively.

For the case of static spacetimes, i.e. for  $\omega = 0$  and therefore  $g_{t\phi} = 0$ ,  $\Omega_{\text{K}} = \pm \sqrt{-g_{\phi\phi,\rho}g_{tt,\rho}}/g_{\phi\phi,\rho}$  and the energy  $E$  and angular momentum  $L$  per mass  $\mu$  of the test particle can be expressed in terms of the metric tensor components

(see e.g. Ryan, 1995),

$$\frac{E}{\mu} = \frac{-g_{tt}}{\sqrt{-g_{tt} - g_{\phi\phi}\Omega_K^2}}, \quad \frac{L}{\mu} = \frac{g_{\phi\phi}\Omega_K}{\sqrt{-g_{tt} - g_{\phi\phi}\Omega_K^2}}. \quad (\text{E.1.17})$$

From here, it is clear that taking the negative branch of the root for  $\Omega_K$  in Eq. (E.1.16) is equivalent to studying a particle with opposite angular momentum, i.e.  $L_{\text{count-rot}} = -L_{\text{co-rot}}$ . Thus, in the static case the magnitude of the energy and angular momentum are invariant under the change  $\Omega_K \rightarrow -\Omega_K$ .

Now we consider the case of stationary space times,  $\omega \neq 0$ . The energy  $E$  and angular momentum  $L$  per mass  $\mu$  are, in this case, given by (see e.g. Ryan, 1995)

$$\frac{E}{\mu} = \frac{-g_{tt} - g_{t\phi}\Omega_K}{\sqrt{-g_{tt} - 2g_{t\phi}\Omega_K - g_{\phi\phi}\Omega_K^2}}, \quad (\text{E.1.18})$$

$$\frac{L}{\mu} = \frac{g_{t\phi} + g_{\phi\phi}\Omega_K}{\sqrt{-g_{tt} - 2g_{t\phi}\Omega_K - g_{\phi\phi}\Omega_K^2}}. \quad (\text{E.1.19})$$

The counter-rotating condition given by the negative branch of Eq. (E.1.16), can be generated by the change  $g_{t\phi} \rightarrow -g_{t\phi}$ , which seems to be a more physical and transparent condition. In contrast to the static case, the counter-rotating orbit has now different energy and different magnitude of the angular momentum due the presence of the dragging of inertial frames, characterized by the metric component  $g_{t\phi}$  (cf. Eq. (E.1.22) below). In a nutshell, the dynamics of counter-rotating orbits of a test-particle can be derived, starting from the positive branch of Eq. (E.1.16), by considering a spacetime with  $g_{t\phi} \rightarrow -g_{t\phi}$ .

For the vacuum case, a similar analysis as the one developed by Herrera et al. (2006), clearly shows that the change in the global sign of  $g_{t\phi}$  is achieved by changing not only the angular momentum of the star,  $J \rightarrow -J$ , but *all the rotational multipolar moments*. For the Kerr metric this change is obtained by changing the sign of the parameter  $a$  (see Appendix E.1.8) while in the PRS solution we need additionally change the sign of the parameter  $s$  associated to *differential rotation*, i.e., by changing  $a \rightarrow -a$  and  $s \rightarrow -s^2$ .

Once we have clarified this important issue about the co-rotating and counter-rotating orbits, we proceed to analyze the functional dependence of the Keplerian frequency on the multipole moments. In the upper panel of Fig. E.2 we plotted contours of constant Keplerian frequency for the PRS solution,  $\nu_{K,\text{PRS}} = \Omega_{K,\text{PRS}}/(2\pi)$ , as a function of the dimensionless angular momen-

---

<sup>2</sup>For the vacuum case, in the solution by Manko et al. (2000), the sign change of  $g_{t\phi}$  is obtained after performing simultaneously the replacements  $a \rightarrow -a$  and  $b \rightarrow -b$ .

tum parameter  $j$  and the quadrupole moment  $M_{2,\text{PRS}}$ , at the ISCO radius. It can be seen that the influence of the quadrupole moment is non-negligible, as evidenced from the departure of the contour lines from vertical lines. The Keplerian frequency grows for increasing  $J$  and  $M_2$ . In the lower panel, we plotted contours of constant ratio  $\nu_{\text{K,PRS}}/\nu_{\text{K,Kerr}}$  as a function of  $j$  and the difference between the quadrupole moment of the PRS solution,  $M_{2,\text{PRS}}$ , and the Kerr quadrupole,  $M_{2,\text{Kerr}}$ .

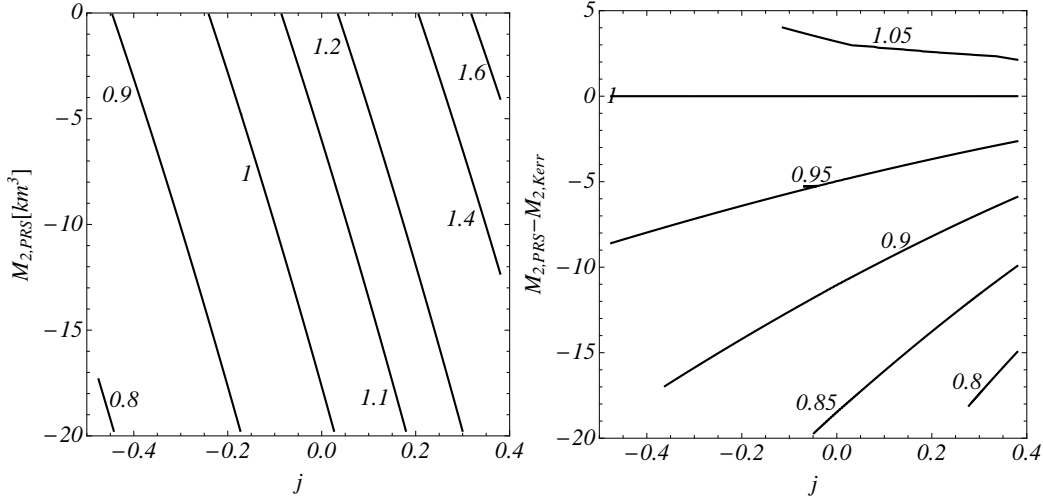


**Figure E.2.:** Left panel: Contours of constant  $\nu_{\text{K}}$  (in kHz) as a function of the dimensionless angular momentum parameter  $j = J/M_0^2$  and quadrupole moment  $M_2$  for the PRS solution, at the ISCO radius, for a compact object with mass  $M_0 = m = 1.88M_\odot = 2.78 \text{ km}$ . Right panel: Contours of constant ratio  $\nu_{\text{K,PRS}}/\nu_{\text{K,Kerr}}$  as a function of  $j$  and the difference  $M_{2,\text{PRS}} - M_{2,\text{Kerr}}$ , at the ISCO radius.

It is appropriate to recall here that because the Keplerian as well as the other frequencies calculated below are evaluated using formulas in the coordinate frame, see for instance Eq. (E.1.16), they must be evaluated at coordinate radii  $\rho$  and not at physical radii given by  $\sqrt{g_{\phi\phi}}$ . In the specific case of the ISCO the frequencies are evaluated at the radius that simultaneously solves the equations  $V = 0$ ,  $dV/d\rho = 0$ , and  $d^2V/d\rho^2 = 0$ , where  $V$  is the effective potential (E.1.15).

### Oscillation and Precession Frequencies

The radial and vertical oscillation (or epicyclic) frequencies are the frequencies at which the periastron and orbital plane of a circular orbit oscillates if we apply slightly radial and vertical perturbations to it, respectively. According to Ryan (1995), in stationary axially symmetric vacuum spacetimes described

by the Weyl-Papapetrou metric (E.1.1), the radial and vertical epicyclic frequencies can be obtained as

$$\begin{aligned} \nu_\alpha^{\text{OS}} = \frac{1}{2\pi} \left\{ -\frac{g^{\alpha\alpha}}{2} \left[ (g_{tt} + g_{t\phi}\Omega)^2 \left( \frac{g_{\phi\phi}}{\rho^2} \right)_{,\alpha\alpha} + (g_{t\phi} + g_{\phi\phi}\Omega)^2 \left( \frac{g_{tt}}{\rho^2} \right)_{,\alpha\alpha} \right. \right. \\ \left. \left. - 2(g_{tt} + g_{t\phi}\Omega)(g_{t\phi} + g_{\phi\phi}\Omega) \left( \frac{g_{t\phi}}{\rho^2} \right)_{,\alpha\alpha} \right] \right\}^{1/2}, \end{aligned} \quad (\text{E.1.20})$$

and the corresponding periastron ( $\nu_\rho^{\text{P}}$ ) and nodal ( $\nu_z^{\text{P}}$ ) precession frequencies as

$$\nu_\alpha^{\text{P}} = \nu_{\text{K}} - \nu_\alpha^{\text{OS}}. \quad (\text{E.1.21})$$

where  $\alpha = \{\rho, z\}$ , respectively, and  $\nu_{\text{K}} = \Omega_{\text{K}}/(2\pi)$  is the Keplerian orbital frequency with  $\Omega_{\text{K}}$  given by Eq. (E.1.16).

In the upper panel of Fig. E.3, we plotted contours of constant nodal precession frequency  $\nu_z^{\text{P}}$  at the ISCO radius as a function of  $j = J/M_0^2$  and  $M_2$  for the PRS solution, at the ISCO radius. We can see now that the influence of the quadrupole moment is quite important. The nodal precession frequency increases for increasing  $J$  and decreasing  $M_2$ , at fixed  $M_0$ . In the lower panel we plotted contours of constant ratio  $\nu_{z,\text{PRS}}^{\text{P}}/\nu_{z,\text{Kerr}}^{\text{P}}$ , at the ISCO radius, as a function of  $j$  and the difference  $M_{2,\text{PRS}} - M_{2,\text{Kerr}}$ , in order to evidence deviations from the Kerr solution. The radial oscillation frequency  $\nu_\rho^{\text{OS}}$  vanishes at the ISCO radius and therefore at such location the radial precession frequency equals the Keplerian frequency, whose contours have been plotted in Fig. E.2.

In Figs. E.4 and E.5 we plotted the nodal precession frequency  $\nu_z^{\text{P}}$  and the radial oscillation frequency  $\nu_\rho^{\text{OS}}$  as a function of the Keplerian frequency  $\nu_{\text{K}}$ , respectively, for both the Kerr and PRS solutions. As an example, we have shown the results for rotating NS models 20 and 26 of Table VI of Pappas and Apostolatos (2012), for the EoS L. The lowest multipole moments of the PRS solution  $M_0$ ,  $J$ ,  $M_2$ , and  $S_3$  have been fixed to the numerical values obtained by Pappas and Apostolatos (2012). In the case of the Kerr solution, only  $M_0$  and  $J$  can be fixed, while  $M_2$ , and  $S_3$  have values induced by the lower moments  $M_0$  and  $J$ . For the PRS solution with  $s = 0$ ,  $M_0$ ,  $J$  and  $M_2$  can be fixed while  $S_3$  cannot be fixed and depends on the lower moments. The results for the PRS analytic model obtained by fixing  $M_0$ ,  $J$ ,  $M_2$ , as well as  $S_3$  are also shown.

The deviations of the quadrupole and current octupole moments given by the Kerr solution from the numerical values of Pappas and Apostolatos (2012) can be used to show the low accuracy of the Kerr solution to describe fast rotating NSs. The accuracy of the PRS solution in describing the ISCO radii of these two models has been shown in Table E.1 of Section E.1.3.

In Figs. E.4 and E.5 we can see the differences of the  $\nu_z^{\text{P}} - \nu_{\text{K}}$  and  $\nu_\rho^{\text{OS}} - \nu_{\text{K}}$  relations between the Kerr and PRS solutions for *realistic NS models*. The devia-

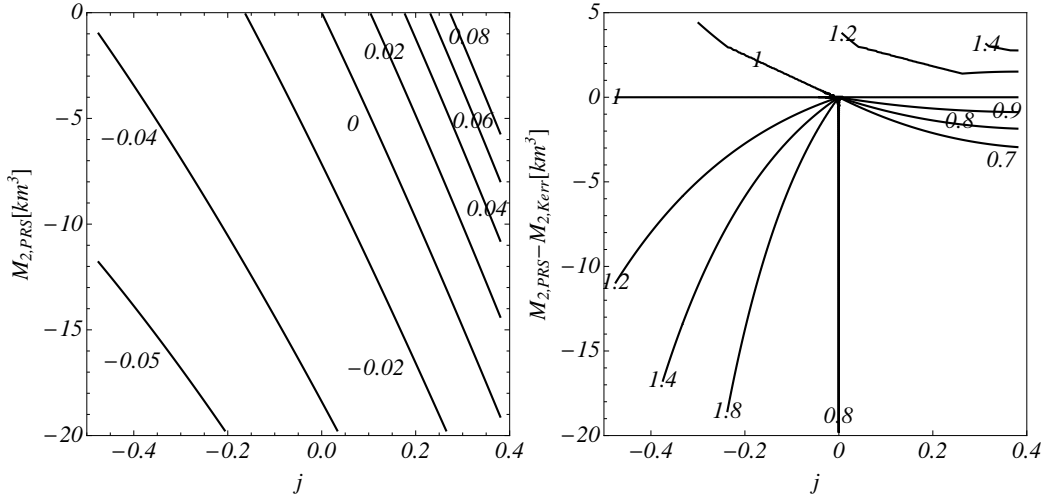


**Figure E.3.:** Left panel:  $\nu_z^P$  (in kHz) as a function of the the dimensionless angular momentum parameter  $j = J/M_0^2$  and quadruple moment  $M_2$  for the PRS solution, at the ISCO radius, for a compact object with mass  $M_0 = m = 1.88M_\odot = 2.78$  km. Right panel: Contours of constant ratio  $\nu_{z,PRS}^P/\nu_{z,Kerr}^P$  as a function of  $j$  and the difference  $M_{2,PRS} - M_{2,Kerr}$ , at the ISCO radius.

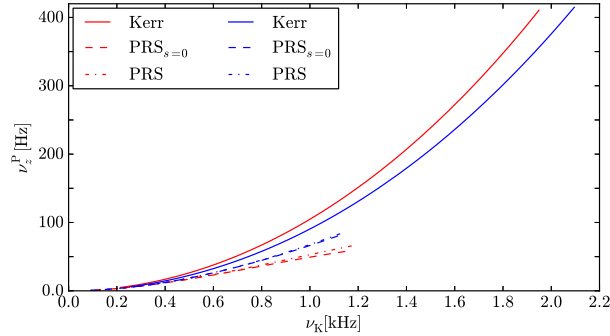


**Figure E.4.:** Nodal precession frequency  $\nu_z^P$  versus Keplerian frequency  $\nu_K$  given by the Kerr and PRS analytic solutions. The lowest multipole moments have been fixed from the rotating NS models 20 (red curves) and 26 (blue curves) of the Table VI of Pappas and Apostolatos (2012) for the EoS L. Model 20:  $M_0 = 4.167$  km ( $2.82M_\odot$ ),  $j = J/M_0^2 = 0.70$ ,  $M_2 = -79.8$  km<sup>3</sup> ( $-1.08 \times 10^{45}$  g cm<sup>2</sup>) and  $S_3 = -401.0$  km<sup>4</sup>. Model 26:  $M_0 = 4.36$  km ( $2.95M_\odot$ ),  $j = J/M_0^2 = 0.56$ ,  $M_2 = -45.2$  km<sup>3</sup> ( $-6.10 \times 10^{44}$  g cm<sup>2</sup>) and  $S_3 = -170.0$  km<sup>4</sup>.

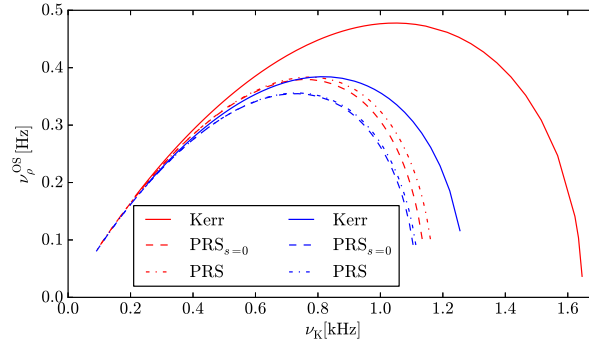


**Figure E.5:** Radial oscillation frequency  $\nu_{\rho}^{\text{OS}}$  versus Keplerian frequency  $\nu_{\text{K}}$  given by the Kerr and PRS analytic solutions. The lowest multipole moments has been fixed from the rotating NS models 20 (red curves) and 26 (blue curves) of the Table VI of Pappas and Apostolatos (2012) for the EoS L. Model 20:  $M_0 = 4.167 \text{ km}$  ( $2.82M_{\odot}$ ),  $j = J/M_0^2 = 0.70$ ,  $M_2 = -79.8 \text{ km}^3$  ( $-1.08 \times 10^{45} \text{ g cm}^2$ ) and  $S_3 = -401.0 \text{ km}^4$ . Model 26:  $M_0 = 4.36 \text{ km}$  ( $2.95M_{\odot}$ ),  $j = J/M_0^2 = 0.56$ ,  $M_2 = -45.2 \text{ km}^3$  ( $-6.10 \times 10^{44} \text{ g cm}^2$ ) and  $S_3 = -170.0 \text{ km}^4$ .

tions of the Kerr solution, especially at fast rotation rates, are evident because of the influence of the deformation (quadrupole  $M_2$ ) of the star as well as, although in less proportion, of the octupole current  $S_3$ . In general, we observe that the larger the angular momentum, the poorer the performance of the predictions of Kerr solution.

We have also shown in Figs. E.4–E.5 the influence of the current octupole  $S_3$  in the determination of the precession and oscillation frequencies. We found that the effect of  $S_3$  is only appreciable for the fastest models. The minor influence, in this case, of the current octupole  $S_3$  is expected from the small values of the parameter  $s$  needed to fit the numerical values of Pappas and Apostolatos (2012). Clearly, larger values of the parameter  $s$  needed to fit realistic values of  $S_3$  will enhance as well deviations from the Kerr spacetime.

The effects of a multipolar structure that deviates from the one of the Kerr geometry on the various quantities analyzed here are relevant for instance in the RPM of the QPOs observed in LMXBs (see e.g. Stella and Vietri (1998); Morsink and Stella (1999); Stella et al. (1999); Stella and Vietri (1999) and Section E.1.6, for details).

### Dragging of Inertial Frames

It is known that a prediction of general relativity is that a rotating object makes a zero angular momentum test particle to orbit around it, namely it

*drags* the particle into the direction of its rotation angular velocity; such an effect is called dragging of inertial frames or Lense-Thirring effect. Consequently, oblique particle orbit planes with respect to the source equatorial plane will precess around the rotation axis of the object. In stationary axially symmetric spacetimes described by the metric (E.1.1) the frame dragging precession frequency is given by (see e.g. Ryan, 1995)

$$\nu_{\text{LT}} = -\frac{1}{2\pi} \frac{g_{t\phi}}{g_{\phi\phi}}. \quad (\text{E.1.22})$$

Many efforts have been done to test the predictions of general relativity around the Earth such as the analysis of the periastron precession of the orbits of the LAsER GEODynamics Satellites, LAGEOS and LAGEOS II, (see e.g. Lucchesi and Peron, 2010) and the relativistic precession of the gyroscopes on-board the Gravity Probe B satellite (see Everitt et al., 2011, for details). The latter experiment measured a frame dragging effect within an accuracy of 19% with respect to the prediction of general relativity.

The smallness of this effect around the Earth makes such measurements quite difficult and has represented a multi year challenge for Astronomy. The frame dragging precession increases with the increasing of the angular momentum of the rotating object and therefore a major hypothetical arena for the searching of more appreciable Lense-Thirring precession is the spacetime around compact objects such as BHs and NSs. The much stronger gravitational field of these objects with respect to the Earth one allow them to attain much faster angular rotation rates and so larger angular momentum.

Stella and Vietri (1998) showed how, in the weak field slow rotation regime, the vertical precession frequency  $\nu_z^{\text{P}}$  (orbital plane precession frequency) can be divided into one contribution due to the Lense-Thirring precession and another one due to the deformation (non-zero quadrupole moment) of the rotating object, both of them comparable from the quantitative point of view. These frequencies could be in principle related to the motion of the matter in the accretion disks around BHs and NSs and thus particularly applicable to LMXBs. For fast rotating NSs and BHs the frequency at which the orbital plane, and so the frame dragging precession frequency, can reach values of the order of tens of Hz (see e.g. Stella and Vietri (1998) and Figs. E.3 and E.4).

Thus, it is clear that an observational confirmation of the relativistic precession of matter around either a NS or a BH will lead to an outstanding test of the general relativity in the strong field regime and, at the same time, an indirect check of the large effects of the frame dragging in the exterior spacetime of compact objects (see e.g. Morsink and Stella, 1999, for details).

Although making independent measurements of the frame dragging effect around BHs and NSs is a very complicate task, it is important to know the numerical values of the precession frequency due to the frame dragging with respect to other relativistic precession effects, e.g. geodetic precession. In

addition, it is important to know the sensitivity of the precession frequency to the object parameters such as mass, angular momentum, quadrupole, and octupole moment.

In the upper panel of Fig. E.6 we plotted contours of constant frame dragging frequency  $\nu_{\text{LT}}$  for the PRS solution, at the ISCO radius, as a function of the the angular momentum per unit mass  $J/M_0$  and the quadrupole moment  $M_2$ , for a compact object mass  $M_0 = m = 1.88M_\odot$ . Correspondingly, in the lower panel of Fig. E.6, we show the differences between the frame dragging precession frequency as predicted by the Kerr and PRS solutions, at the ISCO radius, as a function of  $j = J/M_0^2$  and the difference between the quadrupole moments,  $M_{2,\text{PRS}} - M_{2,\text{Kerr}}$ .

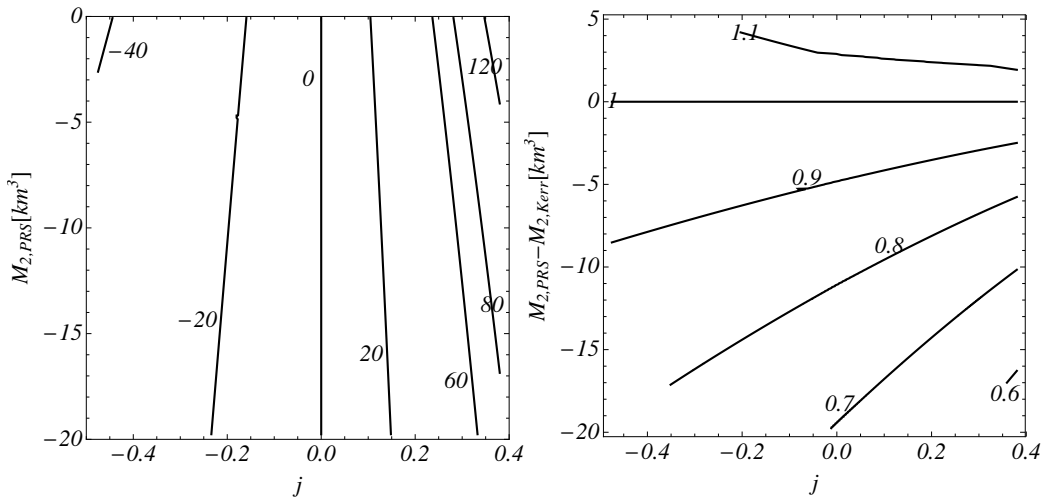


**Figure E.6.:** Left panel: Contours of constant  $\nu_{\text{LT}}$  (in Hz) as a function of the the angular momentum per unit mass  $j = J/M_0^2$  and the quadrupole moment  $M_2$  for the PRS solution, at the ISCO radius, for a compact object with mass  $M_0 = m = 1.88M_\odot = 2.78 \text{ km}$ . Right panel: Contours of constant ratio  $\nu_{\text{LT,PRS}}/\nu_{\text{LT,Kerr}}$  as a function of  $j$  and the difference  $M_{2,\text{PRS}} - M_{2,\text{Kerr}}$ , at the ISCO radius.

The influence of the quadrupole moment in the determination of the frame dragging frequency is evident; the frequency  $\nu_{\text{LT}}$  given by a NS is generally smaller than the one given by a BH as can be seen from the value of the ratio  $\nu_{\text{LT,PRS}}/\nu_{\text{LT,Kerr}} < 1$  obtained for configurations with a quadrupole moment that deviates with respect to the one given by the Kerr solution, namely for  $M_{2,\text{PRS}} - M_{2,\text{Kerr}} = M_{2,\text{PRS}} + ma^2 = mk \neq 0$ , see Eq. (E.1.8).

It is also worth mentioning that frame dragging precession can be affected as well by the presence of electromagnetic fields (Herrera et al., 2006, see) and further research in this respect deserves the due attention.

### E.1.4. Accuracy of Ryan's Analytic Formulas

Following a series expansion procedure in powers of  $1/\rho$ , Ryan (1995) found that the periastron (radial) and nodal (vertical) precession frequencies,  $\nu_\rho^P$  and  $\nu_z^P$  given by Eq. (E.1.20), can be written as a function of the Keplerian frequency  $\nu_K$  as

$$\begin{aligned} \frac{\nu_\rho^P}{\nu_K} = & 3\mathcal{V}^2 - 4\frac{S_1}{M_0^2}\mathcal{V}^3 + \left(\frac{9}{2} - \frac{3M_2}{2M_0^3}\right)\mathcal{V}^4 - 10\frac{S_1}{M_0^2}\mathcal{V}^5 \\ & + \left(\frac{27}{2} - 2\frac{S_1^2}{M_0^4} - \frac{21M_2}{2M_0^3}\right)\mathcal{V}^6 + \left(-48\frac{S_1}{M_0^2} - 5\frac{S_1M_2}{M_0^5}\right. \\ & \left.+ 9\frac{S_3}{M_0^4}\right)\mathcal{V}^7 + \left(\frac{405}{8} + \frac{2243}{84}\frac{S_1^2}{M_0^4} - \frac{661M_2}{14M_0^3}\right. \\ & \left.- \frac{21M_2^2}{8M_0^6} + \frac{15M_4}{4M_0^5}\right)\mathcal{V}^8 + \dots, \end{aligned} \quad (\text{E.1.23})$$

and

$$\begin{aligned} \frac{\nu_z^P}{\nu_K} = & 2\frac{S_1}{M_0^2}\mathcal{V}^3 + \frac{3M_2}{2M_0^3}\mathcal{V}^4 + \left(7\frac{S_1^2}{M_0^4} + 3\frac{M_2}{M_0^3}\right)\mathcal{V}^6 \\ & + \left(11\frac{S_1M_2}{M_0^5} - 6\frac{S_3}{M_0^4}\right)\mathcal{V}^7 + \left(\frac{153}{28}\frac{S_1^2}{M_0^4} + \frac{153M_2}{28M_0^3}\right. \\ & \left.+ \frac{39M_2^2}{8M_0^6} - \frac{15M_4}{4M_0^5}\right)\mathcal{V}^8 + \dots, \end{aligned} \quad (\text{E.1.24})$$

where  $\mathcal{V} = (2\pi M_0 \nu_K)^{1/3}$ ,  $[M_0, M_2, M_4]$  are the lowest three mass moments and,  $[S_1, S_3]$ , are the lowest two current moments. For the PRS solution in the vacuum case,  $M_4 = m(a^4 - 3a^2 + k^2 + 2as)$ .

The above formulas are approximate expressions of the periastron and nodal precession frequencies in the weak field (large distances from the source) and slow rotation regimes. We should therefore expect that they become less accurate at distances close to the central object, e.g. at the ISCO radius, and for fast rotating objects. However, such formulas are an important tool to understand the role of the lowest multipole moments on the values of the relativistic precession frequencies, such as the importance of the higher multipole moments at short distances and high frequencies as can be seen from Eqs. (E.1.23–E.1.24).

At high frequencies, for instance of the order of kHz, deviations from the above scaling laws are appreciable. In Figs. E.7 and E.8 we compare the radial precession and vertical oscillation frequencies,  $\nu_\rho^P$  and  $\nu_z^{\text{OS}}$ , as a function of the

Keplerian frequency  $\nu_K$ , as given by the full expressions (E.1.20) for the PRS solution and by the approximate formulas (E.1.23) and (E.1.24), respectively.<sup>3</sup> The lowest multipole moments  $M_0$ ,  $J$ ,  $M_2$ , and  $S_3$  of the PRS solution have been fixed to the values of two models of the Table VI of Pappas and Apostolatos (2012); Model 2 with  $M_0 = 2.071$  km ( $1.402M_\odot$ ),  $j = 0.194$ ,  $M_2 = -2.76$  km<sup>3</sup> ( $3.73 \times 10^{43}$  g cm<sup>2</sup>),  $S_3 = -2.28$  km<sup>4</sup> and Model 20 with  $M_0 = 4.167$  km ( $2.82M_\odot$ ),  $j = J/M_0^2 = 0.70$ ,  $M_2 = -79.8$  km<sup>3</sup> ( $-1.08 \times 10^{45}$  g cm<sup>2</sup>) and  $S_3 = -401.0$  km<sup>4</sup>.

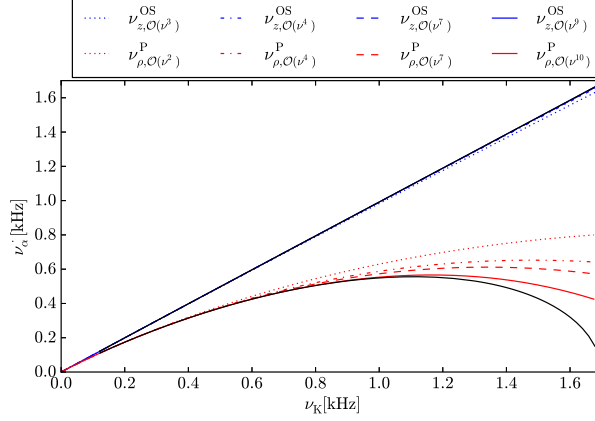


**Figure E.7.:** Comparison of the  $\nu_z^{\text{OS}}-\nu_K$  and  $\nu_\rho^{\text{P}}-\nu_K$  relations given by the PRS solution and the approximate expressions (E.1.23–E.1.24) derived by Ryan (1995). The lowest multipole moments  $M_0$ ,  $J$ ,  $M_2$ , and  $S_3$  have been fixed to the values of the Model 2 of the Table VI of Pappas and Apostolatos (2012):  $M_0 = 2.071$  km ( $1.402M_\odot$ ),  $j = 0.194$ ,  $M_2 = -2.76$  km<sup>3</sup> ( $3.73 \times 10^{43}$  g cm<sup>2</sup>), and  $S_3 = -2.28$  km<sup>4</sup>.

In the  $\nu_z^{\text{OS}}-\nu_K$  relation, the blue dotted curve depicts the contribution from the angular momentum (we plot the series (E.1.24) up to  $\mathcal{V}^3$ ), for the blue dot-dashed curve we added the first contribution from the quadrupole moment  $M_2$  (we cut the series at  $\mathcal{V}^4$ ), for the dashed blue line we added the first contribution from the octupole mass-current (series expansion up to  $\mathcal{V}^7$ ) and finally in the continuous blue line we consider contributions for higher multipole moments and stop the series at the order  $\mathcal{V}^9$ , not shown in Eqs. (E.1.24). For this case, we can see that Ryan’s expressions clearly tend, from the bottom, to the exact result (continuous black curve) obtained by using the PRS solution.

For the analysis of the  $\nu_\rho^{\text{P}}-\nu_K$  relation we followed the same procedure as described above. In this case, the Ryan’s expressions tend from the top to the exact result, the continuous black curve, represented by the PRS solution. It is interesting to see that the introduction of the octupole moment (dashed red

<sup>3</sup>Because the scale of the  $\nu_\rho^{\text{P}}$  and  $\nu_z^{\text{OS}}$  frequencies are very similar, we decided to plot in Fig. E.7  $\nu_\rho^{\text{P}}$  and  $\nu_z^{\text{OS}}$  whose scales are different allowing a more clear comparison with the PRS solution in a single figure.

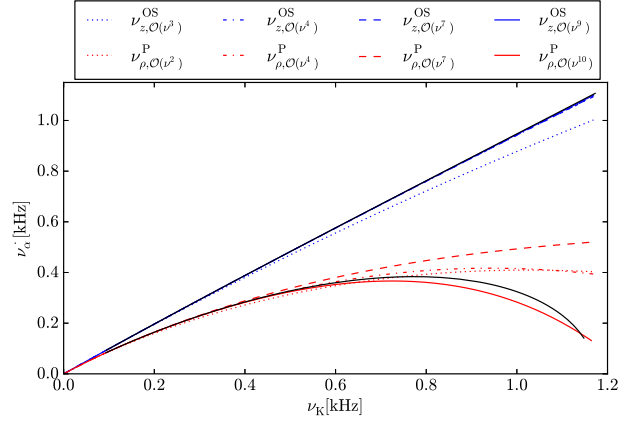


**Figure E.8.:** Comparison of the  $\nu_z^{\text{OS}}-\nu_K$  and  $\nu_\rho^{\text{P}}-\nu_K$  relations as given by the PRS solution and the approximate expressions (E.1.23-E.1.24) derived by Ryan (1995). The lowest multipole moments  $M_0$ ,  $J$ ,  $M_2$ , and  $S_3$  have been fixed to the values of the Model 20 of the Table VI of Pappas and Apostolatos (2012):  $M_0 = 4.167 \text{ km}$  ( $2.82M_\odot$ ),  $j = J/M_0^2 = 0.70$ ,  $M_2 = -79.8 \text{ km}^3$  ( $-1.08 \times 10^{45} \text{ g cm}^2$ ) and  $S_3 = -401.0 \text{ km}^4$

line) makes the approximation to deviate from the exact result, however by including more terms the accuracy is enhanced. As can be seen from Figs. E.7 and E.8 the quantitative accuracy of the Ryan's approximate formulas in the periastron precession frequency  $\nu_\rho^{\text{P}}$  is less than the one obtained in the vertical oscillation frequency  $\nu_z^{\text{OS}}$ .

The importance of the high-order multipole moments such as the quadrupole and the octupole moments is evident in the high-frequency regime. This is in line with the results shown in Figs. E.2–E.3 and in Figs. E.4–E.5. We can see from Figs. E.7 and E.8 that the Ryan's approximate formulas describe more accurately the Model 2 than the Model 20. The reason is that, as we mentioned above, we should expect a better accuracy of the series expansions from low to moderate moderate rotation rates and consequently the same occur for the quadrupole deformations. It is clear that there are appreciable differences both in rotation and deformation between the two selected models; we recall also that the rotation frequency of the star can be expressed as a function of the dimensionless  $j$  parameter as  $\nu_s = GjM_0^2/(2\pi cI) = 1.4(M/M_\odot)^2/I_{45} \text{ kHz}$ .

It is noteworthy that we have checked that the Ryan's series expansions, Eqs. (E.1.23) and (E.1.24), fit quite accurately the exact results if taken up to order  $\nu^{10}$ . In particular the values of the vertical oscillation and precession frequencies are fit better than the corresponding radial ones. For the Model 2 the radial oscillation frequency is well fitted by the Ryan's expression up to Keplerian frequencies of order  $\sim 1.2 \text{ kHz}$  while, for the Model 20, the approximate formulas break down at a lower value  $\sim 0.7 \text{ kHz}$ . These results

are of particular relevance because it makes possible the extraction of the object parameters (for instance the lowest multipoles up to  $S_3$ ) by the fitting of the observed QPO frequencies in LMXBs, providing they are indeed related to the precession and oscillation frequencies of matter in the accretion disk (see Section E.1.6, for details) and for Keplerian motion not exceeding a few kHz of frequency.

### E.1.5. Accuracy of PRS solution

We turn now to analyze the behavior of the Kerr and PRS solutions in predicting results for the Keplerian, frame dragging, and vertical oscillation frequencies, for realistic NSs. In particular, we compare their predictions with the frequencies calculated by Morsink and Stella (1999). Since Morsink and Stella (1999) did not include the values of the octupole current moment  $S_3$ , here we set  $s = 0$  in Eq. (E.1.7) for the PRS solution. For the sake of comparison, we choose the results derived by Morsink and Stella (1999) for the EoS L, because for this EoS the highest rotating parameter  $j$  and quadrupole moment  $M_2$  were found. In addition, the stiffness of such an EoS allows the maximum mass of the NS to be larger than the highest observed NS mass,  $M_0 = 1.97 \pm 0.04 M_\odot$ , corresponding to the 317 Hz (3.15 milliseconds rotation period) pulsar J1614-2230 (see Demorest et al., 2010b, for details).

This regime of high  $j$  and  $M_2$  in realistic models is particularly interesting to test the deviations of the Kerr solution in the description of NS signatures as well as to explore the accuracy of the PRS solution. In Table E.2, we present the results for four different sets of the star spin frequency  $\nu_s$ , namely  $\nu_s = 290$  Hz (M1 and M2),  $\nu_s = 360$  Hz (M3 and M4),  $\nu_s = 580$  Hz (M5 and M6) and  $\nu_s = 720$  Hz (M7 and M8).

Model	$r_+^{\text{MS}}$ [km]	$r_+^{\text{Kerr}}$	$r_+^{\text{PRS}}$	$\nu_K^{\text{MS}}$ [kHz]	$\nu_K^{\text{Kerr}}$	$\nu_K^{\text{PRS}}$	$\nu_{\text{LT}}^{\text{MS}}$ [Hz]	$\nu_{\text{LT}}^{\text{Kerr}}$	$\nu_{\text{LT}}^{\text{PRS}}$	$\nu_z^{\text{PMS}}$ [Hz]	$\nu_z^{\text{PKerr}}$	$\nu_z^{\text{PPRS}}$
M1	15.4	14.90	15.42	1.31	1.363	1.304	39.7	42.248	38.476	18.6	39.697	22.040
M2	22.2	22.16	22.23	0.90	0.906	0.902	19.6	19.676	19.493	17.2	18.809	17.629
M3	15.6	14.89	15.63	1.29	1.380	1.296	49.8	57.001	49.804	17.5	52.608	26.197
M4	21.8	21.62	21.74	0.93	0.937	0.931	26.1	27.245	26.833	21.9	25.670	23.635
M5	16.3	14.18	16.06	1.26	1.514	1.289	84.3	125.75	88.905	-10.5	109.04	31.140
M6	20.6	20.05	20.45	1.01	1.041	1.015	53.5	57.467	54.391	35.8	51.861	42.854
M7	17.0	13.58	16.53	1.22	1.637	1.269	106.7	201.52	116.25	-51.8	166.55	29.804
M8	19.8	18.85	19.65	1.06	1.136	1.077	78.8	90.821	80.895	38.4	79.079	57.187

**Table E.2.:** ISCO radius  $r_+$ , Keplerian frequency  $\nu_K$ , frame-dragging (Lense-Thirring) frequency  $\nu_{\text{LT}}$ , and vertical precession frequency  $\nu_z^{\text{P}}$  of the co-rotating orbits calculated numerically by Morsink and Stella (1999) (upper index MS) and comparison with the corresponding predicted values given by the Kerr (upper index Kerr) and the PRS $_{s=0}$  solution (upper index PRS). The quadrupole moment  $M_2$  have been normalized for convenience to the value  $Q_0 = 10^{43}$  g cm<sup>2</sup>.

In Table E.2, we clearly observe that the results predicted by the PRS $_{s=0}$  solution for the Keplerian and frame-dragging frequencies are in excellent agreement with those calculated by Morsink and Stella (1999) for even highly

massive, rotating and deformed models such as the model M7 with  $M_0 = 2.17M_\odot$ ,  $j = 0.51$  and  $M_2 = -39.4Q_0$ . We notice that Morsink and Stella (1999) reported some configurations with negative values of  $\nu_z$  (see Table E.2). We advance the possibility that this is due to instabilities of the numerical code that occur when the ISCO radius is located very close or inside the surface of the object. Thus, the values of the frequencies given by the analytic solution in these cases are to be considered predictions to be tested for future numerical computations. This fact can be checked within the calculations of Morsink and Stella (1999) by exploring the properties of counter-rotating orbits which produce in general ISCO radii larger than the ones of the co-rotating ones. In Table E.3, we depicted the results in the counter-rotating case where we can notice an improvement of the accuracy of the PRS solution with respect to the co-rotating case.

Model	$r^{\text{MS}}[\text{km}]$	$r^{\text{Kerr}}$	$r^{\text{PRS}}$	$\nu_{\text{K}}^{\text{MS}}[\text{kHz}]$	$\nu_{\text{K}}^{\text{Kerr}}$	$\nu_{\text{K}}^{\text{PRS}}$	$\nu_{\text{IT}}^{\text{MS}}[\text{Hz}]$	$\nu_{\text{IT}}^{\text{Kerr}}$	$\nu_{\text{IT}}^{\text{PRS}}$	$\nu_z^{\text{MS}}[\text{Hz}]$	$\nu_z^{\text{Kerr}}$	$\nu_z^{\text{PRS}}$
M1	18.8	18.35	18.73	0.99	1.023	0.997	21.7	22.61	21.39	29.0	23.88	29.70
M2	25.9	25.82	25.88	0.73	0.734	0.732	12.4	12.43	12.36	13.6	12.95	13.46
M3	19.9	19.39	19.89	0.93	0.960	0.928	24.0	25.79	24.04	32.9	27.61	34.20
M4	26.4	26.33	26.42	0.71	0.715	0.712	14.7	15.08	14.94	16.4	15.88	16.57
M5	23.3	22.22	23.24	0.77	0.816	0.768	28.2	32.59	28.78	41.3	36.31	44.65
M6	28.2	27.94	28.18	0.65	0.660	0.652	20.5	21.19	20.70	24.1	23.03	24.51
M7	25.9	24.37	25.78	0.67	0.731	0.678	28.9	34.62	29.64	43.4	39.56	47.90
M8	29.7	29.18	29.58	0.61	0.623	0.611	23.2	24.40	23.48	28.4	27.12	29.22

**Table E.3.:** Same as in Table E.2, but for the counter-rotating case.

In this line, we consider worth performing numerical computations of the precession and oscillation frequencies of particles around realistic NSs in a wider space of parameters and using up-to-date numerical techniques which will certainly help to establish and elucidate more clearly the accuracy of analytic models. It is also appropriate recalling the recent results of Pappas and Apostolatos (2012) on the computation of the general relativistic multipole moments in axially symmetric spacetimes.

### E.1.6. The Relativistic Precision Model

The X-ray light curves of LMXBs show a variability from which a wide variety of QPOs have been measured, expanding from relatively low  $\sim$  Hz frequencies all the way up to high  $\sim$  kHz frequencies (see e.g. van der Klis, 1995, for details). In particular, such frequencies usually come in pairs (often called twin peaks), the lower and upper frequencies,  $\nu_l$  and  $\nu_h$  respectively. BHs and NSs with similar masses can show similar signatures and therefore the identification of the compact object in a LMXB is not a simple task. If the QPO phenomena observed in these systems are indeed due to relativistic motion of accretion disk matter, the knowledge of the specific behavior of the particle frequencies (e.g. rotation, oscillation, precession) in the exterior geometry of NSs and BHs becomes essential as a tool for the identification of the nature of the compact object harbored by a LMXB.

It is not the scope of this work to test a particular model for the QPO phenomenon in LMXBs but instead to show the influence of the high multipole moments on the orbital motion of test particles especially the role of the quadrupole moment which is of particular interest to differentiate a NS from a BH. There are in the literature several models that describe the QPOs in LMXBs through the frequencies of particles around the compact object, and for a recent review and comparison of the different models we refer to the recent work of Lin et al. (2011). In order to show here the main features and differences between the Kerr and the PRS solutions we shall use the Relativistic Precession Model (RPM).

The RPM model identifies the lower and higher (often called twin-peaks) kHz QPO frequencies,  $\nu_l$  and  $\nu_h$ , with the periastron precession and Keplerian frequencies, namely  $\nu_l = \nu_\rho^P$  and  $\nu_h = \nu_K$ , respectively. The so-called horizontal branch oscillations (HBOs), which belong to the low frequency QPOs observed in high luminosity Z-sources (see e.g. van der Klis, 1995, for details), are related within the RPM model to the nodal precession frequency  $\nu_z^P$  of the same orbits (Morsink and Stella, 1999, see). We will use here in particular the realistic NS models of Morsink and Stella (1999) for the EoS L.

One of the salient features of the RPM model is that in the case of the HBO frequencies, the relations inferred from the first term of the expansions (E.1.23) and (E.1.24)

$$\nu_K = 3^{-3/5}(2\pi)^{-2/5}m^{-2/5}(\nu_\rho^P)^{3/5}, \quad (\text{E.1.25})$$

$$\nu_z^P = (2/3)^{6/5}\pi^{1/5}j m^{1/5}(\nu_\rho^P)^{6/5}, \quad (\text{E.1.26})$$

which implies a nodal precession frequency proportional to the square of the Keplerian frequency has been observed in some sources, for instance in the LMXB 4U 1728–34 (see Ford and van der Klis, 1998, for details). In addition, 6/5 power law relating the nodal and periastron precession frequencies can explain (see Stella et al., 1999) the correlation between two of the observed QPO frequencies found in the fluxes of NSs and BHs LMXBs (see Psaltis et al., 1999, for details). This fact provides, at the same time, a significant test of the Ryan’s analytic expressions.

It is interesting to analyze the level of predictability of the precession and oscillation frequencies on particular astrophysical sources. In Fig. E.9 we show the  $\nu_l$ – $\nu_h$  relation within the RPM model, namely  $\nu_\rho^P$  versus  $\nu_K$  for the models M1–M8 of Table E.2. In the upper panel we show the results for the PRS solution while, in the lower panel, we present the results for the Kerr solution. We have indicated the QPO frequencies observed in the sources GX 5–1 (see e.g. Wijnands et al., 1998; Jonker et al., 2002), 4U 1735–44 (see e.g. Ford et al., 1998), 4U 1636–53 (see e.g. Wijnands et al., 1997), Sco X1 (see e.g. van der Klis et al., 1996), GX 17–2 (see e.g. Homan et al., 2002), GX 340+0 (see e.g. Jonker et al., 2000), Cir X1 (see e.g. van der Klis et al., 1996), 4U 0614+091

(see e.g. Ford et al., 1997), and 4U 1728–34 (see e.g. Strohmayer et al., 1996).

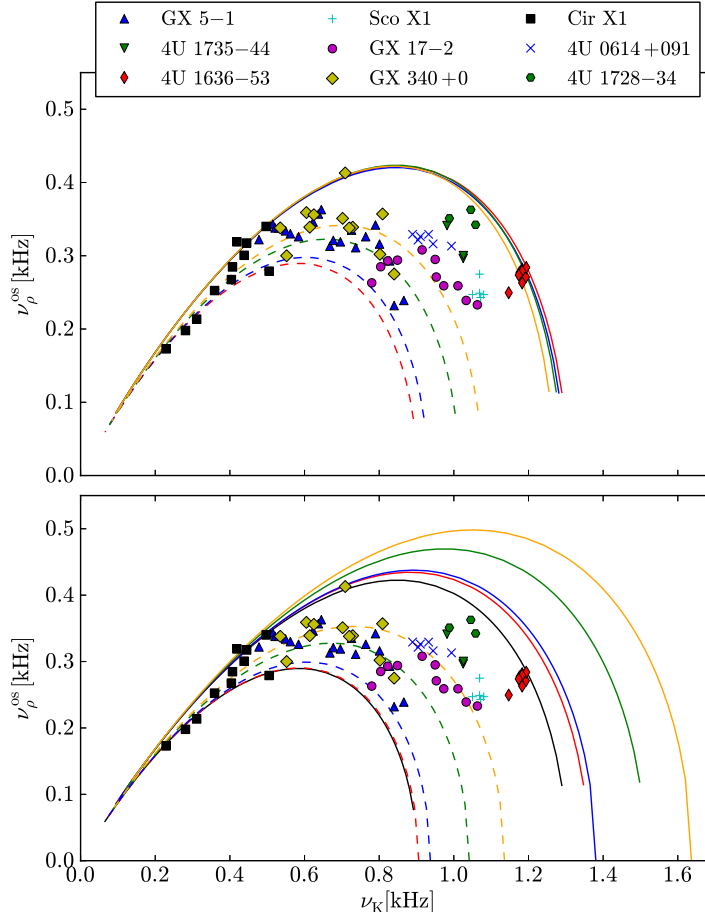


**Figure E.9.:** Periastron oscillation frequency,  $\nu_{\rho}^{\text{OS}}$ , as a function of the Keplerian frequency  $\nu_{\text{K}}$  for the NS realistic models in Table E.2. We indicate the QPO frequencies observed in the sources GX 5–1, 4U 1735–44, 4U 1636–53, Sco X1, GX 17–2, GX 340+0, Cir X1, 4U 0614+091, and 4U 1728–34. The solid curves depict the results for the models M1 (solid) and M2 (dashed) with red lines, for the models M3 (solid) and M4 (dashed) with blue lines, for the models M5 (solid) and M6 (dashed) with green lines while orange lines stands for the results from models M7 (solid) and M8 (dashed). In the upper panel we present the results derived from the  $\text{PRS}_{s=0}$  solution while in the lower panel we present the results for the Kerr solution. In the lower panel we have added, to guide the eye, the inner red dashed and outer red solid curves of the upper panel using black lines.

Both the upper and lower panels of Fig. E.9 have been plotted using the same frequency scales in order to aid the identification of the differences between the Kerr and the PRS solutions. One can notice that all the solid curves in the Kerr solution (lower panel of Fig. E.9) are outside the range of the ob-

served QPO frequencies exemplified, while all dashed and solid curves of the PRS are inside the QPO range. It is then clear that making a fit of the observed QPO frequencies of the selected LMXBs of Fig. E.9 will necessarily require a different choice of parameters in the Kerr and PRS solutions. Therefore, conclusions for instance on the NS parameters (e.g. mass, angular momentum, quadrupole deformation) based on fitting QPOs using the Kerr geometry will deviate from the actual parameters (see e.g. Laarakkers and Poisson, 1999, for details), extractable more reliably from a more complex geometry, such as the PRS one, that allows a better estimate for instance of the quadrupole moment of a compact star.

In Fig. E.9 we show the relation  $\nu_z^P$  versus  $\nu_K$  for the models M1–M8 of Table E.2. For the sake of comparison we show the low frequency branch observed in the LMXB 4U 1728–34 (see Ford and van der Klis, 1998, for details). From the analysis of the pulsating X-ray flux it turns out that very likely the spin frequency of the NS in 4U 1728–34 is  $\sim 363$  Hz (see Strohmayer et al., 1996, for details). Thus, the models M3 ( $M_0 = 1.94M_\odot$ ,  $j = 0.24$ ) and M4 ( $M_0 = 2.71M_\odot$ ,  $j = 0.18$ ) in Table E.2 that correspond to a NS of spin frequency 360 Hz are of particular interest for the analysis of this source. It was suggested by Stella et al. (1999); Stella and Vietri (1999) that the low frequency observed in 4U 1728–34 are likely to be due to excitations of the second harmonic of the vertical motion and therefore a better fit of the lower-higher QPO frequencies of 4U 1728–34 (and of similar sources) will be obtained for the relation  $2\nu_z^P - \nu_K$ . The black curves in Fig. E.10 indicate the  $2\nu_z^P - \nu_K$  relation for the models M3 and M4 (solid and dashed) following the above suggestion. Although the improvement of the fit is evident, we notice that the NS parameters that correctly reproduce the features of 4U 1728–34 are likely in between the models M3 and M4.

### **E.1.7. Concluding Remarks**

We have done an extensive comparison of the orbital motion of neutral test particles in the PRS and Kerr spacetime geometries. In particular we have emphasized on the Keplerian and frame-dragging frequencies, as well as the precession and oscillation frequencies of the radial and vertical motions.

We have evidenced the differences in this respect between the Kerr and PRS solution, especially in the rapid  $\sim$ kHz rotation regime. Such differences are the manifestation of the influence of the high order multipole moments such as the quadrupole and octupole.

The analysis of the deviations between the Kerr and PRS features for given mass and angular momentum of a source studied in this work are useful to distinguish the signatures between BHs and NSs, which relevant to establish a separatrix for the identification of the compact objects harboring in X-Ray Binaries. In the case of BH candidates, these results might become impor-

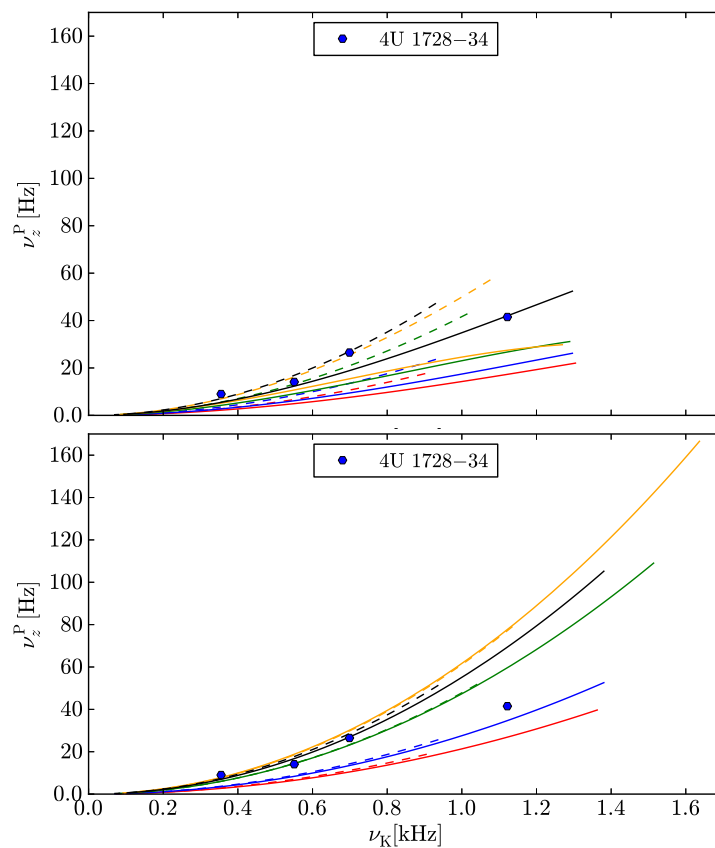


**Figure E.10.:** Nodal precession frequency,  $\nu_z^P$ , as a function of the Keplerian frequency  $\nu_K$  for the NS realistic models in Table E.2. The convention is as Fig. E.9. We indicate the QPO frequencies observed in the LMXB 4U 1728-34 (see Ford and van der Klis, 1998). The black curves indicate the  $2\nu_z^P - \nu_K$  relation for the models M3 and M4 (solid and dashed) following the suggestion of Stella et al. (1999); Stella and Vietri (1999).

tant for testing the no-hair theorem of BHs (see e.g. Johannsen and Psaltis, 2011). Equally important, the application of the precession and oscillation frequencies to the explanation of QPOs in LMXBs possessing a NS, can unveil information on the NS parameters, leading to a possible identification of the behavior of the nuclear matter EoS at supranuclear densities. In this line, the identification of the rotation frequency of NSs in LMXBs from the pulsating X-ray flux  $\nu_{\text{burst}}$ , e.g. the case of 4U 1728–34 (Ford and van der Klis, 1998), 4U 1916–053 (Galloway et al., 2001) and more recently the case of IGR J17191–2821 (Altamirano et al., 2010), will certainly help to constrain QPO models as well as the NS parameters. Additional information coming from recent modeling of the photospheric radius expansion phenomena observed in these systems (see e.g. Munro et al., 2001, for details) during their transient activity with Super-Eddington emission can become of paramount importance if combined with the QPO information.

The generalization of the present work to the electrovacuum case is important to establish the influence of the magnetic dipole and quadrupole moments on the orbital motion of particles around compact objects (see e.g. Bakala et al., 2010; Sanabria-Gómez et al., 2010; Bakala et al., 2012).

Interesting effects on the epicyclic frequencies due to the presence of the magnetic dipole have been already pointed out recently by Bakala et al. (2010) and Bakala et al. (2012). These effects were predicted after neglecting the contribution of the electromagnetic field to the curvature, for  $j = 0$  Bakala et al. (2010) and for  $j \neq 0$  Bakala et al. (2012). In Bakala et al. (2010) the authors assume the model of the star as a dipole magnetic field superimposed on a Schwarzschild black hole. In the second work, they studied the case of a magnetized slowly rotating neutron stars; to build the model they superimpose an dipolar magnetic field on the Lense-Thirring geometry. The effects of the magnetic dipole on the location of the ISCO, within the PRS solution, has been investigated by Sanabria-Gómez et al. (2010).

A complete analysis of the effects due to the emergence of electromagnetic structure on the orbital motion of charged particles is therefore of interest and deserve the appropriate attention. Recent observations have shown that for stars with strong magnetic fields the quadrupole and octupole magnetic terms make significant contributions to the magnetic field (Donati et al., 2006), which indicates that arbitrary higher order multipole components might be required in a realistic model. The presence of a magnetic quadrupole demands the breaking of the reflection symmetry (see Pachón and Sanabria-Gómez, 2006, for details), by means of a slightly change to the Ernst electric potential over the symmetry axis

$$f(z) = \frac{qz^2 + i\mu z + i\zeta}{z^3 + z^2(m - ia) - kz + is}, \quad (\text{E.1.27})$$

a quadrupolar magnetic component  $\mathcal{B}_2 = \zeta$  can be introduced to the PRS solution. Such a change generates just a redefinition of the coefficients  $f_i$  in Eq. (E.1.11). In this way the PRS solution can be readily use to explore the effect of strong magnetic fields with non-dipolar structure.

### E.1.8. Supplementary information

#### Metric Functions

The functions  $A, B, C, H, G, K,$  and  $I$  used to express the metric functions (E.1.13) are given by

$$A = \sum_{1 \leq i < j < k \leq 6} a_{ijk} r_i r_j r_k, \quad B = \sum_{1 \leq i < j \leq 6} b_{ij} r_i r_j, \quad (\text{E.1.28})$$

$$C = \sum_{1 \leq i < j \leq 6} c_{ij} r_i r_j, \quad K = \sum_{1 \leq i < j < k \leq 6} a_{ijk}, \quad (\text{E.1.29})$$

$$H = z A - (\beta_1 + \beta_2 + \beta_3) B + \sum_{1 \leq i < j < k \leq 6} h_{ijk} r_i r_j r_k + \sum_{1 \leq i < j \leq 6} (\alpha_i + \alpha_j) b_{ij} r_i r_j, \quad (\text{E.1.30})$$

$$G = -(\beta_1 + \beta_2 + \beta_3) A + z B + \sum_{1 \leq i < j \leq 6} g_{ij} r_i r_j + \sum_{1 \leq i < j < k \leq 6} (\alpha_i + \alpha_j + \alpha_k) a_{ijk} r_i r_j r_k, \quad (\text{E.1.31})$$

$$I = (f_1 + f_2 + f_3)(A - B) + (\beta_1 + \beta_2 + \beta_3 - z) C + \sum_{1 \leq i < j < k \leq 6} p_{ijk} r_i r_j r_k + \sum_{i=1}^6 p_i r_i + \sum_{1 \leq i < j \leq 6} [p_{ij} - (\alpha_i + \alpha_j) c_{ij}] r_i r_j, \quad (\text{E.1.32})$$

with

$$\begin{aligned}
 r_i &= \sqrt{\rho^2 + (z - \alpha_i)^2}, \quad a_{ijk} = (-1)^{i+j+1} \Lambda_{ijk} \Gamma_{l|mn}, \\
 b_{ij} &= (-1)^{i+j} \lambda_{ij} H_{l|mnp}, \\
 c_{ij} &= (-1)^{i+j} \lambda_{ij} [f(\alpha_l) \Gamma_{m|np} - f(\alpha_m) \Gamma_{n|pl} + f(\alpha_n) \Gamma_{p|lm} - f(\alpha_p) \Gamma_{l|mn}], \\
 h_{ijk} &= (-1)^{i+j+k} \Lambda_{ijk} (e_1^* \delta_{23|lmn} + e_2^* \delta_{31|lmn} + e_3^* \delta_{12|lmn}), \\
 g_{ij} &= (-1)^{i+j} \lambda_{ij} (\alpha_l \Gamma_{m|np} - \alpha_m \Gamma_{n|pl} + \alpha_n \Gamma_{p|lm} - \alpha_p \Gamma_{l|mn}), \\
 p_i &= (-1)^i D_i [f(\alpha_l) H_{m|nps} - f(\alpha_m) H_{n|psl} + f(\alpha_n) H_{p|slm} - f(\alpha_p) H_{s|lmn} \\
 &\quad + f(\alpha_s) H_{l|mnp}], \\
 p_{ij} &= (-1)^{i+j} \lambda_{ij} (e_1^* Y_{23|lmnp} + e_2^* Y_{31|lmnp} + e_3^* Y_{12|lmnp}), \\
 p_{ijk} &= (-1)^{i+j+1} \Lambda_{ijk} (e_1^* \Psi_{23|lmn} + e_2^* \Psi_{31|lmn} + e_3^* \Psi_{12|lmn}), \\
 \lambda_{ij} &= (\alpha_i - \alpha_j) D_i D_j, \quad \Lambda_{ijk} = (\alpha_i - \alpha_j)(\alpha_i - \alpha_k)(\alpha_j - \alpha_k) D_i D_j D_k, \\
 D_i &= \frac{1}{(\alpha_i - \beta_1)(\alpha_i - \beta_2)(\alpha_i - \beta_3)}, \\
 \Gamma_{l|mn} &= H_3(\alpha_l) \Delta_{12|mn} + H_3(\alpha_m) \Delta_{12|nl} + H_3(\alpha_n) \Delta_{12|lm},
 \end{aligned}$$

and

$$\begin{aligned}
 \Delta_{lm|np} &= H_l(\alpha_n) H_m(\alpha_p) - H_l(\alpha_p) H_m(\alpha_n), \\
 H_l(\alpha_n) &= \frac{2 \prod_{p \neq n} (\alpha_p - \beta_l^*)}{\prod_{k \neq l}^3 (\beta_l^* - \beta_k^*) \prod_{k=1}^3 (\beta_l^* - \beta_k)} - \sum_{k=1}^3 \frac{2 f_l^* f_k}{(\beta_l^* - \beta_k)(\alpha_n - \beta_k)}, \\
 \delta_{lm|nps} &= \Delta_{lm|np} + \Delta_{lm|ps} + \Delta_{lm|sn}, \quad h_{l|mnp} = H_3(\alpha_l) \delta_{12|mnp}, \\
 H_{l|mnp} &= h_{l|mnp} + h_{m|npl} + h_{n|plm} + h_{p|lmn}, \\
 \Psi_{lm|nps} &= f(\alpha_n) \Delta_{lm|ps} + f(\alpha_p) \Delta_{lm|sn} + f(\alpha_s) \Delta_{lm|np}, \\
 Y_{lm|nprs} &= f(\alpha_n) \delta_{lm|prs} - f(\alpha_p) \delta_{lm|rsn} + f(\alpha_r) \delta_{lm|snp} - f(\alpha_s) \delta_{lm|npr},
 \end{aligned}$$

being  $\alpha$ 's the roots of the Sibgatullin equation Sibgatullin (1991); Manko and Sibgatullin (1993)

$$e(z) + \tilde{e}(z) + 2\tilde{f}(z)f(z) = 0. \quad (\text{E.1.33})$$

### Kerr's metric in Weyl-Papapetrou quasi-cylindrical coordinates

In order to keep comparisons in the same place, we consider useful to display the Kerr solution in the Weyl-Papapetrou quasi-cylindrical coordinates. For

this case,

$$f = \frac{A\bar{A} - B\bar{B}}{(A - B)(\bar{A} - \bar{B})}, \quad e^{2\gamma} = \frac{A\bar{A} - B\bar{B}}{K\bar{K} \prod_{n=1}^2 r_n}, \quad \omega = \frac{\text{Im}[(A + B)\bar{H} - (\bar{A} + \bar{B})G]}{A\bar{A} - B\bar{B}}, \quad (\text{E.1.34})$$

where for our own convenience we do not present the definition of each term, but present the final combination of them, i.e.,

$$A\bar{A} - B\bar{B} = -8(a^2 - m^2)^3(\rho^2 + z^2) \left( m^2 \sqrt{-2z\sqrt{m^2 - a^2} - a^2 + m^2 + \rho^2 + z^2} \right. \\ \left. \sqrt{(\sqrt{m^2 - a^2} + z)^2 + \rho^2} - 2a^2 \sqrt{-2z\sqrt{m^2 - a^2} - a^2 + m^2 + \rho^2 + z^2} \right. \\ \left. \sqrt{(\sqrt{m^2 - a^2} + z)^2 + \rho^2 + a^2 m^2 - m^4 + m^2 \rho^2 + m^2 z^2} \right), \quad (\text{E.1.35})$$

$$(A - B)(\bar{A} - \bar{B}) = -8(m^2 - a^2)^3(\rho^2 + z^2) \\ (a^2(2m(\sqrt{-2z\sqrt{m^2 - a^2} - a^2 + m^2 + \rho^2 + z^2} \\ + \sqrt{2z\sqrt{m^2 - a^2} - a^2 + m^2 + \rho^2 + z^2}) \\ + 2\sqrt{-2z\sqrt{m^2 - a^2} - a^2 + m^2 + \rho^2 + z^2} \sqrt{2z\sqrt{m^2 - a^2} - a^2 + m^2 + \rho^2 + z^2} \\ + 3m^2 - m^2(2m(\sqrt{-2z\sqrt{m^2 - a^2} - a^2 + m^2 + \rho^2 + z^2} \\ + \sqrt{2z\sqrt{m^2 - a^2} - a^2 + m^2 + \rho^2 + z^2}) \\ + \sqrt{-2z\sqrt{m^2 - a^2} - a^2 + m^2 + \rho^2 + z^2} \sqrt{2z\sqrt{m^2 - a^2} - a^2 + m^2 + \rho^2 + z^2} \\ + 3m^2 + \rho^2 + z^2)), \quad (\text{E.1.36})$$

$$K\bar{K} \prod_{n=1}^2 r_n = 16(m^2 - a^2)^4(\rho^2 + z^2) \sqrt{(z - \sqrt{m^2 - a^2})^2 + \rho^2} \\ \times \sqrt{(\sqrt{m^2 - a^2} + z)^2 + \rho^2}, \quad (\text{E.1.37})$$

$$\begin{aligned}
 \text{Im}[(A + B)\bar{H} - (\bar{A} + \bar{B})G] &= 16am(m^2 - a^2)^3(\rho^2 + z^2) \\
 &(-m^2\sqrt{-2z\sqrt{m^2 - a^2} - a^2 + m^2 + \rho^2 + z^2} \\
 &- \sqrt{-2z\sqrt{m^2 - a^2} - a^2 + m^2 + \rho^2 + z^2} \\
 &\sqrt{(\sqrt{m^2 - a^2} + z)^2 + \rho^2} + a^2\sqrt{-2z\sqrt{m^2 - a^2} - a^2 + m^2 + \rho^2 + z^2} \\
 &- z\sqrt{m^2 - a^2}\sqrt{-2z\sqrt{m^2 - a^2} - a^2 + m^2 + \rho^2 + z^2} \\
 &- m^2\sqrt{(\sqrt{m^2 - a^2} + z)^2 + \rho^2} \\
 &+ a^2\sqrt{(\sqrt{m^2 - a^2} + z)^2 + \rho^2} + z\sqrt{m^2 - a^2}\sqrt{(\sqrt{m^2 - a^2} + z)^2 + \rho^2} \\
 &+ a^2m - m^3 + m\rho^2 + mz^2). \tag{E.1.38}
 \end{aligned}$$

From here, it is clear how changing  $a \rightarrow -a$  will cause only a global change in the sign of the metric function  $\omega$  and therefore only a change in the  $g_{t\phi}$  metric component.



# F. Critical Fields and Non-linear Electrodynamics Effects in Astrophysics

## F.1. On the black hole mass-formula in nonlinear electrodynamics

### F.1.1. Introduction

Black hole solutions to Einstein equations have always attracted the attention of researchers, not only due to their unusual properties, but also from the discovery that they could be one of the most abundant sources of energy in the Universe. From conservation laws, Penrose (1969) has shown primarily how energy could be extracted from a charged black hole.

Christodoulou (1970) and Christodoulou and Ruffini (1971), through the study of test particles in Kerr and Kerr-Newmann spacetimes (Carter, 1968), have quantified the maximum amount of energy that can be extracted from a black hole. These papers deserve some comments. First, this maximum amount of energy can be obtained only by means of the called “reversible processes”. Such processes are the only ones in which black hole configurations can be brought back to their initial states, after convenient interactions with test particles. Therefore, reversible transformations constitute the most efficient processes of energy extraction of a black hole. Furthermore, by studying the interaction between black holes and test particles, Christodoulou (1970); Christodoulou and Ruffini (1971) also introduced the concept of “irreducible mass”. This quantity can never be diminished by any sort of processes and hence would constitute an intrinsic property of the system. Such configuration would constitute the “fundamental energy state for any black hole”. This is exactly the case of Schwarzschild black holes. From this irreducible mass, one can immediately verify that the area of a black hole never decreases after any infinitesimal transformation performed on it. Moreover, one can write down the total energy of a black hole in terms of this quantity (Christodoulou and Ruffini, 1971).

The conceptual asset of effective nonlinear theories of electromagnetism (Ruffini et al., 2010b) is that they allow the insertion of desired effects (eg. quantum, avoidance of singular solutions, etc.) at the classical level in the

problem being addressed. As a first approach, all of these theories are built in terms of the two local invariants constructed out of the electromagnetic fields (Dittrich and Gies, 1998; Landau and Lifshitz, 1975), these invariants assumed to be functions of a four-vector potential in the same functional way as their classical counterpart (i.e., they are gauge independent invariants). We quote for instance Born-Infeld Lagrangian (Born and Infeld, 1934), conceived with the purpose of solving the problem of the infinite self-energy of an electron in the classical theory of electromagnetism. Born-Infeld theory has gained a renewal of interest due to its appearance-like as an effective theory in the low energy limit of String Theory (Rasheed, 1997). Born-Infeld theory has also been minimally coupled to general relativity and it allows for an exact solution (Demianski, 1986; Breton and Garcia-Salcedo, 2007), and this coupling has been studied in a variety of problems (Bretón, 2002; Myung et al., 2008; Olmo and Rubiera-Garcia, 2011). Another worthwhile example of nonlinear electrodynamic theory is the Heisenberg-Euler Lagrangian (Heisenberg and Euler, 1936; Schwinger, 1951). This Lagrangian allows one to take effectively into account one-loop corrections from the Maxwellian Lagrangian coming from Quantum Electrodynamics (QED). This Lagrangian has been extensively studied in the literature (Ruffini et al., 2010b; De Lorenci et al., 2000, 2001). Nonlinear theories of electromagnetism have also been investigated in the context of astrophysics (Mosquera Cuesta and Salim, 2004a,b; Dupays et al., 2008). It has also been claimed that it could be used as a simulacrum of dark energy (Labun and Rafelski, 2010a), and it could play an important role in the description of the motion of particles in the neighborhood of some astrophysical systems (Labun and Rafelski, 2010b).

In connection with the above discussion, the thermodynamics of black holes (Bardeen et al., 1973) in the presence of nonlinear theories of electromagnetism has also been investigated. The zeroth and first laws have been studied in detail (Rasheed, 1997), allowing the raise of other important issues. We quote for example the difficulty of generalizing the Smarr mass for nonlinear theories (Rasheed, 1997). Many efforts have been pursued in this direction, through the suggestion of systematic ways to write down this mass, which has led to some inconsistencies (see e.g. Bretón, 2005). For some specific nonlinear Lagrangians, this problem has been claimed to be circumvented (González et al., 2009).

In this work we shall first deal with static spherically symmetric solutions to general relativity minimally coupled to Abelian nonlinear electrodynamics in the weak field case. We shall be interested in finding general results concerning reversible transformations. Motivated by the previous results, it will be showed how to express the total energy (mass) of any spherically symmetric nonlinear black hole (a black hole solution to a nonlinear theory of electromagnetism) in terms its characteristic parameters (charge and scale fields). This will allow one to investigate the issue related to the extraction of energy from any spherically symmetric black hole in the framework of non-

linear theories.

This paper is organized as follows. In Section II the notation is established and the field equations are stated and solved formally in the spherically symmetric case for any nonlinear theory. In Section III, reversible transformations for nonlinear theories are investigated in details. In section IV the field equations of general relativity are solved for nonlinear theories of electromagnetism in the weak field case. Section V is devoted to the deduction of the total energy of the black hole in terms of irreducible and extractable quantities, when reversible transformations are taken into account. In Section VI variations of the outer horizon associated with the capture of test particles in nonlinear theories of electromagnetism are analyzed. In section VII, motivated by the results of the weak field case, we shall find the energy decomposition of any nonlinear theory of electromagnetism for any range of the electric field. Section VIII closes this paper, with a discussion about the issues raised. Units are such that  $c = G = 1$ . The metric signature chosen is  $-2$ .

### F.1.2. Field Equations

The minimal coupling between gravity and nonlinear electrodynamics depending just upon one parameter can be stated mathematically through the action

$$S = \int d^4x \sqrt{-g} \left( \frac{L_{EH}}{16\pi} - \frac{L_{em}(F)}{4\pi} \right) \doteq \frac{S_{EH}}{16\pi} - \frac{S_{em}}{4\pi}, \quad (\text{F.1.1})$$

where  $S_{EH}$  is the Einstein–Hilbert action and  $S_{em}$  is the action of the electromagnetic theory under interest. Under the variation of Eq. (F.1.1) with respect to  $g^{\mu\nu}$ , and applying the least principle action, one obtains

$$G_{\mu\nu} = 8\pi T_{\mu\nu}^{(em)}, \quad (\text{F.1.2})$$

with  $G_{\mu\nu}$  the Einstein tensor (defined following the convention of Landau and Lifshitz (1975)) and  $T_{\mu\nu}^{(em)}$  the energy-momentum tensor of the electromagnetic field, defined as

$$4\pi T_{\mu\nu}^{(em)} \doteq \frac{2}{\sqrt{-g}} \frac{\delta S_{em}}{\delta g^{\mu\nu}} = 4 L_F^{(em)} F_{\mu\alpha} F_{\nu\rho} g^{\alpha\rho} - L_{em} g_{\mu\nu}, \quad (\text{F.1.3})$$

where  $L_F^{(em)} \doteq \partial L_{em} / \partial F$ ,  $F \doteq F^{\mu\nu} F_{\mu\nu}$ ,  $F_{\mu\nu} = \nabla_\mu A_\nu - \nabla_\nu A_\mu = \partial_\mu A_\nu - \partial_\nu A_\mu$ , being  $A_\mu$  the four-potential associated with the electromagnetic fields.

Application of the Principle of least action in Eq. (F.1.1) concerning the field  $A_\mu(x^\beta)$  gives

$$\nabla_\mu (L_F^{(em)} F^{\mu\nu}) = 0, \quad (\text{F.1.4})$$

since we are interested just in solutions to general relativity in the absence of

sources.

In the static spherically symmetric case, it is possible to solve Einstein equations (minimally) coupled to any nonlinear electrodynamic theory [see Eqs. (F.1.2) and (F.1.3)] and due to the form of the energy-momentum tensor in this case the metric must be of the form

$$g_{\mu\nu} = \text{diag}(e^\nu, -e^{-\nu}, -r^2, -r^2 \sin^2 \theta), \quad (\text{F.1.5})$$

where (Landau and Lifshitz, 1975; Diaz-Alonso and Rubiera-Garcia, 2012)

$$e^\nu = 1 - \frac{2M}{r} + \frac{8\pi}{r} \int_r^\infty r'^2 T^0_0(r') dr', \quad (\text{F.1.6})$$

with  $M$  the total energy (mass) of the black hole as measured by observers at infinity.

The Eqs. (F.1.4) in this special spherically symmetric case reduce just to

$$L_F^{(em)} E_r r^2 = -\frac{Q}{4}, \quad (\text{F.1.7})$$

where  $Q$  as an arbitrary constant representing physically the charge of the black hole.

If one defines

$$E_r \doteq -\frac{\partial A_0}{\partial r} \quad \text{and} \quad \frac{\partial \mathcal{F}}{\partial r} \doteq -L_{em} r^2, \quad (\text{F.1.8})$$

and take into account Eqs. (F.1.3), (F.1.5) and (F.1.7), then Eq. (F.1.6) can be rewritten as

$$e^\nu = 1 - \frac{2M}{r} + \frac{2QA_0}{r} - \frac{2\mathcal{F}}{r}, \quad (\text{F.1.9})$$

where it has been imposed a gauge such that the scalar potential  $A_0$  goes to zero when the radial coordinate goes to infinity, which also holds for  $\mathcal{F}$ .

Horizons in spherically symmetric solutions to general relativity are defined as the solutions to

$$g_{00}(r_h) = e^{\nu(r_h)} = 0. \quad (\text{F.1.10})$$

### F.1.3. Reversible and Irreversible transformations

A way to investigate the motion of test particles in a static spherically symmetric spacetime would be through the solution to the Hamilton-Jacobi equation. The trajectories of the test particles can be obtained by deriving its solutions with respect to the particle constants of motion (energy  $E$ , orbital angular momentum  $L$ , the rest mass  $m$  and the Carter constant) (Carter, 1968; Misner et al., 1973). The energy of the test particle is given by Christodoulou

(1970); Christodoulou and Ruffini (1971); Carter (1968); Misner et al. (1973)

$$E = q A_0 + \sqrt{\frac{e^\lambda}{r^2} \left[ r^4 (p^\theta)^2 + \frac{L^2}{\sin^2 \theta} + m^2 r^2 \right] + (p^r)^2}, \quad (\text{F.1.11})$$

where  $p^\mu \doteq m dx^\mu / d\tau$ ,  $\tau$  an affine parameter along the worldline of the particle and  $q$  its charge. The “+” sign has been chosen in Eq. (F.1.11), because we are interested just in particles traveling to the future (Misner et al., 1973; Deruelle and Ruffini, 1974).

From Eq. (F.1.11), one can see that the only way to apply a reversible transformation in the sense of Christodoulou-Ruffini (Christodoulou, 1970; Christodoulou and Ruffini, 1971; Ruffini et al., 2010b) to a black hole interacting with a test particle is by demanding that the square root term is null. Hence, the minimum energy that the particle (oppositely-charged) could have in a reversible process is given by

$$E_{min} = q A_0(r_+), \quad (\text{F.1.12})$$

where  $r_+$  is the largest solution to Eq. (F.1.10) and is called the outer (event) horizon of the black hole. Expression (F.1.12) is valid only for a particle that arrives on the outer event horizon with zero radial velocity, otherwise, an inevitable loss of energy will happen, and thus the process will become irreversible. In other words, the insertion of any other test particles would not bring the energy of the black hole into its initial configuration.

If the worldline of an arbitrary test particle intersects the outer horizon, then the first law of black hole thermodynamics states that the changes in the energy and charge of the black hole reads:  $\delta M = E$  and  $\delta Q = q$  (Misner et al., 1973), respectively. Hence, from Eq. (F.1.12),

$$\delta M \geq \delta Q A_0(r_+). \quad (\text{F.1.13})$$

#### F.1.4. Weak Field Lagrangians

An interesting and convenient limit for investigating nonlinear properties of Lagrangians is when the fields are small compared to some fundamental fields in the theory, which would introduce scales to the theory (Labun and Rafelski, 2010a). In this limit, one expects that the leading term of the Lagrangian be the linear (Maxwellian) term. When one is interested only in the static spherically symmetric case in the absence of magnetic charge, the general way of writing down the weak field nonlinear Lagrangian is

$$L_{em} = -\frac{F}{4} + \frac{\mu}{4} F^2, \quad (\text{F.1.14})$$

where  $\mu$  is related to the fundamental constants of the theory under interest. The above nonlinear Lagrangian is assumed to be such that its second term is much smaller than the first one. Physically speaking, this term is just a first order correction to Maxwell theory. Hence, a perturbative analysis could be carried out. The sign of  $\mu$  in principle could be arbitrary. Nevertheless, from the inspection of the Euler-Heisenberg Lagrangian, for instance, this constant turns out to be positive (Ruffini et al., 2010b). The same behavior happens if one expands perturbatively the Born-Infeld Lagrangian (Ruffini et al., 2010b; Born and Infeld, 1934; Rasheed, 1997; Demianski, 1986; Breton and Garcia-Salcedo, 2007; Bretón, 2002; Labun and Rafelski, 2010a).

When one interprets nonlinear Lagrangians as the ones related to effective media (Born and Infeld, 1934; Novello et al., 2000a), then one expects that the associated electric field solution should be reduced. This would impose conditions to the sign of  $\mu$ , as we shall show. Nevertheless, it is not ruled out in principle Lagrangians where the associated electric field could increase.

By substituting Eq. (F.1.14) into Eq. (F.1.7) and the first term of Eq. (F.1.8), solving exactly and then expanding perturbatively (or by directly working perturbatively), one can show that

$$E_r(r) = \frac{Q}{r^2} \left( 1 - \frac{4\mu Q^2}{r^4} \right), \quad A_0(r) = \frac{Q}{r} \left( 1 - \frac{4\mu Q^2}{5r^4} \right), \quad (\text{F.1.15})$$

Expressions (F.1.15) are just meaningful if the characteristic distances of the system are much larger than

$$r_c^4 = 4|\mu|M^2\alpha^2, \quad \alpha \doteq \frac{Q}{M}. \quad (\text{F.1.16})$$

As we pointed out before, when  $\mu > 0$ , the modulus of the electric field diminishes in comparison to the pure Maxwellian case, while the opposite happens when  $\mu < 0$ . The former case is exactly what happens in usual media (Landau and Lifshitz, 1960), while the latter could happen in the so-called metamaterials (see e.g. Zhuromskyy et al., 2009).

From Eq. (F.1.14), the second term of Eq. (F.1.8) and Eq. (F.1.15) and assuming Eq. (F.1.16) is valid, it is also easily shown that

$$\mathcal{F} = \frac{Q^2}{2r} \left( 1 - \frac{6\mu Q^2}{5r^4} \right). \quad (\text{F.1.17})$$

When Eqs. (F.1.15) and (F.1.17) are put into Eq. (F.1.9), one obtains

$$e^\lambda = 1 - \frac{2M}{r} + \frac{Q^2}{r^2} - \frac{2\mu Q^4}{5r^6}. \quad (\text{F.1.18})$$

The above result is the same one as obtained in (De Lorenci et al., 2001),

in the corresponding units. Notice that when  $\mu = 0$ , i.e., for the Maxwell Lagrangian [see Eq. (F.1.14)], Eq. (F.1.18) gives the well-known Reissner-Nordström solution (Misner et al., 1973).

The outer horizon can be found perturbatively from Eqs. (F.1.10) and (F.1.18) and the result is

$$r_+ = \mathcal{R}_+ \left( 1 + \frac{\mu Q^4}{5 (\mathcal{R}_+)^5 \sqrt{M^2 - Q^2}} \right), \quad (\text{F.1.19})$$

where we defined

$$\mathcal{R}_+ \doteq M + \sqrt{M^2 - Q^2}, \quad (\text{F.1.20})$$

as the outer horizon in the Reissner-Nordström solution (Misner et al., 1973). Besides, in Eq. (F.1.19), it was assumed that the second term in parenthesis is much smaller than one. Fig. F.1 shows the comparison of the numerical outer horizon and the perturbative solution given by Eq. (F.1.19) for a selected value of  $\mu/M^2$  as a function of  $Q/M$ , for  $0 < Q/M < 1$ .

When one approaches the extreme (extr) value  $Q = M$ , the expression to be taken into account tends to

$$r_+^{(extr)} = M \left\{ 1 + \sqrt{\frac{2\mu}{5M^2}} - \frac{4\mu}{5M^2} + \mathcal{O} \left[ \left( \frac{\mu}{M^2} \right)^{\frac{3}{2}} \right] \right\}, \quad (\text{F.1.21})$$

which is just a solution to Eq. (F.1.18), when one assumes  $M = Q$  and Eq. (F.1.10). The other (perturbative) solutions to this equation are

$$r_-^{(extr)} = M \left\{ 1 - \sqrt{\frac{2\mu}{5M^2}} - \frac{4\mu}{5M^2} + \mathcal{O} \left[ \left( \frac{\mu}{M^2} \right)^{\frac{3}{2}} \right] \right\} \quad (\text{F.1.22})$$

$$r_{ncl}^{(extr)} = M \left\{ \left( \frac{2\mu}{5M^2} \right)^{\frac{1}{4}} + \left( \frac{\mu}{10M^2} \right)^{\frac{1}{2}} + \mathcal{O} \left[ \left( \frac{\mu}{M^2} \right)^{\frac{3}{4}} \right] \right\}, \quad (\text{F.1.23})$$

where  $r_-^{(ext)}$  in Eq. (F.1.22) stands for the nonlinear version of the inner horizon in Reissner–Nordstrom solution, and the solution given by Eq. (F.1.23) has a nonclassical (ncl) version, being intrinsically due to the corrections in the Maxwell theory. Notice that when  $\mu \neq 0$  the inner and outer horizons are never equal in nonlinear theories given by Eq. (F.1.14) in the extreme case. Hence, when corrections are added to Maxwell theory, the degeneracy in the extreme case ( $Q = M$ ) is broken. We stress that Eq. (F.1.23) is just a mathematical solution to Eqs. (F.1.18) and (F.1.10), being physically meaningless, as given by the first term of Eq. (F.1.15) and Eq. (F.1.23), for being it possible the perturbative analysis leading to Eq. (F.1.18). It can be seen as follows. Assume that the charge of the black hole is comparable with its mass (minimum value for being relevant the “nonclassical horizon”), that is

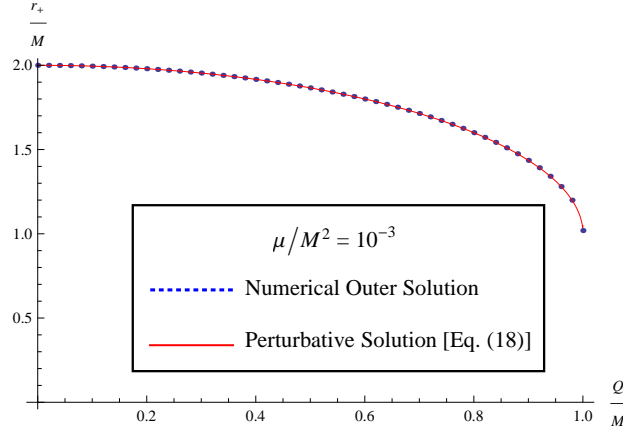


**Figure F.1.:** Plots of the outer horizon for  $\mu/M^2 = 10^{-3}$  as a function of  $Q/M$ . The dotted curve represents a numerical solution to Eq. (F.1.10) and (F.1.18) related to its largest solution (outer horizon). The thick curve represents Eqs. (F.1.19) and (F.1.20). The latter equations are not valid when  $Q = M$ . The proximity to  $Q = M$  up to when the perturbative analysis is meaningful is dictated by  $\mu/M^2$ . The smaller this parameter, the closer one can arrive to  $Q = M$  using perturbative theory. Just for reference, in Euler-Heisenberg and standard Born-Infeld theories,  $\mu \sim 10^{-32}(e.s.u)^{-2}$  (Ruffini et al., 2010b; Born and Infeld, 1934), hence for objects of masses around  $M \sim 10^5 M_\odot$ ,  $\mu/M^2$  when brought to the geometrical system of units ( $\mu[cm^2] = \mu[(e.s.u)^{-2}]c^4/G$  and  $M[cm^2] = M[g]G/c^2$ ) would be approximately  $10^{-4}$ . This would allow one to reach a precision up to four figures concerning  $Q = M$  and yet being meaningful the perturbative analysis given by Eq. (F.1.19). This is due to an ineluctable breakdown of the previous equation when  $\alpha \rightarrow 1^-$ , not a problem with the perturbative equation (F.1.18), which is valid with any precision when this limit is reached. The smaller the ratio  $Q/M$ , the better is the perturbative approximation for the outer horizon, Eq. (F.1.19).

$Q^2 \sim M^2$ . Then, from Eq. (F.1.16) it follows that  $r_c \sim (\mu M^2)^{1/4}$ . From Eq. (F.1.23), however, one has  $r_{ncl}^{(extr)} \sim (\mu M^2)^{1/4} = r_c$ . Since just distances much larger than  $r_c$  are physically meaningful in the realm of our perturbative calculations, it is proved that  $r_{ncl}^{(extr)}$  is not physically relevant. It implies that perturbative changes of the Maxwell Lagrangian just lead to corrections of the Reissner-Nordstrom horizons and naked singularities are present in these theories when  $Q/M > 1$ .

### F.1.5. The Black Hole Mass Formula

Assume a test particle being captured by a black hole under a reversible transformation. In mathematical terms, this means that the equality in Eq. (F.1.13) is to be taken into account and the changes can be considered as infinitesimals. By taking into account the second term in Eq. (F.1.15) and Eq.(F.1.19), one ends up to first order of approximation with

$$\frac{dM}{dQ} = \frac{Q}{\mathcal{R}_+} - \frac{\mu Q^3}{5(\mathcal{R}_+)^5} \left[ \frac{Q^2}{\mathcal{R}_+ \sqrt{M^2 - Q^2}} + 4 \right]. \quad (\text{F.1.24})$$

Since we are supposing that the second term of the above equation is much smaller than the first one, the method of successive approximations can be used. We shall suppose that

$$M(Q) = M^{(0)}(Q) + \mu M^{(1)}(Q), \quad (\text{F.1.25})$$

where the second term of the above expression is thought of as a perturbation. In zeroth order approximation,  $M^{(0)}$  satisfies the differential equation

$$\frac{dM^{(0)}}{dQ} = \frac{Q}{M^{(0)} + \sqrt{(M^{(0)})^2 - Q^2}}. \quad (\text{F.1.26})$$

As it is known, the solution to the above equation is (Christodoulou and Ruffini, 1971)

$$M^{(0)}(Q) = M_{irr} + \frac{Q^2}{4M_{irr}}, \quad (\text{F.1.27})$$

where  $M_{irr}$  is a constant of integration known as the irreducible mass and it accounts for the total energy of the system when the charge of the black hole is zero. Expression (F.1.27) is the Christodoulou-Ruffini black hole mass formula valid for a classical spherically symmetric charged black hole (Maxwell Lagrangian coupled to general relativity). By substituting this expression into Eq. (F.1.20) one obtains  $\mathcal{R}_+ = 2M_{irr}$  and then it follows that  $Q^2/2\mathcal{R}_+ \leq M/2$ , where the equality is valid in the case  $Q = M$ . Hence, up to 50% of the

total mass of a black hole is due to the electromagnetic energy contribution  $Q^2/4M_{irr}$ .

Substituting Eq. (F.1.25) into Eq. (F.1.24) and working now up to first order of approximation, after Eqs. (F.1.26) and (F.1.27) are taken into account, one obtains as a solution to the resulting differential equation

$$M^{(1)}(Q) = -\frac{Q^4}{160M_{irr}^5}. \quad (\text{F.1.28})$$

The above equation is obtained by imposing  $M^{(1)}(0) = 0$ , which is physically clear from our previous considerations. Since energy could be extracted from black holes only when it is charged [see Eq. (F.1.13)], the extractable energy ( $M_{ext}$ ) (or the “blackholic energy” (Ruffini et al., 2010b)) in weak fields nonlinear theories of electromagnetism given by Eq. (F.1.14) is

$$M_{ext}(Q) = \frac{Q^2}{4M_{irr}} - \frac{\mu Q^4}{160M_{irr}^5}. \quad (\text{F.1.29})$$

As it can be checked easily, this is exactly the electromagnetic energy ( $E_{em}$ ) (Ruffini and Vitagliano, 2002; Cherubini et al., 2009) stored in the electric field in the spacetime given by Eq. (F.1.18) viz.,

$$E_{(em)} = 4\pi \int_{r_+}^{\infty} T^0_0 r^2 dr = \int_{r_+}^{\infty} \int_{2\pi}^0 \int_{\pi}^0 T^0_0 \sqrt{-g} d\theta d\phi dr, \quad (\text{F.1.30})$$

where  $(-g)$  is the determinant of the metric, that in Schwarzschild-like coordinates is given by  $r^2 \sin^2 \theta$  [see Eq. (F.1.5)].

From Eq. (F.1.29), one clearly sees that the total amount energy that can be extracted is reduced if  $\mu > 0$ , in relation to the Maxwell counterpart. The positiveness of  $\mu$  is valid both to the Euler-Heisenberg effective nonlinear Lagrangian to one-loop QED as well as to the standard Born-Infeld Lagrangian, as we pointed out before. Hence, in these theories, the extractable energy is always smaller than 50% of the total energy. More precisely, from Eqs. (F.1.19), (F.1.20), (F.1.25), (F.1.27) and (F.1.28),

$$M_{ext} \leq \frac{M}{2} - \frac{\mu Q^4}{320M_{irr}^4 \sqrt{M^2 - Q^2}}, \quad (\text{F.1.31})$$

the equality in this case being true just when  $\mu = 0$ . A clarification about the previous mathematical procedure is in order. Take as examples the weak field standard Born-Infeld Lagrangian (Born and Infeld, 1934) and Euler-Heisenberg Lagrangian (Heisenberg and Euler, 1936; Schwinger, 1951; Ruffini et al., 2010b). As we pointed out before for these theories, our perturbative analysis is valid up to values close to  $\alpha \simeq 1$  just if  $M \gtrsim 10^5 M_{\odot} \sim 10^{10} \text{cm}$ .

Assume besides that the masses of the systems under interest are of this order of magnitude. By re-scaling the masses and the charges of the systems by respectively

$$M = 10^{10}M_{10} \quad \text{and} \quad Q = 10^{10}Q_{10}, \quad (\text{F.1.32})$$

it is simple to see that  $\mu_{10} = 10^{-20}\mu$  is the new quantity that should be considered into the equations, replacing  $\mu$ . For the Lagrangians under interest, one has  $\mu_{10} \sim 10^{-4}cm^2$ . Hence, this would physically justify the perturbative analysis carried out before. In general, one should just conveniently re-scale the theory under interest for applying physically the previous results coming from the method of successive approximations.

### F.1.6. Transformations in the outer horizon

Under the capture of a test particle of energy  $E$  and charge  $q$ , from the first law of thermodynamics of black holes one has that the black hole undergoes the (infinitesimal) given changes  $\delta M = E$  and  $\delta Q = q$ , satisfying Eq. (F.1.13). Since the outer horizon of this black hole is dependent upon  $M$  and  $Q$ , it also undergoes a change. Such a change can be obtained in the scope of the perturbative description we are carrying out and the basic equation for doing so is Eq. (F.1.19).

By using Eqs. (F.1.19), (F.1.20), (F.1.13) and the second term of Eq. (F.1.15), one can easily show that

$$\delta r_+ \geq -\frac{\mu Q^4 \delta \mathcal{R}_+}{5(\mathcal{R}_+)^5 (M^2 - Q^2)} [\mathcal{R}_+ + 3\sqrt{M^2 - Q^2}]. \quad (\text{F.1.33})$$

As it can be seen from Eqs. (F.1.20), (F.1.25), (F.1.27) and (F.1.28),  $\delta \mathcal{R}_+ \sim \mathcal{O}(\mu)$ , then, up to first order in  $\mu$ , we have  $\delta r_+ \geq 0$ . Hence, when reversible transformations are taken into account, the outer horizon of any perturbative nonlinear black hole solution to general relativity remains constant. Under irreversible transformations, however, it increases. This result can be easily seen if one notices that up to first order of approximation in  $\mu$ ,  $r_+ = 2M_{irr}$ . Notice that these results are just valid for  $Q/M < 1$ .

Another way of realizing whether or not there is an increase of the outer radius due to the capture of a test particle is to search the solutions to Eqs. (F.1.10) and (F.1.18) when one performs the changes  $M \rightarrow M + \delta M$  and  $Q \rightarrow Q + \delta Q$ , satisfying Eq. (F.1.13). If one defines generally  $r_+$  as the largest solution to Eqs. (F.1.10) and (F.1.18), then it is simple to verify that  $\delta r_+ = 0$  for reversible transformations. For irreversible transformations,  $\delta r_+ > 0$ . Hence, generically, one has  $\delta r_+ \geq 0$  for an arbitrary infinitesimal transformation undergone by the black hole in nonlinear weak field electromagnetism.

### F.1.7. Energy decomposition for any nonlinear theory

Weak fields nonlinear Lagrangians suggest that the outer horizon of any spherically symmetric  $L(F)$  theory is  $2M_{irr}$  when reversible transformations are considered, for any range of the electric field. Now we shall show that in fact  $r_+$  must be  $2M_{irr}$  for any  $L(F)$  theory whenever one is interested in reversible transformations. This tells us one is able to obtain the total energy of any spherically symmetric nonlinear black hole in an algebraic way, overcoming the tremendous problems in solving differential equations coming from the thermodynamical approach. Also, it gives us the extractable energy from any nonlinear black hole.

Assume that the invariant  $F = -2E_r^2$  is such that  $F = F(r, Q; \zeta)$ , where  $\zeta$  are all the other parameters needed for fixing the units of the theory under interest. From Eqs. (F.1.7)-(F.1.9), one trivially shows that

$$Q \frac{\delta A_0}{\delta Q} = \frac{\delta \mathcal{F}}{\delta Q}, \quad (\text{F.1.34})$$

since the constant present must be zero for accounting for the neutral case. Assume now that  $r_+ = C = \text{const}$ , that is, the outer horizon is an intrinsic property of the system. From Eqs. (F.1.10) and (F.1.34), one shows immediately that

$$\delta M = \delta Q A_0|_{r_+=C}. \quad (\text{F.1.35})$$

It can be easily shown that the above equation is valid just when  $r_+ = C$ . We recall we assumed Eq. (F.1.35) as a law for reversible transformations (energy conservation). Thereby, we showed that reversible transformations are fully equivalent to having constant horizons in spherically symmetric solutions to general relativity. Since Eq. (F.1.35) is valid for any stage of the sequence of reversible transformations for any theory, it is even so when  $Q = 0$  and hence,  $C = 2M_{irr}$ . So, horizons for reversible transformations are dependent just upon the "fundamental energy state" of any black hole,  $2M_{irr}$ . Even more remarkable is that we already know the solution to Eq. (F.1.35), which from Eqs. (F.1.6), (F.1.10) and (F.1.9) is

$$M = M_{irr} + Q A_0|_{r=2M_{irr}} - \mathcal{F}|_{r=2M_{irr}} = M_{irr} + 4\pi \int_{2M_{irr}}^{\infty} r'^2 T^0_0(r') dr'. \quad (\text{F.1.36})$$

The above equation is the generalized Christodoulou-Ruffini black hole mass decomposition formula to any  $L(F)$  theory for any electric field range when the nonlinear electromagnetic theory does not depend upon  $M$ . If this is not the case, one then have an algebraic equation to solve. The extractable energy ( $M - M_{irr}$ ) from any  $L(F)$  can be read off immediately from Eq. (F.1.36).

In the spherically symmetric case, one knows that the horizon area is  $A = 4\pi r_+^2$ . So, Eq. (F.1.36) can as well be written in terms of  $A$ . As we showed

above, for reversible transformations the outer horizon must be kept constant and the mass change must be given by Eq. (F.1.35). Nevertheless, as it is very intuitive, one would expect the total mass of a given black hole to have a definite meaning. In this sense, Eq. (F.1.36) in terms of the black hole area should be the expression for the mass even in the case  $A$  changes. Such a general statement is reinforced by fact it is true for black holes described by the Maxwell Lagrangian (this can be seen in (Smarr, 1973a,b) when one works with its final mass expression,  $M$ , and check it is exactly the same as Eq. (2) of Christodoulou and Ruffini (1971) in the context of reversible transformations). Let us show this should be the case also in nonlinear electrodynamics. Initially recall that the surface gravity (Bardeen et al., 1973) in spherically symmetric solutions of general relativity is (Kothawala et al., 2007)

$$\kappa = \frac{(e^\nu)'|_{r_+}}{2} \quad (\text{F.1.37})$$

where the prime means derivation with respect to the radial coordinate and from Eqs. (F.1.9) and (F.1.10) the above equation can be cast as

$$\kappa = \frac{1}{2r_+} \left[ 1 + 2Q \frac{\partial A_0}{\partial r_+} - 2 \frac{\partial \mathcal{F}}{\partial r_+} \right]. \quad (\text{F.1.38})$$

From Eqs. (F.1.10) and (F.1.34), one can see in the general case that

$$\delta M = A_0 \delta Q + \frac{\kappa}{8\pi} \delta A, \quad (\text{F.1.39})$$

where Eq. (F.1.38) was used. Nevertheless, this is nothing but the generalized first law of black hole thermodynamics for nonlinear electrodynamics (Rasheed, 1997). Since  $M$  as given in Eq. (F.1.36) was derived from Eqs. (F.1.10) and (F.1.34), it is assured its variation satisfies Eq. (F.1.39). Hence, it is the generalization under the physical approach of the parametrization done by Smarr (1973a,b) of the classical Christodoulou-Ruffini black hole mass formula in the context of nonlinear electrodynamics. Besides, Eq. (F.1.36) can be written in the suggestive way as

$$M = QA_0(r_+) + \frac{A}{8\pi r_+} \left[ 1 - 2 \frac{\mathcal{F}(r_+)}{r_+} \right]. \quad (\text{F.1.40})$$

From Eq. (F.1.38), we see that in general the term in the square brackets of the above equation does not coincide with  $2\kappa r_+$ . This could be easily seen in the scope of perturbative theories generically described by Eq. (F.1.14) analyzed by us previously. Nevertheless, for the case of the Maxwell Lagrangian, the term inside the square brackets of Eq. (F.1.40) is  $2\kappa r_+$ . It implies that the generalized Christodoulou-Ruffini black hole mass formula does not keep the same classical (Maxwell Electromagnetism) functional form in nonlinear

electrodynamics.

### **F.1.8. Discussion**

When the first law of thermodynamics of black holes is applied for infinitesimal reversible transformations, one is led naturally after integration to the total electromagnetic energy of a given black hole solution to general relativity in the weak field case, as shown by Eqs. (F.1.29) and (F.1.30). As we showed in this work, this is nothing but a general result coming from reversible transformations, as given by Eq. (F.1.36).

In nonlinear theories, it is known that the propagation of disturbances is steered by the so-called effective geometries (Novello et al., 2000a,a,b). Since this effective geometry is a need just for the propagation of photons, it does not play any role in the description given in this work, once we were just interested in massive and charged particles, the only ones that could canalize the process of energy extraction of a black hole.

As we showed in perturbative nonlinear theories of electromagnetism, a generalization of the Christodoulou-Ruffini black hole mass decomposition formula can always be obtained [see Eqs. (F.1.25), (F.1.27) and (F.1.28)]. For the case where the perturbative nonlinear coupling constant is positive, i.e.,  $\mu > 0$ , the extractable energy is smaller than its Maxwellian counterpart. It means that the extractable electromagnetic energy is always smaller than the half of the total energy. The positiveness of  $\mu$  is compatible with usual media results when this interpretation is given to nonlinear Lagrangians. Hence, we expect this to be exact the case in the Astrophysical scenario, as corroborated by the Euler-Heisenberg and the standard Born-Infeld Lagrangians. This above mentioned energy decrease could be interpreted as related to the self-interaction energy of the field, an unavoidable quantity of energy that must be stored into the system and could not be extracted. It can be visualized as the intrinsic energy stored in usual media when electromagnetic fields are present.

Weak field nonlinear theories of electromagnetism lead to the constancy of the outer horizon ( $2M_{irr}$ , exactly the horizon in the Schwarzschild theory) when reversible transformations are taken into account. For irreversible transformations, it always increases. Due to the generality of the Lagrangian given by Eq. (F.1.14), this suggests it should always be the case for any range of the electric field in any nonlinear theory. This is exactly the case, as we showed, since it is the only way to lead to the equation coming from the law of energy conservation for reversible transformations [the equality in Eq. (F.1.13)]. As a by-product, it allowed us to write down the total mass and the extractable energy (upper limit) of any nonlinear spherically symmetric black hole in terms of its charge, black hole area and the scale parameter coming from the electrodynamic theory under interest. When ir-

reversible transformations are present, for each transformation,  $\delta r_+ > 0$  iff  $(1 - 8\pi T^0_0|_{r_+} r_+^2) > 0$ , as it can be seen by Eq. (F.1.6). From the same equation, it can be checked this is always valid when there exists an outer horizon. Hence, for any  $L(F)$ , the area of the outer horizon never decreases for irreversible processes. We also showed that the generalized Christodoulou-Ruffini black hole mass decomposition formula must be valid in the general case concerning infinitesimal transformations (i.e., those transformations where the black hole area also changes). In general such a mass is not functionally the same as the one obtained in the scope of the Maxwell Lagrangian. Finally, with this generalized Christodoulou-Ruffini black hole mass formula, one can notice that the known first law of black hole mechanics (Rasheed, 1997) is just its direct consequence.



# Bibliography

«On the critical mass: the case of white dwarfs».

In H. Gursky, R. Ruffini, & L. Stella (ed.), *Exploring the universe: a Festschrift in honor of Riccardo Giacconi "Dedicated to Riccardo Giacconi for his sixty-fifth birthday, on the occasion of his being awarded a "Laurea Honoris Causa" in physics at the University of Rome "La Sapienza". Rome, Italy, October 1997* Singapore: World Scientific, 2000, xii, 383 p., *Advanced series in astrophysics and cosmology*, v.13. Edited by H. Gursky, R. Ruffini, and L. Stella. ISBN 9810244231 (2000).

AKSENOV, A.G., RUFFINI, R. AND VERESHCHAGIN, G.V.

«Thermalization of Nonequilibrium Electron-Positron-Photon Plasmas».  
*Physical Review Letters*, **99(12)**, pp. 125003–+ (2007).

ALCOCK, C., FARHI, E. AND OLINTO, A.

«Strange stars».  
*Astrophysical Journal*, **310**, pp. 261–272 (1986).

ALFORD, M., RAJAGOPAL, K., REDDY, S. AND WILCZEK, F.

«Minimal color-flavor-locked-nuclear interface».  
*Physical Review D*, **64(7)**, pp. 074017–+ (2001).

ALLEN, M.P. AND HORVATH, J.E.

«Influence of an Internal Magnetar on Supernova Remnant Expansion».  
*Astrophysical Journal*, **616**, pp. 346–356 (2004).

ALPAR, M.A.

«On Young Neutron Stars as Propellers and Accretors with Conventional Magnetic Fields».  
*Astrophysical Journal*, **554**, pp. 1245–1254 (2001).

ALTAMIRANO, D., WATTS, A., LINARES, M., MARKWARDT, C.B., STROHMAYER, T. AND PATRUNO, A.

«Type I X-ray bursts and burst oscillations in the accreting millisecond X-ray pulsar IGR J17511-3057».  
*Monthly Notices of the Royal Astronomical Society*, **409**, pp. 1136–1145 (2010).

ALTHAUS, L.G., CÓRSICO, A.H., ISERN, J. AND GARCÍA-BERRO, E.

«Evolutionary and pulsational properties of white dwarf stars».  
*Astronomy & Astrophysics Review*, **18**, pp. 471–566 (2010a).

- ALTHAUS, L.G., GARCÍA-BERRO, E., ISERN, J. AND CÓRSICO, A.H.  
«Mass-radius relations for massive white dwarf stars».  
*Astronomy & Astrophysics*, **441**, pp. 689–694 (2005).
- ALTHAUS, L.G., GARCÍA-BERRO, E., ISERN, J., CÓRSICO, A.H. AND ROHRMANN, R.D.  
«The age and colors of massive white dwarf stars».  
*Astronomy & Astrophysics*, **465**, pp. 249–255 (2007).
- ALTHAUS, L.G., GARCÍA-BERRO, E., RENEDO, I., ISERN, J., CÓRSICO, A.H. AND ROHRMANN, R.D.  
«Evolution of White Dwarf Stars with High-metallicity Progenitors: The Role of  $^{22}\text{Ne}$  Diffusion».  
*Astrophysical Journal*, **719**, pp. 612–621 (2010b).
- ANAND, S.P.S.  
«On Chandrasekhar’s Limiting Mass for Rotating White Dwarf Stars».  
*Proceedings of the National Academy of Science*, **54**, pp. 23–26 (1965).
- ANGEL, J.R.P., BORRA, E.F. AND LANDSTREET, J.D.  
«The magnetic fields of white dwarfs».  
*Astrophysical Journal Supplement Series*, **45**, pp. 457–474 (1981).
- ANTONIADIS, J., FREIRE, P.C.C., WEX, N., TAURIS, T.M., LYNCH, R.S., VAN KERKWIJK, M.H., KRAMER, M., BASSA, C., DHILLON, V.S., DRIEBE, T. ET AL.  
*Science*, **340**, p. 6131 (2013a).
- ANTONIADIS, J., FREIRE, P.C.C., WEX, N., TAURIS, T.M., LYNCH, R.S., VAN KERKWIJK, M.H., KRAMER, M., BASSA, C., DHILLON, V.S., DRIEBE, T. ET AL.  
«A Massive Pulsar in a Compact Relativistic Binary».  
*Science*, **340**, p. 448 (2013b).
- ANTONIADIS, J., VAN KERKWIJK, M.H., KOESTER, D., FREIRE, P.C.C., WEX, N., TAURIS, T.M., KRAMER, M. AND BASSA, C.G.  
«The relativistic pulsar-white dwarf binary PSR J1738+0333 - I. Mass determination and evolutionary history».  
*Monthly Notices of the Royal Astronomical Society*, **423**, pp. 3316–3327 (2012).
- ARMITAGE, P.J. AND CLARKE, C.J.  
«Magnetic braking of T Tauri stars».  
*Monthly Notices of the Royal Astronomical Society*, **280**, pp. 458–468 (1996).
- ARUTYUNYAN, G.G., SEDRAKYAN, D.M. AND CHUBARYAN, É.V.  
«Rotating white dwarfs in the general relativity theory».  
*Astrophysics*, **7**, pp. 274–280 (1971).

- AUDI, G., WAPSTRA, A.H. AND THIBAUT, C.  
«The Ame2003 atomic mass evaluation (II). Tables, graphs and references».  
*Nuclear Physics A*, **729**, pp. 337–676 (2003a).
- AUDI, G., WAPSTRA, A.H. AND THIBAUT, C.  
«The Ame2003 atomic mass evaluation (II). Tables, graphs and references».  
*Nuclear Physics A*, **729**, pp. 337–676 (2003b).
- AVANCINI, S.S., MENEZES, D.P., ALLOY, M.D., MARINELLI, J.R., MORAES, M.M.W. AND PROVIDÊNCIA, C.  
«Warm and cold pasta phase in relativistic mean field theory».  
*Physical Review C*, **78(1)**, 015802 (2008).
- BAKALA, P., URBANEC, M., ŠRÁMKOVÁ, E., STUHLÍK, Z. AND TÖRÖK, G.  
«On magnetic-field-induced corrections to the orbital and epicyclic frequencies: paper II. Slowly rotating magnetized neutron stars».  
*Classical and Quantum Gravity*, **29(6)**, p. 065012 (2012).
- BAKALA, P., ŠRÁMKOVÁ, E., STUHLÍK, Z. AND TÖRÖK, G.  
«On magnetic-field-induced non-geodesic corrections to relativistic orbital and epicyclic frequencies».  
*Classical and Quantum Gravity*, **27(4)**, p. 045001 (2010).
- BARDEEN, J.M., CARTER, B. AND HAWKING, S.W.  
«The four laws of black hole mechanics».  
*Communications in Mathematical Physics*, **31**, pp. 161–170 (1973).
- BARSTOW, M.A., JORDAN, S., O'DONOGHUE, D., BURLEIGH, M.R., NAPIWOTZKI, R. AND HARROP-ALLIN, M.K.  
«RE J0317-853: the hottest known highly magnetic DA white dwarf».  
*Monthly Notices of the Royal Astronomical Society*, **277**, pp. 971–985 (1995).
- BAYM, G., BETHE, H.A. AND PETHICK, C.J.  
«Neutron star matter».  
*Nuclear Physics A*, **175**, pp. 225–271 (1971a).
- BAYM, G., PETHICK, C. AND SUTHERLAND, P.  
«The Ground State of Matter at High Densities: Equation of State and Stellar Models».  
*Astrophysical Journal*, **170**, pp. 299–+ (1971b).
- BAYM, G. AND PINES, D.  
«Neutron starquakes and pulsar speedup.»  
*Annals of Physics*, **66**, pp. 816–835 (1971).
- BELL, S.J. AND HEWISH, A.

- «Angular Size and Flux Density of the Small Source in the Crab Nebula at 81.5 Mc/s».  
*Nature*, **213**, pp. 1214–1216 (1967).
- BELVEDERE, R., BOSHKAYEV, K., RUEDA, J.A. AND RUFFINI, R.  
«Uniformly rotating neutron stars in the global and local charge neutrality cases».  
*Nuclear Physics A (in press)*; *arXiv:1307.2836* (2013).
- BELVEDERE, R., PUGLIESE, D., RUEDA, J.A., RUFFINI, R. AND XUE, S.S.  
«Neutron star equilibrium configurations within a fully relativistic theory with strong, weak, electromagnetic, and gravitational interactions».  
*Nuclear Physics A*, **883**, pp. 1–24 (2012).
- BENDER, M., HEENEN, P.H. AND REINHARD, P.G.  
«Self-consistent mean-field models for nuclear structure».  
*Reviews of Modern Physics*, **75**, pp. 121–180 (2003).
- BENHAR, O., FERRARI, V., GUALTIERI, L. AND MARASSI, S.  
«Perturbative approach to the structure of rapidly rotating neutron stars».  
*Physical Review D*, **72(4)**, pp. 044028–+ (2005a).
- BENHAR, O., FERRARI, V., GUALTIERI, L. AND MARASSI, S.  
«Perturbative approach to the structure of rapidly rotating neutron stars».  
*Physical Review D*, **72(4)**, pp. 044028–+ (2005b).
- BERNARDINI, F., ISRAEL, G.L., DALL’OSSO, S., STELLA, L., REA, N., ZANE, S., TUROLLO, R., PERNA, R., FALANGA, M., CAMPANA, S. ET AL.  
«From outburst to quiescence: the decay of the transient AXP XTE J1810-197».  
*Astronomy & Astrophysics*, **498**, pp. 195–207 (2009).
- BERNARDINI, M.G., BIANCO, C.L., CAITO, L., DAINOTTI, M.G., GUIDA, R. AND RUFFINI, R.  
«Grb980425 and the puzzling urca1 emission».  
In R.T. Jantzen, H. Kleinert and R. Ruffini (eds.), *The Eleventh Marcel Grossmann Meeting* (Singapore: World Scientific, 2008).
- BERNARDINI, M.G., BIANCO, C.L., CHARDONNET, P., FRASCHETTI, F., RUFFINI, R. AND XUE, S.S.  
«A new astrophysical “triptych”: Grb030329/sn2003dh/urca-2».  
In E. Fenimore and M. Galassi (eds.), *Gamma-Ray Bursts: 30 Years of Discovery*, volume 727 of *American Institute of Physics Conference Series*, pp. 312–315 (2004).
- BERNARDINI, M.G., BIANCO, C.L., CHARDONNET, P., FRASCHETTI, F., RUFFINI, R. AND XUE, S.S.

- «Theoretical interpretation of the luminosity and spectral properties of grb 031203».  
*ApJ*, **634**, pp. L29–L32 (2005a).
- BERNARDINI, M.G., BIANCO, C.L., RUFFINI, R., XUE, S.S., CHARDONNET, P. AND FRASCHETTI, F.  
«General features of grb 030329 in the embh model».  
In M. Novello, S. Perez Bergliaffa and R. Ruffini (eds.), *The Tenth Marcel Grossmann Meeting. On recent developments in theoretical and experimental general relativity, gravitation and relativistic field theories*, p. 2459 (Singapore: World Scientific, 2005b).
- BERTI, E. AND STERGIIOULAS, N.  
«Approximate matching of analytic and numerical solutions for rapidly rotating neutron stars».  
*Monthly Notices of the Royal Astronomical Society*, **350**, pp. 1416–1430 (2004).
- BERTI, E., WHITE, F., MANIOPOULOU, A. AND BRUNI, M.  
«Rotating neutron stars: an invariant comparison of approximate and numerical space-time models».  
*Monthly Notices of the Royal Astronomical Society*, **358**, pp. 923–938 (2005).
- BERTONE, G. AND RUFFINI, R.  
«Equilibrium configurations of relativistic white dwarfs».  
*Nuovo Cimento B Serie*, **115**, pp. 935–+ (2000).
- BETHE, H.A.  
*Energy production in stars. Nobel lecture.* (1968).
- BHATTACHARYYA, S., STROHMAYER, T.E., MILLER, M.C. AND MARKWARDT, C.B.  
«Constraints on Neutron Star Parameters from Burst Oscillation Light Curves of the Accreting Millisecond Pulsar XTE J1814-338».  
*Astrophysical Journal*, **619**, pp. 483–491 (2005).
- BILDSTEN, L. AND HALL, D.M.  
«Gravitational Settling of  $^{22}\text{Ne}$  in Liquid White Dwarf Interiors».  
*Astrophysical Journal*, **549**, pp. L219–L223 (2001).
- BINI, D., BOSHKAYEV, K., RUFFINI, R. AND SIUTSOU, I.  
«Equatorial circular geodesics in the Hartle-Thorne spacetime».  
*Il Nuovo Cimento C*, **36**, p. 31 (2013).
- BINI, D. AND DAMOUR, T.  
«Analytical determination of the two-body gravitational interaction potential at the fourth post-Newtonian approximation».  
*Physical Review D*, **87(12)**, 121501 (2013).

- BLASCHKE, D., KLAHN, T. AND VOSKRESENSKY, D.  
«Diquark condensates and compact star cooling».  
*ApJ*, **533**, p. 406412 (2000).
- BLASCHKE, D., VOSKRESENSKY, D. AND GRIGORIAN, H.  
«Cooling of Neutron Stars with Color Superconducting Quark Cores».  
*Nuclear Physics A*, **774**, pp. 815–818 (2006).  
ISSN 03759474.
- BOCCALETTI, D. AND RUFFINI, R.  
*Fermi and Astrophysics* (World Scientific, Singapore, 2010).
- BOGUTA, J.  
«Remarks on the beta stability in neutron stars».  
*Physics Letters B*, **106**, pp. 255–258 (1981).
- BOGUTA, J.  
«Chiral nuclear interactions».  
*Nuclear Physics A*, **501**, pp. 637–652 (1989).
- BOGUTA, J. AND BODMER, A.R.  
«Relativistic calculation of nuclear matter and the nuclear surface».  
*Nuclear Physics A*, **292**, pp. 413–428 (1977).
- BOGUTA, J. AND MOSZKOWSKI, S.A.  
«Nonlinear mean field theory for nuclear matter and surface properties».  
*Nuclear Physics A*, **403**, pp. 445–468 (1983).
- BOGUTA, J. AND RAFELSKI, J.  
«Thomas Fermi model of finite nuclei».  
*Physics Letters B*, **71**, pp. 22–26 (1977).
- BOGUTA, J. AND STOCKER, H.  
«Systematics of nuclear matter properties in a non-linear relativistic field theory».  
*Physics Letters B*, **120**, pp. 289–293 (1983).
- BOHR, N. AND WHEELER, J.A.  
«The Mechanism of Nuclear Fission».  
*Physical Review*, **56**, pp. 426–450 (1939).
- BORKOWSKI, J., GOTZ, D., MEREGHETTI, S., MOWLAVI, N., SHAW, S. AND  
TURLER, M.  
«Giant flare from Sgr 1806-20 detected by INTEGRAL.»  
*GRB Coordinates Network*, **2920**, pp. 1–+ (2004).

- BORN, M. AND INFELD, L.  
«Foundations of the New Field Theory».  
*Royal Society of London Proceedings Series A*, **144**, pp. 425–451 (1934).
- BOSHKAYEV, K., IZZO, L., RUEDA, J.A. AND RUFFINI, R.  
«SGR 0418+5729, Swift J1822.3-1606, and 1E 2259+586 as massive fast rotating highly magnetized white dwarfs».  
*Astronomy & Astrophysics accepted; arXiv:1305.5048* (2013a).
- BOSHKAYEV, K., QUEVEDO, H. AND RUFFINI, R.  
«Gravitational field of compact objects in general relativity».  
*Physical Review D*, **86(6)**, 064043 (2012a).
- BOSHKAYEV, K., ROTONDO, M. AND RUFFINI, R.  
«On Magnetic Fields in Rotating Nuclear Matter Cores of Stellar Dimensions».  
*International Journal of Modern Physics Conference Series*, **12**, pp. 58–67 (2012b).
- BOSHKAYEV, K., RUEDA, J.A., RUFFINI, R. AND SIUTSOU, I.  
«On General Relativistic Uniformly Rotating White Dwarfs».  
*Astrophysical Journal*, **762**, 117 (2013b).
- BOWERS, R.L., CAMPBELL, J.A. AND ZIMMERMAN, R.L.  
«Relativistic Baryon Effective Masses and Thresholds for Strongly Interacting Superdense Matter».  
*Physical Review D*, **8**, pp. 1077–1087 (1973a).
- BOWERS, R.L., CAMPBELL, J.A. AND ZIMMERMAN, R.L.  
«Relativistic Many-Body Theory for Strongly Interacting Matter».  
*Physical Review D*, **7**, pp. 2278–2288 (1973b).
- BRACK, M., GUET, C. AND HASTRONOMY & ASTROPHYSICSKANSSON, H.B.  
«Selfconsistent semiclassical description of average nuclear properties-a link between microscopic and macroscopic models».  
*Physics Reports*, **123**, pp. 275–364 (1985).
- BRETÓN, N.  
«Geodesic structure of the Born-Infeld black hole».  
*Classical and Quantum Gravity*, **19**, pp. 601–612 (2002).
- BRETÓN, N.  
«Smarr’s formula for black holes with non-linear electrodynamics».  
*General Relativity and Gravitation*, **37**, pp. 643–650 (2005).

- BRETÓN, N. AND GARCIA-SALCEDO, R.  
«Nonlinear Electrodynamics and black holes».  
*ArXiv High Energy Physics - Theory e-prints* (2007).
- BRETÓN, N., MANKO, V.S. AND AGUILAR SÁNCHEZ, J.  
«On the equilibrium of charged masses in general relativity: II. The stationary electrovacuum case».  
*Classical and Quantum Gravity*, **16**, pp. 3725–3734 (1999).
- BÜRVENICH, T.J., MISHUSTIN, I.N. AND GREINER, W.  
«Nuclei embedded in an electron gas».  
*Physical Review C*, **76(3)**, pp. 034310–+ (2007).
- CAMERON, A.G.W.  
«Pycnonuclear Reactions and Nova Explosions.»  
*Astrophysical Journal*, **130**, p. 916 (1959).
- CAMERON, A.G.W.  
«Neutron Stars».  
*Annual Review of Astronomy and Astrophysics*, **8**, pp. 179–+ (1970).
- CANNIZZO, J.K., LEE, H.M. AND GOODMAN, J.  
«The disk accretion of a tidally disrupted star onto a massive black hole».  
*Astrophysical Journal*, **351**, pp. 38–46 (1990).
- CANUTO, V.  
«Neutron stars».  
In R. Giacconi and R. Ruffini (eds.), *Physics and Astrophysics of Neutron Stars and Black Holes*, pp. 448–527 (1978).
- CARDELLI, J.A., CLAYTON, G.C. AND MATHIS, J.S.  
«The relationship between infrared, optical, and ultraviolet extinction».  
*Astrophysical Journal*, **345**, pp. 245–256 (1989).
- CARTER, B.  
«Global structure of the kerr family of gravitational fields».  
*Physical Review*, **174**, pp. 1559–1571 (1968).
- CASTRO-TIRADO, A.J., DE UGARTE POSTIGO, A., GOROSABEL, J., JELÍNEK, M., FATKHULLIN, T.A., SOKOLOV, V.V., FERRERO, P., KANN, D.A., KLOSE, S., SLUSE, D. ET AL.  
«Flares from a candidate Galactic magnetar suggest a missing link to dim isolated neutron stars».  
*Nature*, **455**, pp. 506–509 (2008).
- CENTELLES, M., DEL ESTAL, M. AND VIÑAS, X.

- «Semiclassical treatment of asymmetric semi-infinite nuclear matter: surface and curvature properties in relativistic and non-relativistic models». *Nuclear Physics A*, **635**, pp. 193–230 (1998).
- CHABRIER, G. AND POTEKHIN, A.Y.  
«Equation of state of fully ionized electron-ion plasmas». *Physical Review E*, **58**, pp. 4941–4949 (1998a).
- CHABRIER, G. AND POTEKHIN, A.Y.  
«Equation of state of fully ionized electron-ion plasmas». *Physical Review E*, **58**, pp. 4941–4949 (1998b).
- CHAMEL, N., FANTINA, A.F. AND DAVIS, P.J.  
«Stability of super-Chandrasekhar magnetic white dwarfs». *ArXiv e-prints* (2013).
- CHANDRASEKHAR, S.  
«The highly collapsed configurations of a stellar mass». *Monthly Notices of the Royal Astronomical Society*, **91**, pp. 456–466 (1931a).
- CHANDRASEKHAR, S.  
«The Maximum Mass of Ideal White Dwarfs». *Astrophysical Journal*, **74**, pp. 81–+ (1931b).
- CHANDRASEKHAR, S.  
«The highly collapsed configurations of a stellar mass (Second paper)». *Monthly Notices of the Royal Astronomical Society*, **95**, pp. 207–225 (1935).
- CHANDRASEKHAR, S.  
*An introduction to the study of stellar structure* (1939).
- CHANDRASEKHAR, S.  
*Ellipsoidal figures of equilibrium* (1969).
- CHANDRASEKHAR, S.  
«The Effect of Gravitational Radiation on the Secular Stability of the Maclaurin Spheroid». *Astrophysical Journal*, **161**, p. 561 (1970).
- CHANDRASEKHAR, S.  
*The mathematical theory of black holes* (1992).
- CHANDRASEKHAR, S. AND FERMI, E.  
«Problems of Gravitational Stability in the Presence of a Magnetic Field.». *Astrophysical Journal*, **118**, p. 116 (1953).

- CHAPMAN, N.L., MUNDY, L.G., LAI, S.P. AND EVANS, II, N.J.  
«The Mid-Infrared Extinction Law in the Ophiuchus, Perseus, and Serpens Molecular Clouds».  
*Astrophysical Journal*, **690**, 496 (2009).
- CHATTERJEE, P., HERNQUIST, L. AND NARAYAN, R.  
«An Accretion Model for Anomalous X-Ray Pulsars».  
*Astrophysical Journal*, **534**, pp. 373–379 (2000).
- CHERUBINI, C., GERALICO, A., J. A. RUEDA, H. AND RUFFINI, R.  
« $e^- - e^+$  pair creation by vacuum polarization around electromagnetic black holes».  
*Physical Review D*, **79(12)**, pp. 124002–+ (2009).
- CHEVALIER, R.A.  
«Neutron star accretion in a supernova».  
*ApJ*, **346**, p. 847 (1989).  
ISSN 0004-637X.
- CHIANG, E.I. AND GOLDREICH, P.  
«Spectral Energy Distributions of T Tauri Stars with Passive Circumstellar Disks».  
*Astrophysical Journal*, **490**, p. 368 (1997).
- CHOI, C.S. AND DOTANI, T.  
«A Flare of AE Aquarii Observed with XMM-Newton».  
*Astrophysical Journal*, **646**, pp. 1149–1159 (2006).
- CHRISTIANSEN, M.B. AND GLENDENNING, N.K.  
«Finite size effects and the mixed quark-hadron phase in neutron stars».  
*Physical Review C*, **56**, pp. 2858–2864 (1997).
- CHRISTIANSEN, M.B., GLENDENNING, N.K. AND SCHAFFNER-BIELICH, J.  
«Surface tension between a kaon condensate and the normal nuclear matter phase».  
*Physical Review C*, **62(2)**, pp. 025804–+ (2000).
- CHRISTODOULOU, D.  
«Reversible and Irreversible Transformations in Black-Hole Physics».  
*Phys. Rev. Lett.*, **25**, pp. 1596–1597 (1970).
- CHRISTODOULOU, D. AND RUFFINI, R.  
«Reversible transformations of a charged black hole.»  
*Phys. Rev. D*, **4**, pp. 3552–3555 (1971).
- CIUFOLINI, I. AND RUFFINI, R.

- «Equilibrium configurations of neutron stars and the parametrized post-Newtonian metric theories of gravitation».  
*Astrophysical Journal*, **275**, pp. 867–877 (1983).
- COHEN, R.H., COPPI, B. AND TREVES, A.  
«Magnetic Configuration in the Neighborhood of a Collapsed Star».  
*Astrophysical Journal*, **179**, pp. 269–276 (1973).
- COOK, G.B., SHAPIRO, S.L. AND TEUKOLSKY, S.A.  
«Rapidly rotating neutron stars in general relativity: Realistic equations of state».  
*Astrophysical Journal*, **424**, pp. 823–845 (1994).
- COPPI, B., PELLAT, R., ROSENBLUTH, M., RUTHERFORD, P. AND GALVAO, R.  
«Resistive internal kink modes».  
*Soviet Journal of Plasma Physics*, **2**, pp. 961–966 (1976).
- DAINOTTI, M.G., BERNARDINI, M.G., BIANCO, C.L., CAITO, L., GUIDA, R. AND RUFFINI, R.  
«Grb 060218 and grbs associated with supernovae ib/c».  
*A&A*, **471**, pp. L29–L32 (2007).
- DAINOTTI, M., BERNARDINI, M.G., BIANCO, C.L., CAITO, L., GUIDA, R. AND RUFFINI, R.  
«The astrophysical tryptic: Grb, sn and urca can be extended to grb060218?»  
*J. Kor. Phys. Soc.*, **56**, p. 1588 (2010).
- DAMOUR, T. AND NAGAR, A.  
«Improved analytical description of inspiralling and coalescing black-hole binaries».  
*Physical Review D*, **79(8)**, 081503 (2009).
- DAMOUR, T. AND NAGAR, A.  
«Effective one body description of tidal effects in inspiralling compact binaries».  
*Physical Review D*, **81(8)**, 084016 (2010).
- DANIELEWICZ, P. AND LEE, J.  
«Symmetry energy I: Semi-infinite matter».  
*Nuclear Physics A*, **818**, pp. 36–96 (2009).
- DAS, U. AND MUKHOPADHYAY, B.  
«New Mass Limit for White Dwarfs: Super-Chandrasekhar Type Ia Supernova as a New Standard Candle».  
*Physical Review Letters*, **110(7)**, 071102 (2013).

- DAVIES, S.R., COE, M.J. AND WOOD, K.S.  
«HEAO-1 observations of the X-ray pulsar 1E2259 + 586».  
*Monthly Notices of the Royal Astronomical Society*, **245**, pp. 268–274 (1990).
- DE JAGER, O.C., MEINTJES, P.J., O'DONOGHUE, D. AND ROBINSON, E.L.  
«The Discovery of a Brake on the White Dwarf in Ae-Aquarii».  
*Monthly Notices of the Royal Astronomical Society*, **267**, pp. 577–+ (1994).
- DE LORENCI, V.A., FIGUEIREDO, N., FLICHE, H.H. AND NOVELLO, M.  
«Dyadosphere bending of light».  
*Astronomy & Astrophysics*, **369**, pp. 690–693 (2001).
- DE LORENCI, V.A., KLIPPERT, R., NOVELLO, M. AND SALIM, J.M.  
«Light propagation in non-linear electrodynamics».  
*Physics Letters B*, **482**, pp. 134–140 (2000).
- DEBYE, P. AND HUECKERL, E.  
*Phys. Zeitschr.*, **24**, p. 185 (1923).
- DEL ESTAL, M., CENTELLES, M. AND VIÑAS, X.  
«Nuclear surface properties in relativistic effective field theory».  
*Nuclear Physics A*, **650**, pp. 443–468 (1999).
- DEMIANSKI, M.  
«Static electromagnetic geon».  
*Foundations of Physics*, **16**, pp. 187–190 (1986).
- DEMOREST, P.B., PENNUCCI, T., RANSOM, S.M., ROBERTS, M.S.E. AND HESSELS, J.W.T.  
«A two-solar-mass neutron star measured using Shapiro delay».  
*Nature*, **467**, pp. 1081–1083 (2010a).
- DEMOREST, P.B., PENNUCCI, T., RANSOM, S.M., ROBERTS, M.S.E. AND HESSELS, J.W.T.  
«A two-solar-mass neutron star measured using Shapiro delay».  
*Nature*, **467**, pp. 1081–1083 (2010b).
- DERUELLE, N. AND RUFFINI, R.  
«Quantum and classical relativistic energy states in stationary geometries».  
*Physics Letters B*, **52**, pp. 437–441 (1974).
- DHILLON, V.S., MARSH, T.R., HULLEMAN, F., VAN KERKWIJK, M.H., SHEARER, A., LITTLEFAIR, S.P., GAVRIIL, F.P. AND KASPI, V.M.  
«High-speed, multicolour optical photometry of the anomalous X-ray pulsar 4U 0142+61 with ULTRACAM».  
*Monthly Notices of the Royal Astronomical Society*, **363**, pp. 609–614 (2005).

- DIAZ-ALONSO, J. AND RUBIERA-GARCIA, D.  
«Thermodynamic analysis of black hole solutions in gravitating nonlinear electrodynamics».  
*ArXiv e-prints* (2012).
- DIB, R., KASPI, V.M. AND GAVRIIL, F.P.  
«Rossi X-Ray Timing Explorer Monitoring of the Anomalous X-ray Pulsar 1E 1048.1 - 5937: Long-term Variability and the 2007 March Event».  
*Astrophysical Journal*, **702**, pp. 614–630 (2009).
- DIRAC, P.A.M.  
*Proc. Cambridge Phil. Soc.*, **26**, pp. 376–+ (1930).
- DITTRICH, W. AND GIES, H.  
«Light propagation in nontrivial QED vacua».  
*Physical Review D*, **58(2)**, 025004 (1998).
- DONATI, J.F., HOWARTH, I.D., JARDINE, M.M., PETIT, P., CATALA, C., LANDSTREET, J.D., BOURET, J.C., ALECIAN, E., BARNES, J.R., FORVEILLE, T. ET AL.  
«The surprising magnetic topology of  $\tau$  Sco: fossil remnant or dynamo output?»  
*Monthly Notices of the Royal Astronomical Society*, **370**, pp. 629–644 (2006).
- DOUCHIN, F. AND HAENSEL, P.  
«A unified equation of state of dense matter and neutron star structure».  
*Astronomy & Astrophysics*, **380**, pp. 151–167 (2001).
- DUBEIBE, F.L., PACHÓN, L.A. AND SANABRIA-GÓMEZ, J.D.  
«Chaotic dynamics around astrophysical objects with nonisotropic stresses».  
*Physical Review D*, **75(2)**, pp. 023008–+ (2007).
- DUERR, H.  
«Relativistic Effects in Nuclear Forces».  
*Physical Review*, **103**, pp. 469–480 (1956).
- DUNCAN, R.C. AND THOMPSON, C.  
«Formation of very strongly magnetized neutron stars - Implications for gamma-ray bursts».  
*Astrophysical Journal*, **392**, pp. L9–L13 (1992).
- DUNCAN, R.C., SHAPIRO, S.L. AND WASSERMAN, I.  
«Neutrino-driven winds from young, hot neutron stars».  
*ApJ*, **309**, p. 141 (1986).  
ISSN 0004-637X.

- DUPAYS, A., RIZZO, C., BAKALOV, D. AND BIGNAMI, G.F.  
«Quantum Vacuum Friction in highly magnetized neutron stars».  
*EPL (Europhysics Letters)*, **82**, p. 69002 (2008).
- DURANT, M., KARGALTSEV, O. AND PAVLOV, G.G.  
*Astrophysical Journal*, in press; *arXiv:1108.3340* (2011).
- DURANT, M. AND VAN KERKWIJK, M.H.  
«Distances to Anomalous X-Ray Pulsars Using Red Clump Stars».  
*Astrophysical Journal*, **650**, pp. 1070–1081 (2006a).
- DURANT, M. AND VAN KERKWIJK, M.H.  
«Extinction Columns and Intrinsic X-Ray Spectra of the Anomalous X-Ray Pulsars».  
*Astrophysical Journal*, **650**, pp. 1082–1090 (2006b).
- DURANT, M. AND VAN KERKWIJK, M.H.  
«Multiwavelength Variability of the Magnetar 4U 0142+61».  
*Astrophysical Journal*, **652**, pp. 576–583 (2006c).
- DURISEN, R.H.  
«Viscous Effects in Rapidly Rotating Stars with Application to White-Dwarf Models. Theory and Techniques».  
*Astrophysical Journal*, **183**, pp. 205–214 (1973).
- DURISEN, R.H.  
«Upper mass limits for stable rotating white dwarfs».  
*Astrophysical Journal*, **199**, pp. 179–183 (1975).
- EDDINGTON, SIR, A.S.  
«On "relativistic degeneracy,"».  
*Monthly Notices of the Royal Astronomical Society*, **95**, pp. 194–206 (1935).
- EMDEN, R.  
*Gaskugeln Anwendungen der Mechanischen Wärmetheorie auf Kosmologische und Meteorologische Probleme* (Leipzig, Teubner, Berlin, 1907).
- ERACLEOUS, M., PATTERSON, J. AND HALPERN, J.  
«A search for periodicities in the X-ray emission from cataclysmic variables».  
*Astrophysical Journal*, **370**, pp. 330–340 (1991).
- ERNST, F.J.  
«New Formulation of the Axially Symmetric Gravitational Field Problem».  
*Physical Review*, **167**, pp. 1175–1177 (1968a).

- ERNST, F.J.  
«New Formulation of the Axially Symmetric Gravitational Field Problem. II».  
*Physical Review*, **172**, pp. 1850–1850 (1968b).
- ERTAN, Ü., EKŞİ, K.Y., ERKUT, M.H. AND ALPAR, M.A.  
«On the Evolution of Anomalous X-ray Pulsars and Soft Gamma-ray Repeaters with Fall Back Disks».  
*Astrophysical Journal*, **702**, pp. 1309–1320 (2009).
- ESPOSITO, P., ISRAEL, G.L., TUROLLA, R., TIENGO, A., GÖTZ, D., DE LUCA, A., MIGNANI, R.P., ZANE, S., REA, N., TESTA, V. ET AL.  
«Early X-ray and optical observations of the soft gamma-ray repeater SGR0418+5729».  
*Monthly Notices of the Royal Astronomical Society*, **405**, pp. 1787–1795 (2010).
- EVERITT, C.W.F., DEBRA, D.B., PARKINSON, B.W., TURNEAURE, J.P., CONKLIN, J.W., HEIFETZ, M.I., KEISER, G.M., SILBERGLEIT, A.S., HOLMES, T., KOLODZIEJCZAK, J. ET AL.  
«Gravity Probe B: Final Results of a Space Experiment to Test General Relativity».  
*Physical Review Letters*, **106(22)**, 221101 (2011).
- FAHLMAN, G.G. AND GREGORY, P.C.  
«An X-ray pulsar in SNR G109.1-1.0».  
*Nature*, **293**, pp. 202–204 (1981).
- FERMI, E. (ed.).  
*Nuclear physics* (1950).
- FERMI-LAT COLLABORATION.  
«Gamma-ray flares from the Crab Nebula».  
*arXiv:1011.3855* (2010).
- FERRARI, A. AND RUFFINI, R.  
«Theoretical Implications of the Second Time Derivative of the Period of the Pulsar NP 0532».  
*Astrophysical Journal*, **158**, pp. L71+ (1969).
- FERRARIO, L., VENNES, S., WICKRAMASINGHE, D.T., BAILEY, J.A. AND CHRISTIAN, D.J.  
«EUVE J0317-855 A rapidly rotating, high-field magnetic white dwarf».  
*Monthly Notices of the Royal Astronomical Society*, **292**, pp. 205–+ (1997).
- FERRARIO, L. AND WICKRAMASINGHE, D.  
«Modelling of isolated radio pulsars and magnetars on the fossil field hypothesis».

- Monthly Notices of the Royal Astronomical Society*, **367**, pp. 1323–1328 (2006).
- FERRARIO, L., WICKRAMASINGHE, D., LIEBERT, J. AND WILLIAMS, K.A.  
«The open-cluster initial-final mass relationship and the high-mass tail of the white dwarf distribution».  
*Monthly Notices of the Royal Astronomical Society*, **361**, pp. 1131–1135 (2005).
- FERRARIO, L. AND WICKRAMASINGHE, D.T.  
«Magnetic fields and rotation in white dwarfs and neutron stars».  
*Monthly Notices of the Royal Astronomical Society*, **356**, pp. 615–620 (2005).
- FERREIRINHO, J., RUFFINI, R. AND STELLA, L.  
«On the relativistic Thomas-Fermi model».  
*Physics Letters B*, **91**, pp. 314–316 (1980).
- FEYNMAN, R.P., METROPOLIS, N. AND TELLER, E.  
«Equations of State of Elements Based on the Generalized Fermi-Thomas Theory».  
*Physical Review*, **75**, pp. 1561–1573 (1949).
- FLANAGAN, É.É. AND HUGHES, S.A.  
«Measuring gravitational waves from binary black hole coalescences. I. Signal to noise for inspiral, merger, and ringdown».  
*Physical Review D*, **57**, pp. 4535–4565 (1998).
- FORD, E.C., KAARET, P., CHEN, K., TAVANI, M., BARRET, D., BLOSER, P., GRINDLAY, J., HARMON, B.A., PACIASAS, W.S. AND ZHANG, S.N.  
«Energy Spectra and High-Frequency Oscillations in 4U 0614+091».  
*Astrophysical Journal*, **486**, p. L47 (1997).
- FORD, E.C. AND VAN DER KLIS, M.  
«Strong Correlation between Noise Features at Low Frequency and the Kilohertz Quasi-Periodic Oscillations in the X-Ray Binary 4U 1728-34».  
*Astrophysical Journal*, **506**, pp. L39–L42 (1998).
- FORD, E.C., VAN DER KLIS, M., VAN PARADIJS, J., MÉNDEZ, M., WIJNANDS, R. AND KAARET, P.  
«Discovery of a Second Kilohertz QPO in the X-Ray Binary 4U 1735-44».  
*Astrophysical Journal*, **508**, pp. L155–L158 (1998).
- FOWLER, R.H.  
«On dense matter».  
*Monthly Notices of the Royal Astronomical Society*, **87**, pp. 114–122 (1926).
- FRASCHETTI, F., BERNARDINI, M.G., BIANCO, C.L., RUFFINI, R., XUE, S.S. AND CHARDONNET, P.

- «Inferences on the ism structure around grb 980425 and grb 980425-sn1998bw association in the embh model».  
In M. Novello, S. Perez Bergliaffa and R. Ruffini (eds.), *The Tenth Marcel Grossmann Meeting. On recent developments in theoretical and experimental general relativity, gravitation and relativistic field theories*, p. 2451 (Singapore: World Scientific, 2005).
- FRENKEL, Y.I.  
*Zeit. fur Phys.*, **50**, p. 234 (1928).
- FRIEDMAN, J.L., IPSER, J.R. AND SORKIN, R.D.  
«Turning-point method for axisymmetric stability of rotating relativistic stars».  
*Astrophysical Journal*, **325**, pp. 722–724 (1988).
- FRIEDMAN, J.L., PARKER, L. AND IPSER, J.R.  
«Rapidly rotating neutron star models».  
*Astrophysical Journal*, **304**, pp. 115–139 (1986a).
- FRIEDMAN, J.L., PARKER, L. AND IPSER, J.R.  
«Rapidly rotating neutron star models».  
*Astrophysical Journal*, **304**, pp. 115–139 (1986b).
- FURNSTAHL, R.J., SEROT, B.D. AND HUA-BIN, T.  
«Analysis of chiral mean-field models for nuclei».  
*Nuclear Physics A*, **598**, pp. 539–582 (1996).
- FURNSTAHL, R.J., SEROT, B.D. AND TANG, H.B.  
«A chiral effective lagrangian for nuclei».  
*Nuclear Physics A*, **615**, pp. 441–482 (1997).
- FURNSTAHL, R.J., SEROT, B.D. AND TANG, H.B.  
«Erratum to “A chiral effective lagrangian for nuclei” [Nucl. Phys. A 615 (1997) 441-482]».  
*Nuclear Physics A*, **640**, pp. 505–505 (1998).
- GAENSLER, B.M., SLANE, P.O., GOTTHELF, E.V. AND VASISHT, G.  
«Anomalous X-Ray Pulsars and Soft Gamma-Ray Repeaters in Supernova Remnants».  
*Astrophysical Journal*, **559**, pp. 963–972 (2001).
- GALAMA, T.J., VREESWIJK, P.M., VAN PARADIJS, J., KOUVELIOTOU, C., AUGUSTEIJN, T., BÖHNHARDT, H., BREWER, J.P., DOUBLIER, V., GONZALEZ, J.F., LEIBUNDGUT, B. ET AL.  
«An unusual supernova in the error box of the  $\gamma$ -ray burst of 25 april 1998».  
*Nature*, **395**, pp. 670–672 (1998).

- GALLOWAY, D.K., CHAKRABARTY, D., MUNO, M.P. AND SAVOV, P.  
«Discovery of a 270 Hertz X-Ray Burst Oscillation in the X-Ray Dipper 4U 1916-053».  
*Astrophysical Journal*, **549**, pp. L85–L88 (2001).
- GAMOW, G.  
*My world line: An informal autobiography*. (1970).
- GAMOW, G. AND SCHOENBERG, M.  
«Neutrino Theory of Stellar Collapse».  
*Physical Review*, **59**, pp. 539–547 (1941).
- GARCIA-BERRO, E., HERNANZ, M., ISERN, J. AND MOCHKOVITCH, R.  
«Properties of high-density binary mixtures and the age of the universe from white dwarf stars».  
*Nature*, **333**, pp. 642–644 (1988).
- GARCÍA-BERRO, E., LORÉN-AGUILAR, P., AZNAR-SIGUÁN, G., TORRES, S., CAMACHO, J., ALTHAUS, L.G., CÓRSICO, A.H., KÜLEBI, B. AND ISERN, J.  
«Double Degenerate Mergers as Progenitors of High-field Magnetic White Dwarfs».  
*Astrophysical Journal*, **749**, 25 (2012).
- GARCÍA-BERRO, E., LORÉN-AGUILAR, P., PEDEMONTE, A.G., ISERN, J., BERGERON, P., DUFOUR, P. AND BRASSARD, P.  
«Evidence of a Merger of Binary White Dwarfs: The Case of GD 362».  
*Astrophysical Journal*, **661**, pp. L179–L182 (2007).
- GARCÍA-BERRO, E., TORRES, S., ALTHAUS, L.G., RENEDO, I., LORÉN-AGUILAR, P., CÓRSICO, A.H., ROHRMANN, R.D., SALARIS, M. AND ISERN, J.  
«A white dwarf cooling age of 8Gyr for NGC 6791 from physical separation processes».  
*Nature*, **465**, pp. 194–196 (2010a).
- GARCÍA-BERRO, E., TORRES, S., ALTHAUS, L.G., RENEDO, I., LORÉN-AGUILAR, P., CÓRSICO, A.H., ROHRMANN, R.D., SALARIS, M. AND ISERN, J.  
«A white dwarf cooling age of 8Gyr for NGC 6791 from physical separation processes».  
*Nature*, **465**, pp. 194–196 (2010b).
- GASQUES, L.R., AFANASJEV, A.V., AGUILERA, E.F., BEARD, M., CHAMON, L.C., RING, P., WIESCHER, M. AND YAKOVLEV, D.G.  
«Nuclear fusion in dense matter: Reaction rate and carbon burning».  
*Physical Review C*, **72(2)**, 025806 (2005).

- GELFAND, J.D. AND GAENSLER, B.M.  
«The Compact X-Ray Source 1E 1547.0-5408 and the Radio Shell G327.24-0.13: A New Proposed Association between a Candidate Magnetar and a Candidate Supernova Remnant».  
*Astrophysical Journal*, **667**, pp. 1111–1118 (2007).
- GEROYANNIS, V.S. AND HADJOPOULOS, A.A.  
«Models of white dwarfs under rapid uniform or differential rotation - Numerical results».  
*Astrophysical Journal Supplement Series*, **70**, pp. 661–677 (1989).
- GEROYANNIS, V.S. AND PAPASOTIRIOU, P.J.  
«Spin-up and Spin-down of Rotating Magnetic White Dwarfs: A Straightforward Numerical Approach».  
*Astrophysical Journal*, **534**, pp. 359–366 (2000).
- GIACCONI, R.  
*The dawn of x-ray astronomy. Nobel lecture.* (2002).
- GIACCONI, R. AND RUFFINI, R. (eds.).  
*Physics and astrophysics of neutron stars and black holes* (1978 Reprinted 2010).
- GINZBURG, V.L.  
«The Magnetic Fields of Collapsing Masses and the Nature of Superstars».  
*Soviet Physics Doklady*, **9**, pp. 329–+ (1964).
- GLENDENNING, N.K.  
«First-order phase transitions with more than one conserved charge: Consequences for neutron stars».  
*Physical Review D*, **46**, pp. 1274–1287 (1992).
- GLENDENNING, N.K.  
«Phase transitions and crystalline structures in neutron star cores».  
*Physics Reports*, **342**, pp. 393–447 (2001).
- GLENDENNING, N.K. AND PEI, S.  
«Crystalline structure of the mixed confined-deconfined phase in neutron stars».  
*Physical Review C*, **52**, pp. 2250–2253 (1995).
- GLENDENNING, N.K. AND SCHAFFNER-BIELICH, J.  
«First order kaon condensate».  
*Physical Review C*, **60(2)**, pp. 025803–+ (1999).
- GNEDIN, O.Y., YAKOVLEV, D.G. AND POTEKHIN, A.Y.  
«Thermal relaxation in young neutron stars».  
*MNRAS*, **324**, pp. 725–736 (2001).

- GNEDIN, O.Y., YAKOVLEV, D.G. AND POTEKHIN, A.Y.  
«Thermal relaxation in young neutron stars».  
*MNRAS*, **324**(3), pp. 725–736 (2001).  
ISSN 0035-8711.
- GÖHLER, E., WILMS, J. AND STAUBERT, R.  
«XMM-Newton observation of the anomalous X-ray pulsar 4U 0142+61».  
*Astronomy & Astrophysics*, **433**, pp. 1079–1083 (2005).
- GOLDSTEIN, A., PREECE, R.D., BRIGGS, M.S., VAN DER HORST, A.J.,  
MCBREEN, S., KOUVELIOTOU, C., CONNAUGHTON, V., PACIESAS, W.S.,  
MEEGAN, C.A., BHAT, P.N. ET AL.  
«A New Derivation of GRB Jet Opening Angles from the Prompt Gamma-  
Ray Emission».  
*arXiv:1101.2458* (2011).
- GOMBÁS, P.  
*Die Statistische Theorie des Atoms und Ihre Anwendungen* (1949).
- GONZÁLEZ, H.A., HASSAÏNE, M. AND MARTÍNEZ, C.  
«Thermodynamics of charged black holes with a nonlinear electrodynamic  
source».  
*Physical Review D*, **80**(10), 104008 (2009).
- GORIELY, S., BAUSWEIN, A. AND JANKA, H.T.  
«r-process Nucleosynthesis in Dynamically Ejected Matter of Neutron Star  
Mergers».  
*Astrophysical Journal*, **738**, pp. L32+ (2011a).
- GORIELY, S., CHAMEL, N., JANKA, H.T. AND PEARSON, J.M.  
«The decompression of the outer neutron star crust and r-process nucle-  
osynthesis».  
*Astronomy & Astrophysics*, **531**, A78 (2011b).
- GREENBERG, J.S. AND GREINER, W.  
«Search for the sparking of the vacuum».  
*Physics Today*, **35**, pp. 24–35 (1982).
- GREGORY, P.C. AND FAHLMAN, G.G.  
«An extraordinary new celestial X-ray source».  
*Nature*, **287**, pp. 805–+ (1980).
- GREINER, J., PEIMBERT, M., ESTABAN, C., KAUFER, A., JAUNSEN, A.,  
SMOKE, J., KLOSE, S. AND REIMER, O.  
«Redshift of GRB 030329.»  
*GCN Circ.*, **2020** (2003).

- GRIGORIAN, H., BLASCHKE, D. AND VOSKRESENSKY, D.  
«Cooling of neutron stars with color superconducting quark cores».  
*Phys. Rev. C*, **71(4)**, pp. 1–8 (2005).  
ISSN 0556-2813.
- GRILL, F., PROVIDÊNCIA, C. AND AVANCINI, S.S.  
«Neutron star inner crust and symmetry energy».  
*Physical Review C*, **85(5)**, 055808 (2012).
- GUDMUNDSSON, E.H., PETHICK, C.J. AND EPSTEIN, R.I.  
«Structure of neutron star envelopes».  
*Astrophysical Journal*, **272**, pp. 286–300 (1983).
- GUDMUNDSSON, E.H., PETHICK, C.J. AND EPSTEIN, R.I.  
«Structure of neutron star envelopes».  
*ApJ*, **272**, p. 286 (1983).  
ISSN 0004-637X.
- HAENSEL, P. AND PICHON, B.  
«Experimental nuclear masses and the ground state of cold dense matter».  
*Astronomy & Astrophysics*, **283**, pp. 313–318 (1994).
- HAENSEL, P., POTEKHIN, A.Y. AND YAKOVLEV, D.G. (eds.).  
*Neutron Stars 1 : Equation of State and Structure*, volume 326 of *Astrophysics and Space Science Library* (2007).
- HAENSEL, P. AND ZDUNIK, J.L.  
«Equation of state and structure of the crust of an accreting neutron star».  
*Astronomy & Astrophysics*, **229**, pp. 117–122 (1990a).
- HAENSEL, P. AND ZDUNIK, J.L.  
«Non-equilibrium processes in the crust of an accreting neutron star».  
*Astronomy & Astrophysics*, **227**, pp. 431–436 (1990b).
- HAMADA, T. AND SALPETER, E.E.  
«Models for Zero-Temperature Stars.»  
*Astrophysical Journal*, **134**, pp. 683–+ (1961).
- HANSEN, B.M.S.  
«Stellar Collisions and Pulsar Planets».  
In M. M. Shara (ed.), *Stellar Collisions, Mergers and their Consequences*, volume 263 of *Astronomical Society of the Pacific Conference Series*, p. 221 (2002).
- HARRISON, B.K., THORNE, K.S., WAKANO, M. AND WHEELER, J.A.  
*Gravitation Theory and Gravitational Collapse* (1965).
- HARRISON, B.K., WAKANO, M. AND WHEELER, J.A.  
*Onzieme Conseil de Physique de Solvay* (1958).

- HARTLE, J.B.  
«Slowly Rotating Relativistic Stars. I. Equations of Structure».  
*Astrophysical Journal*, **150**, p. 1005 (1967).
- HARTLE, J.B. AND SHARP, D.H.  
«Variational Principle for the Equilibrium of a Relativistic, Rotating Star».  
*Astrophysical Journal*, **147**, pp. 317–+ (1967).
- HARTLE, J.B. AND THORNE, K.S.  
«Slowly Rotating Relativistic Stars. II. Models for Neutron Stars and Supermassive Stars».  
*Astrophysical Journal*, **153**, p. 807 (1968).
- HEBELER, K., LATTIMER, J.M., PETHICK, C.J. AND SCHWENK, A.  
«Constraints on Neutron Star Radii Based on Chiral Effective Field Theory Interactions».  
*Physical Review Letters*, **105(16)**, 161102 (2010).
- HEINKE, C.O., RYBICKI, G.B., NARAYAN, R. AND GRINDLAY, J.E.  
«A Hydrogen Atmosphere Spectral Model Applied to the Neutron Star X7 in the Globular Cluster 47 Tucanae».  
*Astrophysical Journal*, **644**, pp. 1090–1103 (2006).
- HEISENBERG, W. AND EULER, H.  
«Folgerungen aus der Diracschen Theorie des Positrons».  
*Zeitschrift fur Physik*, **98**, pp. 714–732 (1936).
- HERRERA, L., GONZÁLEZ, G.A., PACHÓN, L.A. AND RUEDA, J.A.  
*Classical and Quantum Gravity*, **23**, pp. 2395–2408 (2006).
- HESSELS, J.W.T., RANSOM, S.M., STAIRS, I.H., FREIRE, P.C.C., KASPI, V.M. AND CAMILO, F.  
«A Radio Pulsar Spinning at 716 Hz».  
*Science*, **311**, pp. 1901–1904 (2006a).
- HESSELS, J.W.T., RANSOM, S.M., STAIRS, I.H., FREIRE, P.C.C., KASPI, V.M. AND CAMILO, F.  
«A Radio Pulsar Spinning at 716 Hz».  
*Science*, **311**, pp. 1901–1904 (2006b).
- HEWISH, A.  
*Pulsars and High Density Physics. Nobel lecture.* (1974).
- HICKEN, M., GARNAVICH, P.M. AND PRIETO, ET AL., J.L.  
«The Luminous and Carbon-rich Supernova 2006gz: A Double Degenerate Merger?»  
*Astrophysical Journal*, **669**, pp. L17–L20 (2007).

- HIRATA, D., TOKI, H. AND TANIHATA, I.  
«Relativistic mean-field theory on the xenon, cesium and barium isotopes».  
*Nuclear Physics A*, **589**, pp. 239–248 (1995).
- HOENSELAERS, C. AND PERJES, Z.  
«Multipole moments of axisymmetric electrovacuum spacetimes».  
*Classical and Quantum Gravity*, **7**, pp. 1819–1825 (1990).
- HOMAN, J., VAN DER KLIS, M., JONKER, P.G., WIJNANDS, R., KUULKERS, E., MÉNDEZ, M. AND LEWIN, W.H.G.  
«RXTE Observations of the Neutron Star Low-Mass X-Ray Binary GX 17+2: Correlated X-Ray Spectral and Timing Behavior».  
*Astrophysical Journal*, **568**, pp. 878–900 (2002).
- HOWELL, D.A., SULLIVAN, M. AND NUGENT, ET AL., P.E.  
«The type Ia supernova SNLS-03D3bb from a super-Chandrasekhar-mass white dwarf star».  
*Nature*, **443**, pp. 308–311 (2006).
- HOYLE, F. AND FOWLER, W.A.  
«Nucleosynthesis in Supernovae.»  
*Astrophysical Journal*, **132**, pp. 565+ (1960).
- HUGHES, V.A., HARTEN, R.H. AND VAN DEN BERGH, S.  
«A new supernova remnant G109.2-1.0».  
*Astrophysical Journal*, **246**, pp. L127–L131 (1981).
- HULLEMAN, F., TENNANT, A.F., VAN KERKWIJK, M.H., KULKARNI, S.R., KOUVELIOTOU, C. AND PATEL, S.K.  
«A Possible Faint Near-Infrared Counterpart to the Anomalous X-Ray Pulsar 1E 2259+586».  
*Astrophysical Journal*, **563**, pp. L49–L52 (2001).
- HULLEMAN, F., VAN KERKWIJK, M.H. AND KULKARNI, S.R.  
«An optical counterpart to the anomalous X-ray pulsar 4U0142+61».  
*Nature*, **408**, pp. 689–692 (2000).
- HULLEMAN, F., VAN KERKWIJK, M.H. AND KULKARNI, S.R.  
«The Anomalous X-ray Pulsar 4U 0142+61: Variability in the infrared and a spectral break in the optical».  
*Astronomy & Astrophysics*, **416**, pp. 1037–1045 (2004).
- HUND, F.  
*Erg. d. exacten Natwis.*, **15**, p. 189 (1936).

- HURLEY, J.R. AND SHARA, M.M.  
«White Dwarf Sequences in Dense Star Clusters».  
*Astrophysical Journal*, **589**, pp. 179–198 (2003).
- HURLEY, K., BOGGS, S.E., SMITH, D.M., DUNCAN, R.C., LIN, R.,  
ZOGLAUER, A., KRUCKER, S., HURFORD, G., HUDSON, H., WIGGER, C.  
ET AL.  
«An exceptionally bright flare from SGR 1806-20 and the origins of short-  
duration  $\gamma$ -ray bursts».  
*Nature*, **434**, pp. 1098–1103 (2005).
- IBEN, JR., I. AND TUTUKOV, A.V.  
«Supernovae of type I as end products of the evolution of binaries with  
components of moderate initial mass (M not greater than about 9 solar  
masses)».  
*Astrophysical Journal Supplement Series*, **54**, pp. 335–372 (1984).
- IKHSANOV, N.R. AND BESKROVNAYA, N.G.  
«AE Aquarii: The first white dwarf in the family of spin-powered pulsars».  
*arXiv:0809.1169* (2008).
- IKHSANOV, N.R. AND BIERMANN, P.L.  
«High-energy emission of fast rotating white dwarfs».  
*Astronomy & Astrophysics*, **445**, pp. 305–312 (2006).
- ILKOV, M. AND SOKER, N.  
«Type Ia supernovae from very long delayed explosion of core-white  
dwarf merger».  
*Monthly Notices of the Royal Astronomical Society*, **419**, pp. 1695–1700 (2012).
- IMMLER, S., WILSON, A.S. AND TERASHIMA, Y.  
«X-Ray Emission from the Type Ic Supernova 1994I Observed with Chan-  
dra».  
*ApJ*, **573**, pp. L27–L30 (2002).
- IOSILEVSKIY, I.L.  
«Plasma polarization in massive astrophysical objects».  
*Journal of Physics A Mathematical General*, **42(21)**, p. 214008 (2009).
- ISRAEL, G.L., CAMPANA, S., DALL’OSSO, S., MUNO, M.P., CUMMINGS, J.,  
PERNA, R. AND STELLA, L.  
«The Post-Burst Awakening of the Anomalous X-Ray Pulsar in Westerlund  
1».  
*Astrophysical Journal*, **664**, pp. 448–457 (2007).
- ISRAEL, G.L., STELLA, L., ANGELINI, L., WHITE, N.E., KALLMAN, T.R.,  
GIOMMI, P. AND TREVES, A.

- «The Discovery of 13 Second X-Ray Pulsations from the Hydrogen-depleted Subdwarf O6 Star Binary HD 49798».  
*Astrophysical Journal*, **474**, pp. L53+ (1997).
- ITOH, K., OKADA, S., ISHIDA, M. AND KUNIEDA, H.  
«Density Diagnostics of the Hot Plasma in AE Aquarii with XMM-Newton».  
*Astrophysical Journal*, **639**, pp. 397–404 (2006).
- ITOH, N.  
«Hydrostatic Equilibrium of Hypothetical Quark Stars».  
*Progress of Theoretical Physics*, **44**, pp. 291–292 (1970).
- IWAMOTO, K., MAZZALI, P.A., NOMOTO, K., UMEDA, H., NAKAMURA, T., PATAT, F., DANZIGER, I.J., YOUNG, T.R., SUZUKI, T., SHIGEYAMA, T. ET AL.  
«A hypernova model for the supernova associated with the  $\gamma$ -ray burst of 25 april 1998».  
*Nature*, **395**, pp. 672–674 (1998).
- IZZO, L., RUEDA, J.A. AND RUFFINI, R.  
«GRB 090618: a candidate for a neutron star gravitational collapse onto a black hole induced by a type Ib/c supernova».  
*Astronomy & Astrophysics*, **548**, L5 (2012a).
- IZZO, L., RUFFINI, R., PENACCHIONI, A.V., BIANCO, C.L., CAITO, L., CHAKRABARTI, S.K., RUEDA, J.A., NANDI, A. AND PATRICELLI, B.  
*Astronomy & Astrophysics*, *submitted* (2011).
- IZZO, L., RUFFINI, R., PENACCHIONI, A.V., BIANCO, C.L., CAITO, L., CHAKRABARTI, S.K., RUEDA, J.A., NANDI, A. AND PATRICELLI, B.  
«A double component in GRB 090618: a proto-black hole and a genuinely long gamma-ray burst».  
*Astronomy & Astrophysics*, **543**, A10 (2012b).
- JAMES, R.A.  
«The Structure and Stability of Rotating Gas Masses.»  
*Astrophysical Journal*, **140**, p. 552 (1964).
- JOHANNSEN, T. AND PSALTIS, D.  
«Testing the No-hair Theorem with Observations in the Electromagnetic Spectrum. III. Quasi-periodic Variability».  
*Astrophysical Journal*, **726**, 11 (2011).
- JONKER, P.G., VAN DER KLIS, M., HOMAN, J., MÉNDEZ, M., LEWIN, W.H.G., WIJNANDS, R. AND ZHANG, W.

- «Low- and high-frequency variability as a function of spectral properties in the bright X-ray binary GX 5-1».  
*Monthly Notices of the Royal Astronomical Society*, **333**, pp. 665–678 (2002).
- JONKER, P.G., VAN DER KLIS, M., WIJNANDS, R., HOMAN, J., VAN PARADIJS, J., MÉNDEZ, M., FORD, E.C., KUULKERS, E. AND LAMB, F.K.  
«The Power Spectral Properties of the Z Source GX 340+0».  
*Astrophysical Journal*, **537**, pp. 374–386 (2000).
- JUDGE, P.G., SOLOMON, S.C. AND AYRES, T.R.  
«An Estimate of the Sun’s ROSAT-PSPC X-Ray Luminosities Using SNOE-SXP Measurements».  
*Astrophysical Journal*, **593**, pp. 534–548 (2003).
- JURA, M.  
«A Tidally Disrupted Asteroid around the White Dwarf G29-38».  
*Astrophysical Journal*, **584**, pp. L91–L94 (2003).
- KANEKO, Y., RAMIREZ-RUIZ, E., GRANOT, J., KOUVELIOTOU, C., WOOSLEY, S.E., PATEL, S.K., ROL, E., ZAND, J.J.M.I., VAN DER HORST, A.J., WIJERS, R.A.M.J. ET AL.  
«Prompt and afterglow emission properties of gamma-ray bursts with spectroscopically identified supernovae».  
*ApJ*, **654**, pp. 385–402 (2007).
- KASEN, D. AND BILDSTEN, L.  
«Supernova Light Curves Powered by Young Magnetars».  
*Astrophysical Journal*, **717**, pp. 245–249 (2010).
- KASHIYAMA, K., IOKA, K. AND KAWANAKA, N.  
«White dwarf pulsars as possible cosmic ray electron-positron factories».  
*Physical Review D*, **83(2)**, pp. 023002–+ (2011).
- KASPI, V.M., GAVRIIL, F.P., WOODS, P.M., JENSEN, J.B., ROBERTS, M.S.E. AND CHAKRABARTY, D.  
«A Major Soft Gamma Repeater-like Outburst and Rotation Glitch in the No-longer-so-anomalous X-Ray Pulsar 1E 2259+586».  
*Astrophysical Journal*, **588**, pp. L93–L96 (2003).
- KATZ, J.I.  
«The Eddington Limit and Soft Gamma Repeaters».  
*Astrophysical Journal*, **463**, p. 305 (1996).
- KEPLER, S.O., KLEINMAN, S.J., PELISOLI, I., PEÇANHA, V., DIAZ, M., KOESTER, D., CASTANHEIRA, B.G. AND NITTA, A.  
«Magnetic White Dwarfs in the SDSS and Estimating the Mean Mass of Normal DA and DB WDs».

- In K. Werner & T. Rauch (ed.), *American Institute of Physics Conference Series*, volume 1273 of *American Institute of Physics Conference Series*, pp. 19–24 (2010).
- KEPLER, S.O., PELISOLI, I., JORDAN, S., KLEINMAN, S.J., KULEBI, B., KOESTER, D., PEÇANHA, V., CASTANHEIRA, B.G., NITTA, A., DA SILVEIRA COSTA, J.E. ET AL.  
«Magnetic White Dwarf Stars in the SDSS».  
*arXiv:1211.5709* (2012).
- KERR, R.P.  
«Gravitational field of a spinning mass as an example of algebraically special metrics».  
*Phys. Rev. Lett.*, **11**, pp. 237–238 (1963).
- KETTNER, C., WEBER, F., WEIGEL, M.K. AND GLENDENNING, N.K.  
«Structure and stability of strange and charm stars at finite temperatures».  
*Physical Review D*, **51**, pp. 1440–1457 (1995).
- KLEIN, O.  
«On the Thermodynamical Equilibrium of Fluids in Gravitational Fields».  
*Reviews of Modern Physics*, **21**, pp. 531–533 (1949).
- KOBAYASHI, S. AND MÉSZÁROS, P.  
«Gravitational Radiation from Gamma-Ray Burst Progenitors».  
*Astrophysical Journal*, **589**, pp. 861–870 (2003).
- KODAMA, T. AND YAMADA, M.  
«Theory of Superdense Stars».  
*Progress of Theoretical Physics*, **47**, pp. 444–459 (1972).
- KOESTER, D.  
«Convective Mixing and Accretion in White Dwarfs».  
*Astronomy & Astrophysics*, **52**, p. 415 (1976).
- KOESTER, D.  
«White Dwarf Spectra and Atmosphere Models».  
*arXiv:0812.0482* (2008).
- KONACKI, M., LEWANDOWSKI, W., WOLSZCZAN, A., DOROSHENKO, O. AND KRAMER, M.  
«Are There Planets around the Pulsar PSR B0329+54?»  
*Astrophysical Journal*, **519**, pp. L81–L84 (1999).
- KONACKI, M. AND WOLSZCZAN, A.  
«Masses and Orbital Inclinations of Planets in the PSR B1257+12 System».  
*Astrophysical Journal*, **591**, pp. L147–L150 (2003).

- KOTHAWALA, D., SARKAR, S. AND PADMANABHAN, T.  
«Einstein's equations as a thermodynamic identity: The cases of stationary axisymmetric horizons and evolving spherically symmetric horizons».  
*Physics Letters B*, **652**, pp. 338–342 (2007).
- KOTHES, R. AND FOSTER, T.  
«A Thorough Investigation of the Distance to the Supernova Remnant CTB109 and Its Pulsar AXP J2301+5852».  
*Astrophysical Journal*, **746**, L4 (2012).
- KOUVELIOTOU, C., WOOSLEY, S.E., PATEL, S.K., LEVAN, A., BLANDFORD, R., RAMIREZ-RUIZ, E., WIJERS, R.A.M.J., WEISSKOPF, M.C., TENNANT, A., PIAN, E. ET AL.  
«Chandra observations of the x-ray environs of sn 1998bw/grb 980425».  
*ApJ*, **608**, pp. 872–882 (2004).
- KRAMER, M.  
private communication (2010).
- KUBIS, S.  
«Nuclear symmetry energy and stability of matter in neutron stars».  
*Physical Review C*, **76(2)**, 025801 (2007).
- KUIPER, L. AND HERMSEN, W.  
«High-energy characteristics of the schizophrenic pulsar PSR J1846-0258 in Kes 75. Multi-year RXTE and INTEGRAL observations crossing the magnetar-like outburst».  
*Astronomy & Astrophysics*, **501**, pp. 1031–1046 (2009).
- KÜLEBI, B., JORDAN, S., EUCHNER, F., GAENSICKE, B.T. AND HIRSCH, H.  
«Magnetic fields in white dwarfs (Kuelebi+, 2009)».  
*VizieR Online Data Catalog*, **350**, pp. 61341–+ (2010a).
- KÜLEBI, B., JORDAN, S., EUCHNER, F., GÄNSICKE, B.T. AND HIRSCH, H.  
«Analysis of hydrogen-rich magnetic white dwarfs detected in the Sloan Digital Sky Survey».  
*Astronomy & Astrophysics*, **506**, pp. 1341–1350 (2009).
- KÜLEBI, B., JORDAN, S., NELAN, E., BASTIAN, U. AND ALTMANN, M.  
«Constraints on the origin of the massive, hot, and rapidly rotating magnetic white dwarf RE J 0317-853 from an HST parallax measurement».  
*Astronomy & Astrophysics*, **524**, pp. A36+ (2010b).
- KUMAR, H.S. AND SAFI-HARB, S.  
«Variability of the High Magnetic Field X-Ray Pulsar PSR J1846-0258 Associated with the Supernova Remnant Kes 75 as Revealed by the Chandra X-Ray Observatory».

- Astrophysical Journal*, **678**, pp. L43–L46 (2008).
- LAARAKKERS, W.G. AND POISSON, E.  
«Quadrupole Moments of Rotating Neutron Stars».  
*Astrophysical Journal*, **512**, pp. 282–287 (1999).
- LABUN, L. AND RAFELSKI, J.  
«Dark energy simulacrum in nonlinear electrodynamics».  
*Physical Review D*, **81(6)**, 065026 (2010a).
- LABUN, L. AND RAFELSKI, J.  
«QED energy-momentum trace as a force in astrophysics».  
*Physics Letters B*, **687**, pp. 133–138 (2010b).
- LALAZISSIS, G.A., KÖNIG, J. AND RING, P.  
«New parametrization for the Lagrangian density of relativistic mean field theory».  
*Physical Review C*, **55**, pp. 540–543 (1997).
- LAMB, F.K., PETHICK, C.J. AND PINES, D.  
«A Model for Compact X-Ray Sources: Accretion by Rotating Magnetic Stars».  
*Astrophysical Journal*, **184**, pp. 271–290 (1973).
- LANDAU, L.D.  
«On the theory of stars».  
*Phys. Z. Sowjetunion*, **1**, pp. 285–288 (1932).
- LANDAU, L.D.  
*Nature*, **19**, p. 333 (1938).
- LANDAU, L.D. AND LIFSHITZ, E.M.  
*Electrodynamics of continuous media* (1960).
- LANDAU, L.D. AND LIFSHITZ, E.M.  
*The classical theory of fields* (Course of theoretical physics - Pergamon International Library of Science, Technology, Engineering and Social Studies, Oxford: Pergamon Press, 4th rev.engl.ed., 1975).
- LANDAU, L.D. AND LIFSHITZ, E.M.  
*Statistical physics. Part1* (Pergamon Press, Oxford, 1980).
- LATTIMER, J.M. AND PRAKASH, M.  
«The Physics of Neutron Stars».  
*Science*, **304**, pp. 536–542 (2004a).

- LATTIMER, J.M. AND PRAKASH, M.  
«The Physics of Neutron Stars».  
*Science*, **304**, pp. 536–542 (2004b).
- LATTIMER, J.M. AND SCHUTZ, B.F.  
«Constraining the Equation of State with Moment of Inertia Measurements».  
*Astrophysical Journal*, **629**, pp. 979–984 (2005).
- LATTIMER, J.M., VAN RIPER, K.A., PRAKASH, M. AND PRAKASH, M.  
«Rapid cooling and the structure of neutron stars».  
*Astrophysical Journal*, **425**, pp. 802–813 (1994).
- LEE, T.D.  
«Abnormal nuclear states and vacuum excitation».  
*Reviews of Modern Physics*, **47**, pp. 267–275 (1975).
- LEE, T.D. AND MARGULIES, M.  
«Interaction of a dense fermion medium with a scalar-meson field».  
*Physical Review D*, **11**, pp. 1591–1610 (1975).
- LEE, T.D. AND PANG, Y.  
«Fermion soliton stars and black holes».  
*Physical Review D*, **35**, pp. 3678–3694 (1987).
- LEE, T.D. AND WICK, G.C.  
«Vacuum stability and vacuum excitation in a spin-0 field theory».  
*Physical Review D*, **9**, pp. 2291–2316 (1974).
- LEVAN, A.J., WYNN, G.A., CHAPMAN, R., DAVIES, M.B., KING, A.R., PRIDDEY, R.S. AND TANVIR, N.R.  
«Short gamma-ray bursts in old populations: magnetars from white dwarf-white dwarf mergers».  
*Monthly Notices of the Royal Astronomical Society*, **368**, pp. L1–L5 (2006).
- LIEB, E.H. AND SIMON, B.  
«Thomas-Fermi Theory Revisited».  
*Physical Review Letters*, **31**, pp. 681–683 (1973).
- LIEBERT, J., SCHMIDT, G.D., GREEN, R.F., STOCKMAN, H.S. AND MCGRAW, J.T.  
«Two hot, low-field magnetic DA white dwarfs».  
*Astrophysical Journal*, **264**, pp. 262–272 (1983).
- LIN, Y.F., BOUTELIER, M., BARRET, D. AND ZHANG, S.N.  
«Studying Frequency Relationships of Kilohertz Quasi-periodic Oscillations for 4U 1636-53 and Sco X-1: Observations Confront Theories».  
*Astrophysical Journal*, **726**, pp. 74–+ (2011).

- LINDBLOM, L.  
«The role of the viscous secular instability in rotating neutron stars».  
*Astrophysical Journal*, **317**, pp. 325–332 (1987).
- LOAN, D.T., TAN, N.H., KHOA, D.T. AND MARGUERON, J.  
«Equation of state of neutron star matter, and the nuclear symmetry energy».  
*Physical Review C*, **83(6)**, 065809 (2011).
- LORÉN-AGUILAR, P., ISERN, J. AND GARCÍA-BERRO, E.  
«High-resolution smoothed particle hydrodynamics simulations of the merger of binary white dwarfs».  
*Astronomy & Astrophysics*, **500**, pp. 1193–1205 (2009).
- LUCCHESI, D.M. AND PERON, R.  
«Accurate Measurement in the Field of the Earth of the General-Relativistic Precession of the LAGEOS II Pericenter and New Constraints on Non-Newtonian Gravity».  
*Physical Review Letters*, **105(23)**, pp. 231103–+ (2010).
- LUNDQVIST, S. AND MARCH, N.H.  
*Theory of the Inhomogeneous Electro Gas* (1983).
- LYUTIKOV, M. AND GAVRIIL, F.P.  
«Resonant cyclotron scattering and Comptonization in neutron star magnetospheres».  
*Monthly Notices of the Royal Astronomical Society*, **368**, pp. 690–706 (2006).
- MALHEIRO, M., RAY, S., CUESTA, H.J.M. AND DEY, J.  
«General Relativistic Effects of Strong Magnetic Fields on the Gravitational Force: a Driving Engine for Bursts of Gamma Rays in Sgrs?»  
*International Journal of Modern Physics D*, **16**, pp. 489–499 (2007).
- MALHEIRO, M., RUEDA, J.A. AND RUFFINI, R.  
«SGRs and AXPs as Rotation-Powered Massive White Dwarfs».  
*Publications of the Astronomical Society of Japan*, **64**, p. 56 (2012).
- MALOV, I.F.  
«The drift model for AXPs and SGRs in the light of new observational data».  
*Astronomy Reports*, **54**, pp. 925–931 (2010).
- MANCHESTER, R.N. AND TAYLOR, J.H.  
*Pulsars* (1977).
- MANKO, V.S., MARTÍN, J. AND RUIZ, E.  
«Six-parameter solution of the Einstein-Maxwell equations possessing equatorial symmetry».  
*Journal of Mathematical Physics*, **36**, pp. 3063–3073 (1995).

- MANKO, V.S., SANABRIA-GÓMEZ, J.D. AND MANKO, O.V.  
«Nine-parameter electrovac metric involving rational functions».  
*Physical Review D*, **62(4)**, pp. 044048–+ (2000).
- MANKO, V.S. AND SIBGATULLIN, N.R.  
«Construction of exact solutions of the Einstein-Maxwell equations corresponding to a given behaviour of the Ernst potentials on the symmetry axis».  
*Classical and Quantum Gravity*, **10**, pp. 1383–1404 (1993).
- MARCH, N.H.  
«The Thomas-Fermi approximation in quantum mechanics».  
*Advances in Physics*, **6**, pp. 1–101 (1957).
- MARSH, J.S.  
«Magnetic and electric fields of rotating charge distributions».  
*American Journal of Physics*, **50**, pp. 51–53 (1982).
- MARUYAMA, T., TATSUMI, T., VOSKRESENSKY, D.N., TANIGAWA, T. AND CHIBA, S.  
«Nuclear “pasta” structures and the charge screening effect».  
*Physical Review C*, **72(1)**, 015802 (2005).
- MATT, S.P., PINZÓN, G., GREENE, T.P. AND PUDRITZ, R.E.  
«Spin Evolution of Accreting Young Stars. II. Effect of Accretion-powered Stellar Winds».  
*Astrophysical Journal*, **745**, 101 (2012).
- MAZETS, E.P., GOLENTSKII, S.V., ILINSKII, V.N., APTEKAR, R.L. AND GURYAN, I.A.  
«Observations of a flaring X-ray pulsar in Dorado».  
*Nature*, **282**, pp. 587–589 (1979).
- MAZZALI, P.  
talk presented at the congress “Swift and GRBs: unveiling the relativistic universe”, Venice, Italy, June 5-9 (2006).
- MCLAUGHLIN, M.A., REA, N., GAENSLER, B.M., CHATTERJEE, S., CAMILO, F., KRAMER, M., LORIMER, D.R., LYNE, A.G., ISRAEL, G.L. AND POSSENTI, A.  
«Discovery of Pulsations and a Possible Spectral Feature in the X-Ray Emission from Rotating Radio Transient J1819-1458».  
*Astrophysical Journal*, **670**, pp. 1307–1313 (2007).
- MEINTJES, P.J., DE JAGER, C.O. AND ET AL.  
«Persistent Optical-like Pulsed TeV  $\gamma$ -Ray Emission from AE Aquarii».

---

In *International Cosmic Ray Conference*, volume 1 of *International Cosmic Ray Conference*, pp. 338–+ (1993).

MEINTJES, P.J., RAUBENHEIMER, B.C., DE JAGER, O.C., BRINK, C., NEL, H.I., NORTH, A.R., VAN URK, G. AND VISSER, B.

«AE Aquarii - an emitter of pulsed TeV gamma rays resembling optical emission during flares».

*Astrophysical Journal*, **401**, pp. 325–336 (1992).

MEREGHETTI, S.

«The strongest cosmic magnets: soft gamma-ray repeaters and anomalous X-ray pulsars».

*Astronomy & Astrophysics Review*, **15**, pp. 225–287 (2008a).

MEREGHETTI, S.

«The strongest cosmic magnets: soft gamma-ray repeaters and anomalous X-ray pulsars».

*Astronomy & Astrophysics Review*, **15**, pp. 225–287 (2008b).

MEREGHETTI, S., LA PALOMBARA, N., TIENGO, A., PIZZOLATO, F., ESPOSITO, P., WOUTD, P.A., ISRAEL, G.L. AND STELLA, L.

«X-Ray and Optical Observations of the Unique Binary System HD 49798/RX J0648.0-4418».

*Astrophysical Journal*, **737**, 51 (2011).

MEREGHETTI, S., TIENGO, A., ESPOSITO, P., GÖTZ, D., STELLA, L., ISRAEL, G.L., REA, N., FEROCI, M., TUROLLA, R. AND ZANE, S.

«An XMM-Newton View of the Soft Gamma Repeater SGR 1806-20: Long-Term Variability in the Pre-Giant Flare Epoch».

*Astrophysical Journal*, **628**, pp. 938–945 (2005).

MEREGHETTI, S., TIENGO, A., ESPOSITO, P., LA PALOMBARA, N., ISRAEL, G.L. AND STELLA, L.

«An Ultramassive, Fast-Spinning White Dwarf in a Peculiar Binary System».

*Science*, **325**, pp. 1222– (2009).

MESTEL, L.

«On the theory of white dwarf stars. I. The energy sources of white dwarfs».

*Monthly Notices of the Royal Astronomical Society*, **112**, p. 583 (1952).

MICHEL, F.C.

«Radio pulsar disk electrodynamics».

*Astrophysical Journal*, **266**, pp. 188–200 (1983).

- MICHEL, F.C. AND DESSLER, A.J.  
«Pulsar disk systems».  
*Astrophysical Journal*, **251**, pp. 654–664 (1981).
- MIGDAL, A.B., POPOV, V.S. AND VOSKRESENSKIĬ, D.N.  
«The vacuum charge distribution near super-charged nuclei».  
*Soviet Journal of Experimental and Theoretical Physics*, **45**, pp. 436–+ (1977).
- MIGDAL, A.B., VOSKRESENSKIĬ, D.N. AND POPOV, V.S.  
«Distribution of vacuum charge near supercharged nuclei».  
*Soviet Journal of Experimental and Theoretical Physics Letters*, **24**, pp. 163–+ (1976).
- MILLER, L.D. AND GREEN, A.E.  
«Relativistic Self-Consistent Meson Field Theory of Spherical Nuclei».  
*Physical Review C*, **5**, pp. 241–252 (1972).
- MILNE, E.A.  
«The analysis of stellar structure».  
*Monthly Notices of the Royal Astronomical Society*, **91**, pp. 4–55 (1930).
- MIRABAL, N., HALPERN, J.P., AN, D., THORSTENSEN, J.R. AND TERNDRUP, D.M.  
«Grb 060218/sn 2006aj: A gamma-ray burst and prompt supernova at  $z = 0.0335$ ».  
*ApJ*, **643**, pp. L99–L102 (2006).
- MISNER, C.W., THORNE, K.S. AND WHEELER, J.A.  
*Gravitation* (San Francisco: W.H. Freeman and Co., 1973).
- MONAGHAN, J.J.  
«The structure of rapidly rotating white dwarfs».  
*Monthly Notices of the Royal Astronomical Society*, **132**, p. 305 (1966).
- MORII, M., KAWAI, N., KATAOKA, J., YATSU, Y., KOBAYASHI, N. AND TERADA, H.  
«Near-infrared, optical, and X-ray observations of the anomalous X-ray pulsar 4U 0142 + 61».  
*Advances in Space Research*, **35**, pp. 1177–1180 (2005).
- MORII, M., KOBAYASHI, N., KAWAI, N., TERADA, H., TANAKA, Y.T., KITAMOTO, S. AND SHIBAZAKI, N.  
«Search for Near-Infrared Pulsation of the Anomalous X-Ray Pulsar 4U 0142+61».  
*Publications of the Astronomical Society of Japan*, **61**, pp. 51– (2009).

- MORINI, M., ROBBA, N.R., SMITH, A. AND VAN DER KLIS, M.  
«EXOSAT observations of the supernova remnant G109.1-1.0 and the X-ray pulsar 1E 2259+586».  
*Astrophysical Journal*, **333**, pp. 777–787 (1988).
- MORSINK, S.M. AND STELLA, L.  
«Relativistic Precession around Rotating Neutron Stars: Effects Due to Frame Dragging and Stellar Oblateness».  
*Astrophysical Journal*, **513**, pp. 827–844 (1999).
- MOSQUERA CUESTA, H.J. AND SALIM, J.M.  
«Non-linear electrodynamics and the gravitational redshift of highly magnetized neutron stars».  
*Monthly Notices of the Royal Astronomical Society*, **354**, pp. L55–L59 (2004a).
- MOSQUERA CUESTA, H.J. AND SALIM, J.M.  
«Nonlinear Electrodynamics and the Surface Redshift of Pulsars».  
*Astrophysical Journal*, **608**, pp. 925–929 (2004b).
- MOTT, N.F.  
«The Electrical Resistance of Dilute Solid Solutions».  
*Proceedings of the Cambridge Philosophical Society*, **32**, p. 281 (1936).
- MUCCINO, M., RUFFINI, R., BIANCO, C.L., IZZO, L. AND PENACCHIONI, A.V.  
«GRB 090227B: the missing link between the genuine short and long GRBs».  
*Astrophysical Journal*, *accepted; arXiv:1205.6600* (2012).
- MUCCINO, M., RUFFINI, R., BIANCO, C.L., IZZO, L. AND PENACCHIONI, A.V.  
«GRB 090227B: The Missing Link between the Genuine Short and Long Gamma-Ray Bursts».  
*Astrophysical Journal*, **763**, 125 (2013).
- MÜLLER, B., PEITZ, H., RAFELSKI, J. AND GREINER, W.  
«Solution of the Dirac Equation for Strong External Fields».  
*Physical Review Letters*, **28**, pp. 1235–1238 (1972).
- MUNO, M.P., CHAKRABARTY, D., GALLOWAY, D.K. AND SAVOV, P.  
«Millisecond Oscillations and Photospheric Radius Expansion in Thermonuclear X-Ray Bursts».  
*Astrophysical Journal*, **553**, pp. L157–L160 (2001).
- MÜTHER, H., PRAKASH, M. AND AINSWORTH, T.L.  
«The nuclear symmetry energy in relativistic Brueckner-Hartree-Fock calculations».

- Physics Letters B*, **199**, pp. 469–474 (1987).
- MYERS, W.  
«Nuclear masses and deformations».  
*Nuclear Physics A*, **81**, pp. 1–60 (1966).
- MYUNG, Y.S., KIM, Y.W. AND PARK, Y.J.  
«Thermodynamics and phase transitions in the Born-Infeld-anti-de Sitter black holes».  
*Physical Review D*, **78(8)**, 084002 (2008).
- NALEŻYTY, M. AND MADEJ, J.  
«A catalogue of isolated massive white dwarfs. Mass distribution of massive star».  
*Astronomy & Astrophysics*, **420**, pp. 507–513 (2004).
- NEGREIROS, R., RUFFINI, R., BIANCO, C.L. AND RUEDA, J.A.  
«Cooling of young neutron stars in GRB associated to supernovae».  
*Astronomy & Astrophysics*, **540**, A12 (2012).
- NEGREIROS, R., DEXHEIMER, V. AND SCHRAMM, S.  
«Modeling hybrid stars with an SU(3) nonlinear  $\sigma$  model».  
*Phys. Rev. C*, **82(3)**, pp. 1–9 (2010).  
ISSN 0556-2813.
- NG, C., KASPI, V.M., DIB, R., OLAUSEN, S.A., SCHOLZ, P., GUVER, T., OZEL, F., GAVRIIL, F.P. AND WOODS, P.M.  
«Chandra and RXTE Observations of 1E 1547.0-5408: Comparing the 2008 and 2009 Outbursts».  
*arXiv:1008.1165* (2010).
- NG, C.Y. AND KASPI, V.M.  
«High Magnetic Field Rotation-powered Pulsars».  
In E. Göğüş, T. Belloni and Ü. Ertan (eds.), *American Institute of Physics Conference Series*, volume 1379 of *American Institute of Physics Conference Series*, pp. 60–69 (2011).
- NOVELLO, M., DE LORENCI, V.A., SALIM, J.M. AND KLIPPERT, R.  
«Geometrical aspects of light propagation in nonlinear electrodynamics».  
*Physical Review D*, **61(4)**, 045001 (2000a).
- NOVELLO, M., PEREZ BERGLIAFFA, S.E. AND SALIM, J.M.  
«Singularities in general relativity coupled to nonlinear electrodynamics».  
*Classical and Quantum Gravity*, **17**, pp. 3821–3831 (2000b).
- OKAMOTO, M., MARUYAMA, T., YABANA, K. AND TATSUMI, T.  
«Three-dimensional structure of low-density nuclear matter».  
*Physics Letters B*, **713**, pp. 284–288 (2012).

- OLMO, G.J. AND RUBIERA-GARCIA, D.  
«Palatini  $f(R)$  black holes in nonlinear electrodynamics».  
*Physical Review D*, **84(12)**, 124059 (2011).
- OLSON, E. AND BAILYN, M.  
«Internal structure of multicomponent static spherical gravitating fluids».  
*Physical Review D*, **12**, pp. 3030–3036 (1975).
- OLSON, E. AND BAILYN, M.  
«Charge effects in a static, spherically symmetric, gravitating fluid».  
*Physical Review D*, **13**, pp. 2204–2211 (1976).
- OLSON, E. AND BAILYN, M.  
«Internal structure of multicomponent fluids».  
*Physical Review D*, **18**, pp. 2175–2179 (1978).
- OPPENHEIMER, J.R. AND VOLKOFF, G.M.  
«On Massive Neutron Cores».  
*Physical Review*, **55**, pp. 374–381 (1939).
- Ostriker, J.P. AND BodenhaimeR, P.  
«Rapidly Rotating Stars. II. Massive White Dwarfs».  
*Astrophysical Journal*, **151**, p. 1089 (1968).
- Ostriker, J.P. AND Hartwick, F.D.A.  
«Rapidly Rotating Stars.IV. Magnetic White Dwarfs».  
*Astrophysical Journal*, **153**, p. 797 (1968).
- Ostriker, J.P. AND Tassoul, J.L.  
«On the Oscillations and Stability of Rotating Stellar Models. II. Rapidly Rotating White Dwarfs».  
*Astrophysical Journal*, **155**, p. 987 (1969).
- PACHÓN, L.A., RUEDA, J.A. AND SANABRIA-GÓMEZ, J.D.  
«Realistic exact solution for the exterior field of a rotating neutron star».  
*Physical Review D*, **73(10)**, pp. 104038–+ (2006).
- PACHÓN, L.A., RUEDA, J.A. AND VALENZUELA-TOLEDO, C.A.  
«On the Relativistic Precession and Oscillation Frequencies of Test Particles around Rapidly Rotating Compact Stars».  
*Astrophysical Journal*, **756**, 82 (2012).
- PACHÓN, L.A. AND SANABRIA-GÓMEZ, J.D.  
«COMMENTS, REPLIES AND NOTES: Note on reflection symmetry in stationary axisymmetric electrovacuum spacetimes».  
*Classical and Quantum Gravity*, **23**, pp. 3251–3254 (2006).

PACZYNSKI, B.

«Evolution of cataclysmic binaries».

In D. Q. Lamb & J. Patterson (ed.), *Cataclysmic Variables and Low-Mass X-ray Binaries*, volume 113 of *Astrophysics and Space Science Library*, pp. 1–12 (1985).

PACZYNSKI, B.

«X-ray pulsar 1E 2259 + 586 - A merged white dwarf with a 7 second rotation period?»

*Astrophysical Journal*, **365**, pp. L9–L12 (1990).

PACZYNSKI, B.

«GB 790305 as a very strongly magnetized neutron star».

*Acta Astronomica*, **42**, pp. 145–153 (1992).

PAGANI, C., BEARDMORE, A.P. AND KENNEA, J.A.

«Swift J1822.3-1606: Enhanced Swift-XRT position».

*The Astronomer's Telegram*, **3493**, p. 1 (2011).

PAGE, D., GEPPERT, U. AND WEBER, F.

«The cooling of compact stars».

*Nuclear Physics A*, **777**, pp. 497–530 (2006).

ISSN 03759474.

PAGE, D., LATTIMER, J., PRAKASH, M. AND STEINER, A.W.

«Minimal Cooling of Neutron Stars: A New Paradigm».

*ApJSS*, **155(2)**, pp. 623–650 (2004).

ISSN 0067-0049.

PAGE, D., LATTIMER, J., PRAKASH, M. AND STEINER, A.W.

«Neutrino Emission From Cooper Pairs and Minimal Cooling of Neutron Stars».

*ApJ*, **707(2)**, pp. 1131–1140 (2009).

ISSN 0004-637X.

PAGE, D., PRAKASH, M., LATTIMER, J.M. AND STEINER, A.W.

«Rapid Cooling of the Neutron Star in Cassiopeia A Triggered by Neutron Superfluidity in Dense Matter».

*Physical Review Letters*, **106(8)**, pp. 081101–+ (2011).

PAKMOR, R., KROMER, M., RÖPKE, F.K., SIM, S.A., RUITER, A.J. AND HILLEBRANDT, W.

«Sub-luminous type Ia supernovae from the mergers of equal-mass white dwarfs with mass  $0.9M_{\odot}$ ».

*Nature*, **463**, pp. 61–64 (2010).

- PANEL, J.A., ALTHAUS, L.G. AND BENVENUTO, O.G.  
«Mass-radius relations for white dwarf stars of different internal compositions».  
*Astronomy & Astrophysics*, **353**, pp. 970–977 (2000).
- PAPAPETROU, A.  
«Eine rotationssymmetrische Lösung in der allgemeinen Relativitätstheorie».  
*Annalen der Physik*, **447**, pp. 309–315 (1953).
- PAPPAS, G. AND APOSTOLATOS, T.A.  
«Revising the Multipole Moments of Numerical Spacetimes and its Consequences».  
*Physical Review Letters*, **108(23)**, 231104 (2012).
- PARKER, E.N.  
«Acceleration of Cosmic Rays in Solar Flares».  
*Physical Review*, **107**, pp. 830–836 (1957).
- PATEL, S.K., KOUVELIOTOU, C., WOODS, P.M., TENNANT, A.F., WEISKOPEF, M.C., FINGER, M.H., GÖĞÜŞ, E., VAN DER KLIS, M. AND BELLONI, T.  
«Chandra Observations of the Anomalous X-Ray Pulsar 1E 2259+586».  
*Astrophysical Journal*, **563**, pp. L45–L48 (2001).
- PATEL, S.K., KOUVELIOTOU, C., WOODS, P.M., TENNANT, A.F., WEISKOPEF, M.C., FINGER, M.H., WILSON, C.A., GÖĞÜŞ, E., VAN DER KLIS, M. AND BELLONI, T.  
«Chandra Observations of the Anomalous X-Ray Pulsar 4U 0142+61».  
*Astrophysical Journal*, **587**, pp. 367–372 (2003).
- PATNAUDE, D.J., LOEB, A. AND JONES, C.  
«Evidence for a Black Hole Remnant in the Type III Supernova 1979C».  
*arXiv:0912.1571* (2009).
- PATNAUDE, D., LOEB, A. AND JONES, C.  
«Evidence for a possible black hole remnant in the Type III Supernova 1979C».  
*New Astronomy*, **16(3)**, pp. 187–190 (2011).  
ISSN 13841076.
- PATRA, S.K., CENTELLES, M., VIÑAS, X. AND DEL ESTAL, M.  
«Surface incompressibility from semiclassical relativistic mean field calculations».  
*Physical Review C*, **65(4)**, 044304 (2002).

- PENACCHIONI, A.V., RUFFINI, R., IZZO, L., MUCCINO, M., BIANCO, C.L., CAITO, L., PATRICELLI, B. AND AMATI, L.  
«Evidence for a proto-black hole and a double astrophysical component in GRB 101023».  
*Astronomy & Astrophysics*, **538**, A58 (2012).
- PENROSE, R.  
«Gravitational Collapse: the Role of General Relativity».  
*Nuovo Cimento Rivista Serie*, **1**, p. 252 (1969).
- PERES, G., ORLANDO, S., REALE, F., ROSNER, R. AND HUDSON, H.  
«The Sun as an X-Ray Star. II. Using the Yohkoh/Soft X-Ray Telescope-derived Solar Emission Measure versus Temperature to Interpret Stellar X-Ray Observations».  
*Astrophysical Journal*, **528**, pp. 537–551 (2000).
- PERLMUTTER, S., ALDERING, G., GOLDHABER, G., KNOP, R.A., NUGENT, P., CASTRO, P.G., DEUSTUA, S., FABBRO, S., GOOBAR, A., GROOM, D.E. ET AL.  
«Measurements of Omega and Lambda from 42 High-Redshift Supernovae».  
*Astrophysical Journal*, **517**, pp. 565–586 (1999).
- PHILLIPS, M.M.  
«The absolute magnitudes of Type IA supernovae».  
*Astrophys. J. Lett.*, **413**, pp. L105–L108 (1993).
- PIAN, E., AMATI, L., ANTONELLI, L.A., BUTLER, R.C., COSTA, E., CUSUMANO, G., DANZIGER, J., FEROCI, M., FIORE, F., FRONTERA, F. ET AL.  
«BeppoSAX observations of grb 980425: Detection of the prompt event and monitoring of the error box».  
*ApJ*, **536**, pp. 778–787 (2000).
- PIAN, E. ET AL.  
Proposal for Chandra Observations: The X-Ray Remnant of XRF100316D/SN2010BH (2011).
- PIEPER, W. AND GREINER, W.  
«Interior electron shells in superheavy nuclei».  
*Zeitschrift fur Physik*, **218**, pp. 327–340 (1969).
- POPOV, V.  
«From super-charged nuclei to massive nuclear density cores».  
In R. Ruffini & G. Vereshchagin (ed.), *American Institute of Physics Conference Series*, volume 1205 of *American Institute of Physics Conference Series*, pp. 127–131 (2010).

- POPOV, V.S.  
«On the Properties of the Discrete Spectrum for  $Z$  Close to 137».  
*Soviet Journal of Experimental and Theoretical Physics*, **33**, pp. 665–+ (1971a).
- POPOV, V.S.  
«Position Production in a Coulomb Field with  $Z \lesssim 137$ ».  
*Soviet Journal of Experimental and Theoretical Physics*, **32**, pp. 526–+ (1971b).
- POTEKHIN, A.Y. AND CHABRIER, G.  
«Equation of state of fully ionized electron-ion plasmas. II. Extension to relativistic densities and to the solid phase».  
*Physical Review E*, **62**, pp. 8554–8563 (2000).
- POTEKHIN, A.Y. AND CHABRIER, G.  
«Thermonuclear fusion in dense stars. Electron screening, conductive cooling, and magnetic field effects».  
*Astronomy & Astrophysics*, **538**, A115 (2012).
- POTEKHIN, A.Y. AND CHABRIER, G.  
«Equation of state for magnetized Coulomb plasmas».  
*Astronomy & Astrophysics*, **550**, A43 (2013).
- POTEKHIN, A.Y., CHABRIER, G. AND ROGERS, F.J.  
«Equation of state of classical Coulomb plasma mixtures».  
*Physical Review E*, **79**(1), pp. 016411–+ (2009).
- POTEKHIN, A.Y., CHABRIER, G. AND YAKOVLEV, D.G.  
«Internal temperatures and cooling of neutron stars with accreted envelopes».  
*A&A*, **323**, pp. 415–428 (1997).
- PRAKASH, M., LATTIMER, J., PONS, J., STEINER, A. AND REDDY, S.  
«Evolution of a neutron star from its birth to old age».  
*Physics of Neutron Star Interiors*, pp. 364–423 (2001).
- PREDEHL, P. AND SCHMITT, J.H.M.M.  
«X-raying the interstellar medium: ROSAT observations of dust scattering halos.»  
*Astronomy & Astrophysics*, **293**, pp. 889–905 (1995).
- PROCHASKA, J.X., BLOOM, J.S., CHEN, H.W., HURLEY, K.C., MELBOURNE, J., DRESSLER, A., GRAHAM, J.R., OSIP, D.J. AND VACCA, W.D.  
«The host galaxy of grb 031203: Implications of its low metallicity, low redshift, and starburst nature».  
*ApJ*, **611**, pp. 200–207 (2004).

- PSALTIS, D., BELLONI, T. AND VAN DER KLIS, M.  
«Correlations in Quasi-periodic Oscillation and Noise Frequencies among Neutron Star and Black Hole X-Ray Binaries».  
*Astrophysical Journal*, **520**, pp. 262–270 (1999).
- QADIR, A., RUFFINI, R. AND VIOLINI, G.  
«On the rotational energy loss of pulsars».  
*Nuovo Cimento Lettere*, **27**, pp. 381–384 (1980).
- RASHEED, D.A.  
«Non-Linear Electrodynamics: Zeroth and First Laws of Black Hole Mechanics».  
*ArXiv High Energy Physics - Theory e-prints* (1997).
- RAVENHALL, D.G. AND PETHICK, C.J.  
«Neutron star moments of inertia».  
*Astrophysical Journal*, **424**, pp. 846–851 (1994).
- RAVENHALL, D.G., PETHICK, C.J. AND WILSON, J.R.  
«Structure of Matter below Nuclear Saturation Density».  
*Physical Review Letters*, **50**, pp. 2066–2069 (1983).
- REA, N., ESPOSITO, P., TUROLLA, R., ISRAEL, G.L., ZANE, S., STELLA, L., MEREGHETTI, S., TIENGO, A., GÖTZ, D., GÖĞÜŞ, E. ET AL.  
«A Low-Magnetic-Field Soft Gamma Repeater».  
*Science*, **330**, pp. 944– (2010).
- REA, N., ISRAEL, G.L., ESPOSITO, P., PONS, J.A., CAMERO-ARRANZ, A., MIGNANI, R.P., TUROLLA, R., ZANE, S., BURGAY, M., POSSENTI, A. ET AL.  
«A New Low Magnetic Field Magnetar: The 2011 Outburst of Swift J1822.3-1606».  
*Astrophysical Journal*, **754**, 27 (2012).
- REA, N., ISRAEL, G.L., PONS, J.A., TUROLLA, R., VIGANO, D., ZANE, S., ESPOSITO, P., PERNA, R., PAPITTO, A., TERRERAN, G. ET AL.  
«The outburst decay of the low magnetic field magnetar SGR 0418+5729».  
*Astrophysical Journal*, *in press*; *arXiv:1303.5579* (2013).
- REA, N., JONKER, P.G., NELEMANS, G., PONS, J.A., KASLIWAL, M.M., KULKARNI, S.R. AND WIJNANDS, R.  
«The X-ray quiescence of Swift J195509.6+261406 (GRB 070610): an optical bursting X-ray binary?»  
*arXiv:1101.3483* (2011).
- REA, N., ZANE, S., TUROLLA, R., LYUTIKOV, M. AND GÖTZ, D.  
«Resonant Cyclotron Scattering in Magnetars' Emission».

---

*Astrophysical Journal*, **686**, pp. 1245–1260 (2008).

REISENEGGER, A.

«Chemical Equilibrium and Stable Stratification of a Multicomponent Fluid: Thermodynamics and Application to Neutron Stars».

*Astrophysical Journal*, **550**, pp. 860–862 (2001).

REISENEGGER, A.

«Magnetic field evolution in neutron stars».

*Astronomische Nachrichten*, **328**, pp. 1173–+ (2007).

REISENEGGER, A., BENGURIA, R., PRIETO, J.P., ARAYA, P.A. AND LAI, D.

«Hall drift of axisymmetric magnetic fields in solid neutron-star matter».

*Astronomy & Astrophysics*, **472**, pp. 233–240 (2007).

RIESS, A.G., FILIPPENKO, A.V., CHALLIS, P., CLOCCHIATTI, A., DIERCKS, A., GARNAVICH, P.M., GILLILAND, R.L., HOGAN, C.J., JHA, S., KIRSHNER, R.P. ET AL.

«Observational Evidence from Supernovae for an Accelerating Universe and a Cosmological Constant».

*Astronomical Journal*, **116**, pp. 1009–1038 (1998).

RIESS, A.G., STROELGER, L., TONRY, J., CASERTANO, S., FERGUSON, H.C., MOBASHER, B., CHALLIS, P., FILIPPENKO, A.V., JHA, S., LI, W. ET AL.

«Type Ia Supernova Discoveries at  $z < 1$  from the Hubble Space Telescope: Evidence for Past Deceleration and Constraints on Dark Energy Evolution».

*Astrophysical Journal*, **607**, pp. 665–687 (2004).

RING, P.

«Relativistic mean field theory in finite nuclei».

*Progress in Particle and Nuclear Physics*, **37**, pp. 193–263 (1996).

ROMANI, R.W. AND WATTERS, K.P.

«Constraining Pulsar Magnetosphere Geometry with  $\gamma$ -ray Light Curves».

*Astrophysical Journal*, **714**, pp. 810–824 (2010).

ROSSELAND, S.

«Electrical state of a star».

*Monthly Notices of the Royal Astronomical Society*, **84**, pp. 720–728 (1924).

ROTONDO, M., RUEDA, J.A., RUFFINI, R. AND XUE, S.S.

«On the equilibrium of self-gravitating neutrons, protons and electrons in  $\beta$ -equilibrium».

*ArXiv: 1107.2777* (2011a).

- ROTONDO, M., RUEDA, J.A., RUFFINI, R. AND XUE, S.S.  
«Relativistic Feynman-Metropolis-Teller theory for white dwarfs in general relativity».  
*Physical Review D*, **84(8)**, 084007 (2011b).
- ROTONDO, M., RUEDA, J.A., RUFFINI, R. AND XUE, S.S.  
«Relativistic Thomas-Fermi treatment of compressed atoms and compressed nuclear matter cores of stellar dimensions».  
*Physical Review C*, **83(4)**, 045805 (2011c).
- ROTONDO, M., RUEDA, J.A., RUFFINI, R. AND XUE, S.S.  
«The self-consistent general relativistic solution for a system of degenerate neutrons, protons and electrons in  $\beta$ -equilibrium».  
*Physics Letters B*, **701**, pp. 667–671 (2011d).
- ROTONDO, M., RUFFINI, R., XUE, S.S. AND POPOV, V.  
«On Gravitationally and Electrodynamically Bound Nuclear Matter Cores of Stellar Dimensions».  
*International Journal of Modern Physics D*, **20**, pp. 1995–2002 (2011e).
- ROXBURGH, I.W.  
«On Models of Non Spherical Stars. II. Rotating White Dwarfs. With 2 Figures in the Text».  
*Zeitschrift fur Astrophysik*, **62**, p. 134 (1965).
- ROXBURGH, I.W. AND DURNEY, B.R.  
«Structure, Oscillations and Stability of Rotating White Dwarfs».  
*Zeitschrift fur Astrophysik*, **64**, p. 504 (1966).
- RUDERMAN, M.  
«Pulsars: Structure and Dynamics».  
*Annual Review of Astronomy and Astrophysics*, **10**, pp. 427–+ (1972).
- RUDERMAN, M.  
«Spin-Driven Changes in Neutron Star Magnetic Fields».  
*Journal of Astrophysics and Astronomy*, **16**, pp. 207–+ (1995).
- RUEDA, J.A., AZNAR-SIGUÁN, G., BOSHKAYEV, K., GARCÍA-BERRO, E., IZZO, L., LORÉN-AGUILAR, P. AND RUFFINI, R.  
«A white dwarf merger as progenitor of the anomalous X-ray pulsar 4U 0142+61?»  
*Astrophysical Journal Lett.*, submitted (2013).
- RUEDA, J.A., ROTONDO, M., RUFFINI, R. AND XUE, S.S.  
«A self-consistent approach to neutron stars».  
*Journal of Korean Physical Society*, **57**, pp. 560–+ (2010a).

- RUEDA, J.A. AND RUFFINI, R.  
«On the Induced Gravitational Collapse of a Neutron Star to a Black Hole by a Type Ib/c Supernova».  
*Astrophysical Journal*, **758**, L7 (2012).
- RUEDA, J.A., RUFFINI, R. AND XUE, S.S.  
«On the electrostatic structure of neutron stars».  
In R. Ruffini & G. Vereshchagin (ed.), *American Institute of Physics Conference Series*, volume 1205 of *American Institute of Physics Conference Series*, pp. 143–147 (2010b).
- RUEDA, J.A., RUFFINI, R. AND XUE, S.S.  
«The Klein first integrals in an equilibrium system with electromagnetic, weak, strong and gravitational interactions».  
*Nuclear Physics A*, **872**, pp. 286–295 (2011).
- RUFFERT, M. AND JANKA, H.T.  
«Coalescing neutron stars - A step towards physical models. III. Improved numerics and different neutron star masses and spins».  
*Astronomy & Astrophysics*, **380**, pp. 544–577 (2001).
- RUFFINI, R.  
«On the energetics of black holes.»  
In A. Giannaras (ed.), *Black Holes (Les Astres Occlus)*, pp. 451–546 (1973).
- RUFFINI, R.  
«The Role of Thomas-Fermi Approach in Neutron Star Matter».  
In *Path Integrals - New Trends and Perspectives*, pp. 207–218 (2008a).
- RUFFINI, R.  
«The Role of Thomas-Fermi Approach in Neutron Star Matter».  
In *Path Integrals - New Trends and Perspectives*, pp. 207–218 (2008b).
- RUFFINI, R.  
«Title of the Talk».  
In T. Damour and R. Ruffini (ed.), *Proceedings of the 12th Marcel Grossmann Meeting on General Relativity*, World Scientific, Singapore (2009).
- RUFFINI, R., BERNARDINI, M.G., BIANCO, C.L., CAITO, L., CHARDONNET, P., CHERUBINI, C., DAINOTTI, M.G., FRASCHETTI, F., GERALICO, A., GUIDA, R. ET AL.  
«On Gamma-Ray Bursts».  
In H. Kleinert, R.T. Jantzen and R. Ruffini (eds.), *The Eleventh Marcel Grossmann Meeting On Recent Developments in Theoretical and Experimental General Relativity, Gravitation and Relativistic Field Theories*, pp. 368–505 (2008a).

- RUFFINI, R., BERNARDINI, M.G., BIANCO, C.L., CAITO, L., CHARDONNET, P., DAINOTTI, M.G., FRASCHETTI, F., GUIDA, R., VERESHCHAGIN, G. AND XUE, S.S.  
«The role of grb 031203 in clarifying the astrophysical grb scenario».  
In S. Grebenev, R. Sunyaev, C. Winkler, A. Parmar and L. Ouwehand (eds.), *The 6<sup>th</sup> Integral Workshop - The Obscured Universe*, volume SP-622 of *ESA Special Publication*, p. 561 (2007a).
- RUFFINI, R., BERNARDINI, M.G., BIANCO, C.L., CHARDONNET, P., FRASCHETTI, F. AND XUE, S.S.  
«Grb 980425, sn1998bw and the embh model».  
*Advances in Space Research*, **34**, pp. 2715–2722 (2004).
- RUFFINI, R., BERNARDINI, M.G., BIANCO, C.L., CHARDONNET, P., FRASCHETTI, F. AND XUE, S.  
«Theoretical Interpretation of GRB 031203 and URCA-3».  
In B. Aschenbach, V. Burwitz, G. Hasinger and B. Leibundgut (eds.), *Relativistic Astrophysics Legacy and Cosmology - Einstein's Legacy*, p. 399 (2008b).
- RUFFINI, R., BERNARDINI, M.G., BIANCO, C.L., VITAGLIANO, L., XUE, S.S., CHARDONNET, P., FRASCHETTI, F. AND GURZADYAN, V.  
«Black hole physics and astrophysics: The grb-supernova connection and urca-1 - urca-2».  
In M. Novello, S. Perez Bergliaffa and R. Ruffini (eds.), *The Tenth Marcel Grossmann Meeting. On recent developments in theoretical and experimental general relativity, gravitation and relativistic field theories*, p. 369 (Singapore: World Scientific, 2005).
- RUFFINI, R., BIANCO, C.L., CHARDONNET, P., FRASCHETTI, F. AND XUE, S.S.  
«On a possible gamma-ray burst-supernova time sequence».  
*ApJ*, **555**, pp. L117–L120 (2001).
- RUFFINI, R. AND BONAZZOLA, S.  
«Systems of Self-Gravitating Particles in General Relativity and the Concept of an Equation of State».  
*Physical Review*, **187**, pp. 1767–1783 (1969).
- RUFFINI, R., CHAKRABARTI, S.K. AND IZZO, L.  
«Possible multiple components in a GRB: the case of GRB 090618».  
*Submitted to Adv. Sp. Res.* (2010a).
- RUFFINI, R., IZZO, L., PENACCHIONI, A.V., BIANCO, C.L., CAITO, L., CHAKRABARTI, S.K. AND NANDI, A.  
«GRB 090618: a possible case of multiple GRB?»  
*PoS(Texas2010)*, p. 101 (2011).

- RUFFINI, R., ROTONDO, M. AND XUE, S.  
«Electrodynamics for Nuclear Matter in Bulk».  
*International Journal of Modern Physics D*, **16**, pp. 1–9 (2007b).
- RUFFINI, R., ROTONDO, M. AND XUE, S.S.  
«Electrodynamics for nuclear matter in bulk».  
*IJMPD*, **16**, pp. 1–9 (2007c).
- RUFFINI, R. AND STELLA, L.  
«Some comments on the relativistic Thomas-Fermi model and the Vallarta-Rosen equation».  
*Physics Letters B*, **102**, pp. 442–444 (1981).
- RUFFINI, R., VERESHCHAGIN, G. AND XUE, S.  
«Electron-positron pairs in physics and astrophysics: From heavy nuclei to black holes».  
*Physics Reports*, **487**, pp. 1–140 (2010b).
- RUFFINI, R. AND VITAGLIANO, L.  
«Irreducible mass and energetics of an electromagnetic black hole».  
*Physics Letters B*, **545**, pp. 233–237 (2002).
- RUFFINI, R., VITAGLIANO, L. AND XUE, S.S.  
«On a separatrix in the gravitational collapse to an overcritical electromagnetic black hole».  
*Physics Letters B*, **573**, pp. 33–38 (2003a).
- RUFFINI, R., VITAGLIANO, L. AND XUE, S.S.  
«On plasma oscillations in strong electric fields».  
*Physics Letters B*, **559**, pp. 12–19 (2003b).
- RUFFINI, R. AND XUE, S.S.  
«Effective Dyadosphere».  
In Y.-F. Huang, Z.-G. Dai, & B. Zhang (ed.), *American Institute of Physics Conference Series*, volume 1065 of *American Institute of Physics Conference Series*, pp. 289–293 (2008).
- RUIZ, E., MANKO, V.S. AND MARTÍN, J.  
«Extended N-soliton solution of the Einstein-Maxwell equations».  
*Physical Review D*, **51**, pp. 4192–4197 (1995).
- RYAN, F.D.  
«Gravitational waves from the inspiral of a compact object into a massive, axisymmetric body with arbitrary multipole moments».  
*Physical Review D*, **52**, pp. 5707–5718 (1995).

- SALPETER, E.E.  
«Energy and Pressure of a Zero-Temperature Plasma.»  
*Astrophysical Journal*, **134**, pp. 669–+ (1961a).
- SALPETER, E.E.  
«Energy and Pressure of a Zero-Temperature Plasma».  
*ApJ*, **134**, p. 669 (1961b).
- SALPETER, E.E. AND SHAPIRO, S.L.  
«Neutrino and photon emission from a dense, high temperature atmosphere».  
*ApJ*, **251**, p. 311 (1981).  
ISSN 0004-637X.
- SALPETER, E.E. AND VAN HORN, H.M.  
«Nuclear Reaction Rates at High Densities».  
*Astrophysical Journal*, **155**, p. 183 (1969).
- SANABRIA-GÓMEZ, J.D., HERNÁNDEZ-PASTORA, J.L. AND DUBEIBE, F.L.  
«Innermost stable circular orbits around magnetized rotating massive stars».  
*Physical Review D*, **82(12)**, 124014 (2010).
- SASAKI, M., PLUCINSKY, P.P., GAETZ, T.J., SMITH, R.K., EDGAR, R.J. AND SLANE, P.O.  
«XMM-Newton Observations of the Galactic Supernova Remnant CTB 109 (G109.1-1.0)».  
*Astrophysical Journal*, **617**, pp. 322–338 (2004).
- SCALZO, R.A., ALDERING, G. AND ANTILOGUS, ET AL., P.  
«Nearby Supernova Factory Observations of SN 2007if: First Total Mass Measurement of a Super-Chandrasekhar-Mass Progenitor».  
*Astrophysical Journal*, **713**, pp. 1073–1094 (2010).
- SCHAAB, C., WEBER, F., WEIGEL, M. AND GLENDENNING, N.K.  
«Thermal evolution of compact stars».  
*Nuclear Phys A*, **605**, p. 531 (1996).
- SCHMIDT, G.D., BERGERON, P., LIEBERT, J. AND SAFFER, R.A.  
«Two ultramassive white dwarfs found among candidates for magnetic fields».  
*Astrophysical Journal*, **394**, pp. 603–608 (1992).
- SCHMIDT, G.D., WEST, S.C., LIEBERT, J., GREEN, R.F. AND STOCKMAN, H.S.  
«The new magnetic white dwarf PG 1031 + 234 - Polarization and field structure at more than 500 million Gauss».

- Astrophysical Journal*, **309**, pp. 218–229 (1986).
- SCHWINGER, J.  
«On Gauge Invariance and Vacuum Polarization».  
*Physical Review*, **82**, pp. 664–679 (1951).
- SEDRAKYAN, D.M. AND CHUBARYAN, E.V.  
«Internal solution for stationary axially symmetric gravitational fields».  
*Astrophysics*, **4**, pp. 227–233 (1968).
- SEGRÉ, E.  
*Nuclei and Particles* (1977).
- SEROT, B.D.  
«Quantum hadrodynamics».  
*Reports on Progress in Physics*, **55**, pp. 1855–1946 (1992).
- SEROT, B.D. AND WALECKA, J.D.  
«Recent Progress in Quantum Hadrodynamics».  
*International Journal of Modern Physics E*, **6**, pp. 515–631 (1997).
- SHAPIRO, S.L. AND TEUKOLSKY, S.A.  
*Black holes, white dwarfs, and neutron stars: The physics of compact objects* (1983a).
- SHAPIRO, S.L. AND TEUKOLSKY, S.A.  
«Book-Review - Black-Holes White Dwarfs and Neutron Stars».  
*Journal of the British Astronomical Association*, **93**, p. 276 (1983b).
- SHAPIRO, S.L., TEUKOLSKY, S.A. AND NAKAMURA, T.  
«Spin-up of a rapidly rotating star by angular momentum loss».  
*Astrophysical Journal*, **357**, pp. L17–L20 (1990).
- SHARMA, B.K. AND PAL, S.  
«Nuclear symmetry energy effects in finite nuclei and neutron star».  
*Physics Letters B*, **682**, pp. 23–26 (2009).
- SHARMA, M.M., MOSZKOWSKI, S.A. AND RING, P.  
«Compression properties of nuclei with the derivative scalar coupling in the relativistic mean-field theory».  
*Physical Review C*, **44**, pp. 2493–2498 (1991).
- SHARMA, M.M., NAGARAJAN, M.A. AND RING, P.  
«Rho meson coupling in the relativistic mean field theory and description of exotic nuclei».  
*Physics Letters B*, **312**, pp. 377–381 (1993).

- SHIBATA, M. AND SASAKI, M.  
«Innermost stable circular orbits around relativistic rotating stars».  
*Phys. Rev. D*, **58**, p. 104011 (1998).
- SHTERNIN, P.S., YAKOVLEV, D.G., HEINKE, C.O., HO, W.C.G. AND PAT-  
NAUDE, D.J.  
«Cooling neutron star in the Cassiopeia A supernova remnant: evidence  
for superfluidity in the core».  
*Monthly Notices of the Royal Astronomical Society*, **412**, pp. L108–L112 (2011).
- SIBGATULLIN, N.R.  
*Oscillations and Waves in Strong Gravitational and Electromagnetic Fields*.  
(1991).
- SIBGATULLIN, N.R. AND SUNYAEV, R.A.  
«Disk accretion in the gravitational field of a rapidly rotating neutron star  
with a rotationally induced quadrupole mass distribution».  
*Astronomy Letters*, **24**, pp. 774–787 (1998).
- SILVERMAN, J.M., GANESHALINGAM, M. AND LI, ET AL., W.  
«Fourteen months of observations of the possible super-Chandrasekhar  
mass Type Ia Supernova 2009dc».  
*Monthly Notices of the Royal Astronomical Society*, **410**, pp. 585–611 (2011).
- SLATER, J.C. AND KRUTTER, H.M.  
«The Thomas-Fermi Method for Metals».  
*Phys. Rev.*, **47**, pp. 559–+ (1935).
- SMARR, L.  
«Mass Formula for Kerr Black Holes».  
*Physical Review Letters*, **30**, pp. 71–73 (1973a).
- SMARR, L.  
«Mass Formula for Kerr Black Holes».  
*Physical Review Letters*, **30**, pp. 521–521 (1973b).
- SORIA, R., PIAN, E. AND MAZZALI, P.A.  
«A second glance at SN 2002ap and the M 74 field with XMM-Newton».  
*A&A*, **413**, pp. 107–119 (2004).
- SORKIN, R.  
«A Criterion for the Onset of Instability at a Turning Point».  
*Astrophysical Journal*, **249**, p. 254 (1981).
- SORKIN, R.D.  
«A Stability Criterion for Many Parameter Equilibrium Families».  
*Astrophysical Journal*, **257**, p. 847 (1982).

- SOTANI, H., MARUYAMA, T. AND TATSUMI, T.  
«Shear oscillations in the hadron-quark mixed phase».  
*ArXiv e-prints* (2012).
- SPRUIT, H.C.  
«Dynamo action by differential rotation in a stably stratified stellar interior».  
*Astronomy & Astrophysics*, **381**, pp. 923–932 (2002).
- STAIRS, I.H.  
«Pulsars in Binary Systems: Probing Binary Stellar Evolution and General Relativity».  
*Science*, **304**, pp. 547–552 (2004).
- STEFANESCU, A., KANBACH, G., SŁOWIKOWSKA, A., GREINER, J., MCBREEN, S. AND SALA, G.  
«Very fast optical flaring from a possible new Galactic magnetar».  
*Nature*, **455**, pp. 503–505 (2008).
- STEJNER, M. AND MADSEN, J.  
«Gaps below strange star crusts».  
*Physical Review D*, **72(12)**, 123005 (2005).
- STELLA, L. AND VIETRI, M.  
«Lense-Thirring Precession and Quasi-periodic Oscillations in Low-Mass X-Ray Binaries».  
*Astrophysical Journal*, **492**, pp. L59+ (1998).
- STELLA, L. AND VIETRI, M.  
«kHz Quasiperiodic Oscillations in Low-Mass X-Ray Binaries as Probes of General Relativity in the Strong-Field Regime».  
*Physical Review Letters*, **82**, pp. 17–20 (1999).
- STELLA, L., VIETRI, M. AND MORSINK, S.M.  
«Correlations in the Quasi-periodic Oscillation Frequencies of Low-Mass X-Ray Binaries and the Relativistic Precession Model».  
*Astrophysical Journal*, **524**, pp. L63–L66 (1999).
- STEPHANI, H., KRAMER, D., MACCALLUM, M., HOENSELAERS, C. AND HERLT, E.  
*Exact solutions of Einstein's field equations* (2003).
- STERGIOULAS, N.  
«Rotating Stars in Relativity».  
*Living Reviews in Relativity*, **6**, p. 3 (2003).

- STOLZMANN, W. AND BLOECKER, T.  
«Thermodynamical properties of stellar matter. I. Equation of state for stellar interiors.»  
*Astronomy & Astrophysics*, **314**, pp. 1024–1040 (1996).
- STONER, E.C.  
«The limiting density of White Dwarfs».  
*Philosophical Magazine (Series 7)*, **7**, pp. 63–70 (1929).
- STROHMAYER, T.E., ZHANG, W., SWANK, J.H., SMALE, A., TITARCHUK, L., DAY, C. AND LEE, U.  
«Millisecond X-Ray Variability from an Accreting Neutron Star System».  
*Astrophysical Journal*, **469**, p. L9 (1996).
- STUTE, M. AND CAMENZIND, M.  
«Towards a self-consistent relativistic model of the exterior gravitational field of rapidly rotating neutron stars».  
*Monthly Notices of the Royal Astronomical Society*, **336**, pp. 831–840 (2002).
- SUGAHARA, Y. AND TOKI, H.  
«Relativistic mean-field theory for unstable nuclei with non-linear  $\sigma$  and  $\omega$  terms».  
*Nuclear Physics A*, **579**, pp. 557–572 (1994).
- SUH, I.S. AND MATHEWS, G.J.  
«Mass-Radius Relation for Magnetic White Dwarfs».  
*Astrophysical Journal*, **530**, pp. 949–954 (2000).
- SWEET, P.A.  
«The Neutral Point Theory of Solar Flares».  
In B. Lehnert (ed.), *Electromagnetic Phenomena in Cosmical Physics*, volume 6 of *IAU Symposium*, pp. 123–+ (1958).
- TAKAMI, K., REZZOLLA, L. AND YOSHIDA, S.  
«A quasi-radial stability criterion for rotating relativistic stars».  
*Monthly Notices of the Royal Astronomical Society*, **416**, pp. L1–L5 (2011).
- TAMII, A., POLTORATSKA, I., VON NEUMANN-COSEL, P., FUJITA, Y., ADACHI, T., BERTULANI, C.A., CARTER, J., DOZONO, M., FUJITA, H., FUJITA, K. ET AL.  
«Complete Electric Dipole Response and the Neutron Skin in Pb208».  
*Physical Review Letters*, **107(6)**, 062502 (2011).
- TASSOUL, J.L. AND OSTRIKER, J.P.  
«Secular Stability of Uniformly Rotating Polytropes».  
*Astronomy & Astrophysics*, **4**, p. 423 (1970).

- TAUBENBERGER, S., BENETTI, S. AND CHILDRESS, ET AL., M.  
«High luminosity, slow ejecta and persistent carbon lines: SN 2009dc challenges thermonuclear explosion scenarios».  
*Monthly Notices of the Royal Astronomical Society*, **412**, pp. 2735–2762 (2011).
- TAURIS, T.M. AND BAILES, M.  
«The origin of millisecond pulsar velocities.»  
*Astronomy & Astrophysics*, **315**, pp. 432–444 (1996).
- TAURIS, T.M. AND TAKENS, R.J.  
«Runaway velocities of stellar components originating from disrupted binaries via asymmetric supernova explosions.»  
*Astronomy & Astrophysics*, **330**, pp. 1047–1059 (1998).
- TAVANI, M.  
«AGILE Discovery of Gamma-ray Flares from the Crab Nebula.»  
In *American Astronomical Society Meeting Abstracts*, volume 217 of *American Astronomical Society Meeting Abstracts*, pp. 434.06–+ (2011).
- TAYLER, R.J.  
«The adiabatic stability of stars containing magnetic fields-I.Toroidal fields».  
*Monthly Notices of the Royal Astronomical Society*, **161**, pp. 365–+ (1973).
- TENNANT, A.F., BECKER, W., JUDA, M., ELSNER, R.F., KOLODZIEJCZAK, J.J., MURRAY, S.S., O'DELL, S.L., PAERELS, F., SWARTZ, D.A., SHIBAZAKI, N. ET AL.  
«Discovery of X-Ray Emission from the Crab Pulsar at Pulse Minimum».  
*Astrophysical Journal*, **554**, pp. L173–L176 (2001).
- TERADA, Y.  
«White Dwarf Equivalent of Pulsars, Discovered with Suzaku».  
*Astronomical Herald*, **101**, pp. 526–534 (2008).
- TERADA, Y., HAYASHI, T., ISHIDA, M., MAKISHIMA, K., MUKAI, K., DOTANI, T., OKADA, S., NAKAMURA, R., NAIK, S., BAMBA, A. ET AL.  
«Suzaku Discovery of Hard X-ray Pulsations from the Rotating Magnetized White Dwarf, AE Aquarii».  
In *AAS/High Energy Astrophysics Division #10*, volume 10 of *AAS/High Energy Astrophysics Division*, pp. 10.03–+ (2008a).
- TERADA, Y., HAYASHI, T., ISHIDA, M., MUKAI, K., DOTANI, T., BAMBA, A., OKADA, S., NAKAMURA, R., MAKISHIMA, K., MORIGAMI, K. ET AL.  
«Suzaku Observation of a White Dwarf as a new Candidate of Cosmic-ray Origin».

- In F. A. Aharonian, W. Hofmann, & F. Rieger (ed.), *American Institute of Physics Conference Series*, volume 1085 of *American Institute of Physics Conference Series*, pp. 689–692 (2008b).
- TERADA, Y., HAYASHI, T., ISHIDA, M., MUKAI, K., DOTANI, T., OKADA, S., NAKAMURA, R., NAIK, S., BAMBA, A. AND MAKISHIMA, K.  
«Suzaku Discovery of Hard X-Ray Pulsations from a Rotating Magnetized White Dwarf, AEAquarii».  
*Publ. Astron. Soc. Japan*, **60**, pp. 387– (2008c).
- TERADA, Y., ISHIDA, M., MUKAI, K., DOTANI, T., MAKISHIMA, K., NAIK, S., HAYASHI, T., OKADA, S., NAKAMURA, R. AND ENOTO, T.  
«Possible Suzaku detection of non-thermal X-ray signals from a rotating magnetized white dwarf».  
*Advances in Space Research*, **41**, pp. 512–517 (2008d).
- THOMPSON, C. AND DUNCAN, R.C.  
«Neutron star dynamos and the origins of pulsar magnetism».  
*Astrophysical Journal*, **408**, pp. 194–217 (1993).
- THOMPSON, C. AND DUNCAN, R.C.  
«The soft gamma repeaters as very strongly magnetized neutron stars - I. Radiative mechanism for outbursts».  
*Monthly Notices of the Royal Astronomical Society*, **275**, pp. 255–300 (1995).
- THOMPSON, C. AND DUNCAN, R.C.  
«The Soft Gamma Repeater as Very Strongly Magnetized Neutron Stars. II. Quiescent Neutrino, X-Ray, and Alfvén Wave Emission».  
*Astrophysical Journal*, **473**, pp. 322–+ (1996).
- THOMPSON, C., LYUTIKOV, M. AND KULKARNI, S.R.  
«Electrodynamics of Magnetars: Implications for the Persistent X-Ray Emission and Spin-down of the Soft Gamma Repeater and Anomalous X-Ray Pulsars».  
*Astrophysical Journal*, **574**, pp. 332–355 (2002).
- THORNE, K.S.  
«The relativistic equations of stellar structure and evolution».  
*Astrophysical Journal*, **212**, pp. 825–831 (1977).
- THORNE, K.S.  
*Gravitational radiation.*, pp. 330–458 (1987).
- THOROLFSSON, A., ROEGNVALDSSON, O.E., YNGVASON, J. AND GUDMUNDSSON, E.H.  
«Thomas-Fermi Calculations of Atoms and Matter in Magnetic Neutron Stars. II. Finite Temperature Effects».

- Astrophysical Journal*, **502**, p. 847 (1998).
- TIENGO, A., ESPOSITO, P., MEREGHETTI, S., REA, N., STELLA, L., ISRAEL, G.L., TUROLLA, R. AND ZANE, S.  
«The calm after the storm: XMM-Newton observation of SGR 1806-20 two months after the Giant Flare of 2004 December 27».  
*Astronomy & Astrophysics*, **440**, pp. L63–L66 (2005).
- TOLMAN, R.C.  
«On the Weight of Heat and Thermal Equilibrium in General Relativity».  
*Physical Review*, **35**, pp. 904–924 (1930).
- TOLMAN, R.C.  
«Static Solutions of Einstein’s Field Equations for Spheres of Fluid».  
*Physical Review*, **55**, pp. 364–373 (1939).
- TOLMAN, R.C. AND EHRENFEST, P.  
«Temperature Equilibrium in a Static Gravitational Field».  
*Physical Review*, **36**, pp. 1791–1798 (1930).
- TOMIMATSU, A. AND SATO, H.  
«New Exact Solution for the Gravitational Field of a Spinning Mass».  
*Physical Review Letters*, **29**, pp. 1344–1345 (1972).
- TONG, H., SONG, L.M. AND XU, R.X.  
«Non-detection in a Fermi/LAT Observation of AXP 4U 0142+61: Magnetars?»  
*Astrophysical Journal*, **725**, pp. L196–L199 (2010).
- TONG, H., SONG, L.M. AND XU, R.X.  
«AXPs and SGRs in the outer gap model: confronting Fermi observations».  
*arXiv:1101.2289* (2011).
- TONG, H. AND XU, R.X.  
«The timing behavior of magnetar Swift J1822.3-1606: timing noise or a decreasing period derivative?»  
*arXiv:1212.4314* (2012).
- TOROK, G., BAKALA, P., STUCHLIK, Z. AND CECH, P.  
«Modeling the Twin Peak QPO Distribution in the Atoll Source 4U 1636-53».  
*Acta Astronomica*, **58**, pp. 1–14 (2008).
- TÖRÖK, G., BAKALA, P., ŠRÁMKOVÁ, E., STUHLÍK, Z. AND URBANEC, M.  
«On Mass Constraints Implied by the Relativistic Precession Model of Twin-peak Quasi-periodic Oscillations in Circinus X-1».  
*Astrophysical Journal*, **714**, pp. 748–757 (2010).

- TOROPINA, O.D., ROMANOVA, M.M. AND LOVELACE, R.V.E.  
«Bondi-Hoyle accretion on to a magnetized neutron star».  
*Monthly Notices of the Royal Astronomical Society*, **420**, pp. 810–816 (2012).
- TRÜMPER, J.E.  
«Observations of neutron stars and the equation of state of matter at high densities».  
*Progress in Particle and Nuclear Physics*, **66**, pp. 674–680 (2011).
- TRÜMPER, J.E., BURWITZ, V., HABERL, F. AND ZAVLIN, V.E.  
«The puzzles of RX J1856.5-3754: neutron star or quark star?»  
*Nuclear Physics B Proceedings Supplements*, **132**, pp. 560–565 (2004).
- TRÜMPER, J.E., DENNERL, K., KYLAFIS, N.D., ERTAN, Ü. AND ZEAS, A.  
«An Accretion Model for the Anomalous X-Ray Pulsar 4U 0142+61».  
*Astrophysical Journal*, **764**, 49 (2013).
- TUROLLA, R., ZAMPIERI, L., COLPI, M. AND TREVES, A.  
«Spherical accretion onto neutron stars revisited: Are hot solutions possible?»  
*ApJ*, **426**, p. L35 (1994).  
ISSN 0004-637X.
- USOV, V.V.  
«High-frequency emission of X-ray pulsar 1E 2259+586».  
*Astrophysical Journal*, **410**, pp. 761–763 (1993).
- USOV, V.V.  
«Glitches in the X-ray pulsar 1E 2259+586».  
*Astrophysical Journal*, **427**, pp. 984–986 (1994).
- USOV, V.V.  
«Bare Quark Matter Surfaces of Strange Stars and  $e^+e^-$  Emission».  
*Physical Review Letters*, **80**, pp. 230–233 (1998).
- VAN DER KLIS, M.  
«Quasi-periodic Oscillations and Noise in Accreting Black Holes and Low-Magnetic Field Neutron Stars».  
In J. Greiner, H.W. Duerbeck and R.E. Gershberg (eds.), *IAU Colloq. 151: Flares and Flashes*, volume 454 of *Lecture Notes in Physics*, Berlin Springer Verlag, p. 321 (1995).
- VAN DER KLIS, M., SWANK, J.H., ZHANG, W., JAHODA, K., MORGAN, E.H., LEWIN, W.H.G., VAUGHAN, B. AND VAN PARADIJS, J.  
«Discovery of Submillisecond Quasi-periodic Oscillations in the X-Ray Flux of Scorpius X-1».  
*Astrophysical Journal*, **469**, p. L1 (1996).

- VAN HORN, H.M.  
«Physical processes in white dwarfs».  
In S.S. Kumar (ed.), *Low-Luminosity Stars*, p. 297 (1969).
- VINK, J.  
«Supernova remnants with magnetars: Clues to magnetar formation».  
*Advances in Space Research*, **41**, pp. 503–511 (2008).
- VINK, J. AND KUIPER, L.  
«Supernova remnant energetics and magnetars: no evidence in favour of millisecond proto-neutron stars».  
*Monthly Notices of the Royal Astronomical Society*, **370**, pp. L14–L18 (2006).
- VON-EIFF, D., FREYER, H., STOCKER, W. AND WEIGEL, M.K.  
«The relativistic spin-orbit force near the neutron-drip line».  
*Physics Letters B*, **344**, pp. 11–17 (1995).
- VON-EIFF, D., PEARSON, J.M., STOCKER, W. AND WEIGEL, M.K.  
«Relativistic Hartree calculations of nuclear compressional properties».  
*Physical Review C*, **50**, pp. 831–835 (1994a).
- VON-EIFF, D., PEARSON, J.M., STOCKER, W. AND WEIGEL, M.K.  
«Relativistic semi-classical analysis of nuclear surface-symmetry properties».  
*Physics Letters B*, **324**, pp. 279–285 (1994b).
- VRTILEK, S.D., RAYMOND, J.C., GARCIA, M.R., VERBUNT, F., HASINGER, G. AND KURSTER, M.  
«Observations of Cygnus X-2 with IUE - Ultraviolet results from a multi-wavelength campaign».  
*Astronomy & Astrophysics*, **235**, pp. 162–173 (1990).
- WALECKA, J.D.  
«A theory of highly condensed matter.»  
*Annals of Physics*, **83**, pp. 491–529 (1974).
- WANG, Z., CHAKRABARTY, D. AND KAPLAN, D.L.  
«A debris disk around an isolated young neutron star».  
*Nature*, **440**, pp. 772–775 (2006).
- WEBER, F. AND GLENDENNING, N.K.  
«Application of the improved Hartle method for the construction of general relativistic rotating neutron star models».  
*Astrophysical Journal*, **390**, pp. 541–549 (1992).
- WEISSKOPF, M.C., O'DELL, S.L., PAERELS, F., ELSNER, R.F., BECKER, W., TENNANT, A.F. AND SWARTZ, D.A.

- «Chandra Phase-Resolved X-Ray Spectroscopy of the Crab Pulsar».  
*Astrophysical Journal*, **601**, pp. 1050–1057 (2004).
- WICKRAMASINGHE, D.T. AND FERRARIO, L.  
«Magnetism in Isolated and Binary White Dwarfs».  
*Publications of the Astronomical Society of the Pacific*, **112**, pp. 873–924 (2000).
- WIJNANDS, R., MENDEZ, M., VAN DER KLIS, M., PSALTIS, D., KUULKERS, E. AND LAMB, F.K.  
«Discovery of KiloHertz Quasi-periodic Oscillations in the Z Source GX 5-1».  
*Astrophysical Journal*, **504**, p. L35 (1998).
- WIJNANDS, R.A.D., VAN DER KLIS, M., VAN PARADIJS, J., LEWIN, W.H.G., LAMB, F.K., VAUGHAN, B. AND KUULKERS, E.  
«Discovery in 4U 1636-53 of Two Simultaneous Quasi-periodic Oscillations near 900 HZ and 1176 HZ».  
*Astrophysical Journal*, **479**, p. L141 (1997).
- WITTEN, E.  
«Cosmic separation of phases».  
*Physical Review D*, **30**, pp. 272–285 (1984).
- WOLTJER, L.  
«X-Rays and Type i Supernova Remnants.»  
*Astrophysical Journal*, **140**, pp. 1309–1313 (1964).
- WOODS, P.M., KASPI, V.M., THOMPSON, C., GAVRIIL, F.P., MARSHALL, H.L., CHAKRABARTY, D., FLANAGAN, K., HEYL, J. AND HERNQUIST, L.  
«Changes in the X-Ray Emission from the Magnetar Candidate 1E 2259+586 during Its 2002 Outburst».  
*Astrophysical Journal*, **605**, pp. 378–399 (2004).
- WOOSLEY, S.E.  
«Bright Supernovae from Magnetar Birth».  
*Astrophysical Journal*, **719**, pp. L204–L207 (2010).
- YAKOVLEV, D.G., GASQUES, L.R., AFANASJEV, A.V., BEARD, M. AND WIESCHER, M.  
«Fusion reactions in multicomponent dense matter».  
*Physical Review C*, **74(3)**, 035803 (2006).
- YAKOVLEV, D.G., KAMINKER, A.D., GNEDIN, O.Y. AND HAENSEL, P.  
«Neutrino emission from neutron stars».  
*Physics Reports*, **354(1-2)**, pp. 1–155 (2001).  
ISSN 03701573.

- YAKOVLEV, D.G. AND PETHICK, C.J.  
«Neutron Star Cooling».  
*Annual Review of Astronomy & Astrophysics*, **42**, pp. 169–210 (2004a).
- YAKOVLEV, D.G. AND PETHICK, C.J.  
«Neutron Star Cooling».  
*Ann. Rev. A&A*, **42**, pp. 169–210 (2004b).
- YAMANAKA, M., KAWABATA, K.S. AND KINUGASA, ET AL., K.  
«Early Phase Observations of Extremely Luminous Type Ia Supernova 2009dc».  
*Astrophysical Journal*, **707**, pp. L118–L122 (2009).
- ZANE, S., REA, N., TUROLLA, R. AND NOBILI, L.  
«X-ray spectra from magnetar candidates - III. Fitting SGR/AXP soft X-ray emission with non-relativistic Monte Carlo models».  
*Monthly Notices of the Royal Astronomical Society*, **398**, pp. 1403–1413 (2009).
- ZEL'DOVICH, I.B.  
«Nuclear Reactions in Super-Dense Cold Hydrogen».  
*Soviet Journal of Experimental and Theoretical Physics*, **6**, pp. 760–+ (1958a).
- ZEL'DOVICH, I.B.  
«Nuclear Reactions in Super-Dense Cold Hydrogen».  
*Soviet Journal of Experimental and Theoretical Physics*, **6**, p. 760 (1958b).
- ZELDOVICH, Y.B. AND POPOV, V.S.  
«Reviews of Topical Problems: Electronic Structure of Superheavy Atoms».  
*Soviet Physics Uspekhi*, **14**, pp. 673–694 (1972).
- ZHANG, B. AND GIL, J.  
«GCRT J1745-3009 as a Transient White Dwarf Pulsar».  
*Astrophysical Journal*, **631**, pp. L143–L146 (2005).
- ZHU, W.W., KASPI, V.M., MCLAUGHLIN, M.A., PAVLOV, G.G., NG, C.Y., MANCHESTER, R.N., GAENSLER, B.M. AND WOODS, P.M.  
«Chandra Observations of the High-magnetic-field Radio Pulsar J1718-3718».  
*Astrophysical Journal*, **734**, 44 (2011).
- ZHUROMSKYY, O., SYDORUK, O., SHAMONINA, E. AND SOLYMAR, L.  
«Slow waves on magnetic metamaterials and on chains of plasmonic nanoparticles: Driven solutions in the presence of retardation».  
*Journal of Applied Physics*, **106**(10), p. 104908 (2009).